CLRC

COUNCIL FOR THE CENTRAL LABORATORY
OF THE RESEARCH COUNCILS

Central Laser Facility
Rutherford Appleton Laboratory
Annual Report 1995-96

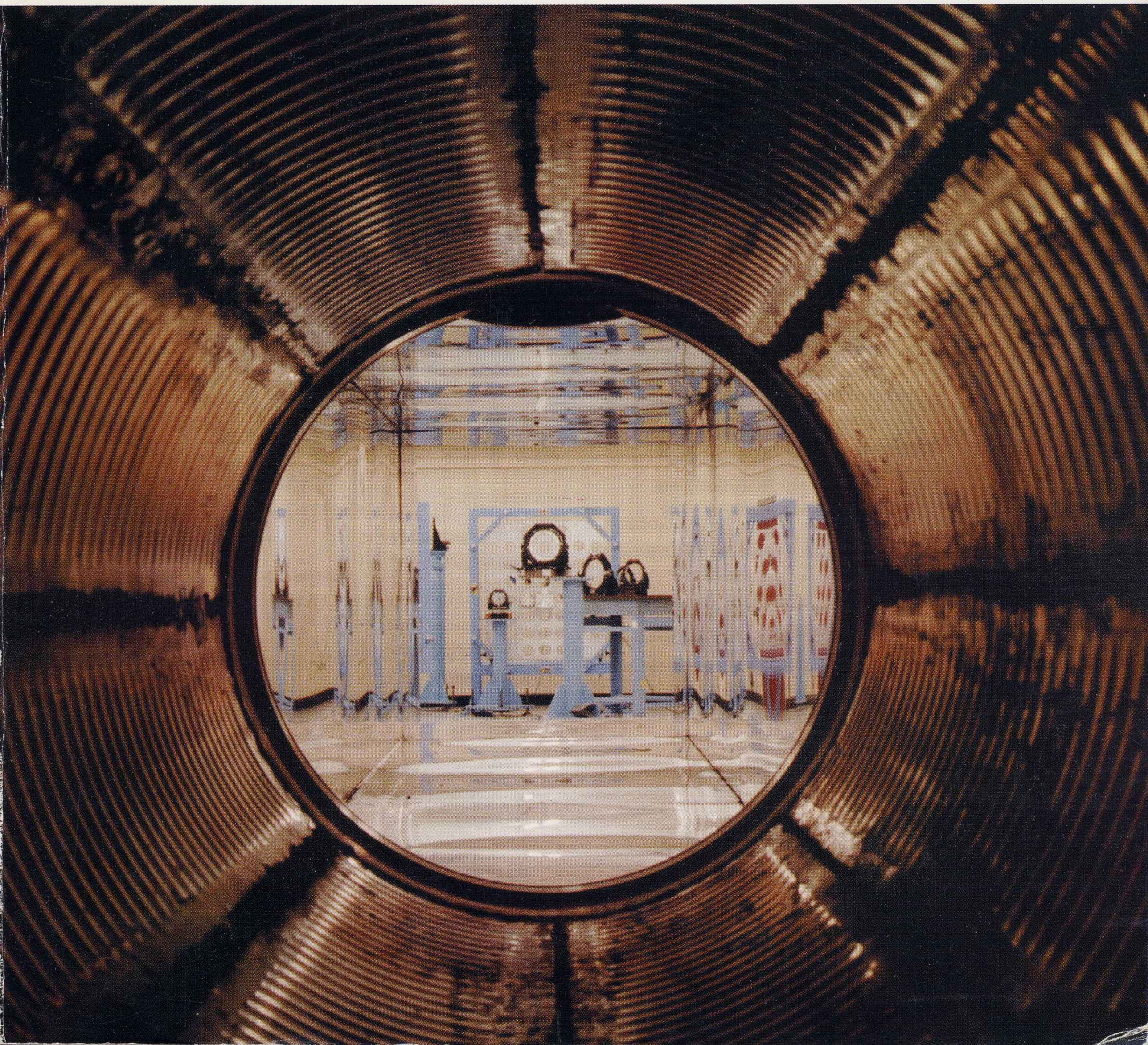

CENTRAL LASER FACILITY

Rutherford Appleton Laboratory

Annual Report 1995 - 96

Central Laser Facility
Rutherford Appleton Laboratory
Chilton, Didcot
Oxfordshire OX11 0QX
Tel. (0)1235 - 445582
Fax. (0)1235 445888

RAL Report TR-96-066

The front cover shows the view through the Titania laser cell into the multiplexing area.

The back cover shows part of the Titania pulsed power area in R2.

ISBN 0902376454

ACKNOWLEDGEMENTS

M H Key

The team producing the Annual Report this year was as follows: production was by Katharine Hale with co-ordination by Nic Allen and Chris Hooker and technical specifications from Chris Reason. Chapter Editors were Steven Rose, Chris Edwards, Mick Shaw, Tony Parker and Graeme Hirst. Section Editors were Colin Danson, Barry Walsh, Peter Norreys, Abdes Djaoui, Dave Pepler, John Collier, David Neely, Pavel Matousek, Kevin Henbest, Ric Allott and Andrew Langley. Publications were collected by David Neely, Andy Kidd and Sue Tavender.

The text has been provided in a mixture of camera ready format and electornic files by facility users and staff and I would like to thank them particularly for supplying their contributions to our schedule.

The document has been reproduced by the RAL Reprographics Section.

PREFACE

M H Key

The last year has been characterised by high productivity in the scientific programmes of the users of the Central Laser Facility (CLF) and by the advent of new opportunities for future developments. There have also been significant changes in funding mechanisms consequent on the reorganisation of the Research Councils. Publications of which 128 are listed in this report, and significant experimental results with both the High Power Lasers and the Lasers *for* Science Facility indicate the scientific productivity.

High Power Laser experiments were sustained entirely last year by the Nd:glass laser, Vulcan. There was particular emphasis on the exploitation of the ultra-high high intensity of Vulcan's chirped pulse (CPA) beam and the routine availability of 10^{19} W cm^{-2}, as high an intensity as any obtained world-wide, enabled important scientific milestones to be reached. The shortest wavelength and highest intensity in XUV harmonics generated in laser interaction with solid targets were achieved. The velocity of the plasma due to light pressure was determined from the Doppler shift of the harmonics. Relativistic channelling of laser light in preformed plasma was observed. Measurements were made of the temperature of high energy electrons and of ion energies in the absorption of laser light at 10^{19} W cm^{-2}. This new science of high intensity interactions was of particular interest in the context of the proposed new fast ignition mechanism for thermo-nuclear fusion. Other fusion related science included the first study at the CLF of hydrodynamic instability in indirect drive and new XUV laser radiographic studies of the hydrodynamics of directly driven targets. X-ray laser research delivered a saturated high brightness and single frequency laser at 19.6 nm which was used for the radiography.

For whole of the reporting year an upgraded high power KrF laser installation Titania, was under construction culminating in an inaugural shot fired on 2nd April 1996. Titania provides UV radiation at the highest intensity and in short pulses at the forefront of international capability. It is now operating for users in the CPA mode and a higher energy Raman laser beam will be provided for users from 1 April 1997.

In the Lasers *for* Science Facility a novel laser based on optical parametric amplification giving two beams of synchronous and independently frequency tunable femtosecond pulses, was brought into operation and produced initial scientific results on transient Raman spectra of photo-excited molecules Four other laboratories of the LSF and the laser loan pool together provided the major part of the scientific output. New nano-fabrication work with patent and industrial potential was carried out with a laser generated soft X-ray source. A picosecond fluorescence confocal microscope gave the distribution within cells of drugs being developed for cancer therapy. Using loan pool lasers the effect of hydration on conformation of a protein was studied. Tests of new theories were made in observation of photo-fragmentation of molecules by high intensity 50 fs pulses.

A change during the year which will be of increasing importance was the introduction by EPSRC of a new system of fully costed 'tickets' for facility access by UK researchers. The tickets will be used from April 1997. They will be bid for and awarded with normal EPSRC research grants and the circa 90% of the funding of the CLF by EPSRC will be based from April 1998, on the sum of the values of the tickets used in the previous year. There will be some discretion in the scheduling process to give tickets for trial experiments and other special purposes but the fraction of such tickets after a transitional period will small. The aim of the new system is to tension the full cost of experiments using central facilities against the cost of directly funded research in the Universities. There are both opportunities and risks in this system. The opportunity is the removal of any funding cap on successful research at the CLF. The risk is that competition for grants could lead to under use and under funding of the facilities. Smaller customers funding research by other UK users included BBSRC, NERC and MRC. Our participation in the EU Large Scale Facilities programme, made 10% of facility time available to EU researchers funded from Brussels.

The EPSRC has moved increasingly towards grant funded support for facility upgrades. In this context work was done during the year to prepare the first phase of a grant funded upgrade to 250 TW power of the CPA system on the Vulcan laser. The next phases of development of the Titania system to implement Raman operation and to provide synchronous Raman and CPA beams have also been refinanced as a grant.

Other changes involve our senior staff. On my return from leave of absence in August 1995, I found the facility in excellent shape after a year's management by my deputy Bill Toner. His retirement in September 1995 was an occasion for us all to thank him for his major contribution to the CLF. More recently the appointment of Chris Edwards as Deputy Head of the CLF has provided an excellent successor to Bill. On a more personal note I shall leave the CLF at the end of September this year to take a new job with the Lawrence Livermore National Laboratory in the USA. I have enjoyed tremendously the 20 years that I have worked in the Central Laser Facility and I shall miss the comradeship of my colleagues at RAL and Oxford and in the visiting research teams of the facility users. I shall also miss my participation in the extremely interesting scientific programme. I plan to maintain some collaborative scientific contacts however, during my future work in the USA.

The opportunities for the Central Laser Facility in the future are many and among these I attach particular importance to the Report of the European Science and Technology Assembly on inertial fusion energy (IFE). The report recommends that the EU should fund co-ordinated activity on IFE in the present centres of expertise in Europe. The CLF could play a significant role in such a programme through its suitability for the study of the science of fast ignition and also that of direct and indirect drive and its expertise with advanced KrF and glass laser technology. More generally there is new emphasis on exploitable science and the CLF will be seeking to undertake more contract work for new customers. I am confident that my successor will find in the CLF a sound base in the portfolio of current work which will provide a springboard for new initiatives to carry the CLF's work successfully into the next century.

INTRODUCTION TO THE CENTRAL LASER FACILITY

C B Edwards

Laser Facilities for Users

The Central Laser Facility is one of the world's leading centres for research using lasers. The CLF operates two unique high power laser installations (Vulcan and Titania), and a range of state of the art commercial table-top systems for multi-disciplinary research in physics, chemistry, biology and materials science.

Vulcan

Vulcan is a uniquely versatile large scale Nd:glass laser installation. Vulcan delivers a maximum of 3 kJ of energy in its six 10cm and two 15cm beamlines to two fully scheduled target areas. Each target area is equipped with frequency conversion optics to enable both 1μ and 0.5μ operation of all beams. Two further target areas are available for lower energy applications. A range of pulse durations are available from 100ps to 20ns in various geometries

An ultra-short pulse (700fs) ultra-high irradiance (10^{19}W.cm^{-2} on target) chirped pulse amplification (CPA) capability is available, with vacuum propagation to target and reflective beam focusing optics. Additional low energy CPA beams are provided for diagnostics with high temporal resolution. The system is fully characterised and equipped with advanced diagnostics. This facility gives users access to extreme conditions and plasma regimes currently unavailable from other facilities.

Titania

On 2 April '96, Dr Paul Williams, Chief Executive of CCLRC, inaugurated the CLF's new high power krypton fluoride laser facility. Titania, an order of magnitude more powerful than its predecessor, will initially operate in CPA mode at the 3-5 TW level with target irradiances at the 10^{19}W.cm^{-2}.

High brightness high energy Raman operation is planned for 1997. Titania's high brightness short wavelength capability is ideal for high harmonic generation experiments and studies of basic laser matter interaction physics at short wavelengths with relevance to laser fusion.

Lasers for Science Facility

The LSF operates a suite of state of the art table-top laser systems and associated instrumentation giving users access to highly tunable (VUV-ir) and variable pulse width (ns to fs) laser radiation. This includes lasers for ns and ps time-resolved resonance Raman spectroscopy (TR^3), a unique dual wavelength multi-kHz femtosecond synchronised pump-probe apparatus based on OPA technology, a femtosecond laboratory, a high average power laser plasma x-ray source and a fast gated (100ps) confocal microscopy laboratory.

Stand-alone, commercial laser systems are available on loan from the Laser Loan Pool for periods of up to 6 months at the user's home laboratory.

Customers

The main customers of the Central Laser Facility are the UK Research Councils, who fund beam time primarily for grant-supported UK University researchers and their overseas collaborators. A small proportion of access is provided by the Research Councils for non-grant funded work to enable rapid access for topical and proof of principle experiments.

The EC provides beam time at the CLF for European researchers through a Large Scale Facility Access contract under the TMR programme.

Access to Facilities

UK access arrangements to beamtime at the CLF in the process of revision. In future, a very large proportion (~90%) of EPSRC access will be provided exclusively to grant supported programmes. Such grants will specify the amount of facility time required, which will be fully costed. Holders of grants will be allocated "tickets" for beam time, which will guarantee access subject only to scheduling considerations. The remaining time will be allocated by the Scheduling Committee for rapid access and for proof of principle experiments to assist in the preparation of a full grant. Arrangements for funding of beamtime for experiments within the remit of BBSRC and NERC programmes differ from the EPSRC model and potential applicants working in these areas should contact the Head of the CLF in the first instance for further information.

European researchers are eligible for beamtime at the CLF funded by the EC through its Large Scale Facilities programme. Further information is available from the Head of the CLF.

Facts and Figures

During the period covered by this report, 19 experiments were scheduled on the Vulcan facility. 69 weeks of beam time were provided for EPSRC experiments in the main target areas. A further 12 weeks were scheduled under the EC Large Scale Facility Access programme.

In the LSF, 122 weeks of facility access were scheduled for in-house EPSRC experiments, 28 weeks for BBSRC experiments and 10.5 weeks for EC access. In the Loan Pool, 72 months of equipment loans were made to EPSRC and 7.5 months to BBSRC supported work.

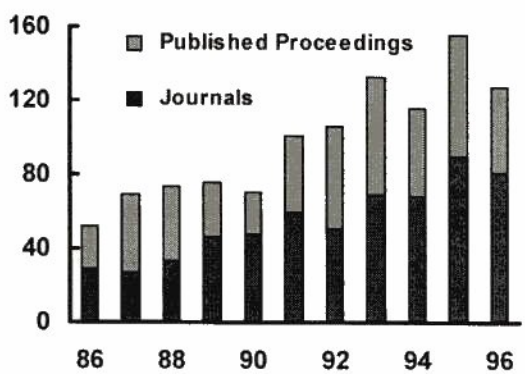

Fig 1: Refereed publications & published conference proceedings

The publication record of the facility is shown in Fig 1. A total of 128 articles were published, with a further 45 in press. While the total published is slightly lower than last year, the number of articles in press is higher by 23.

This is an excellent achievement since only one high power facility was on-line to users during the year.

EFFICIENT XUV HARMONICS GENERATED FROM PICOSECOND LASER PULSE INTERACTIONS WITH SOLID TARGETS

P.A.Norreys[1], M.Zepf[2], S.Moustaizis[3], A.P.Fews[4], J.Zhang[2], P.Lee[5], M.Bakarezos[3], C.N.Danson[1], A.Dyson[5], P.Gibbon[6], P.Loukakos[3], D.Neely[1], F.N.Walsh[1], J.S.Wark[2] and A.E.Dangor[5].

1. Rutherford Appleton Laboratory, Chilton, Didcot, Oxon. OX11 0QX, United Kingdom.
2. Department of Physics, Clarendon Laboratory, University of Oxford, Parks Road, Oxford, OX1 3PU, United Kingdom.
3 IESL/FORTH, University of Crete, P.O.Box 1527, 711 10 Heraklion, Crete, Greece.
4. H.H.Wills Physics Laboratory, University of Bristol, Tyndall Ave., Bristol BS8 1TL, United Kingdom
5. Imperial College of Science, Technology and Medicine, Prince Consort Road, London SW7 2AZ, United Kingdom.
6. Max-Planck-Gesellschaft, Research Unit 'X-Ray Optics', University of Jena, Max-Wien-Platz 1, D-07743 Jena, Germany.

There is currently great interest in the production of coherent XUV radiation by the process of high harmonic generation using high power picosecond laser radiation. Several groups have had considerable success in generating high odd-order harmonics from gases [1] with harmonic orders up to the 141st of Nd:YAG (1053 nm), the 109th of Ti:Sapphire (800 nm) and the 37th of KrF (249 nm) at 67 Å (the shortest wavelength to date) being observed. The high harmonics are produced due to the extreme non-linearity of the atomic polarisability in the intense laser field, with the symmetric nature of the atomic potential dictating that only odd-order harmonics are observed.

In addition to harmonic generation from gaseous targets, there has recently been a renewal in interest in generating high order harmonic radiation from high-power laser interactions with solids. Such high harmonics were first observed in nanosecond experiments using CO_2 lasers (where up to the 46th was observed), where the long laser wavelength (10.6 μm) ensured significant ponderomotive steepening of the plasma density profile. Both odd and even order harmonics are generated via the relativistic current associated with the electrons being dragged back-and-forth across this asymmetric density step. Recently Gibbon has performed PIC-code simulations of laser-solid harmonic generation for sub-picosecond pulses [2]. He concludes that for $I\lambda^2 > 10^{19}Wcm^{-2}\mu m^2$ and modest shelf densities of $N_e/N_{critical} = 10$, up to 60 harmonics can be generated with power conversion efficiencies of 10^{-6}. Importantly, Gibbon's simulations predict that the harmonic *order* is simply determined by ($I\lambda^2$), thus short wavelength lasers should produce shorter absolute wavelengths for a given value of $I\lambda^2$. Also, short wavelength intense lasers may eventually provide a route to shorter wavelength harmonics than have hitherto been generated.

Recently several groups have reported the observation of harmonics from picosecond laser-solid interactions with up to the 15th being observed in the interaction of 800 nm radiation at peak intensities of up to $10^{17}Wcm^{-2}$. However, to date, the extremely high orders that have previously been associated with laser-gas interactions and the nanosecond, long wavelength CO_2 laser-solid work have yet to be reproduced with shorter wavelength picosecond lasers incident on solids. An investigation of harmonic generation from solids with picosecond ultra-high intensity laser pulses is therefore timely.

The work we present in this report constitutes the first conclusive evidence of extremely high order harmonic radiation being produced from a picosecond laser interacting with a solid. Harmonic orders upto the 67th have been observed with laser intensities on target in excess of 10^{19} Wcm^{-2} and with energy conversion efficiencies estimated at ranging from 10^{-4} to 10^{-6}.

The experiment was performed using the Chirped Pulse Amplification beam line on the VULCAN laser at the Central Laser Facility of the Rutherford Appleton Laboratory. The laser produced p-polarised pulses of 2.5 picoseconds duration and energies up to 25 J on target. The contrast ratio was measured to be better than 10^{-6} by the use of a third order auto-correlator. A single shot auto-correlator allowed individual pulse lengths to be measured. The laser beam was focused onto the target by a f4.2, 44 cm focal length off-axis parabolic mirror.

In this experiment, the laser was incident onto the target surface at an angle of 54° to the target normal and the reflected beam was directed into a modified flat field X-UV spectrometer. X-ray and ion penumbral imaging cameras provided high resolution (2 mm) images of the plasma via a proven maximum entropy deconvolution technique. In addition, CR-39 plastic nuclear track detectors provided ion spectra and maximum ion energies associated with the plasma expansion. These laser and plasma diagnostics allowed the intensity on target to be accurately determined for each shot.

The majority of targets consisted of a 2 μm CH layer coated on 200 nm thick 15 μm wide Al cross wires on 1.5 mm optically polished glass slabs. In some cases a 2 μm CH layer was coated onto metal 'sandwich' targets. Targets with a CH overcoat were proven to be the most suitable targets in the experiment due to their lower free-free and bound-free contributions to the spectra.

The modified flat field spectrometer consisted of a Hitachi 1200 l/mm concave aperiodically ruled diffraction grating coupled with an imaging mirror and microchannel plate detector coupled to a CCD detector. The wavelength range was extended from 15 nm to 90 nm by appropriately locating the image plane. The imaging mirror, flat field grating and microchannel plate detector plane were positioned 22.5 cm, 61.5 cm and 85 cm from the target respectively. The imaging mirror was set up with a glancing angle of 4° so that the spectrometer intercepted a total solid angle of $3.2x10^{-5}$ steradians. Ray tracing calculations allowed the dispersion and spectral resolution of the instrument to be accurately determined. The microchannel plate/CCD detector was calibrated against x-ray film and a phoshor/CCD detector. The instrument calibration is accurate to a factor of six, taking into account the uncertainty of the microchannel plate calibration and the reflectivities of the diffraction grating and the grazing incidence mirror.

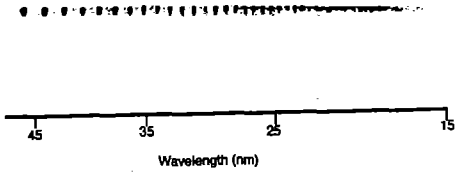

Figure 1. Harmonic spectrum for an incident irradiance of $I\lambda^2 = 1.0x10^{19}Wcm^{-2}\mu m^2$

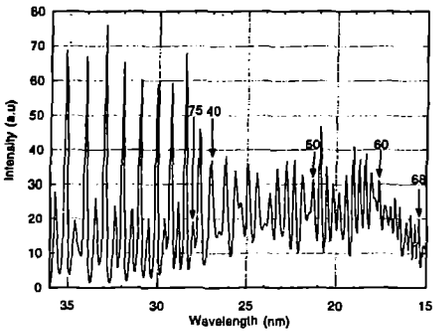

Figure 2. Lineout of Figure 1 after the instrument response function has been removed by a maximum entropy deconvolution procedure.

Figure 1 shows a spectrum taken when 20.7 J of laser energy in 2.6 psec was incident on a target consisting of 2 μm CH coating onto a metal sandwich target (25 μm Mo on 75 μm Pd). The x-ray penumbral images established that the spot size was ~9 μm full width at half maximum (FWHM) diameter, yielding an intensity on target of 9×10^{18} Wcm^{-2}. Figure 2 shows the same spectrum as Figure 1, but harmonic emission can be seen up to 67th order at 15.7 nm in first order diffraction with indications of up to the 75th order in the second order diffracted signal. We have observed that there is no clearly defined cut-off in the harmonic spectra. Instead the harmonics fall into the time integrated background emission. These observations support the argument of Gibbon that the cut-off in the harmonic emission is an artefact of the low temporal and spatial resolution used in calculation of Carman et. al.

Three observed effects - no observable difference in harmonic generation between s and p polarisations, isotropic radiation of the harmonics and relative insensitivity to pre-pulse levels - suggest that the critical density surface is rippled during the interaction. The development of a Rayleigh-Taylor like instability at the critical surface has been observed in 2.5 dimensional PIC simulations when a high intensity laser interacts with a pre-formed plasma. Even with an intensity contrast of 10^{-6} between the 80 psec FWHM duration pedestal (which is the stretched pulse duration in the laser chain) and the 2.5 psec FWHM main pulse, the pedestal level is sufficiently intense to generate a pre-formed plasma at these focused intensities. However, these simulations also predict that the ponderomotive pressure exceeds the plasma pressure in the coronal plasma. This has two effects: the plasma is expelled from the focal region and the critical density is accelerated into the plasma at extremely high velocities, resulting in a density profile similar to that assumed in Gibbon's calculations.

Figure (3) shows a plot of the harmonic order plotted against the energy conversion efficiency into each harmonic for different irradiances. It is interesting to note two features that are apparent. Firstly, the energy into the each of the harmonics increases sharply with a higher laser irradiance on target. Secondly, the conversion efficiency to each harmonic E_W scale as

$$E_\omega = E_{Laser} \times (\omega / \omega_0)^{-x} \text{ Joules} \quad (1)$$

where the exponent x is a function of the irradiance on target. The exponent fitted through all the harmonics decreases with increasing irradiance, changing from x = 5.5 at $I\lambda^2 = 5\times10^{17}$ $Wcm^{-2}\mu m^2$ to x = 3.75 at $I\lambda^2 = 1.0\times10^{19}$ $W\mu m^2cm^{-2}$. These values of the exponent are in very good agreement with those predicted by PIC calculations. Figure (3) suggests that the transfer of energy to the higher harmonics is starting to saturate at irradiances of $I\lambda^2 = 1.0\times10^{19}$ $W\mu m^2cm^{-2}$ because the lower order harmonics are systematically lower than the fitted power law for the 50-67th harmonic orders suggest. This saturation behaviour as the irradiance is increased is also exhibited in PIC calculations and lends some credence to the choice of scaling law fit.

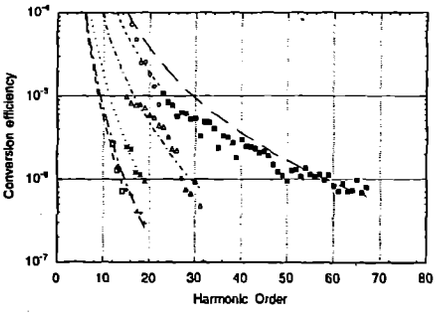

Figure 3. Conversion efficiencies (assuming isotropic radiation) against harmonic order for various irradiances: solid squares, $I\lambda^2 = 1.0\times10^{19}Wcm^{-2}\mu m^2$; open triangles $I\lambda^2 = 5.5\times10^{18}Wcm^{-2}\mu m^2$; open squares $I\lambda^2 = 5.0\times10^{17}Wcm^{-2}\mu m^2$. Curve fits are best fit power laws except $I\lambda^2 = 1.0\times10^{19}Wcm^{-2}\mu m^2$ which is fitted to the 50-68th harmonics to illustrate the onset of saturation for the lower harmonics.

It is interesting to note that for the 38th harmonic the power is 1.8 $MWSr^{-1}$ at an irradiance of 1.0×10^{19} $W\mu m^2cm^{-2}$. If isotropic emission is assumed, then the power radiated in this harmonic is 24 MW. This efficiency is also in pretty good agreement with simulations, taking into account the angular spread of emission seen in the experiment. It is also worth noting that the 56th harmonic of an Ultra-Violet laser such as KrF is in the 'water window' of the spectrum and the intensity requirement for obtaining this harmonic is 1.5×10^{20} Wcm^{-2}.

In conclusion, we have observed harmonic orders up to the 67th at 15.7 nm in first order diffraction with indications of up to the 75th harmonic in second order signal which were created during the interaction of a 2.5 picosecond, 1053 nm laser pulse with a solid target for irradiances of 1.0×10^{19} $W\mu m^2cm^{-2}$. The dependence of both the number of harmonics and their energy conversion efficiency with intensity have been explored. We have shown that there is little difference in the harmonic spectra between both s and p polarisations of the laser beam and with the addition of a pre-pulse. The power into the high harmonics is comparable to the output power of saturated collisional X-UV lasers at similar wavelengths.

REFERENCES

[1] P.A.Norreys, M.Zepf, S.Moustaizis, A.P.Fews, J.Zhang, P.Lee, M.Bakarezos, C.N.Danson, A.Dyson, P.Gibbon, P.Loukakos, D.Neely, F.N.Walsh, J.S.Wark and A.E.Dangor. *Phys Rev Lett* **76** (11) 1832-5 (1996) and all references therein.

[2] P.Gibbon *Phys Rev Lett* **76**(1), 50 (1996) and references therein.

ELECTRON TEMPERATURE AND MAXIMUM ION ENERGY MEASUREMENTS FOR PICOSECOND SOLID TARGET INTERACTIONS BETWEEN 10^{17} Wcm^{-2} AND 10^{19} Wcm^{-2}

F.N.Beg[1], A.R.Bell[1], A.E.Dangor[1], C.N.Danson[2], A.P.Fews[3], M.E.Glinsky[4], B.A.Hammel[4], P.Lee[1], P.A.Norreys[2] and M.Tatarakis[1]

[1]Imperial College of Science, Technology & Medicine, Prince Consort Road, London SW7 2AZ, United Kingdom
[2]Central Laser Facility, Rutherford Appleton Laboratory, Chilton, Didcot, Oxon OX11 0QX, United Kingdom
[3]H.H. Wills Physics Laboratory, University of Bristol, Tyndall Avenue, Bristol, United Kingdom
[4]Lawrence Livermore National Laboratory, Livermore, California, United States of America

The processes of energy absorption in the presence of very steep density gradients is a topic of lively debate at the present time. At high laser irradiances ($I\lambda^2$) a number of collisionless processes become important. These include resonance absorption, vacuum heating, skin-layer heating, and, at normal incidence, $v\times B$ heating. In the absence of ultra-fast diagnostics, time integrated measurements of the energy transference to ions and electrons, and their characteristic temperatures help clarify the validity of the different models. We report here on a series of experiments that were conducted on the CPA beam line of the Nd:glass laser VULCAN and present some of the first measurements of p-polarised laser-plasma interactions with solid targets for irradiances between 3×10^{18} Wcm$^{-2}\mu$m^2 and 10^{19} Wcm$^{-2}\mu$m^2.

The energetic ion emission was recorded by CR-39 plastic nuclear track detectors. CR-39 records charged nuclear particles as tracks which are etched into the surface of the detector after exposure. A separate etch track is produced by each incident ion and the dimensions and depth of penetration of the track enables the energy and atomic number of the ions to be uniquely determined. CR-39 detectors are sensitive to ions with energies $\geq$ 100 keV/nucleon. The detectors were covered in an array of upto 12 Mylar filters which increased in thickness by 2.5 μm and 8 steps of Al of thickness 25 μm. Each step is sensitive to a different energy interval, giving an energy resolution of 0.1 MeV in the range 0.1 - 6.0 MeV. In addition, an aluminium wedge of thickness ranging from 0.2 to 1.1 mm over a 10 mm length was used to measure ions with energies upto 14 MeV. In all shots, one piece of CR-39 was placed in the normal incidence direction, either on the chamber wall at a distance of 55 cm or at the end of an extension tube 2.5 m from the chamber centre. The angular spread of emission was determined by positioning up to seven detectors around the chamber, and the total flux was measured by simply counting the number of tracks in the detectors. At high flux levels where it was not possible to analyse individual particles, the signals under each filter were averaged.

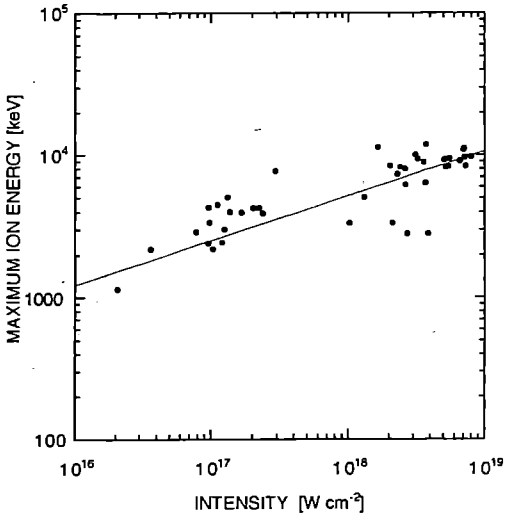

Figure 1. Maximum ion energies recorded in CR-39 detectors

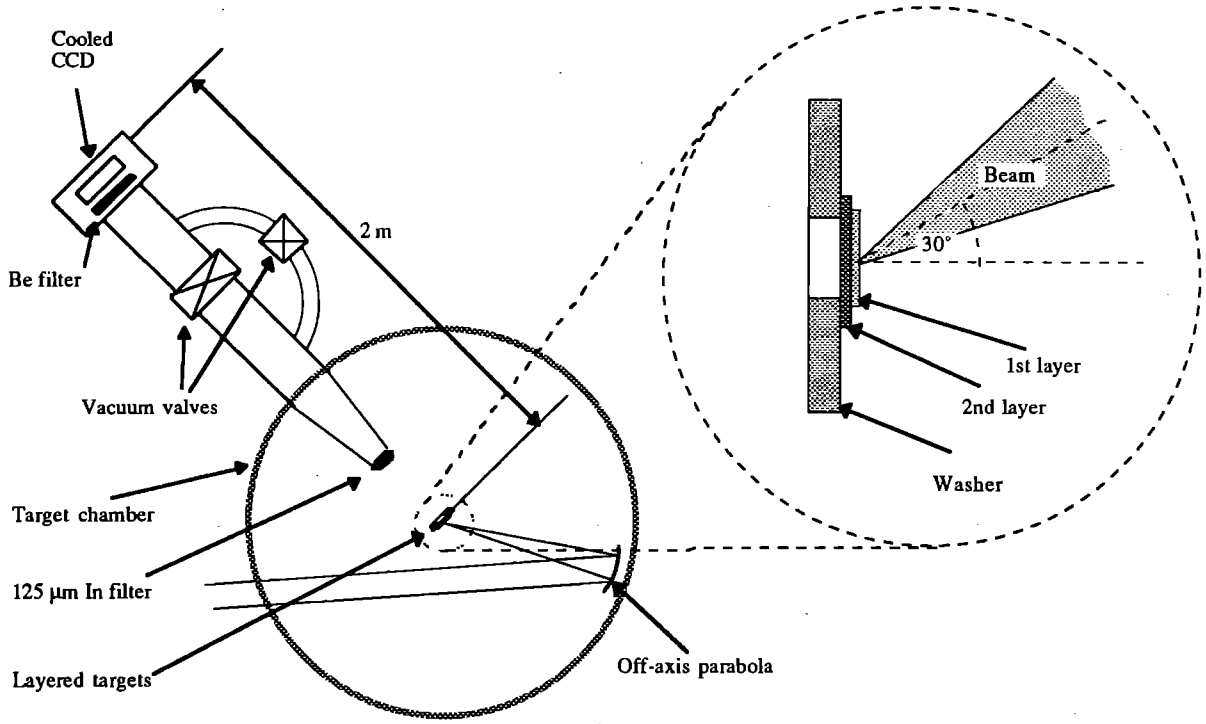

Figure 2. Schematic outline of the x-ray K alpha spectroscopic experimental set-up.

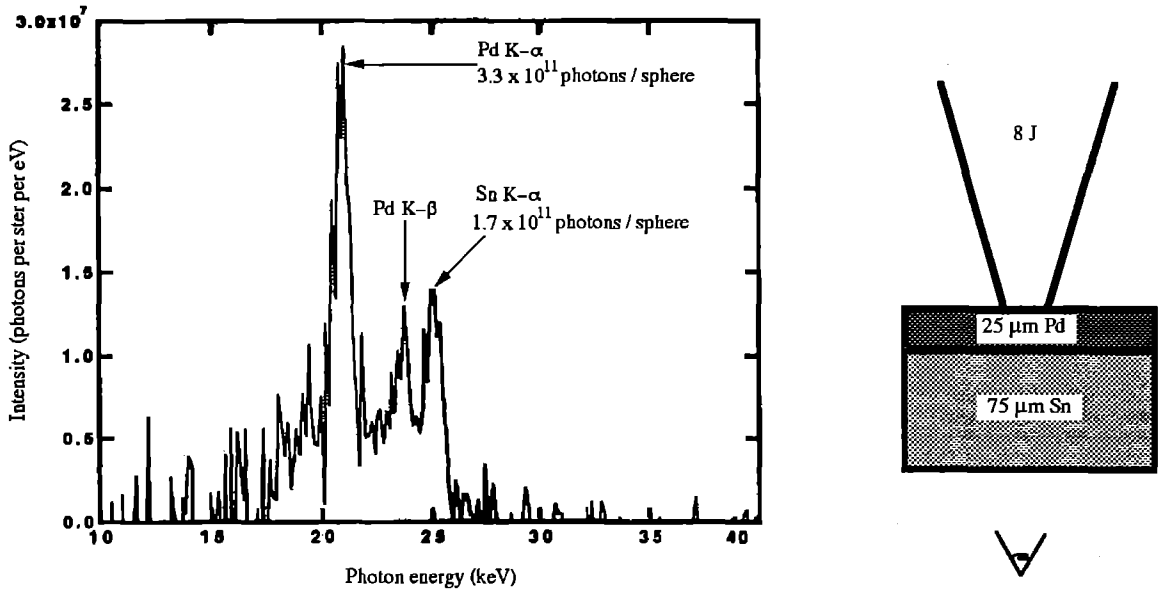

Figure 3. Typical recorded K alpha spectrum.

The energetic ion emission associated with the fast electron driven plasma expansion were predominantly from protons. The ion spectra in most of the shots show an exponential decreasing profile with increasing ion energy, followed by a sharp cut-off. This can be attributed to charge separation which limits the ion velocities by forming a non-neutral electrostatic sheath which truncates the exponential density profile. Figure 1 shows the maximum ion energies plotted against incident irradiance. These scale as:

$$E_{max} = 1.2(\pm 0.3) \times 10^{-2} I^{0.313 \pm 0.03} keV$$

where I is in Wcm^{-2}. This scaling is in quantitative agreement with that reported by Tan, McCall and Williams [1] for longer pulse duration high irradiance experiments, who proved that the maximum ion energies were proportional to the hot electron temperature.

The characteristic temperature of the energetic electrons that generated in the interaction can be characterised by measuring the K_α x-ray emission that the energetic electrons induce when they pass through multi-layer targets. Measurement of the relative K_α x-ray fluorescent emission from two or more layers can yield an estimate of the number and energy of the electrons, taking into account: (a) electron energy loss in the materials, (b) K shell ionisation cross sections, (c) the number of K_α photons produced by an electron of a particular energy (d) the x-ray mass absorption coefficients of the materials in the target [2].

Figure 2 shows a schematic layout of the technique. The targets consisted of: 25 μm Pd on 72 μm Sn, 47 μm Pd on 72 μm Sn, 25 μm Mo on 25 μm Sn and 12 μm Mo on 25 μm Sn with the laser irradiating the Pd or Mo side of the metallic sandwich targets. These medium Z materials were chosen so that the number and energy of the photons detected from each layer lay within the dynamic range of the instrument, and the K shell binding energies were high enough to minimise K_α fluorescence induced from the plasma x-ray emission but were not above the usable range of the detector.

A 16-bit x-ray CCD (Reticon RA1024J with 10^6 13.5 μm×13.5 μm pixels with 4.5 μm thick depletion layer) was used for obtaining the x-ray spectra. The CCD was used in a single hit mode, i.e. where the collection efficiency of the CCD is chosen such that the probability that two photons interacting with one pixel is small. In this mode the value V_p read out from each pixel is directly proportional to the energy of the x-ray photon E_p. After the CCD is exposed, an image, composed of multiple single hits, is captured and stored on a computer. A histogram is then constructed of the number of hits against V_p and, to a first approximation, this histogram gives the x-ray spectrum. In this experiment, an 'isolated event' histogram, i.e a histogram consisting of only those pixels which contain more than 98% of the energy in a square containing 9 pixels, was used to construct the x-ray spectrum, as this greatly increased the signal to noise ratio compared with plain and 'summed event' (the spread charge in the surrounding eight pixels of a centred event is added to the parent pixel) histograms. A typical example of recorded spectrum is given in figure 3.

The response function of the detector is the probability that a photon interacts with a pixel and this can be obtained from the mass absorption co-efficients of silicon with the thicknesses of the dead and the depletion layers in the CCD chip together with the transmission of the 100 μm thick In filter. The detector was calibrated using a 4.1 mCi Cd source for a 180 second exposure. This source decays to Ag by electron capture and the silver emits K shell radiation in the ratio 83.4% at 22 keV and 16.4% at 25 keV. The detector energy response function was found to be linear with $E_p = 0.0818(v_p - 3.01)$ keV for photon energies between 17.5 keV < E_p < 28.5 keV.

The resolution of the spectrometer is given theoretically by:

$$dE = 2.355 \times E_o \left[N^2 + \frac{0.11E}{E_o} \right]^{1/2}$$

where dE is the energy resolution at full width at half maximum (FWHM) in eV, E_o = 3.7 eV is the average energy required to produce an electron hole pair and N is the root mean square readout noise of the CCD obtained by acquiring a 'dark' image (an image taken without x-rays and then processed in the same way as the data shots). From a dark image with N=52, the resolution was found to be 0.5 keV at 25 keV, compared to a minimum without dark noise of 0.2 keV. This agrees with the

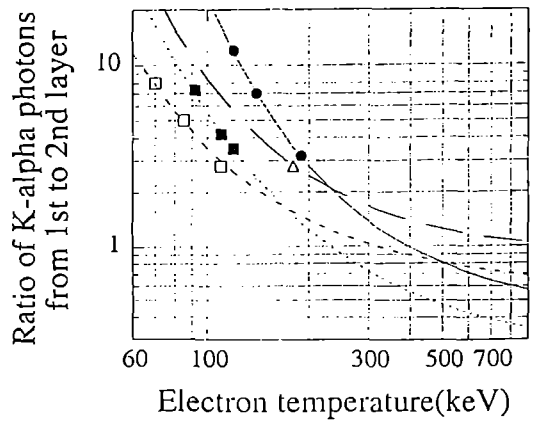

Figure 4. Calculated electron temperatures as a function of the ratio of the K alpha yields from the two layers.

observed linewidths of ~0.5 keV at 20-25 keV which are much greater than the actual linewidths (~0.5 eV). Such a resolution means that the lines from most ionisation stages are indistinguishable.

To obtain an estimate of the number and energy of the electrons by K_α spectroscopy, K shell ionisation cross sections given by

$$s_k = 7.92\times10^{-14}\,\frac{\ln(U_k)}{E_k^{\,2}U_k}\ \text{cm}^2$$

(U_k is the ratio of the electron energy E to the K shell binding energy E_k) which used Spencer's fast electron energy deposition model for electron traversing cold material, x-ray mass absorption coefficients and Krause's data on the number of K_α photons produced for a given electron energy. The targets were modelled as a series of thin planar targets. An electron at energy E_o is propagated through the targets and the total K_α emission is calculated for the detector placed at an angle 35 degrees to the target normal. Figure 4 shows a plot of the calculated ratio of the number of the K_α photons from the first and second layers plotted against electron temperature (i.e. the electrons have a Maxwellian distribution) and the experimentally determined ratios for the different sandwich target materials irradiated. The experimental points lie within the range 70 - 200 keV.

Figure 5 shows a plot of the electron temperature against incident laser energy. Taking the nominal spot size associated with x3.5 diffraction limit, the intensity on target were in the range 1.1×10^{18} - 7.0×10^{18} Wcm^{-2}. However, the maximum ion energies for all the metallic layer targets were, on average, lower than those presented in Figure 1, which suggests that the intensities for these targets were in the range 1×10^{17} Wcm^{-2} to 6×10^{17} Wcm^{-2}.

The absolute yield of K alpha photons from the two layers provides an indication of the energy transferred to the fast electron component in the target. Initial calculations suggest that ~40% of the laser energy is transferred to the energetic electrons directed into the target, but this should be treated cautiously as this result depends upon the assumptions used in describing the energetic electron transport in the target material, where considerations such as resistive inhibition due to the cold electron return current have been neglected [3]. These results which are surprisingly high compared to other published data will be confirmed in a future experimental series.

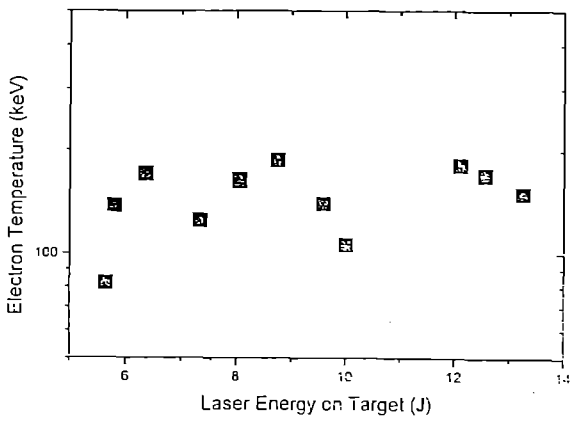

Figure 5. K alpha hot electron temperatures against incident laser energy.

The measurements are consistent either with a profile-steepened resonance absorption process where the hot electron temperature T_{hot} scales as $T_{hot} \propto (I\lambda^2)^{1/3}$ [4], or where the electron temperature is of the order of the ponderomotive potential and $T_{hot} \propto (I\lambda^2)^{1/2}$ [5]. The data certainly rule out models which predict $T_{hot} \propto (I\lambda^2)^{1.0}$ scalings.

In conclusion, we have measured both the maximum ion energies and the hot electron temperature and found that both are consistent with high irradiance measurements with longer pulse durations.

[1] T.H.Tan, G.H.McCall and A.H.Williams. Phys. Fluids **27**, 296 (1984).
[2] P.Lee. PhD thesis, University of London (1996).
[3] B.Luther-Davies, A.Perry and K.A.Nugent Phys Rev A **35**, 4306 (1987).
[4] D.W.Forslund, W.Kinel, K.Lee, E.I.Lindman and R.L.Morse. Phys. Rev. A **11**, 679 (1976).
[5] S.C.Wilks Phys. Fluids B **5**, 2603 (1993).

SPATIAL AND TEMPORAL COHERENCE MEASUREMENTS OF HARMONICS GENERATED FROM INTERACTION BETWEEN PICOSECOND LASER PULSES AND SOLID TARGETS

J. Zhang[1], M. Zepf[1], P.A. Norreys[2], A.E. Dangor[3], M. Bakarezos[4], C.N. Danson[2], A. Dyson[3], A.P. Fews[5], P. Gibbon[6], P. Lee[3], P. Loukakos[4], S. Moustaizis[4], D. Neely[3], F.N. Walsh[3] and J.S. Wark[1]

[1]Clarendon Laboratory, Department of Physics, University of Oxford, Oxford, OX1 3PU, UK
[2]Central Laser Facility, Rutherford Appleton Laboratory, Chilton, Didcot, Oxon, OX11 0QX, UK
[3]Blackett Laboratory, Imperial College, London, SW7 2BZ, UK
[4]IESL/FORTH, University of Crete, P.O. Box 1527, 711 10 Heraklion, Crete, Greece
[5]H.H. Wills Physics Laboratory, University of Bristol, Tyndall Ave., Bristol, BS8 1TL, UK
[6]Max-Planck Gesellschaft, Research Unit 'X-ray Optics', University of Jena, D-07743 Jena, Germany

INTRODUCTION

Tremendous progress has been made in the past decade in the developments of high brightness, coherence XUV sources for applications such as ultra-high resolution biological holography [1], plasma interferometry [2], and the probing of targets relevant to inertial confinement fusion [3]. These sources include both collisional excitation and recombination XUV lasers [4-7], as well as, more recently, ultra-high harmonics generated from gases in strong laser fields [8,9].

XUV lasers have an instantaneous brightness that is many orders magnitude greater than other intense X-UV sources, such as laser produced plasmas, plasma pinches and synchrotrons. However, a satisfactory transverse coherence length of these X-UV lasers appears to be difficult to achieve [7].

To our knowledge, the best spatial coherence demonstrated by an XUV laser showed it to have an effective source size (as defined by the Van Cittert-Zernicke theorem [10]) of 100 ~ 200 μm [11]. On the other hand, the coherence of high harmonics in the XUV regime generated by the interaction of short-pulse, intense lasers with gaseous targets can, in principle, be controlled and optimised relatively easily [8], but the total output energy is still too low for many applications.

In comparison to XUV lasers and harmonics generated from atoms, a new class of XUV sources is now emerging, which has the potential of both high output power and good coherence properties [12-14]. High harmonics generated during the interaction of ultrahigh irradiance ($I\lambda^2$) laser pulses with solid targets were first observed in nanosecond experiments using CO_2 lasers (where up to the 46th harmonic was observed) [15].

A recent experiment has shown that very high harmonics in XUV spectral region can be produced from solid surfaces irradiated by higher intensity, shorter wavelength picosecond laser pulses [16]. The energy conversion efficiency into harmonics is high, up to 10^{-6} for the 68th order. This conversion efficiency is comparable to those of saturated collisional XUV lasers and is much higher than other X-UV sources [4,5]. It is therefore of importance to investigate the coherence of the harmonics generated through this laser-plasma process.

In this paper, we report on our measurements of both the spatial and temporal coherence of the UV harmonic generated during the interaction of a 1053 nm, 2.5 psec laser pulse with a solid target for focused intensities in the range 5×10^{17} to 1×10^{19} Wcm^{-2}.

The measured spatial coherence of the UV harmonics places an upper limit on the effective source size of the higher order XUV harmonics, and thus we will demonstrate that the spatial coherence of these high harmonics exceeds that of current XUV lasers.

EXPERIMENTAL SET-UP

The experiment was conducted using the Chirped Pulse Amplification (CPA) beam line on the VULCAN Nd:glass laser at the Central Laser Facility of the Rutherford Appleton Laboratory [17]. The laser produced pulses of 2.5 picosecond duration at a wavelength of 1053 nm and energies of around 20 J on target. The intensity contrast ratio of the peak of pulse to the pedestal was measured to be better than 10^6 using a third order auto-correlator [17]. The laser beam was focused onto the target by an f/4.2, 44 cm focal length off-axis parabolic mirror.

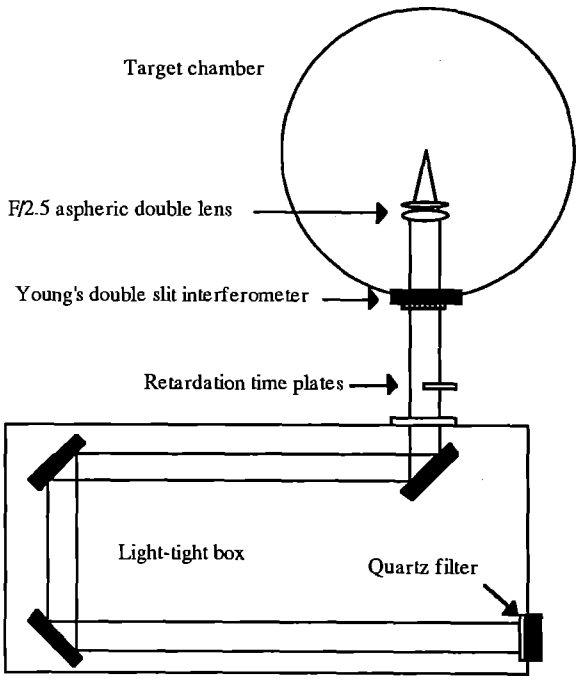

Figure 1. Schematic of the experimental setup for the coherence measurements.

The majority of targets consisted of a 2 μm CH plastic layer coated on 200 μm thick 15 μm wide Al cross wires on 1.5 mm optically polished glass slabs. In some cases a 2 μm CH layer was coated onto metal sandwich targets.

Harmonics of orders up to the 68th were observed in the first order of an XUV grating spectrometer, and up to the 75th in second order of the same instrument. Details of the production of these high order harmonics has been published elsewhere [16].

The coherence measurements, however, were made on the fourth harmonic emission, as optics at this wavelength are readily available. The effective source size determined from these measurements gives an upper limit on the source size for the higher harmonics, although direct measurements of the coherence properties of the higher harmonics are obviously desirable, and will form the goal of future experiments.

The coherence measurements were made using a Young's double slit interferometer. A schematic diagram of the experimental set-up is shown in Figure 1. The slit dimensions were 1.5 cm long and 100 μm wide. The spacing between two slits was varied to measure the spatial coherence, whilst quartz pellicles were placed over one of the slits to provide temporal delay for measurements of the longitudinal coherence.

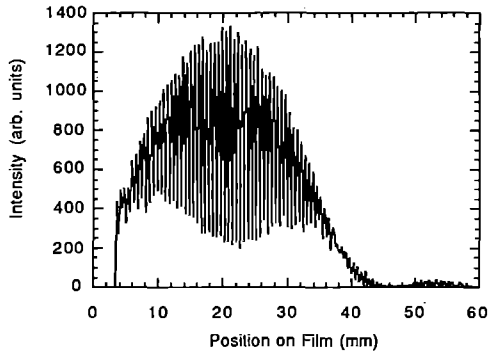

Figure 2. Measured interference pattern from double slits with separation of 5 mm as a function of spatial position on a HP5 film.

The harmonic production at these high intensities was found to be isotropic, as had previously been observed in the earlier CO_2 experiments [15]. An f/2.5 fused silica lens was installed 25 cm away from the source to produce collimated illumination of the slits, and the slits were placed 55 cm from the source. Three UV mirrors operating at 45° were placed after the slits and used as bandpass filters. These mirrors have 99% reflectivity at 268 nm and a bandwidth (FWHM) of 10 nm. A 3 mm thick Quartz filter before the detector was used to block visible and infrared light. The combination of the mirrors and the filter reduced the background radiation, the fundamental, second, and third harmonics from the laser produced plasma to below the threshold for detection. The interference patterns were recorded on ILFORD HP5 optical film, which is insensitive to infrared light. The film was placed 4.38 m from the slits resulting in a minimum fringe spacing of 300 μm, easily seen due to the high spatial resolution of the film. The film was digitised and the optical density was converted to intensity using a calibrated step wedge.

SPATIAL COHERENCE MEASUREMENT

Figure 2 shows the measured intensity distribution of the interference pattern as a function of position on the film obtained with 5 mm separation between the slits at the fourth harmonic. This interference pattern presents high visibility. The double slit interference pattern in figure 2 was modulated by the diffraction from the single slit with a width of 100 μm.

The slit separation was varied to provide a measurement of the spatial coherence. The visibility obtained from measured interference patterns as a function of slit separation is shown in figure 3. The measured visibility can be compared with a model that treats the harmonic source as a uniform disk with a diameter of *2a*. The measured visibility is compared to the Fourier transforms of disk source in figure 3 with diameters of 10 μm and 12 μm respectively, indicating that the time-integrated visibility can be modelled by a uniform disk source with a diameter of 10 ~ 12 μm. The target was rotated so that the angular distribution of the coherence function could be detected. The harmonic radiation was observed to have a significant larger angular distribution than the cone angle of the laser beam. The fringe visibility was insensitive to a change in variations of the angle of incidence angle ranging from 20° to 75° to the target normal. The near isotropic nature of the harmonics is consistent with the source being spatially incoherent, and thus the deduced dimension of the disk source agrees reasonably well with the 9 μm effective source size determined by the x-ray penumbral cameras [16].

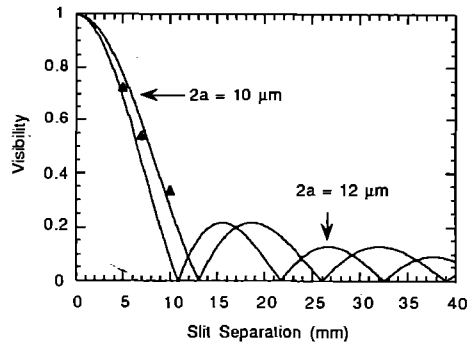

Figure 3. Visibility of the interference pattern versus the slit separation. The solid triangles are the experimental data. The solid lines are theoretical results for 10 and 12 μm disk source sizes respectively.

We expect the higher order XUV harmonics to be produced from regions of higher intensity than those producing the 4th harmonic, and thus would expect the effective source size for higher orders to be less than that deduced here. However, such an argument indicates that 10 ~ 12 μm is also the upper limit for the source size for the XUV harmonics. This should be compared to the effective source size of 100 ~ 200 μm deduced for the most coherent XUV lasers produced to date [11]. This measurement indicates that XUV harmonics have a much better spatial coherence than XUV lasers.

TEMPORAL COHERENCE MEASUREMENT

For the temporal coherence measurement, the spacing in the perpendicular direction between the two slits was kept constant (5 mm). Thin (600 μm) quartz pellicles were inserted behind one of the slits to provide delay along the propagation direction between the two beams from the two slits.

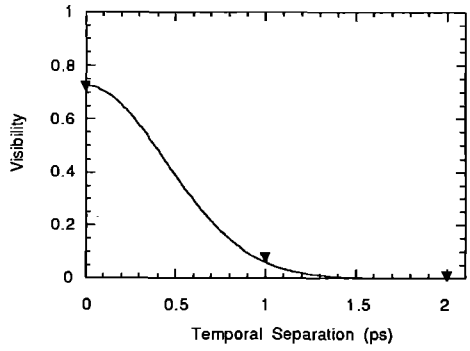

Figure 4. Visibility as a function of retardation time. The solid triangles are the experimental results and the solid line is the theoretical fitted curve assuming quasi-monochromatic light with a Gaussian spectral distribution function.

A temporal coherence measurement result at an irradiance of $5x10^{17}$ Wcm^{-2} is shown in figure 4. The thinnest quartz pellicles were 600 μm thick, resulting in a retardation time between the two beams from the two slits of almost 1 picosecond. The temporal coherence function can be calculated by assuming quasi-monochromatic light with a Gaussian spectral distribution function

$$D(\upsilon-\upsilon_0)=\frac{1}{\Delta\upsilon}\exp\left[-\pi\left(\frac{\upsilon-\upsilon_0}{\Delta\upsilon}\right)^2\right]. \qquad (4)$$

The parameter $\Delta\upsilon$ characterises the width of the line because $D(\upsilon-\upsilon_0)$ is down to 1/e of its maximum value when $\upsilon=\upsilon_0\pm\Delta\upsilon/\sqrt{\pi}$. The best fit of the experimental data gives a coherence time of 0.5 picosecond (solid line). This takes into account of the 5 mm slit separation perpendicular to the propagation direction.

The Fourier transform of the temporal coherence function $\Gamma_{11}(\tau)$ is the power spectrum, which describes the spectral energy distribution of the light source. The temporal coherence $\Gamma_{11}(\tau)$ is therefore related to the bandwidth of the source. In order to determine the bandwidth, a separate measurement of the fourth harmonic emission was carried out using a UV spectrometer with a 1200 line/mm high spectral resolution grating.

The spectrum consists of a spike at the fourth harmonic) and a broad structure associated with self phase modulation [18]. The FWHM of the central spike was measured to be about 0.54 nm. This corresponds to a temporal coherence time of 0.4 picosecond, which agrees reasonably with the direct temporal coherence measurement. However, with increasing irradiance on target, the spectrum is progressively broadened due to the stronger modulation effects. At an irradiance of $3x10^{18}$ Wcm^{-2}, the coherence time is found to be ~ 0.02 ps.

From the direct measurement of the temporal coherence time, and those inferred from measurement of the 4ω bandwidth, the coherence time has been determined to be between 0.02 ~ 0.4 picosecond, depending on the irradiance on target. This coherence time corresponds to a longitudinal coherence length in the range 6 to 120 μm, which is sufficient for applications such as interferometry and holography, where imaging biological samples can typically be no more than 1 μm in depth.

CONCLUSION

It has been shown that the temporal coherence of the harmonics is very dependent on the intensity. It appears that the size of plasma plays an important role in determining the bandwidth of the harmonics generated. Therefore reducing the contrast such that the pedestal level is below that of plasma production levels [19] may significantly reduce the bandwidth of the harmonics and thus improve the longitudinal coherence length.

In conclusion, we have observed high coherence, high power and short wavelength output. These properties, together with the simplicity of selecting the required wavelengths, make these harmonics from the solid surface interacting with intense short laser pulses one of the most promising and competitive sources for applications.

REFERENCES

[1] R.A. London, M.D. Rosen, and J.E. Trebes, Appl. Optics, **28**, 3397 (1989).

[2] L.B. Da Silva, T.W. Barbee, Jr., R. Cauble, P. Celliers, D. Ciarlo, S. Libby, R.A. London, D.L. Matthews, S. Mrowka, J.C. Moreno, D. Ress, J.E. Trebes, A.S. Wan, and F. Weber, Phys. Rev. Lett., **74**, 3991 (1995).

[3] D.H. Kalantar, M.H. Key, L.B. Da Silva, S.G. Glendinning, J.P. Knauer, B.A. Remington, F. Weber, and S.V. Weber, Submitted for publication in Phys. Rev. Lett., (1996).

[4] A. Carillon, H.Z. Chen, P. Dhez, L. Dwivedi, J. Jacoby, P. Jaegle, G. Jamelot, J. Zhang, M.H. Key, A. Kidd, A. Klisnick, R. Kodama, J. Krishnan, C.L.S. Lewis, D. Neely, P. Norreys, D. O'Neill, G.J. Pert, S.A. Ramsden, J.P. Raucourt, G.J. Tallents, and J. Uhomoibhi, Phys. Rev. Lett., **68**, 2917 (1992).

[5] J.A. Koch, B.J. MacGowen, L.B. Da Silva, D.L. Matthews, J.H. Underwood, P.J. Batson, and S. Mrowka, Phys. Rev. Lett., **68**, 3291 (1992).

[6] J. Zhang, M.H. Key, P.A. Norreys, G.J. Tallents, A. Behjat, C. Danson, A. Demir, L. Dwivedi, M. Holden, P.B. Holden, C.L.S. Lewis, A.G. MacPhee, D. Neely, G.J. Pert, S.A. Ramsden, S.J. Rose, Y.F. Shao, O. Thomas, F. Walsh, and Y.L. You, Phys. Rev. Lett., **74**, 1335 (1995).

[7] R.A. London, M. Strauss, and M.D. Rosen, Phys. Rev. Lett., **65**, 563 (1990).

[8] J.L. Krause, K.J. Schafer, and K.C. Kulander, Phys. Rev. Lett., **68**, 3535 (1992).

[9] P. Salieres, A. L'Huillier, and M. Lewenstein, Phys. Rev. Lett., **74**, 3776 (1995). S.G. Preston, A. Sanpera, M. Zepf, W.J. Blyth, C.G. Smith, J.S. Wark, M.H. Key, K. Burnett, M. Nakai, D. Neely, and A.A. Offenberger, Phys. Rev. **A53**, R31 (1996).

[10] P.H. Van Cittert, Physica, **1**, 201 (1934); **6**, 1129 (1939). F. Zernike, Physica, **5**, 785 (1938); Proc. Phys. Soc., **61**, 158 (1948).

[11] J.E. Trebes, K.A. Nugent, S. Mrowka, R.A. London, T.W. Barbee, M.R. Carter, J.A. Koch, B.J. MacGowan, D.L. Matthews, L.B. Da Silva, G.F. Stone, and M.D. Feit, Phys. Rev. Lett., **68**, 588 (1992).

[12] S.C Wilks, W.L. Kruer, and W.B. Mori, IEEE Trans. Plasma Sci., **21**. 120 (1993).

[13] D. von der Linde, T. Enger, G. Jenke, P. Agostini, G. Grillon, E. Nibbering, A. Mysyrowicz, and A. Antonetti, Phys. Rev., **A52**, R25 (1995).

[14] P. Gibbon, Phys. Rev. Lett., **76**, 50 (1996).

[15] R.L. Carman, D.W. Forslund, and J.M. Kindel, Phys. Rev. Lett., **46**, 29 (1981).

[16] P.A. Norreys, M. Zepf, S. Moustaiziz, A.P. Fews, J. Zhang, P. Lee, M. Bakarezos, C.N. Danson, A. Dyson, P. Gibbon, P. Loukakos, D. Neely, F.N. Walsh, J.S. Wark, and A.E. Dangor, Phys. Rev. Lett., **76**, 1832 (1996).

[17] C.N. Danson, L.J. Barzanti, Z. Chang, A.E. Damerall, C.B. Edwards, S. Hancock, M.H.R. Hutchinson, M.H. Key, S. Luan, R.R. Mahadeo, I.P. Mercer, P. Norreys, D.A. Pepler, D.A. Rodkiss, I.N. Ross, M.A. Smith, R.A. Smith, P. Taday, W.T. Toner, K.W.M. Wigmore, T.B. Winstone, R.W.W. Wyatt, and F. Zhou, Opt. Commun., **103**, 392 (1993).

[18] S.V. Bulanov, T.Zh. Esirkepov, and N.M. Naumova, "Properties of spectra of the reflected and transmitted radiation during propagation of relativistically strong laser pulses in underdense plasmas", (unpublished).

[19] Y. Zhang, J. Zhang, S. Pan, Y. Nie, "An estimate of threshold intensity of the leading edge of ultrashort laser pulses in interaction with solid targets", Accepted for publication in Optics Commun., (1996).

IMAGING OF HIGH HARMONIC RADIATION FROM SOLID TARGETS

D.M. Chambers[1], S.G. Preston[1], M. Castro-Colin[1], A. Dyson[2], D. Neely[3], P. Norreys[3], M. Zepf[1], A.E. Dangor[2], M.H. Key[1,3] and J.S. Wark[1]

[1]Clarendon Laboratory, Department of Physics, University of Oxford, Parks Road, Oxford OX1 3PU.
[2]Blackett Laboratory, Imperial College, Prince Consort Road, London, SW7 2AZ.
[3]Rutherford Appleton Laboratory, Chilton, Didcot, Oxon, OX11 0QX.

INTRODUCTION

Recent rapid developments in short pulse, high power laser technology has enabled many advances in the field of harmonic generation [1,2]. The aim of this research is to produce short pulse, coherent XUV radiation at high brightness in order to perform interferometry, holography, spectroscopy and non-linear optics at intensities that, until recently, were only available from optical laser systems. Most of the research in the field of harmonic generation has concentrated on laser interactions with gas targets [3,4]. This exploits the high non-linear susceptibilities of noble gases when the laser field becomes comparable with the Coulomb field within the atoms. The shortest wavelength generated to date is 67 Å in Helium, the 37th harmonic of the 248.6 nm SPRITE KrF laser system [1]. Efficiencies of harmonic generation can reach as high as 10^{-7} at moderate XUV wavelengths [1,5].

The generation of harmonics from laser interactions with solid targets has recently seen renewed interest [6,7]. This process generates both odd and even harmonics as electrons are dragged back and forth across a steep asymmetric density gradient by the intense laser field. Harmonics generated by this process were first observed several decades ago using CO_2 lasers [8]. These experiments relied on long wavelengths and nanosecond time scales to ensure significant ponderomotive steepening of the density profile. Harmonics up to the 46th were observed, although with a fundamental wavelength of 10.6 μm, this corresponds to a harmonic wavelength of 230 nm, far from the XUV region [9].

With the recent advances in high power laser technology, shorter wavelength lasers can now be used for the generation of harmonic radiation from solid targets. Particle-in-cell code simulations have shown that with $I\lambda^2 > 10^{19}$ Wμm^{2}cm^{-2} up to 60 harmonics can be generated with efficiencies of 10^{-6} [10]. A recent experiment on the VULCAN 1 μm laser system produced up to the 68th harmonic (155 Å) [2].

We report on our experiment to image the source of XUV harmonics at ~220 Å from the VULCAN 1 μm laser system. The 48th harmonic has an average brightness of 4.4 x 10^{11} W/(cm^{2}steradian), and the brightest part of the source has an upper limit of 6 μm^2.

EXPERIMENTAL ARRANGEMENT

The experiment was performed using the VULCAN Nd:Glass laser system in CPA configuration [11]. The laser delivered up to 20 J on target, in a typical pulse length of 1 ps at 1.05 μm. The beam was focused using an f/4.2 off-axis parabola, to a 3 x diffraction limited spot of 12 μm FWHM in diameter. The target consisted of an optically polished glass slab 1.5 mm thick coated with 2 μm of plastic (CH), and was at an angle of 55_ to the incident laser beam.

A spherical multilayer XUV mirror, with a 50 cm focal length, and a flat silver-coated mirror were used to relay an image of the source, with a magnification of 6.7 onto Q-plate film, as shown in figure 1. The multilayer had a bandwidth of 25 Å centred at 220 Å, the 48th harmonic, and was at an angle of 45_ to the target normal and 100_ to the incident laser direction. The angle subtended by the plastic target (the XUV source) and the silver-coated mirror at the multilayer mirror was 57 mrad, and the solid angle of the XUV radiation collected by the multilayer was 1.9 x 10^{-5} steradians, giving a diffraction limit of 11 μm to the image at the film plane. A 400 nm aluminium filter, with a transmission of 33 % at 220 Å, was placed over the Q-plate film.

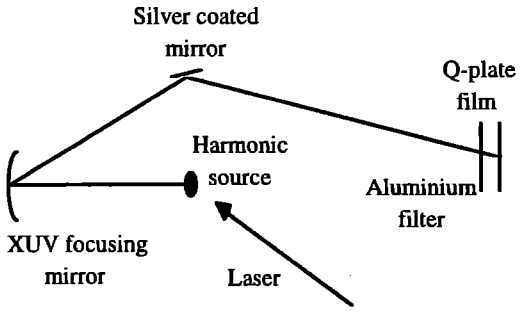

Figure 1. Schematic diagram of the harmonic imaging system.

RESULTS

The Q-plate was densitometered using a Joyce-Loebl densitometer with 22 times magnification, matched optics, and a numerical aperture of 0.25. The ideal setting of both the aperture and step sizes being matched at 2.5 μm was impractical due to problems with low light levels through the system, and the grain size on the Q-plate being of the order of 1 μm. We therefore used an aperture in the densitometer of 400 μm, giving a spot size of 18 μm on the film. Horizontal and vertical step sizes were set to 2.5 μm, the smallest setting available. The image was then deconvolved to recover resolution. Figure 2 shows a deconvolved three dimensional plot of a typical harmonic image, as seen on the Q-plate film. This particular image was taken from an incident laser energy of 17 J focused to an intensity of 4 x 10^{18} W/cm^2.

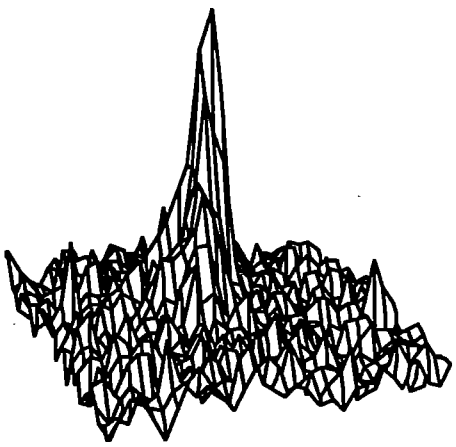

Figure 2. Three dimensional plot of the harmonic image. The area shown is 30 μm x 30 μm.

We now present initial results of two dimensional maximum entropy deconvolutions, to take into account the mismatch in the step size to spot size ratio of the densitometer [12]. Figure 3 shows horizontal and vertical lineouts through the peak of the image of the deconvolved XUV source. These lineouts show the XUV harmonic on top of a wide background fog and thermal plasma emission. The varying intensity of the harmonic is expected from the non-uniform focal spot quality of the VULCAN laser system. This shows the brightest part of the harmonic radiation to be from an area of approximately 6 μm^2. This is at the limit of the resolution of our imaging system, and so the very brightest part of the radiation could be from an even smaller area. These lineouts have been corrected for film response, using the calibration equation calculated by Daido et al [13]. They have not been corrected for the mirror reflectivities or the filter transmission. As the Q-plate image was close to saturation the number of photons calculated from the film response will be a considerable underestimate.

We take a conservative estimate and assume the pulse length of the harmonic emission to be the same as that of the laser pulse of 1 ps, and take the background thermal emission to end at 800 photons/μm^2. Correcting for the transmission and reflectivity of the filter and mirrors, and allowing for the fact that the multilayer mirror's bandwidth allows 6 harmonics to be focused onto the film, increases the intensity by a factor of 15/6 for each harmonic. Taking into account the input solid angle of the imaging system, of 2.4 x 10^{-4} steradians, this gives an average source brightness of 4.4 x 10^{11} W/(cm^2 steradian) per harmonic. It should be noted that a previous experiment indicated uniform harmonic emission into 2^{π} steradians [2], so the solid angle of the collected harmonics is limited by the imaging system not by limitations imposed by the source. This gives an average intensity of the 48th harmonic, at 220 Å, of 2.8 x 10^{12} W/cm^2 at the source, and an energy of 0.33 μJ into all directions. This gives an efficiency from infrared to XUV radiation of 2 x 10^{-8}. In a previous experiment when the VULCAN laser was focused to its highest intensity of 1 x 10^{19} W/cm^2, the 48th harmonic can then be generated with an efficiency of 1 x 10^{-6}, giving two orders of magnitude increase in the energy and brightness of the harmonic [2]. Giving a possible source brightness of more than 10^{13} W/(cm^2 steradian).

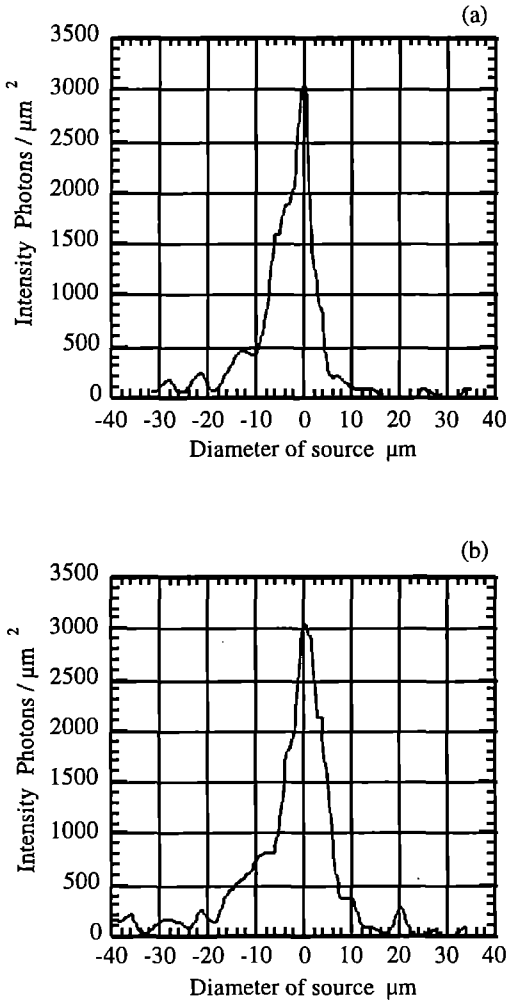

Figure 3. Horizontal (a) and vertical (b) lineouts through the image of the harmonic source, corrected for film response, and deconvolved from the densitometer settings.

CONCLUSION

In conclusion we have demonstrated a coherent XUV radiation source at 220 Å. The brightest part of the source has an upper limit in size of 6 μm^2, the average brightness has a lower limit of 4.4 x 10^{11} W/(cm^2steradian), generated with an efficiency of 2 x 10^{-8}. This is comparable to harmonics produced from gas target sources. More detailed results will be presented in a forthcoming publication.

REFERENCES

(1) S.G. Preston, A. Sanpera, M. Zepf, W.J. Blyth, C.G. Smith, K. Burnett, M.H. Key, J.S. Wark, D. Neely, A.A. Offenberger. Physical Review A, 53, R31-34 (1996).

(2) P.A. Norreys, M. Zepf, S. Moustaizis, A.P. Fews, J. Zhang, P. Lee, M. Bakarezos, C.N. Danson, A. Dyson, P. Gibbon, P. Loukakos, D. Neely, F.N. Walsh, J.S. Wark, A.E. Danger. Physical Review Letters, 76, 1832-1835 (1996).

(3) A. L'Huillier, P. Balcou. Physical Review Letters, 70, 774 (1993).

(4) J.L. Krause, K.J. Schafer, K.C. Kulander. Physical Review Letters, 68, 3535 (1992).

(5) T. Ditmire, J.K. Crane, H. Nguyen, L.B. DaSilva, M.D. Perry. Physical Review A, 51, R902-R905 (1995).

(6) S. Kohlweyer, G.D. Tsakiris, C.G. Wahlstrom, C. Tillman, I. Mercer. Optics communications, 117, 431-438 (1995).

(7) D. von der Linde, T. Engers, G. Jenke, P. Agostini, G. Grillon, E. Nibbering, A. Mysyrowicz, A. Antonetti. Physical review A: Rapid communication, 52, R25-R27 (1995).

(8) R.L. Carman, D.W. Forslund, J.M. Kindel. Physical review letters, 46, 29-32 (1981).

(9) R.L. Carman, C.K. Rhodes, R.F. Benjamin. Physical review A, 24, 2649-2663 (1981).

(10) P. Gibbon. Physical Review Letters, 76, 50-53 (1996).

(11) C.N. Danson, L.J. Barzanti, Z. Chang, A.E. Damerell, M.H.R. Hutchinson, M.H. Key, S. Luan, R.R. Mahadeo, I.P. Mercer, P. Norreys, D.A. Pepler, D.A. Rodkiss, I.N. Ross, M.A. Smith, R.A. Smith, P. Taday, W.T. Toner, K.W.M. Wigmore, T.B. Winstone, R.W.W. Wyatt, F. Zhou. Optics Communications, 103, 392-397 (1993).

(12) Hidden Image computor program, Sehgal corporation.

(13) H. Daido, M.S. Schulz, K. Murai, R. Kodama, G. Yuan, J. Goto, K.A. Tanaka, Y. Kato, S. Nakai, K. Shinohara, T. Honda, I. Kodama, H. Iwasaki, T. Yoshinobu, M. Tsukamoto, M. Niibe, Y. Fukuda, D. Neely, A. Macphee, G. Slark. Journal of X-ray science and technology, 5, 105-120 (1995).

MEASUREMENTS OF THE HOLE BORING VELOCITY FROM DOPPLER SHIFTED HARMONIC EMISSION FROM SOLID TARGETS

M.Zepf[1], M.Castro-Colin[1], D.Chambers[1], A.E.Dangor[3], C.N.Danson[2], A.Dyson[3], A.P.Fews[4], P.Gibbon[5], M.H.Key[1,2], P.Lee[3], S.Moustaizis[6], D.Neely[2], P.A.Norreys[2], S.G.Preston[1], J.S.Wark[1] and J.Zhang[1]

[1]Clarendon Laboratory, Department of Physics, University of Oxford, Parks Road, Oxford OX1 3PU, UK,
[2]Rutherford Appleton Laboratory, Chilton, Didcot, Oxon. OX11 0QX, United Kingdom.
[3]Imperial College of Science, Technology and Medicine, Prince Consort Road, London SW7 2AZ, United Kingdom.
[4]H.H.Wills Physics Laboratory, University of Bristol, Tyndall Ave., Bristol BS8 1TL, United Kingdom.
[5]Max Planck Society, Research Unit 'X-Ray Optics', University of Jena, Max-Wien-Platz 1, D-07743 Jena, Germany.
[6] IESL/FORTH, University of Crete, P.O.Box 1527, 711 10 Heraklion, Crete, Greece.

INTRODUCTION

The use of chirped pulse amplification (CPA) in high power laser systems has lead to irradiances on target that were previously inaccessible in the laboratory. The physics of these interactions is of wide interest for example for new particle accelerators[1], the development of an extremely bright source of highly coherent XUV radiation[2-4]; and in the Fast Ingitor scheme for Inertial Confinement Fusion (ICF) which promises a significant reduction in driver energy requirements for ignition and high gain[5].

In the Fast Ignitor scheme it is required that the critical density surface is pushed close to the dense compressed fuel region (the hole boring phenomenon[6]. Kalashnikov et al[7] have reported measurements of critical density recession velocities for irradiances up to 2×10^{18} Wcm^{-2} for pulses with differing contrast ratios and different angles of incidence. Their results are consistent with a simple model taking into account conservation of mass and momentum including the ponderomotive pressure model first proposed by Kruer and Wilks [8]. In this letter we extend the irradiance range covered to include measurements up to $I = 1.0\times10^{19}$ Wcm^{-2}. We show that the critical density surface is accelerated into the target with a velocity of $v/c = 0.015$ by this irradiance at an oblique angle. Furthermore, it is shown that the inclusion of energy absorption in the momentum conservation expression accounts for the observations.

THE EXPERIMENT

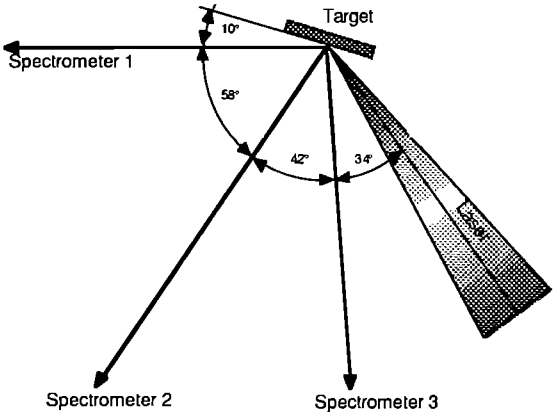

Figure 1 Schematic of experimental lay-out

The experiments were conducted using the 35 TW, 1.054 μm wavelength chirped pulse amplification beamline of the Nd:glass laser VULCAN[9] at the Rutherford Appleton Laboratory. Laser pulses with unto 25 J and pulse durations between 700 fsec and 2.5 psec were delivered onto target by an f/4.2 off axis parabolic mirror. The targets consisted of optically polished glass slabs of 1.5 mm thickness overcoated with 2 mm of plastic (CH). The laser beam was incident on the target at an angle of 54 degrees to the target normal.

Three 0.5 m 1200 lines/mm optical spectrometers were employed with 16 bit Oriel Instaspec CCD camera or Kodak TMAX detectors to measure the spectra of the second, third and fourth harmonics. A modified XUV spectrometer, detailed in reference[5] was used together with double microchannel plate detector to measure the higher harmonic spectra. X-ray and ion penumbral imaging cameras were employed to accurately determine the focal spot size for each shot via a proven maximum entropy deconvolution procedure[10] The optical spectrometers 1,2 and 3 were located at +80°, +22° and -20° relative to the target normal. A schematic outline of the experimental set-up is shown in Figure 1.

Both odd and even harmonics are generated via the relativistic oscillation of the electrons across the steep plasma density gradient which is formed due to the large ponderomotive pressure associated with the laser pulse[10,11] Any shift in the harmonic or fundamental wavelength can therefore be understood as the reflection of a moving mirror. Using third and higher harmonics has the advantage that other laser plasma parametric interactions which could contribute to the spectrum are avoided and the non-linearity of the interaction ensures that these harmonics are generated in a small temporal window around the peak of the drive pulse, reducing the spectral broadening due to a change in velocity in the sampling period. Figure 2 shows a example of a spectra taken simultaneously with spectrometers 1 and 3. Two features are immediately clear: both spectra are significantly broadened relative to the 1.6 nm Full Width at Half Maximum (FWHM) of the fundamental and are significantly red-shifted from the nominal 4ω wavelength. We attribute the broadening to self phase modulation of the incident laser as it propagates through the coronal plasma. The fact that the reflected fundamental displays similar structure and broadening corroborates this interpretation.

In order to measure the recession velocity and direction of the critical density surface unambiguously, at least two spectrometers are required at different viewing angles to distinguish between Doppler motion and possible frequency shifts due to self phase modulation. In the case of oblique incidence, the direction of motion cannot be assumed to be in any given direction, since the ponderomotive force is always normal to the critical density surface, and this depends on the pre-pulse level and the sphericity of the plasma expansion. High contrast pulses would therefore tend to push the plasma in the direction of the target normal, whereas pulses with a lower contrast may exhibit Doppler motion closer to the direction of propagation of the incident laser beam.

RESULTS

The centre frequency of the shifted harmonics was determined by taking the weighted mean of the spectra. Figure 3 shows the angles relative to the target normal deduced from the red shift in

channels 1,2 and 3. The result, a recession along the target normal, is consistent with the interaction of a high contrast pulse and the shifts being due to Doppler motion. The average of our data set is 180° ± 5.6° with respect to target normal.

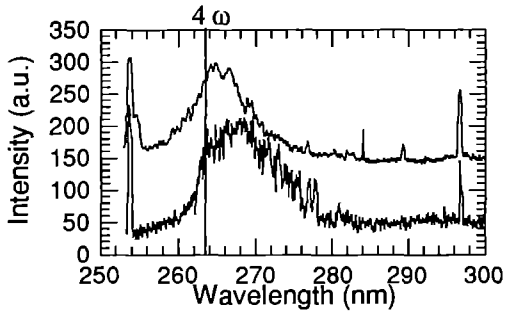

Figure 2 Example of 4th harmonic spectra taken with spectrometers 1 (top) and 3 (bottom). The top spectrum is offset for clarity, the narrow features are Hg-Calibration lines.

The recession velocities plotted against incident irradiance are shown in Figure 4. The spectra change from blue (expansion away from the target) to red shifts at I ~1.0×10^{18}Wcm^{-2}. The recession velocity as a fraction of the speed of light can be estimated from a simple model using number and momentum conservation given by;

$$\frac{v}{c} = \left(\frac{\Delta p}{p_{tot}} \frac{n_{cr}}{n_p} \frac{Zm_e}{M} \frac{I\lambda^2}{2.7\times10^{18}} \right)^{1/2}$$

where $p_{tot}=2I/c$ and Δp is the transferred momentum (taking account of absorption and the angle of incidence) and $n_p(m)$ is the electron plasma density (mass), Z and M are charge and mass of the ions. For normal incidence irradiation, this expression is in good agreement with 2.5 D particle in cell (PIC) calculations[6]. The solid line fit shown in Figure 4 takes into account the oblique angle of incidence and the relative fraction of absorbed and reflected photons predicted by modelling discussed later. This is important because absorbed photons transfer less momentum to plasma at the critical density surface than those reflected. This is illustrated by the dashed line in Figure 4, which shows that when absorption is excluded the theoretical recession velocity is outside experimental errors.

There is good agreement between the model including absorption and experiment at irradiances > 3x10^{18} Wcm^{-2}. Below this, the model breaks down because it does not take into account the transition from the regime where the ponderomotive pressure is balanced or exceeded by the plasma thermal pressure. Indeed, a comparison with the earlier work of Kalashnikov et al. illustrates this clearly. They showed that the transition from plasma expansion to hole boring is below 8×10^{16} W/cm^2 for a low contrast pulse ratio of 10^{-3}:1, while plasma expansion was still observed at 5×10^{17} W/cm^2 for a higher contrast ratio of 10^{-7}:1. This agrees well with our observation of the transition from plasma expansion to hole boring being at approximately 10^{18} W/cm^2 for a pulse with a contrast of 10^{-6}:1.

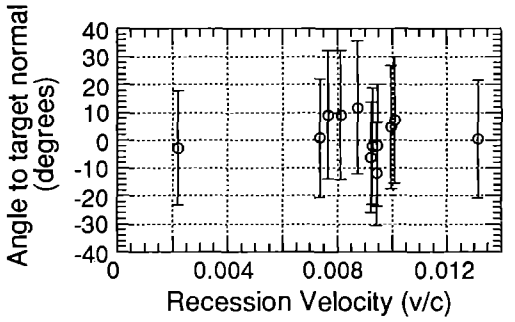

Figure 3 Direction of motion relative to the target normal in degrees. The motion is parallel to the target normal and directed towards the target.

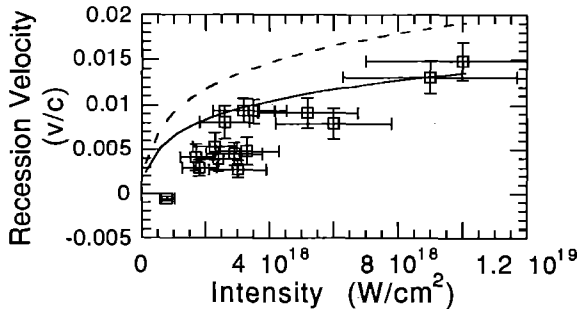

Figure 4 Recession velocities vs intensity. The fits show the theoretical predictions using the model of Wilks et al. The solid line fit includes the angle of incidence and 60% absorption, the dashed line fit excludes the absorbed energy fraction.

The transition from hole boring to plasma expansion depends upon the ratio of laser energy deposited at the critical density surface as hot electrons to that component deposited as thermal energy. It is for this reason that some caution is required when the fractional energy absorption is inferred from the data. We nevertheless note that good agreement has been found between the observed conversion efficiencies into the X-UV harmonics and boosted frame of reference particle-in-cell (PIC) calculations[13] which predict 60 % energy absorption at 45° incidence angle for irradiances between $I\lambda^2$ = 10^{17} and 10^{19} Wcm^{-2} μm^2. Thus, although the absorption fractions inferred from this data set should be treated cautiously, they are physically plausible, but require confirmation in future experiments by more direct methods.

CONCLUSION

In conclusion, we have shown that harmonics generated during the interaction of an ultra-high intensity pulse with solid targets are powerful diagnostic tools of plasma conditions. We have measured the critical density recession velocity to be v/c = 0.015 at I = 10^{19}Wcm^{-2} (which is in quantitative agreement with modelling) and have established the direction of motion to be parallel to the target normal. These observations give relevant basic information for the fast ignition concept.

REFERENCES

[1] A.Modena et al. Nature **377**, 606 (1995)
[2] P.Gibbon. Phys. Rev. Lett. **76**, 50 (1996).
[3] P.A.Norreys et al. Phys. Rev. Lett. **76**, 1832 (1996).
[4] J.Zhang, M. Zepf et al. Phys. Rev .A (accepted April 1996)
[5] M.Tabak et al. Phys. Plasmas **1**, 1626 (1994).
[6] S.C.Wilks et al. Phys. Rev. Lett. **69**, 1383 (1992).
[7] M.P. Kalashnikov et al. Phys Rev Lett **73**, 260 (1994).
[8] W.L.Kruer and S.C.Wilks. Plasma Phys. and Controlled Fusion **34**, 2061 (1992).
[9] C.N.Danson et al. Optics Comm. **103**, 392 (1993).
[10] A.P.Fews et al. Optics Comm. **94**, 259 (1992).
[11] R.L.Carman et al. Phys. Rev. Lett. **46**, 29 (1981).
[12] R.L.Carman et al. Phys. Rev. A **24**, 2649 (1981).
[13] P.Gibbon. Phys. Rev. Lett. **73**, 664 (1994).

INTERACTION OF A SHORT, INTENSE LASER PULSE WITH A PREFORMED PLASMA

M.Borghesi, L.Barringer, L.A.Gizzi*, A.J.MacKinnon, C.Meyer and O.Willi

The Blackett Laboratory, Imperial College of Science, Technology and Medicine, London
* TESRE-CNR, Bologna (Italy)

INTRODUCTION

The propagation of an intense laser pulse through a plasma is a fundamental requirement for a number of applications [1] such as particle acceleration via plasma waves, x-ray laser studies [2], and the Fast Ignitor scheme for ICF [3]. In particular, the Fast Ignitor scheme requires the short laser pulse not only to propagate without considerable energy loss through the underdense coronal plasma, but also to penetrate into the overdense region of the imploding plasma. For a sufficiently powerful, long laser pulse, self guiding of the pulse due to relativistic effects is predicted by theory [4]. Indirect experimental observations of this phenomenon have been reported, in which relativistic channelling of a short pulse in a tenuous plasma was diagnosed via Thomson scattering [5]. A relativistic effect also predicted [6] but not yet experimentally observed, is overdense penetration of a laser pulse at relativistic intensity, due to relativistic increase of the mass of the electrons.

An experimental study of the propagation of a picosecond laser pulse at relativistic intensities through preformed plasmas is presented here.

EXPERIMENTAL ARRANGEMENT

The experiment was performed at the Central Laser facility using the Vulcan laser in the CPA operation mode. The targets used were plastic foils. Their thicknesses varied in the range 0.1-0.5 μm. The plasma was preformed by a 400 ps pulse, frequency doubled in a KDP crystal to $\lambda = 0.527$ μm and focused onto target in a spot of around 200 - 300 μm in diameter, at irradiances below 10^{13} W/cm . Different oscillators (YLF, LML, Ti:Sa) were used throughout the experiment to generate the 1.054 μm interaction pulse. Typical operating parameters for the interaction pulse were 10-20 J on target in a pulse duration of 1-4 ps , focused in a spot of 10-20 μm in diameter. Consequently, intensities above 10^{18} W/cm^2 were obtained on an average shot.

Both heating and interaction beams were focused onto target by an f/5 Off-Axis Parabolic mirror (OAP). The green heating beam was injected into the short pulse beamline through the back of the last turning mirror before the OAP. A small divergence was imposed on the heating beam with a telescope, in order to obtain a heating focal spot much larger than the one of the interaction beam. The delay between heating and interaction pulses could be varied, thus allowing interaction with the plasma at different stages of its evolution.

The plasma was diagnosed with a temporally independent probe pulse, which was split-off of the uncompressed interaction beam. The probe pulse was then compressed on a pair of gratings and frequency doubled in a KDP crystal, resulting in a probe wavelength of 0.527 μm and a pulse duration of few picoseconds. The spatial resolution of the optical system was about 1 μm. A Nomarsky modified interferometer [7] allowed 2-D, time resolved density maps of the preformed plasma to be obtained. Schlieren photography [8] with a sensitivity of 5 mrad, was used to observe the effects of the interaction on the plasma. Polarimetry [8] measurements were also performed in order to detect magnetic fields generated during the interaction. These last measurements, very sensitive to emission noise, required the probe wavelength to be Raman shifted to 622 nm. An f/2.5 lens collected the radiation transmitted through the plasma. Two Streak Cameras, set respectively to collect green and infrared light, were used to observe, with resolution of few picoseconds, the temporal evolution of the transmitted radiation. Spectra of the backscattered radiation were obtained with grating spectrometers using a 1200 lines/mm grating (linear dispersion 15 A/mm).

EXPERIMENTAL RESULTS

Initially, the preformed plasma was characterised via interferometry. In fig.1, an interferogram taken 130 ps after the peak of the heating beam is shown, together with the density map obtained from it. The heating irradiance was 5 x 10^{12} W/cm^2, in a focal spot of about 300 μm in diameter (FWHM). As it can be seen from the reconstructed density profile, density measurements were possible only for electron density values lower than 10^{20} cm^{-3}. In fact, in the high density region closer to the original target position, the density gradients were large enough to refract the probe light out of the collecting optics. The density profile in these regions was inferred by 1-D simulations, performed with the hydrocode MEDUSA.

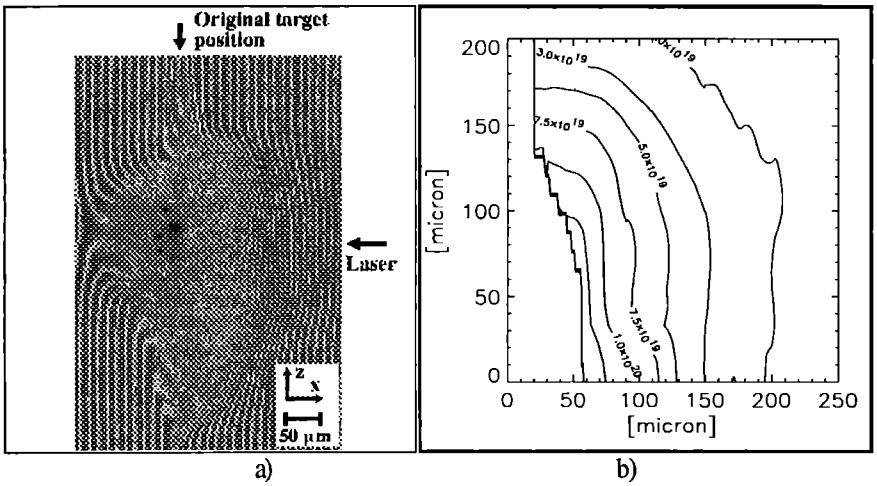

a) b)

Fig. 1. a) Interferogram of the preformed plasma, taken 100 ps after the peak of the heating beam (0.527 μm, 400 ps), for an heating beam irradiance of 5 x 10^{12} W/cm^2. b) 2-D electron density map obtained from the interferogram.

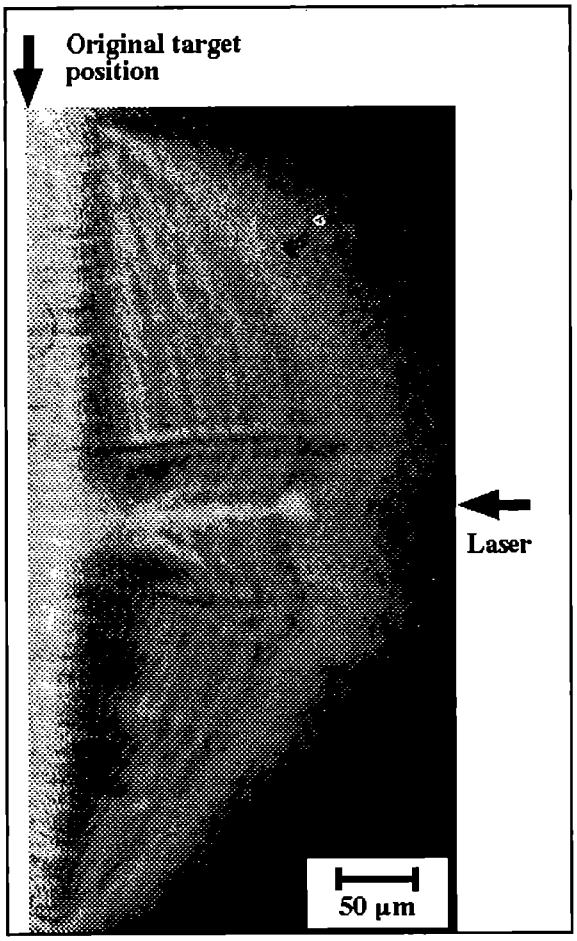

Fig. 2. Time-resolved Schlieren image taken 30 ps after the interaction of an 1 ps, 1.054 µm pulse at irradiance 3.5×10^{18} W/cm^2 with the preformed plasma of Fig. 1. The narrow channel feature visible in the centre of the plasma is due to time integrated second harmonic emission.

INTERACTION WITH UNDERDENSE PLASMAS

The optical probe was also used to diagnose the interaction. In Fig. 2, a Schlieren image of the plasma is shown, taken 30 ps after the interaction with the preformed plasma of Fig.1. The power of the interaction pulse was 10^{13} W. The focal spot was 20 µm in diameter, giving an average irradiance of 3.2×10^{18} W/cm^2. The density distribution 30 ps after the interaction is imaged, with picosecond temporal resolution.

The most striking feature in the image is the narrow second harmonic emission filament visible in the centre of the plasma. This feature, present in a high number of experimental observations, is time-integrated, and corresponds to radiation emitted during the interaction. It can therefore be interpreted as a signature of the spatial extent of the interaction beam in the plasma. The diameter of the channel is about 5 µm, while its length is about 130 µm, i.e. more than 6 times the Rayleigh length corresponding to the diameter size. From comparison with the preformed plasma profile, it can be seen that the laser pulse focuses down to a 5 µm size at a density of 0.05 n_c. It has to be noted that the laser power was well above the threshold for relativistic self-focusing [4] at that density.

Strong channelling of the pulse in near critical underdense plasma was recently predicted by 3-D PIC simulations [9] (fig. 3). The physical mechanisms involved in the channelling process are the following: as the short pulse undergoes relativistic self-focusing, fast electrons are accelerated in the direction of laser propagation, generating large quasi-static magnetic fields. The magnetic fields are in turn effective in pinching the electron current, confining it into a narrow, collimated beam. The propagating laser light follows the electron deflection and, consequently, the pulse channels itself through the plasma.

The results obtained with the other diagnostics seem to confirm the scenario described above. Second harmonic spectra of the backscattered radiation showed a pronounced red shifted broadening, that can be explained as a Self Phase Modulation (SPM) effect in the context of the channelling assumption. As the pulse self-focuses into the channel, ponderomotive expulsion of the electrons, and consequently of the ions, takes place. The pulse then travels through a medium in which the refractive index is rapidly varying, and consequently the phase of the pulse is modulated. Since the derivative of the refractive index stays positive during the pulse propagation, the broadening is on the red side of the spectrum [10]. Two scenarios are plausible: either the interaction pulse undergoes SPM during the propagation (and then transfers the modulation to the second harmonic radiation emitted) or the 2ω itself is directly phase modulated. For the interaction conditions of fig.3 typical broadening observed were in the range 400 - 600 Angstrom.

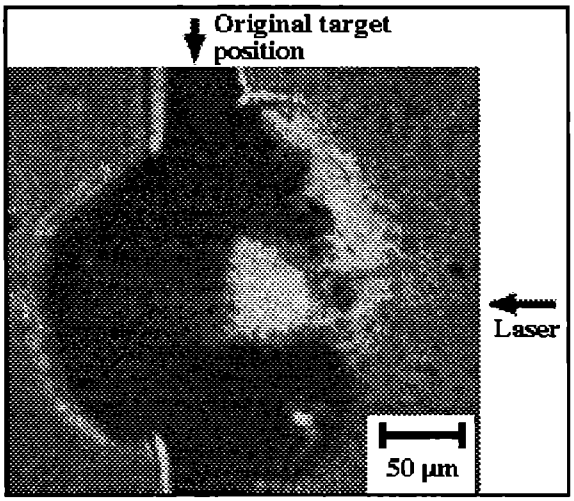

Fig. 3. Polarigram taken during the short pulse interaction with a preformed plasma in the same conditions of fig. 1.

Preliminary measurements of the magnetic fields generated during the interaction were also performed, with a polarimetric technique (for details on the experimental method see M.Borghesi et al., *Measurements of self-generated.*, also in this report). From the polarigram the rotation undergone by different parts of the probe beam, and consequently the magnetic field distribution, can be reconstructed. From the polarigram of fig. 4, taken during the interaction, the presence of two different type of toroidal magnetic fields is suggested. The first (with an amplitude of a fraction of a MG), corresponds to the rotation detectable on the outer edge of the plasma, on the laser side. The second, more intense field (about 2 MG), correspond to the bright and dark regions closely surrounding the laser axis. The direction of the field on the outer edge of the plasma is as expected in case of field generation due to $\nabla n \times \nabla T$ mechanisms [11]. No field was measured in absence of interaction, so the density and intensity gradients generating the fields are produced (or considerably enhanced) by the interaction pulse. Direction and amplitude of the inner field would substantially agree with the PIC code predictions for the quasi-static magnetic fields responsible for pinching the

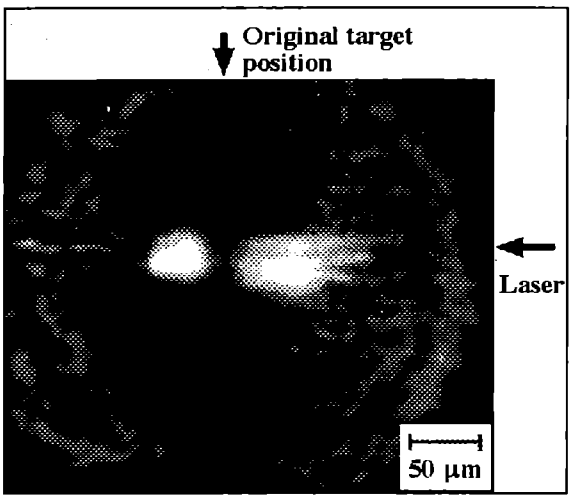

Fig. 4. Time-resolved Schlieren image taken 30 ps after the preformed plasma in conditions close to Fig.2. Three second harmonic emission channels, that coalesce in a single structure, are visible in the picture.

short pulse and confining it into the channel. Further investigations are however necessary to confirm these assumptions.

In some experimental observations, the laser beam appeared to break up into more than one filament, and coalescence of the corresponding emission channels in a single structure was observed. In the Schlieren image of fig. 4, three filamentary structures are visible, that collapse in a single channel as they propagate through the plasma. Such phenomenon was also observed in 2-D and 3-D [9] PIC simulations, and was attributed to magnetic interaction between the filaments.

INTERACTION WITH OVERDENSE PLASMAS

The interaction with an overdense plasma was also studied. In particular, an experimental method for the detection of overdense propagation was devised and tested. In fig. 5 experimental results obtained with the Streak Camera set to collect the green transmitted radiation are shown. It can be seen that the target is transparent to the rising edge of the heating pulse, before a plasma is created. Then, as soon as an initially overdense plasma is created, no heating radiation is transmitted, until the plasma goes underdense. A sharp line is also visible, due to 2ω emission generated by the interaction pulse. This feature can be considered as a time fiducial of the interaction, and used to infer, from comparison with 1-D simulation and interferometric data, at which stage of the plasma evolution the interaction took place. For the situation of fig. 5b, the MEDUSA predictions suggest that the pulse propagated through a plasma of peak density 2×10^{21}cm^{-3} ($2n_c$ for λ=1 µm). The theory [6] predicts an increase of the effective critical density seen by the pulse given by

$$n_{c_{eff}} = n_{c_0}\left(1+\frac{I\lambda^2}{10^{18}}\right)^{0.5}$$

An intensity of 3×10^{18} W/cm^2 is therefore just sufficient to propagate through a plasma of density $2n_c$. Due to the limited number of data available, this has to be considered more a study of feasibility than a conclusive experimental study.

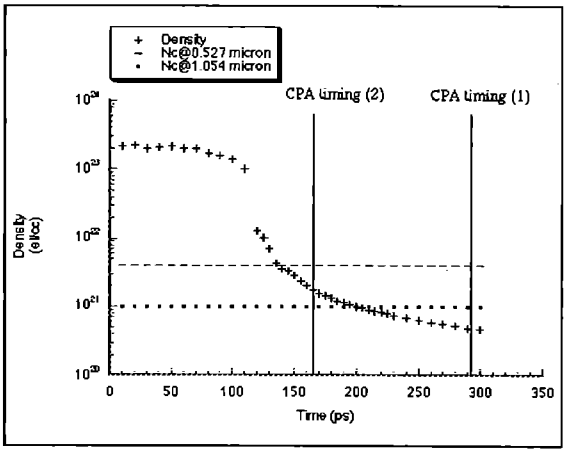

Fig. 5. Temporal evolution of the green radiation transmitted through the plasma, for an heating beam irradiance of 7×10^{12} W/cm^2. In a) the delay between the CPA pulse and the heating beam was 320 ps, and the CPA irradiance 2×10^{18} W/cm^2. In b) the delay was 165 ps and the CPA irradiance 3.5×10^{18} W/cm^2.

Fig. 6. Plasma peak density vs time as predicted by 1-D simulations (MEDUSA 102) for the heating conditions of fig. 5. The vertical lines show the CPA timing in the shots of fig. 5.

CONCLUSION

The interaction of short pulses at relativistic intensities with preformed plasmas has been experimentally studied in different plasma conditions. The propagation in near critical underdense plasmas appeared to be characterised by strong self channelling of the pulse, as predicted by 3D PIC simulations. A preliminary study of the possibility of overdense propagation has also been performed.

REFERENCES

1. W.Tajima and J.Dawson, Phys.Rev.Lett. **43**, 267 (1979)
2. D.C.Eder, P.Amendt, S.C.Wilks,Phys.Rev.A **45**, 6761 (1992)
3. M.Tabak et al, Phys. Plasmas **1**, 1626 (1994)
4. P.Sprangle, E.Esarey, Phys.Fluids B **4**,2241 (1992)
5. P.Monot et al., Phys.Rev.Lett. **74**, 2953 (1995)
6. P.Kaw, J.Dawson, Phys. Fluids **13**, 472 (1970)
7. R.Benattar, C.Popovics, R.Sigel, Rev. Sci. Instruments **50**, 1583 (1979)
8. O.Willi, in *Laser Plasma Interaction 4*, Proceedings of the XXXV SUSSP, St Andrews (1988)
9. A.Pukhov and J.Meyer ter Vehn, Phys. Rev. Lett. to be published (1996)
10. D.Giulietti et al, Opt. Comm. **106**, 52 (1994)
11. J.A.Stamper, Laser & Part. Beams, **9**, 841 (1991)

MEASUREMENT OF MAGNETIC FIELDS GENERATED IN SHORT-PULSE INTERACTION WITH MATTER

M.Borghesi, A.J.Mackinnon and O.Willi

The Blackett Laboratory, Imperial College of Science, Technology and Medicine, London (UK)

INTRODUCTION

Large spontaneous magnetic fields are produced by laser-plasma interactions when a short, powerful laser pulse is focused in a small diameter focal spot on solid targets. The interaction is strongly affected by the presence of these large magnetic fields, through several processes [1]. Recent studies suggested that, for multiterawatt, picosecond interaction pulses, the field produced can be strong enough to pinch the plasma and lead to the formation of plasma jets [2].

Measurements of magnetic fields generated in the interaction of a ps pulse at relativistic irradiance with solid targets and preformed plasmas are reported. At our knowledge, these are the first experimental results available in this interaction regime.

EXPERIMENTAL METHOD

The experiment was undertaken using the Vulcan laser in the CPA operation mode. Pulses of duration 1-3 ps, λ=1.054 μm were focused on 125 μm Al wires with an f/5 off axis parabola. The pulses were produced either by the Ti:Sa or the YLF oscillators: in the first case the pulse was superimposed on a 200 ps pedestal, in the second case on a 70 ps one. The energies deposited on target, in a focal spot of 10 μm diameter, were in the range 10-30 J, corresponding to irradiances in the range 3 10^{18} - 1 10^{19} W/cm^2. The plasma was diagnosed with a temporally independent probe pulse, split-off of the interaction beam before recompression. The probe pulse was compressed on a separate pair of gratings, frequency doubled in a KDP crystal to 0.527 μm and finally Raman shifted in ethanol to 0.622 μm.

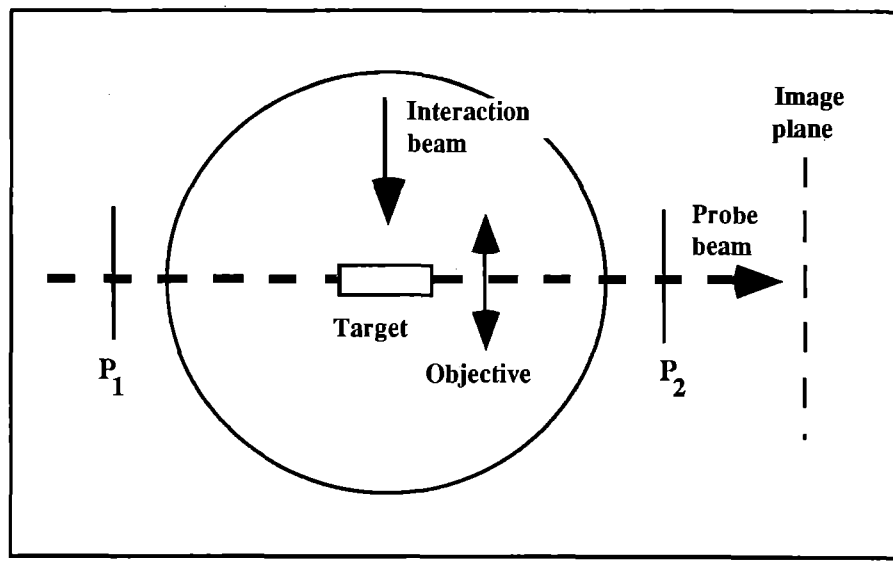

Fig. 1. Diagnostic arrangement for polarimetric measurements.

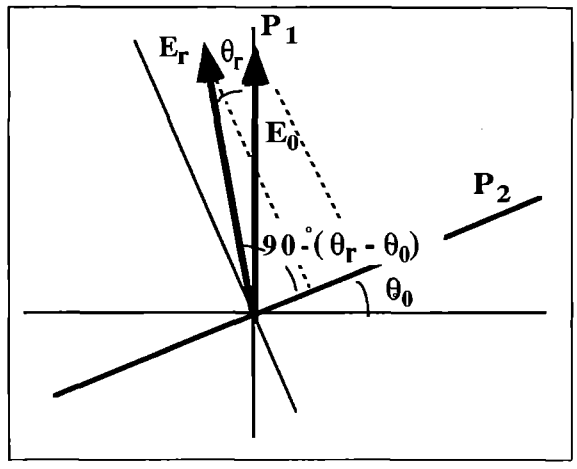

Fig. 2. If the angle between the axes of P1 and P2 is less than 90° clockwise rotations lead to an increase in the transmitted intensity, counter clockwise rotations to a decrease.

Measurements of magnetic fields generated during the CPA interaction with preformed plasmas were also performed. The experimental arrangement used in these measurements is described in [3], also in this report.

The magnetic fields were measured with a polarimetric technique [4]. The experimental set-up is shown in fig. 1. The probe was linearly polarized before the interaction chamber by a polarizer P_1, and analysed after the plasma through a second polarizer P_2. The magnetic fields are detected through local depolarization induced by Faraday rotation effects on the probe beam. It is well known that the effect of the propagation of an e.m. wave through a plasma in the presence of a static magnetic field $\underline{B}$ is the rotation of the $\underline{E}$ vector of the wave by the angle θ_r, given by

$$\theta_r[rad] = 2.6 \cdot 10^{-17} \lambda^2[cm] \int_L n_e[cm^{-3}] \underline{B}[G] \cdot \underline{dl}[cm] \qquad (1)$$

where λ is the wavelength of the radiation, n_e the electron density of the plasma and L the distance travelled in the plasma. The direction of rotation is counter clockwise (for an observer facing

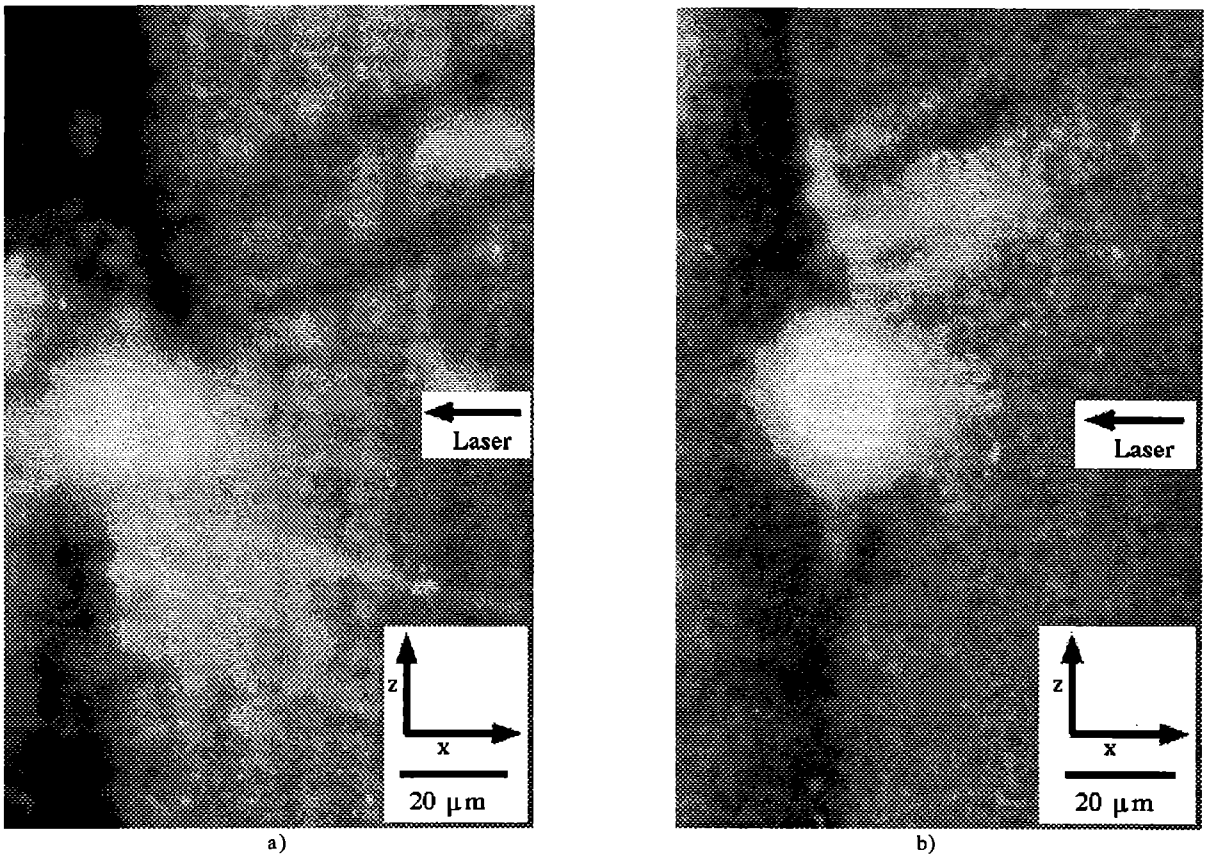

Fig. 3. Polarigrams taken during the interaction of a 1 ps, 9 TW pulse with an Al target. In a), the angle α between the axes of the polarizers was 100° (θ_0 = +10 °), in b) the angle was 80° (θ_0 = -10 °). As expected the dark and bright pattern due to Faraday rotation is inverted, when θ_0 (see fig. 2) is varied from positive to negative values

the probe beam) if B is parallel to the K vector of the probe beam and clockwise if the two vectors are antiparallel. Rotation of the E vector causes intensity variations in the image plane: the regions in the image plane corresponding to zones of the plasmas where magnetic fields are present will be darker or brighter than the background depending on the direction of rotation. If the angle between the polarizer axis is $\alpha = 90 - \theta_0$ (see fig. 2), in correspondence to a rotation by θ_r the transmitted intensity is

$$I_r = I_0 \sin^2(\theta_0 - \theta_r)$$

while the background transmitted intensity is

$$I_r = I_0 \sin^2(\theta_0).$$

Counter clockwise rotations lead in this case to a decrease in transmitted intensity, clockwise rotations to an increase. The opposite happens if the angle between the axes of the polarizers is $90 + \theta_0$. From the intensity distribution in the image plane, a map of rotation angle in the plasma can be obtained, as:

$$\theta_r = \theta_0 - \frac{1}{2}\arccos\left(1 - 2\frac{I_r}{I_0}\sin^2(\theta_0)\right)$$

From θ, via Abel inversion of (1), the product nB can be extracted. If an independent measurement of the density is available, the distribution of magnetic field in the plasma can finally be obtained. In the reported experiment, the density was measured using a Nomarsky modified interferometer [4].

INTERACTION WITH SOLID TARGETS

The analysis of the data is currently in progress, therefore only preliminary results will be shown. Polarimetric measurements were performed at different times during the evolution of the plasma. The temporal resolution of the measurements, depending on the duration of the probe pulse, was a few picoseconds.

Magnetic fields were detected only when the probe pulse was coincident with the interaction pulse. The polarigrams of fig. 3 were taken in the following conditions. The power on target was 9 TW (Ti:Sa oscillator), in a focal spot of 10 μm, resulting in an irradiance of 10^{19} W/cm^2. The two polarizers were 10 degrees off crossed. In the polarigram of fig. 3a, (polarizers +10 degrees off crossed),a dark region and a bright region, corresponding to a toroidal magnetic field surrounding the interaction axis, are visible respectively below and above the intense, central self emission spot. The pattern is inverted in fig. 3b, when the two polarizers were set -10 degrees off crossed. The intensity variations correspond to rotation angles less than 1 degree. In fig. 4a the density profile of the plasma during the interaction is shown. By Abel inverting the rotation angle distribution extracted from the picture (assuming cylindrical symmetry), and dividing by the electron density, the B-field map of fig. 4b is obtained.

The larger magnetic fields observed were of the order of 1 MG, in all the measurements performed in these experimental conditions. The direction of the fields detected is as expected in case of field generation due to $\nabla n \times \nabla T$ mechanisms [1]. As mentioned above, no magnetic fields were detected in measurements at later times (at about 20 ps after the interaction).

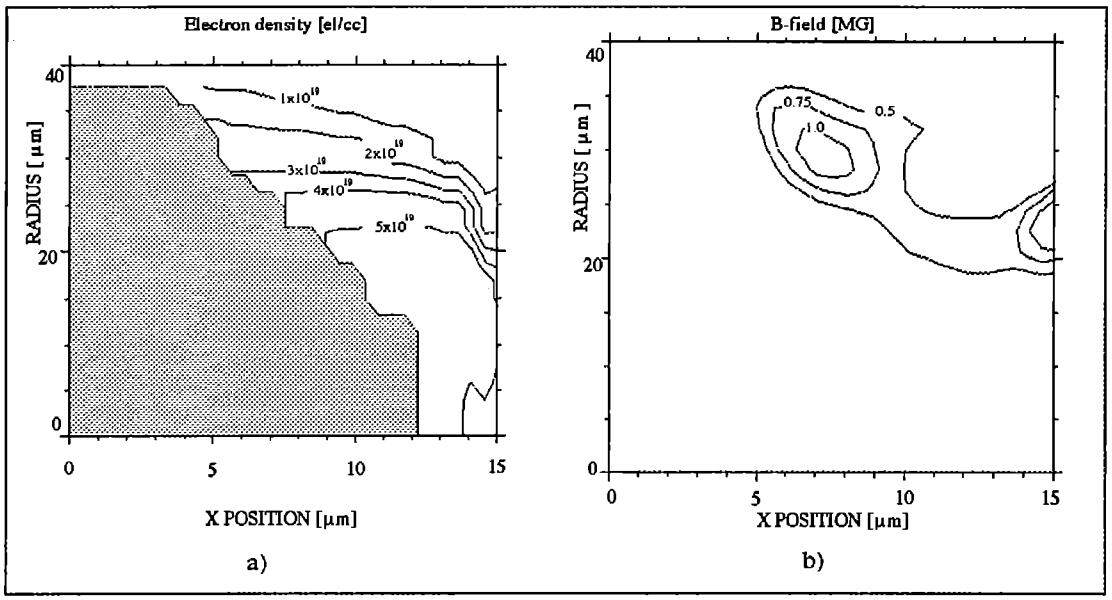

Fig. 4 a) Density profile of the plasma during the interaction, in the conditions of fig. 3. b) B-field map extracted from the polarigram of Fig. 3b. The X position is measured from the target surface, the radius from the interaction beam axis.

Measurements performed using the YLF oscillator gave substantially the same results.

INTERACTION WITH PREFORMED PLASMAS

The same method was also used to measure the magnetic fields generated in the interaction of the CPA pulse with underdense preformed plasmas . The polarigram of fig. 5 was taken during the interaction of a CPA ps pulse at an irradiance of 3 10^{18} W/cm^2 with a preformed plasma. The plasma was produced from a 0.5 μm thick plastic foil by a heating beam at irradiance below 10^{13} W/cm^2 (for details see [3], also in this report). A clear bright-dark pattern is visible along the edge of the plasma, on the laser side. Through the same process described above, the magnetic field distribution of fig. 6 was obtained. The direction of the field on the outer edge of the plasma is also in this case consistent with $\nabla n \times \nabla T$ field generation mechanisms [1]. The rotation angle detected were as large as in the solid targets measurements (about 1°), but in this case, due to the larger size of the plasma and the higher electron density, the corresponding magnetic fields were only of the order of a fraction of a MG. Since no magnetic field was detected in absence of interaction, the density and temperature gradients must have been produced (or enhanced) by the short pulse itself. A second dark and bright pattern, opposite to the one mentioned above, is also visible in the image, in the region closely surrounding the laser axis. The amplitude of the corresponding field can be estimated as 1-2 MG. A discussion about the mechanisms that could be responsible for generating such a field can be found in [3].

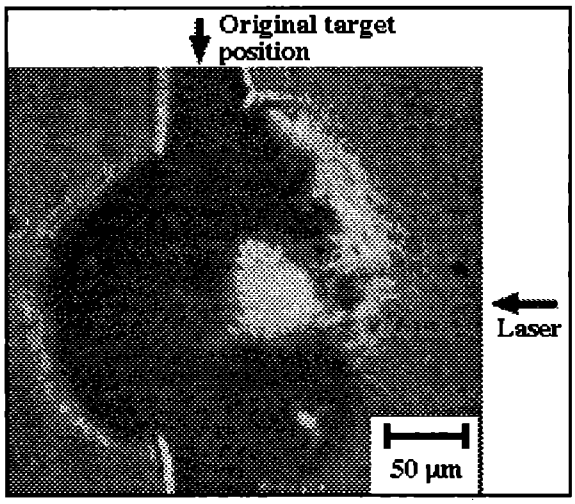

Fig. 5. Polarigram taken during CPA interaction with a preformed plasma

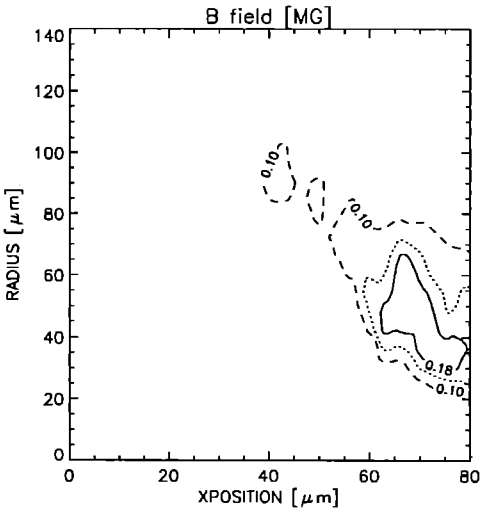

Fig. 6. B field distribution obtained from the polarigram of fig. 5

REFERENCES

1. J.A.Stamper, Las.& Part.Beams, **9**, 841 (1991) and references within.
2. A.R.Bell, Phys.Rev.E, **48**, 2087 (1993)
3. M.Borghesi et al, *Interaction of.an intense, short pulse with a preformed plasma* , in this report
4. O.Willi, in *Laser Plasma Interaction 4*, Proceedings of the XXXV SUSSP, St Andrews (1988)
5. R.Benattar, C.Popovics, R.Sigel, Rev.Sci.Instruments **50**, 1583 (1979)

SHORT PULSE PROPAGATION THROUGH PREFORMED PLASMAS

A.Giulietti[1], M.Borghesi[2], C.Danson[3], D.Giulietti[4], L.A.Gizzi[1], A.Macchi[1] and D.Neely[3]

[1]Istituto di Fisica Atomica e Molecolare del CNR, Pisa, Italy
[2]The Blackett Laboratory, Imperial College of Science, Technology, and Medicine, London, UK
[3]Central Laser Facility, Rutherford Appleton Laboratory, Chilton, UK
[4]Dipartimento di Fisica, Università di Pisa, Italy

INTRODUCTION

The study of the interaction of intense laser pulses with long scalelength plasmas is of crucial importance for laser-driven Inertial Confinement Fusion (ICF). In fact, the conditions of laser-plasma coupling in the expanding underdense *corona* surrounding the ICF capsule are critical in order to determine, for example, the level of energy absorption, the uniformity of energy deposition and the possible generation of fast electrons leading to undesirable target preheating.

Thanks to the recent developments in laser technology, the generation of ultrashort (<1 ps), high-intensity (>10^{17} Wcm^{-2}) laser pulses is nowadays possible. In this regime the oscillating electric field can be comparable with the atomic field, and the electron *quiver* velocity can approach relativistic values; the ponderomotive pressure can be on the order of Gbars. On the other hand the laser pulse duration becomes comparable to the time scale of atomic and plasma processes. The study of laser-plasma interactions in this regime is of great physical interest since the dynamics is typically nonlinear and can lead to a number of new light-induced phenomena [1]. Moreover the propagation of an ultrashort pulse is of crucial interest for a number of scientific applications including the new *fast ignitor* scheme for ICF [2], which is presently being investigated in a number of experiments world-wide.

Our experiment was devoted to the study of the propagation of a short laser pulse with an intensity between 10^{16} and 10^{17} W cm^{-2} through a long-scalelength underdense (n_e<n_c/10), hot (T_e>500 eV) plasma, preformed by irradiation of a thin dot target by opposite pairs of laser beams. The experimental geometry was essentially the same of a previous experiment in which the preformed plasma was accurately characterized and found very suitable as a test bed for the study of coronal interactions [3]. Significant progresses in the chraracterisation of the preformed plasma were achieved in the reported experiment thanks to the use of a ps pulse probe and are described elsewhere in this Report [4].

In the conditions of the experiment, collisional absorption of laser light was virtually suppressed due to the high intensity of the laser pulse. However, the short pulse energy could be absorbed through residual ionization processes in the Al plasma.

In this paper we show and briefly discuss preliminary experimental results concerning the propagation of the short pulse in the plasma.

SET-UP

The experiment was performed in the Target Area East of the Central Laser Facility. The target consisted of a thin (0.4 μm) Al dot with a 0.8 mm diameter, coated on a thin plastic substrate or held by four arms in the shape of a X. Four 600 ps, 1 μm wavelength beams from the VULCAN laser were focused on the target at oblique incidence in opposite pairs to preform the plasma. The heating irradiance on each target side was kept below 10^{14} W cm^{-2}. A detailed description of the production technique and of the diagnostics used for characterising the plasma is presented in [3,4].

The short interaction pulse (1 ps duration and energy up to 10 J) was generated with the CPA technique. A minor portion of the pulse was split, frequency doubled and used as an optical probe for interferometric measurements of the plasma density. The interferometric technique is described in detail elsewhere in this Report [4]. The interaction pulse was focused with either a *f*/15 or a *f*/7.5 optics in a spot smaller than the plasma cross section, in order to avoid refraction effects at the plasma boundary. The short pulse interacted with the preformed plasmas 2-2.5 ns after the peak of the heating beams.

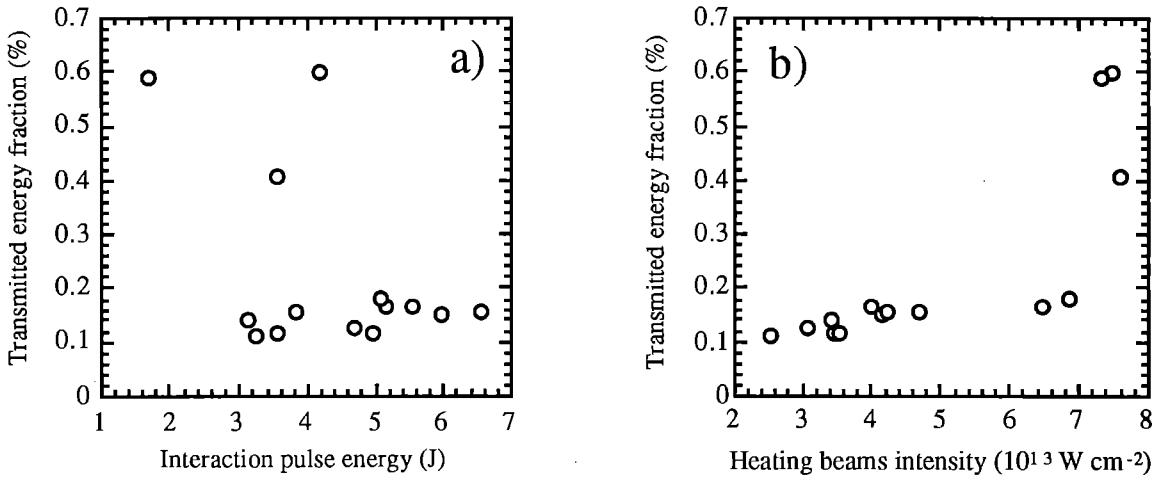

Fig. 1: transmitted energy fraction of the short interaction pulse vs. a) interaction pulse energy and b) heating beams energy.

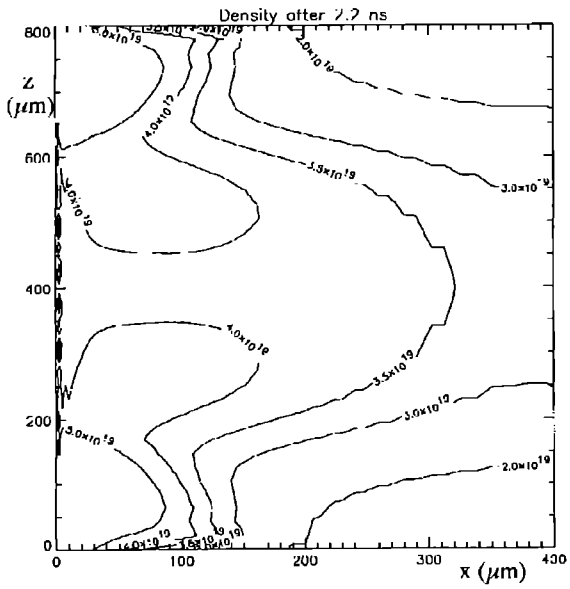

Fig. 2: POLLUX 2-D simulation of the plasma electron density at times corresponding to the short pulse interaction. The original target position is at x=0, y=400. The heating intensity is $8 \cdot 10^{13}$ Wcm^{-2}.

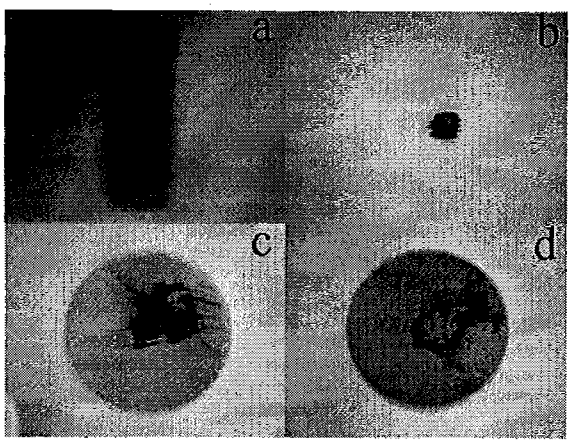

Fig. 3: cross-section images of the short pulse interaction beam a) before interaction: b) after propagation in absence of the plasma; c,d) after propagation in the plasma for two different values of the heating beams intensity (see text).

investigated via calorimetry and beam cross-section imaging of the fraction of the pulse transmitted through the plasma. Density perturbations induced in the plasma by the short pulse were studied by delaying the interferometric probe pulse in order to obtain density maps of the plasma at various instants after the interaction.

STUDY OF SHORT PULSE TRANSMISSION

The characterization of the preformed plasma is described in detail in refs. [3,4]. Here we only discuss results relative to the short pulse propagation.

The energy of the short interaction pulse transmitted through the preformed plasma was monitored using a calorimeter. The background contribution due to plasma self-emission and scattered heating radiation was measured in shots in which only the heating beams were focused on target.

The transmitted energy fraction of the short interaction pulse was studied as a function of both interaction and heating intensity. The results are shown in fig. 1. It can be noticed that in the investigated intensity range the short pulse transmission through the plasma is substantially not related to the energy of the short pulse itself, while it depends from the heating intensity through a sort of threshold mechanism. In other words, the hydrodynamic evolution of the preformed plasma appears to play an essential role in determining the conditions of the propagation process.

For heating intensities above $7 \cdot 10^{13}$ Wcm^{-2}, the density and temperature distribution of the plasma 2 ns after the plasma production seems to be favourable for efficient propagation of the interaction pulse. 2-D hydrodynamic simulations performed using the POLLUX code [5] predicted, for an heating intensity of $8 \cdot 10^{13}$ Wcm^{-2}, the onset of a density depression along the symmetry axis approximately 2 ns after the plasma production (see fig. 2). This suggests that the short pulse propagates with low losses provided a (even weak) density minimum is set along the propagation axis. The influence of the preformed plasma conditions on the short pulse propagation can also be inferred from the cross-section images of the transmitted interaction beam. Fig. 3a shows the beam cross-section before the interaction chamber. The rectangular shape is due to the cut-off from the CPA gratings.

Fig. 4: interferogram of the plasma 300 ps after the interaction with the short pulse. The horizontal arrow shows the short pulse interaction axis. The vertical arrows show the original target position.

Fig. 3b shows the beam intensity profile after propagation in the chamber in absence of the target. Finally, Fig. 3c and 3d show the beam cross section images after propagation through the preformed plasmas at heating irradiances of $5 \cdot 10^{13}$ Wcm^{-2} and $8 \cdot 10^{13}$ Wcm^{-2} respectively.

The background light is due to plasma self-emission and scattered light from the heating beams. From the comparison of the two latter images we see that, when the heating irradiance was higher, the short pulse was sensibly less refracted by the plasma.

DENSITY MAPPING AFTER SHORT PULSE PROPAGATION

As mentioned above, 2-D density maps of the preformed plasma before the interaction with the short pulse were reconstructed from the fringe intensity pattern of the interferograms. Due to the high interferometer sensitivity [3] even weak, small-scale density perturbations, as those induced by the short pulse propagation through the plasma, could be detected from the fringe displacement.

Fig. 4 shows an interferogram taken 300 ps after the interaction of the CPA pulse with the plasma. From this interferogram a density perturbation of about 1/10 of the local electron density was evidenced along the short pulse propagation axis. This density perturbation was likely due to ionization induced by the short pulse.

Since the light collected by the detector was spectrally filtered around 0.527 μm, the picture in fig. 4 is also an image in 2nd harmonic light (time-integrated) of the plasma. The dark features are due to 2nd harmonic produced both by the heating and the interaction pulses, and their analysis is also expected to give interesting information on the physics of the interaction.

CONCLUSION

We studied the propagation of a 700 fs laser pulse in a plasma preformed by irradiation of thin foil targets. The propagation of the pulse appeared to be strongly affected by the preformed plasma conditions, while in the investigated range seemed to be independent from the energy of the pulse itself. The short pulse energy fraction transmitted through the plasma was sensibly higher for heating energies above the threshold value 8 1013 W/cm2. Cross section imaging also showed that above this threshold refraction effects became less severe.

Density perturbations induced by the short pulse propagation were detected via interferometry.

The analysis of the experimental data is however still in progress.

ACKNOWLEDGEMENTS

We acknowledge the continuous and enthusiastic support of the CLF technical staff. The experiment was supported by EC in the framework of the Access to Large Facilities of the Human Capital and Mobility Programme.

REFERENCES

1. P.Mulser, *Theory of short pulse interaction*, in Laser-Plasma Interactions 5, SUSSP publications (1996); P.Sprangle & E.Esarey, Phys. Fluids B **4**, 2241 (1992), and references therein.
2. M.Tabak, J.Hammer, M.Glinsky, W.Kruer, S.Wilks, J.Woodworth, E.Campbell, M.Perry, Phys.Plasmas **1**, 1626 (1994)
3. L.A.Gizzi, D.Giulietti, A.Giulietti, T.Afshar-Rad, V.Biancalana, P.Chessa, C.Danson, E.Schifano, S.M.Viana, and O.Willi, Phys.Rev.E **49**, 5628 (1994); Phys. Rev.E **50**, 4266 (1994)
4. M.Borghesi, A.Giulietti, D.Giulietti, L.A.Gizzi, A.Macchi, O.Willi, *Production and characterization of underdense plasmas for interaction studies,* in this report.
5. G.J.Pert, J.Comput.Phys. **43**, 111 (1981)

PRODUCTION AND CHARACTERISATION OF UNDERDENSE PLASMAS FOR INTERACTION STUDIES

M.Borghesi[1], A.Giulietti[2], D.Giulietti[3], L.A.Gizzi[2], A.Macchi[2] and O.Willi[1]

1 The Blackett laboratory, Imperial College of Science, technology and Medicine, London (UK)
2 Istituto di Fisica Atomica e Molecolare, CNR, Pisa (Italy)
3 Dipartimento di Fisica, Universita' di Pisa, Italy

INTRODUCTION

The study of laser interaction with long scale, underdense plasmas, crucial for ICF applications, requires suitable plasmas to be produced in a controllable way. A well established and flexible method consists in exploding a thin target by irradiating it with laser pulses. By appropriately choosing the pulse and target parameters, plasmas in a wide range of densities and temperature can be obtained with this technique. Both diagnostic development and target design are fundamental issues, in view of a detailed characterisation of these plasmas. In particular, due to the growing interest in short pulse interaction, the development of diagnostics able to resolve physical phenomena on picosecond and subpicosecond temporal scale is strongly required.

The production and characterisation of plasmas produced by symmetrical laser irradiation of thin targets was the object of a previous experimental study by our group [1] performed at the Rutherford Appleton Laboratory in 1992. In that experiment, plasmas were produced by uniform laser irradiation from opposite sides of Al disks coated on thin, narrow stripes. Time resolved X-ray spectroscopy was used to infer the electron temperature, while 2-D electron density maps of the plasma were obtained with an interferometric technique. The resolution available in the interferometric measurements was 100 ps. This limited the readability of the interferograms, since the visibility of the fringes vanished in the inner region of the plasma, where the density variation during 100 ps was large enough to smear out the fringe pattern. A complete density map could be obtained only at late stages of the plasma evolution (typically after 4 ns from the peak of the pulse). An additional problem encountered was the deviation of the plasma from cylindrical symmetry, with the adopted target design.

We report about the progress in the production and characterisation of underdense plasmas achieved in a recent experiment, carried out with the Vulcan laser at the Central Laser Facility.

EXPERIMENTAL ARRANGEMENT

The plasma was produced by four 600 ps, 1.053 μm heating beams of the Vulcan laser, in the configuration reported in [1]. The heating beams were superimposed on target in two opposite pairs in a 650 μm FWHM focal spot for an irradiance on each side below 10^{14} W/cm^2. Each pair was composed of two beams at angles of +13 and -13 degrees to the target plane, respectively. The targets used were Al disks, alternatively coated onto 0.1 μm thick plastic foil support, or held by four tiny Al arms in the shape of a X. This second type of targets was obtained by etching of an Al thin deposit on a plastic foil. The diameter of the dots was 800 μm and their thickness 0.4 μm. A 1 ps Chirped-Pulse Amplified (CPA) beam, frequency doubled to 0.53 μm, was used as an optical probe for interferometric measurements in a line of view parallel to the target plane (see [1]).

A modified Nomarski interferometer [2] allowed to detect the phase changes undergone by the probe beam and thus measure the electron density profiles. The probe line set-up was modified with respect to the configuration of the previous experiment. A confocal optical system (composed of a microscope objective and a f/10 lens) imaged the plasma and recollimated the probe beam. A third lens was used in order to relay the image plane, so that

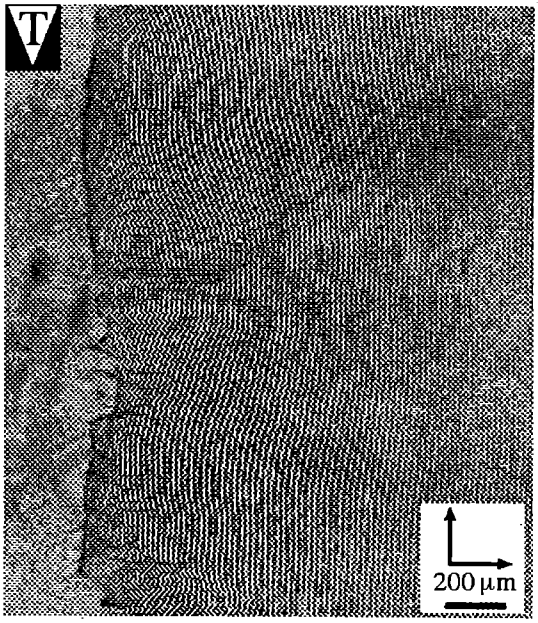

Fig. 1. Interferogram taken 2.2 ns after the peak of the heating pulses. The heating irradiance was 7.2 10^{13} W/cm^2, the duration of the probe pulse about 1 ps. The original target position is indicated by the "T" wedge.

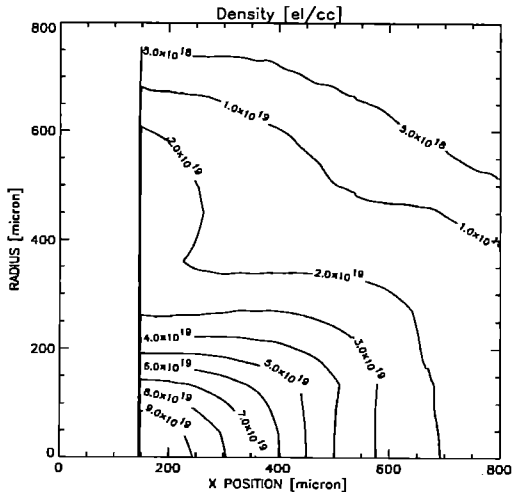

Fig. 2. Density profile obtained from the interferogram of fig. 1. The x position is measured from the original target position, the radius from the main symmetry axis.

spatial filtering could be performed in the Fourier plane of this lens. The Wollanston prism was located close to this plane.

INTERFEROMETRIC CHARACTERISATION

The use of a short pulse optical probe marked a notable progress in the interferometric characterisation of the plasma. An interferogram taken 2.2 ns after the peak of the heating beams is shown in Fig. 1. The target was an Al disk coated on a large plastic foil. The irradiance on target was 7.2 10^{13} W/cm^2 on each side.

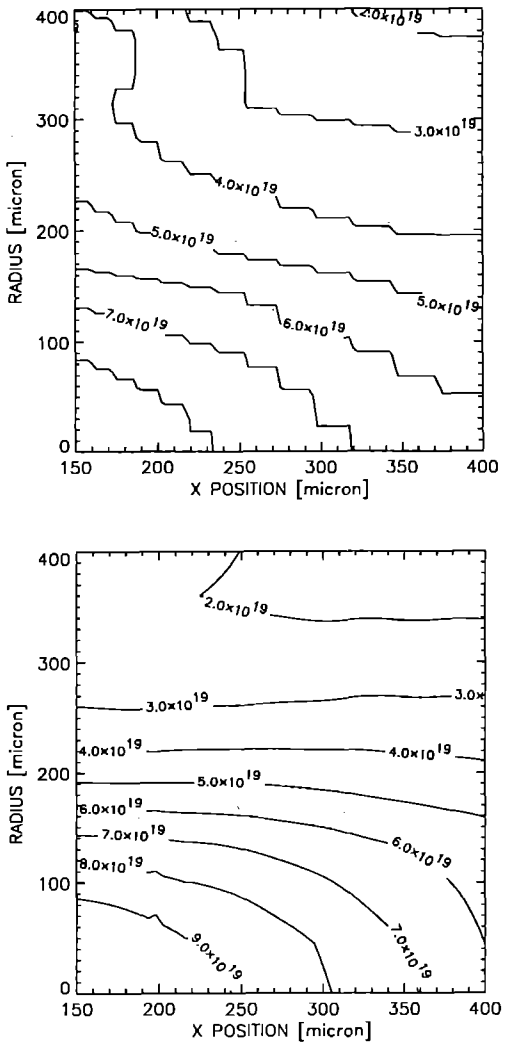

Fig. 3. 2-D predictions for the situation of fig. 2 (above), compared with the experimental profile (below).

The progress achieved is evident from comparison with interferograms obtained with the 100 ps probe [1]. In that case, even at later times, the visibility of the fringes was lost over a considerably wider region: in interferograms taken 3 ns after the plasma production, the region over which the density was not measurable extended longitudinally for 400 μm. With the picosecond probe, it was possible to measure the density profile almost over the length of the whole plasma as early as 2 ns. The density map of fig 2 was obtained from the interferogram using a Fourier transform method for the phase extraction [3], and subsequent Abel inversion [4] of the phase distribution. The Barr algorithm [5] was used to invert the Abel integral.

The hydrodynamic expansion of the plasma was simulated using the 2-D hydro-code POLLUX [6]. In fig. 3 the code prediction for the density profile in the same conditions of the interferogram of Fig. 1 is shown, together with the experimental profile. The substantial agreement with the experimental data gives confidence in 2-D simulations as a reliable and useful tool in designing experiments in this configuration.

TARGET DESIGN

The targets used in the 1992 experiment consisted in Al disks coated on plastic stripes, as wide as the disk diameter. This target design was chosen in order to avoid plasma to be produced outside the Al disks on the line of sight of the probe, since this could result in shadowing of part of the field of view. The drawback of this design was that the plasma produced from this type of targets considerably deviated from cylindrical symmetry. In fact, a plasma was created on the plastic support above and below the Al disk, that confined the Al plasma in the vertical direction. Consequently, the symmetry of the plasma was ellipsoidal rather than cylindrical, with the longer axis along the probe line.

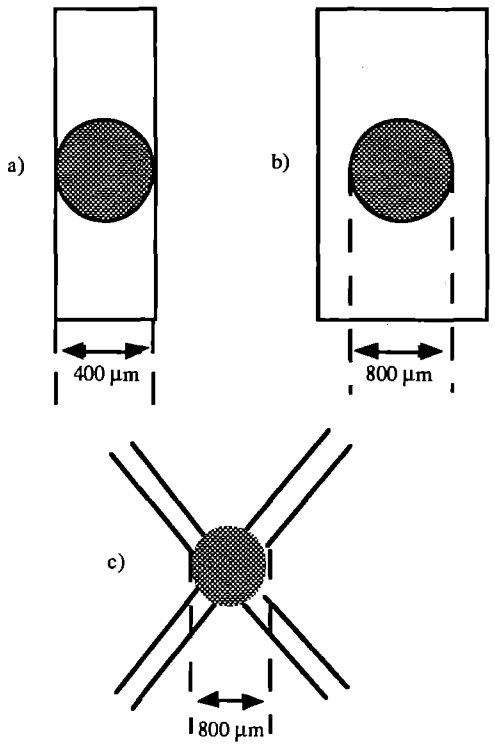

Fig. 4. The different target designs experimented: a) Al disks coated on narrow plastic foils, as used in the 1992 experiments; b) Al disk coated on large plastic foils; c) X-shaped targets.

Since Abel inversion techniques are based on the assumption of cylindrical symmetry, a systematic overevaluation resulted in the density measurements, that led to discrepancies with the numerical predictions [1].

Different target designs were experimented this time. In first place, targets in which Al dots were coated on large plastic foils were used. Plasmas produced from these targets expand with cylindrical symmetry, since a plasma is generated on the plastic support all around the Al disk.

It is not unexpected, then, that the experimental density profile was much closer to the hydrocode predictions, as seen above (fig. 3). Residual, though unsubstantial, discrepancies can be explained keeping in mind that a certain ellipticity of the plasma is however intrinsical, since in the adopted configuration the laser spots are elliptical, rather than circular. However, when using these targets, the shadow of the dense, slowly expanding plasma created on the plastic support obscures the central part of the interferogram. In the interferogram of fig. 1 the shadow extends longitudinally for 150 μm from the original target position.

In interaction studies this limitation can be highly undesirable, since, in order to follow the propagation of an interaction pulse, it may be necessary to visualize the interference fringes over the length of the whole plasma [7]. *X-shaped* targets, in which the Al disk is held by four Al arms, showed to be more suitable for this purpose. Since no plastic is present on the line of sight of the probe, the field of view is not limited by any shadow when using these targets. An interferogram of a plasma obtained from one of these targets is shown in fig. 4. As it can be seen, this particular target design, together with the short duration of the probe pulse,

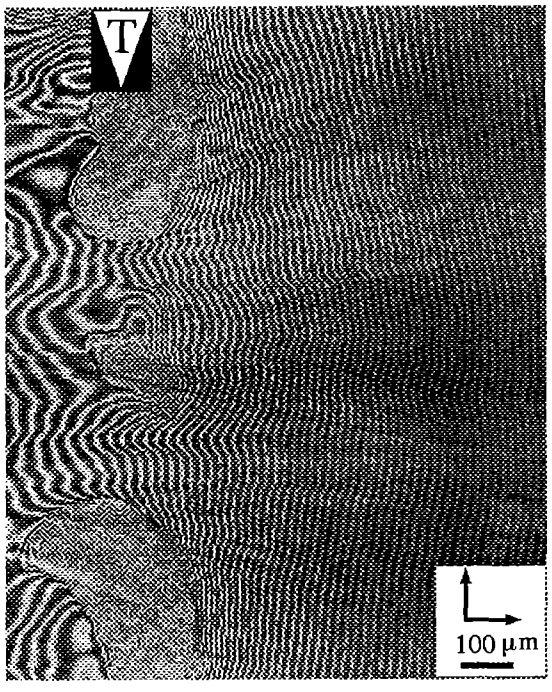

Fig. 5. Intereferogram of a plasma produced from an X-shaped target, taken 2.2 ns after the peak of the heating pulses.

ensured excellent fringe visibility virtually throughout the whole plasma.

Unfortunately the width of the Al arms could not be reduced below 200 μm, due to technical constraints in the target preparation. As a consequence, the plasma produced on the arms by the outer edges of the laser spot introduced a non negligible perturbation to the symmetry of the whole plasma in the region closer to the original target position.

In the interferogram of fig. 5 the longitudinal extent of this region is about 300 μm. An approximate value for the electron density could anyway be obtained in that region, while the deconvolution of the interferogram at distances further away from the original target position did not present any problem.

CONCLUSION

Long scale, underdense plasmas suitable for interaction studies were produced by uniform laser irradiation from opposite sides of thin targets. The plasmas were characterised via optical interferometry with picosecond resolution. The use of a picosecond pulse probe led to relevant progresses in the plasma characterisation with respect to previous results obtained with a lower temporal resolution. Different target design were experimented and their relatives merits compared.

We would like to acknowledge the whole staff of the Central laser facility for the help received in preparing and performing the experiment, and in particular the Target Preparation Area for precious discussions about the target design.

The experiment was supported by EC in the framework of the Access to Large Facilities of the Human Capital and Mobility Programme.

REFERENCES

1. L.A.Gizzi et al, Phys. Rev. E **49**, 5628 (1994)
2. R.Benattar, C.Popovics, R.Sigel, Rev. Sci. Instruments **50**, 1583 (1979)
3. M.Takeda, H.Ia, S.Kobayashi, J.Opt.Soc.Am. **72**, 156 (1982)
4. R.N.Bracewell, Austral.J.Phys. **9**, 198 (1956)
5. W.L.Barr, J.Opt.Soc.Am. **51**, 943 (1961)
6. G.J.Pert, J.Comput. Phys. **43**, 111 (1981)
7. A.Giulietti, M.Borghesi, C.Danson, D.Giulietti, L.A.Gizzi, A.Macchi, D.Neely, *Short pulse propagation though preformed plasmas* in this report

SPECTROSCOPY AND DIAGNOSTICS OF DENSE PLASMAS

D.J. Heading, G.R. Bennett and J.S. Wark

Clarendon Laboratory, Department of Physics, University of Oxford, Parks Road, Oxford, OX1 3PU

INTRODUCTION

The plasma spectroscopy of dense plasmas is a subject of great interest at present. It has relevance to many topics in laser confined fusion and astrophysics, and presents significant theoretical challenges. Of particular significance are the opacity and equation of state of these plasmas. However, until recently, experimental data on the subject has been very limited. Thus theoretical models, used for the interpretation of data, have not been thoroughly tested.

Recent work[1] has shown that dense plasmas can be generated using confined laser ablation. Plasmas of densities of the order of 10^{19} cm^{-3} have been obtained by this technique. The electron temperatures are found to be comparatively low, indicating that the plasmas are non-ideal. However, it is unlikely that the effects of non-ideality will be observable in these spectra[2], but the effects of the breakdown of the basic approximations used for calculating spectral line shapes may be observed.

An important aspect of the plasma both spectroscopically and with respect to the equation of state is the ionisation depression. A number of different theoretical approaches to this have been taken[3-6] but they do not always agree. Again, there is little experimental evidence to distinguish between the theories. Cool, dense plasmas give an opportunity to observe the ratios of the ion species present. This requires a good knowledge of the plasma parameters and also of the atomic populations and oscillator strengths. Thus, much more precise information on the nature of the generated plasmas is required.

At these elevated densities, the spectral lines are very broad. It is thus necessary for care to be used in the analysis of the spectra. We have previously developed a code to facilitate the identification and diagnosis of the plasmas[7]. Before proceeding, improved diagnostics are required. A knowledge of the mass density or plasma pressure for example would greatly facilitate the diagnostic.

EXPERIMENT

Experimental work has been pursued along a number of threads. Previously, high quality spectra of aluminium from a 50 micron foil were obtained[1], and further experiments have been conducted to widen the range of the spectral observations, and to develop further the diagnostics of the plasma. We verify that similar spectra can be obtained using a thin film of Al, rather than a foil. Thus we know the plasma mass density, and this can be used in the diagnostic, and also in hydrodynamic simulations.

The basic confined ablation laser plasma target is shown in figure 1. The laser, in this case the TA4 beam from the Vulcan laser, is incident from the right, and passes through the confining wall. The laser intensity is below the breakdown intensity of the confining wall. The laser is then incident on the target layer, which can be either a 50 micron foil or a thin layer of material. The spectrum is observed from the front of the target.

The laser is focused to a spot size of ~7-10 mm diameter and the incident laser energy 4-8 J in a 4.5 ns pulse. Thus we ensure that the incident intensity is below the quartz breakdown threshold, but above that of the aluminium. Previous studies[8] suggest that 10-15% of the incident laser energy passes through the target if a 300 Å Al foil is used as the target. In the current series of experiments both foil and thin film targets were used. It would appear that our assumption that a skin depth of material was ablated by the laser is indeed correct. However we do have some evidence from thicker film targets that the plasma also erodes the target, and hence the use of a thin film is to be preferred.

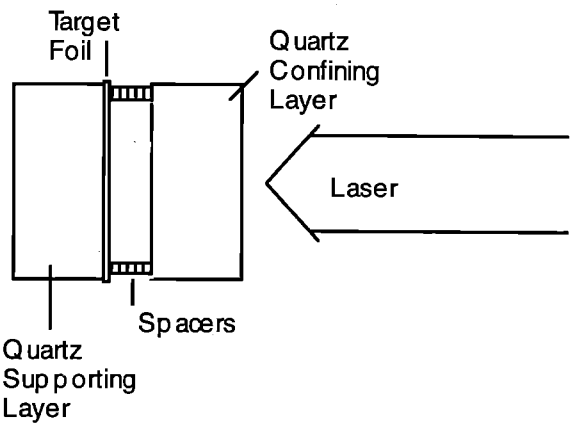

Figure 1: Schematic of confined laser ablation target.

The spectral dispersion is provided by a f = 300 mm grating spectrometer (Bentham M300) fitted with a 50 line / mm grating. This configuration is used because of the very wide spectral lines observed. Using this grating, we are able to observe 250-300 nm of the visible spectrum. However, this is at the expense of having the red end of the spectrum overlapped by second order lines. This is difficult to deconvolve in our spectra due again to the very broad spectral lines. The spectrum was incident on a Hadland 500 optical streak camera, fitted with UV optics. This was operated at 5 ns/mm streak speed, and was coupled to a DarkStar CCD camera. The captured image was saved onto a Macintosh computer for analysis.

We also measured the pressure from the plasma, a technique which has proved to be very successful before for denser plasmas[8]. In this a chromium layer is deposited on the back of the x-cut quartz supporting wall in figure 1. The quartz then acts as a piezo-crystal, and measures the pressure applied to the front surface. Further details of this method have been published elsewhere[8]. The pressure time history was recorded on a 1 MHz digital scope, and was also downloaded to the computer for analysis.

A sample spectrum of an aluminium plasma generated from a 5.55 J incident laser beam, with a 250 Å thin film in a 300 micron gap is shown in figure 2. A number of broad spectral lines can be seen, and these can be identified as the Al I resonance line at 395 nm, ($3s^23p$-$3s^2(^1S)4s$) the Al II line at 466 nm ($3p^2$-$3s(^2S)4p$), and the Al III lines at 452 nm (4p-4d) and 570 nm (4s-4p). Unfortunately, the overlapping orders at around 600 nm have complicated the analysis of the spectrum and detailed results are not yet available. Qualitatively the spectrum is very similar to that observed when the target was a 50 micron foil of Al. The lines observed are the same and the relative intensities are similar.

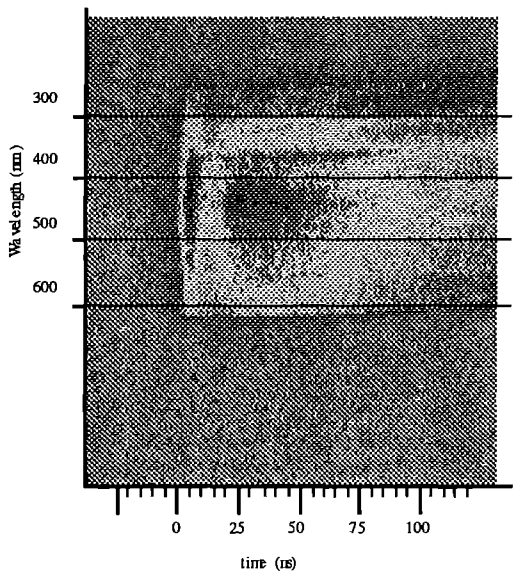

Figure 2: Aluminium emission spectrum from a 250 Å thin film and a 5.55 J laser, with a 300 micron gap.

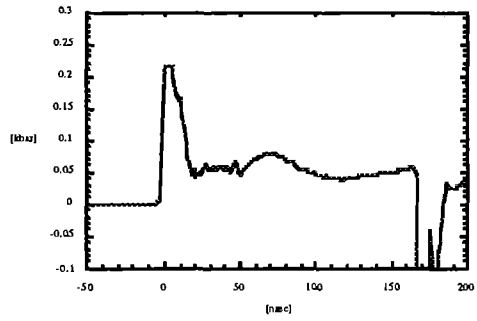

Figure 3: Pressure time history from an aluminium plasma with a 250 Å thin film, 300 micron gap and 5.55 J incident laser energy.

observed are the same and the relative intensities are similar. Preliminary analysis suggests that the plasma conditions are, indeed, within the same range as the previous experiments.

Figure 3 shows the time history of the pressure pulse from the plasma. The initial spike in the pressure, which saturates the detector, is due to the initial free ablation of the foil by the laser. This corresponds to the initial bright emission in figure 2. The pressure then falls, as the plasma expands into the gap. As the plasma hits the confining wall, it expands and heats up. It then recrosses the gap and becomes homogenous. This is shown by the second peak in the pressure and emission at around 60 ns, and the subsequent gently decreasing pressure. Thus, during this time the plasma has a high homogeneity. The late feature in the pressure time history is the reflection of the initial peak, which has recrossed the quartz crystal. A comparison of the measured pressure in the homogenous phase of the plasma (0.05 Kbar) and that from a calculated equation of state from SESAME[9] indicates that the two are in agreement for a cool plasma at ~3 g/cc.

The pressure measurement was not found to be particularly reliable. This was because the plasma resistance was higher than in previous experiments where the plasma was denser. Thus there was more chance of stray capacitative effects affecting the results. Some evidence of this can be seen towards the end of the trace in figure 3, where the pressure increases slightly. The root cause of this effect is still under investigation. Full analysis of the pressure time history requires the use of a full hydrodynamic simulation code, which is under development. This will permit comparison of the observed electron density and temperature from the spectral emission, and the pressure obtained from the x-cut quartz gauge thus yielding information about the ionisation balance and equation of state of this important region of parameter space.

CONCLUSION

We have generated dense plasmas by using confined laser ablation. We have verified that very similar spectra are obtained by using a thin film for a target to those obtained when the target is a 50 micron foil. Thus the mass density of the plasma can be known. The optical diagnostics of the plasmas produced from foils have already been proven, and we have shown that measurement of the plasma pressure can also yield useful diagnostic information. A few technical problems were encountered but these are not insoluble and the simultaneous spectral and pressure measurement of dense, confined plasmas shows great promise for future plasma experiments.

REFERENCES

(1) D.J. Heading, G.R. Bennett, J.S. Wark, R.W. Lee. *Novel plasma source for dense plasma effects.* Phys. Rev. Lett., **74** (18), 3616-3619 (1995).

(2) D.B. Boercker, R.W. Lee, F.J. Rogers. *Strong coupling effects on plasma lineshapes and Thomson scattering signals.* J.Phys.B., **16** 3279-3290 (1983).

(3) D.G. Hummer, D. Mihalas. *The equation of state for stellar envelopes. I. an occupation probability formalism for the truncation of internal partition functions.* Ap. J., **331** 794-814 (1988).

(4) F.J. Rogers. *Equation of state of dense, partially degenerate, reacting plasmas.* Phys. Rev. A, **24** (3), 1531-1543 (1981).

(5) F.J. Rogers, *Equation of State of Partially Ionised Dense Plasmas.* In School Enrico Fermi, Ed. S.Eliezer and R.A.Ricci, North Holland, 77-99 (1989).

(6) J.C. Stewart, K.D. Pyatt. *Lowering of ionization potentials in plasmas.* Ap. J., **144** 1203-1211 (1966).

(7) D.J. Heading, G.R. Bennett, J.S. Wark, R.W. Lee. *Simulations of Spectra from Dense Aluminium plasmas.* J.Q.S.R.T., **54** (1/2), 167-180 (1995).

(8) G.R. Bennett, J.S. Wark, D.J. Heading, N.C. Woolsey, H. He, R. Cauble, R.W. Lee, P. Young. *The production of strongly-coupled plasmas by the laser irradiation of thin metallic films confined within micron-scale gaps by transparent insulators.* Phys. Rev. E, **50** (5), 3935-3942 (1994).

(9) N.G. Cooper. *Sesame '83. Report on the Los Alamos Equation of State Library.* LALP-83-4 (1983).

MEASUREMENT OF SHORT-WAVELENGTH RAYLEIGH-TAYLOR GROWTH IN PLANAR FOIL TARGETS DRIVEN WITH SOFT X-RAY IRRADIATION

R J Taylor, S.Nuruzzaman, C Meyer, O Willi
Imperial College, London, SW7 2BZ, UK

INTRODUCTION

Inertial Confinement Fusion (ICF) uses high powered lasers or particle beams to compress capsules containing fusion fuel to high enough densities, and at high enough temperatures such that a sustained thermonuclear fusion reaction occurs [1]. The driver beams can either impinge directly on the capsule or be first converted to x-rays (indirect drive, ID). One method proposed for achieving indirect drive is focusing high powered laser beams into high Z cavities, or *hohlraums*, such that the laser-plasma interaction on the inner hohlraum wall generates a significant x-ray flux which is distributed throughout the cavity by repeated absorption and re-emission at the cavity wall, bathing the capsule in thermal x-radiation.

The hydrodynamic stability of the imploding capsule poses a major threat to the success of ICF. Imperfections on the capsule surface grow into larger perturbations through fluid instabilities (primarily the Rayleigh-Taylor (RT) instability) which results in degradation of the capsule performance. Understanding this process is crucial for the design of future high gain ICF capsules.

Indirect drive RT growth is generally considered to be dominant at longer wavelength modes, with the shorter wavelengths seen to be more heavily damped during conditions matching the main driver pulse. However, proposed ICF designs feature a long, low-intensity foot to the driving pulse, during which density scalelengths at the capsule surface can be expected to be shorter, and mass ablation rates lower than during the high-intensity main drive phase. Thus there exists a potential window of opportunity for growth of shorter wavelength modes during which coupling to longer modes may occur, representing a dangerous seed to destructive RT growth.

Standard models describing RT growth under Indirect Drive predict a lower cut-off wavelength below which growth is stabilised (negative growth rate), although only one study of RT growth around such wavelengths exists in the literature [2], and this study is hampered since it operates near the resolution limit of the diagnostic employed. Reasonable agreement between experiment and modelling has been obtained at longer wavelengths, where the reduction from classical growth is not extreme, although the most important regime, where the stabilisation results in a reduction of growth rate to below zero has so far remained mostly inaccessible. Here we present measurement of short-wavelength RT growth during acceleration of planar foils, representing a section of the capsule wall, with a diagnostic operating at several times its resolution limit, with the goal of obtaining a more detailed understanding of the RT stabilisation mechanisms at work in Indirect Drive ICF by obtaining measurements at short wavelengths where the stabilisation has its most marked effect on the growth rate.

THE RAYLEIGH-TAYLOR INSTABILITY IN ICF

For a classical RT system (two non-miscible, incompressible fluids in a frame accelerating towards the higher density fluid), sinusoidal interface perturbations of an initial modulation amplitude a_0 and wavenumber $\mathbf{k}$ grow as Eqn.1, with the classical growth rate γ_c given by Eqn.2, where g is the acceleration. This relation holds during the linear regime, i.e. while the perturbation retains a near-sinusoidal shape.

$$a(t) \approx a_0 e^{\gamma_c t} \quad (1) \qquad \gamma_c = \sqrt{\mathbf{k}g} \quad (2)$$

Takabe et al. [3] performed a study of the RT instability under an ablative acceleration (where the fluids are both compressible and miscible), and found that growth followed Eqn.1, with a reduced growth rate γ_T given by the so-called "Takabe formula", Eqn.3, with the term in β relating to ablative stabilisation [4]. Further studies of indirect drive systems in particular [5] identified the constant α as relating to reduction due to the finite density scalelength at the ablation surface, $\alpha = (1+\mathbf{k}L)^{-½}$, $L = \rho/\nabla\rho$. The linear regime is generally considered to prevail while $a \leq \lambda/10$ or thereabouts [6].

$$\gamma_T = \alpha\sqrt{\mathbf{k}g} - \beta\mathbf{k}v_a \quad (3)$$

The constant β lies in the range 2-5, although no single value provides good agreement across a wide range of drive/target combinations. Care must be taken in applying a Takabe analysis since an imploding capsule is in a transient state for much of the duration and thus a steady state Takabe treatment cannot be entirely adequate. The conditions prevailing in this study are akin to the start-up conditions in envisaged high-gain indirect-drive ICF systems due to the limited drive temperatures attainable on Vulcan.

EXPERIMENTAL PROGRAMME

Soft X-ray drive was generated by focusing six beams from the Vulcan Nd:glass laser onto the inner surface of a cylindrical gold hohlraum of diameter 1 mm and length 1.3 mm. Hohlraums were manufactured at RAL [7] and AWE. The two opposing laser entrance holes measured 500μm in diameter, and were formed in the curved wall of the cylinder, centred on an axis which intersects the axis of the cylinder itself. The hohlraum was aligned with a rotation of 30° around its axis, resulting in two sets of 3 horizontally displaced laser spots on the inner walls of the cavity.

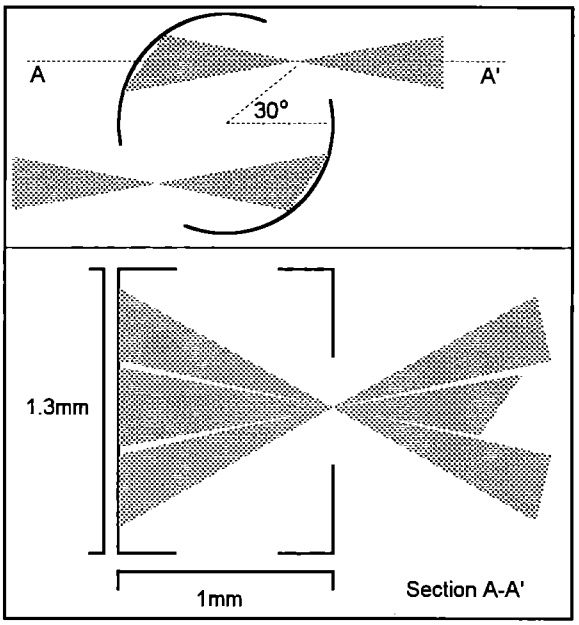

Figure 1 : Hohlraum drive configuration. Two pairs of 3 beams enter the hohlraum through 0.5mm laser entrance holes, and diverge to form two rows of 3 spots on the inner hohlraum wall.

The beams delivered ~600J at a wavelength of 0.527μm in a 1ns pulse, in a geometry represented schematically in Fig.1, generating an estimated equivalent drive temperature of the order of 100eV [12]. Diagnostic holes, also 500μm in diameter, were formed into each of the flat cylinder ends, aligned on the hohlraum axis, to provide a line of sight through the hohlraum and the accelerated foil, which was glued across one diagnostic hole (see Figure 2). Two further beams (also at 0.527 μm, 1 ns pulses stacked to provide 2 ns constant illumination) were incident on a gold backlighter disc, producing a soft x-ray pulse which was used to probe the event. Transmitted x-rays from the backlighter through the target were then selected at an energy of 250±5 eV using a spherical-section multi-layered mirror. This formed an image at 100 times magnification onto an XUV framing camera, in the case of face-on 2D temporally resolved images; or an XUV streak camera for side on data. The side-on measurements were achieved by rotating the hohlraum orientation such that the payload was accelerated vertically, and probed across the horizontal plane. The transverse spatial resolution and modulation transfer function [8] of the XUV imaging system were characterised by recording XUV-backlit images of static meshes of pitch 25μm, which were resolved with an edge-width of better than 3μm. In addition to the hohlraum configuration described here, other designs were occasionally employed. These included shorter (1 mm) and narrower (0.7 mm) hohlraums to control the temperatures achieved, and hohlraums closed at one end, whereby the closed wall performed the role of the backlighter, with the thermal wall emission providing the probe x-rays. This approach was found to be less flexible than having a separate backlighter whose brightness at given times could be controlled independently.

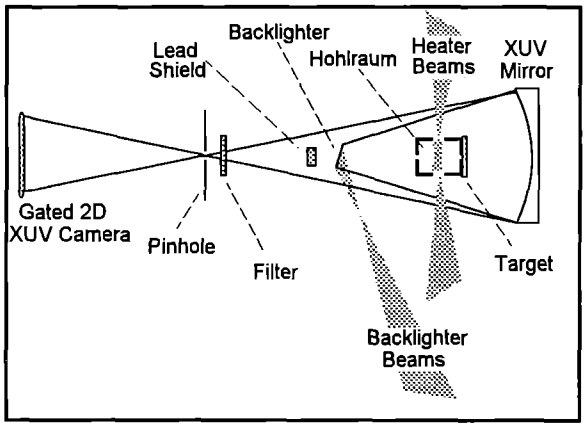

Figure 2 : Experimental configuration (not to scale). X-rays from the backlighter target traverse the length of the hohlraum and are absorbed by the payload foil, which is imaged by the XUV mirror at 100 times magnification onto a 2D gated XUV camera. Direct x-rays are shielded from the camera with a lead block in the line of sight, and a 100nm Aluminium + 200nm Formvar filter is used to remove optical and UV light from the reflected signal.

PAYLOAD DESIGN AND MANUFACTURE

The design of the premodulated payload foil is crucial to this study. Proposed ICF capsules feature a carbon based polymer outer layer [9], and hence it is desirable to use a similar material here, although in order that the target be suitable for probing at XUV energies, and in order that shock transit may occur before the end of the driving pulse, an upper limit is imposed on the thickness (in order that the backlighter is not entirely extinguished). Using a thin foil like this poses some problems for an indirect-drive system, since a pure CH polymer is relatively transparent across significant portions of the drive spectrum, and hence the drive energy is deposited deep into the foil, and global heating occurs, leading to an explosion, rather than the desired scenario where the majority of the energy is deposited in a layer at the surface of the target, and ablative acceleration ensues. In order to combat these problems, Oxygenated polymers were used (Polycarbonate, ρ = 1.2 g/cc, 19% Oxygen by mass and Cellulose Acetate, $\rho \approx$ 1.3 g/cc, ~50% Oxygen by mass), which enjoy both a higher density than typical pure CH polymers, and a higher opacity across the drive spectrum. Simulations predicted that several hundred picoseconds of ablative acceleration would occur with Polycarbonate foils ~15 μm thick irradiated with a typical 1 ns hohlraum pulse. Figure 3 illustrates the drive/target system by comparing an approximate drive spectrum with the mean-free-path (MFP) spectrum in cold Polycarbonate [10].

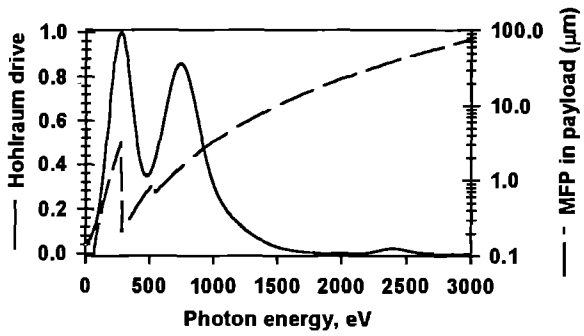

Figure 3: Drive and target spectra. The approximate hohlraum emission spectrum (in arbitrary power units per eV) is shown along with the mean free path (MFP) of those photons in cold Polycarbonate. The majority of the driving energy (hν <1keV) is absorbed within a few microns, and a localised region around 250eV remains sufficiently transparent for the XUV probe to penetrate.

The hohlraum spectrum is estimated given the known positions of Gold band emission [11], combined with an underlying thermal spectrum. The true emission spectrum of the hohlraum can be expected to be of this form, with band emission in the specified places, although the relative magnitude of the bands to each other and the thermal emission requires detailed measurement. The cold Polycarbonate target (at a thickness of 15μm) transmits ~0.1% of the backlighter photons, a value that rises as the foil is heated and the opacity drops. The Oxygenation of the target allows both driving and probing of the payload with XUV radiation, by controlling the lowest XUV opacity to be only what is necessary for transmission of the probe, while the rest of the spectrum enjoys relatively high absorption, particularly for hν > 280 eV above the carbon K-edge, which ensures strong, localised absorption of the drive flux.

A technological challenge was presented by the need for sinusoidally premodulated foils of the above materials at such short wavelengths as were interesting for this study. Conventional techniques for generating modulated foils involved configuring an eximer laser to produce a fringe pattern which illuminated the substrate at sufficient intensity to ablate material. However, this technique was found to be sensitive to the substrate material chosen, and unreliable in terms of producing regular sinusoidal modulation at a known and controllable depth. Hence an alternative method was sought, and since prior success had been obtained at longer wavelengths by casting foils from machined molds, the possibility of obtaining molds for these shorter wavelengths was investigated. Machining at such small scales ($3 < \lambda < 25$ μm) is considerably more difficult than for conventional ($\lambda > 30$ μm) targets, plus achieving a sinusoidal profile is not usually possible. The problem was solved the National Physical Laboratory (NPL), where near-perfect sinusoidal grooves were formed in silicone rubber substrates 25 mm in diameter. The technique involved exposing a glass plate coated with a suitable photoresist to the fringe pattern from an optical interferometer. The interferometer was adjusted to generate the desired wavelength, and the exposure controlled to generate the required depth. Once the photoresist was developed, a silicone rubber

cast was taken, the surface of which accurately reproduced the modulation, and which was robust and inert enough to be used as a mold for casting the payload foils. Modulation depths (peak to peak) of ~5% and ~10% of the respective wavelengths were produced, for wavelengths of 6, 12, 18 and 24 μm. The molds and foils cast from them were characterised at NPL with a Talystep profilometer (a contact stylus device) and at AWE with the non-contact ZYGO interferometric system. Similar results were found, with the foils taking on a negative image of the mold surface on one side, while remaining flat (to ~250Å RMS) on the rear side.

The casting of the foils was achieved by dip coating the mold in either Polycarbonate dissolved in Methylene Di-Chloride, or Cellulose Acetate dissolved in Ethanol. A relatively high concentration was required to achieve the desired thicknesses of ~15μm, and hence it was difficult to maintain the homogeneity of the solution. This resulted in a range of thicknesses being produced, from which the appropriate ones were selected. A further problem was encountered in that the solutions dried very rapidly, and hence a skin would form which then wrinkled leading to clouding of the foil. This was overcome by leaving the coated mold to dry for a few minutes bathed in the vapour of the solvent, which slowed the drying process, and produced highly uniform, clear foils. This technique allowed for rapid, inexpensive production of large quantities of targets, without degradation of the mold, and with the ability to switch between target materials with ease. The depth of the modulation was chosen to be below ~10% of the perturbation wavelength to ensure that some growth occurred in the linear phase. To seed the foils at larger amplitudes would be unrealistic, since by the time such amplitudes are reached in a realistic system, the linear phase would be over and the modulations would be far from sinusoidal. Hence it is important to seed the instability with a single mode at a linear amplitude, in order that it may undergo growth in the same way that it might had it been seeded at much lower amplitude, such as is encountered on the surface of an ICF capsule.

EXPERIMENTAL RESULTS

Modulation growth was observed directly by measuring the evolution of contrast between peak and valley transmission of the backlighter. The modulation in intensity recorded on film is related to the physical state of the foil by Eqn.4,

$$\ln\left(I_{pk}/I_{val}\right) = \int_{I(x,y)=I_{val}} \rho(z)\,\kappa(z)\,dz - \int_{I(x,y)=I_{pk}} \rho(z)\,\kappa(z)\,dz \qquad (4)$$

Where I_{pk} and I_{val} are the peak and valley intensities recorded on film, and the integrals are performed along the line of sight. The opacity κ(z) varies throughout the foil, and is dependent on the local temperature and density, and hence detailed analysis of the results will involve re-creation of the experimental observable from hydrocode simulations. It follows from Eqn.4 that the amplitude of the areal density modulation in the target is related to the ratio of recorded peak and valley intensities through the mean opacity of the sample. Figures 4,5 and 6 show gated (Δt~120ps) images at selected times for foils with 24, 18 and 12μm wavelength modulations respectively. The λ = 24 and 18 μm foils were Polycarbonate, whereas the 12 μm foil was Cellulose Acetate. Growth is observed for each target, although at no time was growth observed for the 6 μm modulation wavelength, nor for λ = 12 μm with Polycarbonate. The 12μm growth was only observed with the more Oxygenated Cellulose Acetate substrate. Figure 7 shows a side-on streak radiograph of a 14μm Polycarbonate foil. The ablated plasma can be seen expanding towards the drive, while the rear of the foil is accelerated away in reaction. The side-on data will be used to match hydrocode simulations such that they reproduce the global hydrodynamic response of the system, after which predictions for growth of target modulations will be compared with the experimental data.

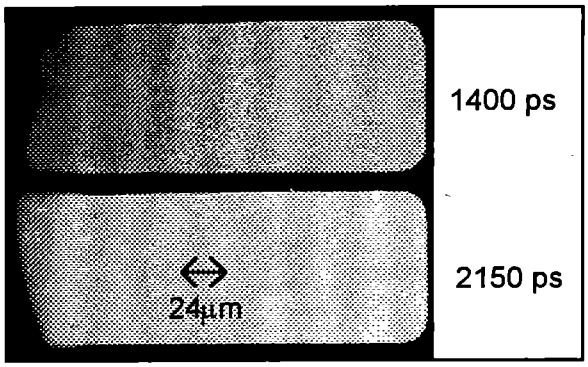

Figure 4: XUV radiographs of a 15μm Polycarbonate foil modulated on the rear (non-driven) side at a wavelength of 24μm, and to a depth of 2.7μm. Frames are shown 1400 and 2150ps after the start of the laser pulse. 526 Joules in a 1ns pulse were delivered into a 1mm diameter, 1.3mm long hohlraum. The light and dark bands correspond to thin and thick regions of the target respectively, caused by RT growth of the seed modulation.

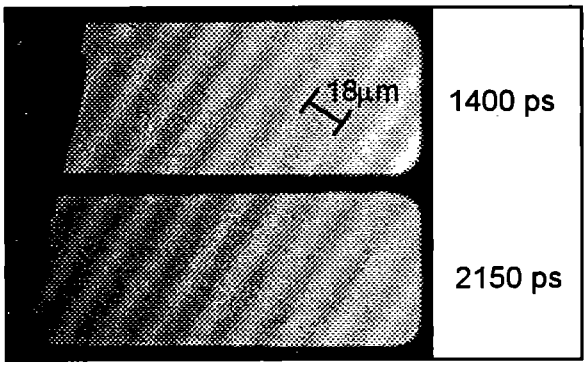

Figure 5: XUV radiographs of a 15.5μm thick Polycarbonate foil modulated at λ= 18μm, to a depth of 0.8μm, with frames at similar times to those in figure 4. In this case 485 Joules was delivered into a 1.1mm long, 0.7mm diameter hohlraum, generating a more intense drive, and the modulations were placed on the front side of the foil.

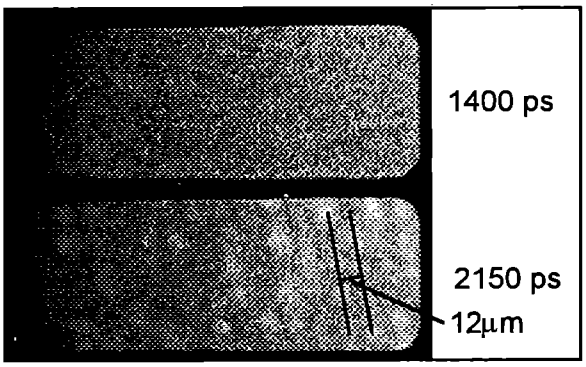

Figure 6: XUV radiographs of a 14.5μm Cellulose Acetate foil modulated on the rear side at λ= 12μm, to a depth of 0.75μm. The higher Oxygen content of Cellulose Acetate renders the foil more opaque, and hence the modulations are not visible until 2150 ps. At this time, the seed perturbation becomes visible, indicating that growth has taken place at a wavelength of 12μm, although the uniform structure is not reproduced. This may be due to dust particles contaminating the foil, or possibly to the hydrodynamic evolution of the target modulation. The foil was driven by a 1.3 mm long, 1 mm diameter hohlraum illuminated with 502 Joules in a 1ns pulse.

PRELIMINARY ANALYSIS

The immediate conclusion of the data obtained is that for Polycarbonate targets of the thicknesses used here, and for the drive conditions used here, the growth rate falls rapidly as the perturbation wavelength drops below 18 μm, such that no modulations were observed for the 12 or 6 μm wavelength targets shot in the course of this study. With the more opaque Cellulose Acetate, however, some growth *was* observed at 12 μm, suggesting that the cut-off for Cellulose Acetate is at a shorter wavelength. The higher Oxygen concentration of Cellulose Acetate (~50% as opposed to 19% for Polycarbonate) can be expected to generate a steeper density gradient as the x-rays are absorbed over a shorter distance at the surface of the target foil, and hence the stabilisation factor α in the Takabe formula should be less severe, and a shorter cutoff should result. This hypothesis was investigated by the means of numerical simulation.

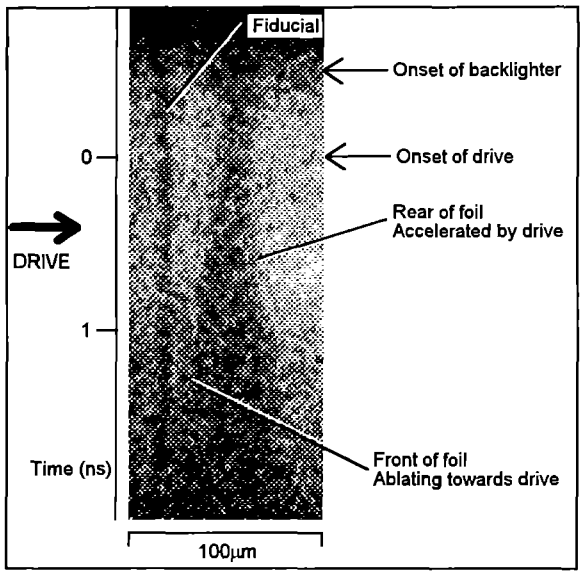

Figure 7: Side-on streaked radiograph of a 14μm Polycarbonate foil modulated on the rear side as in figure 4. The foil was driven by a 1 mm diameter, 1 mm long hohlraum irradiated with 414 Joules in 1ns.

The x-ray pulse shape for typical hohlraum conditions (estimated from x-ray diode measurements and side-on data) was used with the estimated spectrum shown in figure 3 as input for numerical simulations performed with a modified version of the POLLUX hydrocode. The code was modified to support absorption-only x-ray drive, with the assumption that re-emitted radiation in the low-Z target is negligible. 1D Simulations were performed with 15μm thick foils of both Polycarbonate, and the more oxygenated Mylar. Mylar was used as an approximation to Cellulose Acetate to investigate the effect of increased oxygenation (Mylar is 40% Oxygen by mass). The simulations were run to 1ns, and both exhibited a period of near constant acceleration between shock breakout at ~800ps and the peak of the drive pulse at 1ns. Hence the parameters of the Takabe formula were extracted at 900ps, defining g as the centre of mass acceleration, and defining the ablation surface as the location of $\rho_{pk}/2$ for inferring L and v_a. Takabe dispersion relations calculated using these values are shown in Figure 8, along with the classical growth rate given the Polycarbonate case acceleration of 5.8×10^{15} cms^{-2}. A value of $\beta = 3$ was used. The figure illustrates the lower cut-off for the more Oxygenated (and hence higher-opacity) target, a trend which can be expected to continue to Cellulose Acetate, which has more Oxygen than Mylar. The curves are consistent with the general trend illustrated in the data, in that growth falls off rapidly below λ=18μm for a Polycarbonate target, whereas for more oxygenated targets, growth is significant down to a shorter wavelength.

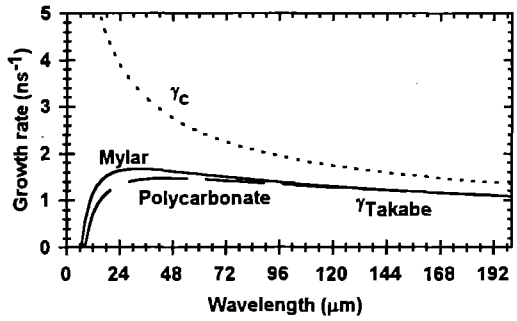

Figure 8. Takabe dispersion relations for Mylar and Polycarbonate targets driven with typical experimental conditions, along with the corresponding classical growth rate. Parameters for the calculation were taken from POLLUX hydrocode calculations.

CONCLUSIONS AND FURTHER WORK

The brief analysis here illustrates that significant RT growth of short-wavelength perturbation can occur during the low intensity start-up phase of an ICF implosion, especially with higher opacity, less explosive targets which retain a steep density gradient at the ablation surface. Proposed ICF capsules feature Carbon-based polymers doped with higher-Z elements such as bromine, which results in an even higher opacity than that considered here. Hence there is significant potential for dangerous seeding of longer-wavelength perturbations from early-time rapid growth of short-wavelength target non-uniformities. Continuing analysis of the data will provide a complete comparison of the experimental data with multi-dimensional hydrocode recreations of the experimental observable, and will hence furnish a more detailed understanding of the ablative RT instability under indirect drive ICF conditions. Further experiments are planned to investigate the coupling of shorter modes, in order to establish the contribution from this to the seed perturbation at destructive wavelengths.

Thanks are due to John Edwards, Brian Thomas, Peter Graham, Pete Hobbs, Tony Tyrell (AWE) and the AWE Target Fabrication team for their invaluable assistance with all aspects of the work, Steven Rose (RAL) for providing opacity calculations for this study, Mike Hutley (NPL) for manufacturing the target molds, John Spencer and colleagues (RAL) for manufacturing the hohlraums, Brian Evans (Reading University) for manufacturing the XUV mirrors, and all VULCAN Laser, Target Area and Target Preparation staff for their support during the experiment.

REFERENCES

[1] J. Kilkenny, "Inertial Confinement Fusion", Laser Plasma Interactions 5, pp. 1-13, SUSSP 1994

[2] B. Remington, Lawrence Livermore National Laboratory, Presentation at Imperial College, 1995.

[3] H.Takabe, *et.al.*, Phys.Fluids **26**, 2299 (1983); H.Takabe, *et.al.*, Phys.Fluids **28**, 3676 (1985)

[4] S.E. Bodner, Phys.Rev.Letts. **33**, 761 (1974)

[5] D.H. Munro, Phys.Rev.A **38**, 1433 (1988)

[6] B.A. Remington, *et al.*. Phys.Fluids B **4**, 967 (1992)

[7] "Manufacture of Planckian Cavities for High-Power Laser Experiments", this publication.

[8] Hecht, "Optics"

[9] L.R. Foreman, Microengineering of Materials: Laser Fusion Targets, Encyclopaedia of Materials Science and Engineering Supplementary Vol 2, R.W. Cahn ed. (Pergamon Press, Oxford) pp. 1067-75.

[10] B.L. Henke, E.M. Gullikson and J.C. Davis *Atomic Data and Nuclear Data Tables*, **54**, No. 2 (July 1993)

[11] C.A Back, *et.al.*, JQSRT, **51**, 19 1994; D.R Kania, *et.al.*, Phys.Rev A **46** 7853, 1992;

[12] J.Lindl, *Phys.Plasmas* **2** no.11, 3933 (1995)

MEASUREMENT OF SINGLE MODE IMPRINT BY XUV LASER RADIOGRAPHY

E. Wolfrum[1], A. Demir[2], D. Kalantar[3], M.H. Key[1,4], N.S. Kim[4], C.L.S. Lewis[5], J. Lin[2], A. McPhee[5], D. Neely[1], B.A. Remington[3], R. Smith[2], G.J. Tallents[2], J. Warwick[5], S.V. Weber[3] and J. Zhang[4]

[1]Rutherford Appleton Laboratory, UK
[2]Essex University, UK
[3]Lawrence Livermore National Laboratory, USA
[4]Oxford University, UK
[5]Queens University, UK

INTRODUCTION

Ignition of thermonuclear burn in directly driven spherical implosions is now a real possibility with megajoule laser facilities planned in the USA and France. A key question determining the robustness of ignition target designs is the level of hydrodynamic perturbations arising from laser speckle and amplified by the Rayleigh Taylor instability. Measurement of hydrodynamic perturbations imprinted on laser driven targets by the smoothed laser speckled patterns envisaged for direct drive has been shown to be possible with high accuracy using XUV laser radiography[1),2),3)]. In recent work the germanium J=0-1 XUV laser operating at 19.6 nm has been used in this manner to study imprint on laser driven aluminium foils (Kalantar et al., ibid.). Data measured for the continuum of modes present in laser speckle is important for assessing the net effect but does not lend itself easily to investigation of the basic physics of the imprint process. We describe here work in which a single one-dimensional optical mode is generated and imprint due to this single optical mode is measured.

EXPERIMENTAL SETUP

We used a Ne-like germanium x-ray laser (Zhang et al, ibid.) as the source for radiographic imaging and an imaging system as described by Kalantar et al (ibid.). The single mode interference patterns were generated in the focal plane of a lens by double rectangular slit apertures. The two selected uniphase wavefront elements interfere to create single mode perturbations of 15 μm and 30 μm periodicity. The fringe pattern is created under an Airy function envelope, determined by the dimensions of the rectangles. The scheme for production of single modes together with a computed 2D intensity distribution is shown in figure 1. 2 μm thick Aluminium foils were irradiated with the VULCAN laser (λ = 527 μm) at average irradiances of $2 \cdot 10^{13}$ W/cm^2 with the pulse shape shown in figure 2a.

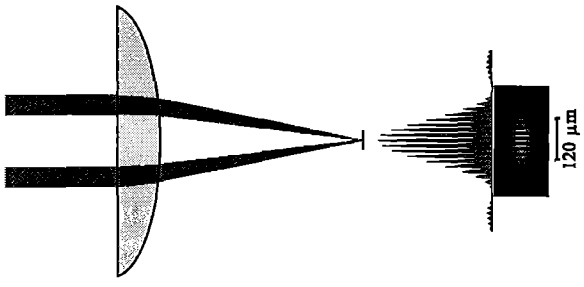

Fig. 1: Optical scheme for single mode studies

MEDUSA SIMULATION

Modelling was performed with the 1D Langrangian code MED103 using a trapezoidal pulse with 200 ps rise time and maximum irradiation of $2 \cdot 10^{13}$ W/cm^2 as shown in figure 2a. The Sesame equation of state for Al yielded the same results as the corrected Thomas Fermi equation of state. The time of shock breakout is determined by the time at which there is significant density increase in the last cell. For the given irradiation it has been calculated to be 240 ps from the start of the pulse, i.e. 40 ps into the flat top phase and 690 ps on the time scale shown. The total density and hydrodynamic pressure profiles are shown in figure 2b at shock breakout time. The main part of the target is being compressed to a density of about 6 g/cm^3 with a hydrodynamic pressure of 2.5 Mbar which is in excellent agreement with independent calculations of the Al shock hugoniot[4)].

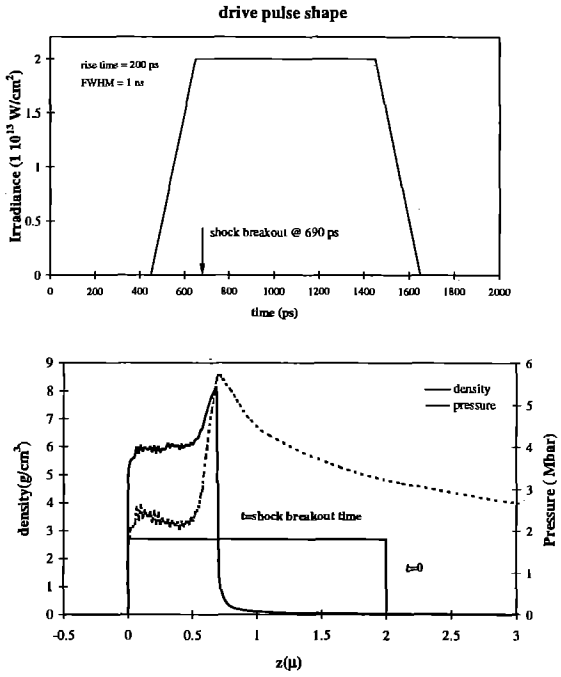

Fig. 2: a) Beam profile used as input for MED103 simulations,
b) Density and pressure at shock breakout time.

The computation also gives the average value of the acceleration a=56.5 μm/ns^2 and the average flow velocity across the ablation front v_a=0.3 μm/ns in the main drive phase. These values have been used with the Takabe formula[5)] in the form

$$\gamma = 0.9\sqrt{ka} - 3kv_a \qquad (1)$$

where k is the wave number, to give a rough estimate of the average Rayleigh Taylor growth rate: γ = 4 ns for 15 μm modes and γ = 2.9 ns for 30 μm modes.

RESULTS

Radiographs were recorded at different times after shock breakout for both modes, 15 μm and 30 μm. Figure 3 shows a 15 μm mode radiograph together with its horizontal lineout taken 200 ps after shock breakout.

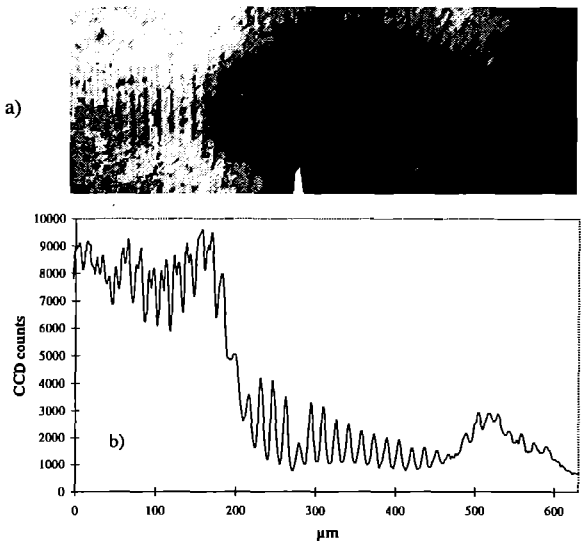

Fig. 3: a) Radiograph of a 2 µm thick Al foil irradiated with single mode fringe pattern of 15 µm periodicity, b) horizontal line profile hereof.

The response of the shocked target visible in the radiographs is comprised of a change in opacity due to the compression of the target and thickness perturbations driven by the single mode. The change in opacity $\Delta\tau_c$, with $\tau_c = \kappa\rho t$, κ the mass absorption coefficient, ρ the density and t the thickness, was evaluated by

$$\Delta\tau_c = \ln\left(\frac{I}{I'}\right) \qquad (2)$$

where I is a linear fit to the radiograph intensities for uncompressed areas and I' the average intensity in the centre of the shocked area. The determination of the correct background due to self emission in the shocked area posed a considerable problem, as there was only one image of selfemission recorded. Because the signal to background ratio generally is rather low, the data have to be considered as preliminary. Care will be taken in upcoming experiments to accurately determine the background and to reduce the background arising from self emission of the target. This could be achieved by reducing the irradiation of the driving beam. The resulting lower temperatures would lead to considerably lower self emission background as a decrease from 5 eV to 4.5 eV results in reduction of black body radiation by one order of magnitude at 19.6 nm. In figure 4 the increase in opacity versus time is plotted, showing a maximum increase by a factor of about 1.65.

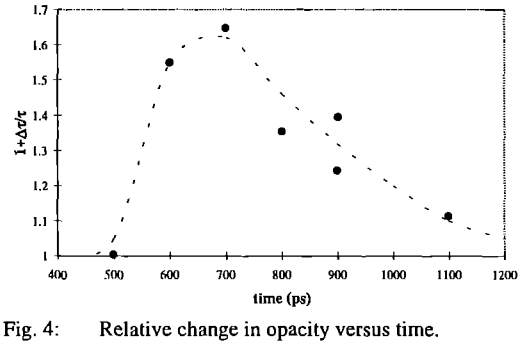

Fig. 4: Relative change in opacity versus time.

The rms amplitudes of the single modes have been derived from the minima and maxima of the fringe pattern in the radiographs, I_{min}, I_{max}:

$$t_{max} - t_{min} = \ln\left(\frac{I_{min}}{I_{max}}\right) * \frac{1}{\kappa\rho} = 2.86\Delta t \qquad (3)$$

where t is the thickness, Δt the rms amplitude of the thickness and the factor 2.86 stems from conversion of maximum amplitude to rms for a sinusoidal curve. Three different background corrections have been carried out: 1) no background correction: The raw data have been used, 2) low background correction: the radiograph with the lowest intensity in the shocked region has been taken as background, 3) high background correction: the image of self emission has been used as background. In figure 5 the fractional rms amplitudes for both, the 15 µ and 30 µ modes versus time are shown for the different background corrections.

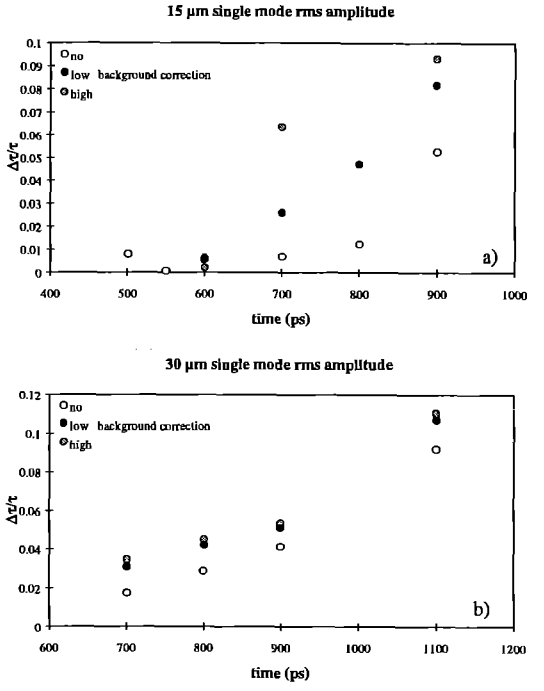

Fig. 5: Single mode fractional rms amplitudes for a) 15µm and b) 30 µm periodicity.

While, due to higher CCD countnumbers, the different background corrections do not affect results for the 30 µm modes, the errors for the 15 µm mode rms amplitudes are intolerably high and an accurate determination of the background is clearly necessary. The Rayleigh Taylor growth factors have been used as multipliers on the mode amplitudes of the imprint shown in figure 5 to estimate the amplitude at shock breakout time, resulting in $\Delta t/t$ of 0.03 for both, 15 µm and 30 µm modes. Full analysis of these data is in progress and will be reported in future publications. This will include comparison with theoretical opacity calculations and 2D hydro calculations of the single mode perturbations.

REFERENCES

1) M.H. Key , T.W. Barbee Jr., L.B. DaSilva, S.G. Glendinning, D.H. Kalantar, S.J. Rose and S.V. Weber. J. Quant. Spectrosc. Radiat. Transfer, 54, 221 (1995)

2) D.H. Kalantar, T.W. Barbee Jr., L.B. DaSilva, S.G. Glendinning, M.H. Key, J.P. Knauer, F. Weber and S.V. Weber. Rev. Sci. Instr.67, 781 (1996)

3) D.H. Kalantar, M.H. Key, L.B. DaSilva, S.G. Glendinning, J.P. Knauer, B.A. Remington, F. Weber and S.V. Weber. Phys. Rev. Lett. 76, 3574 (1996)

4) S.J. Rose, private communications

5) H.Takabe, K.Mima, L.Montierth and R.L.Morse. Phys.Fluids 28, 3676 (1985)

XUV RADIOGRAPHY MEASUREMENTS OF DIRECT DRIVE IMPRINT IN THIN ALUMINUM FOILS USING A GE X-RAY LASER ON VULCAN

D. H. Kalantar[1], A. Demir[2], M. H. Key[3,4], N. S. Kim[3], C. L. S. Lewis[5], J. Lin[2], D. Neely[3], A. McPhee[5], B. A. Remington[1], R. Smith[2], G. J. Tallents[2], J. S. Wark[4], J. Warwick[5], S. V. Weber[1], E. Wolfrum[3], J. Zhang[4]

[1]Lawrence Livermore National Laboratory, Livermore, CA 94550, USA
[2]Department of Physics, University of Essex, Colchester, CO4 3SQ, UK
[3]Central Laser Facility, Rutherford Appleton Laboratory, Chilton, Didcot, Oxon, OX11 0QX, UK
[4]Clarendon Laboratory, Department of Physics, University of Oxford, Oxford, OX1 3PU, UK
[5]Department of Pure and Applied Physics, Queens University of Belfast, Belfast, BT7 1NN, UK

INTRODUCTION

One key aspect for high gain direct drive inertial confinement fusion is the imprint of perturbations in the outer surface of a capsule due to nonuniformities in the direct laser illumination of the capsule. Direct drive implosions are achieved by uniformly irradiating the outside surface of a hollow spherical capsule that contains a layer of fusionable D-T on its inner surface. The laser pulse shape starts with a low intensity 'foot' at 10^{13} W/cm^2 for several nanoseconds before it builds up to more than 10^{15} W/cm^2 during the main drive portion of the pulse. Laser ablation of the capsule surface produces a high pressure that accelerates the capsule shell radially inward in a spherical implosion. During this acceleration, perturbations due to surface roughness and due to imprint from spatial non-uniformities in the laser irradiation undergo Rayleigh-Taylor growth, potentially severely degrading performance.

Our interest is in studying the imprint process and subsequent Rayleigh-Taylor growth of perturbations in a foil target that is irradiated by a low intensity laser speckle pattern. Previous experiments have been done to study laser imprint with an x-ray laser backlighter at the Nova laser using 0.35 μm laser irradiation of a 3 μm Si foil[1,2,3]. In these experiments we irradiated a 2 μm thick Al foil with 0.53 μm laser light at 2-8x10^{12} W/cm^2 using the Vulcan laser. We used a Ge x-ray laser[4] as an XUV backlighter to measure the modulation in optical depth of the foil on a CCD during the initial imprint phase and after Rayleigh-Taylor growth with different laser smoothing schemes. We used a single Vulcan laser beam with a static random phase plate speckle pattern, smoothing by spectral dispersion, and smoothing by ISI. We compared the results with results from a multiple beam overlap of static speckle patterns and SSD smoothed speckle patterns. We also measured the growth of a single wavelength modulation that was imprinted by a single mode optical intensity modulation onto the target. We used Al foil targets since Al has the lowest opacity for the Ne-like Ge x-raylaser wavelength of 19.6 nm. The Al is still highly attenuating, which limits the experiment to thin foils. It also means, however, that the technique is sensitive to small modulations in the thickness of the foil. At 19.6 nm, the product of opacity times density for Al is 2.24 μm^{-1}. With this high an opacity, a thickness variation of only 50 nm results in a 10% change in signal intensity.

EXPERIMENT

We used six beams of the Vulcan laser to generate a Ge x-ray laser. Three of the six beams of 1.05 μm laser light were focused with an overlapping line focus onto each of two 100 μm wide strips of Ge deposited on glass slides. For these experiments we used two 18 mm targets that had a separation of 200 μm, as illustrated in Figure 1. We used 75 ps pulses with a 10% pre-pulse 2.2 ns before the main pulse. Under these conditions, the x-ray laser beam had a divergence of about 30 mrad in the plane of the x-ray laser target surface, and 10 mrad normal to the plane. Details on the ouput characteristics of the Ge x-ray laser are presented separately in this proceedings (J. Zhang *et al*).

We placed a thin (2 μm) Al foil about 3 cm from the output of the Ge x-ray laser. We then used two multilayer mirrors to image the Al foil in the x-ray laser wavelength onto an XUV sensitive CCD (Figure 1). A spherical mirror with a 1 m radius of curvature was placed 53 cm from the Al foil, providing a 16X magnified image of the foil on the CCD at near normal incidence (<0.6°). The CCD was filtered with an additional 0.8 μm Al foil to reduce thermal emission from the foil, and a 45° angle of incidence planar

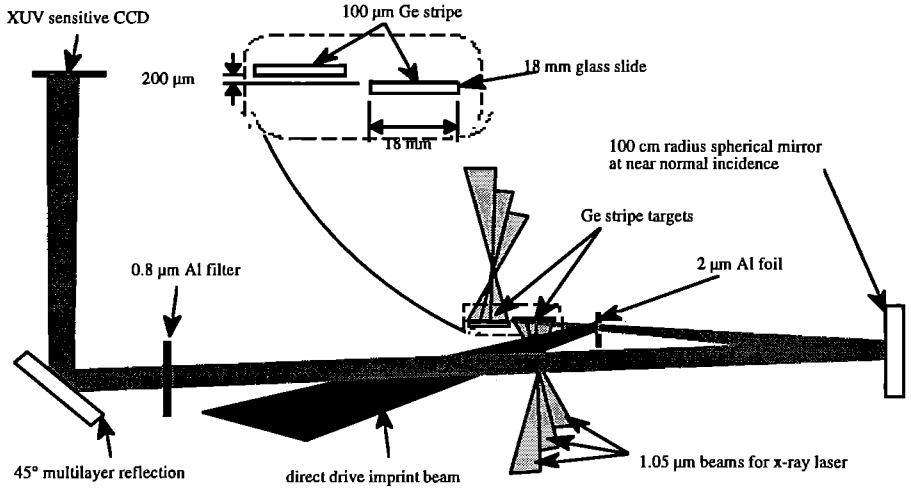

Figure 1: Geometry for the x-ray laser target and XUV imaging system to measure the modulation in optical depth of a thin Al foil due to direct drive laser imprint on Vulcan.

mirror was used to relay the image onto the CCD and spectrally isolate the image from the thermal background noise. The XUV mirror imaging system used near normal incidence reflection from the spherical imaging mirror to minimize spherical aberrations. The resolution of this imaging system was better than 1 μm.

We conducted a series of experiments to study the imprinting of a 0.53 μm laser beam on a thin Al foil by measuring the modulation of the foil as a function of time with various laser smoothing schemes. This modulation was imprinted by variation in optical intensity and enhanced by Rayleigh-Taylor growth at late time.

We used up to two beams of the Vulcan laser as drive beams to directly irradiate the Al foil with the following series of configurations:

1. Multiple mode laser intensity modulation:
   - a) single beam irradiation
     - static speckle pattern
     - 1-D SSD smoothed speckle pattern
     - ISI smoothed speckle pattern
   - b) two beam overlap
     - static speckle pattern
     - 1-D SSD smoothed speckle pattern
2. Single mode laser intensity modulation
   - a) 15 μm wavelength
   - b) 30 μm wavelength

In this report, we present preliminary results from the experiments using a multiple mode laser intensity modulation. Results from the single mode experiments are presented separately in this proceedings (E. Wolfrum *et al*).

RESULTS AND DISCUSSION

In Figure 2, we show optical far field images of the single beam laser focal spot recorded during these experiments on photographic film in an equivalent target plane. This figure shows intensity modulation of a) a static RPP speckle pattern, b) a 1-D SSD smoothed speckle pattern, and c) for an ISI smoothed RPP speckle pattern. Each image shows a 125 μm square region in the focal plane. The static speckle pattern shows small scale modulation in intensity. The irradiation beam was 12 cm in diameter, with a focal length of 1 m. The phase plate elementsize was 0.75 mm, resulting in a minimum speckle size of about 9 μm. The modulation is smoothed with one-dimensional streaks due to the dispersion of the grating used for SSD. The bandwidth of the laser pulse was about 0.5 nm at 0.53 μm, and we used a 300 line/mm gating, providing a dispersion of about 0.17 mrad. We used an RPP with ISI smoothing to generate the smoother irradiation pattern shown in Figure 2c.

We irradiated the 2 μm thick Al foils directly by an intensity of 3-8x10^{12} W/cm^2 of 0.53 μm laser light using the different speckle patterns shown above in Figure 2. We recorded the modulation in optical depth in the foil due to laser imprint and subseqent Rayleigh-Taylor growth using the Ge x-ray laser backlighter. We show several XUV radiographs as modulation in optical depth recorded at 0.2 ns into the laser pulse in Figure 3 for the three cases of imprint due to a static random phase plate (RPP) speckle pattern, a speckle pattern smoothed by spectral dispersion (SSD), and a speckle pattern wth induced spatial incoherence (ISI smoothing). Power spectra for the imprinted modulation measured in these images are shown in Figure 4. These are plotted as power per mode, such that the square root of the integral under the curves is the root mean square (RMS) modulation in the radiograph image. Note that we also show the power spectrum obtained for an undriven target for comparison in this figure.

The RMS modulation in optical depth we measured from the XUV radiographs shown in Figure 3 were 0.37, 0.17, and 0.20. The RMS measured from undriven Al foil targets was 0.13. This corresponds to a surface roughness of about 60 nm. We show the

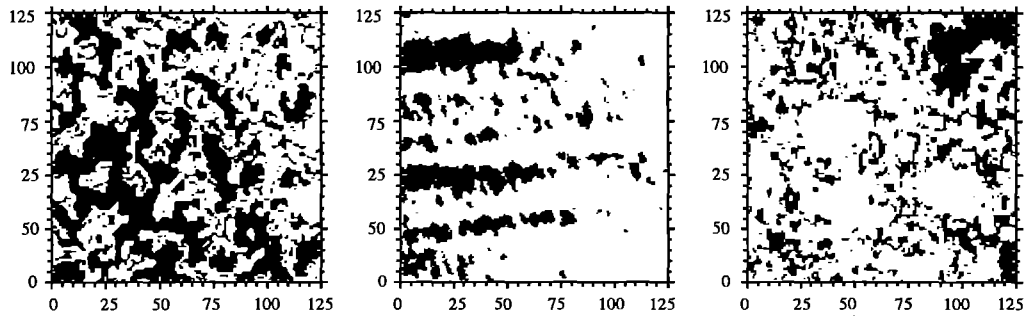

Figure 2: Equivalent target plane images of the laser focal spot recorded with a) a static RPP speckle pattern, b) a 1-dimensional SSD smoothed speckle pattern, and c) an ISI smoothed speckle pattern. The scale is in microns at the target.

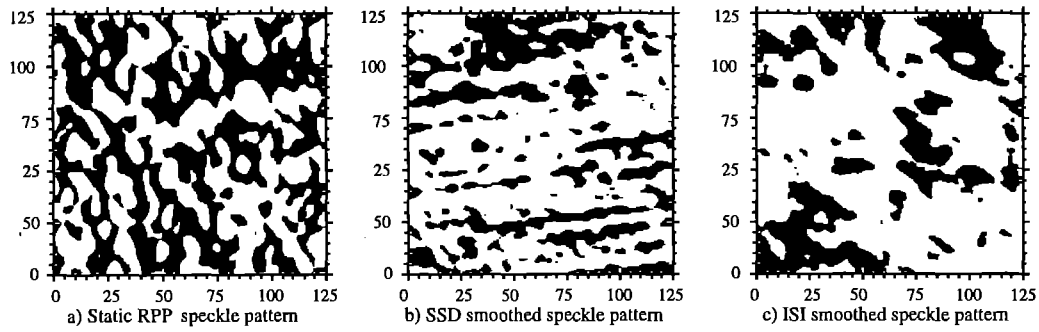

Figure 3: Modulation in optical depth of an Al foil irradiated by a 0.53 μm direct drive laser beam smoothed with a) a static RPP speckle pattern, b) a 1-dimensional SSD smoothed speckle pattern, and c) an ISI smoothed speckle pattern. These images were recorded at 200 ps into the drive pulse using the Ge x-ray laser backlighter . The scale is in microns at the tar get, and they are plotted on the same grayscale from -1.2 to +1.2 in optical depth.

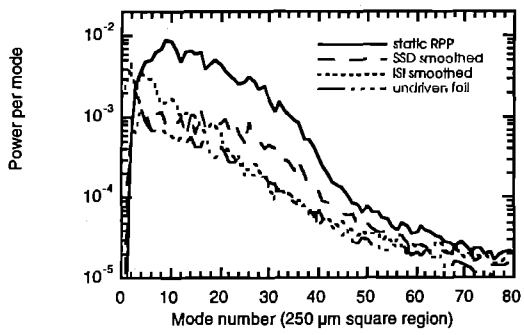

Figure 4: Power per mode calculated from the XUV optical depth modulation measured from the radiograph images shown in Figure 3.

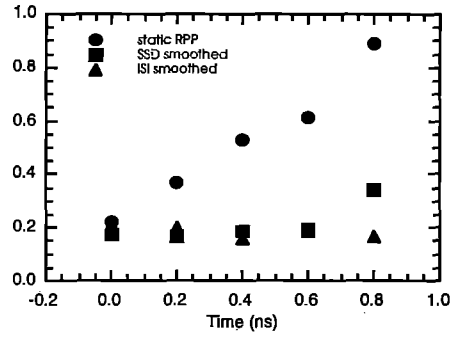

Figure 5: RMS modulation in optical depth of the Al foil measured as a function of time for the static, SSD smoothed, and ISI smoothed drive beams

optical depth modulation as a function of time recorded by XUV radiography in Figure 5. This figure shows that the modulation imprinted due to a static speckle pattern grows faster than for a smoothed speckle pattern. The SSD smoothed case shows a strong reduction in the modulation, but it still grows late in time. The ISI smoothed beam, however, does not show significant growth at any time up to 0.8 ns. In this case, the ISI smoothing technique that is implemented on the Vulcan laser introduces a time skew in the drive beam of about 0.22 ns, so it takes much longer to rise up to the nominal intensity for the 1 ns laser pulse.

We further compared the modulation imprinted in the foil due to overlapping drive beams. We used two beams, both with a 1 ns pulse at 0.53 μm. We overlapped two beams with a static RPP speckle pattern and two beams with an SSD smoothed speckle pattern.

Figure 6 shows XUV radiographs recorded at about 0.2 ns for these two cases with an intensity of about 4-6x10^{12} W/cm^2. The equivalent focal plane image for the overlapped static speckle patterns appears to show smaller scale structure than for a single static RPP speckle pattern in Figure 3a. The image for the overlapped SSD smoothed beams shows streaks in two directions because the dispersion direction on the two beams was orthogonal. The RMS modulation in optical depth with two overlapping static speckle patterns was 0.30. It was 0.17 for the two overlapped SSD smoothed beams. We also conducted preliminary experiments to compare the imprint and RT growth of single mode vs multimode modulations in a thin Al foil. We placed a two-slit aperture in the 0.53 μm laser drive beam that provided an Airy pattern to illuminate the target at about 2x10^{13} W/cm^2. The slits were designed to provide an interference pattern with a single dominant wavelength at 15 μm and 30 μm. We recorded a series of images at different times to measure the growth of the modulation. Preliminary results from these measurements are presented separately in this proceedings.

SUMMARY

These experiments showed that we could make measurements of the modulation imprinted by direct drive on a thin foil using the Ge x-ray laser at the Vulcan laser facility. We made measurements of the imprinted modulation and subsequent Rayleigh-Taylor growth as a function of time with various laser smoothingschemes. We also made measurements of the modulation imprinted by a single mode optical perturbation.

Full analysis of the imprint and subsequent Rayleigh-Taylor growth measurements is in progress, and will be reported in detail in future publications. This will include comparisons of the imprinted modulation with previous experiments made on the Nova laser that used a 0.35 μm laser imprint wavelength, as well as with simulations.

ACKNOWLEDGMENTS

We thank the Vulcan laser operations, target preparation, and engineering groups for their help and cooperation in these experiments. This work was partially supported by the Lawrence Livermore National Laboratory under the auspices of the U.S. Department of Energy under Contract No. W-7405-ENG-48.

REFERENCES

[1] M. H. Key, T. W. Barbee, Jr., L. B. DaSilva, S. G. Glendinning, D. H. Kalantar, S. J. Rose, and S. V. Weber, *J. Quant. Spectrosc. Radiat. Transfer* **54**, 221 (1995).

[2] D. H. Kalantar, T. W. Barbee,, Jr., L. B. DaSilva, S. G. Glendinning, M. H. Key, J. P. Knauer, F. Weber, and S. V. Weber, *Rev. Sci. Instrum.* **67**, 781 (1996).

[3] D. H. Kalantar, M. H. Key, L. B. DaSilva, S. G. Glendinning, J. P. Knauer, B. A. Remington, F. Weber, and S. V. Weber, *Phys Rev. Letters* (in press).

[4] J.C. Moreno, R.C. Cauble, P. Celliers, L.B. DaSilva, J. Nilsen, and A.S. Wan, *Soft X-Ray Lasers and Applications*, Proc. Soc. Photo-Opt. Instrum. Eng. **2520**, 97 (1995).

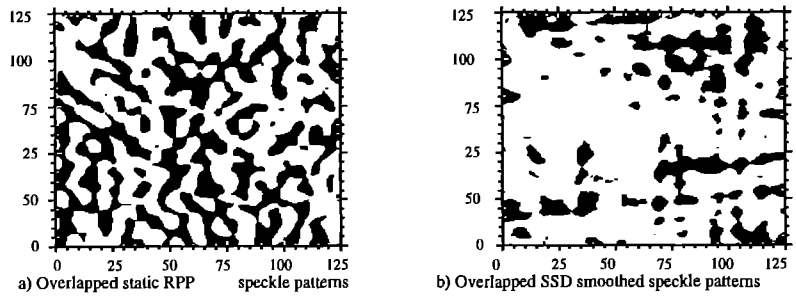

Figure 6: modulation in optical depth of an Al foil irradiated by two overlapping 0.53 μm laser beams with a) static RPP speckle patterns, and b) SSD smoothed speckle patterns.

A STUDY TO OPTIMISE THE TEMPORAL DRIVE PULSE STRUCTURE FOR EFFICIENT LASING ON THE GE J=0-1, 19.6nm LINE

P.J. Warwick[1] A. Bejhat[3] M. Kurkcuoglu[3] C.L.S. Lewis[1] A.G. MacPhee[1] S. McCabe[1] D. Neely[2] G.J. Tallents[3] and E. Wolfrum[2]

[1]Department of Pure and Applied Physics, Queens University of Belfast, BT7 1NN
[2]Rutherford Appleton Laboratory, Chilton, Didcot, OX11 OQX
[3]Department of Physics, University of Essex, Colchester, CO4 3SQ.

INTRODUCTION

Since Boehly et al demonstrated that XUV lasing in Ne-like Ti only occurs when the main optical drive pulse is preceded by a low intensity prepulse[1] there has been wide usage of this technique to produce or enhance J=0-1 lasing on a wide range of elements[2,3,4]. The observation that these lines had a narrow temporal profile, typically 100-200ps, peaking before the maximum of the ns drive beam[4,5] suggested that shorter drive pulses would be more effective. Multiple 100ps drive pulses have since been shown to vastly improve the energy efficiency and brightness of these lasers[6,7]. Comparisons between previous studies are complicated by the use of different target elements, different drive wavelengths and different temporal drive characteristics. The object of this study was to compare several possibilities under standard conditions.

EXPERIMENTAL

Single 18mm slab targets of Germanium were irradiated by 1.054μm pulses from the VULCAN laser. Long pulse drive consisted of 600ps pulses at an average intensity on target of 2×10^{13}W/cm^2, whereas short pulse drive consisted of 100ps pulses at an average intensity of 4×10^{13}W/cm^2. For the short pulse case the number, size and delay between the pulses was varied. Short pulse configurations included: a single pulse; a single pulse preceded at varying times by a single, percent level prepulse (~1-5%); two pulses separated by 400ps and 800ps; two pulses separated by 400ps and 800ps with double, percent level prepulses 2ns early. This is summarised schematically in Fig 1.

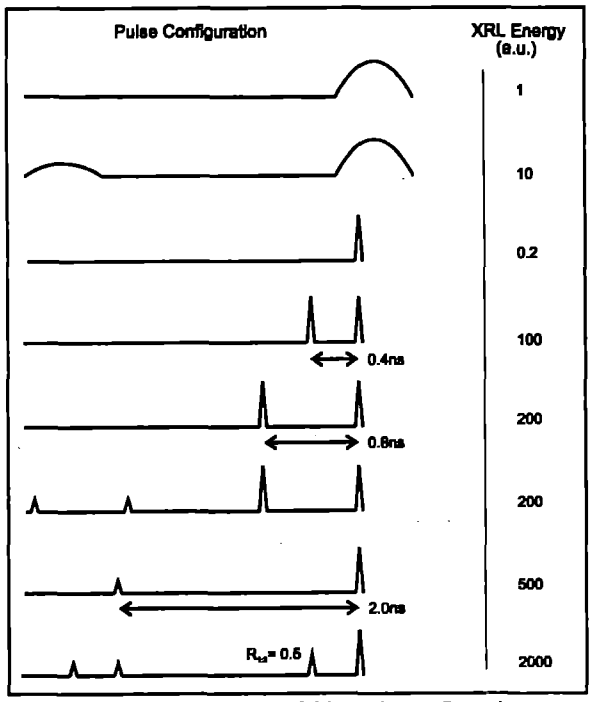

Fig 1 Schematic diagram of drive pulse configurations

The X-ray laser output was monitored using a flat field spectrometer incorporating a cylindrical mirror for spatial resolution. A phosphor-coated fibre-optic was used with a CCD detection system[8], the calibrated sensitivity of which was used to estimate output fluences.

RESULTS

The integrated energy from the Ge J=0-1, 19.6nm line is shown below for different parameter scans. Fig 2 shows the effect of a single, percent level prepulse, preceding the short, main drive pulse by varying times.

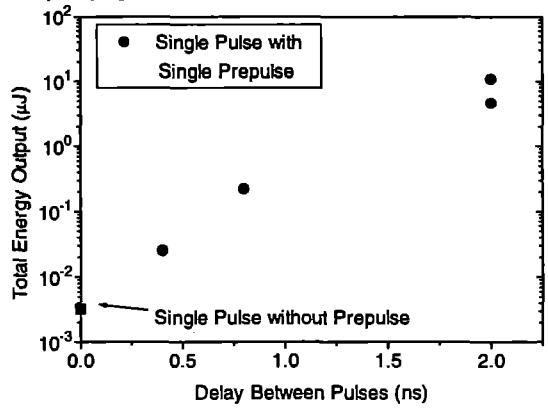

Fig 2 Effect of varying delay between pulse and prepulse

The effect of the prepulse is dramatic. Preceding the main drive pulse by 400ps it enhances lasing output by almost an order of magnitude. At 2ns early lasing output is increased by more than three orders of magnitude over the zero prepulse case.
Contrastingly, we held the time between the two pulses constant at 800ps and varied the ratio of prepulse to main pulse. This data is presented in Fig 3.

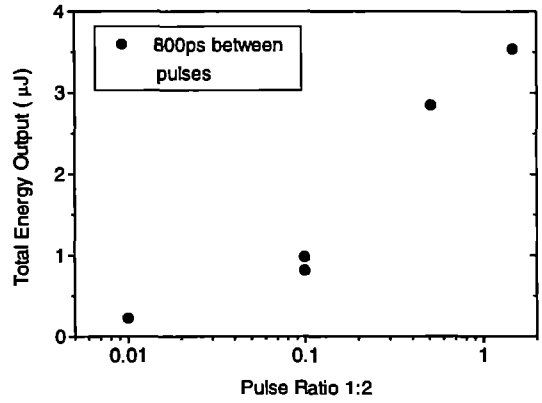

Fig 3 Effect of varying prepulse size at a constant delay time

Lasing output increases by a factor of 15 as the prepulse is increased from 1% to 100% of the main pulse energy.

Fig 4 shows how the long pulse drive compares to the different short pulse drives. Values are again given for the J=0-1 line at 19.6nm. The J=2-1 lines at 23.4nm and 23.6nm contained on

average three times the energy of the J=0-1 line for the single long pulse case. The long pulse prepulse data is taken from previous work[4] using a 2% prepulse, 5ns early and has been normalised to the single long pulse case. In the 2.2.400 and 2.2.800 cases (see figure caption for explanation of notation) the first prepulse was 2ns early with respect to the first of the main pulses.

DISCUSSION

Observing Fig 4 there is considerable scatter in the 2.0.400 and 2.2.800 cases. There appear to be two anomalously low points in the 2.0.400 data and one in the 2.2.800 data. These shots had similar energy on target and uniformity of illumination along the line focus. The errors involved in integrating the relative lasing signals above background are less than ±5% and while there is a large uncertainty in estimation of the throughput of the spectrometer to convert to energy units, this will be a systematic error. The plasma conditions for these spurious shots must have been different in such a way that the optimum conditions for amplification were not always achieved. It is therefore more accurate to talk about the maximum output from a particular configuration rather than the average. The values given in Fig 1 are the maximum observed for each configuration, normalised to the long pulse case.

The effect of a pulse preceding the main drive pulse is to create a pre-plasma which has time to expand to large volume with relaxed density gradients before incidence of the drive pulse. This pre-plasma allows efficient absorption of the drive pulse which then reheats it to create the temperatures and densities necessary for population inversion, while maintaining the shallow gradients necessary to prevent refraction out of the gain zone. There will be a tradeoff between the size of the prepulse and the time with which it precedes the drive pulse. Thus a 1% prepulse at 2ns is more effective than a full pulse at 800ps. Taking the example of a 1% prepulse at 800ps, it can be made more effective by either increasing its size or by increasing the delay between it and the drive pulse. It is interesting that adding two prepulses to the 2.0.800 case appears to make very little difference to the total energy output (although the statistics are poor). It is possible that the principal lasing phase is switching from the second main pulse to the first main pulse after the action of the prepulses. At present we have no time resolved data to determine whether lasing occurs on each of the main pulses in the 2.2.800 case.

Modelling is currently under way to try and develop a better understanding and a facility to predict the sensitivity to prepulse size and delay.

CONCLUSION

The benefits of multiple short pulses over single long pulses, for enhancing lasing on the J=0-1 line, are obvious. The 2.2.400 case for example has an average energy output of three orders of magnitude greater than the long pulse case. The J=2-1 lines on the other hand are in most cases so weak as to be undetectable. With the associated reduction of the total drive energy required, the 2.2.400 case is also extremely energy efficient for an XRL of this length, with an efficiency of roughly 10^{-7}. There is also evidence that short pulse drive leads to much shorter pulse durations than observed with ns drive[6]. Thus the power enhancement will be even greater than three orders. With a spectrally isolated, high energy and short duration beam we have an extremely bright and monochromatic XUV source as demanded by potential applications.

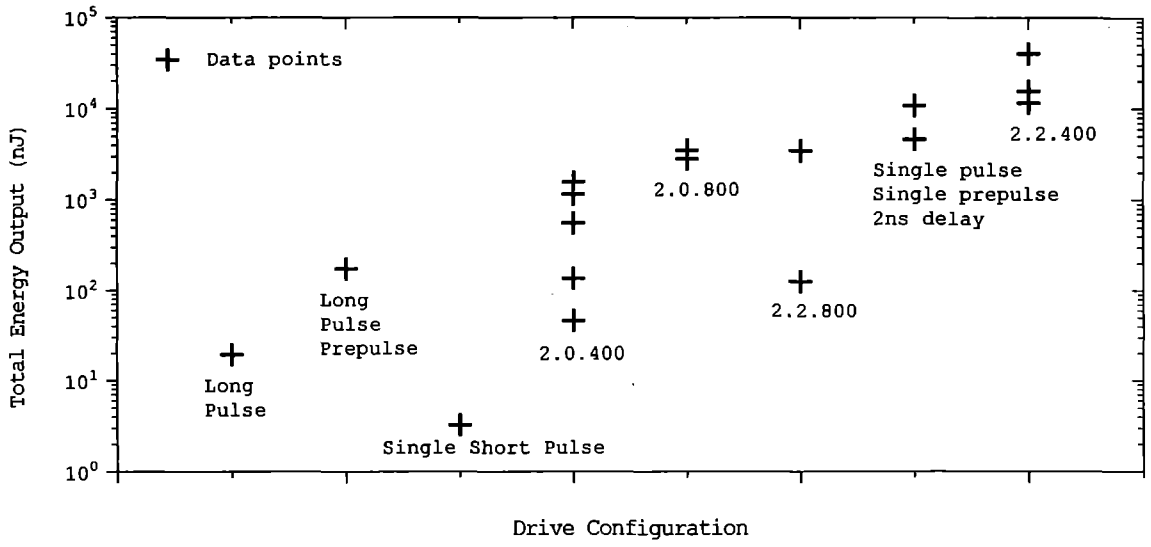

Fig 4 19.6nm X-ray laser output from different drive configurations. In the 2.2.400 notation the first number refers to the number of main pulses, the second to the number of prepulses and the last to the separation between the pulses in picoseconds.

REFERENCES

1. T Boehly, M Russotto, RS Craxton, R Epstein, B Yaakobi, LB DaSilva, J Nilsen, EA Chandler, DJ Fields, BJ MacGowan, DL Matthews, JH Scofield and G Shimkaveg, Phys Rev A, 41, 6962 (1990).
2. J Nilsen, BJ MacGowan, LB DaSilva and JC Moreno, Phys Rev A, 48, 4682 (1993).
3. Y Li, G Pretzler and EE Fill, Phys Rev A, 51, R4341 (1995).
4. GF Cairns, CLS Lewis, ML Lamb, AG MacPhee, D Neely, P Norreys, MH Key, SB Healy, PB Holden, GJ Pert, JA Plowes, GJ Tallents and A Demir, Opt Comm., 123, 777 (1996).
5. B Rus, A Carillon, B Gauthe, P Goedtkindt, P Jaegle, G Jamelot, A Klisnick, A Sureau and P Zeitoun, J Opt Soc Am, 11, 564 (1994).
6. LB DaSilva, RA London, BJ MacGowan, S Mrowka and DL Matthews, Optics Lett., 19, 1532, (1994).
7. AG MacPhee, A Behjat, MJ Lamb, CLS Lewis, D Neely, GJ Tallents, PJ Warwick and EWolfrum, Annual Report of the Central Laser Facility, Rutherford-Appleton Laboratory, 22 (1995).
8. AG MacPhee, CLS Lewis, JE Scott and J Warwick, Annual Report of the Central Laser Facility, Rutherford-Appleton Laboratory, 161, (1994).

THE EFFECTS OF MULTI-PULSE IRRADIATION ON IONISATION BALANCE IN X-RAY LASER MEDIA

A. Behjat[1], G. J. Tallents[1], M. Kurkcuoglu[1], S.P. McCabe[2], C.L.S. Lewis[2], A.G. MacPhee[2], D. Neely[3], P.J. Warwick[2], E. Wolfrum[3]

[1]*Department of Physics, University of Essex, Colchester, C04 3SQ, UK.*
[2]*Department of Pure and Applied Physics, The Queen's University of Belfast, BT7 1NN,UK.*
[3]*The Rutherford Appleton Laboratory, Chilton, Didcot OXON, OX11 0QX, UK.*

1. INTRODUCTION

A soft x-ray laser was first demonstrated[1] in 1984 for neon-like Se^{+24} at wavelengths of 206 and 210 Å on the J=2-1 lines of the 3p-3s transitions. To date, lasing in numerous Ne-like ions has been reported (for example, Ti, Ni, Ga, Ge, As, Se, Br, Rb, Sr, Y, Zn, Nb, Mo, and Ag)[2-5].

Initial experimental results obtained with the Ne-like lasers were not consistent with simple models[6-8] showing that the J=0-1 transitions should dominate the laser output because of their predicted high gain coefficients. Different explanations were proposed to explain the anomaly between the experimental observations of low gain on the J=0-1 lines and the predictions of high gain. Recently, detailed modelling[9,10] showed that the gain region for the J=0-1 line lies in higher density regions compared to the J=2-1 lines and so the J=0-1 lines may be more affected by refraction of the x-ray laser beam as it amplifies in plasmas with large density gradients.

Several methods of minimising refraction and so maximising the distance x-ray laser beams can propagate down amplifying plasma medium have been investigated. In the double-target configuration[11] used at the Rutherford Appleton Laboratory, density gradients in two targets are directed in opposite directions and so the net refraction is reduced. Refraction compensation by bending the targets has also been demonstrated[12-13]. Significant enhancements on the J=0-1 lasing output of neon-like ions (Germanium to Chlorine) when employing different level prepulses have been reported[14-16] and interpreted in terms of reduced refraction. Experimental results[17,18] also indicate that multiple pumping pulses act similarly to prepulses in producing more uniform plasma with enhanced x-ray laser output compared to single pulses.

We present here results from experiments with the Ge^{22+} x-ray laser using double pulse and double pulse with pre-pulse irradiation of stripe Ge targets. Up to 18 mm long Ge stripe targets were irradiated by multipulse irradiation. Various pre-pulse and multipulse configuration have been investigated. The best enhancement on the J=0-1 line at 196Å is produced with two pre-pulses (of irradiance $\approx$ 1%-5% of the main pulses) and two double pulses of approximately equal irradiance due to a reduction in refraction of x-ray laser beam.We show that the ionisation balance of the x-ray laser plasma medium is not affected by such multipulse irradiation, but that the x-ray laser output on the J=0-1 line is significantly enhanced in comparison to single pulse and double pulse (without pre-pulse) irradiation.

2. EXPERIMENTAL DETAILS

The VULCAN glass laser at the Rutherford Appleton Laboratory was modified to produce pairs of 100 ps pulses separated by 400 or 800 ps. Three refracting f/2.5 lens and off axis spherical mirrors[19] were used to produce line foci of 160 mm width and 16 mm length. The foci were overlapped to produce an approximately uniform irradiation on a single 18 mm long target of irradiance ~4 $\times$ 10^{13}W/cm^{-2}. Various pre-pulse and multipulse configurations were used to irradiate the targets . The drive pulses were monitored prior to entering the target chamber by directing the beam leakage through one of the final mirrors onto an optical streak camera. Ge targets consisting of ~ 6 µm thick germanium stripes of 100 µm width deposited onto 1.5 mm thick polished glass substrates were used. The stripes were aligned relative to the main axis of the target chamber using fixed CCD cameras with magnifying optics to spatial and angular accuracies of $\pm$5 micron and $\pm$1mrad respectively.

A grazing incidence cylindrical focusing optic was employed to image the exit aperture of the x-ray laser in the horizontal plane along the entrance aperture of a flat-field grazing incidence spectrometer. This arrangement produced spectra spatially resolved at the exit aperture of the x-ray laser in the direction of the target normal (horizontal), but spatially integrated vertically.

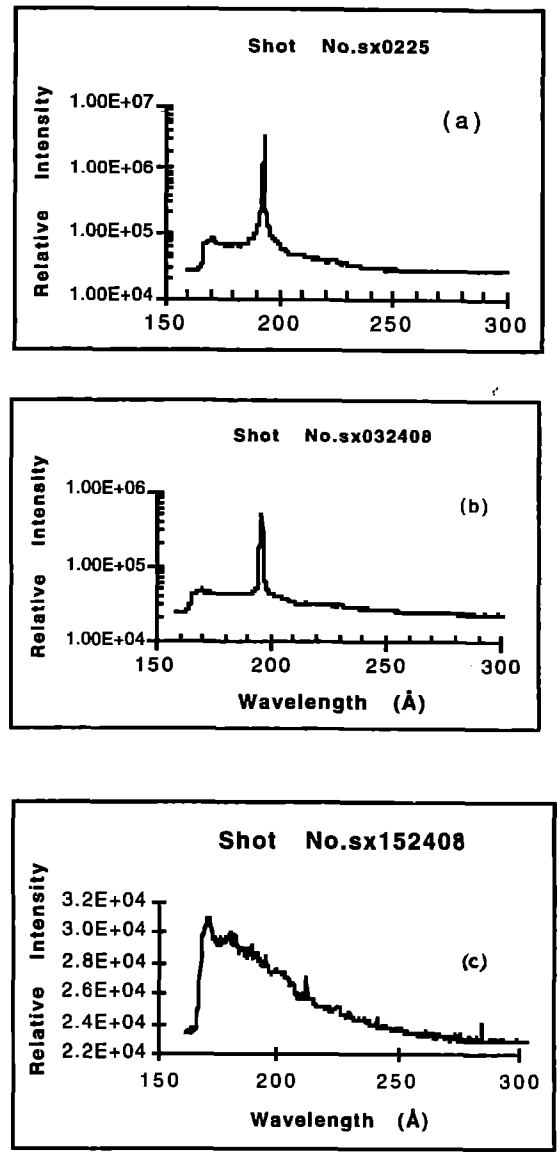

Figure 1 A typical Ge spectrum from the axial spectrometer for (a) double pumping laser pulses with prepulse, (b) double pumping laser pulses without pre-pulse and (c) a single pump pulse. Note that plots (a) and (b) have a logarithmic intensity scale.

The data from the spectrometer was detected using an absolutely calibrated 16 bit CCD system[20]. For this paper, the x-ray laser output recorded by the CCD was spatially integrated numerically in the horizontal direction to give (allowing for filter and reflectivity losses) the total number of x-ray laser photons produced. A space-resolved time integrating KAP crystal

spectrometer incorporating a 16 bit CCD detector was used to monitor the resonance line emission in the wavelength range of 7-10.1 Å and to monitor the uniformity of the line focus plasmas. A 35 micron slit enabled spatial resolution of 60 μm along the plasma length. A pinhole camera with 15 μm pinhole and CCD detection also imaged the plasma to give a measurement of the plasma width as a check of the optical laser focusing.

3. RESULTS

Typical Ge spectra from the flat-field spectrometer from a single pumping laser pulse and from double pumping laser pulses with and without prepulses are shown in Figure 1. The relative intensity values can be compared and show the dramatic increase in output of the J= 0-1 line at 196 Å (which is just visible for a single pumping pulse, see Figure 1c) with double pulsing (Figure 1b) and double pulsing with a pre-pulse (Figure 1a). The number of output photons were obtained from the soft x -ray CCD system by taking into account the absolute sensitivity of the CCD system (0.03 count $hn^{-1}mm^{-2}$), the reflectivity of the grating and silver coated mirror (5% and 80% respectively) and the transmission of an Al filter (0.2 or 0.4 mm thick). The x-ray laser output with a prepulse is systematically much greater than without. A typical spectrum from the KeV spectrometer operated over the range of 7-10.1 Å is shown in Figure 2. The ratio of the intensity of the F-like band (9.4 - 9.6 Å) to the intensity of the Ne-like lines 9.76-10.01 Å was used[21] to monitor the ionisation balance and uniformity of the line focus plasma. It can be seen (Figure 3) that there is no correlation between the ionisation balance as measured by the intensity ratio of the F-like to Ne-like band emission and the x-ray laser output, provided the ionisation is above a certain minimum (a ratio of ~ 0.7).

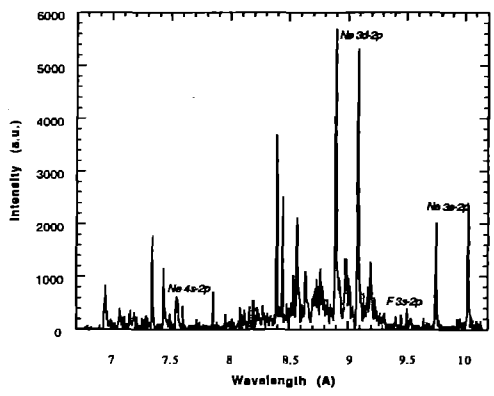

Figure 2 The spectrum of Ne-like and F-like Ge obtained with crystal spectrometer (KAP crystal, 2d=26.6 Å). These results are time and space integrated along the line plasma.

4. DISCUSSION

As the ionisation balance measured by the KeV crystal spectrometer (Figure 3) does not affect the x-ray laser output, it seems that the degree of refraction of the x-ray laser in the plasma medium controls the x-ray laser output. Longer scale-length plasmas produced by the multi-pulse irradiation result in much less refraction and so the J=0-1 line which is produced at higher densities than the J=2-1 lines[9], is refracted less and stays for a longer length in the high density gain region. Since the resonance line ratios are measured from time integrated spectra, further analysis with time resolved data is now required.

5. CONCLUSION

Significant enhancement of lasing for the J=0-1 line at 196Å has been demonstrated by employing a double pulse optical drive. Using a low level prepulse along with the double pulse gives an increase in total output of the x-ray laser of two orders - of - magnitude for the J=0-1 line of neon like Ge. The independence

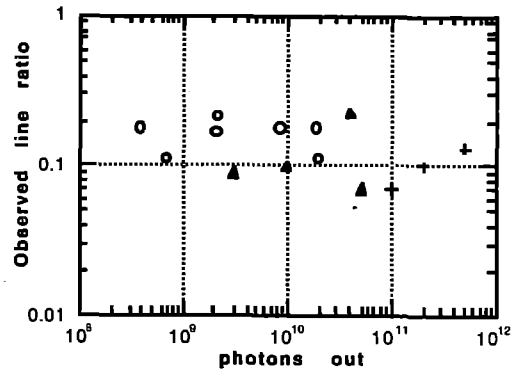

Figure 3 Ionisation balance as measured by the ratio of F-like to Ne-like resonance line emission (see text) as a function of the x-ray laser output. O Double pulse with 400 ps separation. ▲ Double pulse with 800 ps separation. + Double pulse with 400 ps separation and two prepulse.

of the ionisation balance (measured by a crystal spectrometer) with x-ray laser output indicates that the x-ray laser output is mainly determined by refraction of the laser beam as it amplifies in the plasma medium.

REFERENCES

[1] D.L. Matthews et al., Phys. Rev. Lett. **54**, (1985) 110.
[2] J. Nilsen, J.L. Porter, B.J. MacGowan, L.B. Da Silva, and J.C. Moreno, J. Phys. B. **26**, (1993) L243.
[3] C.L.S. Lewis et al., X-ray lasers 1992, E.E. Fill, ed., Institute of Physics Conference Series No. 125 (Institute of Physics, Bristol, UK, 1992) 23.
[4] D.M. O'Neil et al., Opt. Commun. **75**, (1990) 406.
[5] D. Neely et al., Opt. Commun. **87**, (1992) 231.
[6] D.L. Matthews et al., J. dePhysique, **47**, No. NC-6, (1986) 1.
[7] B.J. MacGowan et al., J. Appl. Phys. **61**, (1987) 5243.
[8] T.N. Lee, E.A. McLean, and R.C. Elton, Phys. Rev. Lett. **59**, (1987) 1185.
[9] S.B. Healy et al., J. Phys. B - Atomic Molecular and Optical Physics, Vol. 27, No. 2, (1994) 341.
[10] P.B. Holden and B. Rus, Opt. Commun. 119 (1995) 424.
[11] C.L.S. Lewis et al., X-ray lasers 1990, G.J. Tallents, ed., Institute of Physics Conference Series No. 116, (Institute of Physics, Bristol, UK, 1990) 231.
[12] D. Neely et al., X-ray Lasers 1994, D.C. Eder, D. Matthews eds., AIP Conference Proceedings 332, (1994) 210.
[13] R. Kodama et al., Phys. Rev. Letts., 73, **24**, (1994) 3215.
[14] J. Nilsen, B.J. MacGowan, L.B. Da Silva, and J.C. Moreno, Phys. Rev. A **48**, (1993) 4682.
[15] G.J. Tallents et al., Soft X-ray Lasers and Applications 1995, J.J. Rocca, P.L. Hagelstein eds., SPIE Conference Proceedings, 2520, (1995) 34.
[16] E.E. Fill et al., Soft X-ray Lasers and Applications 1995, J.J. Rocca, P.L. Hagelstein eds., SPIE Conference Proceedings, 2520, (1995) 134.
[17] J.C. Moreno, J. Nilsen, and L.B. Da Silva, Opt. Commun., 110, (1994) 585.
[18] J. Nilsen and J.C. Moreno, Phys. Rev. Lett. **74**, (1995) 3376.
[19] I.N. Ross et al., Applied Optics, **26**, 9, (1987) 1584.
[20] A.G. MacPhee and C. Lewis, X-ray Lasers 1994, D.C. Eder, D. Matthews eds., AIP Conference Proceedings 332, (1994) 441.
[21] G.F. Cairns et al., submitted to J. Phys. B.

MEASUREMENT OF OUTPUT CHARACTERISTICS OF A NEON-LIKE GERMANIUM X-RAY LASER ON THE J = 0→1 TRANSITION AT 19.6 NM

J. Zhang[1], J. Warwick[2], E. Wolfrum[3], M.H. Key[1,3], T.W. Barbee Jr.[6], C. Danson[3], A. Demir[4], S. Healy[5], D. Kalantar[6], N.S. Kim[1], C.L.S. Lewis[2], J. Lin[4], D. Neely[3], J. Nilsen[6], G.J. Pert[5], R. Smith[4], G.J. Tallents[4] and J.S. Wark[1]

[1]Clarendon Laboratory, Department of Physics, University of Oxford, Oxford, OX1 3PU, UK
[2]Department of Pure and Applied Physics, Queens University of Belfast, Belfast, BT7 1NN, UK
[3]Central Laser Facility, Rutherford Appleton Laboratory, Chilton, Didcot, Oxon, OX11 0QX, UK
[4]Department of Physics, University of Essex, Colchester, CO4 3SQ, UK
[5]Department of Computational Physics, University of York, York, YO1 5DD, UK
[6]Lawrence Livermore National Laboratory, Livermore, CA 94550, USA

INTRODUCTION

X-ray lasers from laser produced plasmas have been demonstrated in neon-like ions ranging from chlorine (Z = 17) to silver (Z = 47) [1,2]. Saturation has been observed on J = 2→1 transitions in germanium, selenium and yttrium plasmas and on J = 0→1 transition in zinc plasma [3-5]. Saturated operation is very important because it means that the maximum power possible for a given volume of an excited plasma is extracted by stimulated emission. Saturation also tends to produce an output energy sufficient for applications.

Saturated operation on a single laser line is needed for interferometric applications, but the saturated operation has been observed mostly on J = 2→1 transitions, which give typically doublets of lines with comparable intensities. The yttrium x-ray laser is unique in giving a single line because the short wavelength singlet J = 2→1 transition dominates the spectrum due to an overlap with a J = 0→1 transition, which adds to the gain.

X-ray lasers on J = 0→1 transition are especially interesting as they generate a single line. Recently, saturation has been demonstrated on the J = 0→1 transition at 21.2 nm in a zinc plasma using a prepulse technique [5]. The prepulse heats, ionises and expands the plasma. Between pulses, the plasma cools down and is not as transparent to the optical drive laser and the lasing region of the plasma can directly absorb energy from the main pulse. A larger, more uniform density plasma at the densities required for the J = 0→1 laser line is then generated during the main pulse. The much reduced density gradient allows the J = 0→1 x-ray laser beam to propagate a longer distance at higher density along the excited plasma column and therefore to obtain sufficient amplification for saturation.

We are interested here in producing a saturated neon-like germanium x-ray laser beam on the 19.6 nm J = 0→1 transition for the study of the hydrodynamic imprinting of laser speckle pattern on directly driven laser fusion targets. In order to provide information of the fast evolving plasmas and to reduce blurring due to the hydrodynamic motion of the plasma, it is preferable to have an x-ray laser pulse duration of less than 100 ps. It has been demonstrated that it is possible to produce a 50 picosecond (ps) short pulse 19.6 nm germanium x-ray laser while maintaining a high output energy [6]. Furthermore, the 19.6 nm germanium x-ray laser is just on the long wavelength side of the aluminium L edge which allows one to use readily available aluminium filters which have high transmission at this wavelength.

EXPERIMENTAL SETUP

The experimental set-up is shown in figure 1. Six beams of the VULCAN glass laser with a 75 ps duration at 1.05 μm were used in a standard off-axis focus geometry, where f/2.5 spherical lenses focused three beams from one side of the target chamber to a spot focus which was then imaged by f/2.5 off-axis spherical mirrors to produce a line focus 25 mm long and 100 μm wide. The total energy on each target is about 100 J giving irradiances of ~ $5x10^{13}$ W/cm^2 on target. Deploying the other three beams 180º opposed in another line focus produced a second plasma with opposite density gradient which compensated for refraction deviation of the x-ray laser beam from the first plasma.

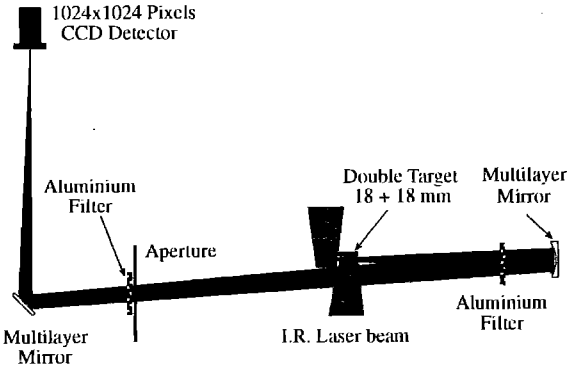

Figure 1. Schematic of the experimental setup.

The prepulse was produced by splitting the oscillator pulse into two pulses before the preamplifiers in the VULCAN laser. A variable prepulse between 10% and 30% of the total energy on target was produced and delivered 2.2 ns in advance of the main pulse. The prepulse level and pulse duration were monitored by a fast photodiode system and streak camera.

The slab targets used in the experiment were 18 mm long 100 μm wide germanium stripes coated on glass substrates. Both ends of the slab target were placed well within the line focus to avoid cold plasmas at the ends of the targets. The targets were aligned off line in a double target mount so that they were parallel with an adjustable radial separation between the surface planes and an axial separation 500 μm between the two targets. Since the x-ray laser pulse duration is comparable to the propagation time, travelling wave excitation for the two successive targets is necessary to achieve sufficient amplification. The three drive beams for the first slab target were therefore timed 60 ps earlier than the other three beams for the second target. The targets were aligned relative to the target chamber axis using a magnifying CCD system to accuracies of ± 1 mrad and ± 3 μm.

In order to measure the output energy of the J = 0→1 germanium x-ray laser, we used a diagnostic consisting of multilayer mirrors, Al filter and a Peltier cooled back thinned XUV CCD detector with 1024x1024 pixels and 24 μm pixel size as shown schematically in figure 1. The mirrors had super-polished (< 0.1 nm RMS roughness) substrates and were coated with 30 layer pairs of molybdenum and silicon. They had a measured peak reflectivity of about 20 % at a central wavelength 19.6 nm with a

Full Width at Half Maximum (FWHM) bandwidth around 1.5 nm. The concave multilayer mirror had 50 cm focal length and was positioned to image the output end of the germanium x-ray laser via a 45° planar multilayer mirror onto the CCD detector at a magnification of 16x. For some shots, a plane 3.0 cm from the laser output end was imaged to provide quasi far field information.

The imaging system was calibrated by placing at the imaging plane a grid target with fine bars repeated each 15 μm. Analysis of this image showed the resolution of the system to be better than 1 μm and calibrated the magnification at 16x. The imaging mirror had an aperture about 25 mm, which gave an acceptance solid angle of 2.5×10^{-3} sterad (50 mrad in radial direction and 50 mrad in the direction parallel to the target surface respectively). Astigmatism in the image was minimised by operating the imaging mirror at less than 0.6° off normal incidence. The planar mirror and the apertures in the path provided screening against broad band thermal XUV emission. The aluminium filters protected against stray laser light and attenuated the x-ray laser beam.

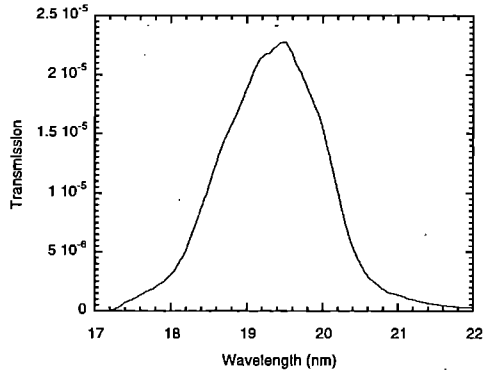

Figure 2. Measured system throughput accounting for multilayer mirrors and aluminium filters.

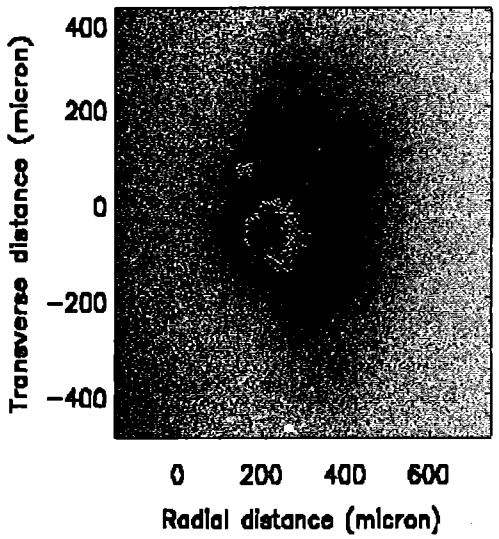

Figure 3. Near field image of the neon-like germanium laser at 19.6 nm from a double target with a 200 μm separation.

We calibrated the reflectivity of each multilayer mirror and the transmission of each filter using XUV radiation from a laser-produced plasma source coupled to a grating spectrometer, similar to Ref. 7. The transmission of a 3.2 μm thick Al filter was measured to be $9 \pm 2 \times 10^{-4}$, which agrees with the calculated value within the uncertainty range. The total throughput of the system, presented in figure 2, shows the high rejection outside the narrow bandpass of the multilayer mirrors. The total uncertainty of the system is estimated to be less than a factor of 2. For some shots, the multilayer mirrors were replaced by two axial flat-field grating spectrometers to give an independent measurement of angular distribution and the output energy of the x-ray laser.

Off-axis diagnostics included two spatially resolving crystal spectrometers coupled to x-ray CCD detectors. Resonance emission from the neon-like and fluorine-like ionisation stages in the wavelength range of 7.0-10.5 Å from the two opposing germanium plasmas were monitored to provide information on ionisation balance and uniformity of the plasmas. The ratio between the fluorine-like and germanium-like resonance lines gave a very sensitive monitor of the uniformity of the illumination on target [8].

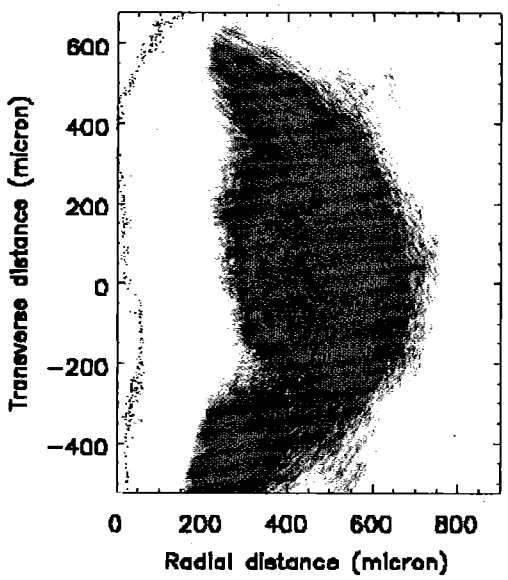

Figure 4. Image of the x-ray laser beam 3 cm from the output plane for double target with 200 μm separation.

OUTPUT CHRACTERISTICS

Figure 3&4 show near field and far field images of the germanium x-ray laser from the double target with a separation of 200 μm in the radial direction. The radial direction is the horizontal axis in the figures with zero corresponding to the original target surface. The target surface position was determined using the thermal emission from the target surface. We observe asymmetric distribution in brightness in the parallel direction both in the near and far field images. We believe this is due to asymmetric amplification caused by a small mismatch of the opposing plasmas in the direction parallel to the target surface. Comparing the near and far field images, we notice that x-ray photons spread over much wider angle in the propagation process in the direction parallel to the target surface than the perpendicular direction. This is plausible since both the opposing plasma and the prepulse technique only improve the propagation in the perpendicular direction. After propogating 3 cm distance, divergence in the prependicular direction is only 6.6 mrad, which agrees with the measurements of anglar distribution using spectrometers. Whereas the divergence in the direction parallel to the target surface was measured to be as large as 30.4 mrad, which was the combination effect of the propagation along the two plasmas.

Since the collection solid angle of the multilayer mirror system overfills the angular distribution of the germanium laser beam, we can estimate the output energy by integrating the total photons emitted from the gain region and using an absolute calibration for the CCD detector and the calibrations for the x-ray multilayer mirrors and aluminium filters (figure 2). The output energy of the germanium laser was estimated to be ~ 0.9 mJ.

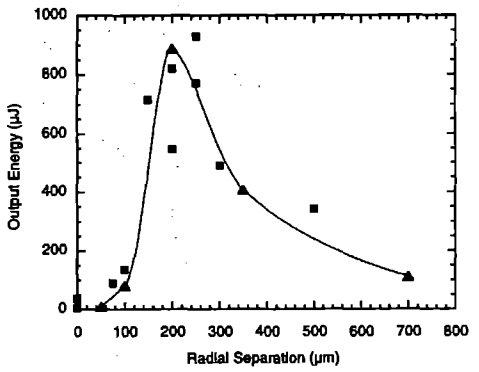

Figure 5. Comparison of output energy measured by the CCD detector via multilayer mirrors and that measured by a flat-field spectrometer on axis.

In figure 5 we show the variation of the output energy against the perpendicular separation between the double targets. The solid triangle with solid line is the measured output energy collected by the imaging mirror. The solid squares represent measurements using the axial flat-field grating spectrometer based on the calibration of the grating (5% reflection at 19.6 nm) and the double reflection filter (5% reflection). The spectrometer has an acceptance angle of 46 mrad in horizontal direction (direction perpendicular to the target surface), which is large enough to collect all the photons from the germanium laser in that direction. But the vertical (direction parallel to the target surface) collection angle of the spectrometer is only 13 mrad, 2.3 times smaller than the divergence angle of the x-ray laser beam. We have therefore taken this factor into account in our estimate. Both measurements show the strong coupling effect at a perpendicular separation around 200 μm. We did not measure the gain duration, but the simulations suggest that the Ge J = 0→1 laser emission has a time duration of 40 ps, which agrees with the experimental experience that the x-ray laser pulse duration is about half of the drive pulse duration [6]. The estimated peak x-ray laser output power is 20 MW. The estimated uncertainty in this measurement is a factor of 2 and is due predominantly to errors in the filter attenuation. Given our best estimates of the source size, the spectral line width (2.5×10^{-3} nm), and the beam divergence (6.6 mrad horizontal by 44 mrad vertical), we calculate a brightness of 7.2×10^{17} W/(cm^2 sr nm). The output intensity, which we can compare with the saturation intensity, is calculated to be 7.9×10^{10} W/cm^2.

The saturation intensity can be estimated by equating the rate of stimulated emission in the laser transition to the total exit rate from the upper state. This assumes that the processes feeding the upper state are unperturbed by the stimulated emission. Applying the Einstein relations between spontaneous and stimulated results in a simple formula for saturation intensity:

$$I_{SAT} = \frac{8\pi\sqrt{\pi}h\nu^3\Delta\nu}{c^2}\frac{E}{A}, \qquad (1)$$

where ν is the frequency of the line, $\Delta\nu$ is the width, E is the total exit rate for electrons from the upper state, and A is the spontaneous radiative decay rate in the lasing transition. To evaluate I_{SAT} we take values for $\Delta\nu$ and E from complete hydrodynamic and kinetic simulations of the germanium slab, using the method described in Ref. 9. Values are taken near the centre of the 75 ps heating laser pulse, when the gain is predicted to peak. The typical plasma conditions are an electron temperature of 880 eV, and an electron density of 3×10^{20} cm^{-3}. The intrinsic line width of the 19.6 nm transition is estimated to be 42 mÅ by combining homogeneous broadening and inhomogeneous broadening (Voigt profile) [10]. The exit rate (E) is calculated to be 1.15×10^{12} s^{-1}, compared with the spontaneous radiative decay rate (A) of 2.15×10^{10} s^{-1}. Electron collisions to other n=3 levels dominate this exit rate. Applying Eq. (1), we estimate that $I_{SAT}=2.0\times10^{10}$ W/cm^2. Although this calculation is a factor of 4 lower than the measured integrated output intensity of 7.9×10^{10} W/cm^2, this is within the theoretical and experimental uncertainty.

CONCLUSION

We have presented output energy measurement of a saturated neon-like germanium x-ray laser. The high brightness and 19.2 nm wavelength of this laser makes it an ideal candidate for radiography experiments. Recent radiography measurements using this 19.6 nm germanium x-ray laser will be described in other section of this annual report.

ACKNOWLEDGEMENTS

The authors would like to thank the VULCAN laser operations, the target preparation and engineering groups of the Central Laser Facility for their help and cooperation.

REFERENCES

[1] Y.L. Li, G. Pretzler, and E.E. Fill, Phys. Rev. A**52**, R3433 (1995).

[2] D.J. Fields, R.S. Walling, G.M. Shimkaeg, B.J. MacGowan, L.B. Da Siva, J.H. Scofield, A.L. Osterheld, T.W. Phillips, M.D. Rosen, D.L. Matthews, W.H. Goldstein, and R.E. Stewart, Phys. Rev. A**46**, 1606 (1992).

[3] A. Carillon, H.Z. Chen, P. Dhez, L. Dwivedi, J. Jacoby, P. Jaegle, G. Jamelot, J. Zhang, M.H. Key, A. Kidd, A. Klisnick, R. Kodama, J. Krishnan, C.L.S. Lewis, D. Neely, P. Norreys, D. O'Neill, G.J. Pert, S.A. Ramsden, J.P. Raucourt, G.J. Tallents, and J. Uhomoibhi, Phys. Rev. Lett. **68**, 2917 (1992).

[4] J.A. Koch, B.J. MacGowan, L.B. Da Silva, D.L. Matthews, J.H. Underwood, P.J. Batson, and S. Mrowka, Phys. Rev. Lett. **68**, 3291 (1992).

[5] P. Jaegle, A. Carillon, P. Dhez, P. Goedkindt, G. Jamelot, A. Klisnick, B. Rus, P. Zeitoun, S. Jacquemot, D. Mazataud, A. Mens, and C. Chauvineau, *X-ray Lasers 1994*, AIP Conf. Proc. **332**, 25 (AIP: New York, 1994).

[6] J.C Moreno, R.C. Cauble, P. Celliers, L.B. Da Silva, J. Nilsen, and A.S. Wan, *Soft X-Ray Lasers and Applications*, Proc. Soc. Photo-Opt. Instrum. Eng. **2520**, 97 (1995).

[7] J.A. Trail, R.L. Byer, and T.W. Barbee, Jr., Appl. Phys. Lett. **52**, 269 (1988).

[9] L.B. Da Silva, B.J. MacGowan, S. Mrowka, J.A. Koch, R.A. London, D.L. Matthews, and J.H. Underwood, Opt. Lett. **18**, 1174 (1993).

[10 G. Yuan, Y. Kato, K. Murai, and R. Kodama, J. Appl. Phys. **78**, 3610 (1995).

A TIME RESOLVED SPECTROSCOPY STUDY OF THE RESONANCE LINE EMISSION IN THE GE XXIII XUV LASER.

G F Cairns[1], S B Healy[2], C L S Lewis[1], G J Pert[2] and E Robertson[1]

[1] Department of Pure and Applied Physics, Queen's University of Belfast, Belfast BT7 1NN.
[2] Department of Physics, York University, York, YO1 5DD, UK

INTRODUCTION

Laser produced plasmas are well tested media for the production of lasing at XUV wavelengths. However current systems which use LPPs as the lasant media still require access to large (kJ/TW) lasers. To aid in the design of experiments to make such schemes operate more efficiently, it is imperative to have reliable simulation codes. These codes simulate the basic hydrodynamics of the plasma and allow us to diagnose the plasma conditions in terms of the plasma electron temperature and density, the densities of the ionisation stages present and the populations of the excited levels. The corresponding experimental information may be provided with spectroscopy studies of the 'harder' X-ray resonance line emission, which tends to be relatively bright and generally well resolved in comparison to other emissions in the relevant high temperature plasmas of current XUV laser systems. Results are presented here which validate the accuracy of the predictions of a particular hydro-atomic code EHYBRID, which has been developed at York.

A comparison is presented of the temporally resolved resonance line emission from the Ne-like Ge XUV laser (pumped with nanosecond pulses) with the predictions for the same emission from the code EHYBRID. The specific lines chosen were the two 3s-2p Ne-like lines at 10.01 (Ne1) and 9.762 Å (Ne2), and the 3s-2p F-like group of lines (F-band) in the 9.4-9.6 Å region. Modification of the code[1] to include 112 excited levels of the F-like ion facilitated a direct comparison between experiment and model of (a) the temporal variation of the emissions and (b) the variation of the peak intensity ratios of the F-like to Ne-like emissions with irradiance on target.

The time resolved data was acquired in two Ge XXIII XUV laser experiments using a crystal spectrometer attached to a streak camera which was mounted so that its line of sight made an angle of ~53° with the axis of the plasma and an angle of ~44° with the horizontal plane through the target (i.e. the view was at an angle $\theta \sim 68°$ with respect to the target substrate normal). The crystal centre was located approximately 25cm from the plasma. The same setup was used in the two experiments which had different pulse lengths and which are referred to as the long pulse and short pulse experiments in this discussion. In the long pulse experiment, a Gaussian shaped pulse of 1.0 ± 0.2 ns FWHM duration was delivered onto target at irradiances from 0.3 - 1.2 x 10^{13} Wcm^{-2} . Targets were typically 18 mm long and 160 μm wide Ge slabs (~ 0.5 μm thick) coated onto polished glass substrates. A shorter drive pulse was used in the other experiment of duration 700 ± 50 ps FWHM. The pulse shape was somewhere between that of a trapezoid and an asymmetric Gaussian with an estimated risetime of ~ 300 ps and a plateau time of ~ 450 ps. Typical irradiances from 1.0 - 2.0 x 10^{13} Wcm^{-2} were delivered to the Ge stripe targets. The latter were typically 22 mm long and 100 μm wide.

EHYBRID is a quasi-2D Lagrangian code which operates in planar geometry and is suitable for modelling slab targets. It has been described in detail elsewhere[2-4]. In order to simulate the experimental drive pulses as closely as possible, asymmetric pulses were used in the code. In each case the modelled pulse had a FWHM equivalent to the real pulse. The rising edge of the pulse was defined by a polynomial which was characterised by a rise-time TOR. This was the time it took for the intensity to go from zero to maximum. The falling edge was defined by a true Gaussian, its profile being determined by the FWHM of the experimental pulse. A pulse with a risetime TOR of 415ps and a falling edge defined by a FWHM of 830ps was used to model the short pulse experiment, whilst a pulse of risetime 600ps and a fall-off defined by a FWHM of 1.25 ns was used in the long pulse case.

The code calculated the excited state populations at regular timesteps. The emission from each cell was calculated at each timestep and the total emission at this time found by summing over all cells. The time-integrated emission E (to be compared with experiment) was then calculated by integrating the output signal over time. This may be expressed as,

$$E = \int \left[\sum_{m} n_i g(\tau) A_{ij} dV \right] dt$$

where n_i is the upper state population for a given transition, A_{ij} denotes the transition rate, and $g(\tau)$ is an escape factor which takes into account the effects of trapping on the emitted radiation. The latter was calculated locally in the code for each cell as part of the C-R model rate equation treatment. The volume element and the cell number are denoted by dV and m respectively. Opacity effects were modelled using escape factors interpolated between those of the Holstein[5] and Sobolev[6] models.

Some loss mechanisms of the incoming drive laser have not been included in the model such as Brillouin and Raman scattering. These have been estimated to account for losses up to as much as 50% of the drive energy[3,7]. (Of the energy supplied in the model, the code calculates an overall absorption, due to Inverse Bremsstrahlung and resonant absorption, of ~80%). If an overall loss of ~50% is assumed, this implies that the actual irradiance input to the code corresponds to ~0.5X the irradiance actually used in the experiment.

RESULTS AND DISCUSSION

The modelled trends of the F/Ne ratios with variation of the pulse length, for a given peak irradiance on target are illustrated in figure 1. Both the peak and time integrated ratios have been generated for two typical irradiances of 1x10^{13} and 2x10^{13} Wcm^{-2}. This shows that the ratios are sensitive to the change in pulse-length up to ~700 ps. For longer pulse-lengths the increase of the F/Ne ratios with increasing pulse-lengths is less pronounced.

Comparisons of the temporal profiles from both experiment and model are shown in figures 2 and 3. Normalisation of intensities was carried out relative to the peak of the Ne1 line in each case. Figure 2 shows the temporal profiles for the long pulse case at irradiances of $I \sim 1.4 \times 10^{13}$ Wcm^{-2} for the experiment and $I \sim 1.5 \times 10^{13}$ Wcm^{-2} for the model. The temporal resolution inherent in the experimental results has not been convolved into the modelled profiles. Doing this would tend to increase the FWHM and to reduce the peak signals of the modelled profiles. However, this is a relatively small effect (~2 %) due to the large FWHM of the emission. The F/Ne ratios are compared in figure 2(b). An

intensity profile of the drive beam used in the model has also been included in this figure. The agreement between the model and experiment is reasonably good. Indeed the F/Ne ratio profiles are very similar apart from the relative temporal offset of ~200 ps. The F-like emission tends to peak early in time relative to the peaks of the Ne-like emission as measured experimentally, which is in contrast to the modelled profiles with the F-band peaking after the peak of the Ne-like lines.

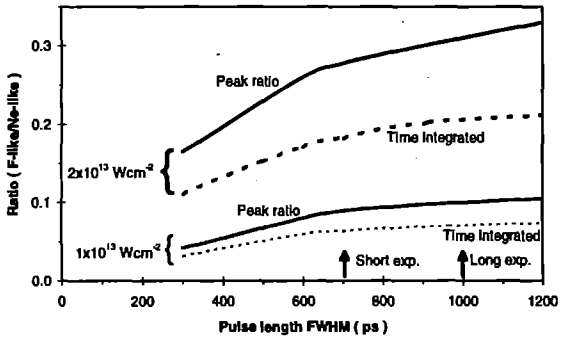

Figure 1 Modelled trends of the F/Ne ratios with variation in pulse length (FWHM).

There is uncertainty in the timing of the experimental traces relative to zero due to the uncertainty in the detection of the continuum signal. If there is a delay in the build up of the measurable continuum then the times measured will be relative to some time reference within the drive pulse, resulting in a systematic shift to earlier times for the experimental results on a time axis set by the modelled pulse profile. Correcting for this would involve a systematic shift to later times for the experimental profiles in the figures which would tend to improve agreement between the experimental and modelled ratio profiles.

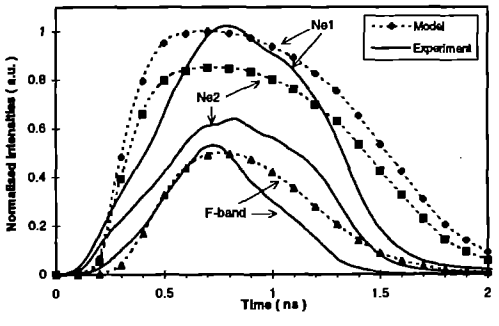

(a)

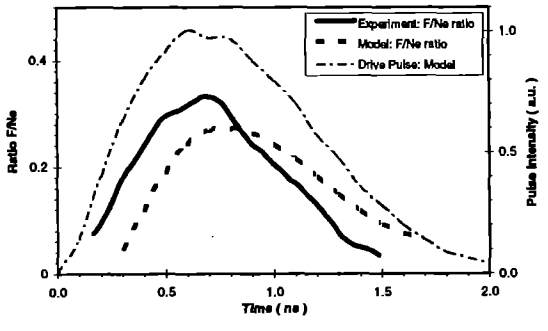

(b)

Figure 2 Comparison of the temporal profiles of the lines in the long pulse case (a) and the corresponding F/Ne ratios (b).

Good agreement was noted between the temporal experimental and model profiles in the short pulse case, as displayed in figure 3. A comparison of temporal profiles with irradiances of ~1.9 x 10^{13} Wcm^{-2} in the experiment and 1.2 x 10^{13} Wcm^{-2} in the model is shown. The irradiances are consistent if unmodelled losses of actual experimental energy are assumed to be ~40 %. The ratio profiles in figure 3(b) are remarkably similar apart from a relative

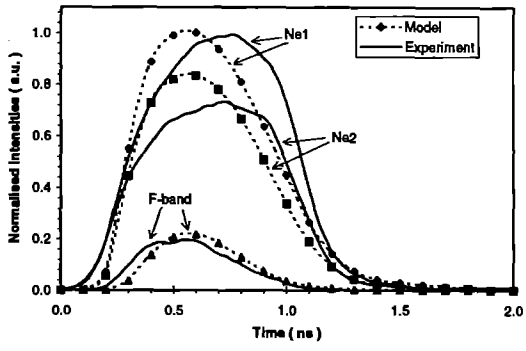

(a)

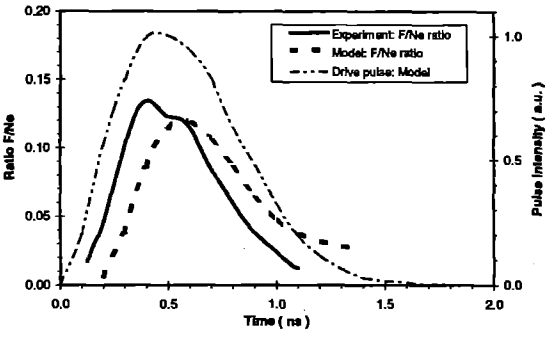

(b)

Figure 3 Comparison of model and experiment line profiles for short pulse case (a) and the corresponding F/Ne ratio profiles (b).

time shift of ~200ps between them, as also observed in figure 2(b). As noted earlier this offset, evident in both the long and short pulse cases, may be due in part to a systematic error in the estimation of time zero for the experimental results. This highlights the importance of a timing fiducial in streak records.

The short pulse experiment results consistently showed the F-like emission to peak early in time relative to the peak of the Ne-like emission. As in the long pulse case, this temporal pattern was reversed in the model. This difference implies that, experimentally, the electron temperature is lower than calculated at later times.

As a further comparison, the peak of the F/Ne ratio profiles were calculated for a range of irradiances in the model spanning those used in the experiments. The peak ratios from both experiments and the corresponding modelling are plotted against the experimental irradiance in figure 4. Two model curves are presented for each case, where the lower model curve assumes unmodelled losses of 50%, (i.e. the code data has been re-plotted with the irradiance multiplied by a correction factor F=2). The model agrees with the experiments in predicting a higher peak ratio for a given irradiance with the long pulse conditions. This is illustrated in the figure for the two uncorrected modelling curves and is consistent with more energy being supplied to the plasma in the long pulse case. The experimental results are expected to lie between the 0 to 50% unmodelled loss limits i.e. within the shaded regions of the diagram.

There is particularly good agreement between the experiment and model for the short pulse results with the data lying well within

the expected region. The trends of the long pulse results from both model and experiment are clearly consistent. However the experimental ratios lie above those predicted by the model. This discrepancy may be due to some unknown systematic error in the experimental data rather than a limitation of the model. The shot to shot variations in the measurements have been shown with typical error bars and do not include systematic errors. These systematic

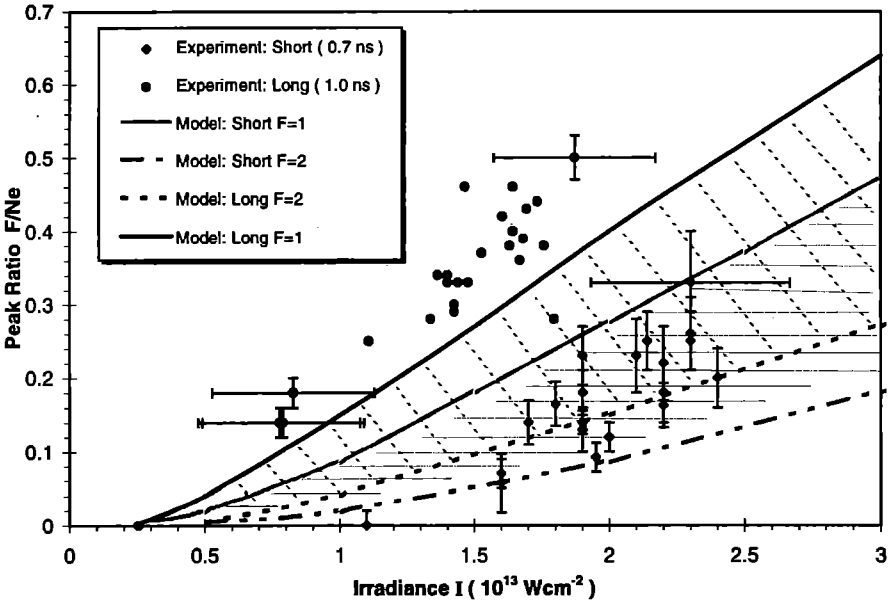

Figure 4 The trends of the peak F/Ne ratios with irradiance on target.

errors, which are principally associated with the energy monitoring calorimeters, the sweep speed of the optical streak cameras and the obscuration on target, are expected to be of the order of ±20%. When the total uncertainties are considered, it can be seen that both sets of results are broadly consistent with the predictions.

When the opacity on a line is important then the plasma dimensions are also important and in turn the angle from which the plasma is viewed. In general the velocity gradients may be different in different directions especially for planar geometries. The spectrometer was therefore viewing the plasma at what could be considered an average position in terms of the influence of the optical depth. The plasma is optically thinnest when viewed normal to the target (velocity gradients steepest) and optically thickest when viewed from the transverse direction (shallower velocity gradients and scale-lengths of ~100 μm). The good agreement noted here between experiment and model is in part due to the fact that the escape factor approximations in the code are based on an averaging of the optical depth experienced. Simple test calculations of the upper and lower limits that might be expected for the opacity τ, given by,

$$\tau = \int k_\nu dl$$

where k_ν is the absorption coefficient and the integral is over the pathlength l, indicated that the bulk of the emission should be produced close to the optically thin regime where precise treatment of radiative transport is not so essential . This reduces to some extent the importance of the direction in which the spectrometer views the plasma, which in this case was at a view angle of ~68° to the target normal. Furthermore, systematic errors associated with opacity treatment of the Ne-like and F-like resonance transitions will tend to cancel when calculating the ionisation balance ratios (F/Ne).

CONCLUSIONS

The measurement of the temporally resolved resonance line emission in the Ge XUV laser has allowed us to carry out a further validation test of the predictions from the hydro-atomic code, EHYBRID. The EHYBRID code was modified to include 112 excited levels of the F-like ion along with the already included 124 excited levels of the Ne-like ion which allowed for the direct comparison with experimental results of the line intensity ratios from the two ion species. The model used escape factors based on the Holstein and Sobolev models to account for opacity effects on the resonance lines. However, our test calculations of the opacity expected on these lines, indicated the system should be close to the optically thin regime for these lines under the current conditions and therefore that the model should not be very sensitive to how the opacity is treated.

The agreement between model and experiment trends was generally good and suggest that the model is realistically simulating the hydrodynamics and atomic kinetics of the plasma. Higher F/Ne ratios were predicted for longer duration pulses at a given irradiance which was in broad agreement with the experimental observations. This further indicates that the same model can simultaneously calculate the Δn=1 (≈keV) and the Δn=0 (sub-keV) transition intensities through population dynamics with a satisfactory degree of accuracy.

A notable feature indicating variance between experiment and model, was the relative timing of the F-like emission to the Ne-like. The model predicts the F-like emission to peak somewhat later in time, several hundred picoseconds, compared to that observed in practice.

REFERENCES

1. E. Robertson, A. Kingston, C.L.S. Lewis, G.F. Cairns, S.B. Healy and G.J. Pert, 1995 *Annual Report to the Central Laser Facility*, (Rutherford-Appleton Laboratory, Chilton, Didcot, UK) TR-95-025 pp 68.
2. G.J. Pert, 1983 *J. Fluid Mech.* **131** 401.
3. P.B. Holden, S.B. Healy, M.T.M. Lightbody, G.J. Pert, J.A. Plowes, A.E. Kingston, E. Robertson, C.L.S. Lewis, D. Neely 1994 *J. Phys. B: At. Mol. Opt. Phys.* **27** pp 341-367.
4. S.B. Healy, G.F. Cairns, C.L.S. Lewis, G.J. Pert, and J.A. Plowes 1995 IEEE J. Select. Topics Quantum Electron. **1** 3 pp 949 - 957.
5. T. Holstein 1947 Phys. Review **72** 12 pp 1212-1233.
6. V. Sobolev 1957 Soviet Astron. **1** 678.
7. C. Garban-Labaune, E. Fabre, C. Max, F. Amiranoff, R. Fabbro, J. Virmont, and W.C. Mead 1985 *Phys. Fluids* **28** 8 pp 2580-2590.

LYMAN-α INTENSITY RATIO CALCULATIONS FROM COLRAD FOR LASER-PRODUCED PLASMAS

J.M.A. Ashbourn[1] and N.N. Ljepojevic[2]
Centre for Computer and Mathematical Modelling,
School of Electrical, Electronic and Information Engineering,
South Bank University, 103 Borough Road, London, SE1 0AA, England

INTRODUCTION

In this paper, we present a brief account of the calculations made by the collisional-radiative code, COLRAD[1], and how the results obtained can be applied to laser-produced plasmas. The particular quantities considered are the excited level populations of hydrogenic species in optically thin high-temperature plasmas, and from these, the Lyman-α doublet intensity ratios have also been calculated. In the laser-produced plasmas considered here, the range of electron densities is approximately 10^{19} - 10^{22} cm^{-3} and the range of electron temperatures is approximately 400 - 1400 eV. The theoretical calculations have been done for a number of hydrogenic ions, including Titanium XXII, Chromium XXIV and Nickel XXVIII[2], but in this particular study for one specific laser-produced plasma, the hydrogenic ion under consideration is Aluminium XIII.

CALCULATION OF INTENSITY RATIOS

The Lyman-α doublet intensity ratio, $\frac{\alpha_{1/2}}{\alpha_{3/2}}$, is the ratio of the intensities of the emission from the $2P_{1/2}$ and $2P_{3/2}$ states down to the ground state, respectively. Since the energy difference between $2P_{1/2}$ level and the $2S_{1/2}$ level is very small, the emissions from the transitions $2S_{1/2} \rightarrow 1S_{1/2}$ and $2P_{1/2} \rightarrow 1S_{1/2}$ cannot be experimentally resolved. Hence the intensity ratios are calculated using the sum of the contributions from the $2S_{1/2}$ and $2P_{1/2}$ states:

$$\frac{\alpha_{1/2}}{\alpha_{3/2}} = \frac{A_{(2P_{1/2}-1S_{1/2})}n(2P_{1/2}) + \mu n(2S_{1/2})}{A_{(2P_{3/2}-1S_{1/2})}n(2P_{3/2})} \qquad (1)$$

where $A_{(2P_{1/2}-1S_{1/2})} = A_{(2P_{3/2}-1S_{1/2})}$ is the transition probability for spontaneous transitions from the 2P sublevels to the ground state, $n(2P_{1/2})$, $n(2S_{1/2})$ and $n(2P_{3/2})$ are the populations of the $2P_{1/2}$, $2S_{1/2}$ and $2P_{3/2}$ levels respectively, and μ is the magnetic dipole transition probability for the transition $2S_{1/2} \rightarrow 1S_{1/2}$.

THE THEORETICAL CODE, COLRAD

The code COLRAD calculates the population densities of the excited atomic levels of hydrogenic ions in a plasma. Collisional-radiative recombination and ionization rate co-efficients are also calculated. The key features of the code are that:

i) COLRAD only calculates the excited level populations for *hydrogenic* ions, and these must be in the range $2 \leq Z \leq 35$, where Z is the atomic number of the element considered. These ions are considered to be present as an admixture in a base plasma;

ii) The code contains the implementation of fine structure level splitting up to $n \leq 4$, where n is the principal quantum number;

iii) The minimum electron temperature which can be considered is $4000Z^2$ K;

iv) The velocity distributions for both electrons and heavy particles are assumed to be Maxwellian;

v) The plasma is assumed to be homogeneous and optically thin for the hydrogenic ion considered.

The calculation of the excited level populations involves the solution of the rate equations in which all the processes which populate and depopulate each level are explicitly considered.

INTENSITY RATIO CURVES

When the Lyman-α intensity ratios are calculated for various hydrogenic ions in a high-temperature plasma, a characteristic curve can be plotted for the ratio values as a function of electron density [2]. It can be seen that at low densities, the ratio has its statistical value close to 0.5, but this increases as the electron density increases with the peak values reached between 10^{18} - 10^{21} cm^{-3}, when there is population transfer from the metastable $2S_{1/2}$ level to the $2P_{1/2}$ level. The ratio then drops off again to its statistical value of 0.5 at higher densities. It is observed that the magnetic dipole contribution can be important for lower electron densities, but that as the electron density increases to above 10^{15} cm^{-3}, it becomes negligible.

[1] Email address: J.M.A.Ashbourn@damtp.cam.ac.uk

[2] Email address: N.N.Ljepojevic@damtp.cam.ac.uk

INFLUENCE OF ION TEMPERATURE

The ion temperature is very often different from the electron temperature, and Figure 1 shows the effect of this on the values of the intensity ratios when the ion temperature is varied around a constant electron temperature of 1 keV by factors of 2, 3 and 4, and 1/2, 1/3, and 1/4. It can be seen from Figure 1, which is for hydrogenic Al XIII in a base plasma of fully ionised hydrogen, that the ratios are reduced quite significantly (up to ~ 12%) from their values with the ion and electron temperatures equal, when the ion temperature is greater than the electron temperature by the given factors, and that they are enhanced when the ion temperature is decreased below the constant electron temperature. Of more direct relevance to laser plasmas is the calculation which is for a self-plasma of aluminium, and again the variations in the intensity ratios are seen when the ion temperature is varied around the constant electron temperature. However, this time they are of the constant electron temperature. However, this time they are of the order of ~ 7%, although for a lower electron density region than before.

COLRAD VERSUS NIMP

A preliminary comparison has been made in collaboration with J.S. Wark and P. Patel of the Clarendon Laboratory, University of Oxford, and S.J. Rose of the Rutherford Appleton Laboratory, between the level populations for $n = 1$ and $n = 2$ from COLRAD and from an average atom code, NIMP. This code uses the time-dependent non-LTE average atom model, and differs from COLRAD in that it does not include the fine structure splitting for the lower levels and so it does not include transitions due to collisions between heavy ions. The comparison was done for electron temperatures of 400 eV, 800 eV and 1400 eV, respectively. It was found that for 400 eV the level populations for both $n = 1$ and $n = 2$ from NIMP were smaller than those from COLRAD by nearly a factor of 2. This discrepancy decreased with increasing electron temperature, so that for a temperature of 1400 eV, the two calculated populations were very nearly identifical.

REFERENCES

1.N.N. Ljepojevic, R.J. Hutcheon, and J. Payne, Comput. Phys. Comm. 44, 157 (1987).

2.J.M.A. Ashbourn and N.N. Ljepojevic, Phys. Rev. A 52, 4966 (1995).

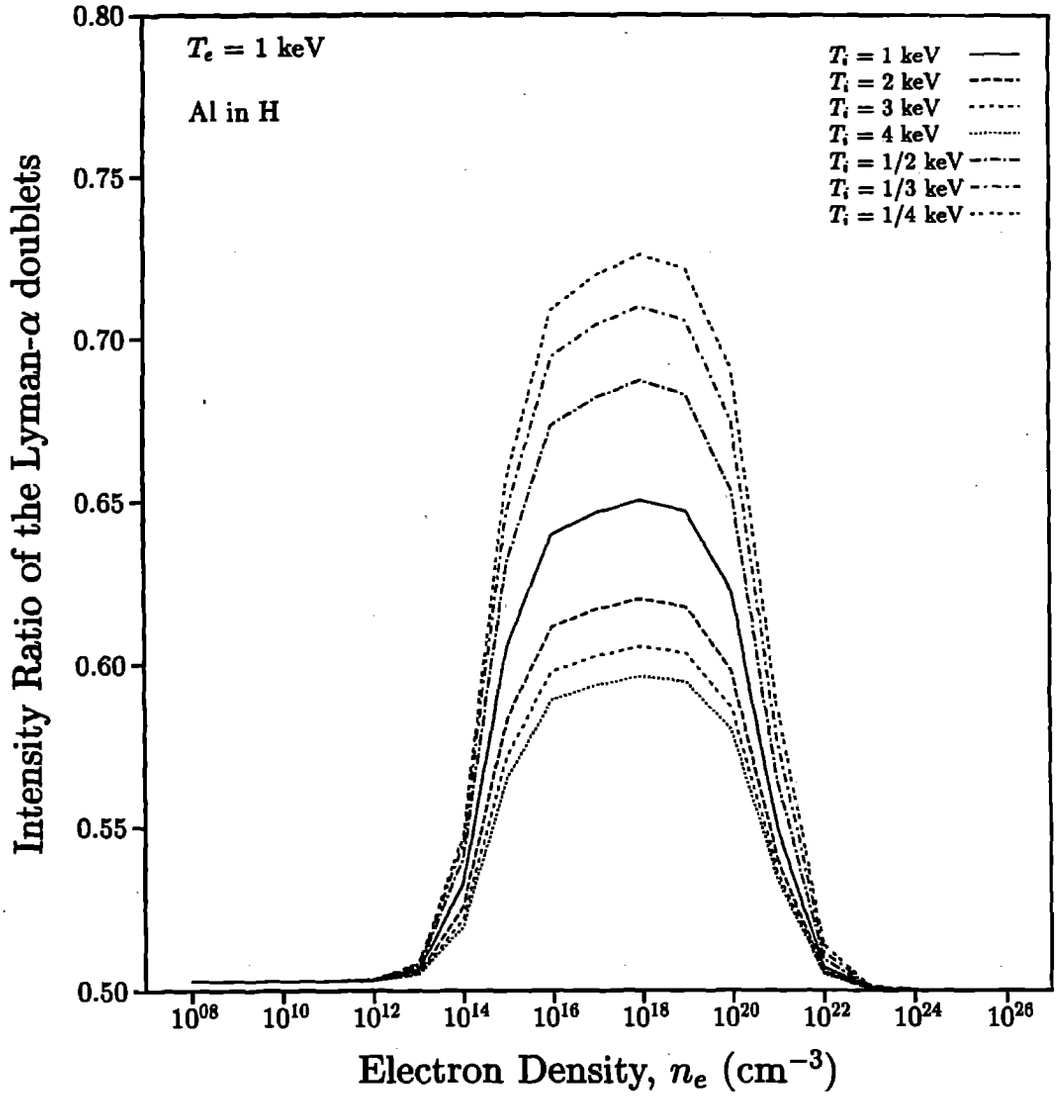

Figure 1

MODELLING OF THE HE-LIKE RESONANCE AND LI-LIKE SATELLITE LINES OF Ti AND Ca PLASMAS

A. Demir, G. J Tallents, Ph. Zeitoun*

Department of Physics, University of Essex, Colchester CO4 3SQ, U.K.
* Now at Laboratoire de Spectroscopie Atomique et Ionique, Bât. 350, Université Paris-Sud, 91405 Orsay Cedex, France

We have modelled He-like resonance and satellite emission from a laser-produced Ti plasma (between 2.6 and 2.66 Å wavelength) and similar emission from a laser produced Ca plasma between 3.17 and 3.22 Å. We show that the emission can be accurately calculated for laser produced plasmas with a relatively straight forward coronal model. The He-like Ca and Ti satellite spectra are thus proposed as useful diagnostics of electron temperatures in laser produced plasmas for temperatures >0.5keV.

Examples of experimental time integrated spectra of Ti and Ca obtained using the 1.3μm iodine laser of ASTERIX[1,2] at MPQ are shown in figure 1 and 2 respectively. The He-like resonance ($1s^2\ ^1S$-$1s2p\ ^1P$), intercombination ($1s^2\ ^1S$ - $1s2p\ ^3P$), forbidden lines ($1s^2\ ^1S$ - $1s2s\ ^3S$), and n=2,3,4,... dielectronic satellite lines were observed. The lines in figure 1 and 2 are identified according to Gabriel's notation[3]. Most of the experimental spectral features are blends of several lines (Figure-1 and 2).

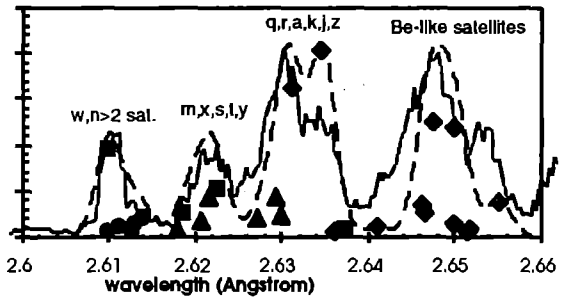

Figure 1 Time and space integrated experimental (solid line) and theoretical (broken line) H-like Ti spectrum. Theoretical positions and relative intensities of all the individual spectral lines considered are also shown. Here the ● shows n=3 satellite lines, ▲ represents n=2 (m,s,t,q,r,a,k,j) satellites, ■ shows the (w,x,y,z) lines and ◆ shows Be-like satellite lines

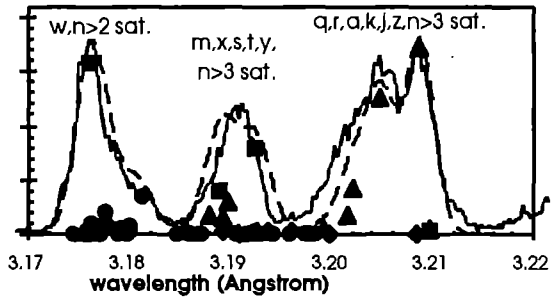

Figure 2 Time and space integrated experimental (solid line) and single temperature (730 eV) theoretical (broken line) He-like Ca spectrum. Theoretical positions and relative intensities of all the individual spectral lines considered are also shown. Here the ● shows n=3 satellite lines, ▲ n=2 (m,s,t,q,a,k,j)satellites, ■ shows the (w,x,y,z) lines, ◆ shows n=4 Li-like satellite lines.

The intensity ratios of the intercombination lines to jkl satellite lines for Ti and Ca have been calculated using the FLY code[4] assuming steady state equilibrium (fig-3 and fig-4). These intensity ratios are constant up to electron densities $\leq 1 \times 10^{21} cm^{-3}$ which indicates that coronal equilibrium[5] applies up to this density. The resonance line emission in the ASTERIX laser produced plasmas is emitted largely from a region close to the critical density of the 1.3 μm laser ($\leq 6 \times 10^{20}$ electron/cm^3).

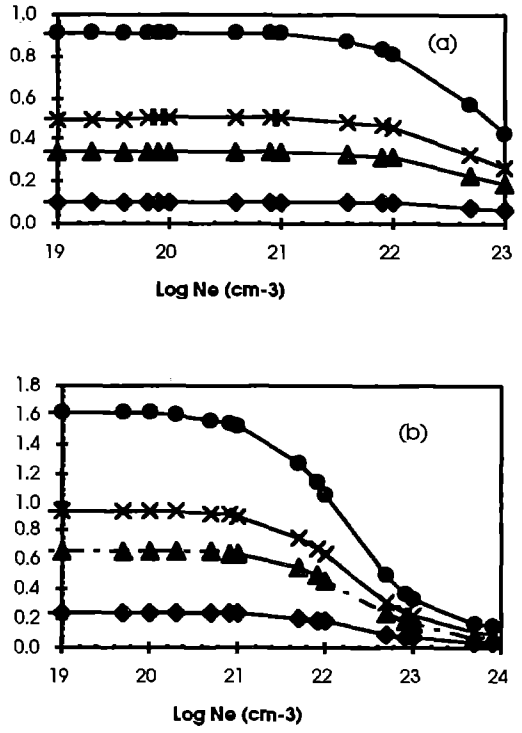

Figure 3 The intensity ratio of the He-like intercombination (x,y) lines to jkl satellite lines (a) of Ti (b) of Ca at different electron temperatures. Here the ● represents 1000- eV, × shows 800 eV, ▲ shows 700 eV, ◆ shows 500 eV

When coronal equilibrium applies, the upper quantum states of the He-like lines can be assumed to be populated by three mechanisms; collisional excitation from the He-like ground state, recombination from H-like ions and inner shell excitation from the Li-like ground state. Recombination from H-like ions can be neglected for the spectra produced at lower electron temperatures as discussed here.

Opacity only affects the resonance line intensities since the oscillator strengths of the resonance lines is much larger than for other lines. The effect of opacity is taken into account in the modelling by an approximate solution of the equation of radiative transfer. The equation of radiative transfer can be written as

$$I_{tot} = \int_{-\infty}^{\infty} \int_{0}^{\infty} \varepsilon(x)\Phi(\lambda) \exp\left[-\int_{x}^{\infty} \frac{\kappa(x)}{\cos(\phi)} \frac{\Phi(\lambda)}{\Phi(0)} dx\right] dx d\lambda \qquad (1)$$

where I_{tot} is the intensity escaping the plasma, $\varepsilon(x)$ is emissivity, $\kappa(x)$ is the absorption coefficient at line center, ϕ is the angle between spectrometer and laser beam, Φ is a line shape function.

The inner integration is over all space x in the plasma in the direction towards the spectrometer and the outer integral is over the wavelength λ of the spectral line from line center.

The approximate solution of the radiative transfer equation for Gaussion line shapes and exponentially decreasing $\varepsilon(x)$ and $\kappa(x)$ is given by ,

$$I_{tot}=I_{peak}\left(1-\frac{\tau}{(2)^{3/2}}+\frac{\tau^2}{2!(3)^{3/2}}-\frac{\tau^3}{3!(4)^{3/2}}+....+\frac{\tau^n}{n!(n+1)^{3/2}}+....\right) \quad (2)$$

where I_{tot} is the intensity escaping the plasma, I_{peak} is the intensity neglecting absorption and τ is the optical thickness of the plasma at line center from the peak emission region to the spectrometer.

In modelling the intensities of the resonance(w), intercombination (x,y) and forbidden (z) lines of Ti, the collisional radiative code FLY was used. The satellites lines were modelled using atomic data calculated by Bely Dubau et al [6]and Bitter et al[7] for Li-like satellite and Be-like satellites lines of Ti respectively. Spectra of titanium calculated assuming coronal equilibrium for a single electron temperatures are shown in figure (5). At low T_e(300 eV), the Be-like satellite lines are stronger than the other lines and the He-like resonance line is weak. When T_e increases (700 eV), the Be-like satellite lines become weak and the He-like resonance line intensities increase. It is necessary to integrate the theoretical spectrum in time and space to obtain a comprehensive agreement with the experimental spectra (figure 1).

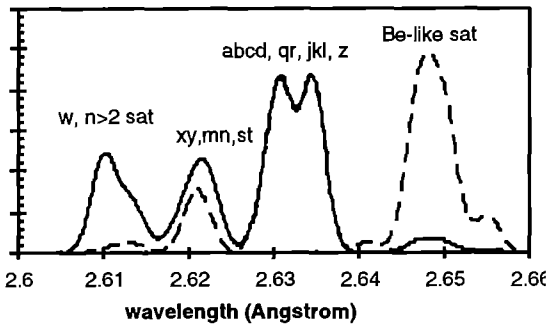

Figure 5 The theoretical spectrum of Ti at different electron temperature 300 eV (broken line) and 700 eV (solid line)

The hydrodynamic and atomic physics code EHYBRID[8] was used to simulate the plasma expansion for the Ti plasma. In the simulation a 450 ps 500 J trapezoidal laser beam irradiates a Ti slab target so that the intensity on the target is $2x10^{13}$ W/cm^2. The time and space integrated He-like Ti spectra (figure 1) was obtained using a post-processor code to integrate in space and time from the ehybrid output calculated He-like and satellite spectra.

To simulate the Ca spectrum, the H-like, He-like and Li-like ground state densities for a single electron temperature calculated by FLY were used but with the principal addition of a calculation of the n>2 spectator electron satellite lines intensities using the data published by Bely Dubau et al.[8]. The calculated theoretical spectrum and experimental spectrum for this temperature is shown in figure (2). The effect of n>2 dielectronic satellite lines on the He-like resonance line is simulated well. Overall the single temperature theoretical spectrum (not time and space integrated) for Ca fits well to the experimental spectrum because the electron temperature are sufficient to ionise Ca to the He-like ionisation stage.

The intercombination line to the Li-like satellite lines can be used as a temperature diagnostic of laser-produced plasmas since these lines are optically thin. Figure 6 shows the line ratios of theintercombination (x,y) plus m,n,s,t to j,k,l,a,b,c,d,q,r plus forbidden (z) lines as a function of temperature. We believe our 'post-processor' model calculations are more accurate than the FLY calculations because of the larger number of satellite lines taken into account

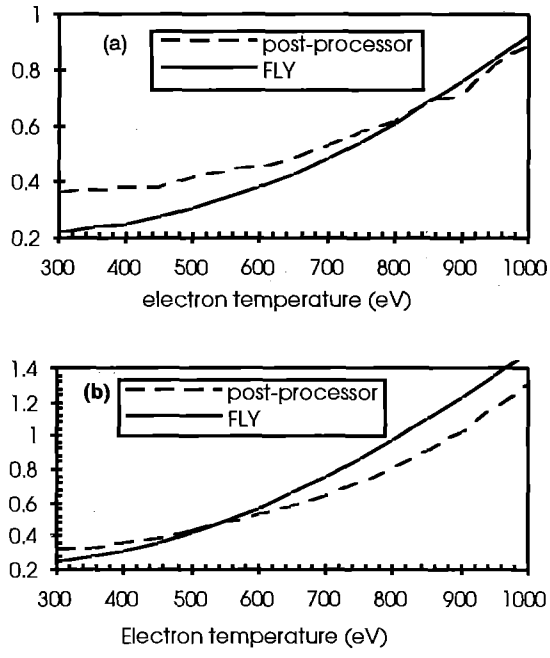

Figure 6 The intensity ratio of intercombination (x,y) plus m,n,s,t to j,k,l,q,r,a,b,c,d satellites plus forbidden (z) lines of (a) Ti and (b) Ca pasmas as a function of electron temperature. The solid line is calculated by the FLY code, while the broken line is calculated by our model.

Time integrated X-ray spectra of helium like titanium, Ti XXI and helium like calcium, Ca XIX, resonance lines emitted from a laser produced plasma have been compared to model calculation of the spectra. We show that the emission can be accurately calculated for laser produced plasmas assuming coronal equlibrium. The He-like Ca and Ti intercombination to jkl Li-like satellites are proposed as useful and accurate diagnostics of electron temperatures in laser produced plasmas for temperatures >0.5 keV.

REFERENCES:

[1]- H. Baumbaker et al, Laser Particle Beams, **11**, 353 (1993)
[2] Demir et al, to be published.
[3] Gabriel A H Mon. Not. R. astr. Soc, **160**,99 (1972)
[4]- Lee R W et al, J. Quant. Spectrosc. Radiat. Transfer. 32, 91(1984)
[5] I. H. Hutchinson, Principles of Plasma Diagnostics, (Cambridge Univeristy Press), 199, (1987)
[6] F.Bely-Dubau et al, Phys.Rev. A 26, No.6, 3459 (1982) [7] M. Bitter et al Phys. Rev. A.32, No.5, 3011 (1985).
[8] G.J. Pert J. Fluid. Mech. Vol. 11 401 (1983)
[9] F. Bely-Dubau et al, Mon. Not. R. astr. Soc. **201**. 1155 (1982)

IONISATION-INDUCED DEFOCUSING OF TITANIA CPA BEAM IN NEON

A Djaoui

Rutherford Appleton Laboratory

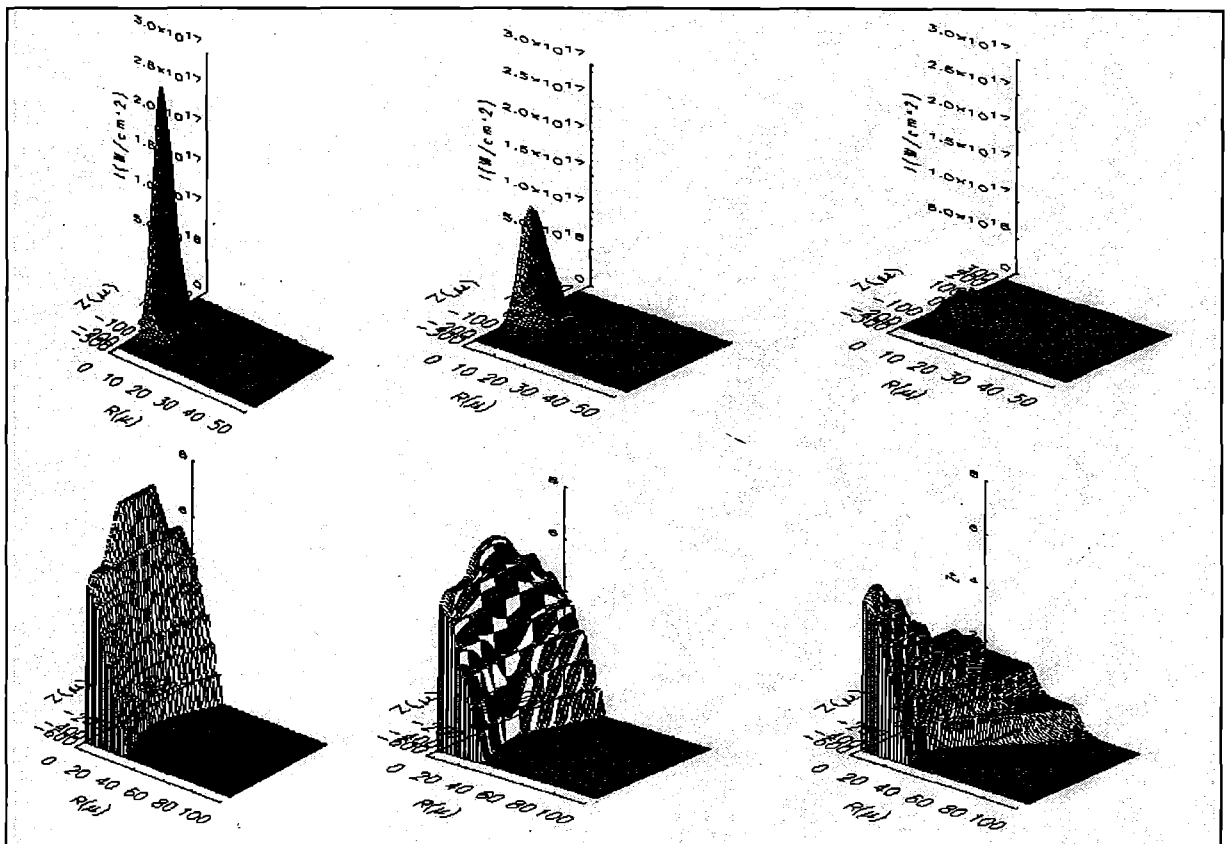

Figure 1: Effect of ionisation induced defocusing on a 400 fs gaussian beam propagating through 1mm neon gas jet. Top row of frames: Intensity profiles at position of ideal focus (Z=0) for 3 ion densities (3.3×10^{16} cm^{-3}, 3.3×10^{18} cm^{-3}, 2.5×10^{19} cm^{-3}). Bottom row of frames: Average ionisation Z* after passage of laser pulse through gas jet as the same densities.

The propagation of an intense laser beam through an initially neutral gas target results in strong field induced ionisation[1]. For non-relativistic intensities, when the effect of the ponderomotive force of the laser on the plasma is negligible, the plasma can be considered as static for the duration of the pulse. Following ionisation, the electron density increases and this results in the reduction of the refractive index of the plasma ($n=(1-Ne/Ncr)^{1/2}$) and an increase in the wave phase velocity ($v_\varphi=c/n$). This leads to a distortion of the wave phase front which then travels faster in regions where the electron density is higher. Since the central region of a laser beam is more intense and creates more ionisation, the beam is defocused as a result of a higher electron density at the centre. This spacial defocusing limits the maximum intensity achieved at the focus and acts as a clamp on the maximum ionisation stage and the maximum density achieved.

We have developed a two-dimensional time-dependent model which solves the paraxial wave equation in cylindrical geometry for a linearly polarised laser propagating in the Z direction. This model is similar to ref 2, but solves the wave equation in a frame of the pulse. This simplifies the equation and allows higher intensities and longer pulses to be studied. This model also goes beyond the work of ref 2 in that it can treat tunnel ionisation for all stages and elements from hydrogen (Z=1) to Krypton (Z=36).

Figure 1 shows the effect of tunnel ionisation defocusing on a moderate intensity (3×10^{17} W/cm^2 at ideal focus) gaussian Titania beam (400 fs, f/10, 3x diffraction limited) propagating through a 1 mm gas jet neon target which extends from -500μ to 500μ . For the lowest density of about 1 torr (first column of frames), the defocusing effect is negligible. The laser intensity at the ideal focus is the same as in vacuum and the density profile is symmetrical with respect to the ideal focus position (Z=0). The ionisation shows a stair-like structure which corresponds to the different ionisation stages. As the density increases to about 100 torr (second column of frames), the intensity at the ideal focus is reduced by more than a factor of two, while the average ionisation is reduced from Z*=8 to Z*=7.3. At about 1 atmosphere (third column), the intensity at the focus is reduced by a factor of 20 and the ionisation to Z*=6. The ionisation profile is very non-symmetrical, showing that the maximum ionisation occurs at the entrance of the beam into the gas jet. It can also be seen that as the beam defocuses a more extended region of the plasma in the radial direction, is ionised to the lower stages.

REFERENCES

1. M. V. Ammosov, N. B. Delone and V. P. Krainov, Zh. Eksp. Teor. Fiz. **91**, 2008 (1986)[Sov. Phys. JETP **64**, 1191 (1987)]
2. S. C. Rae, Opt. Commun. **97**, 25 (1993)

HIGH HARMONIC GENERATION FROM STRONGLY DRIVEN TWO-LEVEL ATOMS

F. I. Gauthey[1,2], C. H. Keitel[1], P. L. Knight[1] and A. Maquet[2]

[1] Optics Section, Blackett Laboratory, Imperial College, London SW7 2BZ
[2] Laboratoire de Chimie-Physique-Matiere et Rayonnement, Universite Pierre et Marie Curie, Paris, France

High harmonic generation from the non-linear interaction of atoms with super intense laser fields has become an efficient and useful source of high frequency coherent light[1]. Idealized models in which the laser Field essentially interacts with a single atomic transition and ionization can be neglected have been quite successful in predicting all essential features of this phenomenon[2].

We investigate the coherent and incoherent contributions of the scattering spectrum of strongly driven two-level atoms. Both contributions to this complete spectrum, the coherent or mean (one time) dipole part and the incoherent or quantum fluctuation part are of significance. The role of the quantum fluctuation part, however, is reduced for a large atomic sample. For large field amplitudes, all spectra reproduce the characteristic features of plateau and cut-off observed in harmonic generation from strongly driven atoms (see Figure 1.a).

One object of the study is to investigate the influence of the initial preparation of the atomic system on the two kinds of contributions of the harmonic spectrum. Particular emphasis is placed on atomic systems which are prepared in a coherent superposition of two atomic levels via a relatively weak laser field prior to the interaction with a super-strong short laser pulse. While the total spectrum is in fact not very sensitive to the initial condition, we find that the coherent contribution to the harmonic generation can display striking variations as a function of the phase of the initial dipole and even totally disappear at a particular phase[3] (see Figure 1.b). This could facilitate the identification of hyper-Raman lines, lines which appear at positions between the harmonics and which are usually overwhelmed by intense harmonics. In particular we point out conditions under which harmonic generation can be inhibited at the expense of the hyper-Raman lines. Our numerical findings are supported by approximate analytical evaluations in the dressed state picture.

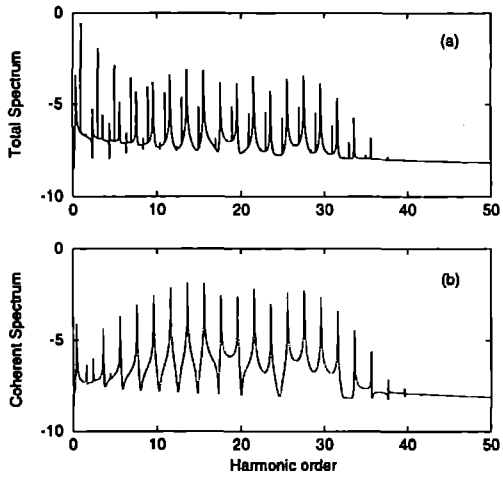

Figure 1: The logarithm of the full spectrum (a) for ground state preparation, and of the coherent part of the spectrum (b) in the case of initial coherence with the dipole initial phase equal to zero. The laser frequency is 0.0258 a. u.,, the Rabi frequency 0.35 a. u. and the levels splitting 0.3 a. u.

For harmonic generation from a sample of atoms in a beam with spatially varying intensity, the intensity dependence of the phase of the harmonics becomes a crucial problem for the coherence properties of the totally generated light at a particular frequency. A recent theoretical study[4] in the case of a model atom with continuum showed that the intensity dependence of the phase of the harmonics of laser driven atoms is linear and substantially stronger in the plateau regime than in the cut-off regime. We investigate the phase coherence of the generated harmonics in the coherent part of the spectrum, and demonstrate that this effect also occurs in the idealized two-level model (Figure 2). This strongly suggests that the sudden change of the phase coherence from the cut-off to the plateau regime is an intrinsic property of non-linear systems, as are the plateau and the cut-off [5].

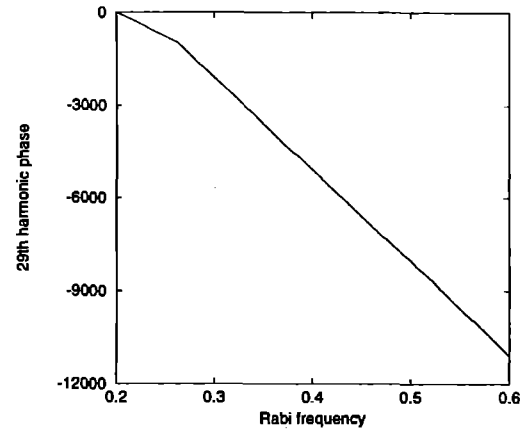

Figure 2: The phase of the 29th harmonic, when considered as a monotonous function of the Rabi frequency. The parameters are the same as in Fig. 1. The change of slope occurs around the cut-off.

REFERENCES

1. For a review, see, e. g., A. L'Huillier, L. A. Lompre, G. Mainfray and C. Manus, Advances in Atomic, Molecular and Optical Physics, ed. by M. Gavrila (Academic Press, New York, 1992); K. Burnett, V. C. Reed and P. L. Knight, J. Phys. B 26, 561 (1993).

2. B. Sundaram and P. W. Milonni, Phys. Rev. A 41, 6571 (1990); K. J. LaGattuta, J. Mod. Opt. 39, 1181 (1992); D. G. Lappas, M. V. Fedorov and J. H. Eberly, Phys. Rev. A 47, 1327 (1993).

3. F. I. Gauthey, C. H. Keitel, P. L. Knight and A. Maquet, Phys. Rev. A 52, 4023 (1995).

4. P. Salieres, A. L'Huillier and M. Lewenstein, Phys. Rev. Lett. 75, 3776 (1995).

5. F. I. Gauthey, C. H. Keitel, P. L. Knight and A. Maquet, in preparation.

PHOTOIONISATION CROSS-SECTIONS OF IRON IONS

G Black, K L Bell and F P Keenan

School of Mathematics and Physics, The Queen's University of Belfast, Belfast, BT 1NN, Northern Ireland

INTRODUCTION

Iron has been found to be an astrophysically abundant element, and is found also in many laboratory-produced plasmas. This makes it a valuable source of information on astrophysical bodies and laser-produced plasmas, as by looking at the X-ray lines arising from these iron ions one may deduce something of the structures and processes of the plasma itself. The highest energy X-ray lines are the K-lines, and so these are of especial importance.

One needs up to date and accurate atomic data on the relevant ions to make sense from these lines, and this report is concerned with photoionisation cross-sections for this purpose.

The K-lines of iron ions are produced as a result of 1s photoejection followed by the relaxation of the ion produced; that is, when a 1s electron is released from the K shell of an iron ion (by a photon) and another electron from a higher shell (such as the L shell) fills the vacant K shell space, thereby releasing a photon of energy.

This process may be investigated in detail using a photoionisation cross-section; this gives the probability per second of a photon releasing an electron from the atom/ion in question, over a range of energies, and can therefore be related to the strength of the K-line.

COMPUTATIONAL THEORY

The heart of the R-matrix method is the representation of a physical system through a mathematically complete set of wavefunctions, Ψ_k, known collectively as a basis set.

These wavefunctions are all fully composed of wavefunctions v_j (known as continuum orbitals) which describe the free electron in the system and also wavefunctions Φ_i (known as target wavefunctions) which describe the target states - that is, all of the system but the free electron:

$$\Psi_k = \sum_{ij} a_{ij}\Phi_i v_{jk} + \sum_{jk} d_j v_{jk}$$

Thus, for the system we have investigated, the free electron is the photoelectron liberated from FeXXIV and the target states are the states of FeXXV, the residual ion.

The main advantage of the R-matrix method over other methods such as the central-field approximation is its ability to include **resonance effects**.

It is clear that, as the R-matrix method is based on the idea of using a complete set, the nearer one gets to a complete set of wavefunctions the more accurate the calculation will be; this is achieved by adding more continuum orbitals and target wavefunctions to the wavefunction representation. Unfortunately, the calculation is limited by computational considerations - having too many of these wavefunctions and continuum orbitals make the calculation extremely long and unwieldy. Therefore, a compromise is made between accuracy and computational resources.

THE CALCULATION

We investigated the process

$$h\nu + FeXXIV \rightarrow e^- + FeXXV$$

This was done in an R-matrix calculation with 35 continuun orbitals and the following 11 target states:

$(1s^2)^1S$, $(1s2s)^{1,3}S$, $(1s2p)^{1,3}P^o$, $(1s3s)^{1,3}S$, $(1s3p)^{1,3}P^o$ $(1s3d)^{1,3}D$.

As presently published orbitals are only for the ground state of FeXXIV, and the '1s hole' states of FeXXV (e.g. $(1s2s)^{1,3}S$) are much different from these due to the absence of a 1s electron from the K shell, it was decided to calculate the one-electron wavefunctions using an ab initio calculation.

Cross-sections were calculated over the photon energy range 0-2700 Rydbergs; these were the total cross-section, the '1s removal cross-section' (the cross-section where only the 1s electron has been removed from FeXXIV) and all the partial cross-sections which leave FeXXV in the **individual n=2 states** (such as $(1s2s)^{1,3}S$).

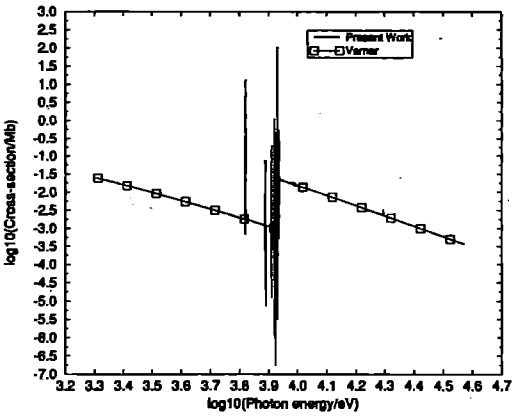

Fig. 1. Comparison of FeXXIV Total Cross-section with Verner et al (1993)

Table 1. Target states energies (in Rydbergs)

Target	Energy Present	Energy Drake (1985)
$(1s^2)^1S$	0.0	0.0
$(1s2s)^3S$	484.426	487.780
$(1s2p)^3P^o$	486.346	490.642
$(1s2s)^1S$	486.593	490.090
$(1s2p)^1P^o$	487.981	492.471
$(1s3s)^3S$	573.443	577.491
$(1s3p)^3P^o$	573.975	578.570
$(1s3s)^1S$	574.022	578.553
$(1s3d)^3D$	574.285	-
$(1s3d)^1D$	574.305	579.352
$(1s3p)^1P^o$	574.424	579.254

RESULTS

We calculated the ionisation potential of FeXXV at 148.815 Rydbergs, in concurrence with Shirai et al (1990); in addition, the good agreement of target state energies with previous calculations (see table 1) shows that our calculation includes a good representation of the target ion. FeXXV.

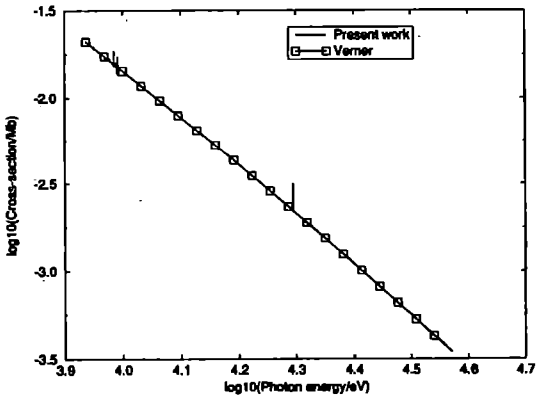

Fig. 2. Comparison of FeXXIV 1s removal Cross-section with Verner et al (1993)

Verner et al (1993, 1995) performed a large number of calculations to find the photoionisation cross-sections of the different subshellsof various atoms/ions, using the relativistic Hartree-Dirac-Slater method, and also fitted these using an analytic expression to provide a quick way of calculating these cross-sections. From this we obtained their results for the total and 1s removal cross-sections of FeXXIV, to compare with our own (see figures 1 and 2 for the total and 1s removal cross-sections respectively).

The total cross-section includes several dramatic resonances (some several orders of magnitude greater than background) which begin at around the excitation energy to the second target state, while the 1s removal cross-section has some few, much smaller resonances.

Our present work compares very well with the work of Verner et al, the 1s removal cross-section differing from Verner's by under 5%, and the total cross-section differing by significantly less than 1%.

Work is underway to repeat these calculations for the case of the FeXXIII ion. This is more complex, and while present results are promising they are not complete.

REFERENCES

1. Verner, D.A., Yakolev, D.G., 1995, A&AS 109, 125.
2. Verner, D.A., Yakolev, D.G., Band, I.M., Trzhaskovskaya, M.B., 1993, ADNDT 55, 23.
3. Shirai, T., Funatake, Y., Mori, K., Sugar, J., Wiese, W.L., Nakai, Y., 1990, Phys. Chem. Ref. Data 19, 127.
4. Drake (1985), unpublished

MAGNETIC FIELD SATURATION MECHANISMS IN LASER-PLASMA INTERACTIONS

M G Haines

Blackett Laboratory, Imperial College, Prince Consort Road, London SW7 2AZ

INTRODUCTION

Departure from one-dimensional symmetry in inertial confinement can lead to the spontaneous generation of magnetic fields, principally through the $\nabla T \times \nabla n_e$ effect. This arises from combining Ohm's law[1].

$$\eta \underline{J} = \underline{E} + \underline{v} \times \underline{B} - \frac{\underline{J} \times \underline{B}}{n_e e} + \frac{q_e \times \underline{B}}{5/2\, P_e} + \frac{\nabla P_e}{n_e e}$$

where ponderomotive and radiation pressure terms are for the moment neglected, and Faraday's law

$$\frac{\partial \underline{B}}{\partial t} = -\nabla \times \underline{E}.$$

As the magnetic field grow, four terms in Ohm's law also grow, and we explore the saturation of the magnetic field by three of these.

REGIME 1

Here resistive effects are assumed to be dominant, ie, $\nabla Pe/n_e e$ is balanced by $\eta \underline{J}$, which by Ampere's law is $\eta \nabla \times \underline{B}/\mu_0$. Distinguishing between scalelengths parallel (L_{11}) and perpendicular ($L_\perp$) to the normal laser irradiation direction, we then have

$$B = \frac{\mu_0 kT}{e\eta} \cdot \frac{L_\perp}{L_{11}} \qquad (1)$$

REGIME 2

When the electron drift velocity exceeds a critical value of order the ion sound speed, C_s, microinstabilities such as lower hybrid turbulence will lead to an anomalous resistivity. A simple model of $|\underline{J}| = nec_s$ leads via Ampere's law to

$$B = \mu_0 n_e \left(\frac{ZkT_e}{m_i} \right)^{1/2} L_\perp \qquad (2)$$

REGIME 3

Another possible saturation mechanism is when the generations of magnetic field is balanced by its convection ($\underline{v} \times \underline{B}$), the convective velocity $\underline{v}$ having a magnitude typically of C_s under steady ablating conditions[2]. This gives

$$B = \frac{1}{L_\perp} \frac{kT_e}{e} \left(\frac{m_i}{ZkT_e} \right)^{1/2} \qquad (3)$$

DISCUSSION

Noting that in regime 2 B is proportional to $L_\perp$ and in regime 3 is inversely proportional to $L_\perp$, B is given by (2) while for large $L_\perp$ it is given by (3). The two scaling laws intersect at $L_\perp = c/\omega_{pi}$, at which point B is equal to $\left(\mu_0 n_e kT_e\right)^{1/2}$ ie there is a balance of magnetic and electron pressure, and the Hall parameter $\Omega_e \tau_{ei}$ is equal to the ratio of the mean free path to the electron collisionless skin depth. If $L_\perp$ equals L_{11} eq (1) gives a value of $\underline{B}$ independent of $L_\perp$ and purely a function of temperature. If it exceeds the value given by the envelope of eqs (2) and (3) it does not apply. At low temperatures or higher Z, it will contribute to the saturation for $L_\perp$ of order c/ω_{pi} Indeed at the triple point where eq (1) equals the value at the intersection of eqs (2) and (3) we obtain $\Omega_e \tau_{ei} = 1$ and the mean free path equals the c/ω_{pe}

REFERENCES

1. M.G.Haines, Plasma Phys and Controlled Fusion, 28, 1705, (1986).

2. R.S.Craxton and M G Haines, Plasma Physics, 20, 487, (1978).

THE WEHRL ENTROPY AND ATOMS IN INTENSE LASER FIELDS

CH Keitel[1] , JB Watson[2] , V Buzek[3], K Burnett[2] and PL Knight[1]

[1]Optics Section, Blackett Laboratory, Imperial College, London SW7 2BZ, U.K.
[2]Department of Physics, Clarendon Laboratory, University of Oxford, Oxford OX1 3PU, U.K.
[3]Institute of Physics, Slovak Academy of Sciences, Dubravska cesta 9, 84228 Bratislava, Slovakia.

The Wehrl entropy[1)] has been as useful tool in the field of quantum optics since its discovery many ago. It is not a measure of the purity of the wavefunction as is the von Neumann entropy nor should it be regarded as a thermodynamic entropy. In terms of measurement theory is was shown to arise from a comparison of the Wigner function of the density operator of the system with that of a coherent state[2)] . More useful for the investigation of atoms with strong laser fields, this entropy was shown to be a convenient measure of the uncertainty of the system in phase space[2)] . This allows to draw a direct connection of the Wehrl entropy with the processes of wavepacket spreading, phase space localization and ionization in the interaction of atoms with strong fields.

The Wehrl entropy can be evaluated from the phase space disbution function Q of the density operator representing the system via

$$S = -\int Q \ln Q \qquad (1)$$

where the integral extends over the phase space variables p and q. It was showns that for a Gaussian distribution the phase space uncertainty area A defined in Fig. 1 can be related to the Wehrl entropy S via

$$S = 1 + \ln[A] . \qquad (2)$$

We have assessed this Wehrl entropy for the interaction of atoms with strong laser fields in the stabilization domain for adiabatic (Fig. 2) and nonadiabatic laser pulses. The Wehrl entropy displays the process of phase space spreading, phase space localization and at the end of the pulse ionization becomes visible.

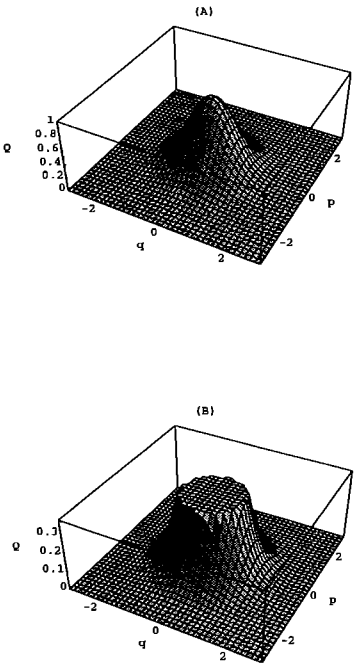

Fig.1. (A) Gaussian wavepacket in phase space. (B) displays the same wavepacket up to the height 1/e of the previous figure. The surface that becomes visble then is related to the Wehrl entropy by equation 2.

REFERENCES

1. A. Wehrl, Rev.Mod.Phys. 50, 221 (1978), Rep. Math. Phys. 16, 353 (1979).

2. V. Buzek, C. H. Keitel and P. L. Knight, Phys.Rev.. 51, 2575 (1995) and Phys.Rev.. 51, 2594 (1995).

3. J. H. Eberly, Q. Su and J. Javanaien, Phys.Rev.Lett. 62, 881 (1989); V. C. Reed, P. L. Knight and K. Burnett, Phys.Rev.Lett. 671415 (1991).

4. J. B. Watson, C. H. Keitel, P. L. Knight and K. Burnett, Phys. Rev. A. 52, 4023 (1995) and Phys.Rev A in press (1996);

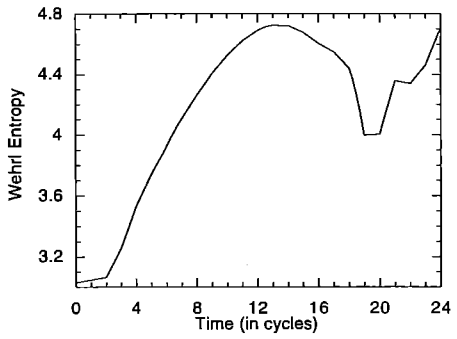

Fig.2. The Wehrl entropy of a atom during the interaction of a pulsed laser field with 24 cycles with an adiabatic sin squared turn-on and turn-off. The electric field strength is 10 a.u. and the frequency 1 a.u., so that we are in the stabilization regime. Wavepacket spreading and localization is visible as is clearly also the ionization towards the end of the laser pulse.

HARMONIC GENERATION WITH FULL ELECTRON CORRELATION IN MODEL He ATOM

D.G. Lappas,[1] A. Sanpera,[2] J.B. Watson,[2] K. Burnett[2], P.L. Knight[1], R. Grobe[3] and J.H. Eberly[4]
[1]Optics Section, Blackett Laboratory, Imperial College, London SW7 2BZ
[2]Clarendon Laboratory, Department of Physics, University of Oxford, Oxford OX1 3PU
[3]Department of Physics, Illinois State University, Normal, IL 61790, USA
[4]Department of Physics and Astronomy, University of Rochester, Rochester, NY 14627, USA

The recent advances in the understanding of harmonic generation (HG) from atoms driven by intense laser fields (~10^{15} W/cm^2) have raised the question of multi-electron effects in the laser-atom interaction. The assumption that inner electronic orbitals are not important for the basic features of HG spectra has not been challenged up to date, mainly due to the success of single-active electron (SAE) theoretical models.[1,2] However, the continuous advances in high-intensity lasers and the trend towards shorter wavelengths, make an investigation of e-e correlation effects[3] necessary. Although 2-e effects have been manifested[4] in electron energy spectra for high-frequency [ω~1 atomic unit (a.u.)] lasers, there has been no corresponding study in the regime of low-frequency tunneling ionization and very high HG. In this work we calculate time-dependent fully correlated 2-e wave functions in the tunneling regime, with ω=0.05 a.u. We confirm the validity of the SAE approaches, at least for a limited range of field strengths (~0.1 a.u.). We detect no essential difference between our 2-e model and an effective SAE one-dimensional quantum system. Nevertheless, strong evidence of correlated double ionization is found for higher field strengths, an effect that establishes a new regime of high-intensity low-frequency e-e correlation.

Our model system[4] consists of two electrons whose spatial coordinates are allowed to move only along one dimension, in the neighbourhood of a nucleus of positive charge, fixed at the origin. The electrons can bypass each other due to the soft core of the Coulomb interaction potential ,[5]

$$V(x) = 1/\sqrt{x^2 + a^2}$$

with a =1 a.u. The same potential form is also used for the electron-nucleus interaction. For the purpose of solving the Schroedinger equation numerically, the 2-e wave function is represented in space on a two-dimensional grid. Starting from the 2-e ground state of the model He atom, the time evolution is performed with the split-operator method. Since first and second derivatives are expressed exactly in momentum space, this method allows for much larger grid spacing than that used in other methods. The calculations were performed on a workstation. The SAE efffective potential model that we used for He has the same soft-core Coulombic form. The value a =0.87 a.u. yields a ground state at -0.740 a.u., the same energy that is needed to remove one electron from our model 2-e He.

The laser pulse has a duration of 6 optical cycles, and a 2-cycle linear turn on and turn off. For maximum field strength of 0.1 a.u. we show in Fig. 1 the decay probability of the initial ground state for both the 2-e and the SAE model. It is remarkable that even the fine details of the two curves match almost perfectly. The differences are too small to indicate any significant 2-e effect. In Fig. 2 we show the HG spectrum of the 2-e system. It is essentially the same as for the SAE model (not shown), and exhibits the standard features of HG. The position of the cutoff [2] is at photon energy equal to the ionization potential of the outer electron plus 3.2 times the kinetic energy of the free electron in the laser field. The ionization potential of the inner electron is at -1.496 a.u. or approximately 30 laser photons. Therefore, any possible inner-electron contribution would extend the cutoff higher by 30 harmonic orders, a shift that would be easily observed, if that were the case.

When the field strength is increased to 0.3 a.u. the situation changes dramatically for the ionization probability, since both electrons can be ionized over the quasi-static potential barrier of the combined nuclear and external potentials. The two electrons can then ionize fast and preferentially in opposite directions. Work in this direction is in progress.

This research is supported by the European Union and the EPSRC.

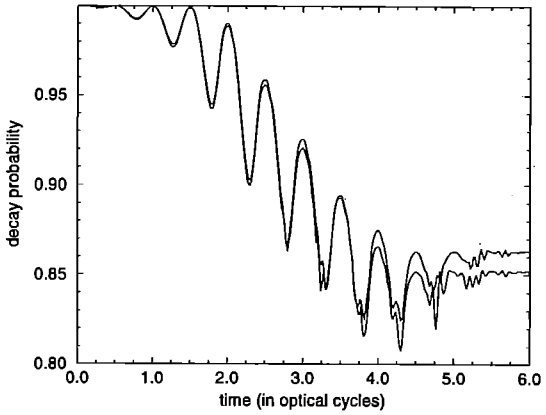

Figure 1 The decay probability of the ground state as a function of time, for the SAE model and the 2-e system. The field strength is 0.1 a.u.

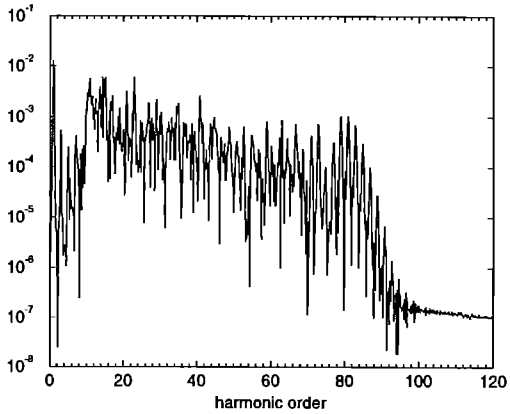

Figure 2 The harmonic generation spectrum for the 2-e system with the same laser parameters as in Figure 1.

REFERENCES

1. A. L'Huillier, L.A. Lompre, G. Mainfray and C. Manus, in "Atoms in Strong Laser Fields", edited by M. Gavrila (Academic Press, New York, 1992), p. 139; K.C. Kulander, K.J. Schafer and J.L. Krause, ibid., p. 247; K. Burnett, V.C. Reed and P.L. Knight, J. Phys. B 26, 561 (1993).
2. M. Lewenstein, P. Balcou, M.Y. Ivanov, A. L'Huillier and P.B. Corkum, Phys. Rev. A 49, 2117 (1994).
3. J. Parker, K.T. Taylor, C.W. Clark and S. Blodgett-Ford, J. Phys. B 29, L33 (1996).
4. R. Grobe and J.H. Eberly, Phys. Rev. A 48, 4664 (1993).
5. Q. Su and J.H. Eberly, Phys. Rev. A 44, 5997 (1991).

THE RECOLLISION PICTURE IN HIGH HARMONIC GENERATION

M Protopapas, DG Lappas, CH Keitel and PL Knight

Optics Section, Blackett Laboratory, Imperial College, London SW7 2BZ

The interaction of atoms with intense laser light has been a rich area of research with many important discoveries[1]. One of these major findings has been high-harmonic generation (HHG); in this process the strongly driven atomic system reradiates energy at odd multiples of the driving frequency. Using HHG it has been possible to generate very short wavelength light[2] with excellent coherence properties and many possible applications.

All HHG spectra show the same generic behaviour: there is a sharp fall from the driving frequency to a plateau, followed by a cut-off for the maximal attainable energy of coherent light. A quasi-classical approach first proposed by Krause, Kulander and Schafer and by Corkum[3] was found to predict accurately the cut-off energy as

$$I_p + 3.17U_p \,, \qquad (1)$$

where I_p is the ionization potential of the atom and U_p the ponderomotive energy of the electron in the incident field.

Insight into the dynamics of the recollision picture is gained by eliminating the ionization process: we start with an electron initially some distance away from the *bare* atomic core generated by tunneling and follow this electron under the influence of a monochromatic laser field. We first use a simple classical model involving one electron, calculate its dipole acceleration and then its spectrum. The electron periodically encounters the nucleus in a sequence of N "recollisions". As N increases the HHG spectrum becomes increasingly well defined. To model a tunneling wavepacket, we use an ensemble of these individual classical electron trajectories. This approach models wavepacket spreading but is, of course, unable to simulate quantum mechanical interference effects.

In our quantum approach, the wavepacket spreads and encounters the core; for the first few encounters, the interaction with the ionic core is not very large and these encounters are "classical-like". What is not classical is the interference between those parts of the wavepacket which are *reflected* by the core and those parts which are still incoming. In fig.1 we have shown with our quantum calculation how the spectrum evolves in time displaying when and how the purely classical and intrinsically quantum components contruct the spectrum. Engineering a single encounter (using time-dependent ellipticity of the super-intense light[4]) leads to a broad-band bremsstrahlung supercontinuum generated within the attosecond timescale of the recollision.

After the first three collisions, the acceleration resembles quite closely that of a single electron trajectory, with, however, a fast amplitude decay due to wavepacket spreading. A windowed Fourier transform of the first collision shows that the associated power spectrum is that of bremsstrahlung (fig.1(a)). After the second and third collision, we see the beginning of harmonic structure (fig. 1(b)) but only for the low order harmonics. Only when the fast frequency components of the dipole acceleration are included do we begin to see anything resembling a true harmonic spectrum (fig.1(c)). If we take the spectrum of the whole dipole acceleration, this now has all the features associated with normal HHG (fig. 1(d)). It is possible to observe, following the trend from (fig.1(a)) to (fig. 1(d)), how the overall efficiency is enhanced, producing a very *clear* cut-off around the expected harmonic order.

Thus, essentially classical dynamics affects the spectrum during the first few encounters of the electron wavepacket with the nucleus; quantum interference effects become crucial once the width of the wavepackets has reached a certain extent. We have shown that a single encounter certainly generates a bremsstrahlung continuum, but with a spectral envelope which is *not* precisely that of the HHG comb of frequencies.

REFERENCES

1. M Lewenstein, Ph Balcou, M Yu Ivanov, Anne L'Huillier and P B Corkum, Phys.Rev.A 49, 2117 (1994) and references therein.

2. J J Macklin, J D Kmetec and C L Gordon, Phys.Rev.Lett. 70, 766 (1993); A L'Huillier and Ph Balcou, Phys.Rev.Lett. 70, 774 (1993).

3. J L Krause, K J Schafer, and K C Kulander, Phys.Rev.Lett. 68, 3535 (1992); P B Corkum, Phys.Rev.Lett. 71 1994 (1993).

4. M Yu Ivanov, P B Corkum, T Zuo and A Bandrauk, Phys. Rev. Lett. 74, 2933 (1995);

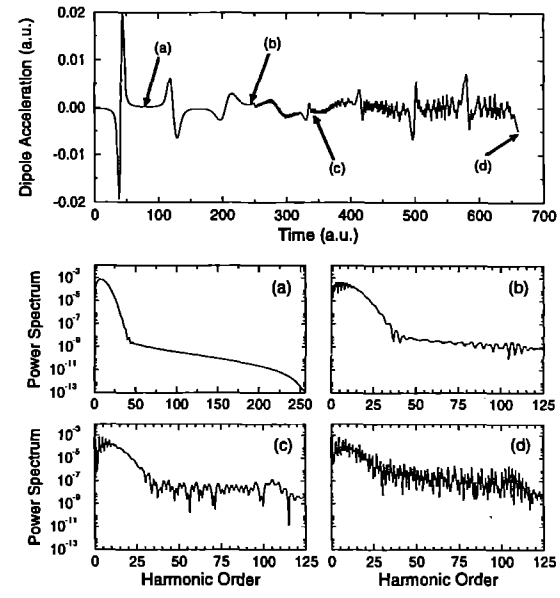

Fig.1. The dipole acceleration (top) and the corresponding power spectra at various points in time as indicated (a) - (d). The maximal electric field strength is 0.1 a.u. , the frequency 0.038 a.u. and the evolution with the square pulse entends over a period of 4 cycles. It displays when and how purely quantum effects modify the power spectrum.

SIMULATION ON VARIATION OF 24.7 NM LINE EMISSION FROM LI-LIKE NITROGEN ION PLASMA WITH A CHANGE OF NITROGEN ION DENSITY

N. S. Kim[1,3], A. Djaoui[2], M. H. Key[1,2], and J. S. Wark[1]

[1]Clarendon Laboratory, Department of Physics, University of Oxford, Parks Road, Oxford OX1 3PU, UK
[2]Rutherford Appleton Laboratory, Chilton, Didcot, Oxon, OX11 0QX, UK
[3]Kumho Information and Telecommunication Laboratory, 572 Sangam-dong, Kwangsan-ku, Kwangju, 506-303, Korea.

Recently experiments were carried out with the aim of producing optical field ionisation and recombinant XUV laser gain in Li-like nitrogen ions [1, 2]. In ref. [2] the experiment was performed at Rutherford Appleton Laboratory (RAL) using a a 300 fsec KrF excimer laser to produce optical field ionisation in a gas jet target. Experimental results showed a non-linear increase of intensity with a increase of nitrogen ion density on Li-like nitrogen XUV transitions including $3d^{5/2}$ - $2p^{3/2}$ (24.7 nm) and $4d^{5/2}$ - $2p^{3/2}$ (18.6 nm). However it was not clear whether this was evidence of XUV laser gain. The simulations described here are designed to address this question .

In this simulation we used a one-dimensional Lagrangian hydrodynamic model in cylindrical geometry which includes tunnel ionization, nonlinear inverse bremsstrahlung, and radial heat conduction (MED104) [3]. An average atom model was used to calculate the average ionization stage and ground and excited state ion densities of the Li-like nitrogen ions. The intensity of 24.7 nm line from each computational zone l is given by

$$I_{l\nu} = \int_0^L I_{l\nu}(z) e^{G_{l\nu} z} dz ,$$

where $I_\nu(z)$ is the spontaneous emission per unit length of the plasma at frequency ν. The total emission in the 24.7 nm line is then obtained by integrating over the linewidth.

The experimental condition is that a KrF excimer laser with 350 fs pulse duration and 5.0×10^{16} W/cm^2 intensity is incident axially into a nitrogen gas. The laser pulse has a Gaussian profile of μm FWHM in the radial direction and in time. The axial intensity of line emission from the Li-like nitrogen ions with a change of ion density was obtained from these simulation results (Fig. 1).

To clarify any evidence of a gain, the emission from plasma lengths of 1 μm and 1 mm was computed. The emission intensities were compared after the line intensity from the 1 μm plasma was multiplied 1000x. The 1 μm plasma length was employed to represent the case of optically thin plasma. As seen in Fig. 2, the emission intensity from the plasma with 1 mm plasma length is two-orders of magnitude less than from 1 μm plasma length x1000. This shows that there is strong absorption of X-ray emission from the elongated nitrogen gas plasma.

We can however see similar non linear increase of intensity with ion density between experimental and simulation results for both plasma lengths when the experimental intensity is normalised to the calculated intensity (as shown in Figure 1). To understand the simulation results better, the dependence of X-ray emission on the plasma length was also calculated. Its results are depicted in Fig.2.

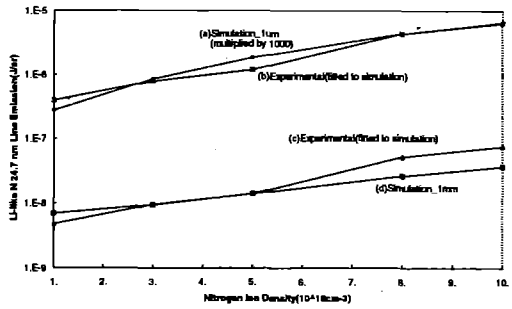

Fig. 1. 24.7 nm line emission from the Li-like nitrogen ion versus ion density. (a) and (c) are simulation results for 1 μm and 1 mm plasma lengths. (b) and (d) are experimental results fitted to the simulation results by rescaling them.

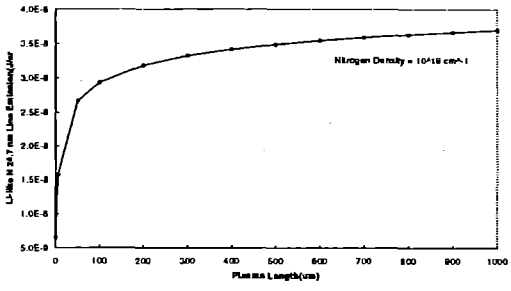

Fig. 2. 24.7 nm line emission from the Li-like nitrogen ion versus plasma length.

From Fig. 2 optically thick saturation of the X-ray emission with an increase of the plasma length is shown. X-ray emission intensity of 6.56×10^{-9} J/sr at 1 μm plasma length was increased up to 3.70×10^{-4} J/sr at 1 mm. So only six times increase of the emission intensity was obtained when the plasma length was increased one thousand times.

These calculations suggest that the experimentally observed increase of intensity with gas density is consistent with an optically thick source and that no XUV laser gain was produced in the experiment.

REFERENCES

1. P. Amendt *et al* SPIE 1860, 140 (1993).
2. A. A. Offenberger, in Proceedings of the Workshop on Ultrashort pulse excimer lasers and their applications, Streatley-on-Thames, 18 Sept. 1995, p.1.82.
3. A. Djaoui and A. A. Offenberger, Phys. Rev. E 50, 4961 (1994).

HARMONIC GENERATION CONTROL

J. B. Watson, A Sanpera and K Burnett

Clarendon Laboratory. Department of Physics. Oxford University. Oxford. (U.K)

INTRODUCTION

While some aspects of harmonic generation are both theoretically and experimentally well understood, the way in which the coherent radiation output can be controlled for practical purposes is still a matter of debate. By controlling harmonic generation we mean the possibility of modifying the spectrum to our convenience by, for example, enhancing only a narrow range of harmonics around a desired energy in the total spectrum. The aim of this article is to show a possible method of controlling the radiation output.

The semiclassical model of harmonic generation [1], correctly asserts the role of the electron's classical returning energies in the harmonic generation process. In particular it suggest that it should be possible to change the spectrum by modifying these trajectories. This idea is reinforced by the experimental data obtained using two different lasers of commensurate frequencies interacting simultaneously with an atom[2]. It appears, therefore, at first sight easier and more beneficial to modify the classical aspects of the process, i.e. the recolliding trajectories than to modify the steps which deal with the intrinsically quantum aspects of it. However, we can produce more profound effects when the ionisation and rescattering events are modified. This can be achieved, for instance, by tailoring the initial state to allow different paths in the recombination event. If the initial state is prepared in a coherent superposition of different bound states, in which only the more loosely bound electron becomes ionised by the action of the field, the harmonic spectrum contains two distinct sets of harmonics. Our aim is to take advantage of this feature, to manipulate the harmonic spectrum.

COHERENT SUPERPOSITION

Our results are based on quantum interference effects that arising during the process of recombination from the continuum into different bound states. We will deal here with the single atom response. (The collective response will be modulated by propagation effects, but keeping the main features of the single atom response). We assume that our initial state is in a superposition of ground and some excited state with a fixed, although arbitrary, phase between both states

$$\Psi(r,t) = \left\{ a|g\rangle + e^{i\phi} b|e\rangle \right\}$$

The laser parameters (I and ω) are chosen such that only the excited state is depleted by ionisation. We do this because it is sufficient to generate high order harmonics, and requires much weaker intensities, to promote the electron into the continuum from the excited state. The emitted radiation spectrum is obtained numerically by solving the time dependent Schroedinger equation and taking the Fourier transform of the acceleration.

The harmonic spectrum obtained from the previous initial state consists of two distinct set of harmonics[3]. The first set of extends to energies up to Ue + 3Up, while the second one appears at the binding energy transition Ug-Ue, and extends up to Ug + 3Up. We can see why this should be so if we assume that harmonics are due to coherent dipole transition between continuum and bound states. An initial bound state amplitude results in a strong dipole moment and therefore enhances such transitions in front of the other ones. We assume that in the tunnelling regime a wavepacket is created in the continuum every half a cycle. In the conditions we have considered, the continuum wavepacket is only due to ionisation from the excited state, and therefore can be characterised by a phase exp(-i Ue ti), where Ue is the binding energy of the field free excited state, and ti refers to the emission time. In the recombination event, characterised by a time tr, the induced dipole between the continuum wavepacket and the excited state will acquire a global phase factor exp(i Ue (tr-ti))= exp(i Ue tc) where tc is simply the time between the wavepacket is created and recollides, i.e. the recollision period. Equivalently, the induced dipole between the continuum wave packet and the ground state will acquire a global phase exp(i (Ug tr -Ue ti))=exp(iUe tc)exp(i Ω tr) where Ω= Ug -Ue is the energy gap between the states of the initial superposition. Due to the periodic nature of the driving field, the overall process of escape and recollision is repeated every half a cycle. That means that since successive wave packets are created and, therefore, recombine at intervals $\tau = T/2 = \pi/\omega$, each successive burst of radiation due to recombination into the ground state differs from the recombination into the excited state by a phase factor exp(i Ω τ). The effect of this phase factor is to shift the harmonic peaks in the second plateau by Ω. To illustrate that effect, we display in Figure 1 the harmonic spectrum corresponding to an initial equally weighted superposition (α=β) of states 1s and 4s for He^+. The laser parameters are λ=2μm and $I = 8x10^{11}\ W/cm^2$ and we use a trapezoidal pulse with a linear turn on in the first two cycles.

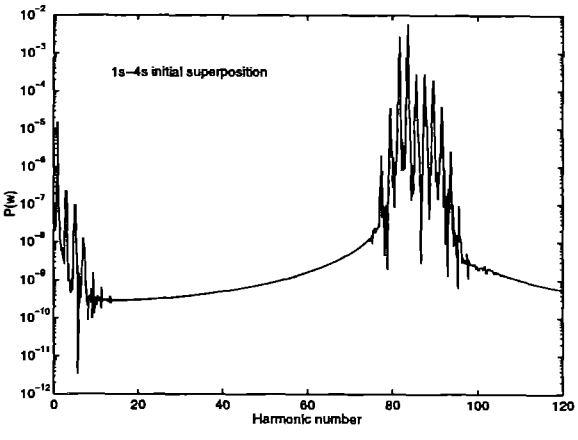

For an equally weighted initial superposition, the conversion efficiency between both plateaux behaves as $(Sg/Se) \approx n^5$ where n is the principal quantum number of the excited state.

REFERENCES

1. J. K. Krause, K. J. Schaffer, and K. C. Kulander, Phys. Rev. Lett. **68,** 3535 (1992).

2. M. Protopapas et al. Phys. Rev A **52**, R2527 (1995) and references therein.

3. J.B Watson, A. Sanpera, X. Chen, and K. Burnett, Phys. Rev A, **55** (1996)., A. Sanpera, J. B. Watson, M. Lewenstein and K. Burnett, submitted to Phys. Rev. A and references therein.

MULTIPLE RECOLLISIONS AND PULSE SHAPE EFFECTS IN HIGH HARMONIC GENERATION

J.B. Watson[1], A. Sanpera[1], K. Burnett[1] and P.L. Knight[2]

[1]Department of Physics, University of Oxford
[2]Blackett Laboratory, Optics Section, Imperial College, London

INTRODUCTION

In this article we will describe some of the critical features of high harmonic generation in a pulsed laser field. In particular we will focus on the loss of harmonic resolution, and the single-atom blueshift that we have previously reported[1]. Before doing so we should first consider the origin of the harmonic peaks observed in a constant field. In order to investigate the features of harmonic generation we will use a model developed by Protopapas *et al*[2], and described elsewhere in this report. The basis of their model is that the harmonic generation can be described by separating two distinct aspects: the behaviour during a single recollision, and the effect of the periodicity of the process. We assume that during each half laser cycle an identical continuum wavepacket is generated. Furthermore since the behaviour of each wavepacket in the field is the same, there is a series of identical recollision events. We can therefore write the harmonic spectrum as the convolution of the response due to a single recollision with a series of delta functions. Applying the convolution theorem we find that the harmonic spectrum is simply the single recollision spectrum modulated by strong peaks at odd harmonics of the laser frequency.

In this discussion we have assumed that each wavepacket only recollides with the core once. In reality there is also a finite probability that the wavepacket will undergo further encounters with the nucleus before it escapes. To include this in our model we consider the single wavepacket response rather than the single recollision response. This consists of several encounters with the nucleus, so there is extra structure (not necessarily harmonic peaks) in the single wavepacket spectrum. The effect of this extra structure is to suppress certain of the harmonic peaks.[3]

PULSE SHAPE EFFECTS

We now turn our attention to the effect of time-dependent pulses on the harmonic spectrum. Clearly if the laser intensity is changing during the pulse then the wavepacket creation and recollision will no longer be strictly periodic. In order to study the effect of this loss of periodicity on the spectrum we have calculated the spectrum using two distinct methods.

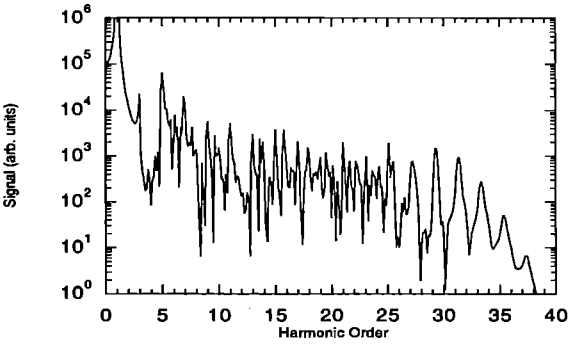

Figure 1

Figure 1 shows the spectrum produced by an 8 cycle pulse of wavelength 372nm, with a field amplitude ramped linearly for intensities between $3.5\times10^{14} W/cm^2$ and $1.5\times10^{15} W/cm^2$, calculated by solving the TDSE over the full duration of the pulse. The plateau region contains peaks at the odd harmonics (as one would expect), but there is also a large amount of structure in between the peaks. In the cut off region there is no significant extra structure, but there is a clear blue-shift of the harmonics[1]. In figure 2 we show the spectra obtained (for the same conditions) by solving the TDSE for a range of different (constant) laser intensities. We then build up the dipole acceleration for our pulse from half-cycle responses calculated at different intensities. The spectrum obtained by sampling the second half cycle (dotted curve) and the fourth half-cycle (solid curve) at each intensity are both shown.

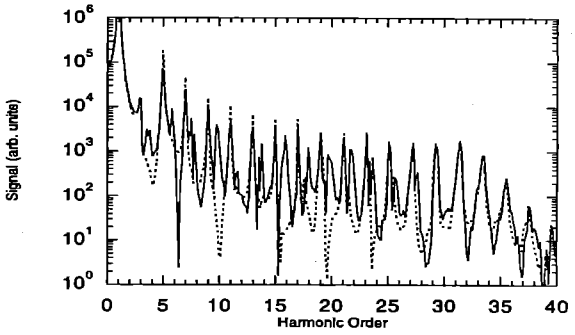

Figure 2

If we compare the dotted curve with figure 1 we find that the main peaks (including the blue-shifted cut-off peaks) are in the correct positions, but that none of the structure between the main peaks is reproduced. When, on the other hand, we sample the fourth half cycle (solid curve) we find that once again we obtain structure between the plateau harmonics. Since we can accurately reproduce the blueshift by combining results obtained at different (constant) intensities, we can conclude that the blue shift occurs because there is a phase shift between the single recollision spectra obtained at different intensities. When the response is Fourier transformed this time-dependent phase shift leads to a blue shift of the harmonics.

In order to explain the extra structure we need to consider the difference between sampling the second and fourth half cycles. If we sample the second half cycle, then only one continuum wavepacket has been produced and therefore we only get the radiation due to the first recollision of a wavepacket. On the other hand sampling the fourth half-cycle also gives contributions due to wavepackets that have recollided more than once. The conclusion is therefore that the extra structure between the main peaks is due to multiple recollisions of each wavepacket. Depending on the laser parameters this extra structure may obscure the main peaks

REFERENCES

1. JB Watson, A Sanpera and K Burnett, Phys Rev A, 51, 1458 (1995).

2. M. Protopapas, D.G. Lappas, C.H. Keitel and P.L. Knight, PRA (Rapid Commun) in press.

3. J.B. Watson, A. Sanpera, K. Burnett and P.L. Knight, submitted to PRA.

X-RAY LINE TRANSFER IN CYLINDRICALLY EXPANDING PLASMAS

P.K. Patel[1], A. Djaoui[2], S.J. Rose[2] and J.S. Wark[1]

[1]Department of Physics, Clarendon Laboratory, University of Oxford, Parks Road, Oxford, OX1 2PU, U.K.
[2]Rutherford Appleton Laboratory, Chilton, Didcot, Oxon, OX11 OQX, U.K.

INTRODUCTION

Calculation of the spectral emission of a plasma is often complicated by the presence of large spatial inhomogeneities. Variations in plasma density, temperature, and velocity, characteristic of laser-produced and astrophysical plasmas, can significantly distort the intensities and shapes of lines in the emission spectrum.[1,2] Gradients in the macroscopic velocity field are of particular importance to the transport of optically thick line radiation since photon re-absorption may be inhibited by the Doppler-decoupling mechanism. Presently we investigate the effects of photon trapping on the x-ray line emission produced by a cylindrical expanding plasma. Such plasmas, produced by the laser-irradiation of thin wire targets, form the basis of many current x-ray laser recombination schemes. We describe a multi-frequency code used to calculate the transfer of hydrogen-like resonance line radiation through a cylindrical plasma.

LINE TRANSFER CALCULATION

The MEDUSA 1-D Lagrangian hydrocode[3] is used to simulate the laser-irradiation of a cylindrical target. The excitation and ionization balance is determined by a time-dependent non-LTE calculation based on the average-atom model.[4] The plasma is assumed to be optically thin to free-free, bound-free, and most bound-bound radiation. Photoabsorption of the optically thick hydrogen and helium-like resonance lines is included - the effect on the bound state populations being accounted for by the use of escape probabilities.[5] The escape probability method is an approximation to the full radiative transfer treatment of line radiation, valid in the limit of steep velocities. In this limit significant absorption of an isolated line can only occur within the Doppler-decoupling distance - that distance in the plasma over which the shift in frequency of a line photon, due to the macroscopic velocity field, is less than the line width - thereby permitting the calculation of a locally defined escape probability for the line. The atomic rate equations can be then be modified to include the effect of photoabsorption simply by adding the escape probability as a multiplicative factor to the local spontaneous emission rate. Equipped with the plasma densities, temperatures, velocities and level populations, we proceed with calculating the spectral emission. In a 1-D simulation we assume an infinitely long wire expanding radially outwards, with zero axial velocity. We wish to model the emission in this plane, normal to the cylinder axis. This is done by a ray-tracing procedure, performed along a set of parallel chords spanning the perpendicular cross-section through the cylinder. A particular chord, or ray, at some distance, y, of closest approach to the wire centre, will intersect, at least once, all those cells with a radius equal or greater than y. The line intensity along the ray from one such cell, m, is given by

$$I_m(\nu) = \sum_l S_m^l(\nu)\left\{1 - \exp\left[-\chi_m(\nu)\Delta z_m\right]\right\} \qquad (1)$$

where S is the source function, χ is the opacity, and Δz is the pathlength of the ray through the cell. The summation is over the number of lines being treated. This radiation is then transported to the edge of the plasma. We account for the absorption by each intervening cell - the absorption coefficients being evaluated at the Doppler-shifted frequency of the incoming radiation. The result is the observed line emission from cell m. We obtain the total intensity at y by summing the contributions from each of the cells along the ray. A spatially-resolved spectrum is constructed by repeating the line transfer calculation for each of the chords.

SIMULATED SPECTRAL PROFILES

As a demonstration we compute the hydrogen-like Ly-α ($1s$-$2p$) emission from an aluminium plasma. The Al Ly-α line has a well resolved doublet fine-structure, with components at 7.175Å ($1s_{1/2}$-$2p_{3/2}$) and 7.180Å ($1s_{1/2}$-$2p_{1/2}$). Doppler profiles are used for each component since the dominant broadening mechanism is thermal Doppler broadening. We simulate a 50μm diameter Al wire uniformly-irradiated by a 1ns (FWHM) Gaussian pulse of 0.53μm light delivering a peak surface irradiance of 4×10^{14} Wcm^{-2}. Maximum emission of Ly-α radiation occurs soon after the peak of the laser pulse. The n=2 excited state fraction decreases rapidly with radius, indicating that the emission will be concentrated close to the surface. Within the first 100μm of the ablation surface the electron temperature is approximately 1400eV, the electron density drops from 5×10^{21} to 5×10^{20} cm^{-3}, and the velocity gradient is a very high 5×10^{9} s^{-1}. The simulated Ly-α spectrum is shown in Figure 1.

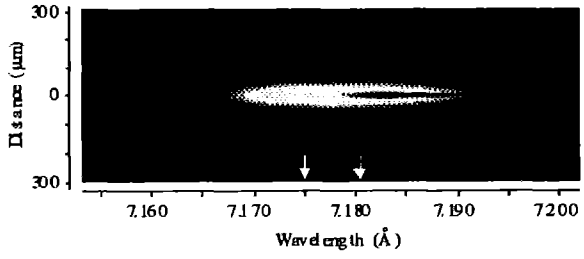

Figure 1 Simulated Al Ly-α spectrum at time of peak laser intensity. Arrows indicate the unshifted positions of the doublet components.

The high expansion velocities have smeared out the emission into a single, highly broadened line bearing no resemblance to the original doublet profile. We note the presence of a dark strip on the long wavelength side, signifying an absence of red-shifted emission at this position. This is due to the wire core shadowing radiation which is emitted by plasma moving away from the observer. At distances greater than the core radius of 25μm we detect emission from both the receding and approaching plasma.

SUMMARY

We have developed a code to compute the spatially-resolved, time-dependent hydrogen-like line emission produced by a cylindrically expanding laser-produced plasma. A comparison of simulated profiles with experimentally recorded spectra will be presented in a forthcoming publication.

REFERENCES

1. J S Wark *et al.* Phys. Rev. Lett., 72, 1826 (1994).
2. A Djaoui, S J Rose and J S Wark. JQSRT, 52, 531 (1994).
3. J P Christiansen *et al*,. Comput. Phys. Commun., 7,271 (1973).
4. A Djaoui and S J Rose. J. Phys. B, 25, 2745 (1992).
5. A I Shestakov and D C Eder. JQSRT, 42, 483 (1989).

MODEL OF NLTE EMISSION FROM PLASMA PRODUCED BY A 300 fs LASER PULSE

K. Nazir†‡ and S. J. Rose‡§

† Atomic Weapons Establishment, Aldermaston, Reading, RG7 4PR, U.K.
‡ School of Physics and Space Research, University of Birmingham, Birmingham, B15 2TT, U.K.
§ Rutherford Appleton Laboratory, Chilton, Didcot, Oxon, OX11 0QX, U.K.

INTRODUCTION

The availability of subpicosecond, high intensity lasers has generated considerable interest[1)2)]. The characteristics of laser generated plasmas are strongly dependent on experimental conditions[2)] (amplified spontaneous emission (ASE) level, pulse length, intensity, target thickness).

Plasmas produced by high power lasers can consist almost entirely of completely stripped nuclei, and of free electrons, but in the majority of cases are partially-ionised, surrounded by a sea of electrons. Transitions of bound electrons from excited states to lower states in ions can produce a major proportion of the radiated power from a laser-plasma. Resonance lines, electric-dipole allowed transitions from excited states to the ground state, generate strong line radiation, which can be used for spectroscopic identification and analysis.

In this short communication, X-ray emission from iron plasmas produced by irradiation of planar solid targets by intense sub-picosecond lasers will be compared with results from a detailed NLTE (Non Local Thermodynamic Equlibrium) radiational model incorporating complete atomic physics data. The analysis of laser-plasma emission using an LTE model and details of the experiments will be reported separately[3)].

THE MODEL

The behaviour of buried layer targets irradiated by high intensity short pulse lasers is modelled using a one-dimensional hydrodynamic simulation code MED103[4)]. As the iron plasma is calculated to be optically thin and the X-ray emission is expected to be dominated by line transitions, we employ a detailed atomic physics model[5] to calculate the spectral emission.

The X-ray intensity at frequency ν is given by

$$I(\nu) = \sum_k \Delta t_k \sum_l S_l \Delta x_{kl} \sum_m N_{klm} g'(\nu) A(\nu) \gamma(\nu) \phi(\nu) \quad (1)$$

where Δt_k is the timestep k, S_l is the cross-section area of cell l, Δx_{kl} is the width of the Lagrangian cell l and N_{klm} is the number density of excited ions of the ionisation stage m in the cell l during timestep k, all of which are taken from the hydrodynamic simulations. $g'(\nu)$ is a degeneracy-correction factor and is given by the ratio of the excited sub-level degeneracy to the total upper configuration-level degeneracy. $A(\nu)$ is the Einstein's probability (per unit time) for a radiative transition of energy $\gamma(\nu)$ to occur, both of which are taken from the atomic physics simulations. $\phi(\nu)$ is the line shape function, which describes the actual frequency spectrum with the line such that $\int \phi(\nu) d\nu = 1$, with the integral extended over a sufficiently large neighbourhood of the line. A Stark width has been assigned to the theoretical spectrum to account for line broadening in the plasma[6)].

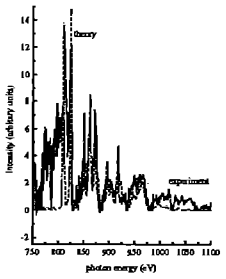

Figure 1: Comparison between measured X-ray intensity (with background subtracted) and theoretical intensity calculated from Eq.(1).

RESULTS

The predicted intensity from Eq.(1) is shown in Fig.(1) for comparison with the measured intensity. The theoretical spectrum shows detailed line features (approximately due to 3–2 transitions above and below the neon-like ionisation stage of iron) as in the experiment. In the simulations only $n = 3 \rightarrow 2$ transitions are included and no account is taken of continuum emission from the plasma. The model assumes the radiating plasma is optically thin to soft X-ray emission, and includes gradient and temporal effects on the plasma radiation.

CONCLUSIONS

Theoretical X-ray line spectra from detailed models of plasma heating and expansion in the hydrodynamic code MED103, and of complete atomic physics from the MCDF code show very good agreement with experiment. The line features around 750–825 eV are attributed to late time emission, whereas features above 825 eV are predicted to be from simultaneously high density and high temperature iron plasmas which exist for a short duration during the incident laser pulse.

REFERENCES

1. S. J. Rose. High-power laser-produced plasmas and astrophysics. Laser Part. Beams, 4, 869 (1991).
2. D. Umstadter *et al.* Intense ultrashort-pulse laser-solid interactions for soft x-ray generation. In SPIE, H. A. Baldis, ed., 1860, 80 (1993).
3. K. Nazir and S. J. Rose. Rutherford Annual Report 1995–96 and all references contained therein.
4. A. Djaoui and S. J. Rose. J. Phys. B: At. Mol. Opt. Phys. 25, 2745 (1992).
5. I. P. Grant *et al.*. Comp. Phys. Comm. 21, 207 (1980).
6. E. Nardi and Z. Zinamon. Phys. Rev. A. 20, 1197 (1979).

MODEL OF LTE EMISSION FROM PLASMA PRODUCED BY A 300 fs LASER PULSE

K. Nasir†‡ and S. J. Rose‡§

† Atomic Weapons Establishment, Aldermaston, Reading, RG7 4PR, U.K.
‡ School of Physics and Space Research, University of Birmingham, Birmingham, B15 2TT, U.K.
§ Rutherford Appleton Laboratory, Chilton, Didcot, Oxon, OX11 0QX, U.K.

INTRODUCTION

The radiative properties of hot dense matter are of interest in both laser fusion and astrophysics[1)2)]. To perform quantative measurements of radiative opacities in the laboratory, the plasma generated are required to be in LTE (Local Thermodynamic Equilibrium)[2)]. The opacity of material in LTE is of great interest in studies of stellar structure and evolution.

In this communication we report a new experiment which employs a subpicosecond high-power laser to generate an iron plasma which is in conditions similar to those found in the diffusive-flow region of main-sequence stars. X-ray emission spectroscopy has been used to perform comparisons with calculated emission based on radiative opacity calculations, as well as provide a global assessment of approximations commonly made in opacity models.

THE EXPERIMENT

The Sprite KrF laser at the Rutherford Appleton Laboratory was used in the Chirped Pulse Amplification (CPA) mode to produce pulses of 300fsec duration at a wavelength of 249nm with an energy of approximately 0.15 J on target, giving intensities in excess of 10^{17} Wcm^{-2} and power of approximately 0.5 TW. Details of the experiments are given by Tallents *et al.*[3)]. In this short communication we present results from the irradiation of plastic (CH) targets with a layer of iron, 1000Å thick, buried 1000Å below the surface. The laser was focussed onto the thin tamper layer of plastic. The time-integrated spectral emission was measured using a mini-crystal spectrometer.

THE MODEL

The behaviour of the buried layer targets in the experiments has been modelled using a one-dimensional hydrodynamic simulation code MED103. In the simulations, We employ a flux-limiter set to 0.2 of the free streaming limit and a laser absorption fraction set to 20% of the incident laser energy. As the iron plasma is calculated to be close to LTE, a result of the high electron collision rates at the iron densities involved, we employ a detailed LTE opacity model to calculate the spectral emission.

The X-ray intensity at frequency ν is given by

$$I(\nu) = \sum_k \Delta t_k \sum_l B(\nu, T_{kl})(1 - \exp(-\rho_{kl} k'(\nu, \rho_{kl}, Tkl)\Delta x_{kl} \quad (1)$$

where Δt_k is the timestep k and Δx_{kl} is the width of the Lagrangian cell l during timestep k. T_{kl} is the electron temperature and ρ_{kl} is the material density of cell l during timestep k, both of which are taken from the hydrodynamic simulations. The opacity $k'(\nu, \rho, T)$ includes the effect of stimulated emission and is interpolated in density and temperature from a table of values calculated by the opacity model IMP[2)].

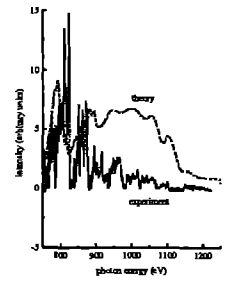

Figure 1: Comparison between measured X-ray intensity (with backgound subtracted) and theoretical intensity calculated from Eq.(1).

RESULTS

The predicted intensity from Eq.(1) is shown in Fig.(1) for comparsion with the measured intensity. The theoretical spectrum shows two broad region (approximately due to 3–2 transitions above and below the neon-like ionisation stage of iron) as in the experiment. The lines which lie towards the low energy region (below 825 eV) are principally the 3–2 transitions in ionisation stages below neon-like. The groups of lines at higher energy are mainly due to the 3–2 transitions in ionisation above neon-like, which are predicted to last for a relatively short period of simultaneously high temperature and density in the iron plasma.

CONCLUSIONS

Comparisons of the theoretical and experimental spectrum shows good agreement particularly for the features resulting from the ionisation stages of neon-like and above which are predicted to exist only at the highest energy density predicted in the experiment (700eV, $8gcm^{-3}$ and $5\,10^{15}\,Jg^{-1}$). The experiment points the way towards a new class of opacity experiments which, by electron conduction heating through short-pulse irradiation of buried layer targets, permits some integrated check of theoretical LTE opacity calculations, in a region of very high energy density.

REFERENCES

1. S. J. Rose. High-power laser-produced plasmas and astrophysics. Laser Part. Beams, 4, 869 (1991).
2. S. J. Rose. Calculations of the radiative opacity of laser-produced plasmas J. Phys. B: At. Mol. Opt. Phys., 25, 1667 (1992).
3. G. J. Tallents *et al.*. Proc. 23rd Europ. Conf. Laser Int. Matter. (Bristol, IOP) (1994).

DEVELOPING COLLISION COEFFICIENTS FOR USE WITH A BOLTZMANN CODE FOR TREATING ELECTRON DISTRIBUTIONS IN A HIGH INTENSITY FIELD

G J Pert

Department of Physics, University of York,
Heslington, York, YO1 5DD

In very strong electro-magnetic fields ionisation essentially occurs through an impact approximation whilst the electro-magnetic field is nearly constant as the electron's state changes. The electron distribution following ionisation is easily calculated from a classical model provided the static electric field emission probability is known[1]. The cycle averaged values are then obtained by direct integration usually using the method of steepest descent to give an asymptotic value[2], although in some cases the exact integral is available[3]. The distribution function of the electron P(ε) after release is calculated from the probability per unit time W(φ) at phase φ and the residual energy ε(φ) of the electron on release at zero velocity and its phase mismatch with the field:

$$P(\varepsilon) = \left(\frac{d\varepsilon}{dt}\right)^{-1} W(\varphi)$$

The residual phase mismatch energy ε is identified with the non-oscillatory , or thermal, motion of the electron as in the impact model of inverse bremsstrahlung[4]. In practice this leads to a two dimensional velocity distribution for the electrons depending on the polarisation and can be easily taken into account. However in this work we will consider only the simplest case where the distribution is assumed to be isotopic.

In this note we examine the characteristics required for a simulation model to treat the time dependent development of the electron distribution considered as a function of the thermal velocity (or energy), i.e. averaged over the radiation driven quiver motion following breakdown in an ionising gas.

Electron-electron collisions relaxing the distribution towards the Maxwellian are well treated by the normal Fokker-Planck collision term[5] for which a satisfactory finite difference algorithm has been developed by Tingbin and Rose[6], although it should be noted that this scheme is only weakly energy conserving.

Electron-ion collisions give rise to electron heating through inverse bremsstrahlung or collisional heating. They may also be treated within the Fokker-Planck approximation since the majority of collisions are long range and involve relatively small electron energy gains provided the integration step is kept reasonably small. The formalism is easily developed by considering a transformation to the quiver frame where the ions are oscillatory. The Fokker - Planck coefficients for this case were calculated long ago by Chandrasekhar[7] for the case of an isotropic distribution and constant ion velocity. Averaging over the field cycle leads to the collision term:

$$\frac{\partial f}{\partial t} = \frac{4\pi}{3} n_i \left(\frac{Ze^2}{m_e}\right) \frac{1}{v^2} \frac{\partial}{\partial v} \left\{ \begin{matrix} u_0^2/v \; \partial/\partial v \left[\ell n \Lambda(v)\right] R(v) f(v) + \\ v^2/u_0 \; \partial/\partial v \left[S(\Delta, u_0/v) f(v)\right] \end{matrix} \right\}$$

where u_0 is the peak oscillation velocity, v the thermal speed n_i the ion number density and $\ell n(\Lambda)$ the Coulomb logarithm modified for the radiation field. For plane polarised radiation the functions R(v) and $S(\Delta, u_0/v)$ have the values:

$$R = \begin{cases} 1/2 & v > u_0 \\ 1/\pi \left\{ \arcsin(v/u_0) - \sqrt{1-(v/u_0)^2} \right\} & v < u_0 \end{cases}$$

$$S = \begin{cases} 0 & v > u_0 \\ 2/\pi \; \tilde{S}(\Delta, u_0/v) & v < u_0 \end{cases}$$

and $\tilde{S}$ is given by

$$\tilde{S}(\Delta, x) = \int_{\arcsin(x^{-1})}^{\pi/2} \ell n\left(\Lambda\left[\Delta, x\sin\theta\right]\right) / \sin\theta \, . \, d\theta$$

the terms Δ and S are equivalent to those calculated earlier in studies of inverse bremsstrahlung[8]. The two terms R and S play entirely different roles in determining the electron distribution. The term R modifies the distribution without changing the total electron energy: it is this term which generates the well-known Langdon form[9]. The term S on the other hand is entirely responsible for the energy gain in inverse bremsstrahlung and hence its equivalence with term calculated earlier[8].

We now turn to the problem of treating inelastic collisions. In this case the energy exchange is no longer small and we cannot continue to use a Fokker-Planck formalism, but must treat the problem within a Boltzmann collision framework.. Numerically this entails exchanging electrons between the various velocity (or energy) cells according to the respective energy overlaps and probability. This is not a trivial problem if it is required that detailed balance be maintained, particularly for ionisation and three-body recombination.

To proceed further we must assume that the detailed ionisation cross section giving the probability of the individual electron speeds is known. In fact in most cases this is not available but the total cross section is known and some approximation as to the relative distribution between the two electrons must be made, for example based on the classical model. To develop the reciprocal rates consider ionisation by an electron of energy $(\varepsilon_0, d\varepsilon_0)$ yielding electrons of energy $(\varepsilon_1, d\varepsilon_1)$ and $(\varepsilon_2, d\varepsilon_2)$. We may write the ionisation rate from a state of energy E_0 to one of energy E_1 in the form:

$$R_+(E_0, \varepsilon_0; E_1, \varepsilon_1, \varepsilon_2) n_e(\varepsilon_0) \; d\varepsilon_0 \\ \delta(E_1 + \varepsilon_1 + \varepsilon_2 - E_0 - \varepsilon_0) d\varepsilon_1 \; d\varepsilon_2$$

and the recombination rate is

$$R_-(E_1, \varepsilon_1, \varepsilon_2; E_0, \varepsilon_0) n_e(\varepsilon_1) d\varepsilon_1 \, n_e(\varepsilon_2) d\varepsilon_2 \\ \delta(E_1 + \varepsilon_1 + \varepsilon_2 - E_0 - \varepsilon_0) d\varepsilon_0$$

where $n_e(\varepsilon)\, d\varepsilon$ is the density of electrons in the energy interval $(\varepsilon, d\varepsilon)$. The equation of detailed balance applied to these rates yields the following reciprocal relationship:

$$g_0\left[\rho(\varepsilon_0)d\varepsilon_0\right]R_+(E_0,\varepsilon_0;E_1,\varepsilon_1,\varepsilon_2)\, d\varepsilon_1\, d\varepsilon_2 = g_1\left[\rho(\varepsilon_1)d\varepsilon_1\right]\left[\rho(\varepsilon_2)d\varepsilon_2\right]R_-(E_1,\varepsilon_1,\varepsilon_2;E_0,\varepsilon_0)d\varepsilon_0$$

where g_0 and g_1 are the statistical weights of states 0 and 1 respectively, and $\rho(\varepsilon)$ the density of free electron states per unit volume:

$$\rho(\varepsilon) = \frac{4\pi(2m_e)^{3/2}}{h^3}\varepsilon^{1/2}$$

For use in a finite difference calculation these rates may be integrated over the three cells of width $\Delta\varepsilon_0$ $\Delta\varepsilon_1$ and $\Delta\varepsilon_2$ to yield a reciprocal weight function $w_{i,j,k}$ to be used to assign the contributions following collision. Thus given three cells centred at ε_0, ε_1 and ε_2 respectively such that $\Delta\varepsilon_2 > \Delta\varepsilon_1 > \Delta\varepsilon_0$ then

$$w_{0,1,2} = \begin{cases} 1/\Delta\varepsilon_2 & 0 > \varepsilon > \tfrac{1}{2}(\Delta\varepsilon_2 - \Delta\varepsilon_1 - \Delta\varepsilon_0) \\ \tfrac{1}{2}(\Delta\varepsilon_2 + \Delta\varepsilon_0 - \varepsilon)/(\Delta\varepsilon_2\Delta\varepsilon_0) - \tfrac{1}{2}\left[\tfrac{1}{2}(\Delta\varepsilon_2 + \Delta\varepsilon_1 - \Delta\varepsilon_0) - \varepsilon\right]^2/(\Delta\varepsilon_2\Delta\varepsilon_1\Delta\varepsilon_0) & \tfrac{1}{2}(\Delta\varepsilon_2 - \Delta\varepsilon_1 - \Delta\varepsilon_0) > \varepsilon > \tfrac{1}{2}(\Delta\varepsilon_2 - \Delta\varepsilon_1 + \Delta\varepsilon_0) \\ \left[\tfrac{1}{2}(\Delta\varepsilon_2 + \Delta\varepsilon_1) - \varepsilon\right]/(\Delta\varepsilon_2\Delta\varepsilon_1) & \tfrac{1}{2}(\Delta\varepsilon_2 - \Delta\varepsilon_1 + \Delta\varepsilon_0) > \varepsilon > \tfrac{1}{2}(\Delta\varepsilon_2 + \Delta\varepsilon_1 - \Delta\varepsilon_0) \\ \tfrac{1}{2}\left[\tfrac{1}{2}(\Delta\varepsilon_2 + \Delta\varepsilon_1 + \Delta\varepsilon_0) - \varepsilon\right]^2/(\Delta\varepsilon_2\Delta\varepsilon_1\Delta\varepsilon_0) & \tfrac{1}{2}(\Delta\varepsilon_2 + \Delta\varepsilon_1 - \Delta\varepsilon_0) > \varepsilon > \tfrac{1}{2}(\Delta\varepsilon_2 + \Delta\varepsilon_1 + \Delta\varepsilon_0) \\ 0 & \tfrac{1}{2}(\Delta\varepsilon_2 + \Delta\varepsilon_1 - \Delta\varepsilon_0) > \varepsilon \end{cases}$$

where ε is the energy mismatch $\varepsilon = |E_0 + \varepsilon_0 - E_1 - \varepsilon_1 - \varepsilon_2|$

Excitation/de-excitation processes and radiative recombination are easily included within this framework.

A code following this prescription has been constructed to model field ionisation at high intensities. Results will be presented at a later date, but good agreement is found with equivalent Monte-Carlo calculations

REFERENCES

1 P.B.Corkum, N.H.Burnett and F.Brunel Phys.Rev.Lett., 62, 1259, 1989

2 M.V.Ammosov,N.B..Delone and V.P.Krainov Sov.Phys. J.E.T.P. 64, 1191, 1986

3 K.A.Janulewicz,M.J.Grout and G.J.Pert J. Phys. B 29,901,1996

4 G.J.Pert J. Phys. A 5, 506, 1972

5 M.N.Rosenbluth, W.M..MacDonald and D.L.Judd Phys.Rev. 107, 1, 1957

6 Z.Tingbin and S.J.Rose Private Communication

7 S.Chandrasekhar Principles of Stellar Dynamics Dover publications, 1942

8 G.J.Pert Phys Rev E 51, 4778, 1995

9 A.B.Langdon Phys.Rev.Lett. 44, 575, 1980

TO INVESTIGATE THE POSSIBILITY OF ACHIEVING AN ELECTRON DENSITY WELL IN X-RAY LASER PLASMAS.

P A Simms , S B Healy and G J Pert.

Department of Physics, University of York, Heslington, York YO1 5DD.

INTRODUCTION

The effective gains of x-ray lasers are known to depend heavily on the refraction that occurs in the high gain regions, due to the large electron density gradients in the lasing plasma. The majority of this refraction occurs in the radial direction (direction of the driving laser pulse), but there is also a high contribution to the losses from refraction in the transverse direction (direction perpendicular to both the driving laser and the x-ray laser output beam) . It is these refraction losses that this work is presently concerned with. The radial refraction can be controlled by the curvature of the target in the direction of the output beam in order to compensate for the bending of the output beam.

A similar method may be used in order to compensate for the transverse refraction losses[1] . This, however, is very difficult to achieve experimentally. This work is therefore aimed at producing a dip in the electron density profile of the plasma. This is done in the radial direction and its purpose is to produce a waveguiding effect along the output direction (ie. to trap the beam at a given electron density). This problem has been looked at in two different ways. Firstly to make the well by using two driving pulses which strike the target at different positions thus giving two overlapping Gaussian profiles that emerge with a dip in the centre. The second and the important way for this report, is to heat the plasma by using a relatively wide low power pre-pulse and then a narrower, more intense main pulse[2] . This has the effect of burning through the plasma and leaving a density profile with a central well. The transition that this work is concerned with is the J = 0 -1 line in germanium which has a wavelength of 196 Å.

THE COMPUTATIONAL MODELS

In order to do these simulations there is a need to use three computer codes. The first code is POLLUX which is used to set up the grid with the density profiles in the gain region. This gives information about the density and the ion and electron temperatures. The data is also read into a 1.5 d langragian hydro/atomic code called EHYBRID[3] . The only difference in the input data for EHYBRID is an increase in the second pulse power. This is to compensate for the much higher heat loss in the transverse direction. This EHYBRID code gives output for the gain of the medium along with the saturation intensity, the density, the temperature, the spontaneous emission rate, the Lorentzian and the Doppler linewidths. All of these values are given on the axis where the values are symmetric in the transverse direction. The next step of this work is to combine the values given from these two codes in order to use them in a third code. This third code is a 3d raytracing code[4] . It is the aim to fit the density profile from the POLLUX code into the grid for the raytracing program and then to use this grid with the relevant values from the EHYBRID code.

RESULTS

Figure 1 shows an electron density profile which was produced by the POLLUX code. It can be seen from this figure that for an electron density of 3e20 to 5e20 that there is a substantial well formed. This well has a dip of 25-35% which is confined to a transverse width of 80 μm. The same data in the EHYBRID code gave a peak gain of 40 cm^{-1} . The electron temperatures achieved in this work peak in the order of 1100 ev. This was achieved by the use of two red laser pulses. Both of these have a time to rise 50 ps and full width half maximum (FWHM) 100 ps. The first pulse has a power 1e13 Wcm^{-2} and a focal spot half width of 50 μm. The main second pulse is started after a time of 500 ps. This pulse has a power of 3e13 Wcm^{-2} and a focal spot half width of only 12.5 μm. This produced a density profile like that one shown in figure 1 after a time of 600 ps.

The densities produced by EHYBRID are higher than that from POLLUX, hence these need normalising before they are used in the raytrace with the POLLUX produced grid.

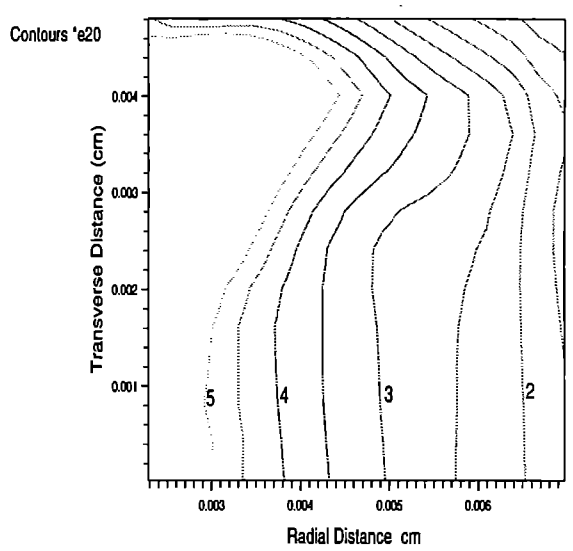

Figure 1 Electron density profile produced by the POLLUX code at a time of 600 ps after the first pulse.

CONCLUSION

A density profile such as the one shown in figure 1 should show strong guiding of the beam. This system should improve the quality of the output beam by increasing the collimation, intensity and brightness of the system. The intensity should increase by a factor of the order of 200 times over a system which has curvature alone[2] . The increase in the intensity of the J = 0 - 1 line (196 Å in germanium) was most noticable due to the ability for this transition to sample the higher gain regions better.

REFERENCES

1. J G Lunney, Appl Phys Lett 48, 891 (1986).

2. J A Plowes, Ph. D. thesis, University of York 1995.

3. P B Holden, S B Healy, M T M Lightbody, G J Pert, J A Plowes, A E Kingston, E Robertson, C L S Lewis and D Neely, J. Phys. B 27, 341 (1994)

4. D J Toft, Ph. D. thesis, Univ. of Hull, 1979.

ELECTRON RESIDUAL ENERGY OF OPTICAL-FIELD-IONISED PLASMAS

MJ Grout, KA Janulewicz and GJ Pert
Department of Physics, University of York.

INTRODUCTION

Optical-field-ionisation by ultrashort pulse lasers has been suggested as a mechanism to produce a cold plasma suitable for recombination x-ray lasers. The three-body electron-ion recombination rate depends on the electron temperature as $T_e^{-9/2}$. Sufficiently cold electrons give a high rate of recombination which with the ensuing cascade relaxation to the upper lasing level will produce a population inversion.

OFI simulations have been compared with experimental electron temperature measurements, and used to determine the effect of space-charge fields induced in the plasma on the electron temperature.

DESCRIPTION OF CODES

The numerical codes used have been described in detail elsewhere[1),2)]. They are based on descriptions of above threshold ionisation[3)] and inverse Bremsstrahlung[4)] as the dominant heating mechanisms present during the pulse. An analytical form may give averaged electron energies under two conditions, firstly, at the peak of both the spatial and temporal profiles, or secondly, at the end of the pulse and averaged over a multimodal spatial profile. The 1D PIC code MULTIPHOTON1 allows for electron movement and thus the creation of space charge fields. The average energy is calculated as for the second condition above.

RESULTS AND CONCLUSIONS

In several experiments only single sets of conditions in helium targets have been considered, thus although our codes give good agreement in most cases this does not allow evaluation of the effect of each parameter. Recently experiments by Blyth *et al*[5)] were performed at various ion densities on helium and neon targets. The laser parameters used were peak intensity 10^{18}Wcm^{-2}; rise time 500fs; FWHM time 350fs; wavelength 248nm; focal spot size (1/e level) 12μm. The results are shown in figure 1 with the experimental values denoted by circles and associated error bars. Blyth *et al* indicated that these energies were measured at the peak of the spatial and temporal profiles, the corresponding analytical code results are shown by the solid-line.

The effect of space charge fields on the electron energy was investigated using MULTIPHOTON1 with a smooth spatial profile and a modulated one. The potential energy of electrons followed the intensity profile as the ponderomotive force displaces the electrons against the restoring space charge field. In the modulated profile case the ponderomotive force is increased due to local gradients from the modes, electrons drift into the lower field region producing electron cavitation shown in figure 2. However at the end of the pulse the potential energy in both cases has returned to very near zero, and the electron cavitation has collapsed. The kinetic energy is only slightly affected. Thus the MULTIPHOTON1 and analytical version (condition 2) results match closely. Blyth *et al* results and simulations for neon are also consistent especially at higher densities.

In conclusion, satisfactory agreement between experimental and simulation results have been found for electron energies. Space charge fields although present do not significantly influence the final energy.

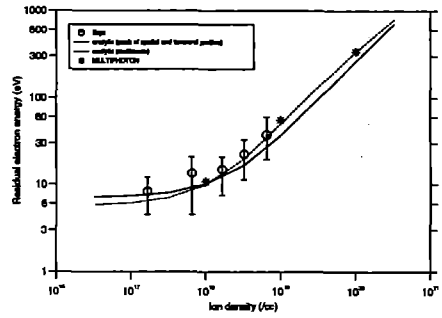

Figure 1 Comparison of experimental and simulation results for helium

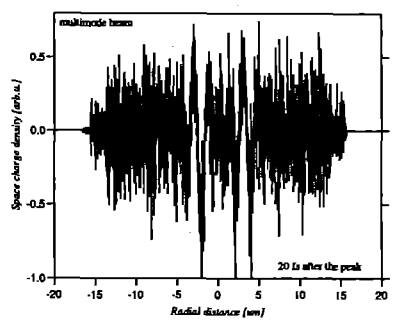

Figure 2 Radial distribution of space charge density 20fs after peak of pulse with multimode beam for helium at ion density 10^{18}cm^{-3}

REFERENCES

1. M.J. Grout and G.J. Pert.
Residual electron energy simulation of optical-field-ionised nitrogen.
CLF RAL Annual Report, RAL-TR-95-025, 88 (1995)

2. K.A. Janulewicz, M.J. Grout and G.J. Pert.
Electron residual energy of optical-field-ionized plasmas driven by subpicosecond laser pulses.
J. of Phys. B, 29, 901 (1996)

3. P.B. Corkum, N.H. Burnett and F. Brunel.
Above-threshold ionization in the long-wavelength limit.
Phys. Rev. Lett., 62, 1259 (1989)

4. G.J. Pert.
Inverse bremsstrahlung in strong radiation fields at low temperatures.
Phys. Rev. E, 51, 4778 (1995)

5. W.J. Blyth, S.G. Preston, A.A. Offenberger, M.H. Key; J.S. Wark, Z. Najmudin, A. Modena, A. Djaoui and A.E. Dangor.
Plasma temperature in optical field ionization of gases by intense ultrashort pulses of ultraviolet radiation.
Phys. Rev. Lett., 74, 554 (1995)

ELECTRON ENERGY DISTRIBUTION FUNCTION OF HELIUM OFI-PLASMA

KA Janulewicz, SB Healy and GJ Pert
Department of Physics, University of York.

INTRODUCTION

Optical-field-ionised (OFI) plasmas, produced with strong, subpicosecond laser pulses have recently become an area of increasing interest. For a non-Maxwellian plasma, with a given residual energy, the electron energy distribution function (EEDF) is necessary to describe correctly the kinetic processes. A comprehensive analysis of plasma effects in the tunnel-ionised low pressure gases has recently been presented[1]. More recently, Glover *et al*[2] derived experimentally the EEDF of helium and traced its time history up to 400 ps after the driving pulse had passed.

MODEL

The EEDF calculations, performed with a particle code, include a full Monte Carlo method to describe ionisation as well as collisional processes in the plasma. The behaviour of the plasma after the ionising, linearly polarised, subpicosecond pulse has passed, is modelled with the 1D-hydrodynamic Lagrangian code which assumes cylindrical symmetry[3]. It is assumed that tunnel ionisation determines the ionisation probability. In the collisional part of the model, an electron exchanges its energy in elastic collisions with ions and other electrons. Most collisions are included into the code as multiple-small-angle Coulomb collisions with a normal angular distribution defined by Monte Carlo methods, although large-angle binary collisions can occur as well. Ions are assumed to be at rest. Despite the unidirectional field, a full 3D-description of the velocity space is achieved.

RESULTS

Our simulations consider helium under conditions identical with those used by Glover[2]. A square profile of the beam cross-section is assumed. When $e-e$ collisions are not included, the electron energy distribution shows an increasing deficit of cold electrons and appearance of a distinct distribution maximum at about 3 eV but still some excess of cold electrons exists when compared to the Maxwellian distribution. Results of simulations with electron-electron collisions included are shown in Fig.1. The profiles presented in Fig.1 are in disagreement with the distribution function obtained experimentally by Glover[2]. The results obtained indicate that the important contribution to the EEDF isotropisation comes from the collisional processes in the plasma (even when the collisional heating contributes lower than 2 eV). This is easily seen in Fig.2, in which the corresponding time history of the residual enegy is presented. In addition to the calculations presented above, we have modelled the behaviour of the cylindrical sample of the OFI-plasma after the ionising pulse, using a 1D-hydrodynamics/atomic physics code[4]. Thermal conductivity seems to be the dominating cooling mechanism in post-OFI-plasmas. It seems possible that such effects as radiation imprisonment or overlapping of the spectra from different regions of the focal volume are present in the experiment.

CONCLUSIONS

The results obtained let us conclude that under the conditions relevant to X-ray lasers, electron-ion and electron-electron collisions contribute significantly to the plasma isotropisation process. Simulations performed with the hydrodynamic Lagrangian code under the assumption of a Maxwellian distribution indicate that thermal conductivity is the dominating and very effective cooling mechanism.

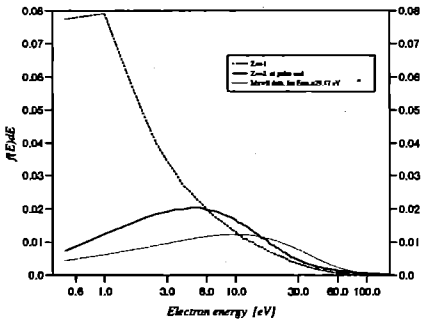

Figure 1 Electron energy distribution function (EEDF) with $e-e$ collisions included calculated for the conditions of Glover experiment: $n_i=10^{18}$ cm^{-3}; I=10^{16} W/cm^2; τ_p(FWHM)=160 fs; τ_{rise}=150 fs; λ=616 μm. Z is the ionisation stage reached.

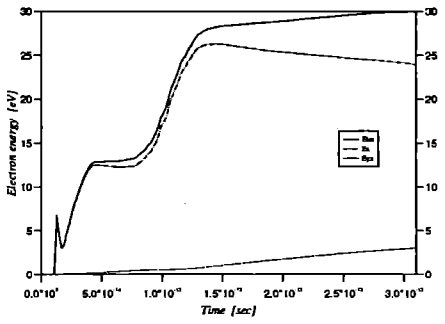

Figure 2 Time history of the residual energy for helium under conditions considered. Total energy (solid line); energy of the parallel component (chain line); energy of the transverse component (dashed line)

REFERENCES

1. W. Leemans *et al.*
Phys. Rev. A, v.46, 1091 (1992)

2. T.E. Glover *et al.*
Phys. Rev. Lett. v.73, 445 (1995)

3. G.J. Pert and S.J. Rose
Appl. Phys. B v.50, 307 (1990):

4. K.A. Janulewicz, S.B. Healy and G.J. Pert
Optics Communications (in print)

SIMULATIONS OF INNER SHELL PHOTOIONIZATION X-RAY LASERS

SB Healy and GJ Pert

Department of Physics, University of York.

The inner shell photoionization x-ray laser is one of the oldest conceptual designs [1] and was studied extensively during the 1970's [2],[3]. It was quickly realised at the time that most of the schemes considered required pumping lasers capable of delivering far greater energies than was available. However, recent advances in laser technology has led to renewed interest in this design [4].

The basic concept is as follows. A high Z 'flashlamp' material, for example gold, is irradiated with an ultra short optical pulse ($\sim 50 - 100 fs fwhm$), producing a highly ionized plasma which is a source of incoherent x-rays. These x-rays pass through a low Z filter which removes the low energy photons. The filtered flux is then incident on the lasant material, which in this discussion will be a neutral neon gas at room temperature. The filtered x-ray flux leads to preferential photoionization of the 1s electrons because at photon energies near the 1s threshold, the 1s cross section is about 10× greater than those of either the 2s or 2p electrons. Consequently a population inversion is set up between the 1s and 2p holes, the former being the upper lasing level. In the case of neon, the lower lasing level is the ground state of the 1st ionization stage, clearly demonstrating the importance of the filtering, as photoionization of the 2p electron directly populates the lower lasing level.

The radiative decay rate of the 1s hole is $\sim 6 \times 10^{12} s^{-1}$, but the gain duration is limited by other transtions. The Auger rate into the Ne^{2+} ion stage is $\sim 4 \times 10^{14} s^{-1}$, but the gain duration is actually limited by collisional ionization of the medium [3]. Although the lasant is initially cold, electrons produced by photoionization and Auger decay have sufficient energy to collisionally ionize the neutral neon and populate the lower lasing level. In the case of neon, the Auger electrons are released with an energy of $\sim 800eV$ with the photoelectron energy determined by the X-ray spectrum. Recently, it has been suggested that this can be alleviated by doping the neon with large concentrations of hydrogen, which acts as a heat sink as it is preferentially thermally ionized by the energetic electrons [4].

A computational model has been developed to investigate this scheme. Although some work has been performed to determine the incoherent X-ray spectrum, in this work the flashlamp/filter is approximated with a black-body spectrum defined by a time dependent temperature (T_b) and assuming all photons below 800eV are filtered out (the difficulties of producing such a source will not be considered here). T_b rises linearly to 600eV in 150fs. With this approximation the problem reduces to a solution of the atomic population kinetics. Only 9 levels are considered, but the major transitions populating and depopulating the lasing levels are included. These are photoionization, collisional ionization, Auger and radiative decay. The electron density is calculated self consistently with the ionic populations and the electron temperature is calculated from the overall energy balance. For the puposes of calculating the collisional ionization rates a Maxwellian distribution is assumed. Given the time scale, it is unlikely that it will be a Maxwellian, but the approximation is sufficient to give reasonable value for the rate. Ion-electron equilibration is not considered as it will be negligible and the laser line width is determined by natural broadening.

Figure 1 shows the time dependent gain at 15Å for A) pure neon gas at $1 \times 10^{20} cm^{-3}$ and B) where the neon has been doped with $10^{22} cm^{-3}$ hydrogen atoms. It is clear that the impurity significantly increases the gain values and duration. The impurity reduced the electron temperature to just 1.5eV at peak gain compared with 340eV in the pure case. In fact, the gain values obtained for the mixture are close to the simulation with all collisions switched off, which represents the maximum achievable gain for the given time dependent blackbody spectrum. However, it is found that unless the impurity is doped in sufficiently large quantities, it can reduce gain. This is because the collisional ionization cross sections only vary slowly beyond the threshold energy. Although, doping the neon with low levels of hydrogen reduces the electron temperature slightly, it also leads to an increase in the electron density and the ionization rate can be increased. Therefore, although the results appear encouraging, areas of the design still appear problematic and require further consideration. Firstly, producing the lasant doped with sufficient quantities of dopant is difficult. In addition the short gain duration necessitates a travelling wave pump, with a pumping pulse tilted at exactly 45 degrees to the lasing direction. Any deviation from the 45 degree tilt will soon result in a mismatch between the propagating signal and the local gain coefficient. Whether this is possible given the indirect nature of the pumping of the lasant is questionable.

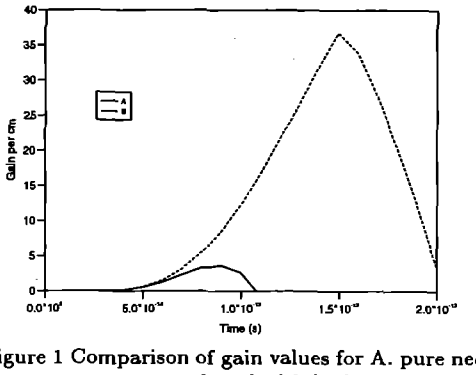

Figure 1 Comparison of gain values for A. pure neon and B. neon doped with hydrogen.

REFERENCES

1. M. A. Duguay and P. M. Rentzepis, Appl. Phys. Lett., 10, 350 (1967).

2. R. C. Elton, Appl Appl. Opt., 14, 2243 (1975).

3. T.S. Axelrod, Phys. Rev. A., 13, 376 (1976).

4. H.C. Kapteyn, Appl. Opt., 31, 4931 (1992).

TRANSIENT HIGH GAINS AT 196Å PRODUCED BY PICOSECOND HEATING OF A PREFORMED GERMANIUM PLASMA.

SB Healy, KA Janulewicz, JA Plowes and GJ Pert

Department of Physics, University of York.

The collisionally pumped X-ray laser has proved to be the most reliable method for generating gain in the XUV region. In this scheme, the lasant material is irradiated with high powered optical pump, stripping the lasant material to a closed shell configuration. For the neon-like scheme considered here, gain is found on transitions between 3p and 3s levels, the former populated by monopole collisional excitation and the latter depopulated by radiative decay. In general the magnitude of the gain increases for higher electron temperatures and/or electron densities. However, the ability of the laser beam to sample the high gain regions is limited by refraction, which depends on the electron density gradients. Most of the early experiments on collisionally pumped systems were characterised by nanosecond pumping pulses, but recently Nickles et al [1] have reported high transient gain ($\sim 19cm^{-1}$) at 326Å with neon-like ions from titanium slab targets irradiated by a combination 1ns and 1ps duration optical pulses at $1.053\mu m$. The experimental work was motivated by computational modelling presented by Shlyaptsev et al [2] which indicated that transient ultra-high gains could be produced in regions of plasma which had been heated sufficiently to ionize to the neon-like ion stage and were then subject to a rapid rise in the electron temperature. Similar computational simulations were presented by Whitney et al [3] and Maxon et al [4].

In this work, we have applied these ideas to the well studied case of neon-like germanium and a more detailed desciption of the results is given in [5]. The simulations are performed with the 1.5D atomic physics/hydrodynamics code EHYBRID [6] and a 3D raytracing code [7]. We consider a germanium slab target of thickness $10^{-4}cm$, width $10^{-2}cm$ and length $1cm$. It is irradiated by a 1ns, peak intensity $5 \times 10^{12}Wcm^{-2}$, trapezoidal background pulse (300ps rise, 400ps flat) and an intense 2ps (0.5ps rise, 1ps flat) main trapezoidal pulse which is switched on after 900ps of the first pulse. The wavelength of both pulses is $1.06\mu m$. The first pulse ionizes the lasant to the neon-like ground state, with an average charge $Z^* \sim 21.5$ and the second pulse rapidly heats the plasma to high temperatures, in excess of 1keV for a main pulse of intensity $10^{15}Wcm^{-2}$. Figure 1 shows the radial gain profiles at the end of the main pulse at this intensity, for the 196Å and 132Å lines. The latter has not been observed experimentally, but the simulations indicate that it should be seen in this case because of the combination of high electron temperature and density. Raytracing calculations indicate it should have a far field deflected angle of $\sim 8mrad$.

Figure 2 shows the ray averaged gain [7] at line centre for the 196Å line at the end of the main pulse as a function of the main pulse peak intensity. This is useful because it clearly indicates the importance of refraction in these systems. Although the peak gain in figure 1 is $\sim 100cm^{-1}$, the averaged value for a $10^{15}Wcm^{-2}$ main pulse is $\sim 25cm^{-1}$ in figure 2. It also shows that a significant gain-length product should be observed for intensities above $1 - 2 \times 10^{14}Wcm^{-2}$ and at slightly higher intensities saturation may be possible from a target of length 1cm. However, a complication arises because the raytracing code does not consider the variation of the gain coefficients as the laser beam propagates through the medium which is found to be significant in these simulations. This approximation is essentially equivalent to the experiment being performed with a travelling wave pump, which would be necessary to achieve the optimum output.

In summary, the simulations indicate that large gains can be generated on the J=0-1, 196Å line by heating a preformed plasma with an intense picosecond pulse. The results also suggest that gain should be observed on the 132Å line.

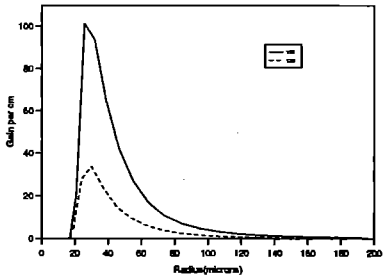

Figure 1: Radial gain profiles of lasing lines after 2ps pulse.

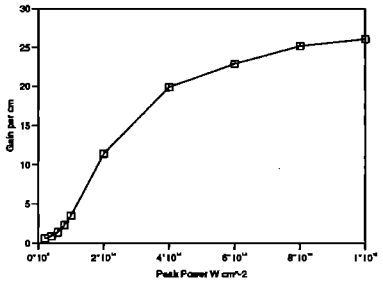

Figure 2 Variation of ray averaged gain at 196Å with main pulse peak intensity.

REFERENCES

1. P.V. Nickles et al, Spie Proceedings 2520, 373 (1995).

2. V.N. Shlyaptsev et al. Spie Proceedings 2012, 111 (1993).

3. K.G. Whitney et al Phys. Rev. E., 50, 468 (1994).

4. S. Maxon et al, Phys. Rev. Lett., 70, 2285 (1993).

5. S.B. Healy et al, submitted to Opt.Comm.

6. P.B. Holden et al, J.Phys . B., 27, 341 (1994).

7. J.A. Plowes et al, Opt. Quant. Elect., 28, 219 (1996)

RAMAN GENERATION OF ULTRA-BROADBAND LIGHT USING NITROGEN

G S McDonald[1], G H C New[1], L L Losev[2], A P Lutsenko[2] and M J Shaw[3]

[1]Imperial College of Science, Technology and Medicine
[2]P N Lebedev Physical Institute
[3]Rutherford Appleton Laboratory

The phenomenon of ultra-broadband multifrequency Raman generation (UMRG) has only recently been discovered and presents a goldmine of new physics with a wealth of possible uses. In addition to frequency conversion, sensing and spectroscopy, a key application lies in the field of inertial confinement fusion. Our previous work has concentrated on the case of hydrogen as the Raman medium and we have predicted that a multifrequency beam with a bandwidth of nearly 50 waves of comparable energy may be generated[1a]. The proposed technique involves using two collinear input beams, with matching temporal profiles, which resonantly drive a rotational transition of the gas (resonant symmetric pumping). For nominal parameters, say a pressure of 1 atmosphere hydrogen and a propagation length of 2 metres, one can maximise the bandwidth of the multifrequency light by varying the pulsewidth and the intensity of the pump beams[1a]. During the last year we have been continuing to extend the understanding of UMRG in hydrogen through the development of analytical models coupled with numerical simulation of the full model equations. Our earlier analysis[1b] yielded a model for the parametric gain which is applicable to dispersionless UMRG under cw conditions. This work has now been extended to incorporate the transient effects which arise from the pulse profiles of the constituent light waves and the dephasing time, T_2, of the polarisation wave in the medium[1c].

We have also extended our investigations to consider the use of nitrogen as the nonlinear medium. The resonant driving of a number of candidate rotational transitions and the optimal conditions under which each can be exploited has been examined. The use of air as the nonlinear medium has very obvious attractions and in this brief communication we report some results on this subject. Experiments demonstrating Raman frequency generation in nitrogen and air have already been performed. However, the configurations that were used are highly non-optimal for bandwidth production. In one case[2a] only around 15 sidebands were generated because a single pump beam was employed; new frequencies had to grow from background noise - a relatively inefficient process. In another set of experiments, Dangor et al[2b] investigated the propagation of two light beams in air and rotational Raman scattering was observed to be the dominant effect. Their configuration generated several sidebands even though the frequency difference of their input beams was around 10 linewidths aways from resonance.

We consider here the resonant symmetric pumping of a single rotational transition (J=8 to 10) of atmospheric nitrogen; defining a Stokes shift of 76cm^{-1}. The pump beam of higher frequency is the second harmonic of a Nd:YAG laser (18900cm^{-1}). We predict that this configuration can lead to a multifrequency beam consisting a number of distinct waves which is 1 to 2 orders of magnitude higher than those previously observed[2]. In Fig 1 we show the role that input pulsewidth plays in determining the growth in bandwidth of the multifrequency beam as it propagates. We generally find that input pulsewidth can have an important limiting effect since, for shorter pulses (of width around, or less than, T_2=130ps), the bandwidth tends to fall off at larger distances. In Fig 2 we consider relatively long input pulses (1ns) and the role that their intensity plays. In contrast to the effect of shorter pulsewidth, for lower intensity beams the bandwidth continues to grow with distance. For example, after propagating a

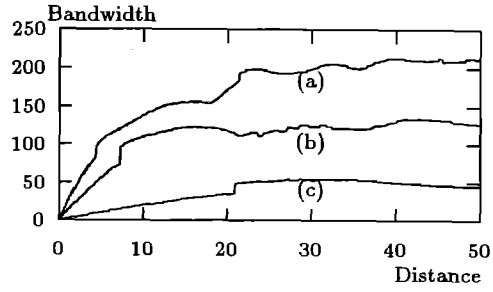

Fig 1 Bandwidth (in units of the Stokes shift) as a function of propagation distance in air (in metres). Square input pulses of intensity 30GWcm^{-2} are considered. Input pulsewidths are (a) 1ns, (b) 130ps and (c) 16ps.

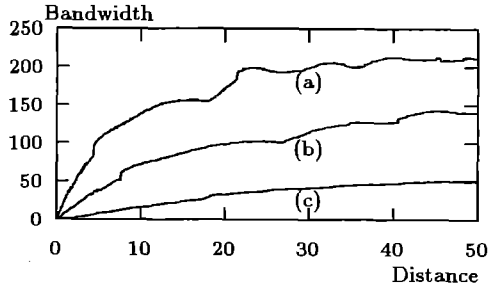

Fig 2 Bandwidth generated as a function of propagation distance in air for 1ns input pulses. The intensity of the launched pulses is a) 30GWcm^{-2}, (b) 10GWcm^{-2} and (c) 2GWcm^{-2}.

distance of 150 metres (not shown) case (b) grows to approximately 180 Stokes shifts while case (c) reaches a bandwidth of around 90 waves. In common with our results for UMRG in hydrogen[1a], we find that input pulsewidths of around an order of magnitude greater that T_2 are optimal. At difference with those results, we find that the highest available input intensities will be optimal (provided that this is not at the expense of having to use highly focused beams[1b]). This new feature has been the subject of analytical investigations and we have found that the explanation lies in the rather sensitive dependence of Raman gain suppression on the Stokes shift. This, in turn, leads to an optimal normalised mistuning parameter[1a] which is orders of magnitude smaller than that found for hydrogen. The experimental confirmation of these predictions presents an exciting task.

REFERENCES

1.a) G S McDonald, G H C New, L L Losev, A P Lutsenko and M J Shaw, Opt. Lett., 19, 1400 (1994), b) L L Losev and A P Lutsenko, Kvantovaya Electron. (Moscow), 20, 1054 (1993), c) L L Losev and A P Lutsenko, Ultrabroadband Parametric Stimulated Raman Scattering in Highly Transient Regime, Opt. Commun. (to appear).

2.a) D Eimerl, D Milam and J Yu, Phys. Rev. Lett., 70, 2738 (1993), b) A E Dangor et al, J. Phys. B, 22, 797 (1989).

HIGH POWER LASER OPERATIONS AND DEVELOPMENT

C B Edwards

Rutherford Appleton Laboratory, Chilton, Didcot, Oxon OX11 OQX

INTRODUCTION

The combination of efficient, cost effective operation of the CLF's high power laser installations with continuous and imaginative development of those facilities is the key to the success of the high power laser programme at the CLF. Only in this way can the scientific productivity of the programme be maximised whilst ensuring the future international competitiveness of the facilities. The CLF has enjoyed an unsurpassed reputation in these two vital areas in the past, and the reports included in this section show that this year is no exception.

The ability to combine operations with development is achieved through collaborations between the operations group staff, the R&D group and the user community. The wide authorship of the reports in this section is evidence of the health of these vital collaborations.

OPERATIONS

An extremely intensive operations schedule for Vulcan during the reporting year has enabled the scientific programme of the facility to maintain its momentum during the construction of Titania and the re-building of Sprite as a preamplifier. This is reflected in the excellent publication record of the programme.

Detailed analysis of the shot statistics and Target Area usage is available elsewhere in this report, but it is interesting to note that a large proportion of the shots delivered (approaching half) were used for the calibration of instruments and characterisation of plasma conditions. This trend is set to continue as the sophistication of diagnostics grows to meet the demands of the front line experiments undertaken on the CLF's high power lasers.

GLASS LASER DEVELOPMENT

In October '95, a major grant was awarded for the upgrade of the CPA capabilities of the Vulcan Nd:glass laser to focused intensities of 10^{20}W.cm^{-2} on target. Work on the upgrade is now well advanced. A new Titanium Sapphire oscillator is already on line, a regenerative amplifier has been used to provide pre-amplification of the ultra-short pulse output of the oscillator and the ultra high power output from the Vulcan CPA beamline has been characterised at the 10^{19}W.cm^{-2} level.

The design of the pulse stretching and compression systems are crucial to the success of the CPA programme at the CLF and much experimental and theoretical work has been performed this year in support of the upgrade.

Also included in this report are details of the technology transfer project with the Instituto Superior Técnico, Lisbon. A 1 TW laser system based on a YLF oscillator with Nd:glass amplification is under construction at the CLF. The system will be shipped to Lisbon and installed in a new laboratory during the next year.

TITANIA COMMISSIONING

The official opening of the Titania facility on 2 April '96 by Dr Paul Williams, Chief Executive of the CCLRC marked the culmination of a year of intense activity in Building R2, formerly the site of the Sprite facility. The new machine is the latest in the line of outstandingly successful KrF laser facilities operated by the CLF, and incorporates the state of the art in many areas of laser and associated engineering including pulse power technology, ultra-high intensity UV optical systems and advanced laser diagnostics.

Some of the most challenging aspects of the engineering, optical design and diagnostics needed for the new machine are described in this section of the report.

INSTRUMENTATION

It has always been the case with low repetition rate sources such as Vulcan and Titania that a consistent and quantitative experimental dataset can only be obtained if a large suite of diagnostics and system instrumentation is maintained on each shot. The development of advanced diagnostics underpins the success of the scientific programme at the CLF, and contributes substantially to maintaining the world leading position of the CLF's high power laser facilities. The reports in this section illustrate the wide ranging work that has been undertaken in the past year.

A particularly significant contribution this year describes the manufacture of Hohlraum cavities for use in the Vulcan programme. Scientists at the CLF have always been interested in the possibility of using Hohlraums as a source of high temperature x-rays, but classification of indirect drive related physics prevented experiments being performed in open laboratories. Recent changes have now opened up this exciting area, and the laboratory has responded to meet user demands for sophisticated targets in support of this new programme.

VULCAN OPERATIONAL STATISTICS

David A. Pepler

Rutherford Appleton Laboratory

A facility development programme and nineteen experiments have been conducted this reporting period (March '95 to March '96), using all four target areas. As shown below in Table 1, most of these experiments were in the two main target areas, west (TAW) and east (TAE). Both of these areas have been used for chirped pulse amplification (CPA) operation with TAE used in this mode for a short pulse plasma interaction experiment early in the year. TAW has been intensively operated throughout the year in CPA mode, with many varied experimental requirements.

A total of 9320 laser shots were fired during the year 4704 of which were to the target areas. Full statistics for the experimental programme are given in Table 1 which indicates the total number of shots, target shots and failed target shots each individual experiment received.

Due to the complexity of the experimental setups nearly half the total number of these shots were required to setup and calibrate the experimental conditions. A total of 1502 disc amplifier shots were fired for laser-plasma interaction studies. TA4 has also continued to be productive delivering an additional 598 (2 minute) shots to target for a broad range of experiments. The breakdown of the relative number of target shots into the four individual areas is indicated in Chart 1.

Chart 1 Relative number of target shots per area

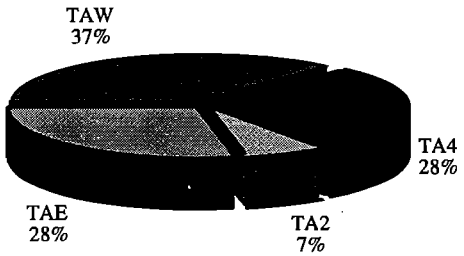

Some down time of the laser was experienced early in the year losing approximately two weeks of experimental time. This was due to a fire in the high voltage capacitor room that supplies the power to the main amplifiers of the laser. Despite this the failure rate of the full energy or full power disc amplifier shots continues to be low at < 3.0 %.

EXPERIMENTAL PERIOD Mar '95 - Mar '96	EXPERIMENT (Total number of shots - Target shots - Failed target shots)			
	TAE	TAW	TA2	TA4
20 Mar - 10 Apr	X-ray laser (80 - 41 - 4)	Relativistic laser propagation (173-63-0)		Plasma opacity (114)
17 Apr - 7 May	CPA interactions in plasmas (268 - 78 - 7)	Optical field ionised X-ray laser (248 - 85 - 1)		
8 May - 5 Jun				Plasma opacity (89)
11 June - 25 Jun		Solid target high harmonic (245 - 118 - 2)	3D Biological imaging (140 - 138 - 2)	Microscopy (20)
26 Jun - 17 Jul				
7 Aug - 20 Aug	X-ray laser (109 - 77 - 7)	Absorption spectroscopy (212 - 63 - 9)		Microscopy (35)
21 Aug - 18 Sept				
25 Sept - 8 Oct	RT using Hohlraums (363 - 113 - 0)	Relativistic laser propagation (479 - 117 - 0)		Spectrometer commissioning (93)
9 Oct - 31 Oct				
6 Nov - 3 Dec	Hydrodynamic studies (171 - 135 - 5)	Harmonics using Li^+ (280 - 74 - 1)		X-ray scattering (92)
4 Dec - 3 Jan				
15 Jan - 4 Feb	Thermal smoothing (475 - 148 - 0)	Solid target CPA (254 - 123 - 3)		Dense cool plasma studies (155)
5 Feb - 25 Feb				
26 Feb - 24 Mar	Facility development (609 - 129 - 0)			
Totals	(1466 - 592 - 23)	(2500 - 772 - 16)	(140 -138 - 2)	(598)

Table 1 VULCAN statistics for the year ending March '96

VULCAN PETAWATT UPGRADE

C N Danson and C B Edwards
Central Laser Facility, Rutherford Appleton Laboratory

VULCAN produces 10^{19} Wcm^{-2} at the focus of its short pulse beam using Chirped Pulse Amplification [1] (CPA). The PetaWatt upgrade will increase that to over 10^{20} Wcm^{-2}, enabling users to carry out important new experiments in X-ray laser research, laser fusion, basic plasma physics and particle acceleration. The CLF is now established as a world leader in ultra-high power experiments. Petawatt operation of VULCAN, coupled with the availability of synchronous kJ multi-beam long pulse operation will provide several years of outstanding physics and will undoubtedly lead to observation of new phenomena.

Phase I of the PetaWatt proposal has been funded by an EPSRC facility upgrade grant of £970k to raise the performance from the current operational level of 35 TW, to over 200 TW. The Phase I programme involves modifications to the existing VULCAN CPA facility as described below:

FRONT END

The existing front end oscillator has been replaced by a commercial 100 fs Titanium Sapphire system [2]. The oscillator has been installed in a purpose built oscillator room and has been operational for user experiments since October 1995.

A recent facility development used this oscillator in conjunction with the Titanium Sapphire regenerative amplifier, developed by Imperial College [3] as part of the Joint Universities Project. Details of this experiment are presented later in this report [4]. Some areas of performance need to be improved before the regenerative amplifier is brought on-line to users. The combined system will give access to the sub-500 fs regime on target, and give improved reliability, productivity, and tunability within the gain bandwidth of the existing glass amplifier chain.

MIXED GLASS OPERATION

Towards the end of the Phase I enhancement, some phosphate laser rods will be replaced with silicate glass, giving increased optical bandwidth, with a potential reduction in pulse duration to ~350 fs. Options for this stage of the enhancement are currently being evaluated.

GRATING CHAMBER

The beam size at the compression stage will be increased, and larger compression gratings will be installed in a purpose built vacuum vessel holding both of the gratings. 42 cm x 21 cm gratings are now available commercially, and with a peak damage threshold of 250 mJ cm^{-2} this will allow in excess of 100 J to be incident on the compression stage. The use of an alternative grating configuration could be employed and is discussed later in this report [5].

INTERACTION CHAMBER

A new, dedicated CPA interaction chamber will be provided for the complex experiments which will be performed with the new facility. The new chamber (as shown in figure 1) will support a wide range of geometries with additional interaction beams, probes and diagnostics. Design studies are currently underway in consultation with users.

SECOND HARMONIC CONVERSION

Second harmonic conversion will be provided as an option at the output of the system, giving additional versatility for experiments with some potential for pulse shortening and enhanced contrast. An experiment will be proposed later in the year to investigate these options.

DIAGNOSTICS

New investment in diagnostics will be essential to exploit the new irradiation facilities. It is proposed to enhance the laser diagnostics including a second harmonic single shot auto-correlator and new diagnostics to detect plasma emission with appropriate temporal resolution. Funding for new diagnostics is included in the Phase I grant which has already produced a new elegant design of single shot auto-correlator described later in this report [6].

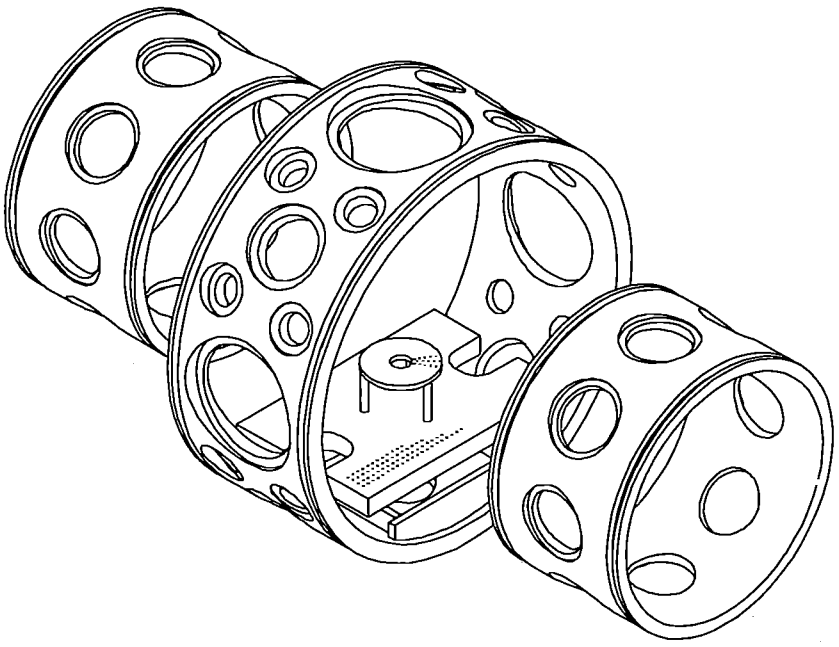

Figure 1 Outline of the new CPA interaction chamber

REFERENCES

[1] D Strickland and G Morou, Opts Comm, 56, p 219-221, 1985.
[2] Spectra Physics Kerr-lens mode-locked fs Tsunami
[3] F Zhou et al., Electronics Letters, Vol 31, No13, p1060-1061, 1995
[4] J.Collier et al., CLF Annual Report 1996
[5] I.Ross et al., CLF Annual Report 1996
[6] J.Collier et al., CLF Annual Report 1996

CHARACTERISATION OF THE VULCAN CPA BEAM GIVING INTENSITIES OF 10^{19} W cm^{-2}

C. N. Danson, N. Bradwell, L. J. Barzanti, J. Collier, A. Damerell, C. B. Edwards, C. Johnson, M. H. Key, D. Neely, M. Nightingale, D. A. Pepler, I. N. Ross, P. Ryves, C. Stephens, N. Thompson, M. Trentelman, E. Wolfrum, F. N. Walsh, and R. Wyatt.

Rutherford Appleton Laboratory, Chilton, Didcot, Oxon OX11 0QX

The process of Chirped Pulse Amplification (CPA) [1] as implemented on the VULCAN glass laser is capable of delivering 30 J to target with pulselengths in the sub-picosecond regime [2]. Results from various experiments [3],[4] have indicated that intensities of 10^{18} - 10^{19} W cm^{-2} have been achieved on target. However, a detailed characterisation of the beam's focal spot intensity distribution was necessary to confirm these results. Measurements of the transmitted energy through pinholes of various diameters placed in the focal plane were used to characterise the intensity distribution. Images from an Equivalent Plane Monitor (EPM) were taken simultaneously with the pinhole transmission measurements and good agreement between the data sets was obtained. The effect of B-integral [5] on the focusability of the beam was also studied and the beam uniformity was examined.

INTRODUCTION

The transmission of energy through a well defined pin-hole provides a useful technique for characterising the intensity distribution obtained at the focal plane of a short pulse high intensity laser system. One of the main limitations when using pin-hole transmission measurements is the effect of 'pinhole closure'. This occurs when a plasma which can refract or reflect the drive beam is formed at the edges of the pin-hole and has sufficient time to expand and either partially or completely fills the pin-hole before the laser pulse has passed through. Plasma formation generally occurs at the ~10^9 Wcm^{-2} level. To avoid plasma formation at the edge of an aperture a contrast ratio of ~10^{10} would be required for the VULCAN CPA laser pulse when using F3 optics. This level of contrast is not available from the CPA system at the fundamental frequency. The spatial and temporal evolution of pinhole closure is very much dependant on the f-number of the focusing optic and the pinhole diameter. For a plasma the lateral expansion velocity may be in the 10^5-10^8 cms^{-1} region which gives a motion of ~10 microns in the timescale of the interaction. Therefore, only when the focal spot and thus the pin-hole radius is a few times 10 microns will pin-hole closure become important. The magnitude of the effect lessens at higher f-numbers due to the larger focal spot sizes having lower intensities and the larger pinhole diameters required. Thus using a longer focal length optic reduces the effects of pinhole closure and also facilitates ease of alignment.

EXPERIMENT

The experimental layout for the characterisation study is shown in figure 1. The stretched and full energy pulse enters the target area and is recompressed to, in this case, ~2 ps by the compression gratings. The beam is apodised to 75 mm x 110 mm to avoid hard edges brought on by clipping at the compression gratings. The pulse is then focused using the 3 m focal length off axis parabola (OAP) and calorimetry is carried out at the exit port. A 5% leakage from the turning mirror in the chamber supplies signal to the laser pulse diagnostics which comprise a single shot autocorrelator and spectrometer as well as an equivalent plane monitor (EPM). Initial null shots indicated that 60% of the energy entering the area was incident on the target plane.

The EPM consists of a 9.6 m focal length lens and two etalons. The first etalon produces a vertical column of beamlets with small optical path difference and a 50% successive energy difference. The second etalon then produces rows of beamlets with larger optical path differences and a 10% successive energy difference. The combination of the two etalons produces a 2d array of spots each representing a different plane in the focusing beam including the focal plane. The array is incident on an 8 bit CCD and the spots are analysed by evaluating the radial energy distribution. Two active pinhole cameras with intensified CCDs were used to check the alignment on a shot to shot basis. Shots were taken with energies ranging from 10J to 20J on target and a pulse length of about 2 ps.

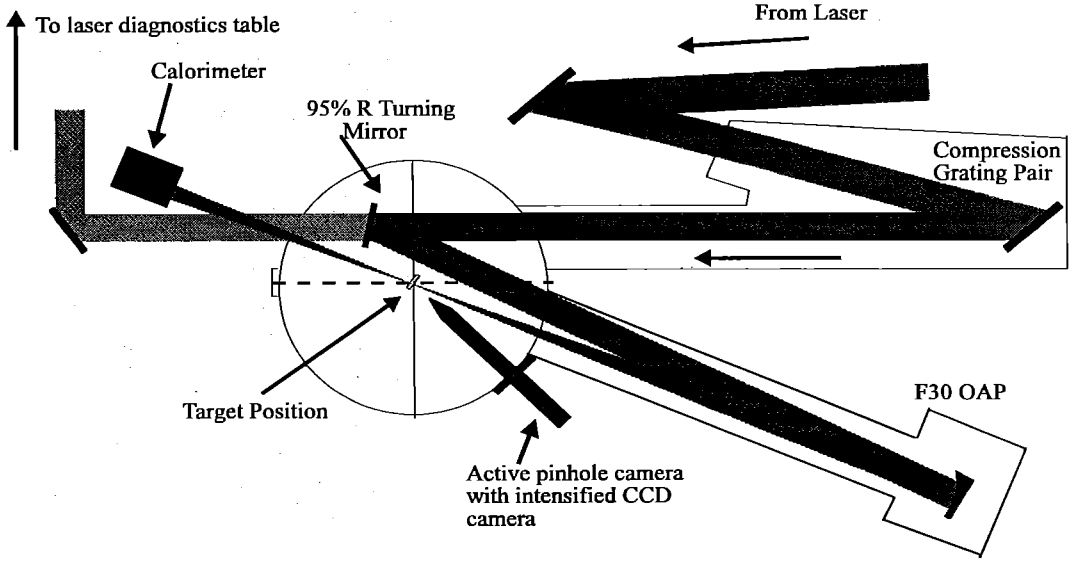

Figure1: Experimental set-up for VULCAN CPA characterisation

RESULTS

The percentage of incident energy transmitted through pinholes of varying diameter measured on high energy (10 - 30 J) shots are shown on figure 2. The two green data points shown on figure 2 represent the amount of energy stopped by a circular disk of diameter D placed at the focal plane. The effect of pinhole closure on the measured data is to reduce the amount of energy transmitted through a hole and increase the amount of energy stopped by a central disk. Hence, pin-hole shots will generally indicate a lower bound and central disk shots an upper bound to the transmission.

The horizontal axis on figure 2 has been normalised to units of the beam diffraction limit ($D_n=2f\lambda/d \approx 60$ μm) defined as the distance between the first minima in the diffraction pattern for a rectangular beam. The beam diameter d is taken as the average size in the horizontal and vertical directions for the rectangular beam d = 0.1 m. A theoretical transmission curve T(D) was initially generated by integrating the transmission through a circle of diameter D placed at the focus of an f = 3 m focal length perfect optic illuminated by a uniform rectangular beam of identical size to the VULCAN CPA beam. Using the generated curve, a fit to the data was obtained using the curve T(mD) where m represents the number of times that the focal intensity distribution exceeds that of a diffraction limited beam.

The fit T(mD) where m=3.5 (shown by the blue line on figure 2) generally shows good agreement between the theory and the experimental results. However, at both D<1.2 and D>5 some discrepancy exists. At D>5 measurement are ~ 4 % lower than the fit. Since plasma closure effects are negligible in this region, these results indicate that a small fraction ~ 4 % of the incident energy is being diffracted significantly further out into the wings of the intensity distribution than would be expected from simple modelling. At D<1.2, the measured transmission falls off dramatically indicating the onset of pinhole closure effects.

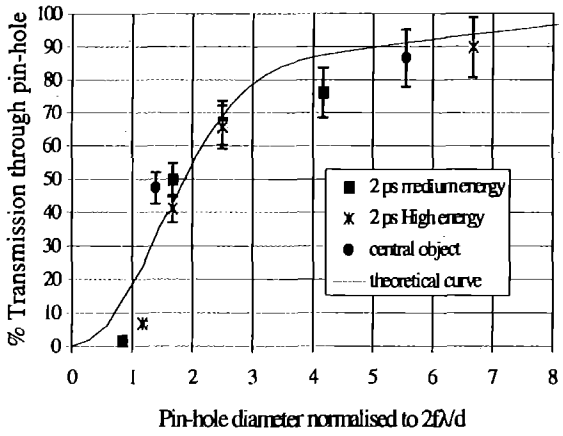

Figure 2: The energy transmitted through pinholes of various diameter. Also shown is the theoretical curve form a uniform rectangular beam of 3.5 times the diffraction limit (see text).

Comparison between the calculated transmission from the EPM data and the experimental measurements also support the onset of plasma closure effects at D~1. The ratio of the energy contained within an equivalent pinhole diameter measured using the EPM data, to the transmitted energy through a pin-hole is close to 1 as would be expected for diameters D many times larger than the diffraction limit. This ratio increases dramatically to ~10 when the pin-hole diameters in question are close to ~1 indicating significant plasma closure effects.

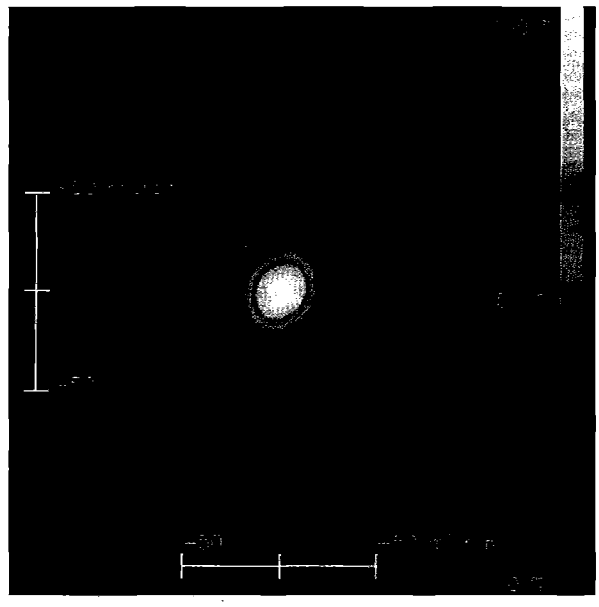

Figure 3: A typical output from the Equivalent Plane Monitor for minimised system B-integral. The scale shown corresponds to the spatial size at the target focal plane.

The effect of B-integral on the beam was examined by placing up to 5 cm of optical quality glass in the recompressed CPA beam and firing full energy shots. The EPM data from low energy (< 0.1 J) shots through the glass demonstrated that the glass had a negligible effect on the transmitted laser beam focal intensity distribution when B-integral due to this additional glass was << 1. Intensity contour maps from the EPM for a total system B-integral of 1 and 14.4 are shown in figures 3 and 4 respectively. The intensity contour map on figure 3 taken at a total system B-integral of 1 (corresponding to the normal situation where the B-integral has been minimised) demonstrates the high quality of the VULCAN CPA beam operating under typical conditions.

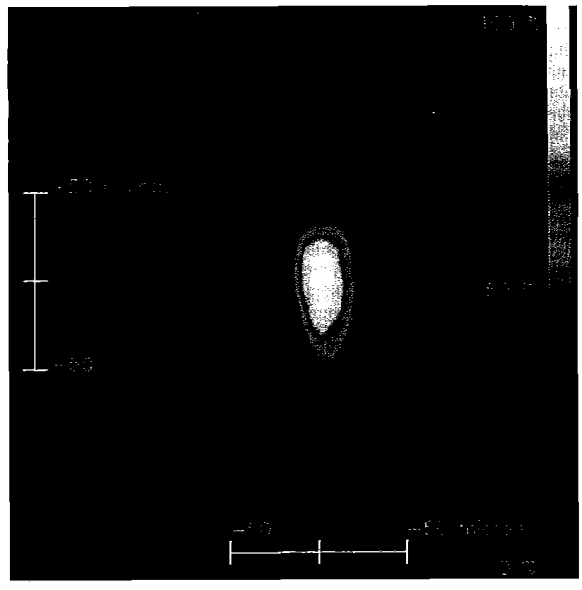

Figure 4: Output from the EPM for a high energy shot with B-integral = 14.4 showing significant focal spot degradation.

The contour map shown in figure 4 where the system B-integral was 14.4 shows some degradation of the intensity distribution but, the beam is still only 5 times the diffraction limit (see table 1). This is a surprisingly good result and is mainly attributable to the high degree of intensity uniformity across the VULCAN CPA beam.

The % total energy T contained within a diameter D was measured from the EPM images and is plotted in figure 6. Due to the limited dynamic range of the CCD camera used in the EPM system, backround subtraction at D>>1 is difficult. Estimates indicate that at these diameters a systematic uncertainty of up to 20% could be present. For the series of shots in question, exposure conditions were almost identical and the relative uncertainity is at the 5% level. The plot indicates that as the B-integral is increased the level of energy contained in the smaller integrating diameters decreases yet the beam is still ~5 times the diffraction limit at a B-integral of 14.

Pinhole size (μm)	% transmitted energy	B-int	Spot size normalised to (2fλ/d≈60μm)
150	66.8	1	3.5
150	54.4	7.7	4.375
100	33.3	13.2	4.175
150	47	14.4	5

Table 1: B-integral data.

The beam uniformity was examined by exposing a high speed IR film in the near field. About a third of the beam size was densitometered with a step size of 50 μm. The appropriate background was subtracted and the digitised data was converted to intensities using a calibration curve for the film given by the following equation;

$$I = D - 0.537D^2 + 0.892D^3 \qquad 0<D<2.5$$

where I is the intensity and D the optical density of the film.

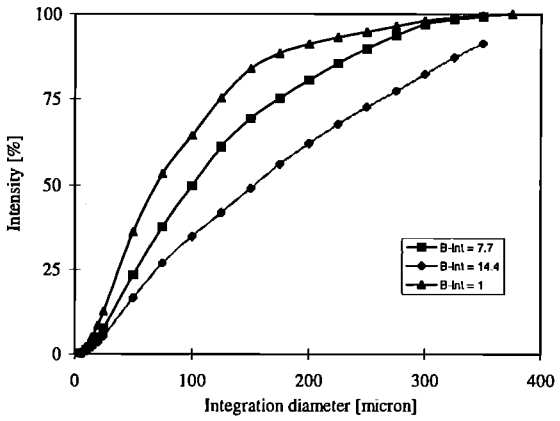

Figure 6: Output from EPM with increase in B-integral

The rms deviation σ_{beam} is calculated from the calibrated intensities yielding a relative roughness of the beam.

$$\sigma_{beam}/I_{avg} = 0.066, \text{ i.e. } 6.6\%.$$

Two different square regions of the area were selected for further analysis. Two dimensional Fast Fourier transforms were calculated and a power spectrum was obtained by summing the power of individual modes in annular zones in the 2D Fourier

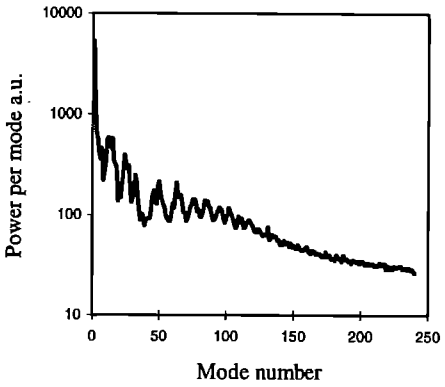

Figure 7: The power spectrum from a near field exposure of VULCAN CPA

transforms. The square root of the power spectrum gives the rms intensity variation per mode.

Figure 7 shows a plot of the power spectrum for the sampled area (24mm x 24mm) of the beam. The plot shows that the low modes dominate indicating that most of the power in the beam is contained in large scalelength perturbations (comparable with sampled area). This indicates that the beam is uniform over large scalelengths and small scale perturbations in the beam have a small effect on beam uniformity. Investigations, both experimental and theoretical, into the effects of beam uniformity and increasing B-integral on the the focusability of the beam are ongoing.

CONCLUSIONS

A characterisation experiment was carried out to determine the focusability of the VULCAN CPA beam and also investigate beam uniformity and B-integral effects on focusability. The beam was shown to be ~3.5 times diffraction limited. The results show that pinhole closure and plasma formation at the aperture of the pinholes have a significant impact on the transmitted energies. It has been observed that despite a high B-integral the beam was still 5 times diffraction limited demonstrating that VULCAN CPA has good uniformity across the beam. When these results are extrapolated to subpicosecond operation using f3 focussing optics it indicates an intensity on target of ~ 10^{19} W cm^{-2}.

REFERENCES

[1] D. Strickland and G. Mourou, Optics Communications, Vol 56, No. 3, pp 219-22, 1985

[2] C N Danson et al, Optics Communications, Vol. 103, No. 5,6, pp 392-397, Dec 1993.

[3] J. Zhang et al, Accepted to Phys Rev A.

[4] A. Modena et al, Nature Vol. 377 p. 606, 19th October 1995

[5] Lasers, A. E. Seigman, page 385-385, University Science Books, Mill Valley, California, 1986

REGENERATIVE AMPLIFICATION IN THE VULCAN AMPLIFIER CHAIN

J. Collier, C. Johnson, C. Danson, L. Barzanti, R. Wyatt, D. Pepler, N. Thompson, M. Nightingale, B. Walsh, and D. Neely

Rutherford Appleton Laboratory, Chilton, Didcot, OXON, OX 11 0QX, UK

INTRODUCTION

A Titanium Sapphire Regenerative Amplifier [1] (REGEN) has been successfully used in the VULCAN Glass laser system to amplify sub-picosecond pulses generated using the Chirped Pulse Amplification (CPA) technique [2]. The high gain of the REGEN enabled its use as a direct replacement for the 9 mm diameter amplifier chain with an ultimate production of 30 J pulses recompressed to 800 fs in the Target Areas. The broad amplifying bandwidth of Titanium Sapphire means, in principle, an ultra-fast pulse should be amplified without a significant loss of bandwidth.

DESCRIPTION

A schematic of the REGEN implementation is shown in Figure 1. The amplifier medium is a Ti:Sapphire rod located at the centre of a stable plano-concave cavity with the concave cavity mirror radius of curvature equal to 4 m. The rod is pumped from both ends by the 2nd harmonic of a Q-Switched Nd:YAG laser. The total pump fluence is approximately 3 J cm^{-2} in a spot slightly larger than the cavity mode diameter of 1.6 mm.

The initial optical 5 nJ, 1053 nm pulses of 120 fs duration are produced by a commercial Kerr Lens Modelocked oscillator [3] in the form of a pulse train with a 12 ns separation. The pulses are stretched in time from 120 fs to approximately 1 ns by an asymmetric doublepass stretcher. Spectral clipping in the stretcher limits the bandwidth of the pulse leaving the stretcher to approximately 12 nm. The output of the stretcher is injected into the REGEN by reflection off the Input thin film polarizer. One pulse from the pulse train is selected as the seed pulse for the amplifier by a quarter wave voltage pulse applied to the Input Pockels cell. The electrical pulse duration is 5 ns and is applied 100 ns after the pump pulse. The 90 degree rotation of input pulse polarization means that the pulse is now trapped in the stable REGEN cavity. The pulse is amplified on successive passes of the crystal as shown in Figure 2.

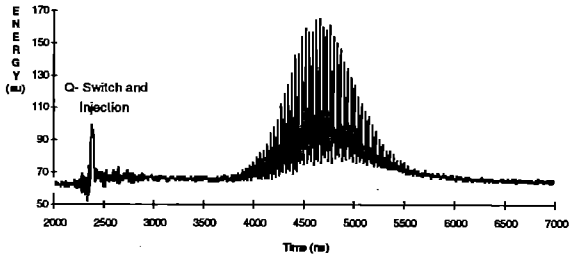

Figure 2: Regenerative amplification of a seed pulse

After a given number of round trips the amplified pulse is switched out of the cavity by reflection off the output polarizer following a quarter wave voltage pulse being applied to the Output Pockels cell. Figure 3 illustrates this, showing the case with and without switch out. The output pulse energy is 1 mJ and is switched out approximately 2 µs after injection. This is equivalent to 170 round trips. The seed pulse energy coupled into the cavity is estimated at 0.2 nJ, significantly less than the original 5 nJ present. This is primarily due to stretcher loss and imperfection and gain narrowing in the REGEN. The net gain is thus $5x10^6$. The cavity losses are estimated to be 4.5% per pass implying a gross energy gain of 9.5% per crystal pass, consistent with a pump fluence of 3 J cm^{-2} [4].

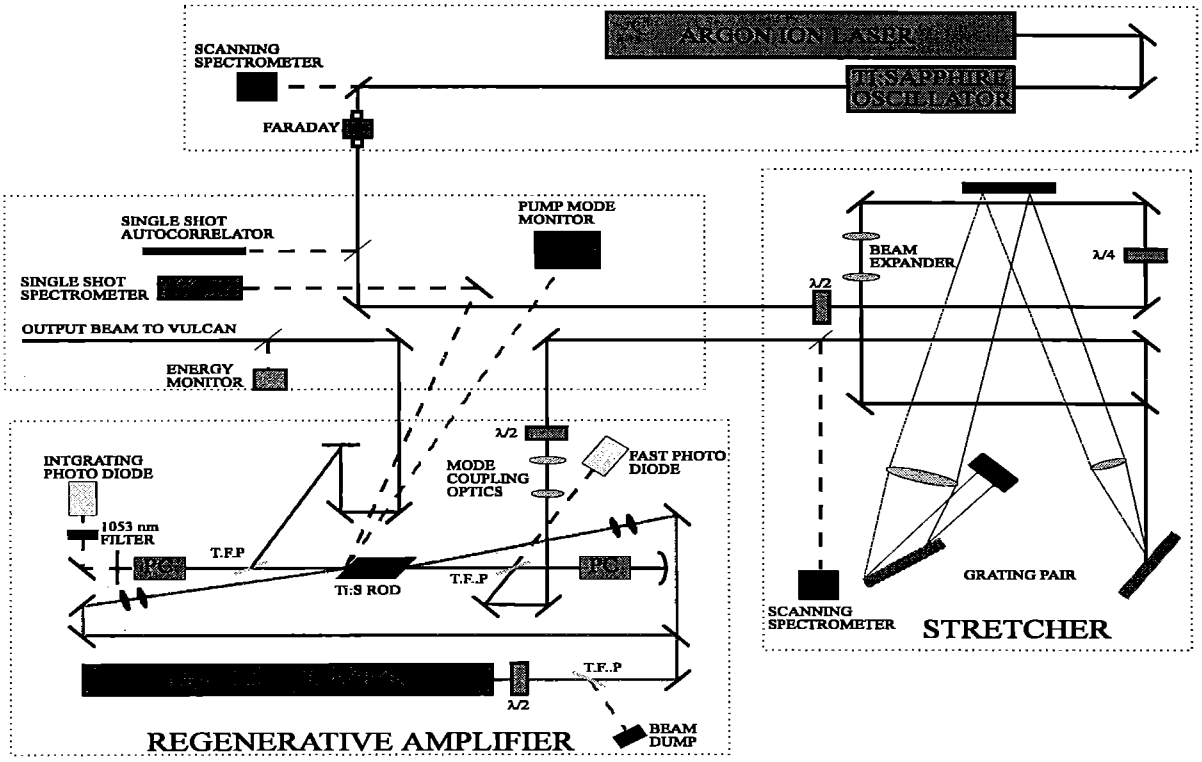

Figure 1 : Regenerative amplifier scheme

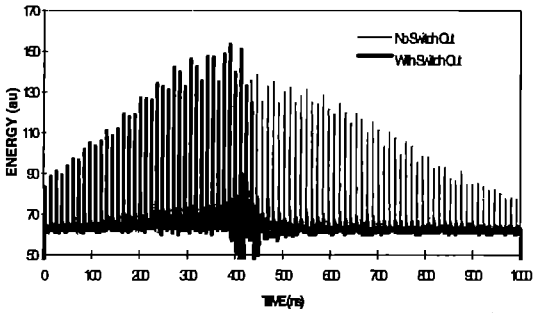

Figure 3 : Pulse build-up. The pulse is switched out just after passing through the peak.

The operating wavelength of the REGEN can be tuned by rotating the polarizers to match the seed wavelength. In the absence of a seed pulse the REGEN will run as a simple pulsed oscillator at a wavelength determined by the polarizers. In principle the REGEN should amplify the full bandwidth of the seed pulse with little or no gain narrowing. The polarizers however have a finite bandwidth, which in single pass produces a negligible effect but for the large number of passes required inside the REGEN cavity can produce a significant bandwidth limiting effect. Figure 4 illustrates this, contrasting the input bandwidth to the output bandwidth after some 680 polarizer passes.

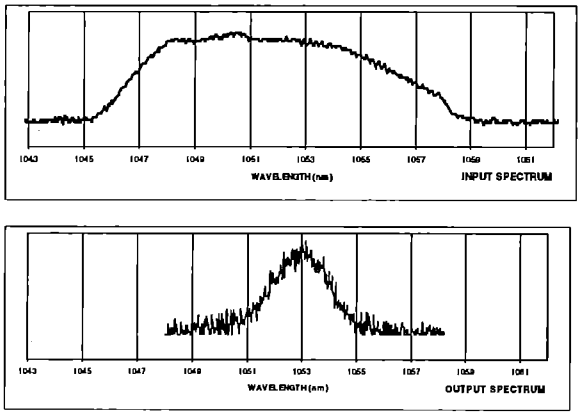

Figure 4 : Illustration of the gain narrowing in the REGEN

The shot to shot energy stability of the REGEN was found to be poor, often exhibiting a 100% fluctuation. This was largely due to random pointing and transverse mode jumping errors of the pump laser, although the low pump fluence and poor seed pulse coupling meant that the REGEN was operating in the small signal gain regime rather than a saturated one. The mode jumping limited the maximum fluence that it was safe to use to 3 Jcm^{-2} from crystal damage considerations. An immediate correction to this problem was not possible.

The effect of a large number of round trips introduces problems in addition to bandwidth narrowing in that it limits the maximum energy that can be extracted due to increased spontaneous fluorescence and also increases the energy instability of the amplifier. With an increase in seed pulse coupling and an increase in pump fluence, energies of 5 mJ at switch out times of 110 round trips should be possible [1].

VULCAN INJECTION

The output pulse of the REGEN was injected into the VULCAN chain at the end of the 9 mm rod amplifier section. The injection process was complicated by the fact that the existing method using the seed oscillator as the master RF timing source could not be used, as the oscillator and REGEN cavities were not frequency locked resulting in only occasional temporal synchronism. The timing sequence used is depicted in Figure 5.

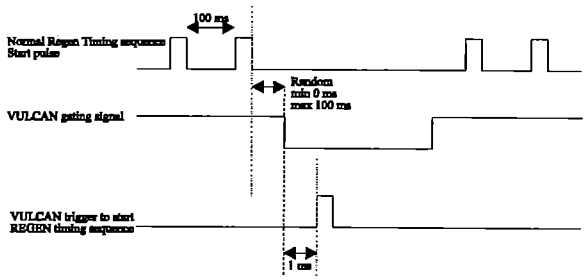

Figure 5 : VULCAN initiated timing sequence

In isolation, the REGEN pump laser flashlamps, Q-Switch, Input and Output Pockels cells were triggered every 100 ms by a pulse synchronously generated with the oscillator. For the VULCAN injection, the VULCAN timing system provided a gating signal to take control of the triggering system followed by a trigger signal for the REGEN that was made synchronous with the oscillator by an RF synchronization unit [5]. The REGEN provided the fast master trigger for the later VULCAN Pockels cell gates.

Following the injection of the REGEN pulses into VULCAN, the compressor gratings in Target Area West were re-tuned to match the different stretcher configuration that was in use. One of the benefits of the use of the REGEN was the availability of a 10 Hz optical cycle in place of the 9 second cycle that previously derived from the firing of the 9 mm amplifiers. This helped significantly in Laser Area and Target Area alignment. Optimization of the compressor gratings ultimately produced recompressed pulses of 800 fs as shown in Figure 6. The FWHM time bandwidth product is 0.35 assuming a $sech^2$ pulse profile. The REGEN was then used in a series of disc shots demonstrating that the system could be operated at full output energy.

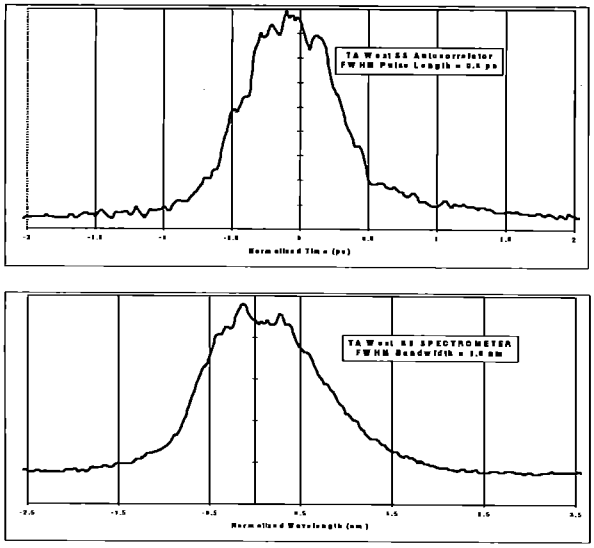

Figure 6 : TA West autocorrelator and spectrometer outputs

REFERENCES

[1] F. Zhou et al, Elec Letters. Vol 31. No 13. (June 1995) 1060
[2] D. Strickland and G. Morou, Opt. Comm. 56, (1985) 219-221
[3] Spectra Physics Tsunami
[4] Stuart *et al*, IEEE Journal Quantum Electronics, 31 (1995), 528
[5] Danson *et al*, Central Laser Facility, Ann. Rept., (1993), p 137

STRETCHER DESIGN FOR THE VULCAN PETAWATT UPGRADE

J. Collier, C. Johnson, C. Danson

Rutherford Appleton Laboratory, Chilton, Didcot, Oxfordshire, OX11 OQX, U.K.

The stretcher design for the Phase 1 PetaWatt Upgrade programme is presented. The stretcher differs from conventional designs because it has been optimised for maximum bandwidth transmission. This has resulted in an asymmetric design. A basic optical pulse stretcher is shown in Figure 1.

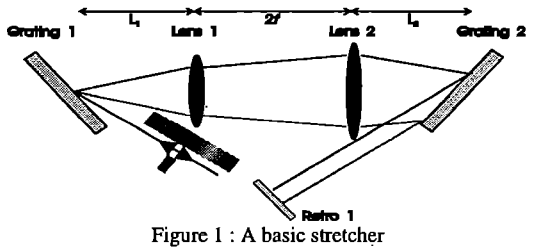

Figure 1 : A basic stretcher

In the absence of the two lenses and with the gratings made parallel, a beam incident on the first grating would diffract onto the second. The system would exhibit negative group velocity dispersion and any pulse would become stretched in time. The insertion of the two lenses of focal length f separated by $2f$ between two orthogonal gratings provides an M=-1 telescopic image of the first grating at $4f$, parallel to the second. If the second grating is placed at a distance less than $4f$ then the system will exhibit an overall positive group velocity dispersion and any pulse will also become stretched in time as in the case without the lenses. At distances grater than $4f$ the system clearly has a negative group velocity dispersion one more. In general CPA systems, the lens-less system is used as the compressor exactly balancing the stretch that the lens based system imposed.

In the design of a CPA stretcher, it is important to transmit the greatest bandwidth possible to enable recompression to as short as pulse as possible and to minimise the deleterious effects of bandwidth clipping in a knife edge manner. The sudden cut-off in frequency that occurs when the spatially dispersed spectrum is clipped by the finite aperture of a lens or grating leads to a reduction in pulse contrast ratio. This is illustrated in Figure 2 showing the reduction in pulse contrast ratio for clipping occurring at two and four times the bandwidth.

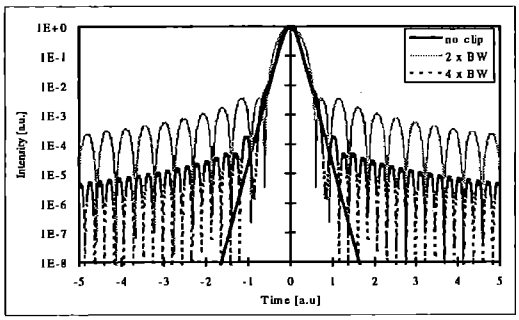

Figure 2: Effect of bandwidth clipping

With reference to Figure 3, assuming sufficiently large gratings, a given stretch factor, grating grove density and incidence angle the maximum bandwidth that can be transmitted through the stretcher is determined solely by the aperture of either the first or second lens. Clipping on the first lens is easily addressed by the choice of lens focal length as will be shown later. The clipping on the second lens occurs at two points. Firstly there is a symmetrical and double sided clip of the spatially dispersed spectrum propagating through the finite aperture $2A$ of Lens 2 and secondly there is the asymmetrical and one sided clipping that occurs when the (still spatially dispersed) diffracted beam off the grating hits one side of

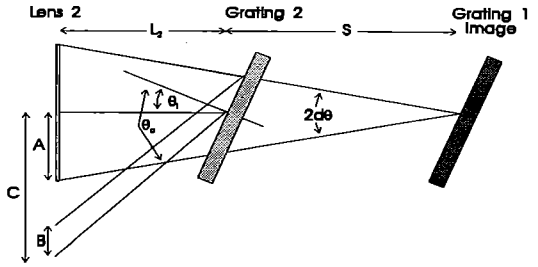

Figure 3: Scheme for the maximum bandwidth calculation

Lens 2. The effect on pulse contrast ratio of the one sided clip is less severe than the two sided clip, yielding a factor 2 difference.

An analysis deriving the relationship between aperture and bandwidth for the case when the one sided clip occurs at the same time as the two sided clip has been performed for $\theta_o > \theta_i$ (*inverted geometry* [1]) The aperture A required for a bandwidth $d\lambda$ is :

$$A = \frac{S\left(\Delta\vartheta + \frac{d\lambda}{2K}\frac{\cos\vartheta_o}{\cos\vartheta_i}\right)}{\left(\frac{2K\Delta\vartheta}{d\lambda} - 1\right)}$$

where :

$$\Delta\vartheta = \vartheta_i - \vartheta_o \qquad K = \frac{\cos\vartheta_o}{N}$$

with (for reference)

$$d\lambda = 2Kd\beta$$

S is the single pass stretch distance and N the grating grove density. A plot of the aperture required to support a given bandwidth is shown in Figure 4 for the proposed PetaWatt Upgrade on VULCAN with inverted compressor geometry [1].

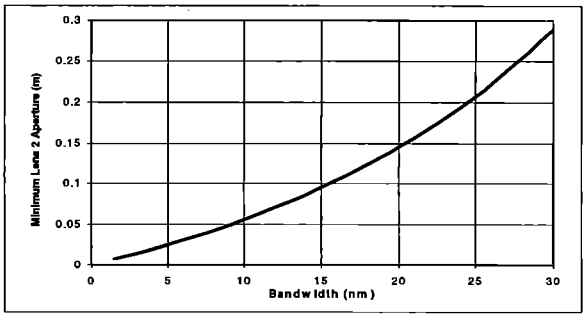

Figure 4 : Minimum Aperture v Bandwidth for the PetaWatt Upgrade Inverted Geometry

Following the determination of the aperture, the distance L_2 is also fixed (for a given stretch distance S). It is simply

$$L_2 = \frac{2KA}{d\lambda} - S$$

and thus L_1 is also determined to be (from the telescope $4f$ imaging requirement)

$$L_1 = 2f - L_2 - S$$

This equation also shows that in addition to a minimum aperture for a given bandwidth there is also a minimum focal length required for the telescope lenses. However, subject to this requirement one is free to choose a value of f such that any clipping that occurs on it is at a bandwidth larger than that occurring on Lens 2. The aperture of Lens 2 for the PetaWatt programme will be 150 mm, transmitting a bandwidth of 20 nm. Additional parameters are $\theta_I = 61°$, $\theta_o = 73°$, $N = 1740 \bullet 10^3$ mm^{-1}, S = 0.75 m, L_2 = 0.5 m, f = 0.75 m and L_1 = 0.25

[1] Trentelman *et al*, CLF Annual Report 1996, Rutherford Lab.

PULSE DEGRADATION ARISING FROM THE FINITE SIZE OF GRATINGS IN A PULSE COMPRESSOR

M. Trentelman, I. N. Ross and C. N. Danson

Central Laser Facility, Rutherford Appleton Laboratory

INTRODUCTION

Modelling is carried out on the Vulcan compressor to calculate the effect of the spectral clipping due to finite grating width. This spectral clipping affects the pulse length as well as the spatial distribution of the pulse in the focal plane. The peak focused intensity, pulse duration and prepulse levels which are of paramount importance to interaction experiments will be limited by the compressor design. Temporal and spatial scanning of the focal spot across the focal plane is another side effect of the spectral clipping but this will not be discussed in detail here.

This contribution discusses calculations of the effect of spectral clipping on these parameters for the proposed compressor for the Peta-Watt Upgrade. The results will also be compared to the more general situation of a perfect sech^2 spectrum. Calculations are made of all these parameters for VULCAN and other spectral profiles, and for double-pass and reverse-geometry in addition to the specified normal design.

MODEL

The compression geometry is shown in figure 1. For the VULCAN compressor the grating widths (W_A , W_B) are both 440 mm, their separation is 2800 mm, 1400 mm and 1000 mm for normal, double-pass and reverse-geometry respectively. The angle of incidence on the first grating is 73.1_ for normal and double-pass geometry an 61.1_ for reverse-geometry. The second grating is positioned such that light at the central wavelength λ_0 (1054 nm) will exactly fill the second grating.

Due to the dispersion at the first grating, an off-centre wavelength will no longer fill the whole of the second grating. As a result the beam at that wavelength will be clipped on one side. The amount and the side of the clipping depends on the wavelength. This is illustrated in figure 1 for wavelengths λ_1 ($\lambda_1 < \lambda_0$). In the output plane of the compressor each wavelength in the beam will illuminate a fraction of the full output aperture. The size w(λ) and off-axis position P(λ) of the fractional aperture are a function of wavelength as shown in figure 2.

The model simply calculates for each point in the focal plane the Fourier transform of the spectrum arriving at that point with appropriate corrections to the spectral amplitude and phase depending on the clipping parameters w(λ) and P(λ).

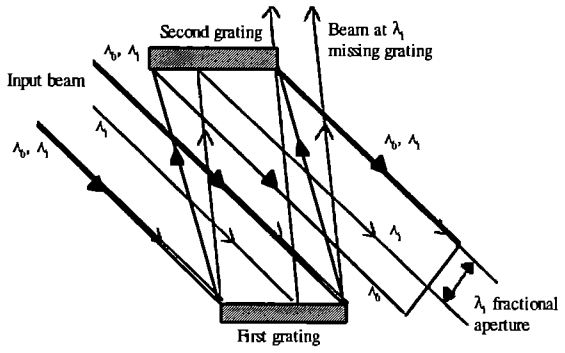

Figure 1 Grating geometry for pulse compression demonstrating the wavelength dependent spectral clipping due to dispersion.

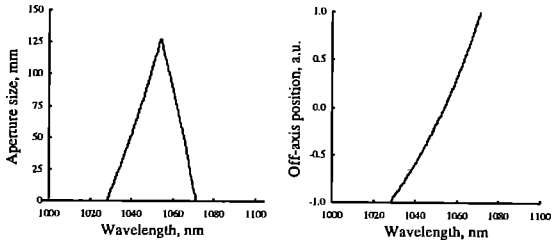

Figure 2 Effective aperture size w(λ) and position with respect to centre ray P(λ) as a function of wavelength.

ON-AXIS RESULTS

For the calculations the output beam is assumed to be brought to a focus by an achromatic and aspheric optic. On the axis in the focal plane all wavelengths will be in phase irrespective of the position on the focusing optic. Therefore, the spectral phase will be independent of P(λ). The spectral amplitude is given by

$$g_0(\lambda)\cdot\sqrt{\frac{w(\lambda)}{w(\lambda_0)}}\cdot\sqrt{\frac{w(\lambda)\lambda_0}{w(\lambda_0)\lambda}}$$

where $g_0(\lambda)$ is the input spectral amplitude, the second term is the spectral clipping at the second grating and the third term takes account of the dependence of the size of the diffraction pattern on both aperture size and wavelength.

The input spectrum which is used as the basis for the calculations is the asymmetric sech^2 shown in figure 3 with a full width at half intensity (FWHI) points of 4 nm and 8.2 nm at the 10 percent points. This asymmetric sech^2 closely matches the calculated curve for the phosphate glass amplification system of VULCAN. Also shown in figure 3 is the clipped spectrum after a single pass through the compressor with 440 mm gratings. The Fourier transform can now be evaluated to give the on-axis temporal profile and this is also shown in figure 3 for the clipped spectrum and the case of an ideal compressor with no clipping.

In table 1 we summarise some of the most important results for comparison. The asymmetric and symmetric sech^2 spectra have the same FWHI. The peak intensity is defined as the peak of the temporal distribution on-axis expressed as a percentage of the peak intensity for the unclipped symmetric sech^2. The energy efficiency refers to the on axis fluence as a percentage of that for an ideal compressor.

The performance of the asymmetric sech^2 is seen to be very similar to that of the symmetric sech^2. Any uncertainty in the asymmetry as a result of differences between different phosphate glasses will consequently lead to little change in the expected compressor performance. In particular it is noted that temporal durations still well under 400 fs can be expected with a peak intensity reduced by 27% and that the prepulse level at 4 ps is increased by only a factor 6 from 2 10^{-8} to 1.3 10^{-7} as compared to the ideal compressor.

An important option to reduce the amount of clipping is to use the compressor in double-pass for which the grating separation is reduced by a factor 2. This reduces the spectral clipping and increases the performance of the compressor. As can be seen from

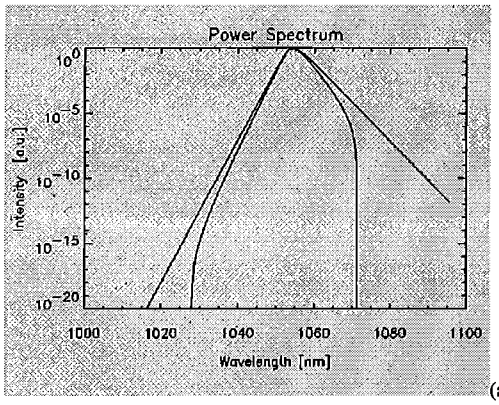

(a)

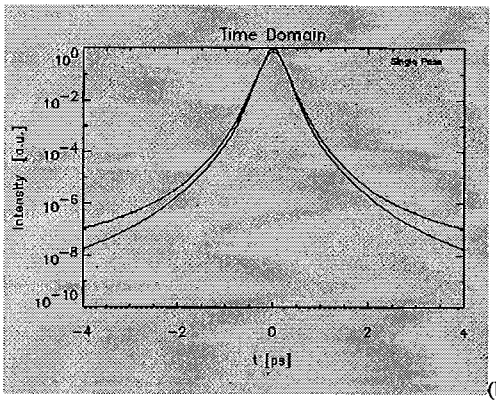

(b)

Figure 3 (a) Spectrum of the asymmetric sech^2 and the clipped spectrum at the output plane of the single pass compressor. (b) The calculated on-axis temporal distributions resulting from the two spectra.

Input spectrum	Asymmetric. sech^2		Symmetric. sech^2		Asymmetric sech^2	Asymmetric sech^2	Asymmetric sech^2
geometry	normal	normal	normal	normal	double pass	300 mm gratings	reverse
	unclipped	clipped	unclipped	clipped	clipped	clipped	clipped
FWHI [fs]	292	341	295	336	315	373	355
10^{-6} [ps]	2.2	5.3	1.8	4.7	4.7	6.2	5.4
prepulse level (4 ps)		$1.3\ 10^{-7}$		$1.1\ 10^{-7}$	$4.4\ 10^{-8}$	$2.9\ 10^{-7}$	$1.3\ 10^{-7}$
peak intensity	99.6 %	73.2 %	100 %	76.3 %	85.7 %	62.7 %	70.0 %
energy efficiency	100 %	84.6 %	100 %	86%	91.8 %	78.3 %	83.6 %
spotsize [μm]	49.48	53.64		53.30	51.58	81.32	
> 2Fλ/W	0.1 %	8.5 %		7.8 %	4.3 %	12.1 %	

Table 1 Summary of results (see text for details).

the table the peak intensity increases from 73.2 % to 85.7 % and the prepulse level at 4 ps is reduced by a factor 3.

Two other significant results are that using reverse-geometry does not significantly change the compressor performance and that the larger gratings of the Peta-Watt programme offer significant performance advantages over the present 300 mm gratings.

DISTRIBUTION IN THE FOCAL PLANE

For off-axis positions y in the focal plane the spatial distribution of spectral amplitude and phase must also be taken into account. Assuming a top hat distribution of intensity on the first grating, the amplitude distribution is a sinc function with argument $\pi w(\lambda)y/F\lambda$ while the phase distribution is $2\pi P(\lambda)y/F\lambda$ where F is the focal length of the optic. A Fourier transform is again used to calculate the temporal profile as a function of off-axis position y.

An example is shown in figure 4 (assuming F = 3000 mm) which gives the fluence distribution for an asymmetric sech^2 spectrum plotted in log form. The spot size to the first minima is 53.6 μm as compared to 49.5 μm for a diffraction limited input beam.

Results on the fluence distribution in the focal plane are also summarised in table 1. The spot size is given for the direction perpendicular to the ruling of the grating and is defined as the distance between first minima. The energy does not go to zero as would be the case for a perfect unclipped monochromatic beam. The spot size in the direction parallel to the grating grooves is not

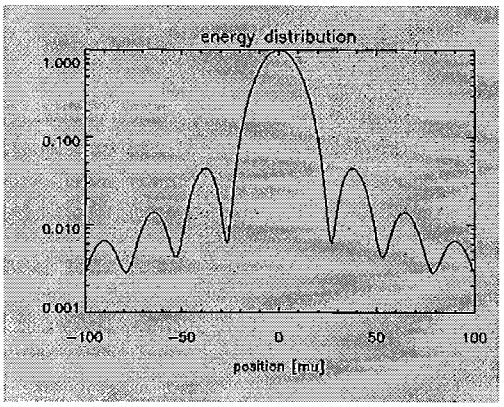

Figure 4 Logarithmic plot of the calculated energy distribution in the focal plane for the clipped asymmetric sech^2 spectrum after passing through the single pass compressor.

affected by dispersion and is just the diffraction limit of the input beam. Therefore, as far as spectral clipping is concerned, this would lead to a spot which is only 8.5% larger than a diffraction limited spot. This percentage is of course independent of the focal length.

COMPARISON OF 'NORMAL', 'DOUBLE PASS' AND 'REVERSED' GRATING GEOMETRY

I.N.Ross, C.N.Danson and M.Trentelman
Rutherford Appleton Laboratory

The grating compressor is a key element in the VULCAN petawatt system and must be optimised to obtain the highest intensity and contrast ratio in the focal spot. Three choices of geometry can be considered: the normal geometry as currently used but with larger gratings; a reverse geometry which exchanges the incident and diffracted beam angles; a double pass geometry.

ANALYSIS

Using the grating equation: $\sin\alpha + \sin\beta = N\lambda$

a) Stretched pulse duration, $\tau_s = \frac{LN^2\lambda d\lambda}{c\cos^2\beta}$

where L = grating spacing, from which the grating separation is calculated

b) Spectral shear due to dispersion on 2nd grating,

$$1 = \frac{LNd\lambda}{\cos^2\beta} \quad \text{or} \quad 1 = \frac{c\tau_s}{N\lambda}$$

This dispersion leads to some energy missing the second grating from all off-centre wavelengths and hence to degradation of the recompressed pulse intensity and contrast ratio.

c) The effects of non-linear chirp due to the grating pair can be calculated from the group delay (T), given by:

$$cT = \frac{S}{\cos\beta} + S\tan\beta\sin\alpha$$

where S = perpendicular separation of grating planes

Using a Taylor expansion :

$$T = T_0 + \frac{dT}{d\lambda}\delta\lambda + \frac{1}{2}\frac{d^2T}{d\lambda^2}\delta\lambda^2 + \ldots.$$

and the ratio of nonlinear to linear chirp is given by

$$\frac{d^2T/d\lambda^2\,\delta\lambda}{2\,dT/d\lambda} = \frac{3N\sin\beta\delta\lambda}{2\cos^2\beta}$$

d) The effects of grating and beam imperfections are assessed by calculating both the resulting time stretch and the resulting output beam divergence. Then a specification results from requirement that these to be less than the compressed pulse duration and the input beam divergence respectively.

Beam imperfections / noncollimation are considered as an input beam pointing error $d\alpha$. The resulting output beam pointing error is just $d\alpha$, while the pulse stretch is given by:

$$c\tau_s = \frac{\cos\alpha}{\cos^2\beta} LN\lambda d\alpha$$

Grating flatness errors are represented by angular errors of ε_1 and ε_2 on the two gratings.

The resulting output beam pointing errors are given by:

$$d\alpha_1 = \frac{\cos\alpha + \cos\beta}{\cos\alpha}\varepsilon_1 \quad , \quad d\alpha_2 = \frac{\cos\alpha + \cos\beta}{\cos\alpha}\varepsilon_2$$

The resulting pulse stretches are given by:

$$c\tau_s = \frac{\cos\alpha + \cos\beta}{\cos^2\beta} LN\lambda\varepsilon_1$$

$$c\tau_s = 0 \quad \text{for } \varepsilon_2$$

RESULTS

Values calculated for N = 1740 l/min; $d\lambda$ = 4 nm; λ = 1.054 μm; τ_s = 500 ps; $[\alpha - \beta] = 12°$; grating length = 2 x grating width = 450 mm; grating efficiency = 90%.

	NORMAL	DOUBLE PASS	REVERSE
Incident angle, α	73.1°	73.1°	61.1°
Diffracted angle, β	61.1°	61.1°	73.1°
Grating spacing for τ_s = 500 ps	2.8m.	1.4m.	1.0m. *
Energy efficiency	40%	35%	67% *
Beam clearance @ midpoint	78 mm		
@ 2nd grating			79 mm
Spectral clipping effects			
Increase in pulse duration	17%	8% *	22%
prepulse level @ 4 ps	1.3×10^{-7}	4×10^{-8} *	1.3×10^{-7}
Non-linear chirp	21 ps	21 ps	63 ps
Grating angle tolerance	±0.3° *	±0.3° *	±0.1°
Grating flatness specification	λ/27 cm^{-1}	λ/54 cm^{-1}	λ/18 cm^{-1} *
Pulse stretch for beam of 3 x DL.	300 fs *	300 fs *	500 fs

* indicates the more advantageous geometry

The following summarises the principle points of comparison between these geometries:

a) The reverse geometry is more energy efficient and does not suffer from propagation problems resulting from hard edge clipping at the gratings. This implies that the laser can be run at a reduced level with lower B-integral.

b) The reversed geometry is more compact and may be easily contained within a single vacuum lank. Significant geometric problems attach to the double pass geometry.

c) The single pass geometries do not give greatly reduced compressor performance.

d) Grating flatness requirements are tight and advise against the double pass geometry.

e) Significant increase in focused intensity is possible if beam divergence could be reduced.

AN ELEGANT ULTRAFAST UNI-AXIAL SINGLE SHOT AUTOCORRELATOR

J. Collier, C. Johnson and C. Mistry

Rutherford Appleton Laboratory, Chilton, Didcot, Oxfordshire, OX11 OQX,U.K.

INTRODUCTION

A new design of an optical pulse autocorrelator for single or multiple pulses is presented having the novel feature of uni-axiality. The design offers a number of distinct improvements over traditional designs. The principal benefits are the extreme simplicity of alignment and operation coupled with a substantial reduction in size and component cost compared to traditional multi-axial systems. The basic design is almost non-dispersive and thus suitable for use with ultra-fast pulses in addition to being virtually insensitive to wavelength (mixing crystal excepted). Fixed and equal group delay in each arm and a fixed, unchangeable calibration are additional features.

DESCRIPTION

As in other autocorrelator devices the technique consists of splitting an input beam into two and then recombining these two beams in a non linear crystal. The non linear crystal is used to produce a Sum Frequency Signal from the two split beams when a pulse is present. Traditional techniques generally use a 50% reflectivity mirror for the splitting process to generate the two arms from the input beam, thereby forcing a bi-axial design. Often the bi-axial design becomes a tri-axial design deriving from the need to carefully match the optical path length of the two arms. A retroreflector is usually used for this purpose generally producing a beam height change. The multi-axial design of these types of autocorrelator generally lead to difficulty of alignment, especially when pulses are only available on a minute by minute basis as

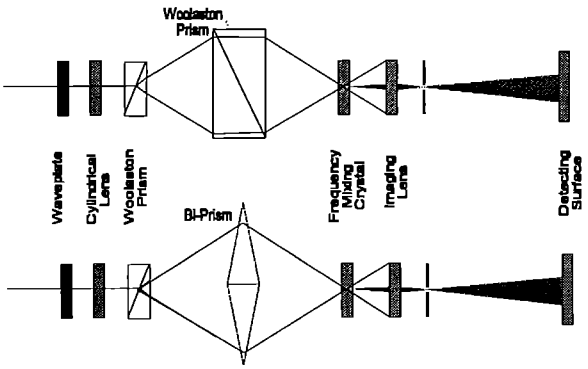

Figure 1 : The basic designs

found in larger laser systems.

The basic design is presented in Figure 1. The input beam, which should have a uniform and constant spatial profile over the input aperture of the system enters via a waveplate. This can have either a quarter or half wave retardation and is used to control the splitting ratio of the two arms. The autocorrelation however is relatively insensitive to this ratio since it derives from the product and not the ratio. Following passage through a cylindrical lens, whose focal plane is coincident with the frequency mixing crystal, the beam is split into two using a Wollaston Prism. A Wollaston Prism is a bi-refringent device that splits an unpolarized input beam into two orthogonally polarized output beams that propagate at two virtually equal angles symmetrically about the input beam direction. The included angle is determined by material properties and the internal interface cut angle. The two diverging beams are then forced to converge by one of two means. Either the two beams are incident on a second Wollaston Prism that has its internal interface angle specifically cut such that the diverging beams are made to converge with a given convergence angle or by use of a symmetric bi-prism. For the design using a second

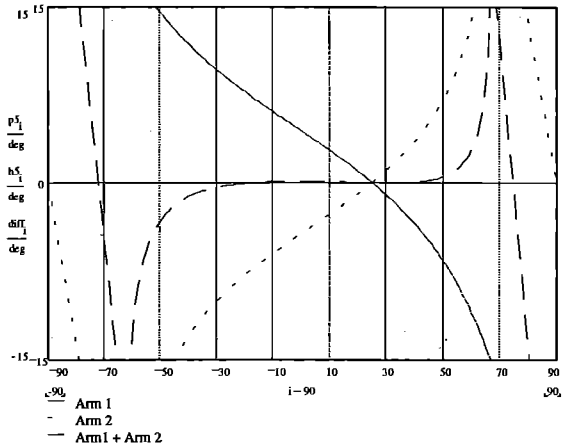

Figure 2 : Arm angles v prism angle

Wollaston Prism the effect of using different cut angles of the second Wollaston Prism is shown in Figure 2. The first Wollaston Prism cut angle is clearly seen as 25 degrees. Note the very slight angular asymmetry at large cut angles which is, if desired, easily compensated for by an equivalent rotation of the first Wollaston Prism. It does not effect the autocorrelation process. The crossover point is arranged to be inside the frequency mixing crystal that is cut for correct phase matching to produce a sum frequency signal from the two orthogonally polarised crossing beams. The sum frequency signal, or effectively the autocorrelation, is then imaged onto a detecting surface such as a CCD camera or linear CCD array in a standard way, utilising a pinhole to prevent residual fundamental or unwanted second harmonic signals reaching the detecting surface. Figure 3 shows the output of the device for 120 fs pulse train at 1053 nm. The device has also been tested with a single 150 fs pulse at 768 nm.

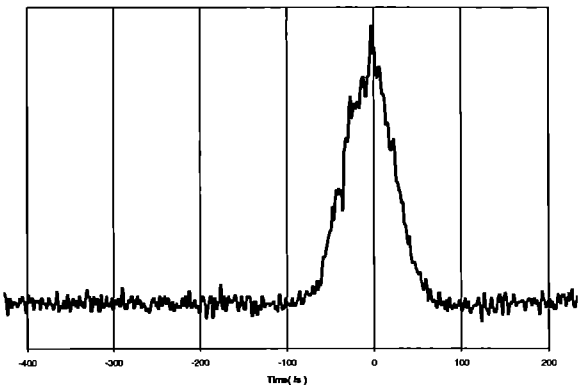

Figure 3 : Autocorrelator output

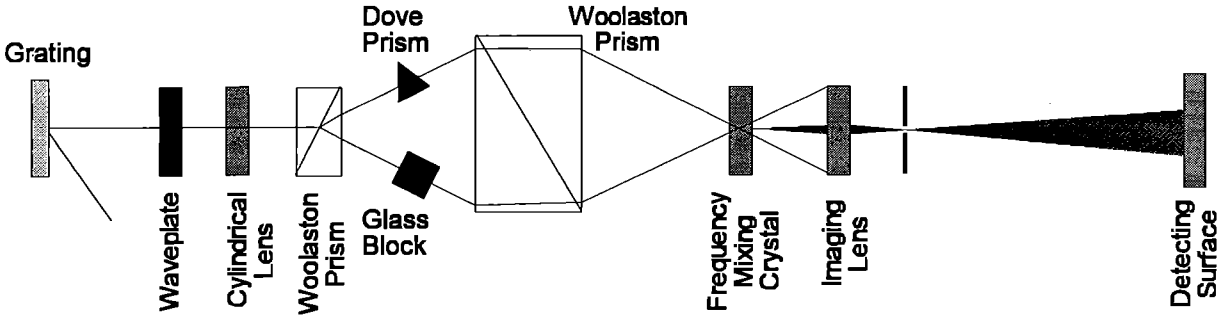

Figure 4 : Modification of the design to accommodate longer pulse lengths

LONG PULSE LENGTH EXTENSION

The minimum pulse length resolvable is limited by material dispersion and the maximum pulse length by the aperture of the device and the crossover angle. The maximum pulse length resolvable can however be significantly increased with the small modification to the device as shown in Figure 4.This is achieved at the expense of an increase in dispersion and thus a corresponding increase in the minimum pulse length resolvable. Injection is by means of a diffraction grating which imposes a temporal shear across the beam which the dove prism inverts in one arm only. The glass block in the other arm compensates for the group delay.

CALIBRATION

One of the important benefits of the basic design is that the group delay is equal in both arms. This clearly simplifies the alignment since the two pulses from each arm are guaranteed to overlap in time at the crossing point. Additionally, the absolute calibration of the device (fs / mm) is also fixed and not adjustable by the user. Calibration of the imaging system is easily achieved by inserting a glass etalon of known thickness into one of the arms of the device thereby providing an exactly known group delay to that arm. A photograph of the autocorrelator appears in Figure 5 highlighting the compactness of the design.

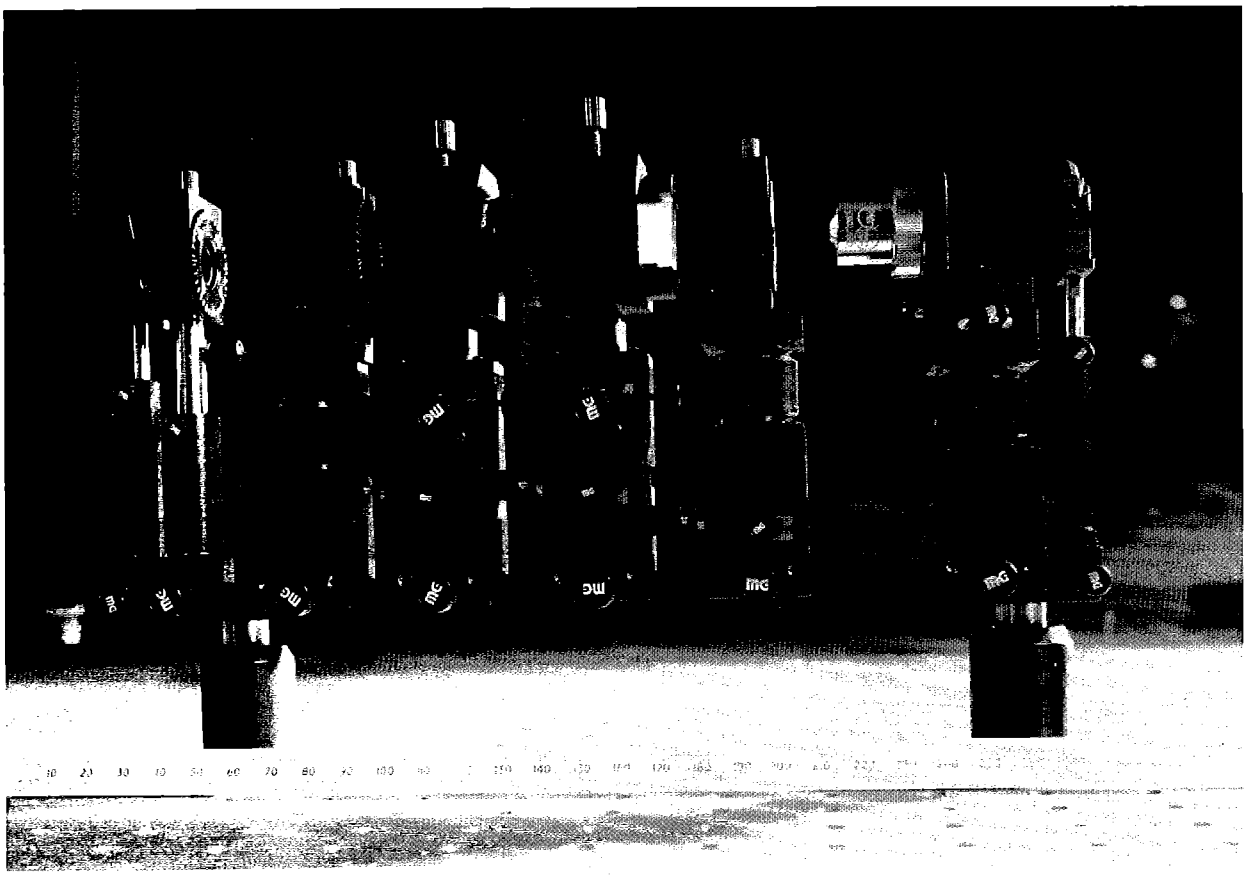

Figure 5 : Photograph of the autocorrelator illustrating its small size

CONSTRUCTION AND COMMISSIONING OF A 1 TERAWATT CPA LASER SYSTEM FOR THE TECHNICAL UNIVERSITY OF LISBON

G N Figueira, J T Mendonça, N Lopes, D Resendes, C N Danson* and C B Edwards*

Grupo de Lasers e Plasmas, Instituto Superior Técnico
* Rutherford Appleton Laboratory

INTRODUCTION

Over the past year and a half a CPA Nd:glass laser system has been under construction at the CLF, following an agreement with Instituto Superior Técnico (IST), Technical University of Lisbon. The comact, table-top laser is based on the Vulcan CPA scheme. Our gaol is to achieve a final energy of 1 J, leading to a peak power below the TW. We describe here the various stages of the complete system and the work done so far.

OSCILLATOR

The oscillator is a diode pump additive pulse mode-locked Nd:YLF laser (Microlase DPM 1000). It delivers 250 mW, 2.6 ps mode-locked pulses centred at 1053 nm at a frequency of 120 MHz. This represents an energy of approximately 2 nJ per pulse. This oscillator has been fully described elsewhere [1], and its design and operation are also similar to the Nd:YLF oscillator used in Vulcan [2]. The oscillator ouput was compressed using fibre/grating techniques. This compression is achieved via an increase of the pulse bandwidth due to self phase modulation during propagation through an optical fibre and subsequent recompression using a pair of diffraction gratings which cancel the group velocity dispersion (GVD) introduced. We measured an eightfold increase in bandwidth (0.5 to 4 nm) using 20 m of single mode optical fibre which allowed the pulse to be compressed to below 400 fs. In the future, we plan to add a commercial device at the output of the oscillator to act as a pulse compressor.

Immediately after the output of the oscillator, a Faraday rotator between crossed polarisers prevents any back-reflection coming from the amplifying stages from entering the laser cavity and disturbing the mode-lock conditions.

STRETCHER

Following the CPA recipe, the pulse must be stretched temporally before amplification to avoid the onset of non-linear effects and beam degradation inside the amplifying media. For that effect, a linear frequency chirp is introduced across the length of the pulse via the GVD that arises by passing a pair of diffraction gratings. In our case, this is accomplished using a stretcher design in all similar to Vulcan's.

The polarisation of the pulse is first rotated to p to suit the gratings. A pinhole is used to clear any unwanted spectral components and to increase the beam width. The two holographic, gold-coated diffraction gratings (Jobin Yvon) have 1740 lines per mm and are blazed for operation at 1064 nm. Working next (~62°) to Littrow's angle, we achieved a diffraction efficiency of more than 90% per grating, or 70% after double passing the two.

A folded, unit magnification telescope is inserted between the gratings, used in an anti-parallel configuration, to provide the necessary frequency chirp [3]. It consists of two 1 m focal length convex lenses put 2 m apart. Each lens, in turn, is 30 cm away from the nearest grating. This distance is fixed both by amplification requirements and space limitations. After the second grating, a retro-reflecting prism sends the beam back through the same path, with a small vertical displacement to allow the chirped beam to pass above the leak mirror before the first one.

Using $\Delta t = 4da^2\lambda\Delta\lambda/c\cos^2\theta_d$, where d is the distance from the grating to the nearest focal point of the lens, a is the grating ruling, λ and $\Delta\lambda$ are respectively the central wavelength and bandwidth, c is the speed of light and θ_d is the diffraction angle, we calculate the stretched pulse length to be approximately 160 ps.

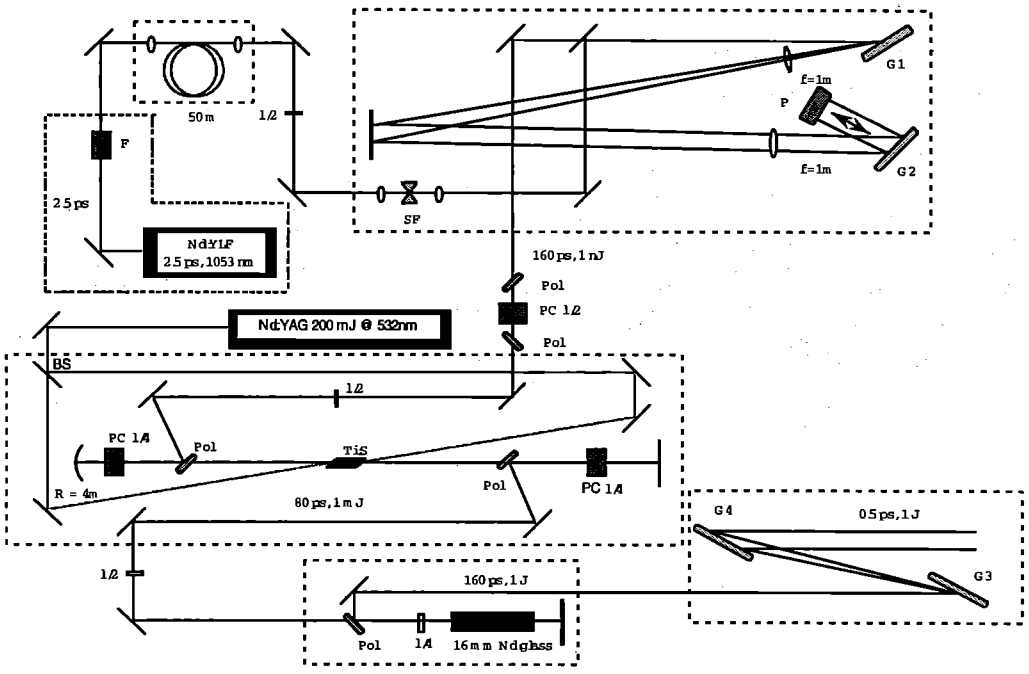

Fig. 1. Schematic of the laser system

TI:SAPPHIRE REGENERATIVE AMPLIFIER

This was based on the design currently being adapted into Vulcan's amplifying chain [4]. The amplifier is formed by a stable resonator cavity consisting of two mirrors, a plane and a 4 m ROC concave one, placed 1.8 m apart. A 2.0 cm long, 7 mm of diameter Ti:sapphire crystal with both ends cut at Brewster's angle, doped at 0.15% wt of Ti_2O_3 with an absorption coefficient at 532 nm of 2.5 cm^{-1}, stands approximately in the centre of the cavity. Before amplification, a single pulse of the mode-locked train is selected by applying a half-wave voltage, short pulse to a Pockels cell between two crossed polarisers, providing a contrast of ~10^5. The pulse is switched into the cavity by a combination of a double passed Pockels cell to which a quarter-wave voltage is been applied and a broadband thin film polariser, placed near the concave mirror. The pulse is trapped inside the cavity long enough for the gain to be depleted, after which its energy starts to decrease. It takes about 120 round trips to attain a maximum energy of a few mJ, corresponding to a total gain of more than 10^6. A second set of Pockels cell / polariser switches the pulse out after the required time (~ 1 ms). These values are only provisional, as this stage is currently under construction.

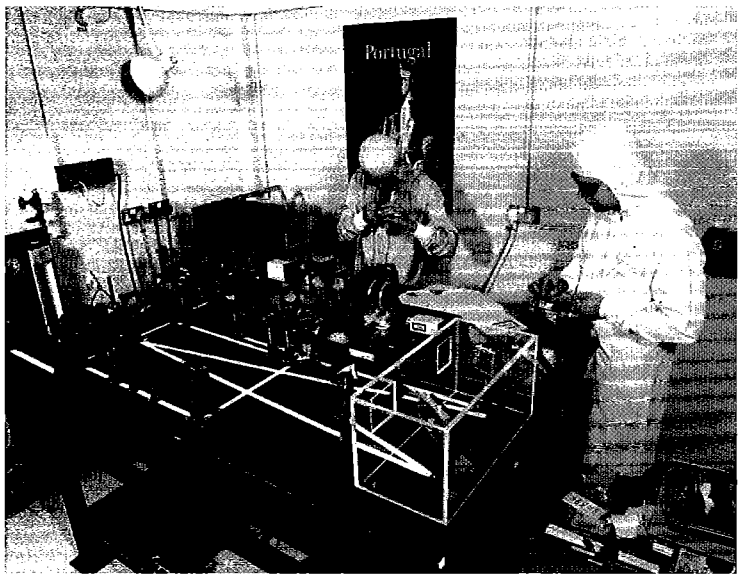

We have made a detailed theoretical study of the amplification process taking place. This study follows that of Stuart *et al* [5] for regenerative amplification at 1053 nm using Ti:Sapphire as gain medium. A model for amplification was developed and a computer simulation written to test it. The model accounts for non-linear effects such as whole-beam self-focusing, mode-size variation due to radial gain profile, gain saturation and gain depletion due to spontaneous emission and ASE. The values calculated with this model are close to what we would expect based on the performance of similar systems. The value obtained for the partial B-integral is less than 1. We intend to develop it further in accordance to the measurements done in the course of assembling this amplifier.

ROD AMPLIFIER

The final amplification stage of the system consists of a 16 mm of diameter Nd:glass rod. The beam diameter is first expanded to 10 mm to extract a greater amount of energy from the rod. A polariser and a quarter-wave plate provide the double pass. With an expected single pass gain of ~30, it will increase the pulse energy to the Joule level.

COMPRESSOR

A pair of large diffraction gratings with the same characteristics as those of the stretcher in a parallel, single-pass configuration are used to provide the opposite chirp needed to compress the pulse length approximately back to its original value. Considering this to be 2.5 ps, we can expect to have a final power the order of a fraction of a Terawatt.

On Fig 1 we have a scheme of the whole system including a fibre at the output of the oscillator, which will allows us to attain a shorter final pulse length (~500 fs) and consequently a higher output power (>1 TW).

APPLICATIONS

The laser system will be installed at IST during the next Summer. A target chamber is being simultaneously developed there, with associated diagnostics. Our primary aim is to study phenomena related with laser-plasma interaction, in particular the generation of large amplitude plasma waves through interaction with ultra-short laser pulses. The electric field associated with such waves can be applied towards accelerating charged particles to high energies, as several recent studies and experiments show [6]. In other experiments we plan to measure the frequency shifts suffered by radiation propagating inside a plasma whose spectral properties have been non-linearly modified by a short, powerful laser pulse.

CONCLUSIONS

We described a CPA Nd:glass laser system being assembled at the CLF based on Vulcan. The system uses a mode-locked Nd:YLF oscillator delivering 2.3ps pulses at 1053nm that subsequently are chirped and stretched to 160 ps using a pair of diffraction gratings. A Ti:S regenerative amplifier raises the pulse energy to the millijoule level. Further amplification is obtained with a 16 mm Nd:glass rod, yielding an output energy the order of 1 J. After the pulse is compressed back to the original duration, a power of a fraction of a TW is achieved. By introducing a pulse compressor this can be substantially increased to more than 1 TW.

The system is currently entering its final stage of construction and will be installed in Lisbon next Summer. There it will be used for laser/plasma interaction experiments.

ACKNOWLEDGEMENTS

The authors wish to thank Dr. John Collier for very useful discussions. G Figueira is supported by grant PRAXIS XXI/BD/5293/95.

REFERENCES

[1] GPA Malcolm, PF Curley, AI Ferguson, Optics Letters 15(1990), 1303
[2] IP Mercer *et al*, Optics Communications 107(1994), 77.
[3] OE Martinez, IEEE Journal of Quantum Electronics 23(1987), 59.
[4] F Zhou *et al*, Electronics Letters 31(1995), 1060; *ibid*, CLF Annual Report 1994, 121
[5] BC Stuart, S Herman, MD Perry, IEEE Journal of Quantum Electronics 31(1995), 528
[6] A Modena *et al.*, CLF Annual Report 1995, 25.

THE NEW TITANIA LASER SYSTEM: AN OVERVIEW

M J Shaw, C B Edwards

Rutherford Appleton Laboratory

On 2nd April 1996 Paul Williams, Chief Executive of the CCLRC, fired the first shot on the Titania laser facility. This event, witnessed by future users, CCLRC staff and representatives of the media, marked the culmination of four years of design, planning and construction of the CLF's 3rd generation krypton fluoride laser.

Exactly one year earlier, Paul had fired the final shot on Titania's predecessor, Sprite. Designed originally a research machine, Sprite was brought on line as a user facility in 1991, and rapidly established a reputation as an extremely productive facility for the study of UV laser interactions with matter. The capabilities of the system were further enhanced in 1993 by the introduction of chirped pulse amplification techniques, making Sprite the world's most intense source of UV laser radiation. Sprite, with some modification, is now incorporated as a pre-amplifier in the Titania architecture.

The installation of Titania was concentrated in four main areas:

i) A new **laser front end** has been constructed in a dedicated laboratory. The system incorporates a Titanium Sapphire oscillator/multipass amplifier delivering 10mJ of near diffraction limited laser output at 748 nm. The multipass amplifier uses a pair of novel double bi-prisms to fold the beam eight times through the Titanium Sapphire crystal. The design is highly efficient, and is the subject of a provisional Patent application. The 748 nm light is then frequency tripled to give over 300μJ at 248nm for injection into the e-beam pumped KrF chain.

ii) The **pulse power area** in building R2 has been re-built to incorporate the 420 mm aperture Titania amplifier. This large amplifier module was extensively tested in a separate laboratory prior to installation in R2, where it proved to be extremely reliable with over 800 shots fired in a comprehensive test programme. The pulsed power for the Sprite amplifier was extensively modified with a new low inductance Marx generator based on the Titania design, removal of the water capacitor and the extension of the pulse forming lines to give 120 ns pulses .

iii) The **multiplexer/ demultiplexer area and Raman bay** has been extended and refurbished to handle the additional beams and longer path lengths required to extract the laser energy from the Titania module and to pump the Raman cells in the Raman laser mode of operation .

iv) A new **target area** has been constructed. The initial operation of the facility will be in CPA mode, using the original Sprite target chamber, with Raman operation becoming available early in 1997.

The first experiments on Titania will use the existing pulse compression gratings. To protect these gratings from damage, the beam is attenuated to 1 J before entering the grating compression chamber. This chamber and the following beam piping to target are of a new design, described in the following section of the report, which provides full mechanical isolation to the mirror and grating mounts from the surrounding vacuum chamber.

Characterisation and monitoring of the short pulse CPA output from Titania presents a significant technical challenge. A novel cross correlation technique has been devised to monitor the compressed pulse duration on-line and is reported below.

A novel windowless Raman amplifier has been designed to overcome the problems associated with transient grating formation on the input window of the final Raman amplifier. These effects, first noticed during Raman experiments using Sprite, impose an upper limit to the pumping intensity of the Raman amplifier. The development of a windowless cell is an important step in optimising the eventual Raman performance of Titania.

The successful completion of the extremely ambitious programme outlined above within one year of Sprite's closure required a high level of commitment and dedication from all staff involved. We now look forward to the resumption of the science programme in new areas which our new facility will open up.

ENGINEERING ON TITANIA

S M Angood, P A Brummitt, A R Damerell, J A C Govans, S Hancock, A R Jackson, W J Lester, H T Medhurst, M R Pitts, C J Reason, D A Rodkiss, C Stephens, G Taylor, R G Williams, D Wood and B E Wyborn

Rutherford Appleton Laboratory

INTRODUCTION

The year has seen a major change for the KrF laser systems at the CLF. Since the last shot on Sprite on 31/3/95, the KrF laser system has been completely re-engineered. This has involved a large amount of engineering work and the efforts of a considerable number of the Engineering and Technology Group and this opportunity should be taken to thank them for all their contribution during the past year. From a laser point of view the changes have been to remove the Goblin amplifier from R2, and install the Titania amplifier in its place with the Sprite module now being the preamplifier, to install a new optical chain to the Sprite target chamber, and install a new front end system. From an engineering point of view this has entailed the almost complete stripping out of the existing Sprite laser system and its services and the erection of a new building complex, the modification and upgrading of Sprite, the installation and integration of Titania, the design and installation of the new optical chain, and the installation and modernisation of the infrastructural services. Throughout this process the aim has been to minimise the down time of the laser as an operational machine and to create a new facility which is functional, meets the design specification and has the potential for future development. An overview of what has been achieved is given in the following paragraphs.

BUILDINGS

A large amount of building work has been completed. Maximum use has been made of the existing Sprite building R2, and with the incorporation of an adjacent building R7 into the system a low cost expansion has been completed (see Fig. 1), with space for possible future upgrades i.e. into the east end of R7 and to the south of R7 where there is an area upon which future buildings could be erected.

The bulk of the laser system has been accommodated in R2 with the pulsed power amplifier modules at the east end. A new Front End Room and an extended Multiplexer Area occupy the majority of the remainder of the building. The CPA and Raman system optical line components will be housed in the modified link building together with the Laser Control Room. These have been joined to the previously erected Target Area in R7 and a new adjacent Target Area Control Room built.

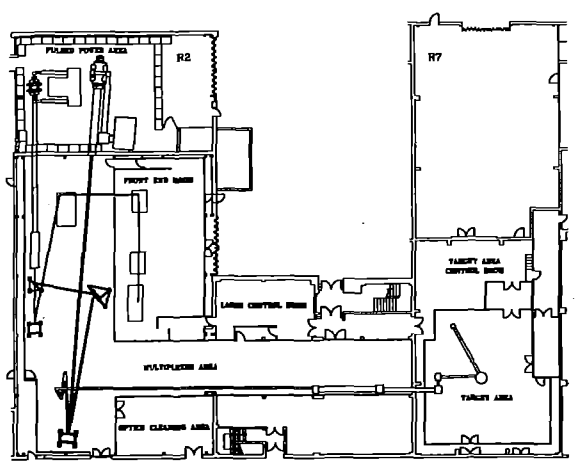

Figure 1. The Titania Laser System

In order to minimise the laser system down time the work was carried out in phases. In phase I the Target Area, the Laser Control Room and the link building modifications were completed while Sprite was still operational. Phase 2 consisted of the stripping out of the Sprite Control Room, the erection of the new Front End Room and work in the Pulsed Power Area. For phase 3 the remaining Sprite Target Area and ancillary rooms were removed and an extension of the Multiplexer Area together with an Optics Cleaning Area were built. The Front End Room and Multiplexer Areas have been built with insulated walls and ceilings and steps have been taken to reduce the solar heat input. Where ever possible equipment producing heat has been minimised, positioned outside the room or is water cooled.

TITANIA MARX

The Titania Marx was refurbished with spark gaps cleaned and a new safety earthing system installed. The tank and internals were transported separately from R7 to R2 and after the position of the tank had been established the internal capacitor stack was installed using a special lifting frame.

SPRITE MARX

A new Sprite Marx was designed, installed and tested. The system included a new tank, a new internal capacitor stack based on the Titania design able to be lifted in and out, a new safety earthing system, a new system of solid resistors [1] and cleaned spark gaps. The completed Marx was tested successfully into dummy loads.

TITANIA DIODE, SWITCHES AND LINES

The design of the Titania Amplifier Module has been reported previously [2] [3] and the satisfactory performance of the laser triggered radial diaphragm switches has already been shown [4]. The amplifier had been tested to design specification in R7 with a reasonably large number of test shots. This equipment was disconnected from its services in R7 and dismantled into large discrete assemblies. The switch diaphragms and optics were cleaned and reassembled. All the equipment had to be carefully transported from R7 and reassembled in R2 with the axis of Titania carefully aligned to the overall optical laser system arrangement and a beam pipe added.

SPRITE DIODE, SWITCHES AND LINES

The overall design of Titania allowed the Sprite diode to stay in its original position to minimise the changes to a working system. However during the stripping out of the old Sprite Marx, Water Capacitor and Pulse Forming Lines it was identified that the diode feedthroughs were in sorry state after many years of use and were in need of refurbishment. Damaged components were replaced, others cleaned and realigned and the system rebuilt symmetrically. New, extended pulse forming lines and refurbished switches were installed and connected directly to the new Marx.

TITANIA AND SPRITE CELL FOILS

Both cells had developed faults and needed to be refoiled. The Sprite cell was removed using the existing jigs and carefully measured before being refoiled and reinstalled in the diode vessel. For servicing Titania the gas vessel was extracted along rails and transferred to a trolley for foiling. A new system has been developed for the etching and gluing of the thin titanium foils to the stainless steel vessel. While the cell was out sacrificial plates

were added to each cathode to try and reduce the wear and tear on the pre foils.

TRIGGER MARX

The Trigger Marx used in R7 has been transferred across to R2 and installed as the single trigger for both the Sprite and Titania pulsed power systems. Modifications were carried out to accommodate the thick trigger cables. Currently further work is ongoing to improve the Trigger Marx's reliability.

LASER TRIGGERING SYSTEM

The Sprite and Titania trigger lasers have been repositioned and services connected. The trigger system has been redesigned with all beams and mirrors etc. enclosed.

CPA LINE

The engineering of the CPA line has involved the design of a vibration isolated beam line, chambers, grating and mirror mounts and is described in more detail elsewhere [5]. A novel mirror mount has been designed and developed as described elsewhere [6].

RAMAN LINE

Although not implemented this year the positioning of components for the CPA line has involved designing the arrangement for the Raman line. This has involved the design of a complex multiplexing and demultiplexing arrangement using a state of the art 3-D CAD package as reported last year [7].

CONTROL SYSTEMS

The Titania, Sprite and Trigger Marx power charging systems have been updated to a system automatically interfacing with the control computer, the Titania and Sprite SF_6 gas control system has been automated and is now capable of being operated from the control computer, a new control and alignment system has been designed and installed in the Target Area and a CPA grating drive system has been implemented. These are described elsewhere [8].

TARGET AREA

The existing Sprite target chamber has been relocated in the new Target Area and services reconnected. A Turbo pump has been installed and all services have been routed to and from the chamber to the control desk in the area and the Target Area Control Room via a service trench to keep the Target Area clear from trailing cables etc. and thus be more flexible for future experimental configurations. The turning mirror/diagnostic chambers and the beam delivery pipe are described elsewhere [5].

WATER COOLING SYSTEM

An automatically controlled water cooling system with two 57KW capacity air blast refrigerated chillers (with the facility for a third unit) has been installed. The water chillers are connected via four stainless steel heat exchangers to the primary cooling circuits which are available in the Titania complex. A dual pumping system has been installed on the chiller circuit to avoid all the cooling being lost on a single pump failure and to allow maintenance to be carried out without affecting operations.

DEIONISED WATER

Two identical deionised water systems have been installed to supply the water electrolyte to the Sprite and Titania pulse forming lines.

OIL SYSTEM

The oil system has had its filtration plant refurbished and solenoid remote operated valves installed which allow the potential for predetermined sequential operation during emptying, cleaning and fill cycles and feedback for computer monitoring or control.

GAS SYSTEM

Gas mains have been installed for all the major gases used. Identical gas handling panels with pneumatically operated valves have been designed and installed for both Sprite and Titania cells.

INTERLOCK SYSTEM

The data table for Cerberus [9] [10], the computerised Interlock system for the Sprite laser system, was successfully updated to take into account the new Titania configuration.

PULSED POWER AREA X-RAY SHIELDING

The combination of Sprite and Titania diodes has increased the x-ray radiation yield in the Pulsed Power Area. Several layers of protection have been added to reduce the level of radiation that personnel are exposed to as low as (reasonably) practical. Firstly lead sheeting has been fitted to both the diodes taking care to minimise shine holes. Secondly the Pulsed Power Area has had a concrete block wall built around it. Care has been taken to overlap blocks to stop direct shine paths and lead wool has been inserted into cracks on the critical angles. Thirdly concrete block walls have been erected behind some of the partitioning.

VACUUM SYSTEMS

Updated vacuum control systems for the Titania diode, Sprite diode and Target Chamber beam line have been designed and installed. The Titania vacuum system incorporates a sophisticated pressure system to protect the end cap window [11].

SAFETY

Throughout these changes careful planning and control has been carried out to ensure that the work was performed in a safe manner and conforms to current Health and Safety legislation. In particular the building work was subject to the new CDM Regulations.

CONCLUSIONS

The closing of the Sprite system and its reincarnation as the Titania laser system has involved a great deal of innovative engineering design, planning and sheer hard work and those responsible should be thanked for achieving such a large amount of work in a limited period in such a professional manner.

REFERENCES

(1) 'Solid resistor tests', A Kidd et al, CLF Annual Report 1994.
(2) 'Design of the Titania amplifier module', S Angood et al, CLF Annual Report 1992.
(3) 'Progress on the Titania amplifier module', S Angood et al, CLF Annual Report 1993.
(4) 'Performance of the Titania laser triggered switches', A Kidd et al, CLF Annual Report 1994.
(5) 'Engineering of Titania CPA system', A Damerell, CLF Annual Report 1995/6.
(6) 'Flexure mirror mount', S Hancock, CLF Annual Report 1995/96
(7) 'Design of the Titania optical system', S Hancock et al, CLF Annual report 1994/95
(8) 'COBWEB, a computerised Control System to serve the gas laser, Titania', C Reason et al, CLF Annual Report 1995/6.
(9) 'Cerberus, a computerised interlock system for the Sprite laser', C Reason et al, CLF Annual Report 1992.
(10) 'Cerberus: a laser interlock system using Arcnet', P Gottfeldt et al, Computing and Control Engineering Journal Dec. 1993.
(11) 'Titania window end cap pressure system', S Angood, CLF Annual Report 1995/96.

ENGINEERING OF TITANIA CPA SYSTEM

A. R. Damerell
Central Laser Facility, Rutherford Appleton Laboratory, Chilton, Didcot, Oxon, OX11 0QX, UK

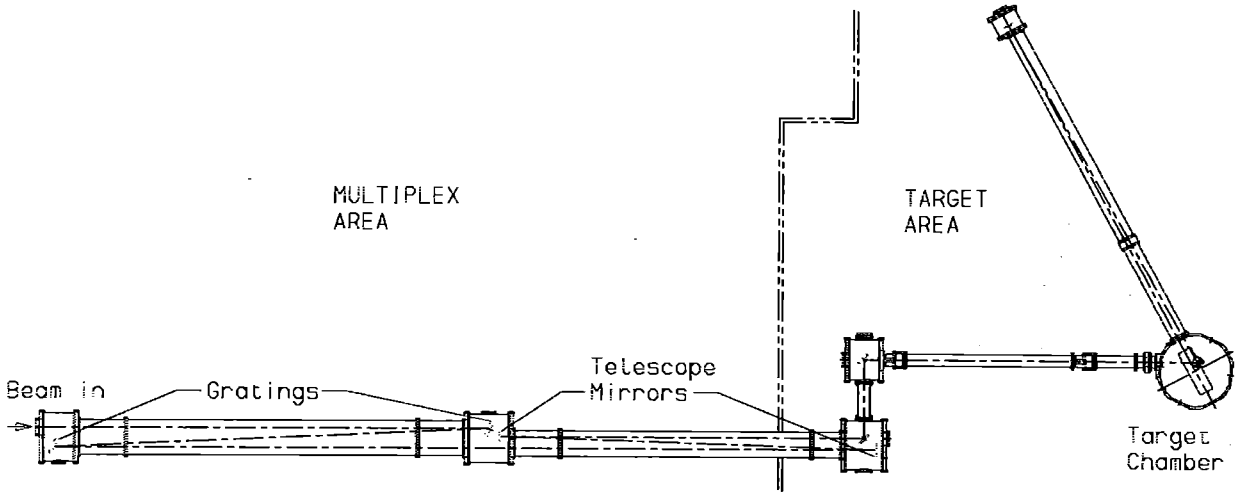

Fig.1 Layout of Titania CPA chamber, beam telescope and beam transport system to the Target chamber

INTRODUCTION

The CPA beam delivery system to the Titania Target Area consists of a pair of compression gratings to compress the pulse from 50 psec to 300 fsec with a separation of 5.5m. The initial beam diameter is 160mm through the compression gratings, the beam is then telescoped down to a diameter of 106mm using a concave mirror of 20m radius followed by a convex collimating mirror of 15m radius. The beam is then transported to the target chamber off a pair of 90° turning mirrors. The reduction in size of the beam has the advantage of enabling existing hardware and beam line optical components including off axis parabolas to be used. There is no loss of power due to the reduction in beam diameter - the power available in target chamber is limited by the damage threshold of the grating pair.

ENVIRONMENTAL CONSIDERATIONS

The physical requirements of the system demand:-
1) The beam must not pass through any optical components after being compressed (i. e. lenses or windows). For this reason the grating pair and all subsequent reflecting optical components are mounted in a continuous vacuum environment.
2) The alignment of the grating pair must remain stable to very fine margins to ensure maximum compression efficiency. The focusing and positioning of the beam in the target chamber also demands very great stability of the beam. In an initial system diagnostic experiment it is required to shoot the beam through, typically, a 10µm diameter pinhole. Hence for these reasons isolation of all the optical beam line components from the various sections of the vacuum envelope is essential to prevent even small movements of the optical components due to the vacuum loads imposed on the vacuum envelope. This vacuum isolation arrangement has also the added advantage of isolating the optical chain from any movement of the vacuum envelope due to thermal stresses induced in the aluminium alloy vacuum envelope.

DESIGN PHILOSOPHY

The initial alignment is to be carried out in air then all subsequent alignment will take place under vacuum. The grating mounts have the ability to adjust the orientation of the rulings to be aligned parallel to each other manually only. A gross motorised rotation drive is provided to rotate the gratings between their operational position and an orientation normal to the incoming beam (for fundamental alignment checks). Both the grating and mirror mounts have coarse manual adjustment and a fine motorised adjustment on both tilt and rotation axes. The resolution of these adjustments is in the region of 10µrad. *Fig.2* shows the design of the vacuum isolation mount -this design incorporates a compensating bellows so that no change of load is experienced whether the CPA chamber is under vacuum or at atmospheric pressure. these bellows units are mounted on substantial steel support frameworks bolted to the common concrete floor plinth. A purpose designed gate valve with a window in the shutter plate is placed in the CPA beam line immediately infront of the target chamber to enable the CPA optics to be held under vacuum while work and alignment are carried out in the target chamber. A three position mirror remotely driven is positioned between the gratings to assist in grating alignment checks.

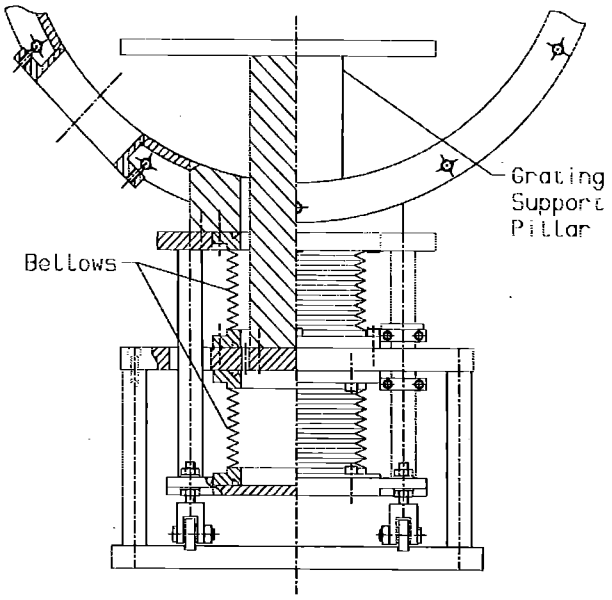

Fig. 2 Vacuum isolation mount.

FLEXURE MIRROR MOUNT

S Hancock

Rutherford Appleton Laboratory

INTRODUCTION

The optical configuration of Titania required input convex mirror's to expand the 9cm beam to maximise the extracted volume of the Titania amplifier, and output convex mirrors to re-collimate the beams at 16cm.

The input/output array was designed to be as compact as possible in order to fit into the optics bay and to minimise any vignetting of the off axis beams. The mirror sizes chosen being 11cm and 18cm, the spacing between mirrors being kept to a minimum.

BASIC DESIGN GEOMETRY

The mounts are required to be as close as possible to each other on the array. All the mirror supporting structure and the operation of the mount has to be carried out from behind the mirror. It is also very desirable that any mirror mount is adjusted about the reflective surface of the mirror to ensure that no aberrations take place.

It was therefore decided to base the design on a class of 4-bar linkage. Fig 1 shows the basic arrangement for the linkage which for a small change in angle "A" results in rotation of the coupler about the virtual pivot point. By arranging to mount the mirror from the coupler so that the front face is in line with the virtual pivot the mirror is adjusted about its reflective surface.

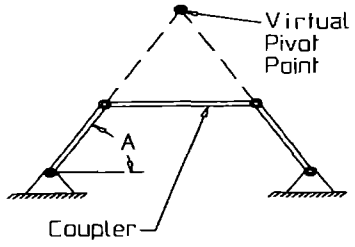

Fig 1

By mounting a second linkage assembly at right angles to the first and attached to the coupler on that assembly the second motion is achieved .This assembly is reversed so as to reduce the overall height by allowing one assembly to fit around and under the first assembly. Fig 2 shows the second linkage assembly.

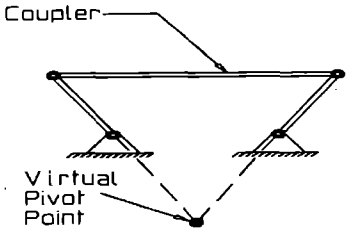

Fig 2

PHYSICAL DESIGN

With such a large number of pivot joints in the basic design it was essential to eliminate any friction in the operating of the mirrors. It was therefore decided that the pivots would have to take the form of flexures. Commercially available flexures are expensive, and require a large force to move them. They would also have required a substantial mounting system. Apart from allowing rotation to take place the pivot must also be a solid support structure for the mirror. Movement of the reflective surface should only take place when the adjustment screws are moved to direct the laser beam.

To achieve this two leaf springs one the full length of the pivot, with a narrow slot half its length machined about its centre. The second spring half as long, is assembled through the slot at right angles to the first spring to form a cross, which is then clamped to form the flexure. Thus allowing a partial rotation of the pivot, while still giving rigid support to the mirror.

The manufactured items of the assembly consist of three castings, four pivot blocks, eight spring assemblies, and thirty-two clamp bars. The base casting which bolts to the support structure of the array carries the horizontal adjusting screw. The intermediate casting is the coupler of the first linkage. The inverted base of the second linkage, and this casting also carries the reaction bar for the two adjusters. The third casting is the coupler for the second linkage and carries the vertical adjusting screw, pillars on this casting will be adjusted to allow for different mirror size's . The mirror will be mounted to this casting. Fig 3 shows a cutaway view of the mirror mount with a 11cm mirror fixed to the front.

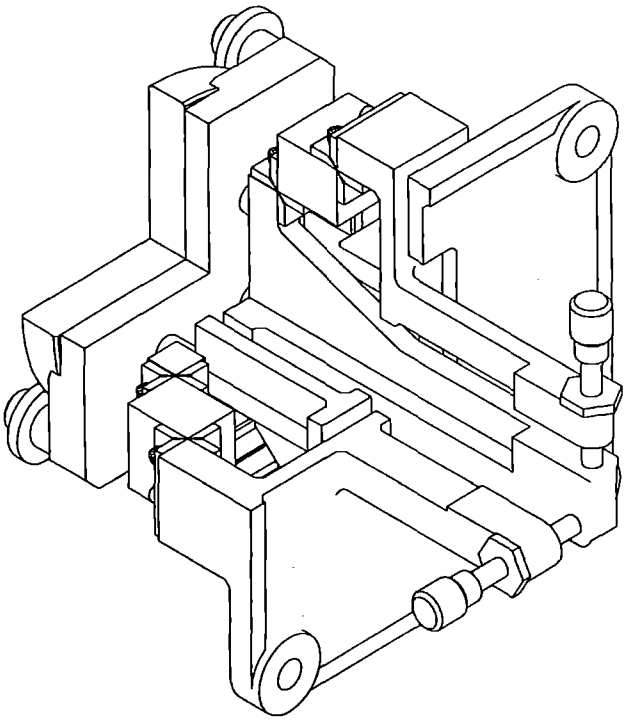

Fig 3

'COBWEB', A COMPUTERISED CONTROL SYSTEM TO SERVE THE GAS LASER, 'TITANIA'

C J Reason, E Divall, A Kidd, W Lester, D Spiller and M Pitts

Rutherford Appleton Laboratory

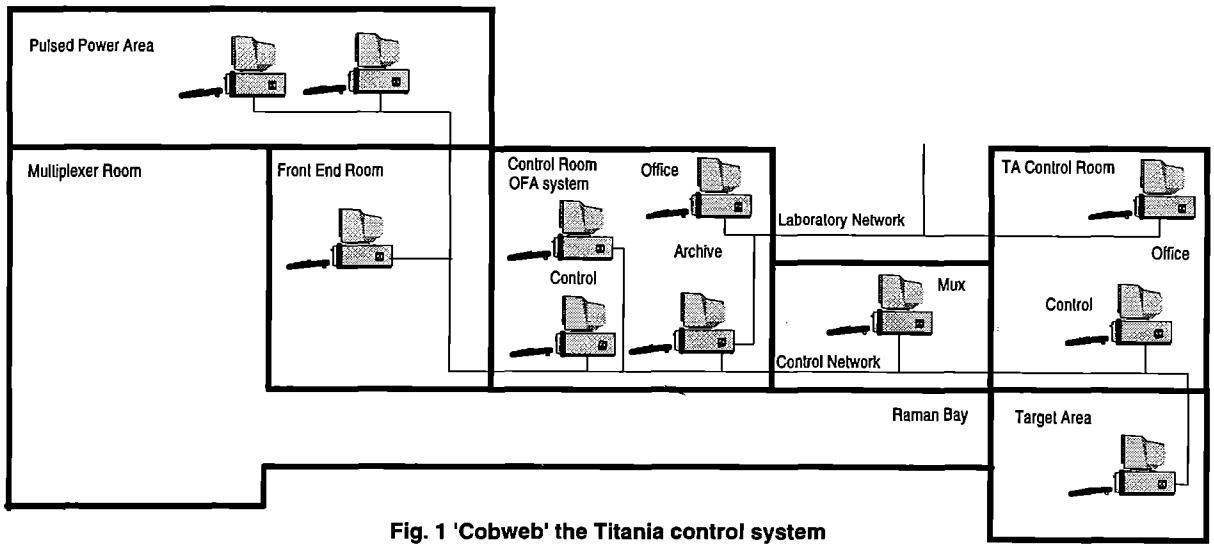

Fig. 1 'Cobweb' the Titania control system

The new gas laser system 'Titania' occupies seven rooms (See Fig. 1) In order to control all the component parts of the laser it was necessary to design a distributed control system with one or more computers in each area. The computer for the Multiplexer area is located outside the area to prevent air turbulence near the beams. It is no longer possible to fire the laser without the assistance of the at least one computer.

It was decided to base the control system on a number of PC's linked by an Ethernet system. The code was written in Turbo Pascal making use of Units to provide the common code on each control computer. Each computer would have a defined set of tasks using appropriate interfaces to control and interrogate the equipment in the particular area. The archiving and analysis computers run separate code.

The computerised interlock system 'Cerberus' is identical to the one used on the Sprite laser with only the tables changed to reflect the changes in the laser system.

The computers chosen for the control system are the laboratory standard Viglen PC's, chosen for their compatibility and reliability. As the control program is to run under DOS the memory requirements were not a problem and new machines were bought with 4 M bytes of memory and 500 M bytes of hard disk. The processor chosen was the most cost effective at the time of purchase and varies from a 33 MHz 486 to 120 MHz P5.

High resolution screens were purchased and new graphics cards installed to allow high resolution screen drivers (1024x768x256 colours) in Turbo Pascal.

A thin wire Ethernet was installed into all rooms in copper. If, in the light of experience, the network suffers from electrical noise pickup then fibre optics can be installed on specific runs. It is most unlikely that noise will be interpreted as a valid packet. More probably, any noise will destroy a valid packet which can be reissued. It was also designed that the network would be quiescent at the time of maximum noise generation.

All computers comprising the control system will sit on the control network and third party equipment computers can also be added to make their data available to the system. The network software is Novell Personal NetWare which makes hard disks and RAM disks available to other computers.

The laboratory network will be run into the control room and the target area control room so that office system computers can attach to it. The archiving computer will also be attached to the laboratory network via a second interface card, thus being attached to both networks. This makes the archive data available to the rest of the world but does not allow any other machine into the control network.

A number of specific cards are installed in computers as appropriate to provide the interface to equipment. Digital I/O is provided by Amplicon PC14AT and PC192 cards, relay control by Amplicon PC263 cards and Analog I/O by Amplicon PC30AT and PC226 cards. These control and read lines directly. The interface to oscilloscopes and Stanford Pulse Units is provided by a single GPIB interface (Amplicon CIO PC2A) and the units 'daisy chained' down a GPIB cable.

The whole control software was written from scratch in Borland Turbo Pascal Version 7, many units were written to deal with the networking between machines, external diagnostics and controls, the shot firing sequence and the graphical user interface.

The control software also incorporated basic code used for automatically pressurising the SF6 gaps and setting/reading the scopes from the old Sprite system. This was updated to give a graphical and more user friendly interface. The scope driving software was rewritten to give a library of commands which will allow any of our current digital scopes to be set-up, read and interchanged with minimum of effort..

Each section is housed in its own units with only key global variables and the graphical/mouse units being shared. The total program uses more than 40 units encompassing over 20000 lines

The emphasis through out the programming has been on a neat and user-friendly interface within the constraints of programming time (see Fig. 2). All panels and menus rely are mouse driven with limited use of the keyboard. To simplify the code and reduce re-compilation time each machine (bar one) runs identical software, with a just a basic initialisation file telling it which machine it is.

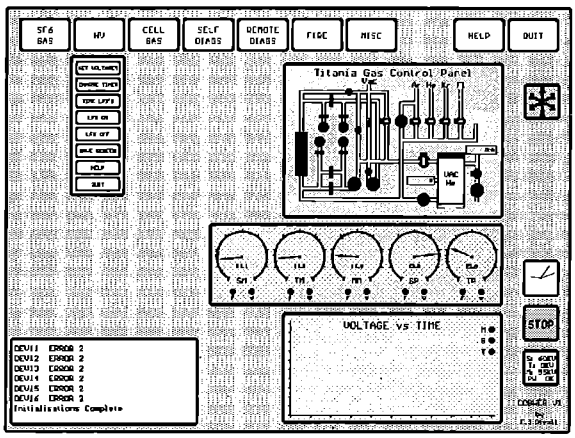

Fig. 2. Typical screen for the control system

The network communications was a new step for us and involved creating our own data transfer protocol to enable the different PC's to talk to one another. This involved setting a ram-drive on each machine containing a file of incoming messages. To send a message the file on the receiving machines' drive would be appended with the corresponding data, this data would then read and deleted by the receiving PC. This method requires careful timing and error checking to prevent the file being 'written to' while the receiver is checking it. Using this method a 'live scope' option was written to allow the operator to monitor and adjust scopes in other areas across the network. The addition of a ram-drive also enabled easy access to the extended memory for rapidly saving screen overlays.

The Pulsed Power Area was the most complex from the control view since the computer had to capable monitoring or controlling external devices on over 100 channels. The shot firing sequence was most involved since the computer initially sets the gas pressures and trigger lasers and arms the scopes. It then synchronises its self to the 8 Hz pulses from the front end room and uses them to derive a 1 Hz output for the trigger lasers and its timing pulses. Whilst remaining in synchronisation it starts each laser charging at the correct relative time so they reach full voltage together. During this charge period it must continuously check/adjust the gas pressures, monitor the charge voltages and relay this information to the control room. At the end of charge it initiates the pre-triggers, fires the lasers, informs the other machines that the shot is over and reads its own diagnostics.

The software is over 90% complete with some software functions still to be implemented. To speed and simplify communications between computers it is proposed to use direct application to application control, thus doing away with the message files. Other future developments include improving the scope software to use the full power of the scopes and a improved graphical display of other computers activities.

Following a Titania laser shot, experimental data is collected in a variety of formats from several sources in a Laboratory-based Archiver and Analysis System. Items stored are Numerical data (Shot number, date and time); digital oscilloscopes (Up to ninety digitised waveforms and associated scope set-up data per shot @ 8K per trace); joule meters (Laser beam energies); sensors on Titania (Gas pressures, charging voltages) and framestores images (of laser beam and parameters @ 260K/ image)

All of this data, which can amount to 1 Mb per shot, is downloaded from the networked PCs of the Titania laser system and stored (temporarily) on the hard drive of the Archiver PC. At the end of each experimental run, the data is transferred to CD ROM and deleted from the hard drives of all networked PCs.

The Archiver PC is responsible for the display and hard copy output of this data. All waveforms can be viewed and printed either individually or simultaneously. Measurements can be made of the waveform characteristics such as peak voltages, gradients, etc. (with a zoom facility for greater resolution).

A suite of analysis codes (pulsed power, electron beam energy deposition, kinetics, optical extraction) provide comparison with the experimental data.

In addition, the user can control the format of the data in the 'Preferences' option. The system is mouse-driven with an absolute minimum of keyboard input. On-line scrollable help is available from every screen in the system.

An office-based system has been developed which will enable users to have remote access via the laboratory network to up-to-date information regarding the status of the current experimental run. This is a Windows-based system written in the programming language Delphi which makes use of OLE (Object Linking and Embedding) and DDE (Dynamic Data Exchange) to link in spreadsheet programs (Microsoft Excel), data bases (Paradox, Access) and graphing packages (FXChart) to provide state-of-the-art visual display and statistical analysis of the archived data.

The office-based PCs collect their data from the Archiver PC via a client-server arrangement, or via the CD ROM relevant to the particular experiment. Up to 100 separate data items are stored in a relational database. Data from different shots can be compared enabling operational details of any experimental run to be continuously available. For example, the behaviour of the Titania output switches (peak voltages, gas pressures, etc.) can be monitored over a period of several hundred shots. Fig. 3 shows the data regarding diode voltage obtained from one of the Sprite pulsed power experiments for a particular shot.

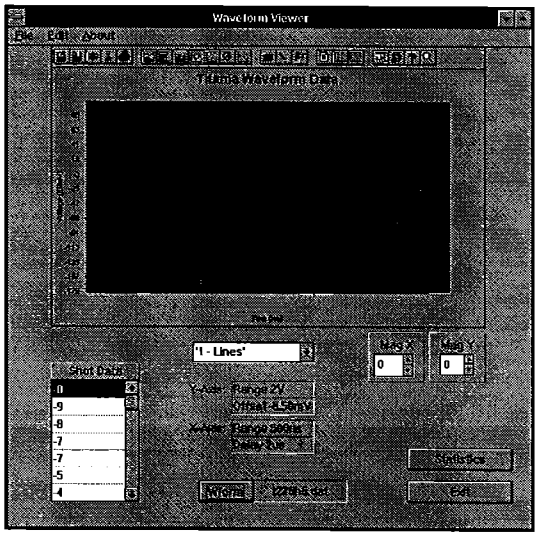

Fig. 3. Sprite amplifier diode voltage.

DEVELOPMENT OF GAS WINDOWS FOR RAMAN AMPLIFIERS

C J Hooker, J Butterworth, J M Dodson, T Hill, P Pickering
Rutherford Appleton Laboratory

INTRODUCTION

The windows of the final amplifier are probably the most highly-stressed optical components in a Raman amplifier chain, as they are required to transmit the full energy of the pumping laser. For efficient pumping the pump beams cannot be much larger than the Stokes beam, which is 150 mm in the Titania system, and the average pump fluence at the window of the final Raman amplifier is expected to be between 0.7 and 0.9 J cm^{-2}. The damage threshold of silica in the picosecond pulse regime is around 2 J cm^{-2}, and for comparison, the window fluence in the Sprite Raman system, in which no window damage was observed, was typically 0.3 J cm^{-2}. In practice, the window will be exposed to a complex interference pattern formed by the 20 pump beams, and from the statistics of such patterns it can be shown that over ~1% of the area, the fluence will be high enough to cause damage in ten shots. The damage will occur in many small spots distributed over the window, with the result that it will act as a weak diffuser. It is known that scatter in the pump and Stokes beams can seed the generation of second Stokes radiation [1], which even at very low levels can significantly reduce the efficiency of the amplifier. Consequently, the useful lifetime of a window is likely to be at most a few tens of shots, and repolishing will become a major part of the running cost of the laser. Alternatives to solid windows are therefore worth investigating.

BACKGROUND

The problem is to contain the Raman medium (methane gas) without a solid window which is liable to damage. If there were no windows at all, pure methane would rapidly escape, as it is far less dense than air. However, a mixture of gases containing some methane, made up to have the same density as air, would remain in place when the retaining shutters were withdrawn (Figure 1a), apart from diffusion and effects due to turbulence. In practice, to avoid any mixing of the methane with the laboratory air, or vice versa, there must be a separate region of inert gas between the methane mixture and the air (Figure 1b), with a shutter on either side. This region is the gas window, and it must also have the same density as air, although to avoid the risk of explosion it must not contain any oxygen. The window gas will be flushed away and replaced after each laser shot.

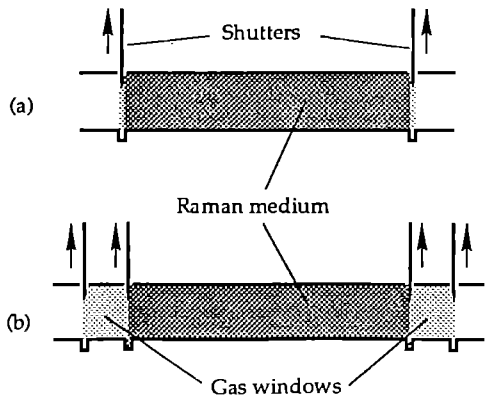

Figure 1. Illustrating the concept of gas windows.

A vertical interface between two fluids of different densities is unstable, so even the slightest density difference will cause the interface to move (Figure 2). Experiments in a water tank with a sliding partition showed that, after an initial acceleration, the speed of the 'tongues' of fluid becomes constant, depending only on the differential density $\Delta\rho/\rho$ between the fluids. In the Raman amplifier, a small amount of gas movement is acceptable, provided it does not cause a significant optical path difference between the top and bottom of the amplifier, and to achieve this the gas mixtures must have not only the same density but also the same refractive index as air. Calculations showed that two suitable mixtures with this property are a Raman medium containing 30% methane, 17.8% neon and 52.2% argon, and a window gas containing 76.9% nitrogen and 23.1% argon.

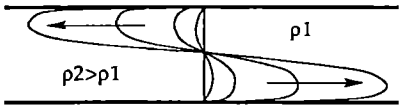

Figure 2. Movement of a vertical interface between two fluids.

The composition of cylinders of pre-mixed gases was stated by BOC to be accurate to ±0.1% of the minority constituent, which with the above mixtures results in a density range of ±0.07%. In the worst case, one would be high and the other low, leading to a density difference of 0.14% at the interface. A computer model of the interface was set up, and run with various values of density difference. With a $\Delta\rho/\rho$ of 0.14% the interface velocity was close to 1 cm s^{-1}, and combining this figure with the calculated differences in refractive indices, the time for a path difference of 0.2 wave (at 268 nm) to develop across the 16 cm aperture of the Raman amplifier would be about 5 seconds in the worst case, and this is ample time to open the shutters and fire the laser.

EXPERIMENTS

To gain practical experience of the operation of a gas window and to confirm the computer predictions, a full-sized test rig was built, shown schematically in Figure 3. It consists of a 16 cm square tube made of Perspex, 80 cm long, with one end closed by an optically parallel window, and the other open. The shutter is placed in the middle of the tube. The shutter blade is a sheet of 1 mm thick stainless steel, which slides in a channel formed by the two sides of its housing. No attempt was made to seal the edges of the shutter, as there is no pressure difference between the two sides, and the depth of the channel and the narrow clearance provide an adequate barrier to diffusion. The shutter is raised and lowered by a pneumatic cylinder, whose speed is controlled by a reduction valve on its gas supply. To set up a density difference between the two sides of the shutter, methanol vapour is added to the air in the closed end of the rig, a volume of 0.35 cm^3 of liquid methanol producing a $\Delta\rho/\rho$ of 0.2% when added to the 11 litres of air in the enclosed volume. The methanol is evaporated in a warmed beaker, fitted with a plunger having a pipe connected to the rig. Once the methanol has evaporated, the air in the beaker can be transferred into the rig by depressing the plunger. The displaced air escapes through another valve, which is then closed.

Establishing the exact concentration of methanol was difficult, as both the plunger of the beaker and the Perspex walls of the chamber gradually absorb methanol, and there was a small un-transferred volume in the beaker and the pipe. A meter used for monitoring the concentration of methanol vapour in the air of the room was placed inside the chamber, and used to calibrate the concentrations produced by evaporating different volumes of

liquid. Standardising the procedures for adding the methanol allowed fairly consistent concentrations of vapour to be obtained.

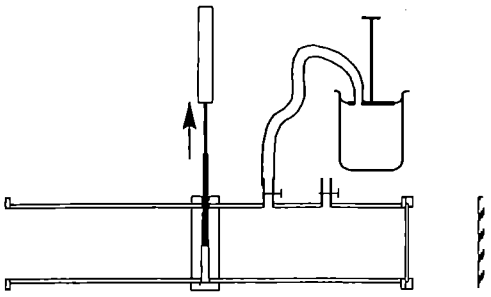

Figure 3. Schematic of the gas-window test rig.

As there is no means of colouring gases to see their movement, it was decided to visualise the gas flow using interferometry, which also permits quantitative measurements of the optical path difference. The apparatus was positioned in the beam of the Zygo interferometer, with the reference flat placed behind the window at the closed end and adjusted to give from five to ten horizontal fringes across the aperture. By measuring the changes in the fringe pattern after the shutter is withdrawn, the speed of movement of the gas can be determined, and the effects of turbulence caused by the shutter itself evaluated. It proved necessary to isolate the rig from the interferometer table, as the movement of the shutter caused enough vibration to blur out the fringes, and the open end of the tube had to be thoroughly shielded from stray air currents before reproducible results could be obtained. Once these precautions had been taken, fringe patterns consistent with the expected type of gas movement (Figure 2) were observed. An example is shown in Figure 4.

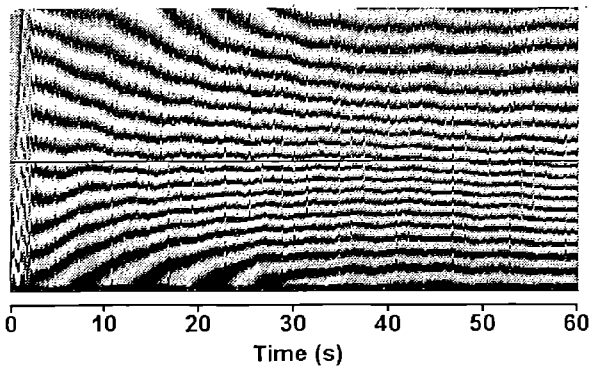

Figure 4. Time variation of the fringe pattern across the aperture of the rig, due to gas movement driven by density differences.

The interferometer frame store was set to repeatedly sample a vertical section of the fringe pattern at the centre of the aperture at intervals of 120 milliseconds. The resulting image (figure 4) shows the fringe positions as a function of time over a period of sixty seconds. In the first two seconds, the shadow of the shutter can be seen as it is raised. Just after that, there is a loss of contrast as the interferometer table vibrated, due to the shutter hitting the stop at the top of its motion. About three seconds after the shutter starts to open, the initial fringe pattern stabilises, with fringes uniformly spaced across the aperture. The increasing gradient of optical path difference (opd) caused by the movement of the gas is shown by the convergence of the fringes (the opd gradient is proportional to the reciprocal of the fringe spacing), and by the appearance of new fringes at the edges of the plot. There is a neutral point near the centre of the aperture (indicated by the horizontal line) where the actual opd does not change significantly. At about t=40 seconds the tongues of gas reach the ends of the rig and new fringes cease to appear because the opd is no longer changing. As the denser gas starts to pour out of the open end of the apparatus, the neutral point drops towards the bottom of the rig, and the corresponding fringe begins to move.

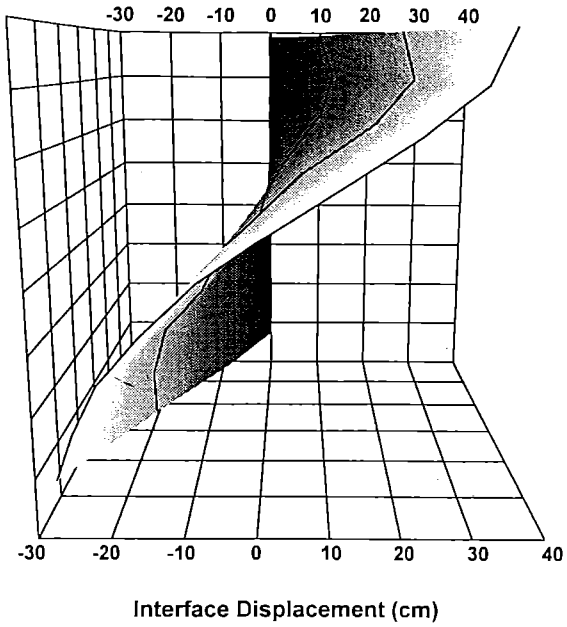

Figure 5. Gas interface movement as determined from Figure 4.

Provided the refractive index of the air containing the methanol vapour is known, the changes in opd measured from the fringes can be used to find how far the interface has moved, and hence deduce its speed. Figure 5 is a 3-D representation of the interface movement during the first thirty seconds of the fringe pattern in Figure 4. The vertical coordinate is distance across the aperture, and time runs from back to front (grid lines are at 5 second intervals). The speed of the interface in this example is 1 cm s^{-1} for a density difference of 0.2% between the two gases, which is rather less than the model prediction of 1.46 cm s^{-1}. The discrepancy may be due to the uncertainty (noted earlier) in the density of the air containing the methanol vapour, but generally the behaviour seems to be as predicted by the code model.

Changes in humidity and temperature will affect the density of the air outside the amplifier. Provided the gas in the amplifier is at the same temperature as the air, the density difference across the interface will not be affected, but variations of air density with humidity, on the other hand, will not be compensated by changes in the Raman gases, and may lead to unacceptably large density differences across the gas interface. At 20°C, the difference in density between air with relative humidities of 30% and 60% (a reasonable range for an indoor environment) is close to 0.5%, i.e. ±0.25% from the average. If an excursion in humidity occurred in conjunction with a worst-case density difference between the gas mixtures, the interface might move between two and three times faster than expected, and the opd after 5 seconds would be around 0.5 wave. In practice, this is probably still acceptable for most experiments, though some form of humidity control in the multiplexer area would help to minimise the effects.

REFERENCES

1. C J Hooker et al, Phys. Rev. Letters **74**, 4197 (May 1995)

A HIGH GAIN MULTIPASS TITANIUM SAPPHIRE AMPLIFIER

I.N.Ross, E J Divall and J.M.D.Lister

Rutherford Appleton Laboratory

INTRODUCTION

Titanium sapphire (TiS) has rapidly become the preferred laser material in many types of laser system, from cw to femtosecond, from single frequency to very broadband and tuneable frequency and from low to extremely high power. Many of these systems require a high level of amplification, in some cases from nanojoules up to 100 mJ and more. Generally because of the large overall gain required, regenerative amplifiers have been used. In many cases however, multipass amplifiers would be preferred because they have less amplified spontaneous emission (ASE), spectral narrowing, self focusing and group velocity dispersion (GVD), but their use has been deterred by an expectation that they are optically complex and are difficult to align and maintain in alignment. We have looked to optimise the design of multipass amplifiers with a view to making them as simple, compact and stable as possible whilst providing a large number of passes to give high overall gain and maximum output power. The principles of the resulting design are of course applicable to a wide range of multipass applications, but have been applied specifically to TiS in the context of the front end driver at 745nm for the TITANIA KrF laser system.

OPTICAL DESIGN

A design of multipass amplifier was sought which provided the TITANIA requirement of at least 6 passes with as simple as possible a geometry and specifically it should minimise the number of mirrors (for maximum stability) and use as far as possible common optics for different passes. A further requirement was to not use image relaying optics from pass to pass which restricts the beams size and hence the achievable output energy and power.

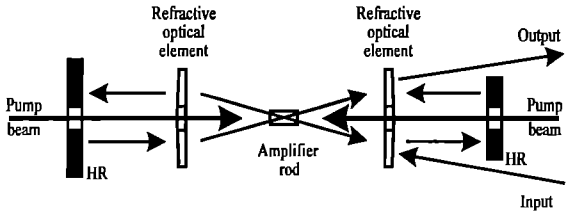

Figure1: Concept for simple multi-pass amplifier

It was found that an optical arrangement as shown schematically in Figure 1 can meet the above requirements and can provide a different number of passes dependent on the specific design of the refractive elements. These schemes have just two flat mirrors both normal to the axis, have a large degree of axial symmetry with all passes at a fixed angle to the axis and can provide for two ended axial pumping of the amplifier rod. Because the designs are compact and can be scaled according to the required beam size there is no need for image relaying within the multipass arrangement.

TITANIA SCHEME

The selected scheme for the TITANIA front end is the 8 pass scheme shown in Figure 2. Each refracting element in this case is a double biprism (realised by working mutually orthogonal biprisms on opposite faces of a silica flat). The two double biprisms are mutually orientated at 45 degrees. Such a scheme allows a circulatory beam within the resonator which returns to its starting point every 8 passes and would repeat the sequence if a modification is not made to allow a beam to be input for the first pass and output again after the eighth pass. In the TITANIA design the selected modification is to cut a slice off one of the double biprisms so that a beam injected onto the nearest end mirror at the correct position and direction will emerge after 8 passes reflected at a different position and direction from this same mirror. Axial holes in all optical elements allowed the passage of pump beams to the TiS rod.

GEOMETRICAL DESIGN

The values of the biprism angles and the spatial dimensions are determined by the required angle to the axis of each beam at the amplifier rod, by the beam size and by the separation of the beams at the biprisms on different passes. The TITANIA design led to a beam angle of 4.3 degrees to the axis (external to the amplifier rod) giving a lateral shear of 0.15 mm between amplified and pump beams at the rod ends, and hence required an angle of 17.6° between the faces of each biprism. The design also called for a beam size of ϕ3 mm on the final pass and for convenience the beam separation at the biprisms was specified to be > 10 mm. In the actual design the rod to biprism distance was 200 mm (giving a beam separation of 11.6 mm at the biprism) and the biprism to mirror distance 142 mm. Thus the mirror separation was 684 mm and the total path length for 8 passes was 5.47m, well within the maximum allowable distance of 27m for propagation of a Gaussian beam of Ø3 mm FWHM.

ALIGNMENT PROCEDURE

The following procedure was adopted for setting up and aligning the multipass amplifier.

i) All components were mounted at the correct separations and centred on a HeNe laser beam (which passed through the rod and element axis holes). Double biprisms were set mechanically at an azimuth angle of 45° to each other.

ii) Using clamped straight edges, both mirrors were translated sideways until the beam passed through the mirror surfaces.

iii) The HeNe was re-centred on the biprisms and rod.

iv) Both mirrors were normalised to the HeNe and translated back to their centred positions.

v) The signal beam was injected off the appropriate end mirror at a position and direction to pass through the rod on the first and second passes. Fine tuning of these same adjustments using an infrared viewer to observe the spots on the double biprisms gave some signal on a detector after the full 8 passes.

vi) Fine tuning of the end mirrors is carried out to maximise the output signal.

vii) Further fine tuning is carried out with an aperture of ~ Ø3 mm placed as close as possible to the TiS rod.

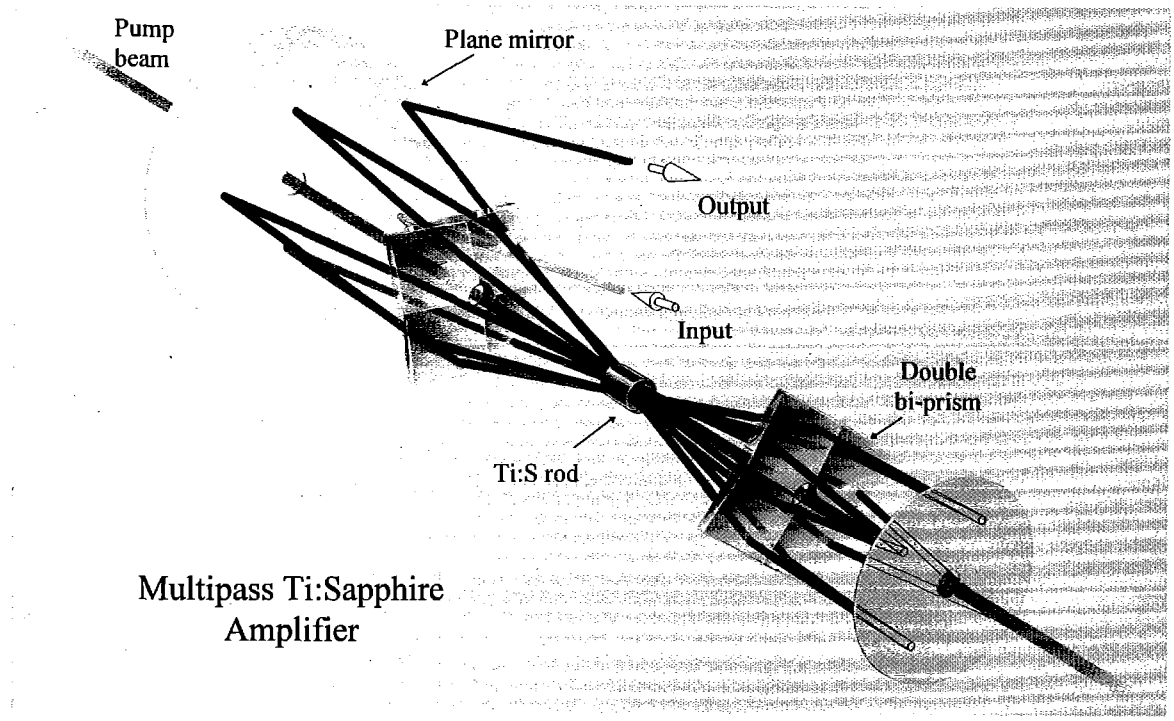

Figure 2: TITANIA 8-pass Ti:Sapphire amplifier

AMPLIFICATION DESIGN

The TiS multipass amplifier is required to amplify from a few μJ to 50 mJ a pulse of ≥50 ps at a wavelength of 745 nm. Taking into account some saturation of amplifier gain, the total small signal gain is $\approx 10^5$ giving a single pass round trip gain of 4.2. Assuming a 90% absorption of the pump beam and a round trip loss of 10%, the pump beam fluence at each end of the rod should be $\approx 1.3 J/cm^2$, or 165 mJ at each end, pumping an area of Ø4 mm.

OPTICS ISSUES

a) B-Integral.

The total B-integral in the TiS amplifier must be very small since it is part of a system with other contributions to the B-integral. An acceptable maximum value may be taken to be 0.5. The total B-Integral = $0.023 \int I\, dl$ for TiS. For the above design, taking into account the amplifier saturation and for a 50 mJ output pulse of duration 50 ps: B = 0.23, well within the specified maximum value.

b) Output Intensity and Fluence.

These are calculated for 50 mJ and 50 ps to be 14 GW/cm^2 and $0.7 J/cm^2$ respectively and are compatible with good harmonic conversion efficiency in the third harmonic generator and with the damage resistance of beam optics.

c) Dispersion and Group Velocity Dispersion (GVD)

For short pulse operation of TITANIA using chirped pulse amplification it is important not to exceed acceptable amounts of dispersion due to prism effects which will result in a pulse front tilt on the recompressed pulse or an acceptable level of group velocity dispersion which will introduce incompressible non-linear chirp onto the beam. Residual dispersion from the multipass TiS amplifier arises from the slightly wedged TiS rod and from the residual uncompensated prism effects due to the beam not passing through one double biprism on its first and final passes.

With a rod wedge of 15 minutes the pulse front tilt due to the TiS rod is 7.5 fs while that of the double biprisms is 48 fs. This pulse front tilt can of course be cancelled by use of a compensating prism.

The total GVD chirp due to passage through the TiS rod and double biprisms is calculated to be 1.15 fs/cm^{-1} giving rise to a change in stretched pulse duration of 172 fs for a 150 cm^{-1} bandwidth pulse of which the non-linear (and hence incompressible) component is estimated to be < 1 fs.

d) Parasitics

The dimensions of the TiS rod (Ø6 mm x 7 mm) and its high index give very high reflective coupling of ASE back into the rod and hence result in the gain being clamped at a very low level unless the reflectivity of the internal reflections is reduced substantially. This can be achieved by using an absorber wrapped around the rod with as good an index matched coupling to the rod as possible. An index of > 1.5 proved sufficiently close to that of the TiS to enable the required gain to be generated.

AMPLIFIER PERFORMANCE

A schematic of the TITANIA front end amplification stages is shown in Figure 3. The multipass TiS amplifier is pumped by up to 500 mJ total from a frequency doubled Q-switched Nd:YAG laser (Continuum). Good pump beam uniformity was achieved by imaging the pump laser nearfield into the TiS crystal. A dye preamplifier enabled the injection of pulses of a few μJ into the TiS amplifier. Small signal gain measurements were conducted with this dye amplifier turned off. The injected beam was passed through a diffraction limited spatial filter to ensure a smooth near Gaussian profile and transmitted through a lens to give a sub-millimetre focal point in the second amplification pass and an output beam size of 2 to 3 mm after the 8th pass.

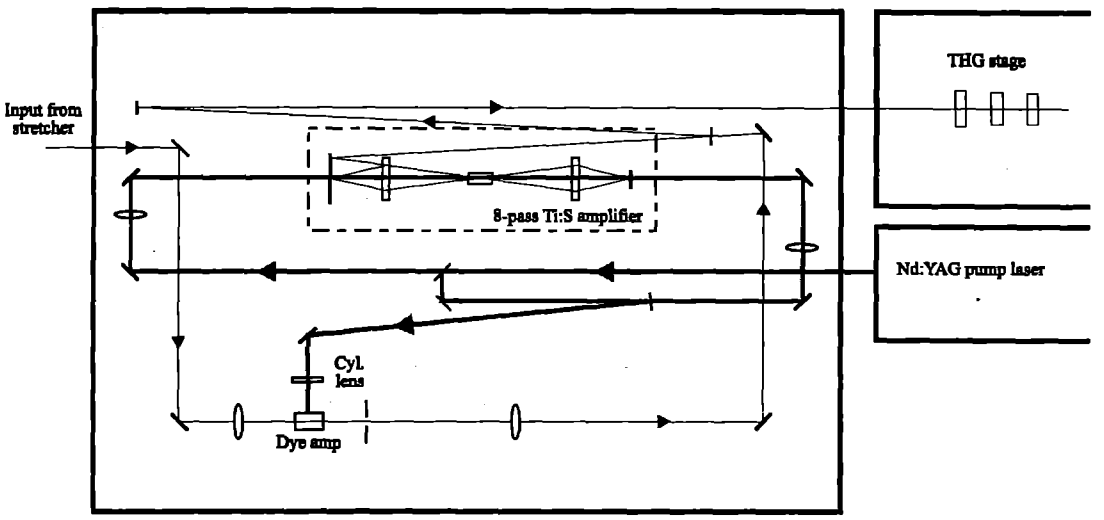

Figure 3: Schematic of the TITANIA front end amplifier system

The measured small signal gain is shown in Figure 4 as a function of the pump energy showing that the amplifier reached its specified gain of 10^5 at a pump energy of 350 mJ. The lower curve shows the steady state gain at an 8 Hz pump prf, somewhat less than the single shot values. This is not fully understood but is shown to be due to thermal effects by virtue of the few seconds required to arrive at the steady state gain value. However it is not a serious problem at the specified gain of 10^5. The achievement of small signal gains as high as 10^7 show that the surface absorber has effectively suppressed the gain clamping due to parasitic oscillation.

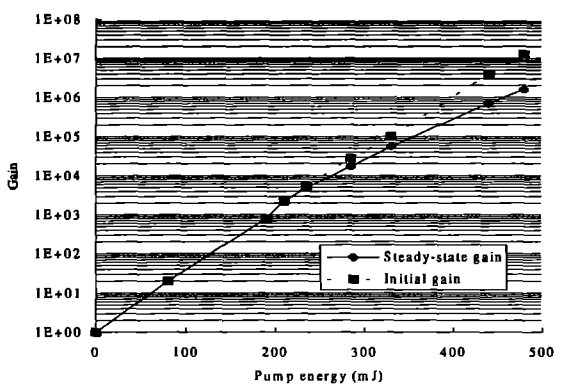

Figure 4: 8-pass amplifier gain as function of absorbed pump energy

Using input pulses of a few μJ, output pulses were amplified up to more than 20 mJ. Further capacity for increase was available but the system is currently limited to this value by a low damage threshold on the output mirror. The near diffraction limited optical quality of the amplified beam is demonstrated in Figure 5 which plots the profile of the third harmonic at 249 nm generated from it.

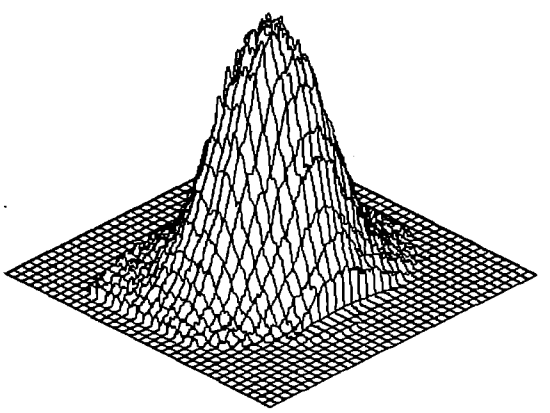

Figure 5: 3D plot of third harmonic beam profile

CONCLUSION

A novel compact 8-pass TiS amplifier has been designed, built and tested and is in continuous use as part of the front end of TITANIA. It meets its design criteria in terms of gain and output energy, has demonstrated good alignment stability and provides good quality beams at the third harmonic for injection into the KrF laser.

MEASUREMENT OF THE TEMPORAL CONTRAST AND PULSE DURATION ON TITANIA CPA THEORY AND PRELIMINARY RESULTS

K Osvay*, I N Ross, J M D Lister and C J Hooker

Central Laser Facility, Rutherford Appleton Laboratory
*On leave from JATE University, Szeged, Hungary

1. INTRODUCTION

Beside energy, pulse duration, far- and near-field distributions, one of the most important parameters of a laser pulse is the so called contrast ratio which gives a measure of how far in time and intensity the main pulse can be regarded to be free of pre- or postpulses as well as the level of amplified spontaneous emission (ASE). Since a solid target can be seriously damaged or even vaporised with an intensity of 10^{10} W/cm^2, in the case of a high power laser producing 10^{19} W/cm^2 focused intensity, the pre-pulse should be down at the 10^{-9} level.

Our aim was to find a suitable process and implement an experimental technique for measurement of the contrast ratio of ultrashort UV pulses, that (i) has a dynamic range of $\geq 10^7$; (ii) operates with input pulse energies as low as 5-10 μJ; (iii) can easily be modified to single-shot operation and (iv) is simple. Among several possibilities considered (phase conjugation, stimulated Raman generation, etc.) the scheme of difference frequency generation seemed to offer the best compromise.

2. THEORY

The basic concept of the measurement is to mix the long KrF pulse at 248.3 (expected to be ≈250 fs with residual stretched pulse structure over ≈50 ps) in a nonlinear crystal with the short fundamental pulse at 744.9 nm (<150 fs). Measuring then the energy of the resulting difference frequency signal at 372.5 nm as a function of the delay τ of the fundamental pulse, the curve of second-order cross correlation can be recorded. Knowing the shape of the fundamental pulse, the temporal shape and contrast of the KrF pulse can be obtained.

2.1 Generation of difference frequency (DF)

Because the interacting fields have relatively broad band spectra, the mathematical treatment needs to take into account the effect of group velocity mismatch in the mixing crystal. Thus, the input fields (1 and 2) and the generated difference frequency output field (d) can be written in the form [1]

$$E_j(z,t) = E_j^0 \cdot f_j(t - \hat{k}_j z) \cdot \exp\left[i\omega_j(t - \hat{k}_j z)\right] \qquad (1)$$

where f_j and $\hat{k}_j = dk_j/d\omega_j$ (j=1,2,d) are the temporal envelopes and the reciprocal group velocities, respectively. The envelope of the generated field at $\omega_d=\omega_2-\omega_1$ is

$$f_d(t,L,\tau) = \sqrt{2\pi}\cdot e^{-i\omega_2\tau}\int d\omega' e^{i\omega' t}\int d\omega' F_1(\omega'-\omega'') \times F_2(\omega'') e^{-i\omega''\tau} e^{i\Delta k_{eff} L/2}\cdot \mathrm{sinc}\left(\Delta k_{eff} L/2\right) \qquad (2)$$

which is a resolution of the wave equations of non-linear polarization at the end of a crystal of L length. Here $F_j(\omega)$ is the Fourier-transform of $f_j(t)$, $\Delta k=|k_d-(k_2-k_1)|$ is the phase mismatch, $\Delta\hat{k}_{d1} = \hat{k}_d - \hat{k}_1$ and $\Delta\hat{k}_{21} = \hat{k}_2 - \hat{k}_1$ are the group velocity mismatches, and $\Delta k_{eff} = \Delta k + \Delta\hat{k}_{d1}\omega' + \Delta\hat{k}_{21}\omega''$.

2.2 Cross Correlation

At the low conversion efficiency approximation, the cross correlated energy density is obtained from (2) as

$$\mathcal{E}_{cc}(\tau) = \int_{-\infty}^{\infty} (C_0 L)^2 \cdot \left|f_d(t,L,\tau)\right|^2 dt \qquad (3)$$

where C_0 is the constant determined by the crystal, the interacting frequencies and the peak power of the generating field.

From the integration of eq.3 the temporal properties of E_{cc} can be derived. In the following, the duration (intensity FWHM) of the pulses *1*, *2* and *d* are denoted by Δt_1, Δt_2 and Δt_d respectively, while Δt_{cc} is the temporal FWHM of the cross correlation curve. Since the phase mismatch can experimentally be made very small, Δk=0 is assumed in all cases.

2.2.1 Zero group velocity mismatches ($\Delta\hat{k}_{d1}L=0$, $\Delta\hat{k}_{21}L=0$):

$$\Delta t_{cc} = \left(\Delta t_1^p + \Delta t_2^p\right)^{1/p} \qquad (4)$$

where p=2 and 1.615 for Gaussian and sech^2 pulses, respectively. That is, if $\Delta t_i \gg \Delta t_j$ then $\Delta t_{CC} \approx \Delta t_i$.

2.2.2 Zero fundamental group velocity mismatch ($\Delta\hat{k}_{21}L=0$)

Compared to eq.5, Δt_{cc} varies very little (typically a few percent) with $0 < \Delta\hat{k}_{d1}L < \infty$.

2.2.3 Zero group velocity mismatch between the generated and the pump pulse ($\Delta\hat{k}_{d1}L=0$)

α. $\lim_{\Delta\hat{k}_{21}L\to 0} \mathcal{E}_{cc}(\tau)$ = the case 2.2.1

β. $\lim_{\Delta\hat{k}_{21}L\to \infty} \mathcal{E}_{cc}(\tau) \Rightarrow \Delta t_{cc} \approx \Delta\hat{k}_{21}L$

γ. $\lim_{\Delta t_2/\Delta t_1\to \infty} \mathcal{E}_{cc}(\tau) \Rightarrow \Delta t_{cc} \approx \Delta t_2$

Thus, the theoretical investigation can conclude that the temporal shape of the resulting cross correlated energy density is very close to the long pulse shape for $\Delta t_2 > \Delta t_1$. This statement is also valid for small amounts of group velocity mismatch.

3. EXPERIMENTAL

3.1 Setup

Because of the demanding requiremets, care was required in designing the cross correlator. In particular the type and optimum length of crystal as well as the choice of lenses depended not only the spectral bandwidth of the generating pulses, the beam divergence [2], the two photon absorption, the self phase modulation [3-4] and the damage threshold of the nonlinear crystals [5], but also the features of optimal focusing of femtosecond pulses [6].

The schematic of the multiple shot cross correlator can be seen in Fig.1. The generating pulse at 745 nm originates directly from the TITANIA oscillator: 16 % of the main beam is split off before the stretcher. This 745 pulse is delayed appropriately and amplified in two dye cells, filled with Rhodamine 700 of 0.24 g/l and 0.1 g/l, respectively and pumped by 15 % of the pump laser for the main stretched beam preamplifiers. The energy of the amplified pulses is typically 100 μJ with an ASE content less than 1:500.

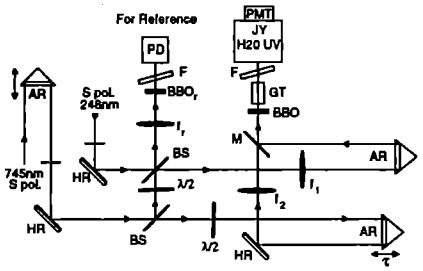

Figure 1: The layout of the multiple-shot cross correlator

The incoming KrF (Ø=3 mm) and 745 (Ø=7 mm) beams are focused onto a type I BBO crystal of a length L=0.6 mm by spherical lenses with focal lengths f_1=500 mm and f_2=300 mm, respectively. The 8 Hz repetition-rate DF signal is detected by a photomultiplier. To achieve the highest signal-to-noise ratio, three filtering steps are applied: a monochromator and a BG39 filter (F) to completely reject the generating pulses as well as the background light and a Glan-Thompson prism (GT) to reject the non-phase-matched S-polarised second harmonic signal generated by the 745 beam in favour of the P-polarised DF (the polarisation contrast is 1:66).

3.2 Preliminary results

The first measurements have been carried out in the TITANIA front end room. The KrF pulse to be measured was split off (about 9 %) from the beam of the stretched seed pulse for TITANIA and compressed in a four-pass single-grating compressor. The energy of the KrF pulse at the entrance of the correlator was measured to be 5-10 μJ. A typical scan is shown in Fig.2. Each dot is an average of ≈120 shots. The prepulses are probably due to internal reflections in the BBO crystal while the very broad pedestal suggests that the stretcher of the main beam and the compressor of the KrF beam do not match very well. The achieved contrast ratio is 4×10^{-7}. The lower limit is that of the residual non-phasematched second harmonic of the 745 beam which in fact just exceeds the noise level by 20%. The upper limit is the peak power of the KrF pulse, that will of course be higher for the output of TITANIA.

The exact shape and duration of the main peak cannot exactly be obtained from the above contrast measurement because of the very high saturation of the PMT tube above the 10^{-2} level on Fig.2. For this the DF signal needs to be substantially reduced. Figure 3.a and b show a scan with an ND=2 filter between BBO and GT, and the spectrum, respectively. The spectrum is asymmetrical ($\Delta\lambda$=0.58 nm) and the spikes may arise from an etalon-type effect. The temporal shape of the KrF pulse is also asymmetrical (Δt=0.94 ps). As suggested by the contrast measurement the pulse is not compressed to the transform limit.

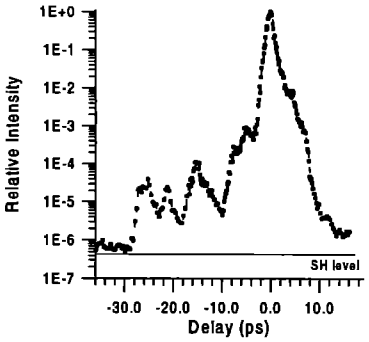

Figure 2. Contrast ratio measurement of the TITANIA seed pulse at 248 nm.

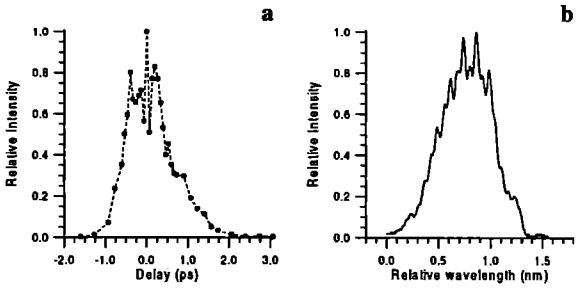

Figure 3. The detailed temporal shape (a) and the corresponding spectrum (b) of the KrF pulse

4. SINGLE-SHOT MEASUREMENTS ON TITANIA

The measurements on the TITANIA output will be done in the multiplexer room. The KrF pulse for the cross correlator will be a few percent of the diagnostic beam split off from the compressed pulse of TITANIA. The 745 beam generated as described above will be delivered in a closed beam pipe along the wall and delayed in a 16-pass delay line in order to compensate for the optical path of the KrF beam in TITANIA.

The modification of the cross correlator for single-shot measurements has two requirements. One has a smaller time window (2.1 ps) for which the temporal shape of the main KrF pulse (i.e. the duration) can be recorded while for the other the pulse stucture (i.e. the contrast ratio) is to be measured by scanning with the larger time window (8.5 ps). The time-windows are introduced along a line focus by use of pulse front tilts from a prism and a grating, respectively.

5. REFERENCES

[1] A P Baronavski et al., IEEE **QE-29** (1993) 2980
[2] A Penzkofer et al, Appl.Phys.B **47** (1988) 71
[3] I N Ross et al, J.Mod.Optics **37** (1990) 555
[4] C J Hooker et al, Opt.Comm. **103** (1993) 153
[5] Laser Handbook Vol.5
[6] Z L Horváth et al, Opt.Comm. **108** (1994) 333

EFFICIENT BROADBAND SUM FREQUENCY GENERATION USING CHIRPED PULSES

K Osvay and I N Ross

Central Laser Facility, Rutherford Appleton Laboratory
*On leave from JATE University, Szeged, Hungary

1. INTRODUCTION

Much recent interest in the development of lasers has centred around the generation of very broad spectral bandwidth pulses, either because this is required for ultrashort pulses or because it is demanded by the application physics. The main limitation to efficient broad bandwidth frequency conversion originates from the dispersion of the non-linear crystal [1]. For TITANIA, pulses of bandwidth 150 cm^{-1} (corresponding to Gaussian pulse of ≈100 fs) must be efficiently produced by the third harmonic generator. Because this bandwidth requires the third harmonic crystal to be ≤0.25 mm thick for the conventional design the overall conversion efficiency is power limited to ~2 %. To overcome such sever restrictions on efficiency various techniques have been developed [2-5].

In this paper an alternative technique is proposed in which the generating beams to be mixed in the nonlinear material are chirped at different chirp rates such that the phase matching condition can be met at all times.

2. THEORY

The principal of the scheme is demonstrated in Figure 1. The phase-matching condition is satisfied, at some angle in the nonlinear medium, for the central frequencies of the generating beams (ω_1^0 and ω_2^0) and sum frequency beam (ω_s^0). Then for a frequency offset at the sum frequency there can be found a pair of frequencies $\omega_{1,2}^-$ and $\omega_{1,2}^+$ in the generating beams which are also phase matched at the same crystal angle. If the sum frequency has its frequency varying linearly with time (chirped) there are corresponding chirps on both generating beams for which the phase matching condition is met over the full bandwidth.

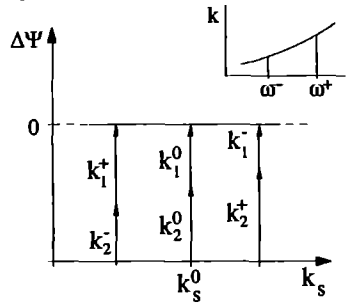

Figure 1. The phase matching condition for the proposed new frequency conversion scheme.

For the analytical description we consider a collinear Type I mixing process, where the well collimated generating ordinary $\omega_1<\omega_2$ waves propagating in z direction produce the generated extraordinary ω_s wave. Following from the general solution of the coupled wave equations in a nonlinear crystal, the mismatches

affecting the efficiency, and hence the bandwidth of the frequency conversion, can be described by the total phase mismatch of the process

$$\Delta\psi(t,z) = \psi_s(t,z) - \psi_1(t,z) - \psi_2(t,z), \qquad (1)$$

where

$$\psi_i(t,z) = \omega_i t + k_i z .$$

For perfect generation $\Delta\psi=0$ should be satisfied in time and in space simultaneously, that is

$$\omega_s(t) = \omega_1(t) + \omega_2(t), \quad k_s(z) = k_1(z) + k_2(z). \qquad (2)$$

To consider the more general case of broad bandwidth pulses, the frequencies are assumed varying with time while the wave vectors change in space. Expanding them into series, the equations following from the time and space dependence of $\Delta\psi$ in eq.(1) are

$$\omega_{s0} = \omega_{10} + \omega_{20}, \quad \beta_s = \beta_1 + \beta_2 \qquad (3)$$

and

$$k_{s0} = k_{10} + k_{20}, \quad k'_{s0}\beta_s = k'_{10}\beta_1 + k'_{20}\beta_2 \qquad (4)$$

respectivelly, where β_i is the linear chirp parameter defined by $\omega_i=\omega_{i0}+\beta_i t$, $\omega_{i0}=\omega_i(t=0)$ and k'_{i0} is the reciprocal group velocity at ω_{i0}. Note, that eq.(3.a) and (4.a) give the ordinary phase matching condition and determine the phase matching angle. The solution of eq.(3.b) and (4.b) at the phase matching angle gives the first order compensation, that is

$$\beta_1 = \left(1 - \frac{\Delta k'_{s1}}{\Delta k'_{21}}\right)\beta_s = A_1\beta_s, \quad \beta_2 = \frac{\Delta k'_{s1}}{\Delta k'_{21}}\beta_s = A_2\beta_s \qquad (5)$$

where $\Delta k'_{21} = k'_{20} - k'_{10}$ and $\Delta k'_{s1} = k'_{s0} - k'_{10}$ are the reciprocal group velocity mismatches between the generating and generated waves. This solution is in full agreement with the qualitative physical picture described above. Eq.(5) means that (i) the requirement of first order compensation can be fulfilled by introducing linear chirp (β_1, β_2) into the initial fields, so it can be interpreted as *chirp-assisted group velocity matching* (CGV); (ii) the ratio of these necessary chirps is determined by the group velocities of the generating and generated waves.

Assuming perfect CGV matching, the residual total phase mismatch due to second order effects (add second order terms to eq.(1)-(2)) at the end of a crystal of length L is

$$\Delta\psi^{CGV} = \frac{\beta_s^2 L^3}{2c^2}\Delta k'' \qquad (6)$$

where $\Delta k'' = k''_{s0} - A_1^2 k''_{10} - A_2^2 k''_{20}$ and k''_{i0} is the group velocity dispersion at ω_{i0}. Equation (6) is exactly what could be expected, namely that upon propagation through the crystal there is a residual phase mismatch due to uncompensated group velocity dispersion.

The chirp of the generated field seems to be arbitrary. It can be shown, however, that β_s has an optimum value determined by group velocity dispersion [6] through eq.(6) as well as by the need for high conversion efficiency [7].

3. RESULTS

The calculations presented are made for a frequency tripling process via sum frequency generation ($\omega_t+2\omega_t\rightarrow3\omega_t$) using Gaussian pulses in BBO with length L=1000 μm. The input transform limited pulse duration is τ_{10}=50 fs. If the acceptable total phase mismatch is π/2, Fig.2.a shows the generated bandwidth $\Delta\bar{\nu}_s^{CGV}$ ($=\Delta\omega_s^{CGV}/2\pi c$) vs. wavelength of λ_t. For comparison, the bandwidth achievable by the traditional method $\Delta\bar{\nu}_s^0$ ($=\Delta\omega_s^0/2\pi c$) under the same conditions is also displayed. Since the dispersion increases with frequency, the gain in generated bandwidth compared to the traditional method is more significant at shorter wavelengths.

The bandwidth of the generated pulse is dependent on the crystal length through β_S and the duration of the generated pulse in a quite complicated way [7]. In Fig.2.b the bandwidths $\Delta\bar{\nu}_s^{CGV}$ and $\Delta\bar{\nu}_s^0$ are plotted as a function of crystal length for BBO. The limitation to increasing the crystal length to an arbitrary high value while maintaining broadband conversion is set by the increasing chirp on the pulses by the crystal itself (see (ii) of Section 2 in [7]). For TITANIA this technique would allow crystal lengths in excess of 1 mm with a large consequent improvement in conversion efficiency.

The analysis can be extended to include higher order dispersion [7]. As can be seen from equation (1)-(2), if higher order terms are included, there is still a solution to the phase matching condition which yields nonlinear equations relating the required chirps on each beam and hence to a requirement for slightly nonlinear chirps on the generating beams. Other than for extreme cases of high dispersion and crystal length, however, linear chirps can be used efficiently without exceeding the 'normal' bandwidth limit of the process.

The main conclusions established are: (i) the bandwidth generated has an asymptotic value as a function of crystal length; (ii) the advantages of CGV technique are increased in the cases where the dispersion is higher, and (iii) the phase matching condition can theoretically be satisfied for arbitrarily wide bandwidth by suitable design of higher order chirp coefficients.

4. REFERENCES

[1] A Penzkofer, F Ossig, P Qiu, Appl.Phys. B **47** (1988) 71

[2] O E Martinez, IEEE J.Quant.Electron. **QE-25** (1989) 2464

[3] M J T Milton, T J McIlveen, D C Hanna, P T Woods, Opt.Commun. **87** (1992) 273

[4] G Szabó, Z Bor, Appl.Phys. B **58** (1994) 237

[5] T R Zhang, H R Choo, M C Downer, Appl.Opt. **29**, (1990) 3927

[6] I N Ross, K Osvay, Opt.Quant.Electr. **28** (1996) 83

[7] K Osvay, I N Ross, J.Opt.Soc.Am. B **13** (1996) in press

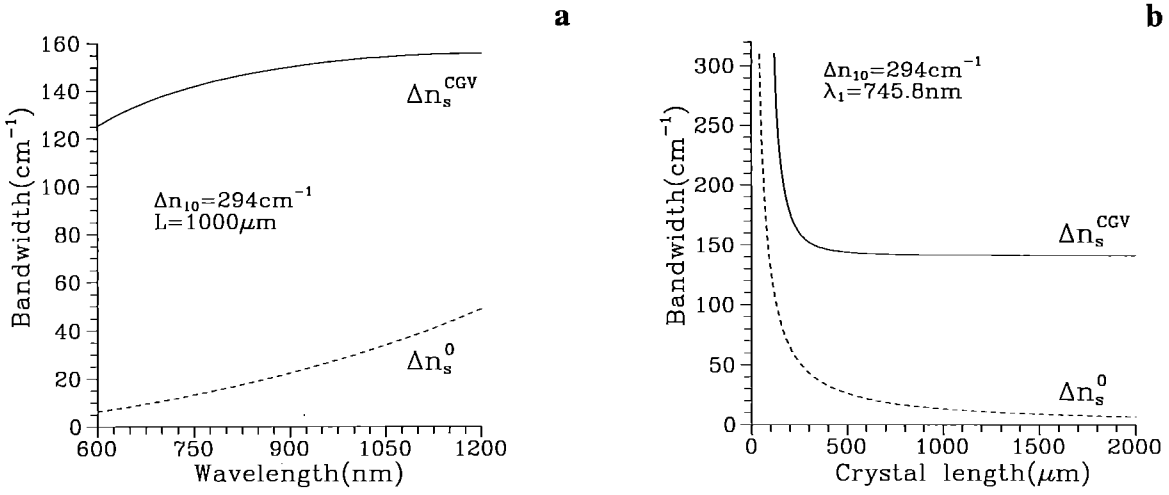

Figure 2. The generated bandwidth in BBO with and without CGV compensation as a function of wavelength of λ_t (a) and of crystal length (b).

CHARACTERISATION OF A HIGH-DENSITY GAS JET FOR LASER PLASMA INTERACTION STUDIES

A Behjat[1], G J Tallents[1], D Neely[2]

[1]Department of Physics, University of Essex, Colchester, CO4 3SQ, UK.

[2]Central Laser Facility, Rutherford Appleton Laboratory, Chilton, OX11 0QX, UK.

INTRODUCTION

Pulsed gas jets are now widely used as high power laser targets. The ion densities (up to ~10^{21} cm^{-3}) found in gas jets are required for optical field ionisation x-ray laser experiments[1-3], incoherent x-ray generation[4-5], particle acceleration experiments[6], spectroscopy and harmonic generation studies[7,8]. A large volume of uniform, sub-critical plasma can be created, making the gas jet a suitable target.

Simple free expansion gas jets have been investigated [9,10] with small opening nozzle diameter. Supersonic low density gas jets which are suitable for molecular beam and cluster research have also been studied[11]. In these gas jets high pressure gas expands and cools within a tapered expansion nozzle to produce a supersonic low density region. To model and interpret laser interaction with a gas jet requires ideally a detailed knowledge of the density profiles present and their time evolution. In this paper, we use a Mach-Zehnder interferometer and employ an Abel inversion technique to characterise a free expansion gas jet.

ABEL INVERSION METHODS

In interferometery, the average value of phase shifts along a chord through the medium is measured. It is necessary to deduce local values of the refractive index from the available phase shift chordal measurements. Gas jets are cylindrically symmetric, which enables us to deduce the radial distribution of refractive index from the phase shift measurements using Abel inversion. Assuming a cylindrically symmetric refractive index variation n(r), the phase shift chordal measurements $\phi(y)$ can be written as

$$\phi(y) = \int_{-\sqrt{R^2-y^2}}^{+\sqrt{R^2-y^2}} (n_r - 1) dx \,. \qquad (1)$$

Re-arranging this expression so that the integration is with respect to r gives

$$\phi(y) = 2\int_y^R (n_r - 1) \frac{rdr}{\sqrt{r^2 - y^2}} \qquad (2)$$

The Abel inverse transform theorem states that

$$n_r - 1 = -\frac{1}{\pi} \int_r^R \frac{d\phi}{dy} \frac{dy}{(y^2 - r^2)^{1/2}} \qquad (3)$$

Several methods[12] for solving the Abel transform equation have been studied. A recent review[12] recommends polynomial curve fitting to the $\phi(y)$ data which leads to analytic solution for $\frac{d\phi}{dy}$ and analytic solution for $n_r - 1$ By substituting the 6th order polynomial fitting function to the phase shift $\phi(y)$ in the above integral, the refractive index is evaluated as simply

$$n_r - 1 = -\frac{1}{\pi} \left\{ 2cu + 4e\left(ur^2 + \frac{u^3}{3}\right) + 6g\left(ur^4 + 2\frac{u^3}{3} r^2 + \frac{u^5}{5}\right) \right\} \qquad (4)$$

where $U = \sqrt{R^2 - r^2}$ and c, e, and g are the coefficients of the polynomial fit to the phase shift, viz.

$$\phi(y) = a + by + cy^2 + dy^3 + ey^4 + fy^5 + gy^6 \,. \qquad (5)$$

EXPERIMENTAL SET-UP

A Mach Zehnder interferometer was constructed inside the TA4 target chamber at RAL using a low energy, ns probe beam from the VULCAN laser. Two Al mirrors (25 mm diameter) with flatness of λ/20 and two similar half silvered splitting mirrors were used to construct the interferometer. The 1.053 μm beam of the VULCAN laser was frequency doubled and used as a probe in the line of view normal to the gas jet flow. Pre-alignment and normalisation of the interferometric optics was carried out using a low power Green He-Ne (543 nm) laser diverted parallel and coincident with the main probe beam.

Neon and Nitrogen gas jets with backing pressure over the range of 13-17 atm have been characterised. A high pressure solenoid valve [13] controlled the output of gas from a high pressure reservoir. The opening time of the gas jet solenoid valve relative to the probe beam and duration of opening was controlled by pulse and delay generator. The gas valve opening times were in the range of 0.1 to 2 msec.

The fringe pattern generated by the phase shift induced on the probe beam by the gas jet integrated along the line of sight of the interferometer was detected by two CCD detectors and recorded using a frame store system (CEO). Two objectives with different magnification were used for the two Mach Zehnder image planes. Interference filters for the 0.53 μm wavelength probe beam were used to minimise back ground illumination of the CCD detectors.

DATA ANALYSIS

The phase shift produced by the gas jet was evaluated by measuring the displacements of fringes from their unperturbed positions (compared to the background fringes which were generated in the absence of the gas jet). Typical interferograms obtained from the CEO frame store computer system are shown in Figure 1. By counting the number of the fringes crossed moving along the y direction, a sampling of fringe shifts ($\delta\phi$) for a given distance from the gas jet surface was measured. The 6th order polynomial fitting function to the phase shifts was determined and used in the inverse Abel inversion integral (equation 4) to calculate the radial refractive index of the gas jet.

Figure 1-Typical interferograms of the N_2 gas jet at backing pressure of 70 atm.

RESULTS

The radial refractive index of an N_2 gas jet with backing pressure of 70 atm at different positions above the nozzle tip are shown in Figure 2. From these refraction index values, the radial density of the gas can be estimated as shown in Figure 3. The density is assumed[14] to be proportional to n^2-1. The axial density of the N_2 gas jet with backing pressure of 70 atm was found to drop

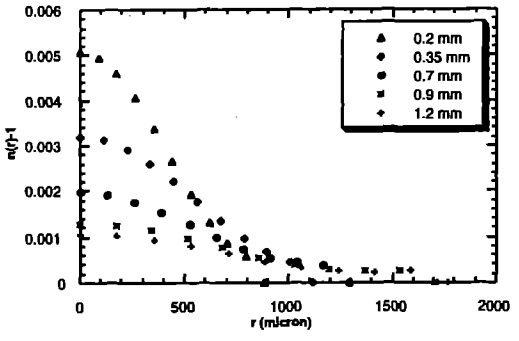

Figure -2 Refractive index measured for N_2 gas jet with backing pressure of 70 atm at different position above the 1 mm nozzle tip (0.2, 0.35, 0.7, 0.9 and 1.2 mm).

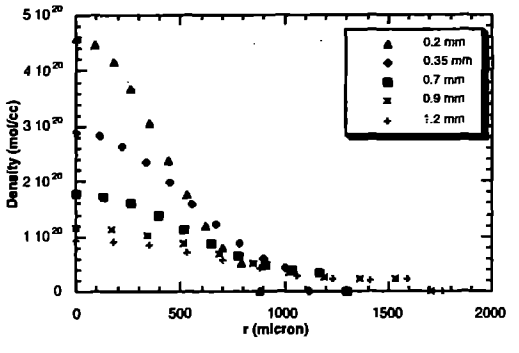

Figure 3 Radial density profile of the N_2 gas jet for backing pressure of 70 atm and 0.2, 0.35, 0.7, 0.9 and 1.2 mm from the nozzle tip.

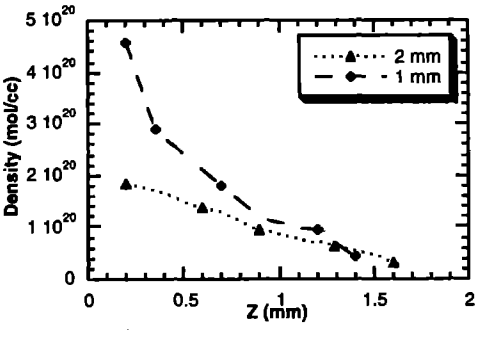

Figure 4 Axial density versus distance from the nozzle tip for 1 and 2 mm nozzle (N_2 gas jet with backing pressure of 70 atm) at time of 15 msec.

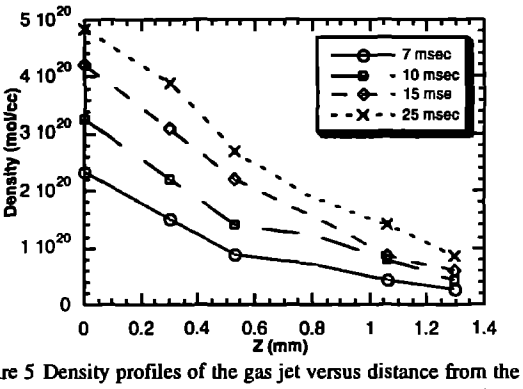

Figure 5 Density profiles of the gas jet versus distance from the 1 mm nozzle tip for N_2 gas jet with backing pressure of 70 atm at different time.

exponentially with distance from the nozzle with a scale length of ~1 mm for both 1 and 2 mm nozzle (figure 4). The radial density scale lengths of N_2 gas jet at the same backing pressures was about 0.5 mm for 1 mm nozzle. The time evolution of the density profile was measured by taking interferograms at various times through the gas flow (Figure 5).

CONCLUSION

We have characterised a gas jet which is suitable as a low mass long scale-length target for laser plasma interaction studies and XUV recombination x-ray laser experiments. A Mach Zehnder interferometer was used and the Abel inversion technique was employed to measure density in a cylindrical gas jet at backing pressure over the range of 13-70 atm with a 1 or 2 mm diameter circular nozzle. The axial density of the N_2 gas jet with backing pressure of 70 atm was found to drop exponentially with distance from the nozzle with a scale length of ~1mm. The radial density scale length of the N_2 gas jet at the same backing pressure was about 0.5 mm for a 1 mm nozzle and is approximately Gaussian in shape.

REFERENCES

[1] N.H. Burnett and P.B. Corkum, J. Opt. Soc. Am. B 6 (1989) 1195.

[2] N.H. Burnett and G.D. Enright, IEEE J. Quant. Electron. 26 (1990) 1797.

[3] H. Fiedorowicz et al., Phys.Rev.Lett. 76, 3 (1996) 415.

[4] H. Fiedorowicz et al., Laser and Particle Beams, 12 (1994) 471.

[5] H. Fiedorowicz et al., Appl. Phys. Lett. 62, 22 (1993) 2778.

[6] A. Modena et al., Nature 377(1995) p606.

[7] Fill et al., Phys. Rev. E 51,6 (1995) 6016.

[8] C.G. Wahlstrom, X-ray lasers 1994, D.C. Eder, D. Matthews eds., AIP Conference Proceedings 332, (1994) 313.

[9] D.L. Musinski etal., Plasma Phys. 24 (1982) 731.

[10] Y.M. Li and R. Fedosejevs, Meas. Sci. Technol. 5 (1994) 1197.

[11] B. Farizon et al., Nuclear Instruments and Methods in Physics Research B 101 (1995) 287.

[12] M.J. Buie et al., J. Quant. Spectrosc. Radiat. Transfer. 55, 2 (1996) 231.

[13] Hycontrol LTD., Larchwood House, Worcestershire B98 7DP, Uk, Solenoid valve type V52H ABA20502.

[14] M. Born and E. Wolf, Principles of optics, Pergamon Press (1970)88.

SOLID DEUTERIUM TARGET ASSEMBLY

S.Angood

Rutherford Appleton Laboratory

INTRODUCTION

A recent VULCAN solid target Chirped Pulse Amplified interaction experiment had a requirement to shoot a solid deuterium target located at the centre of the target area west chamber. As Deuterium solidifies at 14 degrees Kelvin clearly, a cryogenic target mount was required.

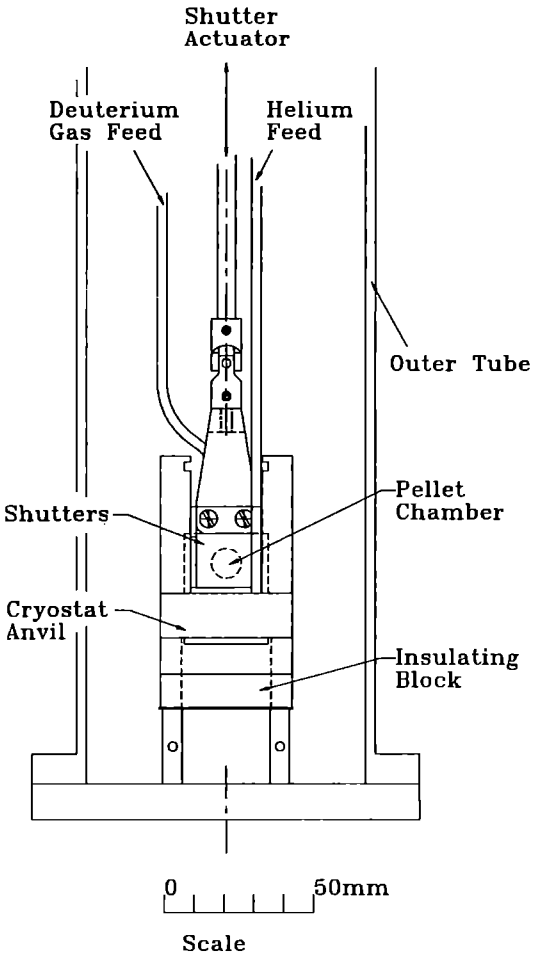

Fig 1. Schematic diagram showing a face on view of the cryogenic target mount.

DESIGN

To enable these temperatures to be reached, liquid helium is used as a cooling agent. Standard procedure is to use a reservoir dewar as the supply and deliver the helium to the cryostat via a vacuum transfer line. In theory, with no other sources of heat input to the system a temperature of 4 Kelvin, the temperature of the liquid helium can be achieved. Any material added to the system will increase this achievable temperature. It was estimated that with inevitable heat inputs mainly through conduction the actual temperature of the cryostat would be 10 Kelvin. During the design stage, the main thermal problem would be that the warm deuterium gas flowing into the cold cryostat would raise its base temperature. A temperature rise of only 4 degrees would be enough to stop the deuterium solidifying. Options to reduce the temperature rise were:-

1) Extra cooling capacity by increased flow rate of liquid helium through the cryostat housing.
2) Increased thermal inertia by increasing the mass of the cryostat housing.
3) Pre-cooling of the deuterium before entry into the cryostat housing.

The final solution was to balance the cooling capacity and thermal inertia within the cryostat housing whilst introducing warm gas in a slow and controlled manner. Pre-cooling the gas was ruled out due to the possibility of the 2.5 mm ID feed tube being blocked with frozen gas before the pellet chamber had a chance to fill.

The cryostat incorporates a copper anvil, cooled by liquid helium which flows through internal passageways. The anvil also forms the target mount. This is a copper wall 5 mm thick with a 10 mm diameter hole through its width. Two shutters slide against each face of the wall creating an internal chamber within the anvil. The faces of the shutters were optically polished to provide a good surface finish for the deuterium pellet. The shutters are operated by an air cylinder on top of the chamber and are not designed to give an effective seal, as any small leak paths around the shutters are sealed by escaping gas freezing up during the first few seconds of a gas fill. A small tube feeds into the top of the target mount to supply the gas. An outer tube mounted to the top of the chamber acts as a barrier to heat radiation and also supports the cryostat (see fig 1).

Temperature monitoring is simple, consisting of carbon resistors which are placed in contact with the cryostat body, these give a reading on a remote display. This readout is in ohms an not degrees, but after initial trials a reference point at which solid deuterium could be made was established.

OPERATION

Before any cooling can take place, the gas feed must be evacuated to eliminate any water vapour as this would freeze and block the tube. The initial requirement for pellet production is to sufficiently cool the cryostat. This is achieved with the shutters closed and the helium dewar pressurised to 1 psi. From room temperature this takes 40 to 50 minutes. Once the required temperature is achieved, warm deuterium gas is fed into the cryostat at 10 psi via a regulator an flow meter. The purpose of the meter is to indicate when the flow of gas into the pellet chamber has stopped. At this point a pellet has been formed and the gas supply is isolated. With the shutters closed and sufficient cooling, a pellet can be held for 1 hour without any visible deterioration. To allow beam to target interaction, the shutters are raised by remote switching from the target area control room.

RESULTS

This design and operation regime allowed a 97% success rate in producing pellets with an average target production time of 7 minutes from a full laser shot. A full data set was obtained using solid deuterium targets and is reported in the high intensity interaction section of this report.

A DETECTION SYSTEM FOR 'WATER WINDOW' X-RAYS

G Eker[1], G J Tallents[1], A Behjat[1], D Neely[2], E Wolfrum[2], A D Stead[3] and T W Ford[3]

[1]Department of Physics, University of Essex, Wivenhoe Park, Colchester, CO4 3SQ, U.K.
[2]Rutherford Appleton Laboratory, Chilton, Didcot, Oxon, OX11 0QX,U.K.
[3]Biology Department, Royal Holloway (University of London), Egham, Surrey, TW20 0EX, U.K.

INTRODUCTION

Soft X-ray contact microscopy has been used to image living biological material at RAL for several years[1]. It is desirable to use very short pulses of soft X-rays such as thoes created by laser-produced plasmas to avoid sample motion and blurring during the exposure of the sample. Soft X-rays in the so called water window (23-44 A) region are often used by biologists because in this region the absorption of x-rays by oxygen is low compared to the absorption by carbon. Here, water (largely oxygen) is transparent, but protein (largely carbon) is not[2]. The X-rays are absorbed by the carbon in the specimen and pass through the water and impact photoresist. The photoresist is etched using standard lithography techniques to create an image of the sample[3]. It has been found that 20 joule, ~1 ns duration laser-produced plasmas can produce sufficient soft X-ray fluence at distances of ~ 10 mm for single shot, short-duration exposures onto standard photoresists.

A silicon photodiode (AXUV-100) reverse biased at 5 volts was used to monitor the water window flux of X-rays during an experiment to image biological samples onto photoresist. Silicon photodiodes operate by the absorption of light photons to generate a flow of current in an external circuit. Photodiodes can be used to detect the presence of small fluxes of light and can be calibrated to measure the intensity of light accurately. Although X-UV silicon photodiodes have a band gap cut-off wavelength of 1.1 microns, the optical bandwidth can be limited by depositing an appropriate thin film of a suitable material directly on the surface of the detector or by placing thin foils of material in the photon path before the detector. Here we also limit the wavelength by using a reflection filter. By choosing to reflect X-UV radiation at an appropriate grazing angle, we have manufactured a filter which only allows radiation of wavelength >2.3 nm to pass. Combined with a K-edge transmission filter, this allows us to define the band-pass of the filter system to the water window (23-44 A). The foil filter and reflection filter select are shown schematically illustrated in figure 1.

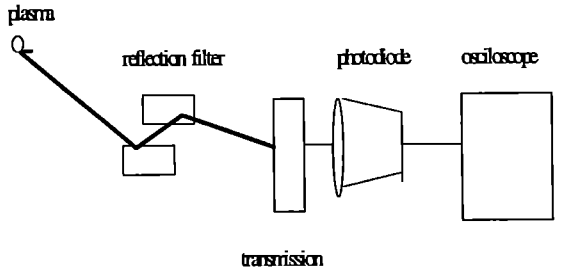

Figure 1 Schematic diagram showing the location of the reflection filter and transmission filter when used with the photodiode.

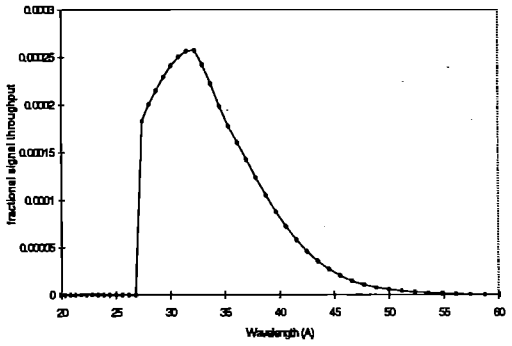

Figure 2: The throughput obtained using a combination of a transmission (2 μm thickness of Ti) and reflection (two reflections at 5° grazing angle on Ge) filters.

The reflection filter absorbs short wavelength emission while the transmission filter gives a sharp rise in the throughput above an absorption edge. Two reflections on germanium of thickness 300 nm with the radiation incident at 5 degree were used as the reflection filter. The transmission filter consisted of 2.μm of Titanium foil. The combined reflection and transmission filters have the throughput shown in figure 2.

The radiation emitted from a laser generated plasma consists of broad band continuum on which line emission is superimposed. The line emission principally arises from electron excitation from the ground state of an ion plus recombination from more highly ionised ions which is then followed by radiative de-excitation of excited state electrons. There appears a set of line spectra corresponding to each shell for a particular element and the energy associated with each transition is dependent on the elements atomic number Z. It is therefore possible to constrain the line emission to some wavelength range by choosing Z, while at the same time adjusting the laser irradiance on target to obtain a suitable plasma temperature to excite the ion species of interest. Targets of yttrium (Z =39), molybdenum (Z=42), and tungsten (Z=74) which have line emission in the water window region were used for the present investigation.

We have measured the spectral emission from these elements using a flat field spectrometer. In order to produce stereoscopic imaging of biological samples two plasmas were produced using two approximately 13 Joule in 1 ns pulses focused onto a target with 30 mm between the two focal spots. A flat field diffraction grating (≈1200 lines/mm) was located at a distance of 237 mm from the entrance slit of a soft X-ray spectrometer and focused the emission from the entrance slit onto the detector plane which was situated at 235 mm behind the grating. A standard grazing angle setting for the flat field gratings of 3.02 degrees was used and a 0.9 mm slit was employed to spatially resolve the two plasmas.

In our experiment, the spectra were recorded on Ilford Q-plate film and read out using a densitometer with step size of 10 μm. For thick emulsion films, such as Ilford Q-plates, optical density is related to the incident X-UV flux by[3]

$$D = \ln (1 + CI) D_{sat} \qquad (1)$$

where D_{sat} is the saturation density of the film, I is the intensity corresponding to an optical density D and C is a constant dependent on the properties of the particular film. For Q-plate, C and D_{sat} are 0.18 and 1.27 respectively[4]. From equation (2) optical density can be converted to intensity and these values can be compared to the recorded photodiode intensity in the water window region. The photodiode measured the total emission from both plasmas on each shot. The wavelength scale was calculated from the grating line spacing and the geometry and was cross-calibrated against known emission lines for a carbon spectra (Lyman-α at 3.37 nm and Helium-α at 4.03 nm) measured with the same spectrometer and a carbon target. The emission spectra for yttrium is shown in figure 3 .

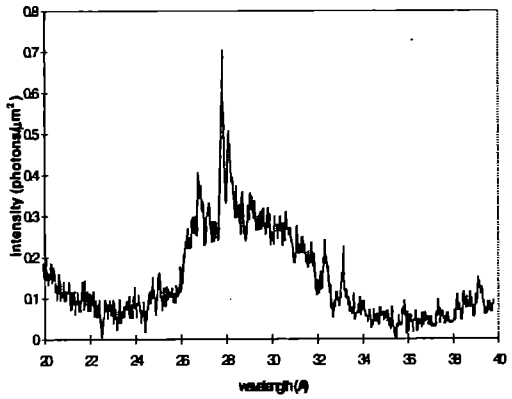

Figure 3 A yttrium spectrum recorded on Q-plate film using the flat-field spectrometer.

The photodiode was connected to an oscilloscope which measured the current flow through 50 ohms (figure 4). Allowing for the photodiode filtering and the grating reflectivity, the temporal integrated photodiode signal and wavelength integrated spectrometer recorded x-ray flux can be compared (figure 5).

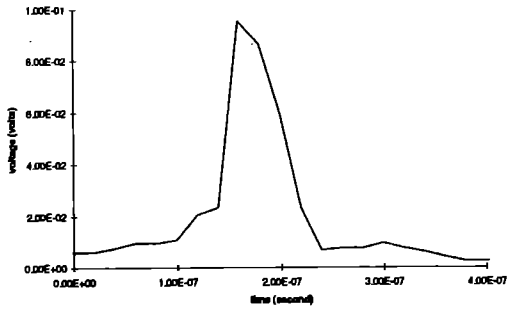

Figure 4 A soft X-ray diode output voltage signal is plotted against time.

We have for the flux I (photons/sr.) recorded by the photodiode

$$I = (T_{si} \cdot R_s \Omega)^{-1} \int V \, dt \qquad (2)$$

where T_{si} is the transmission of the 0.25 μm Silicon thick overlay on the photodiode, $\int V.dt$ is the integrated diode signal output voltage, R_s =50 ohm and Ω (= 2.25×10^{-7} sr.) is the solid angle of the photodiode and reflection filter system.

The measured yttrium spectra integrated over the spectral bandwidth of the photodiode system is plotted against the photodiode signal in figure 5.

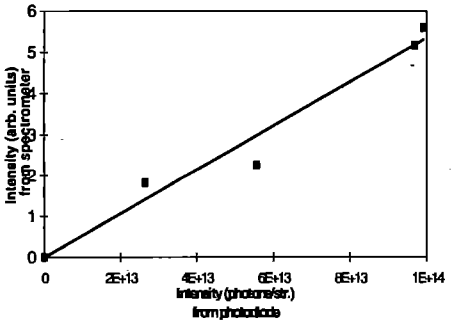

Figure 5 Intensity measured by the spectrometer after multiplication by the throughput of figure 2 and integration over wavelength as a function of the photodiode recorded intensity.

It can be seen from figure 5 that the filtered photodiode and flat field spectrometer have a linear relationship. Since the signals measured using the flat-field were filtered to be in the linear film response region, therefore, the diode is operating in a linear regime. The photodiode is clearly a useful and accurate device for direct detection of water window emission.

REFERENCES

1 Cotton, R.A., Dooley, M.D., Page, A.M., Stead, A.D, Ford, T.W. Annual Report to the Laser Facility Committee, 50-53 (1992).

2 London, A.R., Rosen, D. M., Maxon, M.S., Eder, C.E., Hagelstein, P.L. J. Phys. B: At. Mol. Opt. .Phys. 22., 3363-3376 (1989).

3 Bijkerk, F., Louis, E., Wiel, M.J., Turcu, I.C.E., Tallents, G.J., Batani, D., J. X-Ray Sci. and Technol. 3, 133-151 (1992).

4 Krishnan, J., Ph D. thesis, University of Essex, sec.3.3, 64-66 (1994).

5 Henke, B.L., Kwok, S.L., Uejio, T.Y., Yamanada, H.T., Young, G.C., Palmer, M.H., J. Opt. Soc. Am. 1, p818 (1984).

REPORT ON PRELIMINARY EXPERIMENT ON X-RAY SCATTERING IN TA4

D. Riley
Queen's University Belfast

INTRODUCTION

The purpose of this experiment was to demonstrate the feasibility of a larger scale X-ray scattering experiment in which 5-10 keV X-rays would be scattered from a radiatively heated plasma and detected with a cooled CCD detector. Because of the low energy in a single beam available in TA4, the scaled experiment was designed to show that photons scattered from a cold foil of similar total mass to the proposed plasma targets could be scattered in sufficient numbers and be detected by the CCD system, with minimal background noise.

EXPERIMENT

Figure 1 shows the outline of the experimental arrangement. What is not shown is the plastic sheeting used as shielding to prevent X-rays from the target wire from hitting the chamber walls and fluorescing or scattering into the CCD from the target mounting and drive structures inside the chamber.

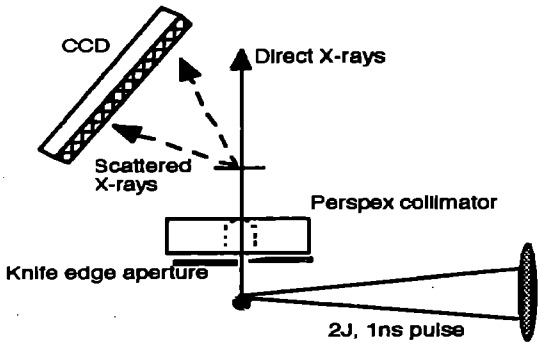

Figure 1. Schematic of experiment

The laser was tightly focussed onto a 250 μm Al wire by obscuring on the end of the wire. Since the best focus for the lens and beam used is typically 50μm the intensity on target was of order 10^{14} Wcm^{-2}. By observing the scatter of the Ar-ion alignment laser the wire could be moved such that the plasma was created on the correct side of the wire. A telescope system was used to align the targets in position, so that sufficient X-rays would travel through the knife edge aperture and perspex collimator. The aperture and collimator were designed to allow a cone of X-rays with solid angle $1.5x10^{-2}$ Sr to hit the target foil. The CCD detector was filtered with 25μm Be, so that only Al K-shell X-rays would be transmitted. In a preliminary experiment, the direct X-rays were incident on a Tlap crystal and dispersed onto the CCD detector. It was seen that, as expected, by far the brightest line was the Al He-α line. By filtering the detector heavily and placing it directly in front of the aperture, a clearly defined 'footprint' was seen with a very flat topped profile with few photons (~5) outside the main imprint, showing that the beam was well collimated and confirming the expected angular spread. Accounting for filter transmission, repeated shots showed that about $8x10^8$ photons were incident on target. However, by deliberately inducing slight mis-alignment it was seen that an order of magnitude reduction could be caused. This showed that, in a full experiment, reproducible alignment and monitoring of transmitted photons will be important.

As a null experiment, the CCD was placed in it's proper position as in figure 1, but no target was in place. In this case there should be no signal measured after all background sources of fluorescence were carefully screened out with plastic foil. The main effect was achieved in screening the Al wire target itself, such that the ablated plasma was contained within an enclosed box, this had the effect of eliminating fluorescence effects from the plasma impact with the chamber wall. In practice it was possible to achieve null shots with only one or two pixels with counts above the noise level.

After the null result was satisfactorily achieved and reproduced, a thin foil of Be (7.5μm) was placed in the beam on a target support, which was in place during the null tests. The target sampled by the beam was then approximately a 3mm diameter disk of Be foil.

RESULTS

Figure 2. shows a histogram of results from 3 shots showing the counts converted to photon energy on the x-axis and frequency of occurrence on the y-axis. We can see that there is a definite peak at the He-α photon energy. The r.m.s. read noise was 2 counts per pixel, with a similar shot noise for He-α photons, which explains the spread in the peak. The peak is superimposed on a spectrum falling off with photon energy. This spectrum could be explained by photo-absorption in the target (18%) which results in recombination radiation. This does not explain the pixels with counts above the He-α energy. It is possible that absorption of higher energy transitions may account in part for this. Also due to noise, there were a large number of pixels with 1-5 counts superimposed on the photon signal these may partially explain the pixels with higher counts.

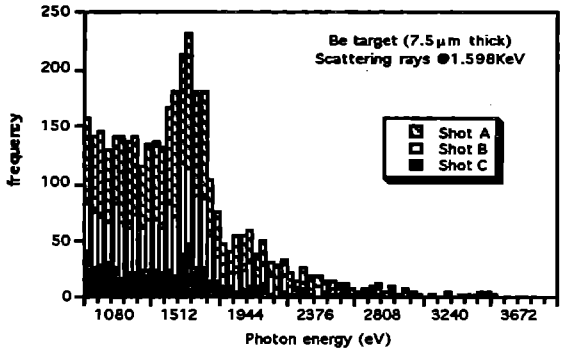

Figure 2. Results from Be target

Using the data from figure 2, we can estimate, the cross section by accounting for QE (72%) at the He-α wavelength, transmission of target (82%) and filter (52%) and number of target atoms(~$6.5x10^{18}$). From the data above, the average cross section is around $7x10^{-25}$ cm^2/Sr, which, to within the uncertainty of the measurements, is what is expected for a target with low Z atoms.

CONCLUSION

This preliminary experiment established three important points. Firstly, the cooled CCD detector can record individual scattered photons. Secondly, it is possible to screen the experiment such that background photons due to scattering off target mounts and chamber walls are eliminated. Finally, when scattered photons were recorded, the number detected was, to within experimental error, consistent with expectation.

In the scaled up experiment, the absorption of X-rays by the target will be less than 1% thus reducing significantly the contribution of recombination radiation. The preliminary expeiment also highlighted the importance of good alignment of the source of scattering X-rays, and the probable need for shot to shot monitoring.

MANUFACTURE OF PLANCKIAN CAVITIES FOR HIGH-POWER LASER EXPERIMENTS

J Spencer[1] and R J Taylor[2]
[1]Space Science Division, RAL
[2] Imperial College, London, SW7 2BZ, UK

Inertial Confinement Fusion (ICF) [1] and more general programmes of experimental research into radiation transport physics [2] require an intense source of X-rays, which can be used to rapidly heat matter to extremes of temperature, and in the case of ICF, implode a capsule containing Hydrogen isotopes until the density and temperatures exceed those requisite for a sustained thermonuclear fusion reaction to occur. The VULCAN facility at RAL is capable of delivering hundreds of Joules of energy in a billionth of a second to an area less than one millimetre square, but the energy is delivered as monochromatic green light, and while the physics of the interaction of such light with matter is a field of vigorous study in itself, the ability to convert the laser light to an X-ray flux is extremely desirable in terms of pursuing the study of radiation physics.

An efficient method of converting laser light to X-rays is to shine it onto the inner wall of a small cavity made from a high-Z material such as Gold (known as a Planckian cavity, or *hohlraum* [3]). Where the laser strikes the wall, a plasma is rapidly formed, and efficient conversion (50-80%) of the laser light to soft X-rays (photon energy hν; $0 < h\nu < 3000$ eV) occurs. These X-rays are emitted in all directions, but since the cavity is mostly closed (apart from the laser entrance and diagnostic holes), it is inevitably absorbed somewhere, and before long the entire inner wall of the cavity becomes a plasma, emitting and absorbing X-rays. If a spherical capsule is placed in the centre of this cavity, it feels near uniform drive from the X-ray field, and implodes, or alternatively, a section of the hohlraum wall may be replaced with a sample which will feel the same X-ray flux as the rest of the cavity wall, and be heated accordingly. To give an idea of the temperatures that can be achieved by this technique, the Vulcan laser can raise a 1 mm diameter, 1.3 mm long cylindrical hohlraum to temperatures approaching 130eV, or 1.5 *million* degrees centigrade, and all within 1 billionth of a second. Exposed to such treatment, matter behaves in strange ways, and is the subject of intense study at laboratories around the world.

A recent relaxation of classification rules has provided the opportunity to study the heating of material by hohlraums to civilian researchers, and hence the Imperial College group wished to field an experiment to study aspects of ICF [4]. For this they required Gold hohlraums, which were within the manufacturing capability of the Microwave Workshop in Space Science at RAL. More used to manufacturing components for satellites, the tools and techniques were readily adapted to the manufacture of these small gold cavities. The basic design specification is shown in Figure 1, and consists of a hollow Gold cylinder of diameter 1 mm and length 1.3 mm, closed to 0.5 mm diameter at each end, and with opposing 0.5 mm holes formed in the curved wall. These latter holes allowed the 6 laser beams to enter, and illuminate the inner wall in two rows of 3 spots.

The geometry of the laser illumination is described in more detail elsewhere in this report [4]. The diagnostic holes in the ends of the hohlraums provided a line-of-sight through the cavity, with the sample to be heated fixed across one hole, and the other open to allow a probe beam of X-rays through the hohlraum such that a shadow image of the sample could be recorded while it was heated. The sample in this case was to be a thin plastic foil, the inside surface of which is evaporated by the X-ray flux, causing the remainder of the foil to recoil, reaching a velocity of ~100,000 MPH.

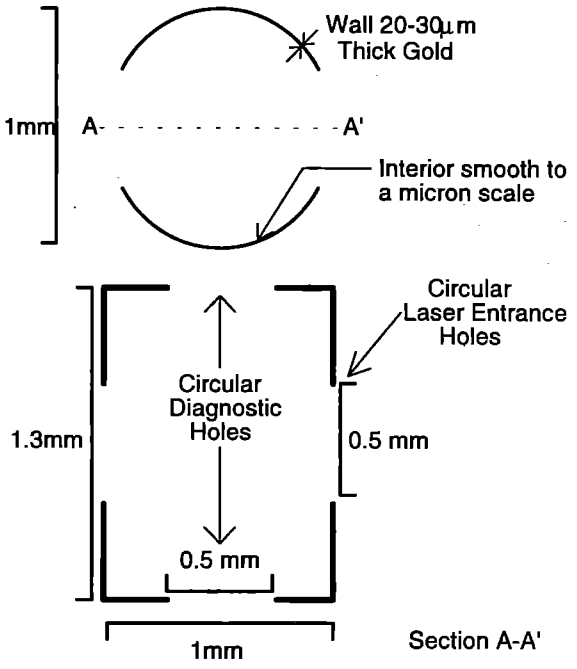

Figure 1: Hohlraum design specification. A Gold cylinder with ends closed to a diameter of 0.5 mm and a wall thickness of 20-30μm was required. Laser Entrance Holes were to be formed at a diameter of 0.5 mm in the curved wall, and an interior finish smooth to a micron scale was required.

The temperature reached inside the cavity is related to the amount of Gold that must be heated by the X-rays. Less Gold for the same amount of energy results in a higher temperature, and hence the inner surface area of the cavity needs to be controlled. The gross dimensions of the cavity determine the area in the first instance, but a secondary effect which can be significant is the surface finish of the interior. A very bumpy surface can expose significantly more gold to the heating process than would otherwise be exposed by a perfectly smooth surface, and hence the design required that the surface finish be smooth down to a micron scale. Non-uniformities on this scale are less important, because the plasma formed by the X-rays will wash them out. The final design requirement was that the wall be sufficiently thick to lend rigidity to the structure, yet thin enough so that the beams could penetrate the holes at an angle without clipping the edges (see [4]). Hence a wall thickness of 20-30μm was decided upon.

The manufacturing process in essence is based around tried and tested techniques developed at other laboratories [5], with some refinements developed at RAL. First, a Copper mandrel is machined to the shape of the inner surface of the hohlraum. The mandrel starts the process as 1/8" dowelling, which was then threaded at one end. A length of 4-5 cm was used to allow for multiple mandrels to be cut from the end without the need for re-threading a new piece each time. The high-precision lathes of the Microwave Workshop were then used to turn down the end of the dowelling to the required 1 mm diameter at high accuracy, with a neck cut 1.3 mm from the end of the mandrel to a diameter of 0.5 mm, which would later become one of the 0.5 mm diagnostic holes.

Past this neck, the dowelling was opened up to the original 1/8" diameter. The surface finish on the mandrel after this machining process was typically of a very high standard, but any residual roughness from play in the cutting tools or lathe spindle was removed by polishing with a fine diamond compound until an acceptable finish was obtained.

At this stage, the Laser Entrance Holes were formed by drilling through the mandrel. Burrs were removed, and the hole plugged with snug-fitting PTFE sleeving, leaving a mandrel ready for the electro-plating process, as illustrated in Figure 2. Prior to the Gold layer, a flash layer of Copper was deposited to fill any slack between the PTFE sleeve and the mandrel, and then the 20-30μm Gold layer was electro-formed, leaving a Gold-plated mandrel ready for post-machining.

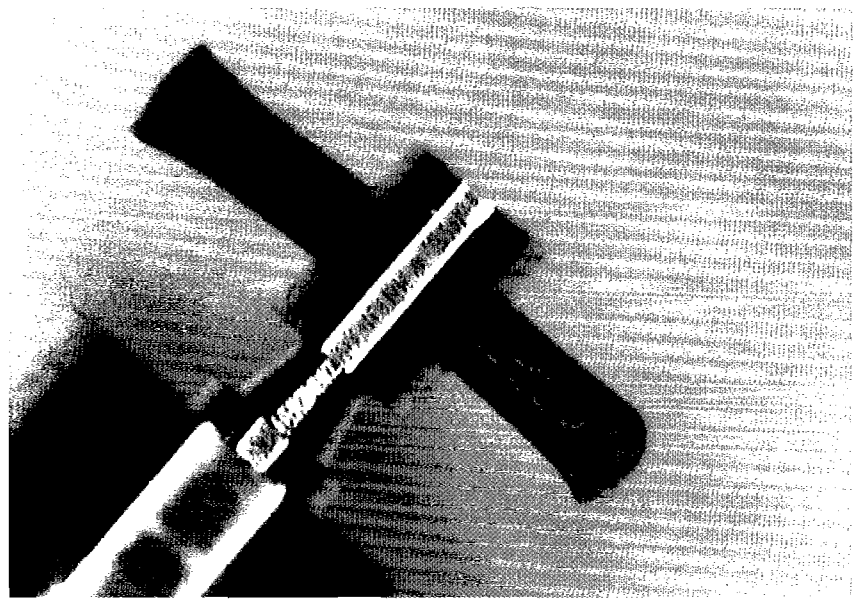

Figure 2: A machined copper mandrel ready for the electro-plating process.

The plated mandrel was returned to the lathe, and the second diagnostic hole was precision-drilled at a diameter of 0.5 mm in the end. Drilling through the soft, flat Gold layer into the copper core caused little or no burring, and so the only remaining task was to part the mandrel from the 0.5 mm neck, to leave the coated hohlraum with its Copper fill. The PTFE sleeving was removed, and the hohlraum leeched in Nitric Acid to remove the Copper. This process left the Gold shells, clear of any trace of Copper and with the inner surface a copy of the exterior of the mandrel prior to electroplating. The hohlraums were rinsed in water, and cleaned in an ultrasonic bath prior to being mounted as targets for the Laser experiments. A finished hohlraum is shown in Figure 3.

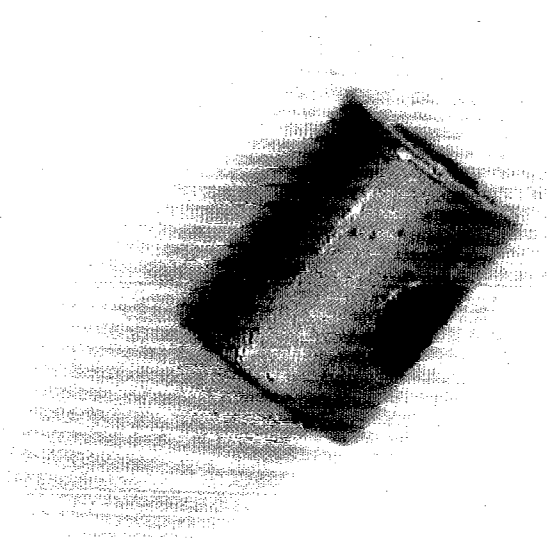

Figure 3: A completed hohlraum

Thanks are due to the rest of the RAL Space Science Microwave Workshop team, and to John Edwards, Brian Thomas, Pete Hobbs and the Target Fabrication Staff at AWE, Aldermaston for their invaluable advice and assistance throughout this work.

REFERENCES

[1] J. Kilkenny, "Inertial Confinement Fusion", Laser Plasma Interactions 5, pp. 1-13, SUSSP (1994)

[2] For example: J.Edwards *et al*, Physical Review Letters, **67**, 3780 (1991); T.S.Perry *et al.*, Physical Review Letters, **67**, 3784 (1991)

[3] H.Nishimura *et al.*, Physical Review A, **44**, 8323, (1991); R.Sigel *et al.*, Physical Review A, **38**, 5779, (1988)

[4] R.J.Taylor *et al.*, Measurement of Short-wavelength Rayleigh-Taylor Growth in Planar Foil Targets Driven with Soft X-Ray Irradiation, (This publication)

[5] Pete Hobbs, AWE Aldermaston, (Private Communication); L. Foreman, "Inertial Confinement Fusion", Laser Plasma Interactions 5, pp. 219-230, SUSSP (1994)

LINEARITY OF A NEW INEXPENSIVE CMOS X-RAY DETECTOR

M.E. Kurkcuoglu[1], D. Neely[3], G J. Tallents[1], A. Behjat[1], C.L.S. Lewis[2], S.P. McCabe[2], A.G. MacPhee[2], P.J. Warwick[2] and E. Wolfrum[3],

[1] Department of Physics, University of Essex, Colchester, CO4 3SQ, UK.
[2] Department of Pure and Applied Physics, The Queen's University of Belfast, Belfast, BT7 1NN, UK.
[3] The Rutherford Appleton Laboratory, Chilton, Didcot OXON, OX11 OQX, UK.

INTRODUCTION

In the diagnosis of X-ray lasers and laser-plasmas, CCD cameras are often used for the detection of the X-ray flux [2] by converting the beam radiation into an electrical signal. This signal can be amplified and measured using several available software options such as the CEO (in house software) and OFA[1] programs.

In this paper, we present the calibration of a CMOS (Complementary Metal Oxide Silicon) camera (ASIS-1011-B manufactured by VLSI VISION LTD.) for X-ray sensitivity. The camera has 312x287 pixels of size 19.6x16 microns. One of the significant features of this camera is the considerable saving in cost compared to purpose-designed X-ray CCD cameras due to its manufacturing simplicity. The camera only costs ~ £100 (excluding the ~10 Volt power supply).

EXPERIMENTAL

The CCD camera was calibrated for sensitivity at wavelengths between 8A-10.1A against the spectrum (see figure 1) recorded by a (KAP) crystal spectrometer viewing Ge plasma emission[3] (Ne-like 3d-2p, 3p-2s and 3s-2p spectral lines). Two 150 mm diameter beams (beams 7 and 8) of 100 ps duration from the VULCAN Nd:YAG laser were focused onto a 5 mm long Ge slab targets in TAE. By using f/2.5 aspheric lenses inside the chamber and a pair of counter-rotating cylindrical lenses outside the chamber, a line focus was generated[4] on the Ge slab target. The emission was spectrally resolved with the crystal spectrometer using a 35 mm entrance slit covered with a 25 mm Be filter, 280 mm away from the source.

A 25 micron Al and 6.2 micron Alumunized-Mylar filters plus 6, 12, 18, 24, 30, 36 micron Mylar filter steps were placed in front of the CCD chip. Images of the X-ray flux through these filters were obtained using the CEO and OFA image grabbing/analysis programs. The original spectra of the Ge plasma were obtained from the crystal spectrometer using the CCD IMAGE image grabbing package after taking account of the 25 mm Be filter transmission of the spectrometer.

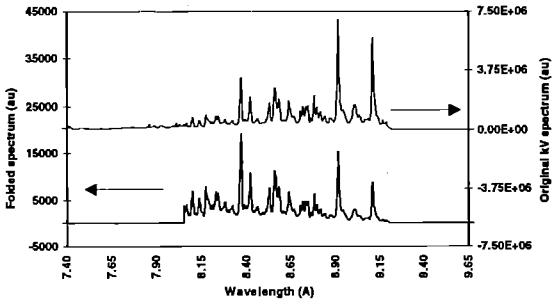

Figure 1 Original and folded (25μm Al. plus 42μm Mylar)spectra obtained from the crystal spectrometer

RESULTS

Folded spectra were obtained by multiplying the original spectra by the transmission effect of each of the CCD's filtering (figure 1). The calibration curve was assembled by integrating in wavelength the folded spectral intensity for each filtering system and plotting this against the measured intensity from the camera (figure 2).

It was found that the output signal voltage from the CCD is independent of the power supply voltage over the range 7.5-12V. A signal calibration of the CEO framestore system showed that a reading of ~ 63 units (the vertical axis in figure 2) corresponds to 1 volt output voltage from the CCD. As can be observed in figure 2, the CCD camera has a linear response to the incident X-ray flux up to a saturation output level of ~1 volt from the CCD camera.

CONCLUSION

An inexpensive camera has been used to detect x-ray emission from laser-produced plasmas and found to have a linear response to the incident x-ray flux over the majority of the output range. The camera is suited for detecting x-rays in pinhole cameras and other similar applications.

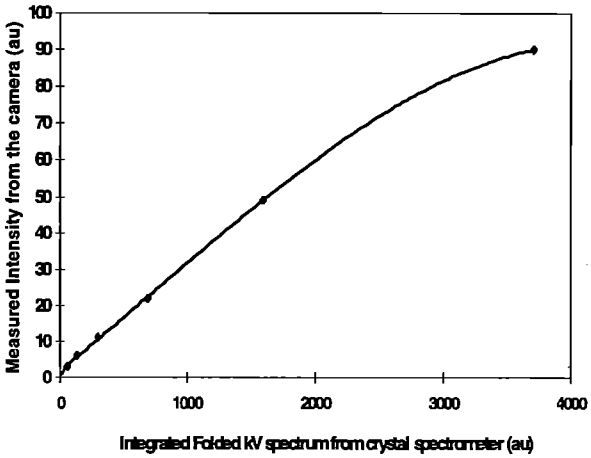

Figure 2 The calibration curve of the CCD camera response

REFERENCES

1. D Hardie et al, 'Calibration of a CCD System for Film Densitometry' SERC Central Laser Facility, Ann. Rep., 61, (1992).
2. A MacPhee et al, 'CCD Imaging from 20eV to 8keV' SERC Central Laser Facility, Ann. Rep.,161-162, (1994).
3. A MacPhee et al, 'CCD Imaging from 0.7keV to 8keV with Multi-Pinned Technology' SERC Central Laser Facility, Ann. Rep.,135-136, (1993).
4. G F Cairns et al, 'New X-Ray Laser Target Chamber Geometry' SERC Central Laser Facility, Ann. Rep.,131, (1993).

LASERS *for* SCIENCE FACILITY PROGRAMME

Anthony W. Parker

The year began with the final stages of the reorganisation to establish 5 laser laboratories within the LSF. These are; The Nanosecond Science Laboratory, The X-ray and UV Laboratory, The Femtosecond Laser Laboratory, The Ultrafast Spectroscopy Laboratory and The Laser Microscopy Laboratory. This diverse range of pulse widths (ns to fs) and wavelengths (VUV to infrared) ensures the LSF maintains a versatile scientific programme across chemistry, biology, physics and material science.

A major development has been the design and building a doubly tunable femtosecond laser system. The apparatus is based on optical parametric amplifier technology and will be used mainly for transient absorption and time-resolved Raman spectroscopy. The opening report for this section demonstrates the unique capabilities of the system to investigate relaxation dynamics in photoexcited molecules by measuring Raman excitation profiles of singlet excited states. The benefit of moving fs transient absorption from the Femtosecond Laboratory has allowed optimisation of the 50 fs laser source for programmes investigating: (i) Photofragmentation comparing measurements made on the symmetry of fragmentation with newly developed theory. (ii) Femtosecond mass spectroscopy whereby the utilisation of ultrashort pulses enables large and stable molecule ions to be created facilitating the identification of the parent molecule. (iii) High harmonic generation - 10^7 photons per pulse at 124 nm at 10 Hz has been achieved. Each of these topics are fully covered in the Physics Section of this report.

The new solid state OPO laser technology has also found its way into the Nanosecond Laboratory replacing the 10 year old excimer/dye laser system. A new activity has been the setting up of a unique time-resolved confocal microscope system which begins formal scheduled operation during mid 1996. To date the microscope has studied the cellular distribution of drugs being developed for the treatment of cancer by photodynamic therapy. The preliminary investigations show how different local environments (e.g. pH, $[Ca^{2+}]$) within the cell alter the photochemical activity of the drug.

The laser plasma X-ray source hosted European Scientists to investigate the radiobiology of yeast cells and established that irradiation by soft X-rays particularly damages the cellular wall and membrane and this impairs anaerobic processes but aerobic ones remain active. Futhermore, this year's Annual Report contains a new section entitled Nanoengineering resulting from work using the X-ray source for the fabrication of sub-micron structures.

Within the Loan Pool the policy to replace lasers once they have reached 5 years of age has continued through EPSRC funding. The award has also allowed the purchase of data acquisition and laser monitoring equipment to aid user experiments. Again gas phase chemistry and spectroscopy has featured highly in the programme. Highlights include: Determining how the conformation of a protein molecule depends on the level of hydration and the imaging of an ion cloud created from the interaction of a pulsed laser with a freely expanding gas jet.

Finally, the new name of the LSF aims to reflect the present mission of the facility to enhance the use of lasers throughout all scientific disciplines.

PICOSECOND TIME-RESOLVED RAMAN EXCITATION PROFILE OF QUATERPHENYL

P Matousek[1], A W Parker[1], M Scully[1], P F Taday[1], M Towrie[1] and W T Toner[2]

[1]Rutherford Appleton Laboratory
[2]Clarendon Laboratory, University of Oxford

INTRODUCTION

Following the photoexcitation of a molecule in solution, any excess excitation energy is redistributed internally and transferred to the solvent as heat on timescales which overlap with changes in geometry and the formation of a new chemical relationship with the solvent. The time resolved resonance Raman scattering technique is a powerful tool for the study of these intimately related non-radiative processes, but the strong enhancement of the scattering close to resonance also varies strongly with probe wavelength, and measurements of the Raman excitation profiles of the spectra are necessary for the interpretation of band intensity data. This report describes the first measurements[1] of the Raman excitation profile of an excited state molecule and presents a first analysis. The data were obtained using a new laser-OPA system giving independence of pump and probe beam tuning over a wide spectral range[2].

This work follows from studies[3-5] of stilbene and other dyes which were stimulated by the observation that several bands in the Stokes spectrum of S_1 *trans*-stilbene (S_1tS) shift significantly to the blue and decrease in width in the 25 picoseconds immediately following photoexcitation[6,7]. Several dye-like molecules show similar dynamic shifts and linewidth narrowing effects in the Stokes spectra[8,9]. Some, such as quaterphenyl[9], also show relative intensities varying with time.

In the anti-Stokes spectrum of photoexcited *trans*-stilbene[10,11], the intensities of several bands decrease markedly with time, relative to their neighbours (in the case of the *c.*1570 cm^{-1} band, by a factor of at least 20), tracking the time dependent frequency shift. The spectra also give ratios of the anti-Stokes to the Stokes intensities of all the bands in the 1100 to 1600 cm^{-1} region which are very much higher than would be expected on the basis of a Boltzmann population distribution (in the case of the *c.*1530 cm^{-1} band, by a factor of ~ 150), even at times as late as 50 ps, when spectral changes have ceased and thermal equilibrium is fully established. In the absence of an excitation profile, no firm conclusion could be drawn on the causes of these effects.

METHOD

The laser system is described elsewhere[2]. A photoexcitation pump at a wavelength of 277 nm was obtained from the third harmonic of the output of a Ti-Sa regenerative amplifier operating at 830nm. The second harmonic was used to pump a tunable Optical Parametric Amplifier seeded by white light continuum generated by a small part of the 830 nm beam, to give the tunable probe. The time resolution of this system extends down to ~ 150 fs, and is determined by the transform limit of a variable resolution spectral filter in the probe beam. A spectral resolution of 20 cm^{-1} was chosen for this experiment giving a probe pulse length of 700 fs. The pump beam chirp gave a pulse length estimated at ~ 500 fs, avoiding any possibility of non-linear artifacts. Resonance Raman intensities were observed to rise sharply from zero to full intensity at between -1and +1 ps pump/probe time delay.

Colinear pump and probe beams having parallel polarisations were focused to a spot ~ 70μm in diameter on the surface of a jet of the sample solution flowing from a nozzle and photons scattered through 90° were collected and analysed in a spectrometer equipped with a cooled CCD detector. Quaterphenyl was chosen for the first trials of the new system in view of its very large cross-section. The dye was dissolved in dioxane at millimolar concentration.

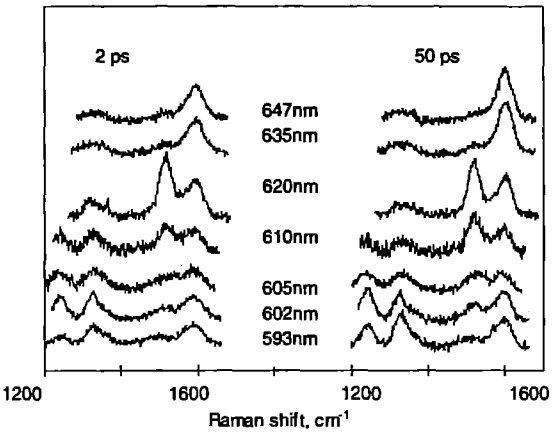

Figure 1 Raman spectra at 2 and 50 picoseconds after photoexcitation, for various probe wavelengths. The pump wavelength was 277 nm.

Stokes spectra for seven probe frequencies between 15400 and 16900 cm^{-1} at time delays of 2 and 50 ps following photoexcitation are shown in Figure 1. The intensities of some bands can be seen to depend markedly on both the probe frequency and the pump-probe time delay. The spectra were fit to Lorentzian profiles convolved with a gaussian of fixed width (20cm^{-1}) to represent the resolution of the spectral filter system and spectrometer. The band close to 1600 cm^{-1} contains several components which could not be resolved unambiguously, and the intensities attributed here to c. 1585cm^{-1} are the sum of the components used in fitting it. Band intensities obtained in this way were used to obtain the excitation profiles shown in Figure 2 of the *c.*1585 and *c.*1515cm^{-1} bands, which show the most marked effects.

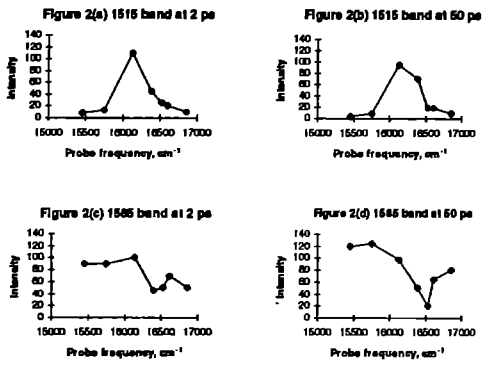

Figure 2 Raman excitation profiles of the c. 1515 and c. 1585 cm-1 bands derived from the data shown in figure 1.

RESULTS AND DISCUSSION

A very sharp variation of the relative resonance enhancement with probe frequency can be seen in Figure 2, in both cases. The profile of the *c.*1515 cm^{-1} band can be fit to a resonance with a full width at half maximum of around 500 cm^{-1}. The sharp resonance is centered at ~16250 cm^{-1} probe frequency (615nm). We identify it with the sharp peak at 212 nm in the ground state absorption spectrum[12], which locates the level whose Raman spectrum we are observing at 324nm. The assumption that this is S_1 v=0 is consistent with the ground-state absorption spectrum, which has a threshold at 340 nm and peaks at 298 nm. The sharp feature in the excitation profile is therefore most likely due to a S_1, v=0 to S_n, v=0 resonance.

Although the spectra for early times in Fig 1 show significant differences from the late time), it is evident from Fig 2 that the early and late time excitation profiles can be described by the same structure. The spectral differences are, however, real. For example, the decrease in intensity of the 1515 cm^{-1} band between 2 and 50 ps which can be seen at a probe wavelength of 610nm (frequency of 16400 cm^{-1}) can also be seen in Figure 4 of reference 9 if the intensity of this band is compared with the others. Such a change could be produced by a small shift in probe frequency, of the order of 100cm^{-1} (4 nm). Spectrophotometer measurements of the temperature dependence of the ground state absorption spectrum show an easily observable increase in the separation of the broad S_1 peak from the sharper S_n peak as the temperature decreases, amounting to ~ 3% of the separation for a 46° temperature difference. We may therefore be observing a change in the excitation profile in which the resonance enhancement peak shifts to higher frequencies as the S_1 quaterphenyl looses excess photoexcitation energy by cooling to bath temperature.

We note that a sharp resonance of this kind in stilbene would account for the strong enhancement of the anti-Stokes spectrum discussed in reference 10 and that changes in resonance enhancement of the kind observed in quaterphenyl could also account for a significant part of the stilbene anti-Srokes intensities.

In the case of the *c.*1585 cm^{-1} band, the intensity drops by a factor of ~ 2 as the probe beam is tuned over the width of the resonance affecting the 1515 cm^{-1} band. The excitation profile resembles the interference of a resonance with a flat background at a relative phase of ~90°. This would require the involvement of two electronic S_n states, one of which is distant, or very broad. Interference of this kind has been observed[13] in ground state resonance Raman scattering.

We conclude that the wavelength-dependence of the quaterphenyl Raman band intensities arises from a resonance enhancement which has a width ~500 cm^{-1}. A change in resonance frequency with time may be responsible for much of the time-dependence of the Raman intensities. The excitation profile of the 1585 band suggests the enhancement in this case is due to the interference of terms from two higher electronic states.

We thank our collaborators, R E Hester, D L Faria and J N Moore, for their participation in the earlier work cited and many useful discussions.

REFERENCES

1. A W Parker, P Matousek, P F Taday, M Towrie, W T Toner and R H Bisby, Proc New Delopments in Ultrafast Time-resolved Vibrational Spectroscopy, Tokyo (1995).
2. P Matousek, A W Parker, W T Toner and M Towrie, Opt Comm (1996) *in press*.
3. R E Hester, P Matousek, J N Moore, A W Parker, W T Toner and M Towrie, Chem Phys Lett, **208** (1993) 471.
4. J N Moore, P Matousek, A W Parker, W T Toner, M Towrie and R E Hester *in* Time-Resolved Vibrational Spectroscopy VI (1994), Springer Proceedings in Physics **74**, p89.
5. W T Toner, R E Hester, P Matousek, J N Moore, A W Parker and M Towrie, *in* Time-Resolved Vibrational Spectroscopy VI (1994), Springer Proceedings in Physics **74**, p115.
6. W L Weaver, L A Houston, K Iwata and T L Gustafson, J Phys Chem **96** (1992) 8956.
7. K Iwata and H Hamaguchi, Chem Phys Lett **196** (1992) 462.
8. R M Butler, M A Lynn and T L Gustafson, J Phys Chem, **97** (1993) 2609; D L Morris, Jr. and T L Gustafson, Appl PhysB, **59** (1994) 389; J Phys Chem **98** (1994) 6275.
9. M Towrie, P Matousek, A W Parker, W T Toner and R E Hester, Spectrochimica Acta **A 51** (1995) 2491.
10. A W Parker, P Matousek, W T Toner, M Towrie, D L A de Faria, R E Hester and J N Moore, ProcXIV Int Conf on Raman Spectroscopy (1994), Extra booklet, pE-9; P Matousek, A W Parker, W T Toner, M Towrie, D L A de Faria, R E Hester and J N Moore, Chem Phys Letters, **237** (1995) 373.
11. J Qian, S I Schultz and J M Jean, Chem Phys Lett, **233** (1995) 9.
12. The dye handbook (Coherent).
13. G E Galica, B R Johnson, J L Kinsey and M O Hale, J Phys Chem, **95** (1991) 7994.

TIME RESOLVED RESONANCE RAMAN OF CAROTENOID RADICAL CATIONS

S. M. Tavender[1], R. Edge[2], D. J. McGarvey[2], A. B. Robertson[2], J.H.Tinkler[2], T.G. Truscott[2] and A. W. Parker[1]

[1]Lasers *for* Science Facility, Rutherford Appleton Laboratory, Chilton, Didcot,Oxon. OX11 OQX
[2]Department of Chemistry, University of Keele, Keele, Staffs. ST5 5BG

INTRODUCTION

Carotenoids are believed to have multi-functional roles in biological systems. In the chloroplasts of green plants[1,2] they serve to protect the photosynthetic system from photodynamic (photo-oxidative) damage. This is achieved by the quenching of chlorophyll triplet states, preventing formation of damaging singlet oxygen and possibly by direct quenching of singlet oxygen. Carotenoids also function as accessory light-harvesting pigments in the antenna systems of photosynthetic organisms, absorbing light energy in the spectral region where the chlorophyll absorption is weak. In addition, they may participate in the photosynthetic electron transfer chain with formation of carotenoid radical cations. Although there is no direct evidence that carotenoid radical cations are involved in normal photosynthetic electron flow, absorption changes following photoexcitation of chloroplasts have been attributed to a carotene radical cation within the photosystem II reaction centre[3]. Similarly, carotene radical cations have been observed in 'blocked' reaction centres[4]. In models of the photosynthetic system a porphyrin is covalently linked to a carotenoid and a quinone. Photoexcitation of this triad molecule leads to the formation of the carotenoid radical cation[5]. Carotenoids are also able to act as lipid soluble antioxidants by quenching singlet oxygen and harmful free radicals. Several studies[6] have established that β-carotene reduces the risk of diseases such as cancer possibly by radical scavaging to produce carotenoid radical ions.

In previous work we concentrated on the shorter (7 and 8 double bonds) carotenoids which absorb at 760 nm and 820 nm respectively. In this study we present the time resolved resonance Raman spectra of a series of longer chain carotenes containing up to 11 double bonds and also those containing oxygen (xanthophylls). The structures of the carotenoids studied are shown in Fig 1 along with the absorption maxima of the radical cations.

PHOTOCHEMISTRY

The carotenoid radicals have been generated by our well-established technique involving electron transfer from triplet 1-nitronaphthalene (NN):

$$NN \longrightarrow {}^3NN \qquad (1)$$

$$^3NN + Car \xrightarrow[OR]{355nm} NN^{\bullet-} + Car^{\bullet+} \qquad (2)$$

$$^3NN + Car \longrightarrow NN + {}^3Car \qquad (3)$$

The quenching of ^3NN involves a solvent dependent competition between energy transfer and electron transfer producing triplet carotenoid or radical cation respectively[7]. Hence to increase the yield, studies on the carotenoid radical cations were carried out in polar environments such as methanol, acetonitrile and Triton-X. For example with NN and 7,7-dihydroβ-carotene $\Phi_{\text{electron transfer}}$ is 0.3 in methanol and 0 in hexane.

EXPERIMENTAL

For all ns-TR[3] experiments reported here the pump laser wavelength was 355 nm (typically 0.35 mJ) and probe laser wavelength 810 nm (typically 1-2 mJ). The time delay between pump and probe lasers was 2 μs (the maximum of the cation intensity) and the laser repetition rate was 20 Hz. Spectra were collected for between 30 and 60 minutes. The concentration of carotenoid was 2×10^{-5} mol dm^{-3} and NN 10^{-3} mol dm^{-3}. The solvent was methanol. All solutions were flowed and recycled with the exception of 15,15-cis-β-carotene which showed signs of photodegradation. This sample was flowed to waste. It has been shown that 15,15-cis-β-carotene photoisomerises to give the trans isomer i.e. trans β-carotene.

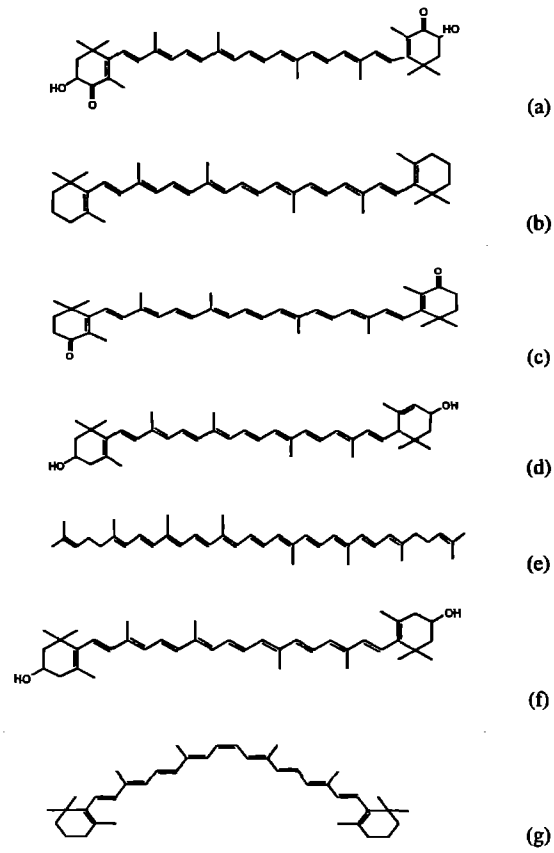

Fig 1 Carotenoid structures. (a) astaxanthin (11, 860 nm), (b) β-carotene (11, 940 nm), (c) canthaxanthin (11, 860 nm), (d) lutein (10, 910 nm), (e) lycopene (11, 920 nm), (f) zeaxanthin (11, 940 nm), (g) 15,15-cis-β-carotene (11, -). Number of double bonds and absorption maxima of radical cations from ref 7 in brackets.

RESULTS AND DISCUSSION

The time resolved resonance Raman spectra of the seven carotenoids studied are shown in Fig 2. The band positions have been determined by spectral fitting of the data using Raman[9]. Assignments are given in Table 1.

A weak underlying fluorescent background signal was observed for the pump probe experiments and this could not be reproduced by the pump only or probe only experiments. This background was removed by subtracting a polynomial curve fitted to each baseline. The wavelength maximum for this curve was different for each radical cation and this indicates that the background is fluorescence from the radical cation.

It is interesting to note that all the radical cation spectra are extremely similar and follow the same trends as described in our earlier work on shorter chain carotenoids[7]. That is, the bands in the 1500 cm^{-1} region, assigned as C=C stretching, exhibit a downward shift in frequency relative to the ground state reflecting a decrease in bond order and the bands around 1180 cm^{-1} assigned as C-C stretching show an upward shift from the ground state position indicating an increase in bond order.

carotenoid	astaxanthin	β-carotene	canthaxanthin	lutein	lycopene	zeaxanthin	15,15 -cis-β-carotene	septapreno-β-carotene*	7,7-dihydro β-carotene*	Assignment
Raman Frequency (cm^{-1})	938 1004	928 1006	975 1004	940 1000	971 1021	941 1003	939 1001	957 1008	949 1009	C-H out-of-plane deformation or CH_3 rocking
	1153 1189	1138 1185	1155 1190	1144 1185	1151 1188	1144 1185	1144 1186	1132 1173	1188	C-C stretch
	1275 1314 1451	1270 1301 1433	1274 1297 1437	1274 1308 1415	1286 1412 1453	1270 1307 1434	1272 1312 1412	1269 1442	1287 1303	C-H in plane bending or CH_3 deformation
	1502 1534	1499 1531	1502 1533	1502 1535	1492 1525	1501 1533	1497 1528	1517 1536	1514 1541 1563	C=C stretch

Table 1. *refers to reference 7.

We first examine the non-oxygen containing carotenoids. As the number of double bonds within the polyene chain (i.e. not including those within the β-ionone-ring) increases, there is a downward shift for the C=C stretching frequency, i.e. 1517 & 1536 cm^{-1}, 1499 & 1531 cm^{-1} and 1492 & 1525 cm^{-1} respectively for 7, 9 and 11 polyene chain double bonds. In a similar fashion, the C-C stretching frequency shifts upwards. This is explained by the electron loss centre being completely delocalised over the polyene chain and the net change to the radical cation structure lessens as the number of C=C units increases. Next we consider the xanthophylls. Firstly, in zeaxanthin the OH is uncoupled from the π-system by two C-C bonds. This allows the system to behave the same as other 9-double bonded polyene chain systems and this is observed with the Raman spectrum equivalent to β-carotene. This is further evinced by lutein which has an asymmetric structure with only one of the β-ionone-ring double bonds coupling with the π-system and 9 double bonds in the polyene chain. From the above discussion we can expect the cation radical spectrum to resemble β-carotene and this is the case.. For astaxanthin and canthaxanthin the C=O's are coupled to the π-system. However, the Raman band positions for both these carotenoids are yet again equivalent to the β-carotene. We believe this is evidence that the centre for electron loss is restricted within the polyene chain and does not extend to the β-ionone-ring. Furthermore, carotenoid radical ions have a bathochromic shift in absorption maxima dependent on the number of double bonds. Astaxanthin and canthaxanthin with a total of 13 double bonds (including polyene chain β-ionone-ring and C=O's) have absorption maxima ~50 nm lower than β-carotene supporting our conclusions drawn from the Raman spectra that the radical centre is not delocalised over the β-ionone-ring and C=O's. This is also expected because of the repulsive nature of the C=O's to positive charge. For the non-oxygen containing carotenoids the Raman data does not agree with the absorption data where the bathochromic shift only correlates with the total number of double bonds.

REFERENCES

1. J. C. Goedheer, Ann.Rev. Plant Physiol., 23, 87 (1972).
2. M. Chessin, R Livingston, T.G. Truscott, Trans Faraday Soc. 62, 1519 (1966).
3. P. Mathis, A.W. Rutherford, Biochem. Biophys. Acta 767 217 (1984).
C.C. Schenck, B. Diner, P. Mathis, K. Satoh, Biochim. Biophys Acta 680, 216, (1982).
4. A. Telfer, J. De Las Rivas, J. Barber, Biochem. Biophys Acta 106, 1060 (1991).
5. T.A. Moore et al, Nature 307 630 (1984)
6. M. Matthews-Roth, N Krinsky, Photochem. Photobiol. 42, 35 (1985)
7. J.H. Tinkler, S.M. Tavender, A.W. Parker D.J. McGarvey, L. Mulroy and T.G. Truscott, J Am Chem Soc. 118 1756 (1996).
8. T.J. Hill, E.J. Land, D.J. McGarvey, W. Schalch, J.H. Tinkler and T.G. Truscott, J.Am. Chem. Soc. 117, 8322 (1995)
9. Raman fitting programme CCLRC 1994.

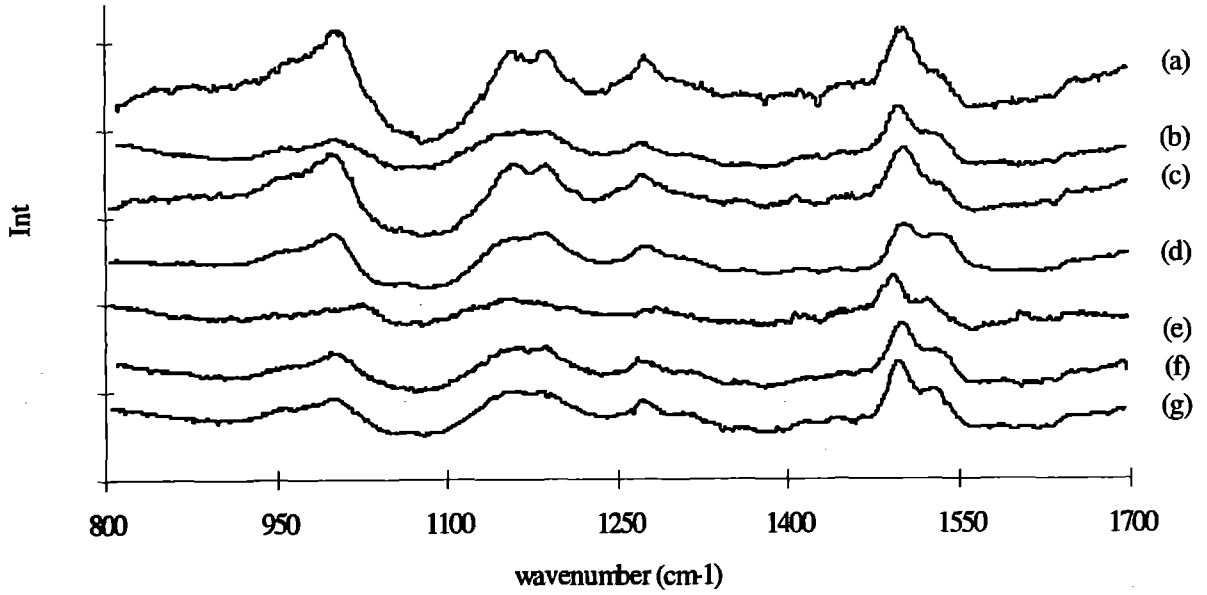

Fig 2. Time resolved resonance Raman spectra of carotenoid radical cations. (a) astaxanthin, (b) β-carotene, (c) canthaxanthin, (d) lutein, (e) lycopene, (f) zeaxanthin, (g) 15,15-cis-β-carotene. All spectra are subtracted (pump/probe minus probe only) and normalised to solvent bands.

1-NITRONAPHTHALENE TRIPLET EXCITED STATE, RADICAL ANION AND ELECTRON TRANSFER REACTION WITH TRANS-STILBENE : A ns-TR^3 STUDY

T. Fournier [1], G. Scholes [2], D. Phillips [2], S. Tavender [1], A.W. Parker [1]

[1]Laser for Sciences Facility, Rutherford Appleton Laboratory
[2]Chemistry Department, Imperial College of Science, Medicine and Technolology

INTRODUCTION

Molecules containing the nitro group are involved in many electron-transfer processes both in the gas phase and in solution. Although there has been a fair amount of work concerning the steady-state photochemistry of aromatic nitrocompounds[1-4], as well as transient absorption studies[5], only vibrational spectroscopies (Raman and infrared absorption) are able to yield direct structural information about the chemical intermediates.

The lowest triplet excited state of 1-nitronaphthalene (NN) has long been suspected of having a different character depending on solvent polarity[5], changing from an n-p* to a p-p* when going from non polar to polar solvents. However, what really attracted our interest in this molecule was the recent observation at RAL[6] that NN is able to undergo both electron transfer (35%) and energy transfer (65%) reactions with carotenoids in methanol (polar) while only energy transfer takes place in n-hexane (non-polar). In order to better understand the relationship between structure and electron transfer reaction we have investigated the lowest triplet excited state and the radical anion of NN in different solvents by nanosecond time-resolved resonance Raman spectroscopy (ns-TR^3). We compared the reactions with carotenoids with that with trans-stilbene (a very good electron donor and a very efficient Raman scatterer).

EXPERIMENTAL

The ns-TR^3 experimental set-up has been described previously[7]; 360 nm laser light (0.5 to 1.5 mJ, 15 ns FWMH) was used to pump ground-state NN while 448, 452, 456, 520, 540, 560, 580 and 640 nm (0.3 to 1 mJ, 15 ns) served as probe for triplet NN (^{3}NN); 452 nm was used to detect NN^- and 448 nm to detect $tS^{+\cdot}$.

Carbon tetrachloride (CCl_4), cyclohexane, dichloromethane (DCM), methanol (MeOH), dimethylsulfoxide (DMSO) and acetronitrile (MeCN) (Aldritch) were of spectroscopic grade and used as such while water was of Analar quality. All chemicals -1-nitronaphthalene, sodium nitrite ($NaNO_2$), trans-stilbene (tS)- were purchased from Aldritch (purity>98%) and used as such. For the triplet state studies the concentration of the solutions of NN was kept between 1 and 3 mM; the radical anion was detected using 3 mM NN and 5 or 10 mM $NaNO_2$ in an MeCN/water mixture (95/5 v/v) and the electron transfer reaction with tS was observed in 5 mM NN and 10 mM tS solutions.

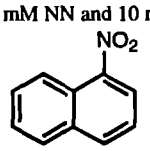

1-nitronaphthalene

RESULTS AND DISCUSSION

Triplet excited state

Porter et *al.*[6] showed that the peak of the main absorption band of triplet nitronaphthalene shifts from *ca.* 520 nm in non-polar solvents (n-hexane) to over 600 nm in very polar solvents (N,N'-dimethylformamide). In each solvent no change in Raman bands positions was observed by varying the probe wavelength from 520 to 640 nm, that is by probing from the blue to red tails of the triplet absorption band. Further very minor changes in the relative intensities of the spectral bands were detected. However some significant differences are observed between the spectra recorded from polar and non-polar solutions as is illustrated figure 1. Most of the bands appear upshifted in polar solvents compared to non-polar solvents (see table 1), with the notable exception of the 1554 cm^{-1} band in CCl_4 which downshifts to 1547 cm^{-1} in MeCN. The two other most remarkable changes are the shift of the 1027 cm^{-1} band in CCl_4, which goes from being overlapped with the 1021 cm^{-1} band to being clearly separated at 1040 cm^{-1}, and the shift from 1112 to 1120 cm^{-1} which is accompanied by an important increase in relative intensity.

^{3}NN in CCl_4 (cm^{-1})	^{3}NN in MeCN (cm^{-1})	NN^- in MeCN/water (cm^{-1})	tentative assignments
		1002	*
1021	1022	1025	*
1027	1040	1038	*
1075	1077	1076	*
1112	1120	1122	n CN
1146	1144	1156	*
1176	1184	1176	*
1195 (sh)			*
		1229	*
		1253	*
1264	1272	1273	*
1310	1315		*
1319	1323	1326 or 1338	$n_s NO_2$
1347	1350	1351	*
1384	1383	1382	*
1417	1424		*
1446	1454	1454	*
		1502	*
1513	1518		*
1554	1547	1553	$n_{as} NO_2$
1567	1569	1566	*
1587	1583		*

Table 1 Vibrations of ^{3}NN in non polar and polar solvents and of the radical anion between 1000 and 1600 cm^{-1}.

By comparison with other nitro compounds and particularly nitrobenzene[8] we tentatively assign the *ca.* 1320 cm^{-1} band to the NO_2 symmetric stretch, the *ca.* 1567 cm^{-1} band to the NO_2 asymmetric stretch and the 1120 cm^{-1} band to the CN stretch. The other bands encompass a variety of CC stretches, in- and out-of-

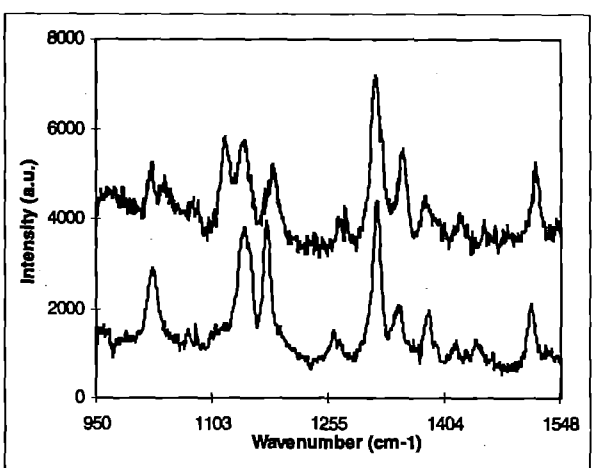

Fig.1 Resonance Raman spectrum of ^{3}NN [top] in MeCN (2 mM) and [bottom] in CCl_4 (1.6 mM). λ_{pump}=360 nm. λ_{probe}=540 nm.

plane CH bends and ring deformations as well as possible unidentified overtones and combination bands. No more precise assignments are available for the moment for all vibrations are Raman allowed due to the symmetry of the molecule. Ab initio calculations are being carried out to help us in this task. The shifts to higher frequencies in polar solvents could be linked to a shortening of bond lengths and an increase in the conjugation between the aromatic part of the molecule and the nitro group but for the lower frequency of n_{as} NO_2. However we must remain cautious in our interpretation especially since the observed frequencies do not correspond to pure vibrational modes in the same way as was demonstrated by Shlyapochnikov *et al.*[8] for nitrobenzene.

Radical anion

The radical anion of NN ($NN^{-\cdot}$) was produced by the diffusion-controlled electron-transfer reaction between triplet NN and ground-state nitrite. Although $NN^{-\cdot}$ has two characteristic absorption bands[4] at 600 and 660 nm these are very weak (e *ca.* 1000 $M^{-1}.cm^{-1}$) making a 452 nm probe wavelength although in a region where both $NN^{-\cdot}$ and ^3NN absorb a better choice. The TR^3 spectra (figure 2) show the formation of the radical anion over the

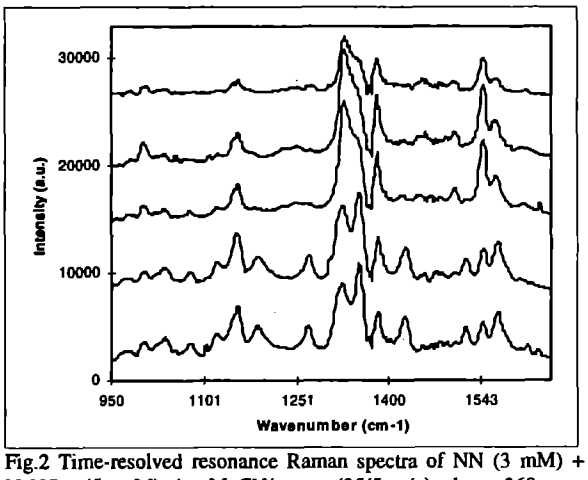

Fig.2 Time-resolved resonance Raman spectra of NN (3 mM) + $NaNO_2$ (5 mM) in MeCN/water (95/5 v/v); l_{pump}=360 nm, l_{probe}=452 nm. From bottom to top the delays between pump and probe are : 0,10, 100, 200 and 1000 ns.

first 250 ns and its slower decay over the next few ms (when the beams are temporally overlapped, dt = 0 ns, a mixture of ^3NN and $NN^{-\cdot}$ is observed). The resonance Raman spectrum of the anion is mainly characterised by bands at 1002 and 1156 cm^{-1}, three overlapping bands at 1326, 1338 and 1351 cm^{-1}, and bands at 1382, 1502, 1553 and 1566 cm^{-1}; Either the band at 1326 cm^{-1} or the one at 1338 cm^{-1} can be assigned to the NO_2 symmetric stretch. All the bands observed between 1000 and 1600 cm^{-1} for ^3NN and $NN^{-\cdot}$ are summarised in table 1.

Electron transfer reaction with trans-stilbene

Triplet NN reacts with carotenoids by both electron and energy transfer reaction in polar solvents but only transfers energy in non-polar solvents. To compare what happens with another electron donor we investigated the reaction of ^3NN with trans-stilbene in various solvents. tS is a well-known electron donor which also possesses the useful property for us of being an extremely good Raman scatterer. The reaction was studied in CCl_4 (non-polar), DCM (medium polarity) and MeCN (polar). We were surprised to detect ground-state tS (see figure 2) since it is not in resonance at 452 nm (e < 100 $M^{-1}.cm^{-1}$). Further in MeCN the TR^3 spectra proved the formation of the radical cation of tS; we can see on figure 3 the formation and the decay of $tS^{+\cdot}$ as characterised by the rise and fall in intensity of its *ca.* 1600 cm^{-1} band. However no such reaction could be detected in CCl_4 or DCM, illustrating once again the importance of the solvent's role in the electron transfer reaction to ^3NN.

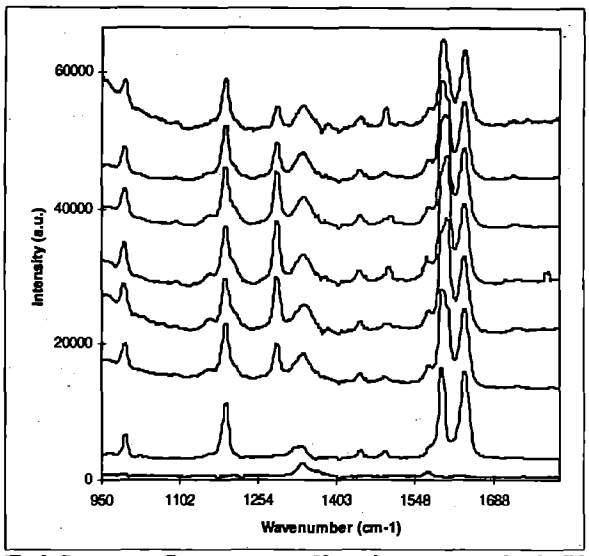

Fig.3 Resonance Raman spectra [from bottom to top] of NN (5mM), of tS (10mM) -both probed at 452 nm- and of NN (5mM) + tS (10mM) pumped at 360 nm and probed at 452 nm with the following delays : 0, 25, 45, 100, 250 and 500 ns. Solvent MeCN.

When the thermodynamic possibility of the electron transfer reaction is considered we can see that the free energy of the reaction,

$$DG = E_{ox} - E_{red} + C - E_{triplet} \qquad (1)$$

($E_{ox/red}$ oxidation and reduction potentials of the donor and acceptor respectively, $E_{triplet}$ energy of the triplet state, C coulombic correction due to the interaction of the ions formed in a dielectric media), is *ca.* 0 eV for both the reaction with carotenoids and with tS. The exact value, being dominated by C, that is by the solvent polarity, is small (|DG|<0.1eV). The rate of electron transfer, according to Marcus' theory, is :

$$k_{et} = FC \cdot \exp(-DG^{\#}/k_BT) \qquad (2)$$

$$\text{with } DG^{\#} = (DG+l)^2/4l \qquad (3)$$

where l is the reorganisation energy, k_B the Boltzmann factor, T the temperature and FC the Fanck-Condon factor. Consequently, in the reactions between ^3NN and carotenoids and tS, two factors control the electron transfer rate : the reorganisation energy and the Franck-Condon factor. The latter is directly linked to structural factors while the former is the sum of the internal and external reorganisation energies, i.e. the intramolecular and the solvent rearrangement after the electron transfer has taken place. So the electron transfer probability in a particular solvent will be determined by the particular structures of the molecules and by the amount of solvent reorganisation. It is our belief that the changes in the TR^3 spectra of ^3NN observed for the various solvents hold subtle clues to the switching from an energy transfer to an electron transfer process. That is to say the electron transfer quenching is not solely favoured because of the increase in rate of ion separation. A definitive assignment based on ab initio calculation should enable us to establish these facts.

REFERENCES

1. O.S. Khalil, H.G. Bach, S.P. McGlynn, *J. Mol. Spectr.*, 1970, **35**, 455.
2. G.N. Lewis, M. Kasha, *J. Am. Chem. Soc.*, 1944, **66**, 2100.
3. D.S. McClure, *J. Chem. Phys.*, 1949, **17**, 905.
4. W. Kemula, R. Sioda, *Naturwissensch.*, 1963, **23**, 708.
5. C. Capellos, G. Porter, *J. Chem. Soc. Faraday Trans. 2*, 1974, **70**, 1159.
6. J.H. Tinkler, S.M. Tavender, A.W. Parker, D.J. McGarvey, L. Mulroy, T.G. Truscott, *CLF Annual Report 1994-95*, 130.
7. E. Vauthey, A.W. Parker, B. Nohova, D. Phillips, *J. Am. Chem. Soc.*, 1994, **116**, 9182.
8. V.A. Shlyapochnikov, L.S. Khaikin, O.E. Grikina, C.H. Bock, L.V. Vilkov, *J. Mol. Struct.*, 1994, **326**, 1.

RESONANCE RAMAN STUDIES OF DMABN - A PRELIMINARY REPORT

G D Scholes,[1)] T Fournier,[2)] A W Parker,[2)] and D Phillips[1)]

[1]Department of Chemistry, Imperial College of Science, Technology & Medicine, London SW7 2AY
[2]Rutherford Appleton Laboratory

INTRODUCTION

A large number and variety of molecules which exhibit intramolecular excited state charge separation have been characterized. A class of these are thought to possess a "Twisted Internal Charge Transfer" (TICT) state and exhibit characteristic dual fluorescence.[1] 4-(dimethylamino)benzonitrile (DMABN) is the most well-known of the TICT molecules. Only the higher energy of the two emission bands is seen in non-polar solvents, or for systems in which the -$N(Me)_2$ group is constrained to be in the plane of the aromatic ring. The red-shifted emission observed in polar solvents is attributed to the TICT state; twisted intramolecular charge transfer because it is often assumed that the charge transfer state is produced when the -$N(Me)_2$ group is orthogonal to the aromatic ring.[2,3] Whether or not the dimethylamino group in DMABN really does twist markedly is not known for certain,[4] however the molecule does display some interesting photophysical properties. Recent *ab initio* calculations undertaken at Imperial College[5] together with the preliminary resonance Raman data reported here are adumbrating a particularly interesting picture and should help to elucidate some of the most topical questions debated in the literature.

A time resolved infra red study of the DMABN TICT state has been reported recently.[6] The CN stretch was observed and its frequency suggests that an electron is transferred to the antibonding orbital of the CN group. No information regarding the $N(Me)_2$ group was obtained however. We have begun to undertake ground state and transient resonance Raman studies of DMABN in various solvent environments in order to elucidate further the structure and nature of the ground and excited states of DMABN.

EXPERIMENTAL SECTION

DMABN was obtained from Aldrich and used without further purification. Samples in spectroscopic grade solvents (carbon tetrachloride, chloroform and dichloromethane) were made up to concentrations of *ca.* 1 mM, degassed by argon bubbling and were flowed through a Spectrosil B quartz silica tube. The Raman signal was collected at right angles to the laser pump/probe beams and sample flow direction using a Spex Triplemate 1400 spectrograph and a back illuminated liquid nitrogen cooled CCD detector (Princeton Instruments CSMALN/CCD-1024/TKB/I system). The TR^3 set-up has been described previously.[7] A pump wavelength of 308 nm and a probe wavelength of 500 nm were used. Spectra were collected for 90 minutes.

RESULTS

Ground state. Using the probe only (500 nm) some quite intense ground state classical Raman bands for DMABN were observed. Such a spectrum is depicted in Figure 1(a) for carbon tetrachloride solvent (solvent bands subtracted). The most intense bands are seen to lie at 1166 cm^{-1}, 1181 cm^{-1} and 1612 cm^{-1}. *Ab initio* calculations[5] suggest that both the 1166 cm^{-1} and the 1612 cm^{-1} bands correspond to aromatic ring in-plane deformation modes. The 1181 cm^{-1} peak is most likely a combination band. In Figure 1 (b) the 750 to 1000 cm^{-1} region is shown for DMABN in CCl_4 (ε = 2.24), CH_3Cl (ε = 4.81) and CH_2Cl_2 (ε = 9.08) solvents. These measurements will be repeated "in resonance", but even the present data suggests that there is a frequency shift for the *ca.* 800 cm^{-1} band in going from a non-polar to a polar solvent.. According to the *ab initio* results, this frequency is due to a vibration involving the aromatic ring and the nitrile nitrogen, which (given that the ground state of DMABN is fairly polar (m Å 6 D)) may explain this solvent-dependence.

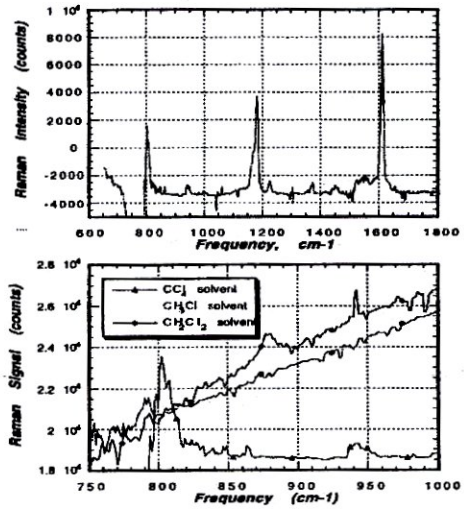

Figure 1. (a), top, DMABN ground state classical Raman spectrum in carbon tetrachloride solvent. (b), bottom, comparison of the 750 to 1000 cm^{-1} region for various solvents.

Excited state. Using the ns TR^3 set-up it was hoped that the excited (TICT) state Raman spectrum could be charcterized in a range of solvents. Marked changes have been observed previously in the transient absorption spectra of DMABN in solvents of various dielectric constant [8]. However, the transient Raman signal was very difficult to detect due to an overwhelming fluorescence background. A transient signal was detected in CCl_4 solvent at 1395 cm^{-1}, but this signal originates from the DMABN triplet excited state.

REFERENCES

1. W. Rettig, Top. Curr. Chem., 169, 254 (1994).
2. E. Lippert, W. Lüder and H. Boos, in *Adv. Mol. Spectros.* vol. 1, Ed. A. Mangini (Pergamon, NY, 1962).
3. W. Rettig, Angew. Chem. Int. Ed. Engl., 25, 971 (1986).
4. K. A. Zachariasse, T. von der Haar, A. Hebecker, U. Leinhos and W. Kühnle, Pure Appl. Chem., 65, 1745 (1993).
5. G. D. Scholes, I. R. Gould and D. Phillips, J. Am. Chem. Soc. (to be submitted).
6. M. Hashimoto and H. Hamaguchi, J. Phys. Chem., 99, 7875 (1995).
7. E. Vauthey, D. Phillips and A. W. Parker, J. Phys. Chem., 96, 7356 (1992).
8. T. Okada, N. Mataga and W. Baumann, J. Phys. Chem., 91, 760 (1987).

IMPROVED INSTRUMENTATION AND TECHNIQUES FOR THE TIME RESOLVED DETECTION OF SINGLET OXYGEN LUMINESCENCE

T. C. Oldham,[1] A. Beeby,[2] A. W. Parker,[3] C. F. Stanley,[2] A. Telfer,[4] J. Barber[4] and D. Phillips[1]

[1] Department of Chemistry, Imperial College of Science, Technology and Medicine, London SW7 2AY
[2] Department of Chemistry, University of Durham, South Road, Durham DH1 3LE
[3] Rutherford Appleton Laboratory, Chilton, Didcot OX11 0QX
[4] Department of Biochemistry, Imperial College of Science, Technology and Medicine, London SW7 2AY

INTRODUCTION

We have previously reported studies of singlet oxygen ($^1O_2$) luminescence at 1270 nm using the North Coast Scientific EO817-P liquid nitrogen cooled Ge photodiode at RAL.[1] The near-IR luminescence signal comprises two components: the grow-in and decay of the $^1O_2$ luminescence (which is of interest), and a fluorescence spike (which is not of interest). In the case of red emitting $^1O_2$ sensitisers such as the phthalocyanines, this spike may be orders of magnitude more intense than the $^1O_2$ signal, giving rise to two problems: the spike prevents information about early time kinetics, particularly the risetime, of the $^1O_2$ decay being extracted from the signal; and at high gains needed to detect $^1O_2$, the spike saturates oscilloscope amplifiers leading to distortion of the decay. Two strategies to address these problems and improve $^1O_2$ detection are discussed in this report, namely the determination of the origin of the spike in order to reduce its intensity, and switching the diode signal in order to control the input to the measuring oscilloscope. A third strategy, the development of faster detectors is currently under investigation at Imperial College. We also describe measurements of $^1O_2$ luminescence in two interesting biological systems (Photosystem two and photosensitised microbes) which have helped explain some poorly understood physiological observations.

ORIGIN OF THE FLUORESCENCE SPIKE

Three sources for the fluorescence spike may be postulated: 1270 nm fluorescence from the sensitisers; leakage of visible sensitiser fluorescence through blocking regions of interference filters; and near-IR emission from filter substrates subjected to excitation by sensitiser fluorescence.[2] Our preliminary studies[3] supported the third postulate. A more detailed study has now been undertaken.

Figure 1 Sensitiser emission wavelength dependence of the fluorescence spike intensity

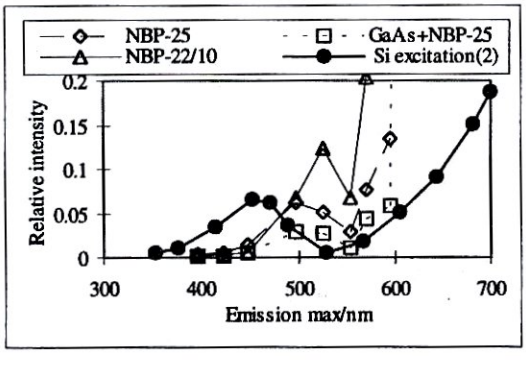

Nine laser dyes with emission maxima in the range 390-820 nm where prepared with optical densities of ≈ 0.05 at 355 nm. Using 355 nm excitation the spike intensity for each of these dyes was measured at three (non-saturating) laser powers using the RAL Ge diode.[1] Sample emission was filtered using one of two 1270 nm narrow bandpass interference filters (NBP) from Infrared Engineering. In some cases, additional filters or substrate materials were placed in front of the NBP. After correcting the spike intensities for absolute emission intensities and laser power fluctuations, the spike intensities were plotted as a function of sensitiser maximum emission wavelength. Figure 1 shows some typical data sets. The most common filter substrate is silicon and its excitation spectrum according to Scurlock et. al.[2] is also shown.

Figure 1 shows that although the wavelength dependence of the spike intensity displays a local maximum at blue-green wavelengths, as predicted by Scurlock et. al., it does not correlate with their Si excitation spectrum. The use of a variety of different substrates and filters to reduce the intensity of visible fluorescence incident on the NBP had no effect on the shape of the spike intensity profile, although Si and GaAs blanks reduced the spike intensity relative to elements which did not provide additional blocking beyond 900 nm. These data do not support the conclusions of Scurlock et. al. or our earlier interpretation.

The two nominally identical NBP's displayed very different behaviour. The transmission spectra of the filters revealed an 18 nm spectral hole at 760 nm in the blocking region of NBP-22. Leakage of fluorescence here accounts for the greater red wavelength dependence of spike intensity for this filter. Use of a monchromator at Durham University to resolve spectrally the emission confirmed this and in addition showed that, while both styryl 9 and disulfonated aluminium phthalocyanine ($AlPcS_2$) emit at 1270 nm, a large proportion of their spike is due to fluorescence leaking through the blocking region of the NBP's, notwithstanding the spectral hole. Using a Cu^{2+}/NH_3 solution filter to provide additional blocking in the region of 600-800 nm considerable reductions in spike intensity were achieved.

We conclude that the dominant contribution to the fluorescence spike observed during $^1O_2$ measurements is sensitiser fluorescence leaking through the blocking regions of the NBP. The sensitiser emission wavelength dependence of the spike intensity (Figure 1) is identified as the wavelength dependence of the Ge responsivity curve. For far red emitting sensitisers, there is also a contribution from direct fluorescence at 1270 nm, but this dominates only for styryl 9. Significant reductions in spike intensity can be achieved by supplementary blocking at the sensitiser fluorescence maximum.

GATING THE FLUORESCENCE SPIKE

To eliminate saturation of DSO amplifiers, we have developed an electronic switch enabling the oscilloscope and the signal from the detector to be grounded for the duration of the spike. Switching is achieved using an analogue switch chip controlled by a variable width TTL pulse, the width of the pulse determining the ground (gate) time. Use of the switch enables $^1O_2$ measurements to be made with greater accuracy and in previously impossible systems. Full details of the technique are being published elsewhere.[4]

Figure 2 shows the effect of varying the switch gate width on the oscilloscope response to the near-IR emission from a mixture of rose bengal (small spike, $^1O_2$ sensitiser) and styryl 9 (large spike, not a $^1O_2$ sensitiser) in methanol. Without the switch, undershoot following the spike is indicative of amplifier saturation. By increasing the gate width, the saturation is reduced until the decay

becomes invariant for gate widths of 2 μs or more. The measured decay time is 10.1 μs, in good agreement with the literature value for the lifetime of $^1O_2$, τ_Δ, in methanol of 10.6 μs. The switch can also be used to eliminate more subtle distortions. For a sample of $AlPcS_2$ in methanol, OD_{355} = 0.544 pumped with 1.09 mJ/pulse at 355 nm, τ_Δ and the initial intensity were measured as 13.0 μs and 3.8 mV respectively without the switch, and 10.0 μs and 5.1 mV with a 3 μs gate, yet the ungated signal was not obviously subject to saturation effects. In a further application, using a 700 ns gate we measured the lifetime of $AlPcS_2$ sensitised $^1O_2$ in oxygen saturated water as 4 μs, in good agreement with the literature.

Figure 2 Effect of switch gate width on signal distortion for a mixture of rose bengal and styryl 9 in methanol

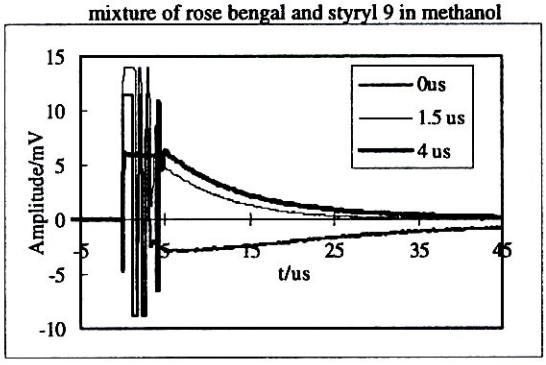

We recommend use of the switch in all situations where the spike is significantly more intense than the $^1O_2$ decay. In its current form, the minimum useable gate width is 100 ns and the switching transient is insignificant 200 ns after the gate reopens for large $^1O_2$ signals, and 1 ms for small $^1O_2$ signals. Elimination of saturation effects is achieved by increasing the gate width until the decay becomes independent of gate width. Application of the switch enables quantum yield and lifetime measurements to be made for previously inaccessible systems and improves accuracy in all systems.

DETECTION OF $^1O_2$ IN PSII REACTION CENTRES

Protection of oxygenic photosynthetic organisms against the potentially lethal effects of $^1O_2$ is normally achieved *in vivo* via the rapid quenching of chlorophyll triplets by carotenoids. This mechanism does not operate in Photosystem two (PSII). Isolated PSII reaction centres (RC's) generate ^{3}P680 (primary electron donor chlorophyll triplets) in 30% yield without appreciable generation of carotenoid triplets. It has previously been shown that isolated PSII RC's do generate singlet oxygen which is only partially quenched by the carotenoids.[5] Two problems remain. First, if P680 is generating the $^1O_2$ then the decay of ^{3}P680 should have the same rate as the grow-in of the $^1O_2$ signal (when $\tau_T < \tau_\Delta$ as is the case for these measurements in D_2O). This had not been observed. Secondly, since $\tau_T < \tau_\Delta$ the risetime of the $^1O_2$ signal should be dependent upon the oxygen concentration while the decay time should not, contrary to observations by Yruela et.al.[6]

To address these issues the decay of ^{3}P680 in isolated PSII RC's was remeasured at 20 °C rather than 4 °C as previously and found to be significantly faster. The near-IR luminescence of isolated PSII RC's was measured using the RAL system[7] over a range of time scales in air saturated D_2O buffer, oxygen saturated D_2O buffer and in the presence of NaN_3. The NaN_3 (non-$^1O_2$ emission including the spike) signal was subtracted from the other decays prior to fitting. The kinetic parameters extracted (Table 1) show good correlation between the ^{3}P680 decay rate and the $^1O_2$ grow-in rate, and also that the grow-in rate but not the decay rate of the $^1O_2$ signal is oxygen concentration dependent as expected. $\tau_{\Delta,decay}$ is less than the 60 μs expected in D_2O due to residual water retained in the RC's during preparation and the possible influence of the buffer salts and detergent on the $^1O_2$ decay rate constant.

Table 1 Isolated PSII RC triplet (T) and $^1O_2$ (Δ) lifetimes at 20 °C in D_2O buffer

Lifetime	Air saturated	O_2 saturated
τ_T/μs	20±1	4.5
$\tau_{\Delta,rise}$/μs	15±4	5±1
$\tau_{\Delta,decay}$/μs	46±4	41±3

ROLE OF $^1O_2$ IN MICROBE LETHAL PHOTOSENSITISATION

Toluidine blue (TB) is an effective sensitiser for the lethal photosensitisation of a range of micro-organisms; however the mechanism of cell kill seems to be organism dependent. Lethal photosensitisation experiments at the Eastman Dental Hospital have yielded the results shown in Table 2.[7]

Table 2 Conditions for lethal photosensitisation of microbes

Organism	Can be killed by TB in solution?	Takes up TB from solution?	Can be killed by bead bound TB?
S. sanguis (Gram +ve)	✓	✓	✓
P. gingivalis (Gram -ve)	✓	✓	X
C. albicans (Yeast)	✓	Slightly	X

We detected $^1O_2$ (as verified by absence of signal following Ar purging) in a D_2O suspension of TB sensitised sepharose beads. using a 2 μs gate on the switch to eliminate distortions. In pure D_2O, the decay showed a rise time of 3.2 μs, interpreted as the TB triplet lifetime, and a decay time of 60 μs, typical of $^1O_2$ in D_2O. In the beads, the triplet lifetime was extended to 6.9 μs, while the decay time was 34 μs. The shorter lifetime is believed to be due to incomplete exchange of H_2O and D_2O during bead preparation but this is yet to be verified.

We conclude that incorporation of TB into sepharose beads does not deactivate $^1O_2$ pathways to lethal photosensitisation. While $^1O_2$ is sufficient to kill organisms with simple cell walls such as the Gram positive bacterium, it is not sufficient (even necessary?) to kill the organisms with substantial cell walls. We propose, consistent with physiological studies by other workers,[8] that the more complex organisms require some interaction of the sensitiser with the cell wall which is inhibited by incorporation of the sensitiser into beads. The most likely process is electron transfer and in future we will be seeking evidence of transient TB radical ions.

REFERENCES

1. A. Beeby, S. Bishop, A.W. Parker, M.S.C. Simpson and D. Phillips, C.L.F. Ann. Rep., RAL-92-020, 227 (1992).
2. R.D. Scurlock, K.-K. Iu and P.R. Ogilby, J. Photochem., 37, 247 (1987).
3. T.C. Oldham and D. Phillips, C.L.F. Ann. Rep., RAL-TR-95-025, 153 (1994-95).
4. A. Beeby, A.W. Parker and C.F. Stanley, (submitted).
5. A. Telfer, S.M. Bishop, D. Phillips and J. Barber, J. Biol. Chem., 269, 13244 (1994).
6. I. Yruela, M.S. Churio, T. Gensch, S.E. Braslavsky and A.R. Holzwarth, J. Phys. Chem., 98, 12789 (1994).
7. M. Bhatti, T. Burns, Z. Jackson and M. Wilson, unpublished results.
8. M. Paardekoper, A.W. De Bruijne, J. Van Steveninck and P.J.A. Van den Broek, Photochem. Photobiol., 61, 84 (1995).

FLASH PHOTOLYSIS OF PHTHALOCYANINE SENSITISERS FOR PDT:THE EFFECT OF PH ON SOME PHOTOPHYSICAL MEASUREMENTS OF CLINICAL DISULPHONATED ALUMINIUM PHTHALOCYANINES

R.Ostler & D.Phillips

Department of Chemistry, Imperial College of Science, Technology & Medicine, South Kensington, London, SW7 2AY

Clinical disulphonated AlPcS2 is a mixture of water soluble disulphonated isomers currently undergoing clinical trials as a PDT sensitiser.

The present study is a continuation of the work presented earlier[1] which demonstrated a dependence of the triplet state lifetime and quantum yield on pH.

Triplet state data were obtained by nanosecond flash photolysis, using a pump beam of 670 nm and a probe beam of 490 nm. Samples were degassed by argon bubbling. Triplet state quantum yields were obtained by comparison with chlorophyll a in diethyl ether, (ϕ = 0.53).

The solutions used in this study were of constant AlPcS2 concentration (≈ 5.0 μM) in phosphate buffered saline (PBS) of constant ionic strength. Optical densities did not exceed 0.8 at the pump wavelength. The use of PBS rather than NaCl (as used previously) to maintain constant ionic strength was prompted by the use of the former as a biological buffer and also enabled us to monitor the effect of some common oxyanions.

NaCl solution			PBS solution		
pH	τ_T	ϕ_T	pH	τ_T	ϕ_T
1.3	190	0.11	2.5	281	0.1
2.1	211	0.115	4.5	477	0.155
2.85	282	0.126	5.5	500	0.133
4.0	343	0.136	6.5	490	0.19
6.9	424	0.269	7.5	494	0.22
8.25	387	-	8.75	482	0.5
11.75	420	0.54	10.0	447	0.57
13.38	466	0.52	11.3	444	0.57

The quantum yields and lifetimes exhibit different pH dependencies with the results from solutions containing PBS and NaCl concurring. These are therefore plotted together.

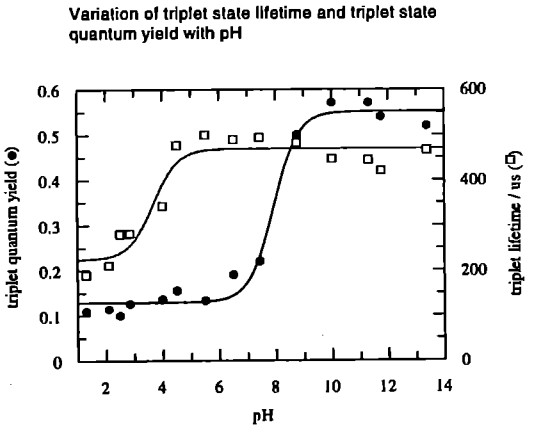

FIG 1

From Fig 1 it can be seen that the triplet quantum yield and triplet lifetime values appear to pass through pK_a values of approximately 8.0 and 3.5 respectively.

Triplet absorption spectra were obtained for pH 1.75 and pH 11.0 in pbs. (see Fig 2)

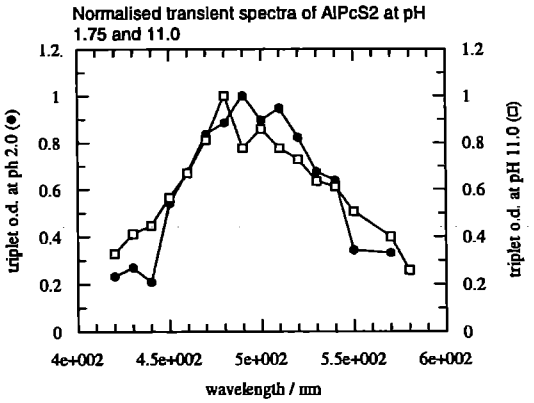

FIG 2

As shown in Fig 2 there is a general similarity in the spectral shape of the two species. Differences in absolute triplet o.d values are ascribed to the pH dependent concentration of the ground state monomer which gives rise to the triplet active species, (the dimer / aggregated species not contributing to the data obtained.).

The transient spectra appear to indicate that the triplet species at the pH extremes are very similar, if not identical. This would suggest that the major source of variation arises from ground state effects. We have found that the concentration of monomer species is dependent on pH, with increasing dimerisation occuring at low pH, $AlPcS_2$ being monomeric at high pH. The pH dependent dimerisation would be expected to have a marked effect on the observed ϕ_T. Triplet lifetime values are thought to depend on ground state quenching of the triplet state, this being rapid at low pH. The increase in the rate of this process is thought to be increased as a result of one of the water ligands on the aluminium being replaced by a labile chloride (pK_a ~ 3.5)[2], the subsequent loss of which would allow the close approach of quenching molecules and a subsequent decrease in the observed lifetime.

REFERENCES

1. Flash Photolysis of Phthalacyanine sensitisers for PDT. R.B. Ostler & D.Phillips. RAL Annual Report 1995

2. Savitsky et al, J. PhotochemPhotobiol B.Biol 13, 1992

THE PHOTOLYSIS OF ADSORBED MOLECULES

C.J.S.M. Simpson[1], P.T. Griffiths[1], H.L. Wallaart[1] and M. Towrie[2]

[1] Department of Physical and Theoretical Chemistry, Oxford University
[2] Rutherford Appleton Laboratory

INTRODUCTION

Our objective in these experiments is to understand the dynamics of the photolysis and ejection of products from molecules physisorbed onto dielectric surfaces. Over the past year we have made investigations into the photolysis of 3-cyclopentenone [1], by studying the desorbed CO, and into NO dimers, $(NO)_2$ [2] and alkyl nitrites [3] by investigations into the desorbed NO. Where possible we have compared our results with those obtained from similar dissociation processes occurring in the gas phase.

EXPERIMENTAL

The ultra-high vacuum chamber and laser system is described in detail elsewhere [1]. The MgF_2 surface is cooled to around 50 K and then dosed with between one and two monolayers.

An excimer laser is used to photolyse the adsorbed molecules. Low desorption laser fluences and even illumination of the crystal face are used to avoid any significant change in the structure of the surface layer during the collection of the REMPI spectra.

The frequency doubled output of an excimer pumped dye laser system is used to ionise the desorbed products of dissociation. The ion current is recorded as a function of dye laser frequency to produce a REMPI spectrum. These provide a complete description of the rotational and vibrational (v,J) state of the CO or NO product.

The delay between desorption and ionisation laser shots is controlled by a digital delay unit. By varying this delay, we are able to investigate the dependence of the (v,J) state of the desorbed products on its velocity.

RESULTS AND DISCUSSION

1. 3-Cyclopentenone

The photolysis of this molecule at 193 nm in the gas phase has been investigated by Jimenez *et al.* [4]. Dissociation occurs with nearly unit quantum yield to give butadiene and CO(v,J). 14% of the CO is born in (v"=1) and the remainder is born in (v"=0) with rotational temperatures of T_{rot}(v"=0)=3500 +/- 140 K and T_{rot}(v=1) = 7500 +/- 400 K. The rotational energy of the CO product was found to be proportional to its translational kinetic energy.

Our own experiments have shown that, within experimental error, CO is desorbed from the photolysis of adsorbed 3-cyclopentenone with the same vibrational population as in the gas phase. The rotational temperatures are much lower: the highest observed temperatures are 600 K for (v"=0) and 900 K for (v"=1). The rotational temperature of the desorbed CO was also found to depend on its kinetic energy, with an approximately linear relationship being observed.

We consider that the photolysis of 3-cyclopentenone is modified by adsorption. The amount of energy which may pass into rotation and translation is restricted, perhaps by some constraint of the molecules upon the surface. The rotational and translational degrees of freedom would then appear to be relaxed by collisions with surrounding molecules with the degree of relaxation depending upon the number of collisions which the desorbing molecule undergoes before leaving the surface. In this way, there is relaxation of both of these modes prior to desorption. The large quantum of CO vibration means that vibrational relaxation does not occur on the timescale of desorption.

2. NO Dimers

In condensed phases, NO forms a dimer. This has a structureless absorption centred around 220 nm [5], and can be photolysed at 248 nm using the output of an excimer laser. Since there is only one product of dissociation, this system is relatively simple to interpret. However, there are no gas phase data with which to compare our results.

Our preliminary investigations are described elsewhere [6]. We have now found that the velocity of the desorbed NO is of particular importance: the observed rotational distribution changes from a Boltzmann (Trot=320 K) to a Gaussian form with increasing velocity. For NO desorbed with velocities below 500 ms^{-1}, a rotational temperature of 320 K is observed. This temperature increases with increasing velocity, rising to 700 K at 1000 ms^{-1}. Above 1500 ms^{-1}, the distribution is well-characterised by a Gaussian function, shown in Figure 1.

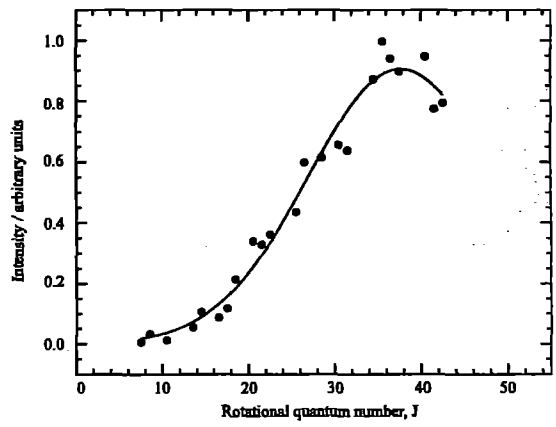

Figure 1: The rotational distribution of NO(v"=2) desorbed from NO dimers, measured for a velocity of 1500 ms^{-1}

We consider that collisional deactivation of the rotational and translational degrees of freedom is responsible for the observed change in the rotational distribution with velocity. NO is born on the surface with a Gaussian distribution of rotational states, and is subsequently relaxed by collisions with surrounding molecules prior to desorption. The longer the NO remains on the surface, the greater the degree of relaxation of rotational and translational energies.

3. Alkyl nitrites

These molecules show a structured absorption in the ultra-violet region between 300 and 400 nm. This corresponds to the $A^1A'' \leftarrow X^1A'$ ($\pi^* \leftarrow n$) transition with a simultaneous excitation of the localised N=O stretching mode [8]. The electronically excited molecule dissociates within 300 fs to give NO and an alkoxy fragment, RO [9]. The vibrational distribution of the NO depends on the initial vibrational excitation, and hence on the dissociation wavelength., with the distribution peaking one quantum below the initial excitation[8].

$$RONO\ (X^1A') + h\nu \rightarrow RONO\ (A^1A'',v) \rightarrow RO + NO(v\text{-}1,J)$$

We have shown that the vibrational distribution of NO produced from the photolysis of adsorbed alkyl nitrites mimics that seen in the gas phase [9].

We have now turned to the study of the rotational distribution of the NO produced in these processes. In the gas phase, a Gaussian distribution of rotational states is seen.

Huber and co-workers have recently studied the dissociation of alkyl nitrite cluster $[RONO]_n$ [10]. They have shown that two types of NO are produced: the first has a rotational distribution resembling that seen in the dissociation of the monomer; the second has a much lower degree of rotational excitation, with a Boltzmann distribution of rotational states (T_{rot}=250 K).

We have found that the rotational distribution of the desorbed NO depends crucially on its velocity, see Figure 2. At the highest velocities observed, 1900 ms^{-1}, an approximately Gaussian distribution of rotational states is seen, although there is a slightly more population in the lowest rotational states than is predicted by the fitted function. We have already shown that, at velocities below 500 ms^{-1} NO is desorbed with a rotational temperature of 400 +/- 100 K [10], and we have now found that, at intermediate velocities, the distribution is well-fitted by a function which is a weighted sum of Boltzmann and Gaussian functions. Only the relative intensities of these two functions change with velocity, in the case of *iso*-butyl nitrite, a temperature of 500 +/- 200 K and a Gaussian function with J_{max}=32.5 and ΔJ=8 is seen. For tert-butyl nitrite, we observe a temperature of 600+/- 300 K and J_{max}=26.5 with ΔJ=4.

We propose that NO is born on the surface with a Gaussian distribution of rotational states. Those molecules which are desorbed without colliding with the surrounding molecules show this original distribution. Through collisions, the rotational and translational energies of NO molecules are relaxed to Boltzmann distributions. Thus NO is desorbed in two forms: one form is highly rotationally and translationally excited, while the other is desorbed with lower velocity and significantly less rotational excitation.

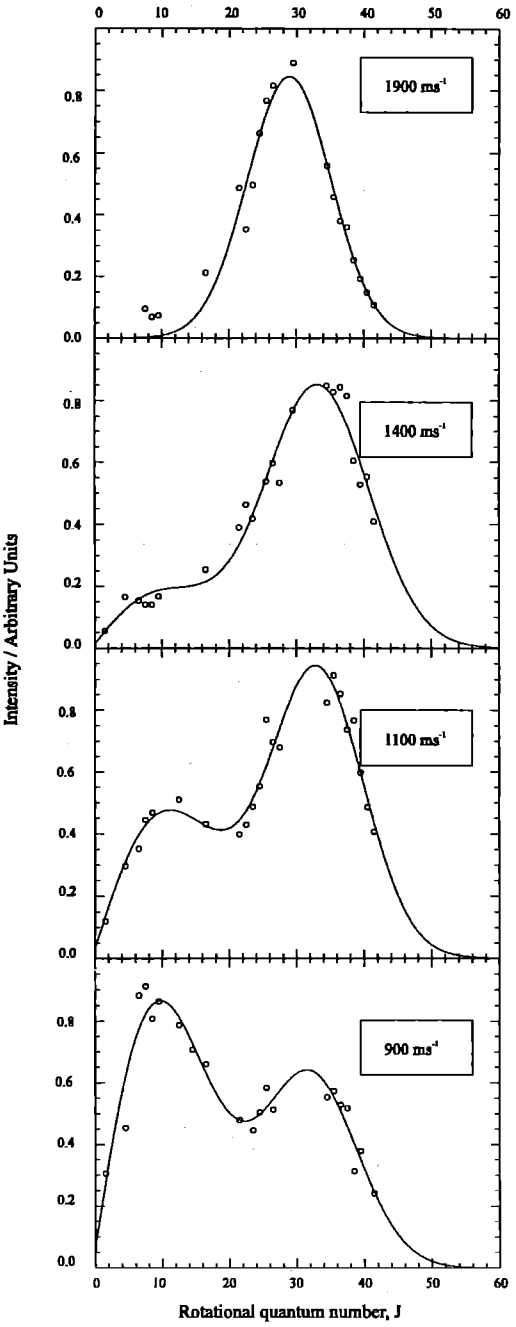

Figure 2: The rotational distributions of NO desorbed from *iso*-butyl nitrite, measured as a function of its velocity.

REFERENCES

1. C.J.S.M. Simpson, P.T. Griffiths, R. Lovegrove, P. Matousek and M. Towrie,
Chem. Phys. Letters, 246, 269 (1995).
2. C.J.S.M. Simpson, P.T. Griffiths, J.M. Curry and M. Towrie,
Chem. Phys. Letters, 250, 342 (1996).
3.C.J.S.M. Simpson, P.T. Griffiths, H.L. Wallaart and M. Towrie,
submitted to Chem. Phys. Letters.
4. R. Jimenez, S.H. Kable, J.-C. Loison, C.J.S.M. Simpson, W. Adam and P.L. Houston,
J. Phys. Chem, 96, 4188 (1992).
5.J. Billingsley and A.B. Callear,
Trans. Faraday Soc. 67 589 (1971).
6. J.M. Curry,
Part II Thesis (University of Oxford, 1990).
7. H. Reisler, M. Noble and C. Wittig in :
Molecular Photodissociation Dynamics, eds M.N.R. Ashfold and J.E. Baggott (Royal Society of Chemistry, London, 1987) p.162
8. M. Nonella, J.R. Huber, A. Untch and R. Schinke,
J. Chem. Phys. 91, 194 (1989).
9. C.J.S.M. Simpson, P.T. Griffiths and M. Towrie,
Chem. Phys. Letters, 234, 230 (1995).
10. E. Kades, M. Rosslein, U. Bruhlmann and J.R. Huber,
J. Phys. Chem 98 13557 (1994).

PHOTODISSOCIATION OF JET-COOLED NITROSO-COMPOUNDS: ALIGNMENT OF THE NO FRAGMENT

C. Ning and J. Pfab

Department of Chemistry, Heriot-Watt University, Edinburgh, EH14 4AS

INTRODUCTION

The photodissociation of C-nitroso-compounds into NO and carbon-centred radicals has provided interesting model cases for studies of unimolecular dissociation. Absorption of visible photons by the $\pi^* \leftarrow$ n transition results in photodissociation of the C-N bond on a time scale ranging from microseconds down to less than a picosecond.[1] Most C-nitroso-compounds reveal diffuse gas phase (n,π^*) absorption spectra indicating rapid predissociation to alkyl radicals and NO.[1,2] Recently v-J correlation effects and two-channel behaviour have been seen in the translational energy distributions of the NO fragment produced by photolysis of 2-chloro-2-nitrosopropane (CNP).[3] The photodissociation of trichloronitrosomethane (TCNM - CCl_3NO) also produces NO with a non-statistical rotational state distribution and equal populations of the Λ-doublets.[4] The present work was undertaken to identify and measure NO alignment effects in an attempt to further characterise the dissociation dynamics of the parent molecules.

EXPERIMENTAL

Fig.1 shows a schematic of the experimental set-up for the alignment measurement of CNP and CCl_3NO. Samples containing typically 1% of the nitroso-compound with helium as the carrier gas were used to minimise clustering effect.

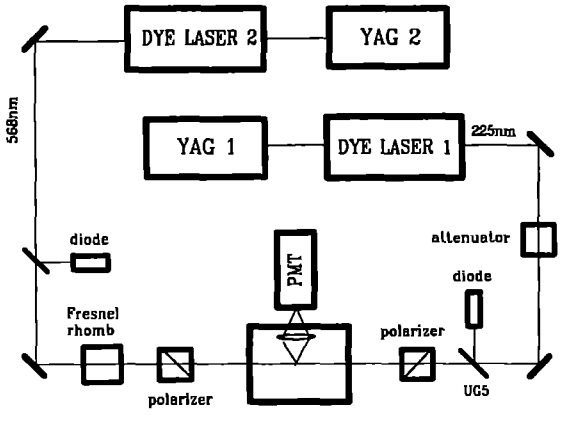

Fig 1 Experimental set-up used for the NO photofragment alignment measurements

Samples were jet-cooled by expansion through a pulsed nozzle with 0.5 mm orifice. The co-axially counterpropagating photolysis and probe lasers intersected the jet at a distance of about 8 mm from the nozzle.

The polarisation of the 568 nm photolysis beam (5 mm diameter, 9 mJ pulse energy) from the loaned YAG pumped Rh6G dye laser (Spectron SL-800/Quantaray PDL-2) was controlled by a Fresnel rhomb in combination with a polarizer and its power monitored by a diode. The NO fragment was probed by polarised LIF near 225 nm with the frequency doubled output of a Lumonics YAG pumped coumarin dye laser. Synchronisation with a timing jitter smaller than 5 ns and a delay of 15 ns between photolysis and probe laser pulses was accomplished with a delay generator. The probe laser beam was polarised horizontally using a calcite polarizer. The LIF signal of NO was detected by a photomultiplier, processed by a gated integrator-boxcar averager and stored in a lab computer. The LIF signal and probe laser energy were checked carefully to avoid saturation effects.

RESULTS

Fig 2 shows a comparison of normalised, polarised LIF spectra of NO from the photolysis of 1% CNP seeded in helium at 568 nm.

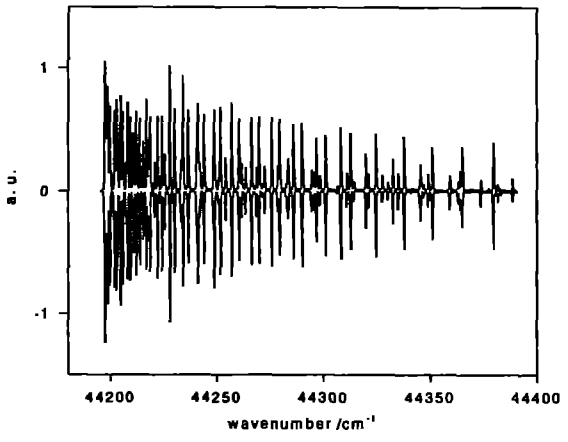

Fig.2: High energy section of the polarised LIF spectra of NO from the 568 nm photolysis of CNP:Upper spectrum recorded with vertical and lower, inverted spectrum with horizontal polarisation of the photolysis beam.

The power corrected and normalised spectra displayed start from the head of the Q_{11} branch near 226.1 nm and include transitions up to J"=27.5 around 225.1 nm. The alignment values for NO with J > 15.5 were calculated using Dixon's formulae for the high J limit[5] and are shown in figure 3 for transitions from four different branches.

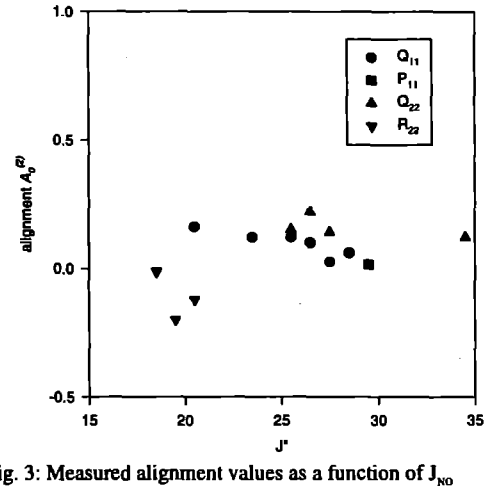

Fig. 3: Measured alignment values as a function of J_{NO} for 568 nm CNP photolysis

Measurements based on the strong Q_{11} branch transitions are most accurate and provide alignment values close to zero for J ranging from 20.5 to 27.5. The single P_{11} branch transition J = 29.5 measured also yielding a value of zero. Transitions from the weaker other two branches are from the upper spin-orbit manifold and also gave values close to zero with a maximum of 0.26 from the R_{22} branch. Given an experimental uncertainty of at least 50% for these measurements we conclude that the NO fragment from photolysis of CNP at 568 nm is not aligned significantly.

Fig.4 shows the measured alignment of NO from the 568 nm photolysis of CCl_3NO under identical experimental conditions.

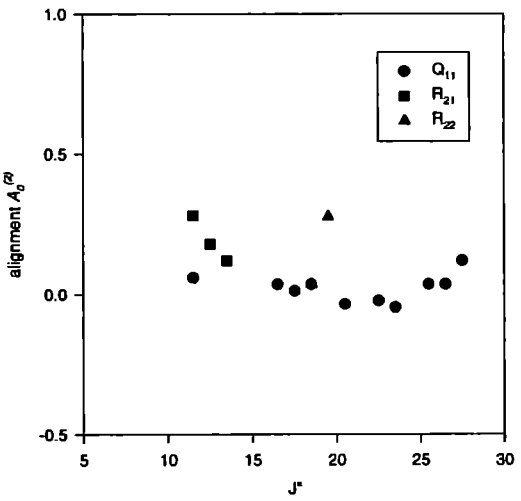

Fig. 4: Alignment as a function of J_{NO} for 568 nm TCNM photolysis.

The Q_{11} branch again yields consistent values close to zero, and the results from the other branches of the upper spin-orbit manifold showed little scatter with a maximum value of 0.25. We can therefore conclude that NO from the photolysis of TCNM at 568 nm is also not aligned significantly within our experimental error.

DISCUSSION AND CONCLUSION

The 300 K absorption and jet-cooled NO photofragment yield spectra of CNP and TCNM in the visible appear diffuse., although they are not continuous revealing crude vibronic features at low temperature in the jet or in low temperature hydrocarbon glasses. The fluorescence is too weak in both cases to permit detection indicating that photodissocation might be prompt. The translational energy distribution (in the case of CNP) and the rotational state distributions of the NO photofragment can be interpreted as statistical implying energy randomization or as dynamically controlled. For TCNM we have measured decidedly non-statistical rotational state distributions showing that photodissociation from S_1 takes place on a time scale that is too short for complete energy randomisation. and suggesting that fast dynamics is involved significantly. We have now shown that the photolysis of both compounds at 568 nm, where the excess energy available for partitioning into fragments is about 3000 cm^{-1} , does not produce NO with a significant alignment. Our results imply S_1 excited state lifetimes of the parent longer than 1 ps and confirm that photodissociation of both species cannot proceed by a direct mechanism at this wavelength. Measurements at shorter wavelengths will reveal whether excitation into steeper portions of the S_1 potential or to the S_2 state lead to aligned NO.

REFERENCES

1. H. Reisler, M. Noble and C. Wittig, in *MolecularPhotosdissociation Dynamics*, ed. M.N.R. Ashfold and J.E. Baggot (Royal Society of Chemistry, London, 1987), ch. 4.

2. J.L. Dyet, M.R.S. McCoustra and J. Pfab, J. Chem. Soc. Faraday Trans. **86**, 2049 (1990).

3. J.L. Tomer, M.C. Wall, B.P. Reid and J.L. Cline, J. Chem.Phys. **102**, 6100 (1995).

4. A.W. Simpson, V.M. Young and J. Pfab, to be published.

5. R.N. Dixon, J. Chem. Phys. **85**, 1866 (1986).

A STUDY OF HYDRATED MOLECULAR CLUSTERS USING TWO COLOUR, MASS SELECTED R2PI SPECTROSCOPY

P W Joireman, R W Randall, J M Dickinson, E Robertson, and J P Simons[1)]

[1)] Physical and Theoretical Chemistry Laboratory, Oxford OX1 3QZ

INTRODUCTION

The tertiary structure of a protein, a determinant of its function, is built upon the conformational choices made by its constituent residues within their local solvent environments.[1] A molecular beam proved by laser spectroscopy provides an ideal laboratory to study such effects. Chromophores, such as tyrosine, phenylalanine, or tryptophan,[2,3] contain flexible side chains that can adopt different conformations with respect to the aromatic system. The separate conformers will give rise to distinct spectral bands whose position and intensity will depend on the strengths of the interactions between the aromatic system and the side chain. Additionally, weakly bound complexes of the chromophore with different solvent molecules can be formed in beam expansions, making possible direct studies of the effect of specific solvent molecules on conformational choice.

We have probed the conformational properties of dihydrocinnamic acid (HCA), 3-phenyl-1-propionic acid, an analogue of phenylalanine, and its complexes with water. Previous conformational analyses of similar systems have been largely based on vibronically resolved spectra, symmetry arguments, and theoretical calculations,[2,3] with few rotationally resolved spectra.[3b] For example, HCA has been studied previously by Martinez, et. al.[3a] using fluorescence excitation methods. Their work revealed two strong bands in the region of 37650 cm^{-1} that were assigned as origin bands of two conformers. Here, we present resonant two-photon ionisation (R2PI) spectra of these two bands and other bands produced by complexing HCA with water, from which reasonable structures and relative energetics are deduced.

II. EXPERIMENTAL

The experimental apparatus consisted of a Nd:YAG laser (Spectron SL805; 1.1 W/355 nm, 10 Hz) is used to pump a grating tuned dye laser (Lambda Physik FL2002, 15 mW/530 nm, 10 Hz), the doubled output of which serves as pump and photoionisation laser in a one-colour R2PI experiment, and pump laser only in a two-colour R2PI. A second Nd:YAG laser (Spectra-Physics GCR-11; 1.5 W/532 nm, 10 Hz) pumps a dye laser (Spectra Physics PDL-3, 11 mW/585 nm) which is frequency doubled and used as the photoionisation laser in the 2-colour R2PI experiment. The doubled dye laser outputs are combined co-linearly and directed into the interaction region of a differentially pumped time-of-flight mass spectrometer (R. M. Jordan, Co.),[4] at right angles to the expansion axis of a pulsed molecular beam (General Valve, Series 9, 800 μm orifice). Rotational band contours were obtained by narrowing the bandwidth of the FL2002 pump laser using an intracavity etalon. The sample was heated (T=120--140 °C) and entrained in helium, total pressure 3-4 bar. Water solvent incorporated into the carrier gas by bubbling helium through a room temperature water sample and combining this flow with the main carrier using a needle valve. Mass-resolved photoionisation signals are sampled by a digitising oscilloscope (Tektronix TDS 520) and recorded as a function of pump laser wavelength.

III. RESULTS AND INTERPRETATION

One-colour R2PI spectra of HCA–$(H_2O)_n$, where n=0 to 3 respectively, are shown in Fig. 1 (below). The two most intense bands appearing in the monomer mass channel (n=0), labelled A and B, are the two bands previously observed by Martinez, et al.[3a] and assigned to two conformers of HCA. Introducing water into the expansion produced several new bands in the spectrum whose identities were probed by detecting in different mass channels (n=1-3) Correlations of the observed band positions between lead to the following assignments. Bands appearing to the red of the band B are assigned to water complexes of conformer B (n=1 to 3), each cluster exhibiting a nearly constant red shift from the previous band position. The first feature to the red of band A consists of two closely separated (ca. 2 cm^{-1}) bands. These are assigned to water complexes of conformer A, n=1, 2. The n=3 complex of conformer A appears to the blue of the monomer band origin. Both n=3 complexes appear to exhibit significant vibrational activity. Their origins are accompanied by progressions of 17 cm^{-1} (A) and 16 cm^{-1} (B), each displaying a qualitatively different Franck-Condon profile. The bands appearing at 37567 cm^{-1} and 37582 cm^{-1} for the n=2 water complex could not be assigned and may be hot bands or a different isomer of the complex. R2PI spectra for the n=4, 5 complexes exhibit only a single feature in the region of 37686 cm^{-1}. Extended wavelength scans 300 cm^{-1} to the red and blue of the band origin for conformer A produced no additional features assignable to water complexes.

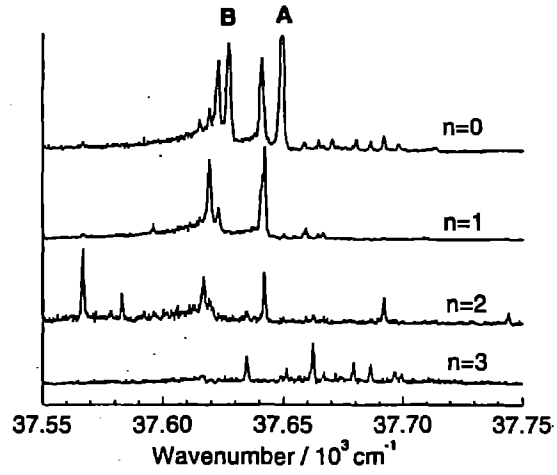

It is clear from the spectra in Fig. 1 that the water clusters undergo extensive fragmentation after photoionisation, thus contaminating the spectra in lower mass channels. In order to reduce the amount of fragmentation and facilitate band assignments, two-colour R2PI experiments were implemented (λ_{probe} = 292.5 nm). The results are shown in Fig. 2 (next page) for HCA--$(H_2O)_n$, n = 0 to 3. Comparisons of these spectra with those in Fig. 1 are revealing. The most intense bands in Fig. 1, n=1 are due to HCA--$(H_2O)_2$, A and B. Similarly, the most intense bands in Fig 1, n=2 are due to HCA--$(H_2O)_3$, A and B. The corresponding two-colour spectra, Fig. 2, n=1 and n=2, exhibit their most intense peaks at the band position assigned as arising from the water cluster being monitored in that mass channel. This observation is consistent with a fragmentation mechanism in which the one-colour

photoionisation step deposits sufficient energy into the complex to preferentially remove one water molecule, leading to a dominant band in the n mass channel from the complex with (n+1) water molecules. The two-colour photoionisation does not supply sufficient energy to the ion to favor the previous mechanism.

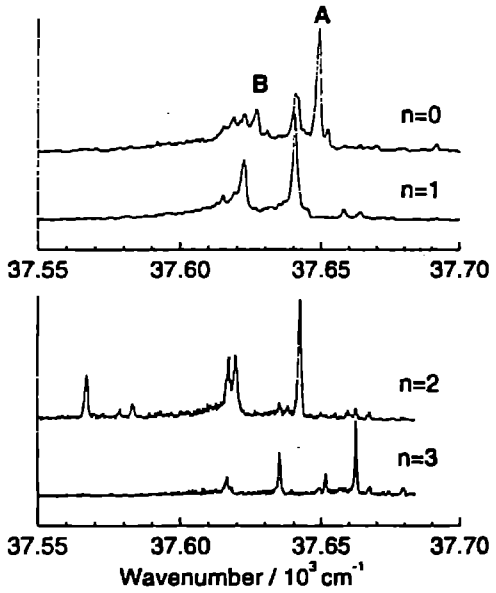

Rotational band contours (not shown for lack of space) were measured by fluorescence excitation at 0.08 cm^{-1} resolution for conformers A and B of HCA. The contour of conformer B is predominantly b-type, whereas that of conformer A exhibits a significant amount of a-type character. Rotational band contours from R2PI for the water complexes (n < 3) were also measured. Qualitatively different contours are again observed. However, the contours for each water complex display the same band polarisation as the monomer to which the solvent is attached, indicating that water solvation does not significantly affect the direction of the optical transition moment within the inertial frame.

IV. DISCUSSION

We now use these results to deduce likely structures of the two observed conformers of HCA. The appearance of any rovibronic band contour is critically dependent on six parameters, ΔA=(A'-A'')/A'', ΔB, ΔC, the band polarisation, the temperature and the experimental resolution. The data are not sufficient to allow exact specification of all six parameters. However, reasonable estimates of their values may be obtained from informed initial estimates and grid searches on each parameter.[5] Estimates of the rotational constants of ground state molecular structures were obtained from microwave structural data.[6] Two side chain conformations are suggested by experimental and theoretical work on similar systems, an *anti* conformation[3,7] (side chain extended) and a *gauche* conformation[7] (side chain folded back toward the ring). The band was initially assumed to be polarised along the short axis of the phenyl ring (ie., perpendicular to the axis directed along the C--C_α substituent bond), similar to the behaviour observed for other monosubstituted benzene derivatives.[8]

Our assumption of the HCA transition moment (TM) direction and the higher symmetry of the *anti* conformer implicates it as conformer B. Grid searches implemented on all the parameters using the calculated *anti* rotational constants converged to the following values: ΔA = -4%, ΔB= 0% and ΔC=-1%, 100 % b-type polarisation, T=(4 +/- 1) K, and 0.08 cm^{-1} resolution. A band contour calculated using these values shows a good fit to the experimental. The experimental and calculated contours reveal only minor differences, specifically a slight mismatch in the intensities of some sub-bands and a small difference in the 'Q band positions, confirming our assignment of conformer B as the *anti* conformer. A band contour calculated using the ground state rotational constants for the *gauche* conformer, using similar values for ΔA, ΔB, ΔC, and a short axis polarised TM, does not reproduce the experimental spectrum.

The simulated band contour just discussed is, however, also different from that observed experimentally for the *gauche* isomer. Grid searches implemented for all parameters using the projection of the TM on the inertial frame cannot reproduce the observed band contour. When the band polarisation was varied without regard to the inertial projections of our assumed TM, the grid searches converged to the following values: ΔA = -2 %, ΔB=-1 % and ΔC=0 %, 70 % a-type, 20 % b-type, and 10 % c-type hybrid polarisation, T=(4 +/- 1) K, and 0.08 cm^{-1} resolution. No combination of side-chain torsional angles can reproduce this polarisation based on inertial arguments alone. The observed contour is reproducible and possibly owes its unique structure to an electronic contribution to the transition dipole.[9] This effect may be due to a significant interaction between the ring and side chain causing the TM to rotate toward the side chain, or a TM oriented along the long molecular axis of the phenyl ring. Regardless of the mechanism responsible, the effect is strikingly large in view of the small frequency shift between the two monomer origins.

Work on modelling the HCA--$(H_2O)_{n=1,2}$ complexes is still in progress. Initial indications suggest that the first water binds to the side chain as a proton acceptor. Subsequent addition is to the side chain[2b] for the anti conformer while for the gauche conformer a significant interaction with the aromatic ring is postulated.[10]

[1]L. Stryer, *Biochemistry*, 4th ed. (W. H. Freeman Co., New York, 1995).

[2](a) T. R. Rizzo and D. H. Levy, *Lasers and Mass Spectroscopy* ed. D. M. Lubman, (Oxford University Press, Oxford, 1990) p. 402, and references therein; (b) J. Sipior and M. Sulkes *J. Chem. Phys.* **98**, 9389 (1993), and references therein.

[3](a) S. J. Martinez, J. C. Alfano and D. H. Levy J. Mol. Spec. **145** 100 (1991); (b) S. J. Martinez, J. C. Alfano and D. H. Levy *J. Mol. Spec.* **152**, 80 (1992).

[4]D. M. Lubman and R. M. Jordan *Rev. Sci. Instrum.* **56**, 373 (1985).

[5]B. D. Howells, J. McCombie, T. F. Palmer, J. P. Simons, and A. Waters *Farad. Trans.* **88**, 2587 (1992).

[6](a) V. Amir-Ebrahimi, A. Choplin, J. Demaison, G. Roussy *J. Mol. Spec.* **89**, 42 (1981); (b) W. Caminati, D. Damiani, G. Corbelli, B. Velino, C. W. Bock *Mol. Phys.* **74**, 885 (1991).

[7](a) N. Okabe and T. Suga *Acta. Crystalallographica. C* **51**, 1324 (1995); (b) P. J. Breen, J. A. Warren, and E. R. Bernstein *J. Chem.. Phys.* **87**, 1927 (1987); (c) P. D. Godfrey, L. D. Hatherley, and R. D. Brown *J. Am. Chem. Soc.* **117**, 8204 (1995).

[8](a) A. R. Bacon and J. M. Hollas Faraday Discuss. Chem. Soc. **86**, 129 (1988); (b) H. Abe, N. Mikami, and M. Ito *J. Phys. Chem.* **86**, 1768 (1982).

[9]P. A. Hepworth, J. McCombie, J. P. Simons, J. F. Pfanstiel, J. W. Ribblet, D. W. Pratt *Chem. Phys. Lett.* **236**, 571 (1995).

[10]A. J. Gotch and T. S. Zwier *J. Chem. Phys.* **96**, 3388 (1992).

IMAGING MOLECULAR PHOTODISSOCIATIONS

M N R Ashfold,[1] L J Rogers,[1] S H S Wilson[1] and B J Whitaker[2]

[1]School of Chemistry, University of Bristol, Bristol BS8 1TS
[2]School of Chemistry, University of Leeds, Leeds LS2 9JT

EPSRC grant no. GR/J79225 provided funds to introduce an ion imaging capability within our existing photofragment translational spectroscopy programme. Unfortunately, at the outset of this grant, the excimer laser with which we had intended to 'tag' the photofragments of interest by resonance enhanced multiphoton ionisation (REMPI) failed catastrophically. A tuneable pulsed laser was essential if we were to be able to progress with developing the experiment, and the six month loan of a Nd-YAG pumped dye proved a perfect stop gap whilst funds were sought (successfully) to acquire a replacement excimer laser to dedicate to this experiment. Without the loan laser the experimental development would have been set back a full six months.

Our ion imaging experiment incorporates a number of unique features, principally in the way in which the image is captured and processed. Tagging of the fragment of interest (e.g. Cl atoms by 2+1 REMPI at 235 nm), produced by photolysis in the source region of the reaction chamber, produces an ion cloud which expands with a velocity and angular distribution determined by the fragmentation dynamics. Carefully designed bias electrodes accelerate the resulting ions onto a pair of microchannel plates (MCPs); species discrimination is assured since different ion masses show different times-of-arrival at the MCPs. The resulting secondary electrons are accelerated onto a fast phosphor screen which is viewed by a gated image intensified CCD camera. Each ion arrival appears as a bright 'blob', occupying just a few pixels of the 512x512 pixel array. Custom designed software allows us to establish whether any given 'blob' satisfies user specified thresholds for size and brightness. For those that pass this discrimination test, the computer finds the centroid and stores a count at the appropriate x,y-coordinate. During the loan period we were able to confirm that the software is able to process up to 30 'blobs' per laser shot, at a 10 Hz rep. rate. This data processing strategy should obviate most of the non-uniformities (*e.g.* variable response of the MCPs, phosphor screen and CCD array) which, traditionally, cause raw ion images to deviate from the expected cylindrical symmetry.

The loan laser was crucial in providing signals which (i) established that the camera worked as intended, (ii) validated the software - testing discrimination levels and data transfer rates, and (iii) highlighted design flaws in our ion imaging spectrometer. These largely centred around stray and non-uniform fields. Progress is illustrated by the accompanying figure, which displays images of NO molecules seeded in a mild expansion with Ar and tagged by 1+1 REMPI using a laser wavelength *ca.* 226 nm taken early (fig. 1a) and at the end (fig. 1b) of the loan period. The gross distortion of the early images is all too obvious! The height and width of the latter image reflect the spread of velocities in the NO/Ar beam and the spatial width of the gas pulse respectively (as well as some residual blurring due to field inhomogenieties and space charge effects); such compact images were only obtained after incorporation of a differentially pumped skimmed beam chamber (thereby reducing the pressure in the source region), further improvements in the uniformity of the extraction fields and the replacement of Penning gauges (with their strong associated magnetic fields) with ionisation gauges. At the time of writing (March 1996) the experiment is now starting to work in earnest, as evidenced by the image of tagged Cl atoms resulting from horizontally polarised 355 nm photolysis of jet-cooled Cl_2 seeded in Ar [fig. 1(c)].

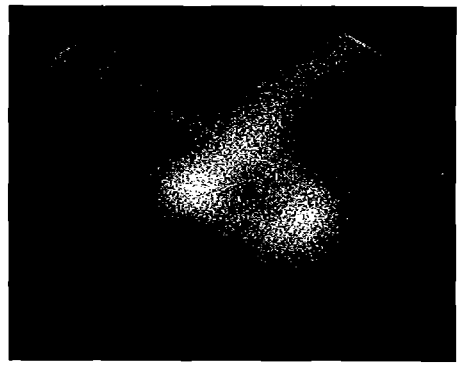

Fig. 1(a)

Fig. 1(b)

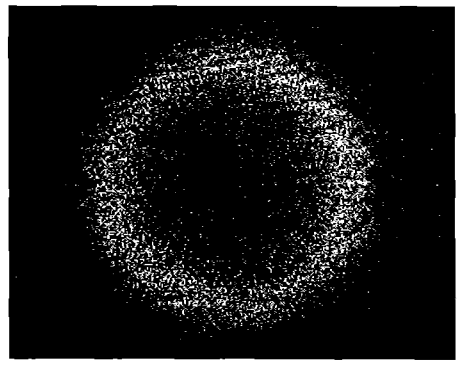

Fig. 1(c)

Figure 1. (a) and (b): Images of NO^+ ions, formed by 1+1 REMPI (at 226 nm) of a mild expansion of NO seeded in Ar at early (a) and later (b) stages of development. (c) shows the image of Cl^+ ions (tagged by 2+1 REMPI at 235 nm) resulting from 355 nm photolysis of Cl_2 with $\varepsilon_{photolysis}$ aligned parallel to the TOF axis.

LASER-INDUCED FLUORESCENCE SPECTROSCOPY OF JET-COOLED LASER-DESORBED PHTHALOCYANINES

F.L. Plows and A.C. Jones

Department of Chemistry, The University of Edinburgh

INTRODUCTION

There is great interest in the electronic structure and excited state properties of the porphyrins because of their extensive occurrence in photobiological systems and, in particular, because of their central role in the energy transfer and electron transfer processes of photosynthesis. The phthalocyanines (tetraazatetrabenzoporphyrins) have a close structural similarity to the biologically important porphyrins and can be considered synthetic biophysical model systems.

The phthalocyanines are very involatile and, therefore, have not been amenable to study in conventional supersonic jet experiments. Previously, we have shown that the porphyrins and phthalocyanines can be readily vaporised, without thermal decomposition, by pulsed infrared laser desorption [1,2], facilitating their study under jet-cooled conditions. We report here on the use of laser desorption supersonic jet spectroscopy to investigate the laser-induced fluorescence excitation spectra of free base phthalocyanine (H_2Pc), magnesium phthalocyanine (MgPc), zinc phthalocyanine (ZnPc) and chloroaluminium phthalocyanine (ClAlPc).

The molecular structure of free base phthalocyanine is shown in Figure 1. In MgPc and ZnPc, the two central protons are replaced by a divalent metal ion. In ClAlPc, the central trivalent aluminium cation has an axial Cl^- ligand. The laser desorption laser photoionisation mass spectrum of ClAlPc indicates that the axial ligand is retained in the laser-desorbed molecule [3].

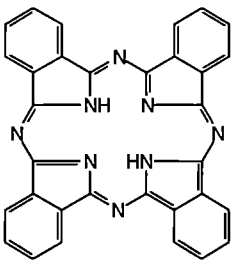

Figure 1. The molecular structure of free base phthalocyanine

The results presented here demonstrate that even very large laser-desorbed molecules like the phthalocyanines can be jet-cooled sufficiently to give well resolved vibronic spectra.

EXPERIMENTAL

The use of laser desorption as a source of molecules for supersonic jet spectroscopy requires the production of a stable supply of sample vapour pulses for extended periods of time. Furthermore, in order to produce sufficient jet-cooling to give well resolved vibronic spectra, the desorbed molecules must be efficiently entrained in the high pressure throat of a pulsed supersonic expansion. In our experiments these conditions are achieved using a desorption nozzle assembly which has been described in detail elsewhere [4]. This consists of a pulsed supersonic valve (General Valve Corporation Series 9) fitted with an extension block into which the desorbed molecules are released and where they are entrained into the supersonic expansion. The sample is prepared as a solid disc of diameter 25mm and thickness about 3mm. The sample is mounted on a motor-driven holder which allows it to be moved continuously relative to the desorption laser beam during the experiment; desorption can be carried out continuously from the same sample for several hours.

Desorption was achieved using a pulsed TEA CO_2 laser (Alltec 854MS) which outputs up to 300mJ of 10.6μm radiation in a 100ns pulse. The desorbed phthalocyanine molecules were entrained in a supersonic beam produced by expansion of 20-30bar of helium through a 0.8mm diameter nozzle. Fluorescence was excited using a Nd:YAG-pumped dye laser system (Spectron 805G Nd:YAG/ Quanta Ray PDL2 dye laser with WEX UV accessory). The excitation laser beam crossed the expansion 5-10mm downstream of the desorption nozzle. Undispersed fluorescence was collected by a 50mm focal length f/1 lens and detected by a Hamamatsu R928 photomultiplier tube. The signal was processed by a SRS SR250 gated integrator and stored on a PC. The experiment was carried out at a repetition rate of 10Hz and the signal was averaged over 30 laser shots. The relative timing of the pulsed valve, desorption laser and excitation laser was controlled by a SRS DG535 digital delay generator.

RESULTS AND DISCUSSION

The origin regions of the LIF spectra of H_2Pc, MgPc, ZnPc and ClAlPc are shown in Figure 2. The wavenumbers of the 0-0 transitions are given in Table 1. The S_0-S_1 transition energies of the three metallophthalocyanines are higher energy than that of the free base and show a dependence on the central metal ion. For each molecule, the spectrum consists of an intense 0-0 transition and relatively weak vibronic structure. This indicates a symmetry-allowed electronic transition between two states with very similar equilibrium geometries. The phthalocyanine macrocycle has fourfold symmetry and the metallophthalocyanines containing a divalent metal ion (that maintains the planarity of the macrocycle) have D_{4h} symmetry. In free base phthalocyanine, the fourfold symmetry is broken and the molecule has D_{2h} symmetry. Molecular orbital calculations [5] predict that the first excited singlet state of the D_{4h} metallophthalocyanines is a doubly degenerate ^1E_u state. Under the D_{2h} symmetry of H_2Pc, the degeneracy is lifted to give $^1B_{3u}$ (S_1^x) and $^1B_{2u}$ (S_1^y) states. The spectra reported here are consistent with these assignments.

In Table 1, the 0-0 transition wavenumbers measured for the isolated, ultracold phthalocyanines in the present work are compared with the results of previous studies in the high temperature vapour phase [6] and in n-alkane Shpolskii matrices at 4.2K [7]. The high temperature vapour phase spectra are broad and unstructured. The Shpolskii spectra show well-resolved vibronic structure but the spectra are complicated by the occupancy of multiple sites by the phthalocyanine molecules. The data given in Table 1 are for the thermally most stable site (in an annealed matrix). In the matrix, the 0-0 transition of the metallophthalocyanines is split into a doublet, due the crystal-field-stabilised Jahn-Teller effect. The 0-0 transition of H_2Pc is split due to the existence of molecules in two tautomeric states. These splitting effects introduce further complexity into the.

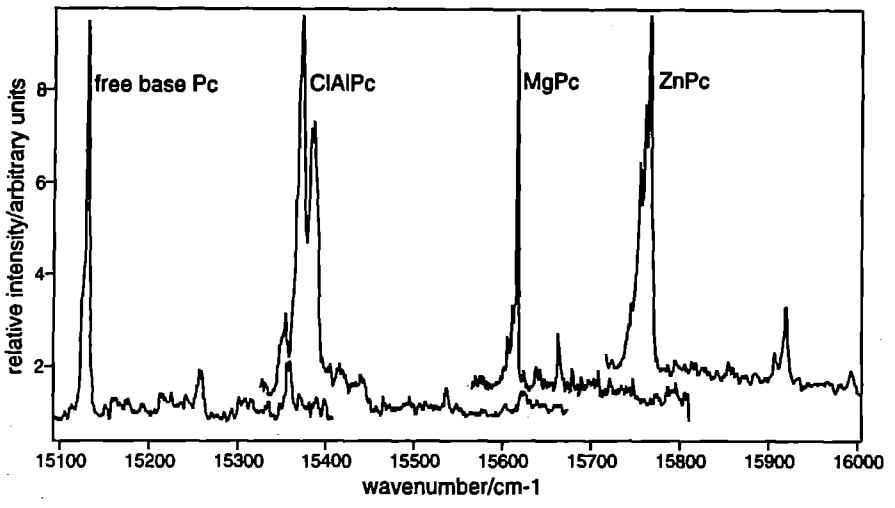

Figure 2. The origin regions of the S_0 - S_1 LIF excitation spectra of free base phthalocyanine, chloroaluminium phthalocyanine, magnesium phthalocyanine and zinc phthalocyanine

spectrum. Under the isolated molecule conditions of the supersonic jet, these complexities are eliminated.

As shown in Table 1, the 0-0 transitions in the supersonic jet spectra are shifted some 600cm^{-1} to the blue of the static gas absorption peaks. This shift is attributed to the presence of intense hot band absorptions in the vapour phase spectra which were recorded at temperatures in excess of 750K.

The data presented in Table 1 also show that the supersonic jet spectra are blue-shifted by more than 700cm^{-1} relative to the Shpolskii spectra. This indicates that, even in a 'non-interacting' n-alkane matrix, there is a substantial solvent-induced stabilisation of the S_1 state relative to the ground state. The magnitude of the solvent perturbation appears to be greater for the metal-substituted molecules than for the free base and to depend on the nature of the central metal ion.

	Jet-cooled 0-0/ cm^{-1}	Vapour [6] 0-0/ cm^{-1} (T/K)	Shpolskii matrix [7] 0-0/ cm^{-1} (4.2K)	Wavenumber shift jet - vapour / cm^{-1}	Wavenumber shift jet - matrix / cm^{-1}
H_2Pc	15131	14577 (773)	14411	554	720
			14475		
ClAlPc	15373	-	14503	-	870
			14543		
MgPc	15615	15015 (793)	14878	600	737
			14898		
ZnPc	15766	15128 (829)	14885	638	881
			14914		

Table 1. Comparison of the results of the present jet-cooled experiments with those of previous studies in the high temperature vapour phase and in Shpolskii matrices at 4.2K

REFERENCES

1. A.C. Jones, M.J. Dale, G.A. Keenan and P.R.R. Langridge-Smith, Chem.Phys.Lett. 1994,**219**,174
2. M.J. Dale, A.C. Jones, P.R.R. Langridge-Smith, K.F. Costello and P.G. Cummins, Anal. Chem. 1993,**65**,793.
3. S.J. Wright, Private Communication.
4. F.L. Plows and A.C. Jones, RAL Report TR-95-025 1995,144.
5. A.J. McHugh, M. Gouterman and C. Weiss, Theoret.Chim. Acta. 1972,**24**,346.
6. L Edwards and M. Gouterman, J.Mol.Spec. 1970,**33**,292.
7. T.H. Huang, K.E. Rieckhoff and E.M. Voigt, J.Chem.Phys. 1982,**77**,3424

ACKNOWLEDGEMENTS

FLP is grateful to the EPSRC for the provision of a studentship.

STUDY OF METAL COMPOUNDS BY HIGH RESOLUTION ELECTRONIC SPECTROSCOPY

J.M. Brown, G. van den Hoek, Y. Ito and C.J. Whitham

Physical and Theoretical Chemistry Laboratory
Oxford University

1. BACKGROUND

The objective of the research programme is the determination of the structural properties, both the geometric structure and electronic distribution, of several involatile metal-containing molecules from their electronic spectra. The work is fundamental research with important implications for valence theory in chemistry. The species which we study are at the limit of, or slightly beyond, the capabilities of present day *ab initio* calculations. We have recorded the spectra of several transition metal dihalides and have so far determined the structures of $NiCl_2$ and $Cucl_2$; this is the first time this has been done reliably. The complexity of the spectra shows that it would be extremely difficult to obtain this information by theoretical calculation. We have also worked on the group IIIA hydroxides and oxides, in particular InOH and In_2O. These species have not been obtained in the gas phase before.

There is considerable motivation for this research outside the strictly academic context. The transition element compounds play an important role in catalysis and the development of more powerful agents depends upon a better understanding of their valence properties. The group IIIA hydroxides and oxides are of relevance to the nuclear power industry because they could be formed in the event of a nuclear accident (in the high temperature reaction between steam and indium which is a component of the control rods).

2. PRINCIPLE OF EXPERIMENT

We have been recording the gas phase electronic spectra of involatile compounds using LSF equipment for over six years. The molecules are formed in the vapour phase by heating a suitable precursor in a furnace and then cooled in a free jet expansion of an inert carrier gas. The spectra are recorded by irradiating the sample with a dye laser and detecting the total (i.e. undispersed) fluorescence as the excitation wavelength is tuned. Experiments have also been carried out in which fluorescence excited by a fixed frequency laser is dispersed to give information on the vibrational and rotational levels of the lower electronic state.

3. PROGRESS REPORT

A loan period of the Quanta Ray PDL-3 dye laser pumped by the Quanta Ray Nd:YAG laser including the WEX UV accessory lasted from March to September 1995. During this period, studies have been made of the spectra of several molecules.

3.1 Laser ablation studies

As an alternative to the high temperature generation of molecules, we have designed and constructed a laser ablation source. In this, radiation from a pulsed Nd:YAG laser is focused onto a slowly rotating metal rod. A small amount of the metal is vaporised to give a plasma which in turn reacts with a secondary gas to form the desired product species. The species is again subjected to a supersonic expansion so that it is confined to a few rotational and vibrational levels; this considerably simplifies its electronic spectrum.

The apparatus was aligned and the various timing sequences established by recording spectra of previously known species, namely calcium atoms and CaOH. The latter experiment proved more difficult than expected because of the softness of the rating calcium rod.

Once the apparatus was working satisfactorily, we attempted to record a spectrum of the molecule AlO_2 entrained in argon. A search was conducted within the range of Rh6G dye (555-580 nm) but no signals were recorded.

3.2 Nickel dichloride, $NiCl_2$

We have worked extensively on the electronic spectrum of nickel dichloride over a period of several years. Two main band systems have been studied, one at 460 nm and the other at 360 nm. The latter is particularly complicated and resistant to analysis. In an attempt to shed more light on the UV system, we have searched to shorter wavelengths and discovered another set of bands around 340 nm, see Figure 1. They appear to have a similar structure to the 360 nm system but it is not yet clear if they are related to this other system.

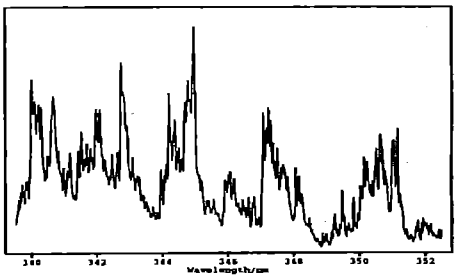

Figure 1 $NiCl_2$ fluorescence excitation spectrum measured with the pulsed laser around 340 nm

3.3 Indium suboxide, In_2O

We have recorded the first gas phase spectrum of the high temperature molecule In_2O in previous experiments with LSF lasers, in the near-ultraviolet around 390 nm. Experiments by other workers with a matrix-isolated sample suggest that there is another electronic transition from the ground state centred around 520 nm, in the green part of the spectrum. We have searched extensively for bands in this system, generating In_2O by the efficient reduction reaction, In_2O_3 and In at 950°C. However, no spectral features were seen in the range 465 to 560 nm.

3.4 Copper dichloride, $CuCl_2$

Copper dichloride has a strong electronic transition in the visible region of the spectrum, with a band origin at 643 nm. We have studied this band system in detail and confirm that it involves (primarily) a $^2\Pi_u$ - $^2\Pi_g$ transition. The vibrational structure is extensive and we have recorded survey spectra with LSF laser out to 550 nm. Theoretical calculations suggest that there should be a $^2\Sigma_u^+$ state lying a few thousand cm^{-1} above the $^2\Pi_u$ state. We have therefore extended the survey scans below 550 nm in an attempt to identify the $^2\Sigma_u^+$ - $^2\Pi_g$ transition. The data need to be investigated before we can be certain that we have identified this transition.

3.5 Titanium chloride compounds, $TiCl_n$

We have made a preliminary search for $TiCl_n$ species where n =1, 2 or 3, in the reaction products of chlorine (in argon), with titanium metal at high temperatures. Initial observations have been confined to the diatomic molecule, TiCl.

SECOND HARMONIC GENERATION OBSERVATIONS OF LIQUID SURFACES

M.J. Crawford, C.G. Hickman, W.J. Bullock and A.J.G. Fordyce and J. G. Frey

Department of Chemistry, University of Southampton, Southampton, SO17 1BJ

In the SHG experiment laser radiation is focused at an interface. A second order non-linear interaction leads to a small fraction of the radiation being doubled in frequency. The doubling process is dipole forbidden in an isotropic medium and so no signal is obtained from the two bulk liquid phases surrounding an interface. However, at the interface itself, the symmetry is broken and a harmonic signal can be recorded both from the bare interface and from molecules adsorbed in an ordered manner at the interface. The adsorbed molecules can be investigated selectively since most molecules of interest have a suitable visible or UV electronic absorption and can be selectively observe in the SHG process by tuning the laser close to the molecular resonance, resulting in an enhancement to the SHG signal. The intensity and polarisation of the SHG signal provides information on the number of molecules adsorbed and their average orientation.

The Ti:Sapphire system was used at either 800 nm or 750 nm and provided ca 50 fs pulses at 80 MHz. The laser radiation was focused at the interface with the polarisation controlled using a half-wave plate. The second harmonic radiation obtained in reflection was separated from the much more intense reflected fundamental radiation using filters and a monochromator, and detected using a gated photon counting system. For some experiments the polarisation of the second harmonic was also measured.

Crown Ether, 4-nitrobenzo-15-crown-5

The crown ether, 4-nitrobenzo-15-crown 5, has a detectable SHG signal at the water air interface. As the crown ether is insoluble in water it is spread on the water surface by adding a small quantity of the crown ether in a chloroform solution. Experiments using the Langmuir trough show that once a monolayer has been formed the surface pressure increases as the number density of the crown ether is increased either by reducing the area or by adding more chloroform solution, Figure 1. The SHG signal, Figure 2, similarly increases for low concentrations but levels off once a

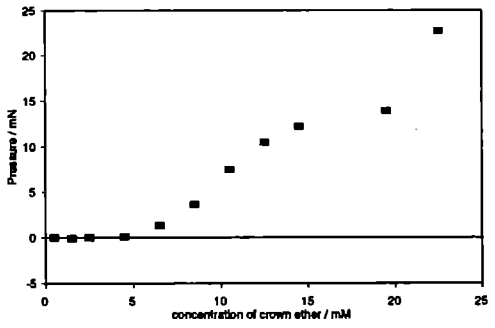

Figure 1 Surface Pressure of the Crown Ether Film

fully compressed layer is formed.

As a comparison the SHG response from the surface of a dichloroethane solution with the crown ether present was observed, Figure 3 This shows the adsorption isotherm of the crown ether at the surface of dichloroethane. The isotherm can be fit with a Langmuir isotherm but more data at higher concentrations is required. This will enable a comparison with the molecular size determined from the experiments with the crown ether layer supported on the water sub-phase.

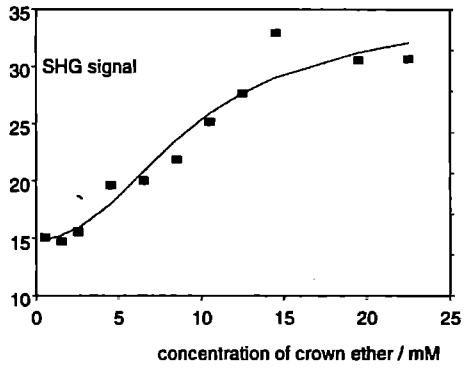

Figure 2 SHG from the Crown Ether Film

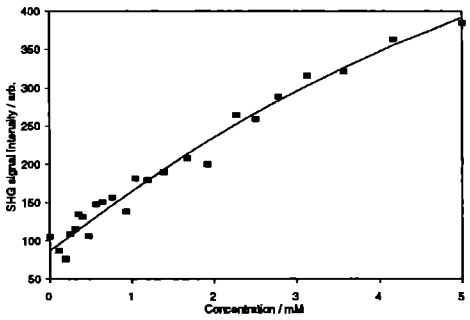

Figure 3 SHG from the Crown Ether at the Air/Dichloroethane interface

SHG Fluctuations

The interfacial selectivity of the SHG process immediately focuses consideration to the small number of molecules adsorbed at an interface. The small number of molecules involved in generating the SHG signals means that the observed intensities are not constant but will fluctuate as the number of molecules in the observation region (typically a diameter of 10-100 microns and one molecular layer thick) changes. These fluctuation reflect directly the rate at which the molecules move over the interface and diffusive motions on time scales longer than about 1s can be observed ether to the interface. The diffusion of small molecules within a surface (or interfacial) film can thus be observed, as can the diffusive motion of the macromolecular units that make up a structured interface.

The most favourable probe molecule we have studied in the Ti:Sapphire laser wavelength region is p-nitroaniline. In the most favorable conditions a count rate of 1000-2000 counts/s for p-nitroaniline at the air/water surface was obtained. The 'static' SHG polarisation data is being analysed to provide information on the ordering of the p-nitroaniline at this interface. The large SHG signal means that it was practical to record the signal in a sequence of 1s bins by connecting the time gated photon counter to a PC. An example of the sequence of counts recorded is shown in figure 4)

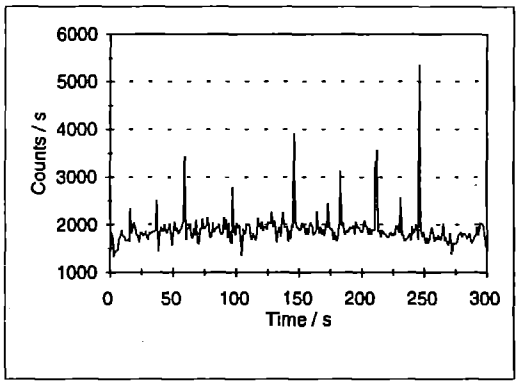

Figure 4 SHG Signal from p-nitroaniline at the air/water interface as a function of time

The time sequence of count data is analysed in terms of the autocorrelation function. Figure 5. The autocorrelation has not been corrected for the average signal level.

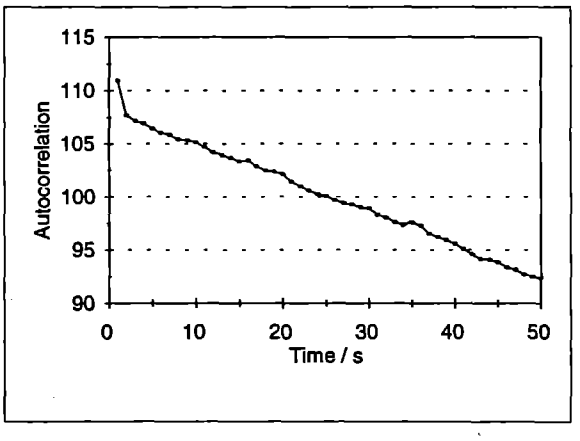

Figure 5 Autocorrelation obtained from the data in Figure 4 (uncorrected for the mean level)

The data shows an autocorrelation, extending over an unexpectedly long time scale. The tiime scale of th emajor feature in Figure 5 is too long to correspond to the microscopic motions of the p-nitroaniline. It is probable that the time scale is in fact that for the motion of some aggregated species moving on the liquid surface. Such an agregate will give a large SHG signal when it is in the laser beam focuss and nothing when it has moved outof the focal region. The time scale would then correspond to the difussion of this particle round the surface. This is consistent with the linearly decreasing autocorrelation which is predicted for two dimensional diffusion of a particle (N.J.B. Green, Kings College, London).

Once we have the opportunity to collect more data from this system under different conditions (for example a greater range of concentrations and within a compressed LB film) we will be able to interpret more of the data.

We would like to thank all the staff at the laser facility for making these investigations possible.

HARMONICALLY GENERATED VUV WAVELENGTHS USING 50 FS PULSED LASER RADIATION

A C Flexen[1], R J Donovan[1], R R J Maier[1],
A J Langley[2], W Shaikh[2]

[1]Department of Chemistry, The University of Edinburgh, West Mains Road, Edinburgh, EH9 3JJ
[2]Rutherford Appleton Laboratory

INTRODUCTION

High-order harmonic generation has been developed in recent years to provide a source of coherent laser radiation with wavelengths extending into the XUV and soft X-ray regions of the electromagnetic spectrum[1]. This has been possible due to the development of lasers with ultrashort pulse lengths, on the femtosecond timescale[2]. These sources are able to produce significantly higher peak intensities than conventional laser sources. Intensities developed are typically of the order 10^{14}-10^{15}W cm^{-2} which is necessary for efficient high-order harmonic generation (HG).

The high-order HG process is based on the non-linear polarisation response of atoms and molecules, to the strong electric field component of applied radiation. An atom or molecule may scatter incident radiation of frequency ω yielding radiation at frequencies equal to an odd integer multiple of the fundamental radiation, $n\omega$, where $n \geq 3$. Only odd multiples or orders of the fundamental frequency are produced under gaseous, isotropic conditions. Harmonic wavelengths are produced in the same direction as the applied fundamental beam and have similar pulse width characteristics. Harmonic orders with n as high as 10^2 have been generated using pulsed jets[3]. This approach may therefore provide a source of useable short wavelength radiation with subpicosecond pulse widths[4,5].

In the preliminary work described here we have used a static gas cell (with MgF_2 windows) to produce the 3rd and 5th harmonics of 750 nm radiation (i.e. 250 nm and 150 nm radiation respectively) using argon and xenon as the harmonic media. Conversion efficiencies and spectral characteristics of the harmonics generated were measured and the suitability of application to VUV spectroscopy considered.

EXPERIMENTAL

The experimental arrangement is shown on figure 1. Laser pulses of around 50 fs pulse length were generated by a CW argon-ion pumped mode-locked titanium sapphire laser. Pulses were amplified in an Nd:YAG pumped three stage dye-amplifier, yielding 750 nm radiation with pulse energy 100 μJ at a repetition rate of 10 Hz. This provided peak intensities, when focused, of the order of 10^{14}Wcm^{-2}. Laser radiation was directed and focused into a 30 cm length, 25 mm diameter cell containing the generating medium at pressures ranging from 1 to 760 Torr. Harmonics were separated from the fundamental using a monochromator and detected with a photomultiplier tube (PMT). Third harmonic radiation at 250 nm was observed using a 0.25 m monochromator. For the 5th harmonic a grating monochromator was used which could be evacuated to $<10^{-6}$ Torr and a solar-blind PMT (Hamamatsu R1459) was used for detection. Signals were amplified and measured on a digital oscilloscope. The stability and pulse energy of the fundamental beam was monitored by detecting the second harmonic (375 nm) using a photodiode.

RESULTS AND DISCUSSION

The main aims of the work carried out were to determine the optimum experimental conditions for generating harmonic radiation up to the 5th order, to estimate the number of photons produced for each harmonic observed and to study the characteristics of the generated radiation. The ultimate aim is to use this technique as a source of short wavelength radiation for spectroscopy.

Several gases were studied as possible media for HG including xenon, argon, helium and nitrogen. Harmonic generation was only observed in xenon and argon. It was found that a higher conversion efficiency was measured using Xe compared to Ar at the same pressure. However, under the same conditions of focusing and laser power, the third harmonic in Xe exhibits a maximum intensity at 100 Torr (before falling to a minimum at around 350 Torr and slowly rising again to a plateau at 760 Torr) whereas Ar displays a continuously rising pressure-intensity relationship up to 760 Torr. By comparing the maximum observed signals for the third harmonic in Xe and Ar, it was estimated that the conversion efficiency in Xe was approximately ten times higher than that in Ar. A difference in the pressure-intensity relationship of the fifth harmonic signal in xenon and argon was also observed, with Xe displaying a maximum intensity at 30 Torr before falling to effectively zero around 200 Torr. In Ar the signal rises with pressure up to the measurable limit at 760 Torr. Both argon and xenon have similar fifth harmonic conversion efficiencies, with Xe slightly more efficient. A 25 cm focal length lens was found to produce the optimum signal in both gases. The peak intensity developed at the focus using this lens was estimated to be 5×10^{14}Wcm^{-2}. Shorter focal length lenses promoted plasma formation in the generating cell and this reduced the efficiency of harmonic generation.

The number of photons generated for each harmonic in xenon was estimated using the known sensitivity of the photomultiplier and the efficiency of the grating. An estimated 10^4 photons were generated per pulse for the third harmonic in xenon at 100 Torr, representing a conversion efficiency of 2×10^{-6}. A cubic relationship between the 250 nm output and the 750 nm pump intensity was observed.

The number of fifth harmonic photons per pulse generated in Xe at 30 Torr was estimated to be 5×10^4, representing a conversion efficiency of 10^{-10}. The relationship between the intensity of the fifth harmonic and the fundamental was found to be linear, suggesting that the fifth harmonic had joined the plateau of harmonics[6].

The spectral profiles of the third and fifth harmonics were measured. The spectra fitted reasonably well to Gaussian curves. The important parameters obtained are listed in Table 1. The spectral width measurements correspond to the full width half maximum of the band profiles analysed.

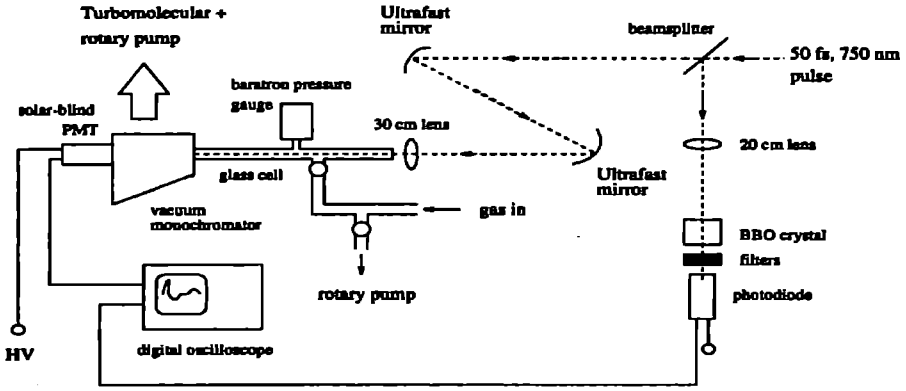

Figure 1: Experimental arrangement for harmonic generation.

CONCLUSION

It has been shown that high order harmonics can be successfully generated using intense femtosecond pulses with a relatively simple experimental arrangement. Although the estimated number of fifth harmonic photons generated per pulse appears to be low (conversion efficiency of 10^{-10}), this value may prove to be an underestimate. Further work is planned to check the efficiency of harmonic generation. Higher harmonics will also be studied and extended to lower XUV wavelengths (higher orders) using the same laser system and a windowless vacuum system with the generating medium introduced as a pulsed jet.

Harmonic (medium)	Wavelength nm	Width nm
5th (Ar)	150	3.4
3rd (Xe)	250	3.4
5th (Xe)	150	2.1

Table 1 : Spectral characteristics of 3rd and 5th harmonics in Xe and Ar.

REFERENCES

1. C.-G. Wahlstrom, Physica Scripta **49** 201 (1994).
2. G. Mourou and D. Umstadter, Phys. Fluids B, **4** 2315 (1992).
3. K. Miyazaki, H. Sakai, G.U. Kim and H. Takada, Phys. Rev A, **49** 548 (1994).
4. P. Balcou, P. Salieres, K.S. Budil, T. Ditmire, M.D. Perry and A. L'Huillier, Z. Phys. D, **34** 107 (1995).
5. P. Erman, A Karawajczyk, E. Rachlew-Kallne, E. Mevel, R. Zerne, A.L'Huillier and C.-G.Wahlstrom, Chem. Phys. Lett., **239** 6 (1995).
6. P. Balcou and A. L'Huillier, Phys. Rev. A, **47** 1447 (1993).

LASER CUTTING AND SMOOTHING OF DIAMOND COATED FIBRES

Michael N.R. Ashfold,[1] Sarah E. Johnson,[1] Robert J. Lade[1], Graham Meaden[2] and Peter G. Partridge[2]

[1]School of Chemistry, University of Bristol, Bristol BS8 1TS
[2]Interface Analysis Centre, University of Bristol, Bristol BS8 1TS

INTRODUCTION

The strength, hardness and elastic modulus values for natural or synthetic diamond grit exceed those of any other material. Not surprisingly, one of the major markets for particulate diamond is in composites for cutting and superabrasive grinding. Chemical vapour deposited (CVD) polycrystalline diamond films exhibit many of the properties of natural diamond and are also being considered for cutting tool applications. One recent development, pioneered at Bristol,[1,2] has been the manufacture of diamond fibres by hot filament CVD onto wires and ceramic fibres. Such fibres may be superior to current commercial fibres for reinforcing metallic and ceramic matrix composites. Their exceptional hardness and stiffness, however, associated with a relatively low strain to fracture, presents major difficulties when it comes to cutting or machining these fibres. Such operations thus become a critical area of activity in the processing of these materials. Here we report preliminary investigations of the potential of Nd-YAG laser ablation as a means of sectioning individual diamond coated fibres and a diamond fibre Ti-alloy composite testpiece.

EXPERIMENTAL

Fibres have been prepared using a purpose designed and built hot filament reactor (Thomas Swan and Co. Ltd.) to deposit diamond onto tungsten wires (20-100 μm diameter) and Sigma SiC fibres (100 μm diameter containing a 15 μm diameter W core). The diamond coating thickness scales linearly with deposition time; fibres have been prepared with up to 97% diamond volume fraction. Test pieces of diamond fibre metal matrix composite material were prepared by aligning a number of continuous diamond fibres, each sputter coated with Ti, embedding them in Ti-6Al-4V alloy at 900°C and either hot vacuum pressing under superplastic conditions or hot isostatic pressing. The inter-fibre spacing in these preliminary test-pieces was chosen to be of the order of the individual fibre diameters.

RESULTS AND DISCUSSION

The fundamental (1064 nm), second and third harmonic outputs (532 nm and 355 nm respectively) of the Spectron Nd-YAG loan laser, operating at 10 Hz, were steered onto the sample in turn, using two 90° prisms and a spherical and cylindrical lens combination to produce a line rather than a spot focus. Figs. 1 and 2 show SEM photographs of representative cuts obtained using the 355 nm output. Consistent with previous studies of laser ablation of other materials, this UV wavelength was found to be much more effective at cutting the fibres than either of the longer wavelengths (for a given pulse energy). Fig. 1 demonstrates that UV laser ablation provides a most convenient means of sectioning diamond coated W-wires, yielding a much cleaner finish than any we have achieved using a sharp blade. More informative, from the mechanistic viewpoint, are the results of experiments such as that illustrated in fig. 2. Here ablation was deliberately halted part way. Inspection of SEM images such as this shows that diamond ablates faster than tungsten at 355 nm, and that some of the ablated tungsten redeposits on the fibre surface in the immediate vicinity of the cut. Laser Raman studies suggest some local graphitisation of the diamond at the cut edges.[3]

During the loan period we were able to make preliminary investigations of the way the cut rate of an individual fibre varies with incident fluence. These show that there is a distinct threshold fluence/intensity below which no ablation occurs, above which the cut rate appears to scale roughly linearly with fluence. Equivalent experiments were performed whilst jets of oxygen and argon were directed at the area under ablation, with a view to minimising the redeposition of sputtered tungsten.

If individual fibres are hard to cut mechanically, the composite testpieces provide even more of a challenge. Nonetheless, fig. 3 shows one of our earliest demonstrations that these samples can also be sectioned by UV laser ablation. Progress in this area would undoubtedly benefit from the higher photon and pulse energies, the higher repetition rates, and the greater beam uniformity provided by the latest excimer lasers. We are actively seeking such a laser to advance these preliminary studies further.

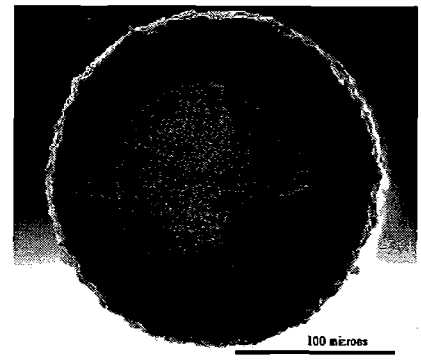

Fig.1

Fig. 2

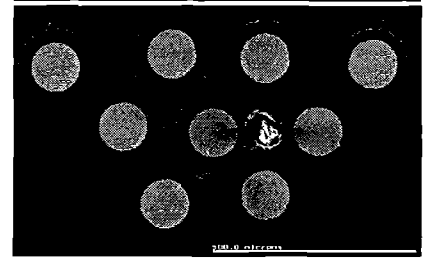

Fig. 3

REFERENCES

[1] P.W. May et al. *Diamond and Rel. Mater.* 4, 794 (1995)
[2] P.G. Partridge, P.W. May and M.N.R. Ashfold, *Mater. Sci. and Technol.* 10, 177 (1994)
[3] G. Meaden, P.G. Partridge, M.N.R. Ashfold, E.D. Nicholson and A. Wisbey, *J. Mater. Sci.* 31, xxx (1996)

USE OF FOCUSED LASER PLASMA GENERATED SOFT X-RAYS TO SIMULATE THE BIOLOGICAL EFFECTS OF DENSELY IONISING RADIATIONS

BD Michael[1], AG Michette[2], M Folkard[1], KM Prise[1], SJ Pfauntsch[2], CJ Buckley[2], G Schettino[2], M Forsberg[3], ICE Turcu[4] and R Allott[4]

[1]Gray Laboratory Cancer Research Trust, PO Box 100, Mount Vernon Hospital, Northwood, Middlesex, HA6 2JR
[2]Department of Physics, King's College London, Strand, London WC2R 2LS
[3]Department of Medical Radiation Physics, University of Stockholm, Stockholm, Sweden
[4]Central Laser Facility, Rutherford Appleton Laboratory, Chilton, Didcot, Oxfordshire OX11 0QX

INTRODUCTION

Densely ionising radiations such as α-particles are known to have a much higher biological effectiveness for inactivating and mutating cells than X-rays and other sparsely ionising radiations. The difference is believed to be related to increased clustering of damaged sites on DNA and its fragmentation, both of which occur preferentially at high ionisation densities. The induction of these complex types of DNA damage is characteristic of how ionizing radiations act. For a given type of radiation, the spectrum of complex damages induced reflects how the structure of the track maps on to that of DNA. These processes are the subject of studies using Monte Carlo modelling and experimental work with cell and DNA systems comparing the actions of radiations having different track structures. It is clear that clustering of ionisations at the nanometer level is particularly important and that this relates both to the dimensions of the DNA helix and to its higher-order structure. Energy is deposited around the tracks of charged particles by δ-rays (electrons) to a maximum radius which depends on the particle velocity – 10s or 100s of nanometers for many radiations of practical interest. Within this region, the density of ionization varies by a number of orders of magnitude, in approximately inverse proportion to the square of the radial distance from the particle track. As a consequence, experiments using charged particles actually compare the effective average *as seen by the cell* of a wide range of ionization densities. The attraction of generating an artificial "high-LET" track of focused soft X-rays is that it can be tailored to deliver a very much more uniform distribution of ionization density than occurs in the real track of a charged particle. The uniformity of the focused laser plasma X-ray track should therefore offer certain advantages for probing the underlying effects of ionisation density that govern the biological effectiveness of charged particles. In attempting to mimic some of the important features of high-LET tracks, a key requirement is to deposit the energy within the cell nucleus in a comparable time interval and the ability of the laser plasma to deliver single ~7 ps pulses appears to satisfy this requirement.

We have recently developed a system to irradiate cells individually with counted numbers of protons or $^3He^{++}$ ions to measure their effectiveness at the ultimate low-dose level, that of a single traversal of the cell nucleus. This system has also been designed to probe the distribution of sensitive targets in cells with micron resolution. In addition, we have recently received a grant award from the BBSRC to develop a focused soft X-ray microprobe (based on a conventional microfocus source) for individual cell irradiations which will allow us to probe targets with ~100 nm resolution. Both of these systems employ computerised imaging, cell recognition and micropositioning control. In future work, we intend to use one of these systems in conjunction with the laser plasma source. The methods for mammalian cell culture and irradiation and for assaying radiation effects, such as cell kill, micronucleus induction and DNA damage are well established in our laboratory. The main aim of our initial pilot study (26 Feb - 15 Mar 1996) was to align and test the focusing zone-plate system and obtain output data to confirm that sufficient dose could be delivered within a single pulse, as had been indicated by our earlier estimates.

METHODS

Trains of 8 laser pulses at 248 nm were focused on to a Mylar tape target to excite the Lyman-α line of hydrogenic C^{5+} at 3.37 nm (367 eV). Photons emerged from the source chamber through a 100 nm thick aluminised silicon nitride window. A 91 μm diameter apodised zone plate was used, with a focal length of 2.7 mm, together with an order-sorting aperture (typically of 20 μm diameter) before the focal point. The zone plate and aperture were mounted in an assembly equipped with micrometer adjustments which were used for alignment. An off-line microscope was used and in addition, a newly delivered microscope ordered for the BBSRC-funded X-ray microprobe project was installed on-line and tested. The output of the source was monitored by a silicon diode installed inside the source chamber. The output after the silicon nitride window was measured using a silicon diode which had been calibrated for pulse height using a reference Am-241 α-particle source. The space between the zone plate and diode was purged with helium.

RESULTS

Measurement of the X-ray output with and without the zone plate in position allowed its efficiency to be measured and it agreed with previously determined values. The order-sorting aperture was scanned in the x-y plane and the corresponding changes in transmitted beam measured by the diode were found to vary in accordance with the expected performance of the zone plate. With the aperture positioned for optimum focusing of the first-order diffracted photons, we measured an average output corresponding to 300 keV, i.e. about 800 photons, for an 8-pulse train.

CONCLUSIONS

The measurements of output demonstrated that, even before any of the potential improvements are made, it is possible to deliver ~300 keV to a cell nucleus, enough to achieve readily quantifiable responses. For example, experience with our proton microbeam shows that we can detect the effect (measured as micronucleus induction) of a single proton traversal, corresponding to an energy deposition of only ~50 keV in the nucleus. Much of the scheduled period was required to establish the necessary techniques for accurate positioning and alignment of the focusing system and insufficient time remained to irradiate cells.

We hope to carry out a further pilot study in which cell irradiations will take place. In addition, a number of improvements can be made to increase the output. These include: the use of a CaF_2 lens in place of the existing silica lens used to focus the UV, cleaning and re-alignment of the UV optics, installing a larger diameter zone plate with improved efficiency and working at a shorter distance from the source. To be offset against these improvements is a decrease in output (~2-fold) in selecting a single 7 ps pulse. We estimate that taking all of these factors into account, it will be possible to deliver up to between 1.5 and 7 MeV in a single pulse. Focused to a spot of about 150 nm diameter, this should provide ionization densities that model those occurring in densely ionising charged-particle tracks.

YIELDS OF SSB AND DSB IN PLASMID DNA IRRADIATED WITH 248nm PHOTONS: ROLE OF HYDRATION

K.M. Prise,[1] B.D. Michael,[1] R.A. Meldrum[2] and C.W. Wharton[2]

[1]Gray Laboratory Cancer Research Trust, PO Box 100, Mount Vernon Hospital, Northwood, Middlesex, HA6 2JR
[2]School of Biochemistry, University of Birmingham, Edgbaston, Birmingham, B15 2TT.

INTRODUCTION

An understanding of the effectiveness of different radiations of differing ionisation density requires detailed knowledge of track structure and information on the energy dependence of lesion induction. For high energy ionising radiations the most frequent energy loss event is in the order of 10's of eV. Despite this, very little information has previously been available as to the energy dependence of lesion production by ionising radiation in DNA. Modelling studies which have made predictions regarding the types of damages likely to be induced in DNA by different qualities of radiations have had to make basic assumptions regarding the energy required to induce even the most simple break in the DNA helix backbone (see for example Charlton *et al.* 1989, *Int. J. Radiat. Biol,* **56,** 1; Nikjoo and Goodhead; 1989 *Int. J. Radiat. Biol,* **55,** 513). Our studies involve the generation of action spectra for the formation of ssb and dsb in a model plasmid DNA system for both synchrotron photons (7-150eV) and photons from a pulsed laser source (248nm; 5eV). The use of laser sources has allowed us to critically study the role of the hydration state of the DNA on both the spectrum and yields of DNA damage which is difficult with synchrotron sources due to the low photon flux and limited penetration. Using 248nm photons we have measured both the effect of hydration and laser intensity on the yields of single-strand (ssb) and double-strand breaks (dsb) in irradiated pBR322 DNA.

RESULTS AND DISCUSSION

DNA (0.25μg) was spread onto glass coverslips and irradiated either in solution (0.068mM EDTA, pH 7.0) under ambient conditions or under a vacuum of 10^{-3} torr. Samples were analysed by gel-electrophoresis to determine the fractions of the supercoiled, relaxed and linear forms of the plasmid. The intensity of the laser was varied to cover a range from 4 J m^{-2} per pulse to 1400 J m^{-2} per pulse. The quantum efficiencies for both ssb and dsb induction under these conditions are shown in figure 1. For

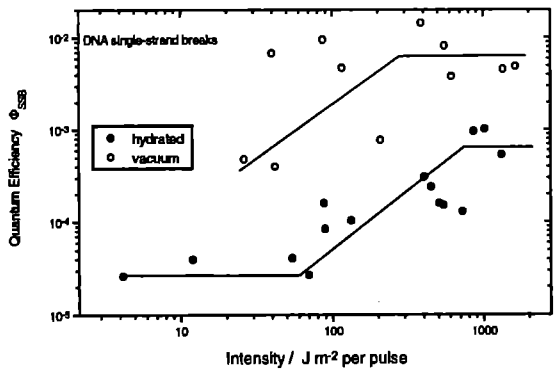

Figure 1 Quantum efficiency of ssb induction

ssb induction an effect of intensity was observed for both hydrated and dry DNA systems and the yields of ssb in dry DNA were ~10-fold higher than DNA irradiated in a fully hydrated state. For plasmid DNA irradiated in solution the induction of dsb changed from a quadratic response (dsb produced by 2 ssb's being formed close together on opposite strands) at low intensities to a linear-quadratic relationship at intensities above 200 Jm^{-2} (evidence of a component for direct induction of dsb). Direct induction of dsb was only observed at intensities of greater than 200Jm^{-2} per pulse at a constant level independent of intensity (Figure 2). In

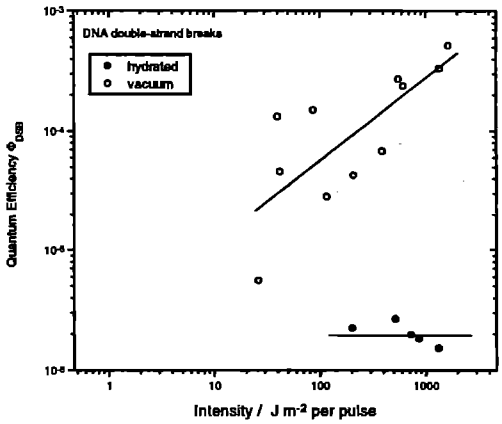

Figure 2 Quantum Efficiency of dsb induction

particular, under hydrated conditions the induction of dsb principally involves a two photon event from the marked effect of intensity suggesting that ionisation is required. With DNA irradiated under vacuum direct induction of dsb was observed at all intensities studied with the quantum efficiency increasing with increasing intensity. These data indicate that water plays a critical role in determining the effectiveness of 248nm photons and in the mechanism of dsb production. The similar increase in quantum efficiency of ssb and dsb under vacuum conditions mirrors the similarity we have observed in the action spectra for ssb and dsb induction with synchrotron photons (7-150eV; Michael *et al.* 1994 *Int. J. Radiat. Biol,* **66,** 569; and unpublished data). Here, despite the range of energies the ratio of ssb to dsb remains around 20. This suggests that there is a common precursor for both lesions with a 1 in 20 relative probability that a dsb will be formed. This may be via a radical transfer mechanism which has been postulated to occur under some conditions with ionising radiation (Siddiqi and Bothe 1987 *Radiat. Res,* **112,** 449). The quantum efficiencies for both ssb and dsb formation under vacuum conditions are similar to those observed in the 7-11 eV range with synchrotron photons. In hydrated DNA the mechanism is, at low intensities, a two radical mechanism, leading to the formation of two ssb, which if formed close enough together, will form a dsb. At higher intensities direct formation is observed with a change in the ratio of ssb to dsb.

In conclusion, this preliminary study has shown that the hydration state of the DNA has a significant effect on both the yield and mechanism of strand break formation in DNA exposed to 248nm photons. The development of a laser plasma VUV source at the Central Laser Facility (Turcu, Allott *et al.*) will allow us to cricitcally study the role of hydration at higher energies (10-40eV) directly relevent to ionising radiation.

193NM LIGHT INDUCED SINGLE STRAND BREAKS IN DNA: A TIME RESOLVED STUDY.

P. O'Neill[1], S. Botchway[1], T. Melvin[1], A.W. Parker[2] and P. Cullis[3]

[1]MRC Radiation and Genome Stability Unit
[2]Rutherford Appleton Laboratory
[3]Leicester University

INTRODUCTION

The various biological effects of ionising radiation and UV light such as cellular inactivation, transformation and radiation mutagenesis are thought to be as a consequence of chemical modifications to DNA.[1] Of all the lesions, non repairable DNA double strand breaks (dsb) have been implicated in cellular inactivation by ionising radiation.[2] The initial chemical events occurring in DNA following ionising radiation arise by the interactions of water radicals, namely the hydroxyl radical, with DNA, and the direct deposition of energy within DNA (direct effects). The damage produced upon interaction of the OH radical with DNA and model systems has been well documented[3] whereas much less is known about the chemical events following direct energy deposition in DNA.

The majority of the information about the radicals formed from the direct effects of ionising radiation comes from esr studies[4] on DNA irradiated at 77K. Two types of species are produced namely electron loss and electron gain centres which are localised upon the base moieties. With the advent of lasers which produce light at <200nm, photolysis is an alternative approach to study ionisation of DNA.

Monophotonic ionisation of the nucleic acid base moiety is a major process within the DNA or polynucleotide matrix upon exposure to 193nm light (ϕ_r 0.03 - 0.11). Although a large proportion of the initial ionisation of DNA by the 193nm light is predicted to occur at the guanine residue, migration of the oxidative damage to the guanine residue takes place between neighbouring bases[5]. Further, irradiation of single or double-stranded DNA with 193nm light results in strand breakage by a monophotonic process in extremely low yields (< 2% of the total photoejected electron yield). The major sites for 193nm light induced DNA ssb occur at guanine[6].

Rayleigh light scattering is a technique which has enabled direct measurement of the timecourse of the strand breakage process from changes in the molecular weight of the biopolymer. This technique has previously been used to show that ssb induced in DNA by hydroxyl radicals results from transfer of the radical site from the nuclei base moiety to the sugar backbone by a hydrogen abstraction.

The following studies were undertaken to assess whether strand breakage of DNA, caused by exposure to 193nm light, but visualised after electrophoresis, occurs as a result a prompt radical process or by a 'labile' diamagnetic product of guanine. Further, since there is little information known about the DNA radicals responsible for strand breakage as caused by the *'direct effect'* of ionising radiation, the following study was undertaken to assess the mechanism of ssb induction by 193nm light in DNA and polynucleotides. The consequences of exposure of the single stranded polyribonucleotides poly A,C and U and three DNA samples from calf thymus, *micrococcus lysodeikticus* and *clostridium perfringens* to a 20ns pulse of 193nm light was probed by transient optical absorption spectroscopy and Rayleigh light scattering.

193nm induced strand breakage in polynucleotides

PolyC and polyU

The transient optical absorption spectra after photolysis, with 193nm, of an oxygen, saturated solution of single stranded polyC (pH=8) were determined. The change in optical absorption with time at 300 nm for polyC is shown in Figure 1. The initial component of the optical absorption decays with a half-life of ~ 7 ms to yield a species, which absorbs in the wavelength region 300-400nm. The decrease of light scattering intensity (LSI) with time upon 193nm irradiation of poly C, under identical conditions to those for absorption changes, is shown in Figure 1. These changes represent at least two pathways to ssb. The proportion of strand breakage which occurs via the 'prompt' process is 50% and occurs within 4 ms. There is no significant change in optical absorption at early times corresponding with this 'prompt' formation of strand breakage. The slow component of the strand breakage, as detected by RLS occurs at a similar rate to that for the decay of the optical absorption at 300nm.

With polyU, similar time dependent changes in LSI were obtained on irradiation of an oxygenated, aqueous solution of poly U (pH=7.9) with 193nm light. The slow component of strand breakage corresponds with the decay of the one-electron oxidised species of polyU as determined at 290nm. The relative contributions to the different processes leading to strand breakage and the reaction half-lives are given in Table 1.

polyA

With polyA, strand breakage detected upon 193nm photolysis of an oxygenated polyA solution (pH=8) occurs mainly by a 'prompt' process (>90%). At 330nm, the absorption maximum for the adenine radical, the optical absorption was found to decay slowly, indicating that strand breakage does not involve the major adenine radical species within poly A within 0.5s.

DNA

Three different DNA samples (CP, CT, ML) were chosen, containing different proportions of the base pairs adenine/thymine: guanine/cytosine (%GC, CP=31%, CT=43%, ML=75%), to assess if there is an influence of base composition on ssb induction within 0.5s. The single stranded DNA samples (pH=7.6-8) in oxygenated aqueous solution were irradiated with a short pulse of 193nm laser light. The resulting LSI changes with time for CT DNA are displayed in Figure 1 as a representative example. From the time dependence of these LSI changes, strand breakage occurs by at least two processes; a 'prompt' process and a slower process. The loss of optical absorption at 320nm following photoionisation of the DNA samples, occurs with a half-life of 40ms similar to that for strand breakage (Figure 1).

The data for the three DNA samples are collected in Table 1. The efficiency of strand breakage per photo-electron previously determined is also included in Table 1.

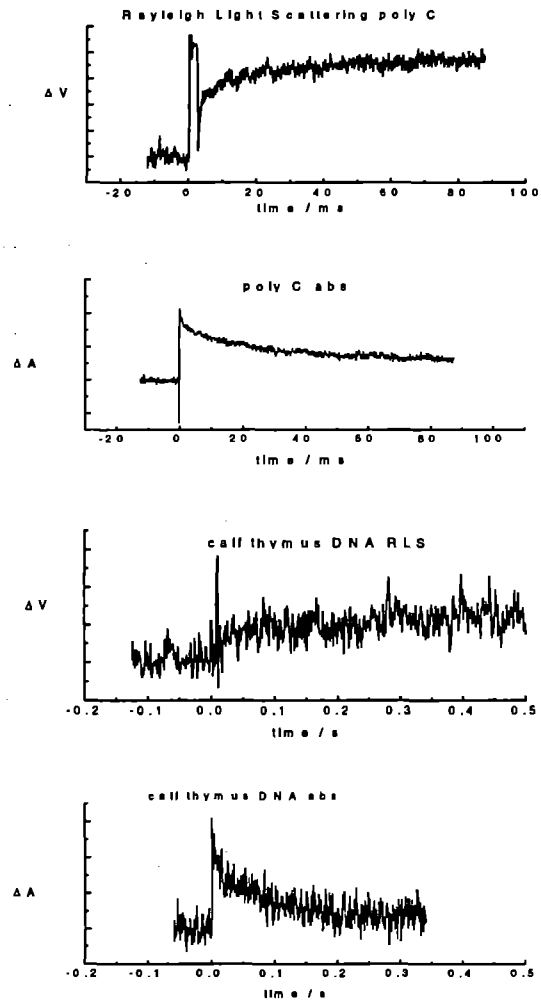

Figure Timecourse for the changes in RLS and transient optical absorption (abs) at 300 nm for poly C and calf thymus DNA.

Table 1 Contribution of the fast component of and the half life of the slower component of LSI change following 193 nm photo-ionization of various ss- polynucleotides and DNA samples with different base compositions.

Poly-nucleotide	% Fast Component	$t_{1/2}$ TRLS	$t_{1/2}$ Optical	f_{ss}/f_r -
Poly C	<50%	6-7 ms	7.0 ms	0.32
Poly U	60%	40 ms	40 ms	
Poly A	>90%	-	-	0.015
DNA ML (72% G:C)	<10%	40 ms	-	
DNA CT (43%G:C)	<10%	46 ms	40 ms	0.011
DNA CP (31%CP)	<10%	40 ms	-	

DISCUSSION

From these studies it is demonstrated that 193 nm photolysis of Poly C, Poly U and the three different ssDNA samples in solution induces, within 0.5s, ssb by at least two processes; a 'prompt' and a slow component. With polyA only 'prompt' strand breakage occurs. The optical absorption spectra determined after photo-ionisation of polyC, polyU, polyA and ssDNA have previously been assigned to their corresponding one-electron oxidised species. The decay of these one electron oxidised base radicals, occur on a similar time scale to that of the slower component of ssb formation. It is suggested that the one electron oxidised nucleobase radicals are the precursors to the slower component of the strand breakage process.

It is proposed that the slow component of strand breakage involves transfer of the radical site from the nucleobase to neighbouring sugar moiety by a rate determining H-atom abstraction reaction. Depending on the site of H-atom abstraction, the resulting sugar radicals lead to strand breakage involving a non-rate determining, heterolytic elimination of the phosphate ester bond. This process is in competition with the radical cation chemistry of the nucleobases involving two different reactions, hydration or deprotonation. Using model systems, deprotonation of the radical cation of cytidine occurs at C(1)'.

For the 'prompt' component of strand breakage, observed to varying degrees for the polynucleotides and DNA, a corresponding decay of the radicals which absorb at >300nm was not observed. There are several possible precursors to this 'prompt' strand breakage. One is that the strand breakage is initiated by a weakly absorbing radical; the second is that it occurs from an ionisation process such as formation of one electron oxidical phosphate radical. Sugar radicals at C(4)' and C(2)' are not expected to be produced directly by 193nm light but via a base radical transfer as discussed above. Prompt strand breakage arising from a one-electron oxidised phosphate radical as precursor may occur, since phosphate could contribute a relatively large component to the photo-ejected electron yield, especially with polyU and polyC. Once a one-electron oxidised phosphate is formed, possible pathways include i) transfer of the electron hole to its more easily oxidised base moiety although this process may depend on the ease of oxidation of the base. ii) Transfer of phosphate radical site via a hydrogen atom abstraction to the sugar moiety. iii) Direct photocleavage of the phosphate sugar. Both ii) and iii) would lead to strand breakage which is not mediated by any interaction of the nucleic acid base moiety

Therefore, photolysis of DNA with 193nm light leads to strand breakage involving a free radical pathway. One electron oxidised nucleic acid base radicals formed by 193nm photoionisation of DNA and polynucleotides are the major precursors to strand breakage. The rate of strand breakage of DNA is not affected by neighbouring base composition. The major pathway for loss of these base radicals does not however lead to strand breakage but to base or sugar modifications. Ionisation of the phosphate backbone may also contribute to prompt strand breakage depending on the absorption cross-section of the individual components. In DNA, the *'direct effects'* of radiation of the base moieties leads to localisation of the hole at guanine which is a precursor to strand breakage but with an efficiency < 1%.

REFERENCES

1. P O'Neill and E M Fielden. Adv. Radiat. Biol., 17, 53-120 (1993).
2. D Blöcher. Int. J. Radiat. Biol., 54, 761-771 (1988). T J Jenner, C M de Lara, P O'Neill and D L Stevens. Int. J. Radiat. Biol., 64, 265-273 (1993). M Frankenberg-Schwager. Radiat. Environ. Biophys., 29, 273-292 (1990).
3. C von Sonntag. "The Chemical Basis of Radiation Biology". Taylor & Francis, London, England. p.515 (1987). W A Berhard. Adv. Radiat. Biol., 9, 199-280 (1981). S Steenken. Chem. Rev. 89, 503-520 (1989).
4. P J Boon, P M Cullis, M C R Symons and B W Wren. J. Chem. Soc. Perkin Trans.2, 1393-1399 (1984). W A Bernhard, N Mroczka and J Barnes. Int J. Radiat. Biol., 66, 491-498 (1994). D Becker and M D Sevilla. Adv. Radiat. Biol., 17, 121-180 (1993).
5. T Melvin, S W Botchway, A W Parker and P O'Neill. J. Chem. Soc., Chem. Commun., 653-654 (1995).
6. T Melvin, M A Plumb, S W Botchway, P O'Neill and A W Parker. Photochem. Photobiol., 61, 584-591 (1995).

TIME-RESOLVED SPECTROSCOPY OF THE FREE RADICAL SITE IN PEA SEEDLING COPPER AMINE OXIDASE

Roger H Bisby[1], Stephen A Johnson[1], Susan M Tavender[2] and Anthony W Parker[2]

[1]Department of Biological Sciences, University of Salford, M5 4WT
[2]Rutherford Appleton Laboratory

Copper amine oxidases are widely distributed enzymes noted for the presence of a TOPA (trihydroxyphenylalanine) quinone residue at the active site[1,2]. The X-ray structure of the E.coli enzyme has recently been determined[3] and shows the spatial relationship between the TOPA quinone site and the copper ion which is the second redox site in the enzyme. In the catalytic cycle, the amine substrate reacts with the TOPA quinone to form the corresponding aminoquinol. This is in equilibrium with a TOPA-derived free radical and Cu(I). Our objective is to use time-resolved resonance Raman spectroscopy to determine the nature and involvement of intermediate species, including the transient free radical, in the mechanism of pea seedling copper amine oxidase.

In the last annual report we showed the progress that had been made in obtaining the steady-state resonance Raman spectrum of the free radical site that is formed in anaerobic solutions of pea seedling amine oxidase after reduction with amine substrate. This work has now been published[4]. Figure 1 shows the steady-state resonance Raman spectra obtained using both ^{14}N- and ^{15}N-containing substrates. The shifts in some of the peaks in the spectra indicate that an atom of nitrogen is incorporated into the radical site on reaction of amine with the TOPA quinone.

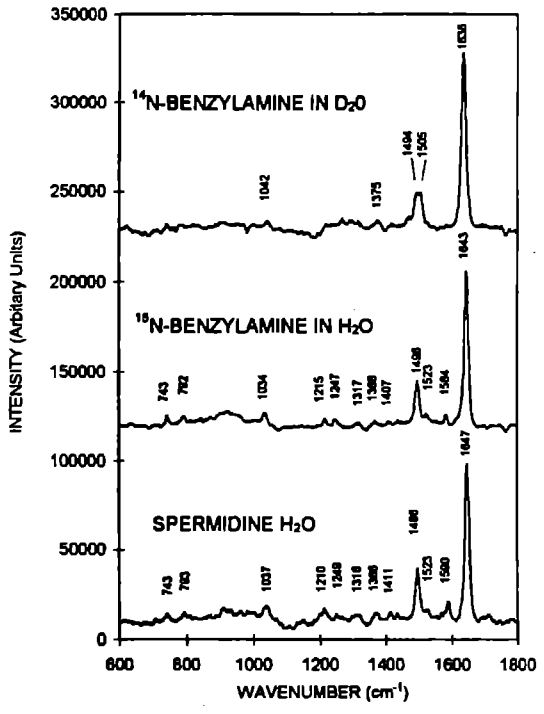

FIGURE 1 - Steady-state resonance Raman spectra of the free radical site in pea seedling copper amine oxidase in anaerobic aqueous solutions at neutral pH. The spectra were obtained using the 457.9 nm line from an Ar+ laser.

This supports the conclusion that the radical is a semi-iminoquinone. The differences in the spectra observed in Figure 1 when measured in H_2O and in D_2O also suggest that the radical site contains a strongly bound proton.

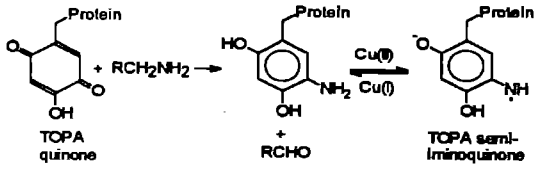

In order to provide more insight into the structure and reactivity of the semi-iminoquinone radical site in amine oxidases, further TR[3] work has been undertaken with 4-aminoresorcinol (4-AR), which may be regarded as a suitable model for the aminoquinol form of the enzyme intermediate after substrate reduction[5]. The free radical formed by one-electron oxidation of 4-AR has been studied by both pulse radiolysis and laser flash photolysis, using respectively triplet duroquinone and the Br_2^- radical as oxidants. In the pulse radiolysis experiment (Figure 2) the radical form from the reaction of Br_2^- with 4-AR at pH 7 showed an absorption maximum at 460 nm, whereas at pH 2 the peak maximum shifts to 430 nm. Formation of the species absorbing at 460 nm was observed in time-resolved resonance Raman spectra using a probe wavelength of 460 nm (Figure 3A). At this wavelength both the durosemiquinone radical anion and the 4-AR radical are in resonance, but several peaks may be assigned to the 4-AR radical after subtraction of the DQ^- spectrum. At pH 5.2 the 4-AR radical spectrum appears similar to that from the amine oxidase, with a major peak at 1648 cm^{-1} almost identical to that in Figure 1, and a subsidiary peak at 1520 cm^{-1} which appears to correspond to the 1496 cm^{-1} peak in the amine oxidase spectrum.

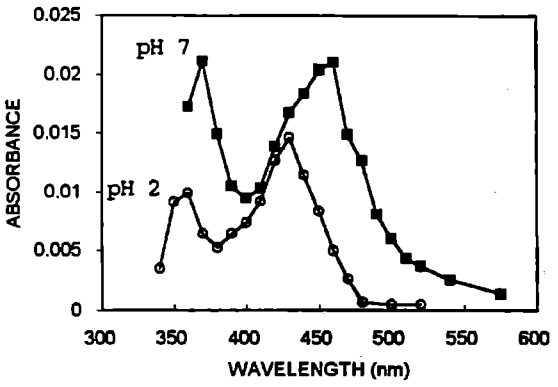

FIGURE 2 - Transient absorption spectra of radicals from oxidation of 4-AR by Br_2^- at pH 2 and pH 7 obtained by pulse radiolysis.

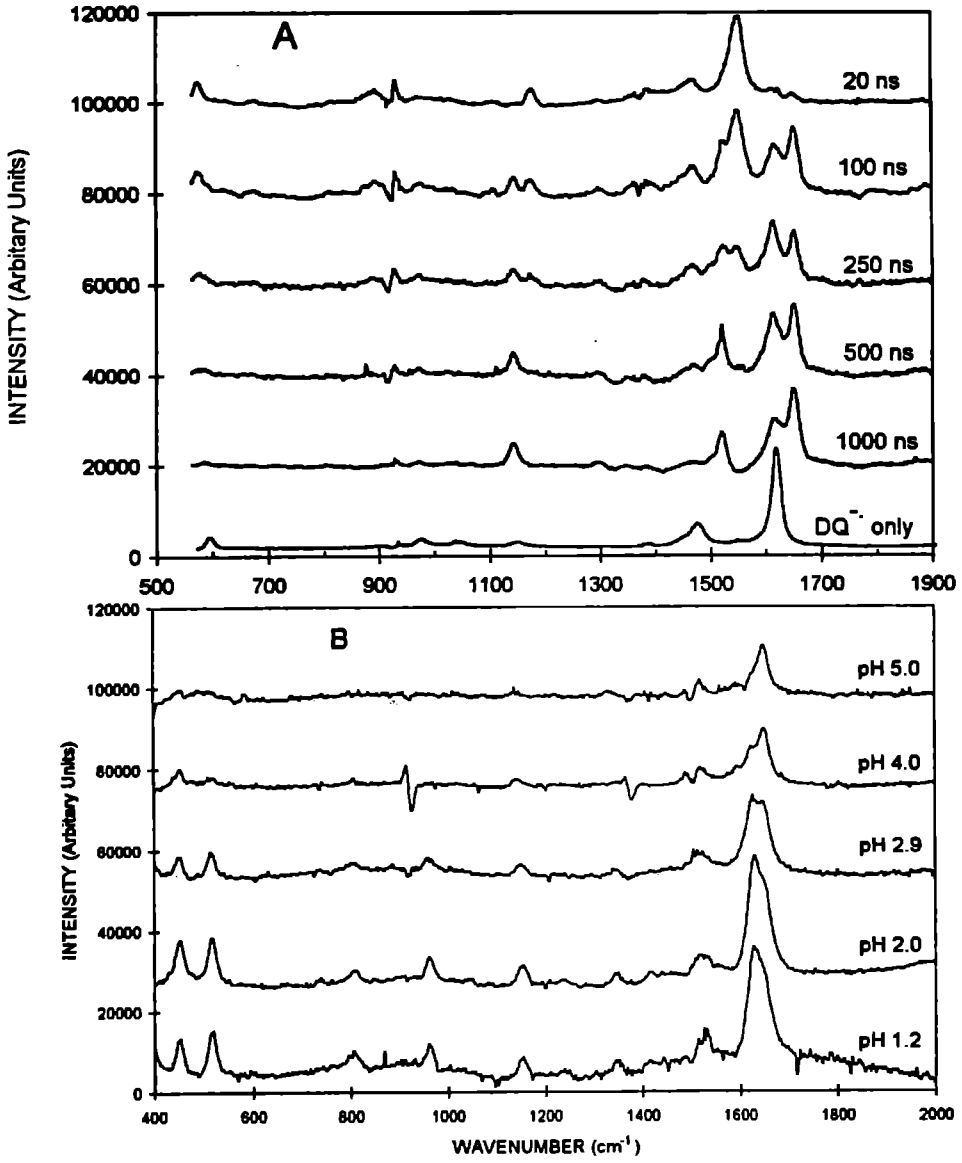

FIGURE 3 - A:- Time-resolved resonance Raman spectra obtained during the reaction of triplet duroquinone with 4-AR in H_2O/MeCN(50%v/v) at pH 5.2 [λ(pump)=340nm, λ(probe)=460 nm]; B:- resonance Raman spectra of radicals from oxidation of 4-AR with ^{3}DQ measured as a function of pH [λ(pump)=355 nm, λ(probe)=430 nm. Δ t=1μs]

Since the latter has been assigned to the mixed C-O/C-N stretching vibration of the TOPA-derived semi-iminoquinone radical, this shift may result from a particular environment in the enzyme, such as hydrogen bonding or interaction with the copper ion. The resonance Raman spectra of radicals from 4-AR over a range of pH shown in Figure 3B are the result of subtraction of durosemiquinone spectra at identical pH values and show only peaks due to 4-AR radicals. Protonation of the radical form at pH 5 (C-C stretch at 1648 cm^{-1}) is clearly observed as the pH is reduced to pH 1.2 (C-C stretch at 1629 cm^{-1}). The pK_a appears to be in the region of 4 and remains to be more accurately determined in pulse radiolysis experiments.

Furthermore, it is expected that the charge of each radical might be determined by the effect of ionic strength on the second order decay constant.

REFERENCES

1. S.M. Janes, D. Mu, D. Wemmer, A.J. Smith, S. Kaur, D. Maltby, D. Burlingame and J.P. Klinman (1990) Science 248, 981-987.

2. P.F. Knowles and D.M. Dolley (1994) Metal Ions Biol.Syst. 30, 361-403.

3. M.R. Parsons, M.A. Convery, C.M. Wilmot, K.D.S. Yadov, V. Blakeley, A.S. Coner, S.E.V. Phillips, M.J. McPherson and P.F. Knowles (1995) Structure 3, 1171-1184.

4. S.A. Johnson, R.H. Bisby, S.M. Tavender and A.W. Parker (1996) FEBS Letters 380, 183-187.

5. M.Mure and J.P. Klinman (1993) JACS 115, 7117-7127.

FAST SOLUTION RELEASE FROM PHOTOSENSITIVE LIPOSOMES: AN ALTERNATIVE TO COVALENTLY 'CAGED' REAGENTS

Roger H. Bisby, Steven A. Johnson, Andrew C. Mitchell and Christopher G. Morgan

Department of Biological Sciences, University of Salford, Salford M5 4WT, UK.

INTRODUCTION

Release of a solute with biological activity by photolysis of covalently 'caged' derivative is now a widely used technique for rapid and localised delivery[1-3]. The most widely used derivatives are 2-nitrobenzyl derivatives which release the caged compound on photolysis at 300-320 nm. Because there are some inherent problems with this approach, including low quantum yield for solute release, damage to other molecules by the short wavelength light required for cage photolysis and the formation of by-products toxic to cellular systems, we have considered alternative strategies to achieve cellular delivery and rapid controlled release of reagents.

Previously we have described a novel photosensitive liposome system[4-7] based on a photochromic lipid molecule 'Bis-AzoPC' [1,2-bis(4-(4-n-butylphenylazo)phenylbutyroy)-phosphatidyl choline] (Figure 1). This lipid exists in a photostationary state which is predominantly composed of the *trans*- isomer under visible light illumination, but which is converted to a *cis*-enriched photostationary state on exposure to near-ultraviolet light. On exposure to ultravoilet light, conversion of Bis-AzoPC to the *cis*-photostationary state disrupts the bilayer membrane leading to rapid leakage of contents[6].

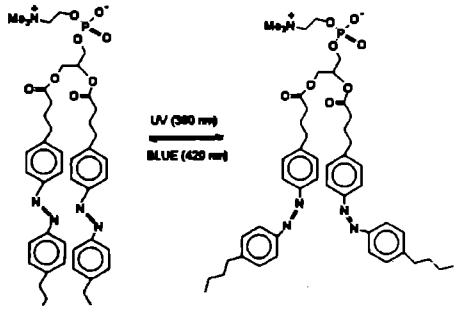

FIGURE 1 Trans-to-cis isomerisation of Bis-AzoPC on UV illumination.

A wide variety of water-soluble materials including biologically important ions such as calcium and copper and drugs such as methotrexate[8] can easily be encapsulated under mild conditions without the need for specialised apparatus, and photo-induced release of such solutes from liposomes containing Bis-AzoPC has already been demonstrated[9,10]. In addition, liposomes might be appropriate as vehicles to introduce reagents into cells by endocytosis, minimising the reagent's exposure to degradative species until release is triggered.

One of the important advantages of some covalently caged molecules with biochemical and physiological activity is that release, on a timescale of microseconds to seconds, may be triggered by a flashlamp or laser pulse. For those examples with the fastest rates of release, the timescale is comparable with that obtained in stopped flow experiments. However caged compounds are widely applied to situations, such as imaging of cells and tissues in which stopped flow and related techniques are inappropriate. In these circumstances, photo-initiated release of solutes initially entrapped within a liposome system may be an attractive alternative to the use of covalently caged species. The purpose of the present experiments was to determine the kinetics of solute release from photosensitive liposomes of dipalmitoylphosphatidylcholine containing Bis-AzoPC. For this purpose calcein was used to represent a typical low molecular weight polar solute which may be encapsulated within a liposome. When entrapped at high concentrations within lipid vesicles the fluorescence of calcein is markedly self-quenched. Calcein release from within a vesicle may therefore be readily monitored by an increase in fluorescence as the dye is diluted into the bulk aqueous solution. We show that under suitable conditions, rapid release of calcein can be initiated by a single laser photolysis pulse.

RESULTS AND DISCUSSION

Initial experiments were undertaken with a low power density, diffused laser beam (ca.0.1mJ mm^{-2}) at 355 nm. In this case no release of caclein, as evidence by an increase in fluorescence intensity, was observed when the sample was exposed to a single laser pulse. Figure 2 shows the result of an experiment at 20°C involving a train of six pulses, each separated by 33 ms. In this experiment there was little dye released until after the fifth laser pulse had irradiated the sample, after which the release proceeded relatively slowly over several hundred milliseconds. Increasing the spacing between pulses to several seconds gave similar results, as did experiments at 35°C except that the fraction of calcein ultimately released was greater at the higher temperature. These results indicate that a threshold level of photoisomerisation of Bis-AzoPC was required to initiate leakage.

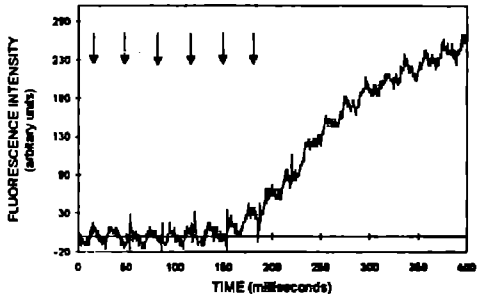

FIGURE 2 Increase in fluorescence intensity due to calcein release from liposomes containing Bis-AzoPC after exposure to six low intensity laser pulses (marked by vertical arrows) at 355 nm.

In contrast it was found that in experiments using the higher power density of the direct dye laser beam (ca 2 mJ mm^{-2}), rapid release could be initiated by a single laser pulse. The result at 25°C is shown in Figure 3. The rate of calcein release from the liposomes inducted by a single laser pulse appeared biphasic, and was fitted well to a double exponential process. Most of the build-up in fluorescence intensity occurred in the rapid phase with a time constant of 6.0±0.5 ms. The slower phase had a time constant of 70±10 ms. These were not thermal effects of the laser pulse, since control experiments using liposomes not containing Bis-AzoPC did not release calcein under any conditions tested, despite the fact that their dye contents would strongly absorb the

incident radiation. The use of the higher power density laser beam therefore induces solute release from within the Bis-AzoPC / DPPC liposomes at 20°C on a timescale comparable with that of the usual stopped-flow technique.

The rate of calcein release in response to a single high intensity laser pulse is markedly temperature dependent as also shown in Figure 3 for experiments performed between 5 and 35°C (below the phase transition temperature of DPPC liposomes). The time constant for the predominant fast component for dye release varied from about 6 milliseconds at 25°C to greater than 100 milliseconds at 5°C.

The release rate at temperatures between 25 and 35°C could not be accurately measured because of saturation of the detector during and shortly after the laser pulse in the present experimental apparatus, as indicated by a transient coincident with the laser pulse as seen in Figure 2. Fitting the rate data obtained at 5°C intervals between 5°C and 25°C to the Arrhenius equation gave an activation energy of 101±13kJ mol^{-1}. Using this value and assuming that the system obeys the Arrhenius law up to the transition temperature, a rate of release of 0.81 ms^{-1} (τ=1.2 ms) at 35°C is calculated.

The marked temperature dependence suggests that the physical state of the lipid bilayer might well be important in the dye release process. As is well known, liposomes of pure DPPC undergo a gel:liquid-crystalline phase transition at around 37-41°C, with a transition profile and midpoint temperature determined by a variety of factors such as liposome size, lipid purity and thermal history of the sample[11]. Our previous experiments have established that liposomes of DPPC containing *trans* Bis-AzoPC retain a similar phase transition to those of DPPC alone, and dispersions of *trans* Bis-AzoPC also show a similar co-operative phase transition at approximately 41°C, though with marked hysteris between heating and cooling cycles[7]. The phase transition of Bis-AzoPC is abolished by isomerisaton to the *cis* photostationary state.

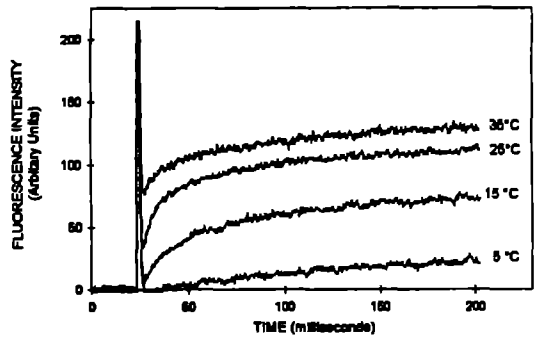

FIGURE 3 Increase in fluorescence intensity due to calcein release from liposomes containing Bis-AzoPC at temperatures between 5 and 25°C on exposure to a single high intensity laser pulse at 355 nm

Interpretation of the effect of isomerisation of Bis-AzoPC in mixtures with DPPC is complicated by the fact that liposomes fuse together after photolysis[8], and this causes a time-dependent change in thermal properties. The fusion process is likely to proceed through initiation of locally disordered regions in the bilayer membrane where the relatively bulky *cis* isomer of Bis-AzoPC interferes with bilayer packing. The relatively slow release of calcein at low temperature also argues for a release mechanism involving dislocations or channels in the ordered bilayer structure whose dimensions are similar to those of the trapped marker. The effective size of such defects would be markedly affected by temperature in the neighbourhood of a lipid phase transition. The behaviour in a lipid bilayer host of azobenzene-containing lipids similar to those used in this study has been investigated by Song et al[12] who find spectroscopic evidence of aggregate formation in some circumstances. It is well known that solute release from liposomes of pure gel-phase lipids is markedly increased at the midpoint of a phase transition[13] where regions of ordered and disordered lipid coexist, and indeed this has been proposed as a method to control localised delivery of soluble drugs trapped within liposomes[14]. Millisecond release of liposome contents is unlikely to be caused by an overall transition in the membrane to the fluid, liquid crystalline state, since these transitions in pure DPPC bilayers occur on a timescale of tens of milliseconds[15].

The present results show that the DPPC-Box-AzoPC liposome system investigated here could be readily applied to effect rapid release of a variety of relatively low molecular weight polar solutes. The results described here have appeared in more detail in the literature[16]. It is likely that such liposomes will find applications as 'cages' for reagents which are difficult to modify using conventional chemical techniques, and in particular the release of metal ions or metal ion chelators appears promising in view of our earlier work[9,10].

REFERENCES

1. Guerny, A.M. and Lester, H.A. (1987) Physiol. Rev. 67, 583-617.
2. McCray, J.A. and Trentham, D.R. (1989) Rev. Biophys. Chem. 18, 239-270.
3. Adams, S.R. and Tsien, R.Y. (1993) Ann. Rev. Physiol. 55, 755-784.
4. Morgan, C.G., Thomas, E.W., Yianni, Y. P. and Sandhu, S. S. (1985) Biochim. Biophys. Acta 820, 107-114.
5. Sandhu, S.S., Yianni, Y. P., Morgan, C.G., Taylor, D.M. and Zaba, B. (1986) Biochim. Biophys. Acta 860, 253-262.
6. Morgan, C.G., Thomas, E.W., Sandhu, S.S., Yianni, Y.P. and Mitchell, A.C. (1987) Biochim. Biophys. Acta 903, 504-509.
7. Morgan, C.G., Sandhu, S.S., Yianni, Y.P. and Dodd, N.J.F. (1987) Biochim. Biophys. Acta 903, 495-503.
8. New, R.R.C. (1990) Liposomes: a practical approach, IRL Press, Oxford.
9. Morgan, C.G., Mitchell, A.C. and Chowdhary, R.K. (1991) Proc. SPIE 1525, 391-396.
10. Bisby, R.H., Morgan, C.G. and Munro, L.H. (1992) Free Rad. Res. Commun. 16, 65-71.
11. Taylor, K.M.G. and Morris, R.M. (1995) Thermochimica Acta 248, 289-301.
12. Song, X., Perlstein, J and Whitten, D.G. (1995) J. Amer. Chem. Soc. 117, 7816-7817.
13. Jansen, M. and Blume, A. (1995) Biophys. J. 68, 997-1008.
14. Ueno, M., Yoshida, M. and Horikoshi, I. (1991) Bull. Chem. Soc. Jpn. 64, 1588-1593.
15. van Osdel, W.W., Johnson, M.L., Ye, Q. and Biltonen, R.L. (1991) Biophys. J. 59. 775-785.
16. Morgan, C.G., Bisby, R.H., Johnson, S.A. and Mitchell, A.C. (1996) FEBS Letters 375, 113-116.

METABOLIC INTERFERENCE OF SOFT X-RAYS ON YEAST CELLS

E.Turcu[1], R.Allot[1], N.Lisi[1], D.Batani[2], M.Milani[2], G.Leoni[2], A.Conti[2], A.Masini[2], F.Previdi[2], R.Casati[2], R.Bonadio[2], N.Correale[2], M.Costato[3], A.Pozzi[3]

[1]Rutherford Appleton Laboratory
[2]Physics Department University of Milano, Italy
[3]Physics Department University of Modena, Italy

INTRODUCTION

Saccharomyces cerevisiae yeast cells were studied from the point of view of their metabolic activity related to radiation damage produced by soft X-rays. Oscillatory effects in CO_2 production, related to fermentation, were measured under different conditions and for different chiral nutrients. Calculations of soft X-rays (0.9keV) penetration depth suggest that radiation damage does not significantly affect the inner parts of the cell, but only the structures of the wall-membrane-cytoplasm configuration.

THE RADIATION SOURCE

Trying to minimise DNA X-rays induced damage which takes place inside the nucleus we choose soft X-rays, produced by CLF, instead and assuming that cellular biological material attenuates X-rays following the Bouguet-Beer law the suitable procedure consist of making use of X-rays with photon energies hv between 530eV and 1keV. Here the decay exponent which is very large while, for instance, we recall that X-rays with hv≈1.2keV are allowed to travel 5μm of biological material and hence can penetrate to the cell nucleus. On the other side also X-Rays in the "Water Window" region (below 530eV) should be avoided giving a low attenuation coefficient. In our experiment soft X-rays in the selected energy range have been produced by shooting a thin teflon (CF_2) stripe target (100micron thickness). Both atomic components of Teflon are ionised to He- and H-like ions and emit respectively in the energy range 304 to 490eV and 731 to 1103 eV. Carbon emission in the water window is then removed by a sequence of Al, mylar and hostaphan filters positioned before the cell sample. Their role is to cut off unwanted portion of the X-rays spectrum together with the UV light from the excimer laser. A low flow of He gas at 1atm of pressure is relevant to reduce effects of debris production consequent to the laser-target interaction [1].

DOSIMETRY

We were interested in the generation of autonomous information on structural cellular parameters since in literature there are conflicting opinion about wall thickness [2] and we needed precise information for the characterisations of the cells to determine the strain we were working with:*Saccharomyces cerevisiae Hansen.* Cells have then been analysed with: optical microscopy, SEM microscopy, TEM microscopy, soft X-ray contact microscopy, Coulter Counter. Typical measured sizes are:

Average radius	3 - 4 micron
Membrane thickness	≈0.2 micron
Nucleus radius	≈1 micron

These parameters are fundamental in order to determine the amount of energy deposited by X-rays.

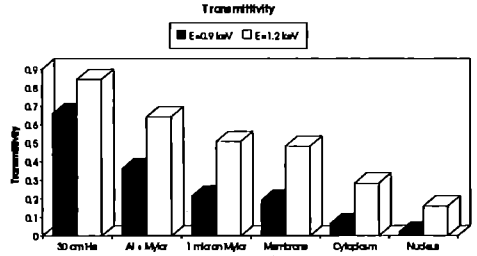

Fig.1

We calculated the doses absorbed by each of the main cell "compartments" of the cell (membrane, cytoplasm and nucleus) unlike most of the work done in X-ray dosimetry [3], in the case of yeast cells, where average density and absorption coefficients are assured. This gives a deeper insight into the cell activity that can be damaged. In fig.1 the attenuation histogram of soft X-rays (0.9keV) is presented.

It is possible to estimate the dose that is deposited in a cell portion by considering the infinitesimal energy dE absorbed between x and x+dx, integrated on the thickness, and dividing it by the mass. The doses are measured by a pin diode with by the same filters of the biological sample to give a one to one correspondence with the actual dose delivered.

PREPARATION OF BIOLOGICAL SAMPLES

The biological target is made of yeast cells (*Saccharomyces cerevisiae*). The cells are commercial dry ones that are hydrated about half a hour before the irradiation procedure. A suspension ($2x10^7$cells/ml is the typical concentration) is obtained by adding deionized water. Then the suspension is filtered in a Venturi tube and the cells are deposited on a paper filter to form a monolayer. After a short period for drying the filters, they are deposited onto a hostaphan film so that yeast cells were hosted in a sandwich made of hostaphan from one side and paper filter on the other. The sandwiches are then deposited into an automatic handling robot that is mutuated by [4] (the hostaphan film facing the X-ray source) and the X-ray dose could be delivered. The thickness of the hostaphan filter (whose composition is analogous to mylar) was 1 micron. After irradiation filters are deposed in sealed bottles with the different nutrients and deionized water, so the measurement of the pressure can start. Different behaviours were observed even in the very simple configuration mode of yeast suspension in nutrient media of different type. The presence of the phosphate buffer is avoided in order to directly link biological performances to energetic-enzymatic dynamics.

THE EXPERIMENT

The investigation is based on the measurement of pressure changes in sealed bottles where CO_2 production can be monitored as a consequence of glycolysis.

Detailed involved processes are complex and they are linked to O_2 consumption, to enzymatic activities, due to the presence of different nutrient sugars, and to the appearance of oscillations, with different periods. Intermediate investigations aims at:

1.Optimisation of the biological target and its support

2.CO_2 production on line noninvasive follow up in aerobic and nonaerobic regimes in cell cultures fed with glucose yaken as controls.

3.CO_2 production follow up in aerobic and non aerobic regimes in cell cultures fed with glucose irradiated at different doses and dose rates (with "normal" teflon target).

4.CO_2 production follow up in aerobic and non aerobic regimes in cell cultures fed with αD-glucose, L-glucose, and L- and D-mannose in absence of irradiation.

5.CO_2 production follow up in aerobic and non aerobic regimes in cell cultures fed with αD-glucose, L-glucose, and L- and D-mannose, irradiated at different doses and dose rates.

6.Morphological analysis of the samples before and after irradiation (microscope, SEM, TEM and X-ray Microscope)

7.The technique gives information on the autorecovery of the cell system in particular in the time lapse between 0-400s and seems very promising. A hypothesis is that mixing irradiated cells with cells from a fresh non irradiated culture cooperative effects can rise in the cell population.

PERFORMANCES AND RESULTS

Here we summarise the major achievements: 1 The system allows both short term long term measurements: we acquired data starting from a few minutes after irradiation up to 72 hours with high sensitivity.

2.A reasonable statistical analysis can be performed; actually we have commonly used the 16 channels available in the D/A card.

Statistically evidence has been obtained of:

•Monotonic increase of pressure as function of time [5].

•Nonmonotonic response of the monitored parameter to the dose (fig.2)

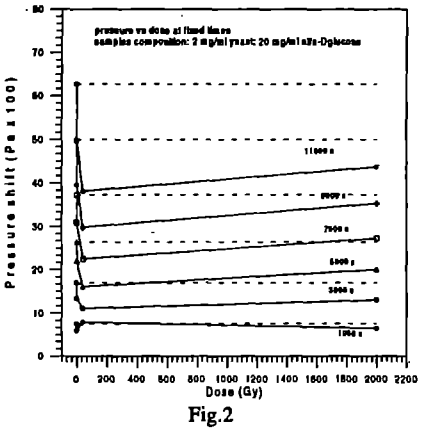

Fig.2

•Later on Delayed Luminescence analysis [6] has been performed on the same samples sharing a monotonic response to the dose: this confirm thus proving the high sensitivity exhibited by the response of CO_2 production to inner dynamics in yeast cells.

3.The analysis of the produced gas (responsible for pressure increase) can be performed by mass spectrometry. The identification of the output gases can be performed by incubating yeast cells in a suitable conditioned atmosphere (Argon) and then following their metabolic activity. The fig3 shows the difference in gas composition after 12 hrs: it is easy to identify the presence of produced CO_2 (mass no 44).

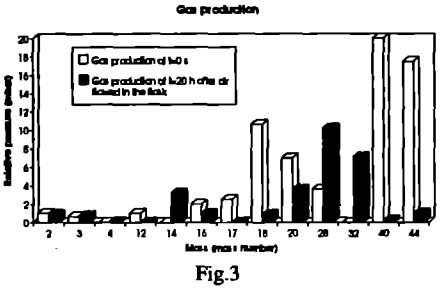

Fig.3

•Slowing down and change of the sign of derivative as shown in Fig4 for the case of yeast with a αD-glucose as nutrient. Follow up lasted 14 hours.

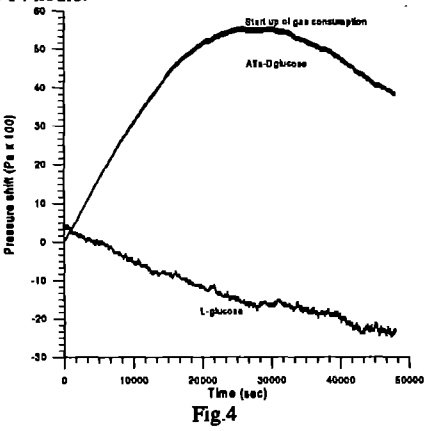

Fig.4

4.We could evaluate the role of sugar metabolic activity consequently monitored by the pressure changes. Actually it can be noted that sugars of different chirality show significant differences in gas production. The use of L-sugar leads to pressure reduction inside the bottles, that means changes in the sign of the pressure. Changes in the sign of the relative pressure is also observed in sample with D-sugar after 14 hours of observation as shown in fig4.

•Recovery mechanism is shown by the trend of the gas production.

•Oscillations on the range of 1 minute (see fig5). This parameter gives information that allows to discriminate between irradiated and nonirradiated samples, and different chiral nutrients and gives adue to the identification of different enzymatic cycles at work.

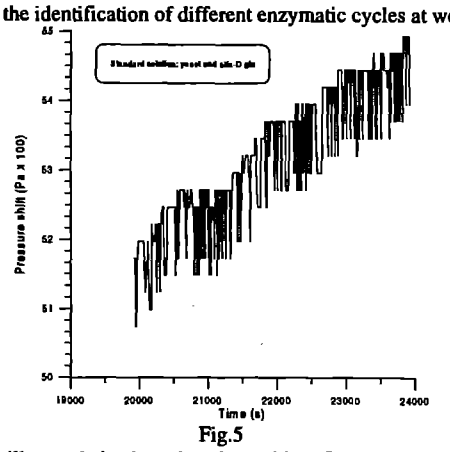

Fig.5

The oscillatory behaviour has been identified through Fourier analysis; in particular some data were previously filtered using FIR filters and neural networks. Results are shown in fig.6.

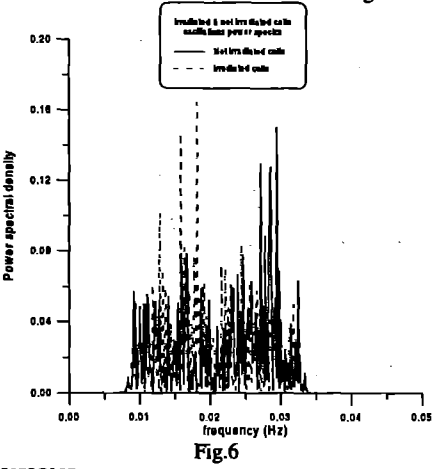

Fig.6

CONCLUSIONS

We have presented a new technique in yeast biophysics experiment which is based on irradiation of yeast cells with soft X-rays and measurement of CO_2 production with semiconductor pressure detectors. The use of soft X-rays produce relative damaging, in particular to wall and membrane. Hence it seriously affected anaerobic processes leaving aerobic respiratory processes, active at mitochondrial level, practically unaltered. The technique seems to be capable to provide a powerful and very sensitive insight into the regulatory processes at the cellular level: the cooperation aspects that can be at work in cell suspension and the mechanisms responsible for yeast photosensitivity.

This procedure has proven to be a useful tool for elucidating enzymatic dynamic properties of glycolysis and fermentation in yeasts, in particular the cyclic aspects of the glycolytic loop (for whole cell population and not only for single cells.)

REFERENCES

[1]IC Turcu et al., SPIE, 2015, 1993.

[2]R Hoelzel, I Lamprecht, Biochim Biophy Acta, 1104, 195, 1992

[3]D Frankenberg, D T Goodhead,M Frankenberg-Schwager, R Harbich, D ance, R E Wilkinson, Int J Radiat Biol, 50 727, 1986

[4]ICE Turcu, GJ Tallents, IN Ross, D Batani, RA Meldrum, Physica Medica, 10, N3, July-Sept 1994.

[5]IC Turcu, M Milani, D Batani et al, Laser & Tech, 1996

[6]F Musumeci, A Triglia, F Grasso, A Scondino, D Sotko, Nuovo Cimento D, 16,1994

THE SEPARATION OF SPATIAL AND TEMPORAL EFFECTS OF HIGH LET RADIATION

D.L Stevens, S.J. Marsden, M.A Hill, ICE Turcu*, R Allott*

Radiation and Genome Stability Unit, MRC Harwell, OXON, OX11 0RD
*Rutherford Appleton Laboratory, Chilton, Didcot, OXON OX110QX

INTRODUCTION

The time allocation in Period I April 1995 was used to study the effect of hypoxia on survival of V79 cells irradiated with very short (≈10 ps) 1.2 keV ultra-soft x-ray pulses. The effect of lack of oxygen on cell survival differs between high LET (alpha-particles, neutrons, etc.) and low LET (hard x-ray, gamma rays, etc) irradiations making it a relevant biological end point to study.

The question that this research aims to answer is are radiobiological differences between high and low LET radiations. due to spatial or temporal differences?

Alpha-particles (high-LET) traverse mammalian cells at time scales on the order of picoseconds, depositing a dose of the order of 0.2 Gy in a linear heavily ionising track. With the High Brightness Picosecond X-ray Source a dose equivalent to one alpha-particle per cell can be given in approximately 10 ps

Low LET radiations deposit small doses (of the order of mGy) per event, distributed over the whole cell. So irradiations of doses equivalent to those received form high LET particles by other low LET sources take times where chemical and biochemical/biological processes are already occurring[1].

So this source is unique in that it can irradiate samples with the usual spatial aspects of low-LET radiations but in a time period approaching that of high-LET radiations. If, surprisingly, biological differences dependent on LET were found to be due to the differing time scales of energy deposition, rather than spatial differences, it would radically alter our understanding of the mechanisms of radiation action and have implications for practical problems including radiotherapy[2].

RESULTS AND DISCUSSION

Three survival experiment were carried out on V79 cells under normal (air with 5% CO_2) gassing conditions, and four under hypoxic conditions where the oxygen levels in cells, surrounding biological medium and gas flowing in sealed biological dishes was minimised by flowing 5%CO_2 in nitrogen through dishes. The irradiation assembly as used by R Meldrum et al[3] was adapted to hold our sealed irradiation dishes and to allow gassing to take place whilst over the irradiation chamber.

The data obtained suggest that there is an oxygen enhancement ratio of about 2.5 (fig below). This value is comparable with data from our laboratory for 1.5 keV ultra-soft X-rays delivered over minutes from a continuous cold cathode source $(2.0 \pm 0.1)^2$ (An OER of 1 is obtained for high LET radiation.) These results suggest that it is the spatial distribution of energy deposition rather than any temporal aspects of any radiation that distinguish between high and low LET radiation characteristics.

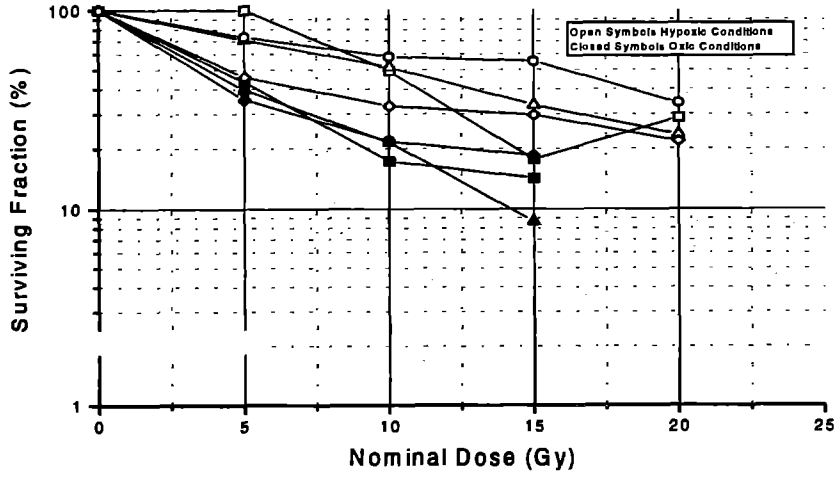

REFERENCES

1. P O'Neill, E M Fielden
Molecular aspects of DNA damage and its modification,
In "Radiation Carcinogenesis and DNA Alterations"
Editors F J Burns et al, Plenum Press, N.Y.

2. D T Goodhead.
Spatial and temporal distribution of energy
Health Physics, Vol.55, No2, (August), pp231-240, 1988

3. R A Meldrum, J Edgerton, W Meaking, C W Wharton, A Damerell.
The kinetics and mechanism of the repair of soft x-ray damage in mammalian cellular DNA.
SERC Central Laser Facility, Annual Report 1992 pp 200-201.

INTRACELLULAR FLUORESCENCE LIFETIME IMAGING OF DISULPHONATED ALUMINIUM PHTHALOCYANINE

A.D. Scully[1,4], A.J. MacRobert[2], S. Botchway[3], P. O'Neill[3], A.W. Parker[1], R.B. Ostler[4] and D. Phillips[4]

[1]LSF, Rutherford Appleton Laboratory
[2]National Laser Medical Centre, UCL Medical School
[3]MRC Radiobiology Unit
[4]Department of Chemistry, Imperial College of Science, Technology and Medicine

INTRODUCTION

One of the most rapidly developing areas in the field of photomedicine over the past ten years has been the exploration of the use of light-activated molecules, known as photosensitisers, in the selective destruction of malignant tumours [1]. The photosensitisers are retained preferentially in the malignant tumour cells and upon irradiation with red light (600-800 nm) generate cytotoxic species, such as singlet oxygen, which are believed to react with and destroy local tissue [1]. This treatment, called Photodynamic Therapy (PDT) is currently undergoing clinical trials. Among the most promising photosensitisers for PDT is disulphonated aluminium phthalocyanine (AlSPc), which has been studied extensively over the last five years [2].

A knowledge of the distribution of sensitisers in cells and tissues is essential for improvement in understanding of the photosensitisation mechanism and the determination of optimal treatment times and dosimetry. The intrinsic fluorescence from AlSPc provides a convenient means of probing its intracellular localisation. Investigations of the intracellular localisation of sensitisers using steady-state fluorescence imaging microscopy have relied on the assumption that the distribution of fluorescence intensity provides an accurate representation of the distribution and actual intracellular concentration of the sensitiser. However, the intensity of fluorescence from fluorophores is often found to be a function of the nature of its local environment. Chemical and physical properties of the environment such as polarity, pH, oxygen concentration and interactions between the fluorophore and specific ionic species can have a pronounced effect on the intrinsic fluorescence decay time of the fluorophore, and this in turn affects the intensity of the steady-state fluorescence emission. Furthermore, aggregation of a fluorescent sensitiser may result in the formation of a species that has significantly different fluorescent properties to the monomer [3]. It is not possible to account for these effects using steady-state fluorescence imaging microscopy.

Fluorescence lifetime imaging microscopy provides a solution to these problems. The main feature of fluorescence lifetime measurements is that lifetimes are usually independent of probe concentration, photobleaching and other artifacts affecting fluorescence intensity measurements. Time-resolved fluorescence detection can thus be used to determine fluorescence lifetime maps which are necessary for the determination of the true spatial distribution of a probe molecule. Moreover, it can enhance contrast between the fluorescence arising from distributions of different probe species with similar spectral characteristics and provides a means of discriminating against background autofluorescence.

In this work we report on the development of a fluorescence microscope having sub-nanosecond time resolution imaging capabilities. This is achieved through the use of a detector that is capable of greater than an order of magnitude shorter gate duration than detectors used in other comparable apparatus reported to date. Results obtained using this system for the measurement of the intracellular distribution of AlSPc in V79-4 mammalian cells are presented. These results are believed to constitute the first reported [4] sub-nanosecond gated fluorescence microscope images and open the way for higher precision measurements of intracellular phenomena using fluorescent probes.

FLUORESCENCE MICROSCOPE

The excitation source consists of a cavity dumped dye laser (Spectra Physics, model 3500) that is pumped synchronously by a mode-locked Nd^{3+}/YAG laser (Spectron, model SL901). The duration of the dye laser pulses is approximately 10 ps. The excitation wavelength used in this work was 610 nm and the dye laser pulse repetition rate was 0.8 kHz. The dye laser pulses were directed to the port of an inverted microscope (Olympus, IMT-2) using a 1 mm diameter PMMA fibre optic cable (Toray), the output of which was magnified and imaged in the back focal plane of the microscope objective lens. The microscope was fitted with a dichroic mirror (Omega Optical, 670DRLP02) and a long-pass filter (Schott, RG665).

The detector is comprised of an 18 mm diameter gated optical image intensifier (GOI) (Kentech Instruments, Didcot, U.K.) capable of gate durations ranging from ~120 ps to ~1 ns, and a luminous gain of $\sim 10^3$ in a single-stage microchannel plate. Further details of this device have been published previously [29]. A pulse/delay generator (Farnell) was used to supply an appropriate trigger signal to the GOI high voltage pulser unit. This signal was routed *via* a switchable cable delay unit that was built in-house and which is capable of introducing minimum incremental delays of 0.5 ns into the timing of the GOI trigger pulse. The phosphor output is coupled using a f/0.85 camera lens (Fujinon, CF25L) to the chip of an 8-bit scientific grade CCD camera (Cohu, 4910) capable of on-chip integration times of tens of seconds at room temperature. Camera control is performed using a commercial framegrabber package (Oxford Framestore Applications). All images presented here were measured using a Nikon 60X oil immersion (NA 1.4) microscope objective and represent a field area of 110 x 82.5 μm.

RESULTS AND DISCUSSION

A steady-state fluorescence intensity image of V79-4 cells is shown in Figure 1.

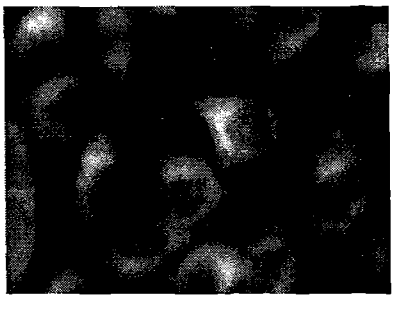

Figure 1. Fluorescence intensity image of V79-4 Chinese Hamster lung fibroblasts stained with AlSPc

The cellular uptake of the sensitiser is seen clearly in this figure, with significantly higher fluorescence intensity observed in the perinuclear regions than in the nucleus. A similar pattern of inhomogeneous intracellular spatial distribution of fluorescence intensity was reported recently [2] for leukaemic K562 cells. It has been proposed that AlSPc selectively partitions into lysosomal membranes, mitochondria and the Golgi apparatus. However, fluorescence intensity images alone are insufficient for the discrimination between the effects of inhomogeneous sensitiser localisation and localised quenching on the overall fluorescence intensity map. Time-resolved fluorescence imaging is required in order to distinguish between these two effects.

Figure 2 shows four sequential sub-nanosecond time-gated images of the same cells shown in Fig. 1, the fluorescence intensities having been scaled so as to fill the available grey levels.

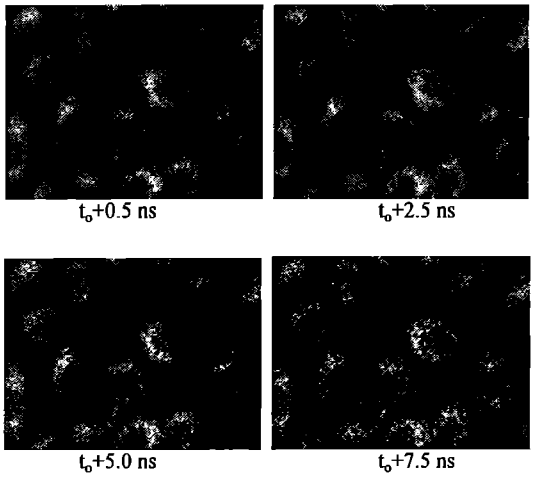

Figure 2. Gated fluorescence images of the cells shown in Fig.1 measured using a gate width of 0.5 ns.

The spatial distribution of fluorescence intensity remains unchanged up to 7.5 ns after excitation and is essentially identical to that observed in the steady-state fluorescence intensity image shown in Fig. 1. The independence of the fluorescence lifetime of AlSPc on intracellular distribution can be inferred from these results. This is borne out by the lack of any corresponding spatial variation in fluorescence lifetime, as illustrated in the fluorescence lifetime map shown in Fig. 3.

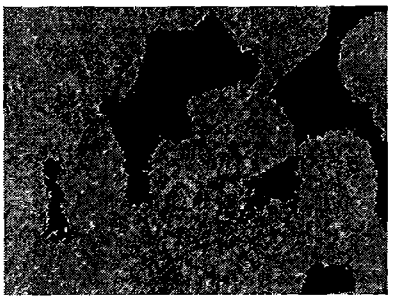

Figure 3. Fluorescence lifetime map of the cells shown in Fig.1.

Therefore, the spatial distribution observed in the steady-state fluorescence image in Fig. 1 is attributed to a genuine distribution of AlSPc concentration within the cells. The intracellular fluorescence lifetime of ~ 4.5 ns obtained in this work for AlSPc in V79-4 cells is similar to values reported [2] for this molecule in PBS buffer solution.

The time resolution of time-gated fluorescence measurements is limited by the jitter in timing of the triggering of the GOI, which is made up of contributions principally derived from the electronics in the GOI high voltage pulser unit and the pulse/delay generator. The peak-to-peak jitter of the intensifier used in the apparatus described in the present work is $\leq$ 40 ps, and the combined jitter of the cavity dumper sync out and pulse/delay generator signal is estimated to be ~ 400 ps. However, with the use of a low-jitter digital pulse/delay generator (Kentech Instruments), acquired since the measurements reported here were made, the latter value has now been reduced to < 100 ps. This places an upper limit of approximately 140 ps on the total peak-to-peak jitter associated with the timing of any image. Consequently, this apparatus has the potential to measure with acceptable precision apparent fluorescence lifetimes that are significantly shorter than 1 ns, and to detect the presence of multi-exponential fluorescence decay behaviour.

Multi-exponential functions are usually used for the analysis of the complex, non-exponential fluorescence decay profiles often obtained for fluorescence probes in biological systems [2,5]. Furthermore, most measurements of multi-exponential fluorescence decay profiles using TCSPC are performed on a single-point basis and so generally only offer site-specific information. The detection of multi-exponential fluorescence decay characteristics is not a requisite for the determination of intracellular perturbations on the fluorescence lifetime of a fluorescence probe, and in many cases it is sufficient to monitor variations in the *apparent* intracellular lifetime through the use of a fluorescence lifetime map. However, such information is necessary for a distinction to be made between effects such as quenching of the excited-state and the presence of contributions by multiple fluorescent components. One approach to the problem of detection of these more subtle effects on the fluorescence decay characteristics from gated fluorescence images involves the measurement of time-gated images at several times along the fluorescence decay profile. This requires the use of gate durations that are short on the timescale of the fluorescence decay to be measured and minimal jitter in the timing of the gates. Non-linear least-squares analysis of the integrated intensities measured at each pixel and delay time will yield values for the two lifetimes at each pixel. Deviations from exponential decay behaviour should be detectable using this approach, provided a sufficiently large number of channels are collected and an adequate signal to noise ratio is attainable. The very short gate durations and low jitter associated with the intensifier used in the apparatus described here makes this system ideally suited to such measurements and this is one aspect of further development to the apparatus that is currently being pursued.

REFERENCES

1. R. Bonnett Chem. Soc. Rev. 24, 19 (1995).
2. M. Ambroz, A.J. MacRobert, J. Morgan, G. Rumbles, D. Phillips J. Photochem. Photobiol. B:Biol. 22, 105 (1994).
3. L.E. Bennett, K.P. Ghiggino, R.W. Henderson J. Photochem. Photobiol. B:Biol. 3, 81 (1989).
4. A.D. Scully, A.J. MacRobert, S. Botchway, P. O'Neill, A.W. Parker, R.B. Ostler, D. Phillips, J. Fluorescence (submitted for publication).
5. S. Hirayama (1992) in J.F. Rabek (Ed.), *Progress in Photochemistry and Photophysics Voume 6*, CRC Press, Florida, pp. 1-42.

PHOTOLUMINESCENCE FROM HIGHLY EXCITED CDTE/CDMNTE MULTIPLE QUANTUM WELLS

N. Cain, M. O' Neill, J.E. Nicholls, T. Stirner, W.E. Hagston, and D.E. Ashenford[1)]

Departments of Applied Physics and Engineering Design and Manufacture[1)]
The University of Hull

The optical nonlinear effects of bandfilling and bandgap renormalisation were studied by means of photoluminescence (PL) of highly excited CdTe/CdMnTe quantum wells. We find that excitons survive with little change in energy to carrier densities > 10^{12} cm^{-2}. This is in contrast to earlier experiments carried out on GaAs/AlGaAs[1] and CdTe/CdMnTe[2] quantum wells which are interpreted in terms of free electron-hole recombination. The samples were excited at 7 K by pulses from a 10 ns Nd^{3+}:YAG-pumped dye laser at 630 nm. Mesas of 100 µm diameter were etched into the material to ensure uniform excitation

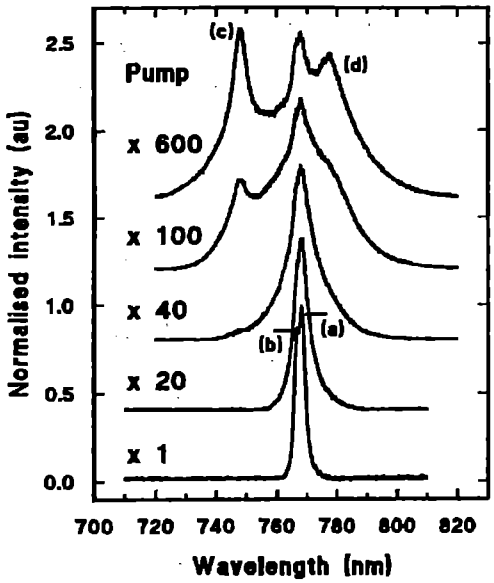

Figure 1 Power dependent PL spectra from sample one. The pump power is given in multiples of 16 kW cm^{-2}.

Figure one shows the PL from sample one as a function of the excitation power. As the pump power increases, the emission spectra broaden because of phase-space filling of the conduction and valence bands. Many sharp peaks are observed which are identified as follows. For the lowest pump power of 16 kW cm^{-2}, the free electron 1-hole 1 (e1-h1) exciton transition is observed as a shoulder (b) to the main peak (a) which is identified as a biexciton since it grows superlinearly with excitation power and has the predicted binding energy of 3 meV. For the highest pump power, two more peaks (c) and (d) are clearly observed. Comparisons with the PL spectra of thin CdTe layers suggest that the low energy broad peak (d) originates from the CdTe buffer layer. The intense high energy peak (c) is observed in all of the investigated samples and in each case originates at the wavelength of the e1-h3 transition as shown in the photoluminescence excitation spectra. A lineshape analysis of PL spectra including excitonic and free electron-hole recombination was made to estimate the photoexcited carrier density and temperature. The exciton recombination was modelled using Lorentzian lineshapes and the free electron-hole PL was analysed by means of Fermi-Dirac statistics. Carrier densities > 10^{12} cm^{-2} and temperatures of ≈ 100K were found for the highest excitation conditions. Using the Thomas-Fermi approximation, the effect of three dimensional screening on the exciton binding energy was calculated. The results suggest that the exciton binding energy decreases with carrier density and, at the highest densities used in the experiment, the Mott transition is reached with the exciton resonance disappearing into the continuum. More complete many-body calculations, incorporating bandfilling and quasi-two-dimensional Coulombic and exchange screening, support these conclusions[3)]. However, in the experiment, the exciton transitions are retained and do not shift significantly in energy with carrier density. We believe that the reduced screening results mainly from biexciton formation. The effect of Auger recombination is also being considered.

When the sample is highly excited, the integrated intensity ratio of the forbidden e1-h3 and allowed e1-h1 exciton resonances is 1.4:1 This compares with relative strengths of 1:18 observed in photoluminescence excitation at low excitation densities and in agreement with calculations. Figure 2 shows how the PL intensity integrated over the full spectrum as well as the e1-h1 and e1-h3 excitonic components vary The total PL shows a sublinear increase with excitation power indicating some nonradiative recombination. For pump powers greater than 10^{-3} the e1-h1 exciton transition saturates while the strength of the e1-h3 exciton increases superlinearly with power. The saturation of the e1-h1 transition is surprising since phase space filling is expected to increase the probability of PL. The influence of carrier collisions on the decrease of oscillator strength is being considered. The superlinear increase of the e1-h3 transition with power is not necessarily an indication of stimulated emission Such a mechanism requires a superlinear increase of PL with carrier density which does not increase linearly with pump power.

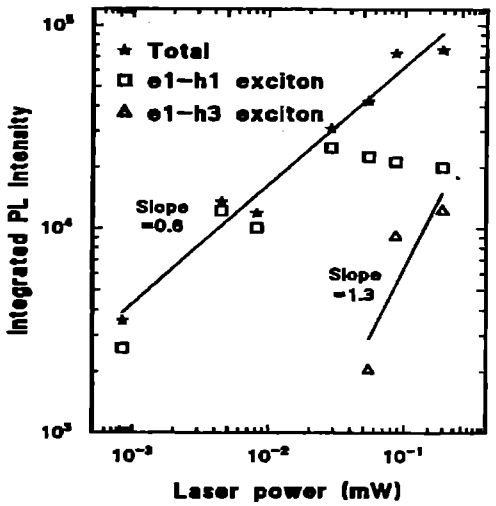

Figure 2 Pump power dependence of total PL intensity and e1-h1 and e1-h3 excitonic contributions

In conclusion, excitonic transitions are observed at carrier densities above the expected Mott transition. The e1-h1 exciton saturates at high densities but the transition does not shift in wavelength as expected.

REFERENCES

1, E Lach, A Forchel, DA Broido, TL Reinecke, G Weimann and W Sclapp, Phys. Rev. B 42 5395 (1990)

2 G Bacher, F Daiminger, A Forchel, A Waag, Th Litz and G Landwehr, J. Cryst. Growth 138 856 (1994)

3 S Nojima, Phys. Rev. B 51 11124 (1995)

ULTRA-VIOLET EXCITONIC LASING IN CdZnS/ZnS MULTIPLE QUANTUM WELLS

K.B. Ozanyan, J.E. Nicholls, M. O' Neill, L. May, J.H.C. Hogg, W.E. Hagston, B. Lunn[1] and D.E. Ashenford[1]

Departments of Applied Physics and Engineering Design and Manufacture[1], University of Hull

INTRODUCTION

UV lasing in ZnS/ZnCdS QW structures grown on GaAs by the MOCVD technique has been demonstrated by Yamada et al. under the conditions of optical pumping[1] and current injection[2]. In these works the gain mechanism involved has been discussed mainly in the light of phase-space filling in the low-energy side of an inhomogeneously broadened exciton resonance in analogy with a convincing work on ZnSe-based structures[3]. In our current work we supply spectroscopic data as evidence for the excitonic lasing mechanism from low Cd-composition ($0.03 \le x \le 0.20$) QW structures grown on GaP by MBE under the conditions of optical excitation. In the case of the lowest Cd-composition we observe lasing at wavelengths as low as 333 nm at 8K, which, to our knowledge, is the shortest lasing wavelength yet reported in a semiconductor heterostructure.

EXPERIMENT

Multilayer stacks, nominally composed of a 500 nm thick ZnS buffer and 50 ZnCdS/ZnS (4nm/8nm) periods, were grown on (001) GaP by MBE from 6N elemental Zn and Cd sources and ultra-pure S (Asahi) contained in a valved cracker (EPI). Laser structures were formed by cleaving 5 mm wide stripes of the wafer into resonators with a cavity length of 1 mm. The structures, with uncoated mirror facets, were carefully mounted on the cold finger of a variable temperature continuous-flow cryostat (Oxford Instruments). They were pumped with UV pulses obtained by frequency doubling the pulses from a tunable dye laser (Quanta-Ray PDL-2) pumped with the frequency-doubled output (532 nm) of a Q-switched Nd-YAG laser (Spectron SL805G). At the maximum gain of the DCM dye used, the system delivered 1 mJ, 6 ns pulses in the UV. The power incident on the sample was controlled by a set of neutral density filters calibrated in the UV. The photoemission from the sample either in front-face or in edge configuration was focused on a monochromator, equipped with a GaAs photomultiplier tube.

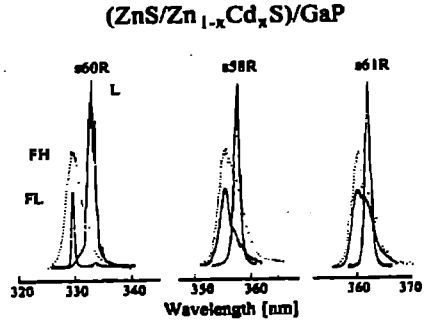

Figure 1 Emissions from laser structures at 8 K. L - stimulated emission, FH - front-face emission at threshold, FL front face PL with low energy excitation

RESULTS AND DISCUSSION

Fig. 1 shows the low-temperature lasing spectra from structures with three different quantum-well depths, with Cd compositions of 0.03 (s60R), 0.18 (s58R) and 0.20 (s61R). Lasing in the structure with the lowest Cd-composition, resulting in the shortest stimulated emission wavelength, 333nm (at 8K), was observed up to temperatures as high as 80 K, while the deeper-well samples lased at 300 K, as shown below. The laser emission is red-shifted with respect to the PL emissions taken in front-face geometry. The PL bands under high-power pulsed excitation conditions continuously evolve from those taken under low-power CW conditions, as evidenced by additional spectra taken at intermediate densities.

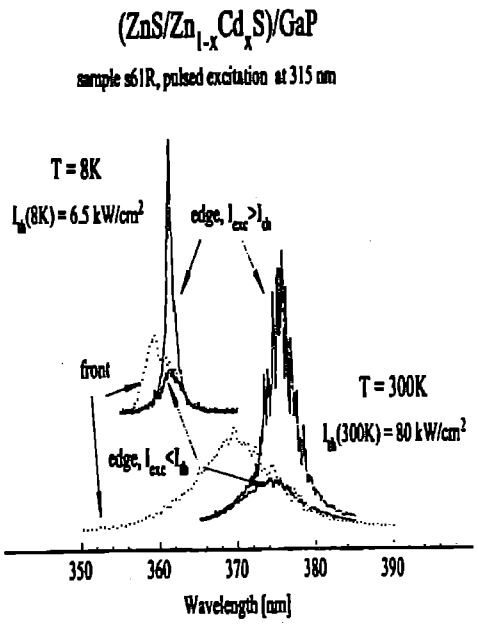

Figure 2 Emission from sample s61R at 8K and 300K

Fig. 2 shows the emission from the lasers at 8K and 300K with Cd composition 0.20. In addition to the spontaneous emission (taken in front-face geometry), the edge emission is also shown, at pumping below as well as above the lasing thresholds. The latter is measured as the bending point of the plot of the integrated near-bandgap emission against the excitation density. The thresholds are measured as 80 kW cm^{-2} and 6.5 kW cm^{-2} at temperatures of 300K and 8K respectively. Lasing shown in the first two figures was achieved by excitation at 315 nm which corresponds to a photon energy larger than the bandgap of the ZnS barriers. The spontaneous emission spectra in front-face geometry were taken with pumping close to the lasing threshold.

Fig. 3 shows the low temperature stimulated emission excitation (SEE) spectrum of sample s61R across the barrier bandgap region. The experimental points were calculated, for each pump photon energy by integrating the recorded stimulated emission band, and joined by spline interpolation as a guide to the eye. The increasing errors at the lowest energies result from the falling pump laser intensity. The energy positions of the free exciton (FX) and the bandgap (Eg) of unstrained ZnS are shown with arrows.

Barrier excitons have been reported to be prominent in the SEE spectra of ZnSe-based lasers with excitonic gain[4]. Fig 3 shows that this applies to ZnS/ZnCdS as well. Analysis of relative heights is however hindered by the fact that they depend on mediatory processes like trapping, as well as on the spectral dependence of the absorption coefficient. However ambipolar diffusion lengths up to 0.2 μm have been observed in other II-VI materials[5], so vertical diffusion in our structure would also tend to suppress the effect of different excitation depths at the two energies. Although the SEE data strongly emphasises the role of the excitons in the lasing process, further evidence is needed to reveal the particular gain mechanism.

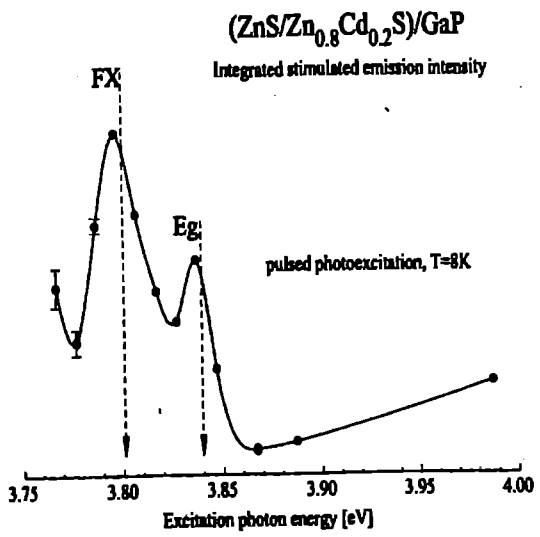

Figure 3 SEE spectrum of sample S61

The low-excitation PLE from the structures (FL in fig. 1) can be interpreted in the following way. Excitonic PL from bulk $Zn_{1-x}Cd_xS$ in the range $0 \le x \le 0.17$ has been calibrated with Cd-composition data obtained by Rutherford Backscattering Spectroscopy. Accounting for the exciton binding energy at x=0 (ZnS) and its expected change with x, we use

$$E_{g_{ZnCdS}} = 3.839 - 2.139 \cdot x \quad [eV]$$

for the bandgap in the composition range $0 \le x \le 0.2$. The above linear dependence in this range agrees with the parabolic dependence derived from (e-A^0) PL in $Zn_{1-x}Cd_xS$ by Yokogawa et al.[7] over the whole range of compositions to account for the bowing at x>0.2 The values from eq.(1) are additionally corrected for the strain shifts in the QW structure. Using the band offset value Q_c=0.84[7], simple calculations for Cd-compositions x=0.03, 0.18 and 0.20, in agreement with the data from DCXRD and Auger Electron Spectroscopy, yield for all three samples bandgap energies about 48-55 meV higher than that experimentally determined from the PL peaks. This is in full agreement with the expected depth of the excitons in a 4 nm $Zn_{1-x}Cd_xS$ ($0 \le x \le 0.2$) QW. Therefore we find enough evidence to attribute the most prominent PL peaks, labelled FL in fig. 1, to excitonic transitions in the QWs in all three samples. The broadening of the FL emissions towards higher Cd-composition can be fully accounted for by alloy broadening effects. At higher excitation (FH in fig. 1) we observe homogeneous broadening that convoluted with the FL bands results in the observed spectral shapes. Carrier-carrier scattering increases with the excitation density and at room temperature the linewidths are mainly homogeneously broadened.

Thus we observe the lasing transitions (L in fig. 1.) occurring at the low-energy side of bands that evolve without spectral shifts from excitonic transitions in the QWs. However, to assign the lasing to a particular excitonic gain mechanism it is necessary to account for possible spectral shifts induced by the edge geometry and multiple passes in the resonator[3]. Indeed, fig. 2 shows that the spontaneous edge emission is red-shifted with respect to the front-face PL, probably because of self-absorption. The observation of primary importance, however, is that at low threshold values (< 10 kW cm^{-2}) the lasing emerges just on top of the spontaneous emission band, ruling out exciton-LO phonon as well as exciton-exciton processes as possible suppliers of gain. Departures from this occur when the carrier confinement deteriorates (in shallower wells or at higher temperature) and the thresholds rise. The laser line shifts gradually towards lower energies and is more than 46 meV away from the spontaneous emission if the threshold exceeds 250 kW cm^{-2}.

The critical carrier density for the transition to an electron-hole plasma[7], given by $\pi^{-1}a_B^{-2}$, was estimated to be 3 x 10^{13} cm^{-2}. Although comparisons are aggravated by uncertainties in the value of the dielectric function, needed to convert the observed exciton binding energy into an appropriate value for the exciton Bohr radius a_B, we find that the critical density may be obtained for pump powers greater than 100 kW cm^{-2}. Also, even below the critical density free carriers may contribute to optical gain when the homogeneous broadening (observed in front-face geometry) exceeds the exciton binding energy. Indeed, as shown in fig. 2, a red-shift is observable already at 80 kW cm^{-2}

In conclusion, we demonstrate, for the first time, stimulated emission at 300K from ZnS/ZnCdS QW structures grown on (100) GaP substrates by MBE. In QW structures with the lowest Cd-composition, optically pumped lasing at wavelengths as low as 333 nm (at 8K) is observed. We present spectroscopic evidence for the excitonic nature of the low-excitation PL, front-face PL close to the threshold, spontaneous edge emission and lasing, which suggests that the stimulated emission involves states in the low-energy tail of an inhomogeneously broadened excitonic resonance. However, while lasing is excitonic at low thresholds, EHP transition is possible if the pump power approaches 100 kW cm^{-2}. Further optimisation of the structures with respect to optical confinement may bring the room temperature threshold value for reasonably shallow QWs well below that figure.

REFERENCES:

1 Y.Yamada, Y.Masumoto J.T.Mullins and T.Taguchi Appl. Phys. Lett. **61**, 2190 (1992).

2 T.Taguchi, C.Onodera, Y.Yamada and Y.Masumoto, Jpn.J.Appl. Phys, **32** L1308 (1993).

3 J.Ding, M.Hagerott, T.Ishihara, H.Jeon and A.V.Nurmikko Phys.Rev.B **47**, 10528 (1993).

4 Y.Kawakami, B.C.Cavenett, K.Ichino, S.Fujita and S.Fujita, Jpn.J. Appl.Phys, **32** L730 (1993).

5 P.Chen, J.E.Nicholls, M.O'Neill, J.H.C.Hogg, W.E.Hagston, B.Lunn and D.E.Ashenford, accepted for publication in J.Crystal Growth.

6 T.Yokogawa, T.Ishikawa, J.L.Merz and T.Taguchi, J.Appl.Phys. **75**, 2189 (1994).

7 S.Schmitt-Rink, D.S.Chemla and D.A.B.Miller, Adv.Phys. **38**, 89 (1989).

THE DYNAMICS OF MULTIPHOTON IONISATION AND DISSOCIATION OF DIATOMIC MOLECULES, STUDIED BY SHAPING OF FEMTOSECOND LASER PULSES

A J Giles[1], M R Thompson[1], J H Posthumus[1], L J Frasinski[1], K Codling[1], A J Langley[2] and W Shaikh[2]

[1]J J Thomson Physical Laboratory, University of Reading, Whiteknights, Reading, RG6 6AF, UK
[2]Central Laser Facility, Rutherford Appleton Laboratory, Didcot OX11 0QX, UK

The multielectron dissociative ionisation (MEDI) process that occurs when diatomic molecules are exposed to intense laser fields (intensities generally in excess of 10^{14} W/cm^2) is characterised by the break up of the molecule into two charged fragment ions with considerable kinetic energy [1]. In the classical Coulomb explosion of doubly charged molecular iodine I_2^{2+}, the I^+ ions take about 150 fs to separate to twice the equilibrium internuclear distance of I_2. This means that the diatom can reach high charge states while the internuclear distance is small. Subsequent dissociation along Coulombic potential curves leads to fragment energies which are a substantial fraction of the Coulomb explosion energy Q_1Q_2/R_e (atomic units), where Q_1 and Q_2 are the charges of the dissociation products and R_e is the equilibrium internuclear separation of the neutral molecule. We use pulse shaping to study the dynamics of the MEDI process.

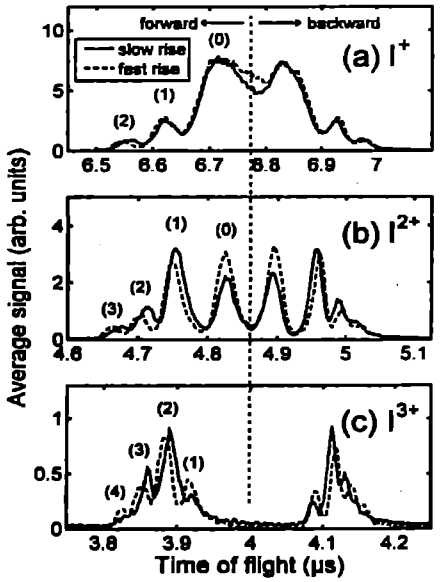

Figure 1. TOF spectra of iodine ions.

For the first experiment we used 70 fs pulses at 750 nm [2] and with focused intensities close to 10^{15} W/cm^2. The interferometer used for the pulse-shaping is of the Michelson type with a 70% beamsplitter [3]. We used a time delay of 0.8 of the pulse width (FWHM) and could switch rapidly between pulses that had rise times similar to pulses of 55 fs width and ones of 100 fs width, simply by changing from destructive to constructive interference. The trailing edges of the two pulses were unaffected.

The I^+, I^{2+} and I^{3+} TOF spectra for both constructive and destructive interference, averaged over 10,000 laser shots are shown in Figs. 1 (a), (b) and (c). One sees forward and backward peaks in the spectra, corresponding to fragment ions of the same energy but moving initially in opposite directions. The forward peaks in Fig. 1 are labeled with the charge state of the other ion of the fragmentation channel. The spectra show conclusively that the separation of the peaks (and therefore the kinetic energy release) decreases with increasing rise time.

Figure 1 b shows a significant amount of the asymmetric (0, 2) dissociation channel of I_2. We assume that in a field-free situation the lowest states in I_2^{2+} will dissociate into the (1, 1) channel. However, in the presence of a strong laser E-field, we will have a excitation of charge transfer states, from which the (0, 2) channel originates.

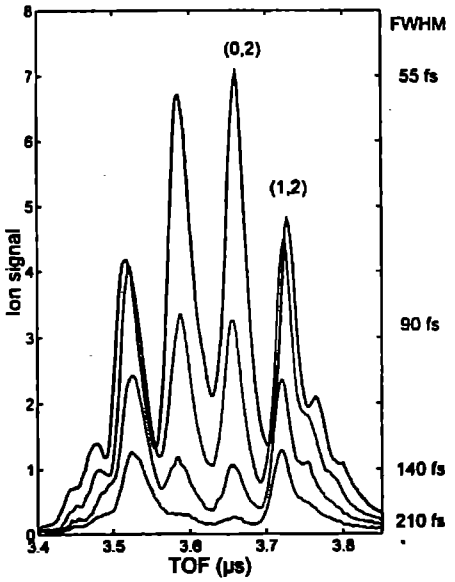

Figure 2. TOF spectra of I^{2+} ions.

We investigated the behaviour of the (0, 2) channel of I_2 with various pulse durations. Besides using the near-Fourier transform limited pulses of 60 fs, we also used pulses that were stretched by making use of the group velocity dispersion when passing through materials such as glass. This introduces a chirp on the pulses, but we have no reason to believe that a variation of a few nm in wavelength will have an effect on the MEDI process. Furthermore, we used positive as well as negative chirp and both gave the same result, indicating that the observed variations were only due to the change in pulse shape.

Figure 2 shows I^{2+} TOF spectra for several pulse lengths. The spectra show that the (0, 2) channel disappears as the pulse is lengthened.

REFERENCES

[1] K. Codling, and L.J. Frasinski, J. Phys. B **26** 783-809 (1993)

[2] A.J. Langley, W.J.Noad, I.N. Ross, and W.Shaikh, Appl. Opt. **33** 3875 (1994)

[3] A.J. Giles, J.H. Posthumus, M.R. Thompson, L.J. Frasinski, K. Codling, A.J. Langley, W.Shaikh, and P.F.Taday, Opt. Comm. **118** 537-541 (1994)

THE FIELD-IONISATION, COULOMB EXPLOSION MODEL FOR UNDERSTANDING THE DISSOCIATION DYNAMICS OF MOLECULES IN INTENSE LASER FIELDS

J H Posthumus, M R Thompson, A J Giles and K Codling

J J Thomson Physical Laboratory, University of Reading, Whiteknights, Reading, RG6 6AF, UK

Short pulse lasers in the visible and infrared can now easily provide electromagnetic E-fields that exceed the internal bonding fields of the outer shell electrons in atoms and molecules. Due to the large number of photons involved, one expects to explain the core of the ionization data by a simple classical approach, and indeed for atoms the appearance intensities are predicted quite well by barrier suppression [1]. However, molecules have been puzzling physicists for several years.

In several experiments the kinetic energy of the ions turned out to be independent of the laser pulse rise time [2]. More precisely, the kinetic energy release, E_K, of a fragment channel (Q_1, Q_2) appeared to be given by (we make use of atomic units)

$$E_K = C_m Q_1 Q_2 / R_e$$

where R_e is the equilibrium distance of the neutral molecule and the molecule specific constant $C_m = 0.45$ for the light molecules N_2, CO and O_2, and $C_m \approx 0.7$ for Cl_2 and I_2. This led to the idea of laser-induced stabilization at the critical internuclear distance, R_c, similar to vibrational trapping in H_2^+, but involving more electrons [3]. R_c is given by

$$R_c = C_m^{-1} R_e$$

At the end of the pulse, the stabilisation would cease to exist, and Coulomb explosion from R_c would follow, yielding exactly the observed kinetic energies. We showed that R_c is the point of electron localization and that it is indeed the same for all fragmentiation channels [4].

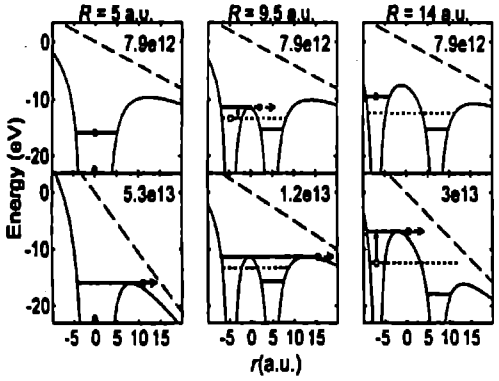

Figure 1. Determining the classical appearance intensities as a function of internuclear separation

In spite of that, we recently showed that the data on I_2 taken at 750 nm wavelength, are explained better by the field-ionisation, Coulomb explosion model [5]. The critical distance turns out to be the distance at which enhanced ionisation occurs, indeed quite the opposite of stabilisation.

We consider a molecule aligned with the laser E field. We use a symmetric double-well potential U in which the outer electron moves. U is given by

$$U = -\frac{Q/2}{|x + R/2|} - \frac{Q/2}{|x - R/2|} - \mathcal{E}x$$

where $Q = Q_1 + Q_2$ is the sum of the atomic core charges, x is axial position, R is the internuclear position and $\mathcal{E}$ is the laser E field. The energy level E_L of the outer electron in this double well can be approximated by [4]

$$E_L = \frac{(-E_1 - Q_2/R) + (-E_2 - Q_1/R)}{2}$$

where E_1 and E_2 are the known ionization potentials of the atomic ions.

Figure 1 illustrates the procedure for the $I^+ + I^+$ channel of iodine. At an internuclear separation of $R = 5$ a.u. the energy level is well above the central potential barrier. The situation is atom-like. At $R = 7.5$ a.u. and beyond, the central barrier rises above the energy level of the electron. Due to the localization of the electron, the level in the well on the left will be raised by a sufficiently strong E field up to the level of the central barrier. This is indicated by the vertical arrows in figure 1. Comparing the energy levels at $R = 5$ a.u. and $R = 9.5$ a.u., both at an intensity of 7.9×10^{12} W/cm^2, we notice how much less bound the electron is at the larger nuclear separation and indeed it takes only an intensity of 1.2×10^{13} W/cm^2 for over-the-barrier ionization. However, beyond $R = 10$ a.u. the central barrier, which now rises above the outer barrier, becomes the single obstacle for ionization and since the level of the inner barrier increases as a function of R, so does the appearance intensity. The latter value is thus the optimum ion separation, which maximizes the ionization process. Notably, the optimum separations for all (Q_1, Q_2) channels are virtually the same. This is because the enhanced ionisation is closely ralated to electron localisation, which, as we showed earlier, starts at virtually the same nuclear separation for all fragmentiation channels [4]

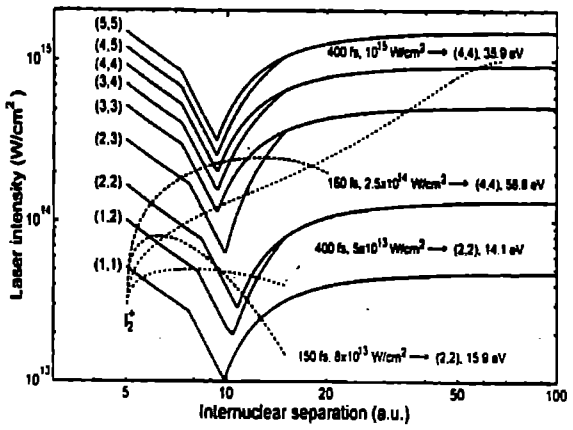

Figure 2. Classical appearance intensities (solid curves) and classical trajectories (dashed curves)

The classical appearance intensity for the fragmentation channels (Q_1, Q_2) are represented by the solid curves in figure 2.

We try to simulate an experiment on I_2 with classical trajectory calculations. The first ionisation step is assumed to occur at the equilibrium distance (5.04 a.u.). We assume that the I_2^+ ions are very unstable in the intense laser field and start to dissociate soon after they have been formed, for example at an intensity of 3×10^{13} W/cm^2.

The fate of a particular molecule clearly depends on where it is located in the laser focus. The dashed curves in figure 2 illustrate this for 150 fs and 400 ps pulses, by tracing the temporal evolution of the laser intensity versus the internuclear separation for molecules in a few different regions of the focus. Those located in a focal region where the 150 fs pulse reaches an intensity of 8×10^{13} W/cm^2, see figure 2, will contribute to the (2, 2) channel with a total kinetic energy release of 15.9 eV (C_m = 0.74). With a pulse duration of 400 fs and at an intensity of 5×10^{13} W/cm^2 the (2, 2) channel, with an energy of 14.1 eV, will result (C_m = 0.65). If we compare the two (2, 2) curves, we notice that the shorter pulse length gives the higher energy, because the transient repulsive states were created at smaller internuclear distances. The main contribution, from the final transition, is made at roughly the same R for both pulse lengths. The energy shift is therefore only small and may go unnoticed experimentally

	Experiment			Theory		
Channel	E_{55}	E_{100}	E_{400}	E_{55}	E_{100}	E_{400}
(1, 1)	4.9	4.8	2.9	5.3	5.3	3.9
(1, 2)	9.7	8.9	7.3	10.7	10.4	7.6
(2, 2)	17.6	16.5	12.1	20.9	19.6	14.1
(2, 3)	26.0	23.8	19.5	28.9	26.6	21.8
(3, 3)	39.0	35.5	16	40	37	32.1
(3, 4)	50.3	47.2	---	51	47.6	---
(4, 4)			16	65.7	61.2	35.9
(4, 5)			---	80.2	74.8	---
(5, 5)			17	97.7	91.9	40.1

Table 1. Kinetic energy releases for 55, 100 and 400 fs pulses

Table 1 lists the experimental and theoretical peak energies for various pulse lengths. Despite the simplicity of the model, the agreement is very good. Not only are the absolute values in nearly all cases correct within 10%, the energy shifts as a function of pulse length are also well reproduced. Furthermore, we notice that at 400 fs both the experiment and the model show PDI. Also, experiment as well as theory show the absence of the (3, 4) and (4, 5) channel at 400 fs. However, the parent of the PDI peaks in the experiment clearly is the (2, 2) channel, whereas in the calculations it is the (3, 3) channel. We have to bear in mind though, that the PDI peaks have very broad energy distributions [6], which encompass the theretical values.

We now turn our attention to the spectra shown in figure 2 of Giles *et al* in this annual report, in which we see the (0, 2) channel disappear when the pulses are stretched from 55 to 210 fs. We can make a rough estimate of the laser intensity required for excitation of charge transfer states as follows. The kinetic energy release of the (0, 2) channel is approximately 1.5 eV. The potential energy of $I + I^{2+}$ at $R \approx 6$ a.u. is therefore $IP_1 + IP_2 + 1.5$ eV = 31.1 eV, where IP_1 and IP_2 are the first and second ionisation potential of atomic iodine. For $I^+ + I^+$, the potential energy is approximately $2\times IP_1 + 1/R$ (a.u.) = 25.4 eV. Charge transfer will be effective if $\mathcal{E}R$ can make up the difference, where $\mathcal{E}$ is the electric field strength. This corresponds to an intensity of 4×10^{13} W/cm^2.

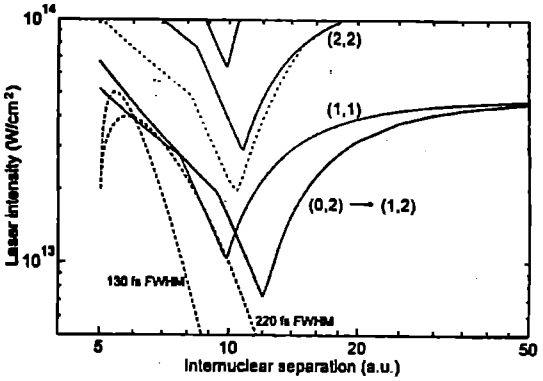

Figure 3. The classical appearance intensity for the (0, 2) to (1, 2) transition (bold line). The dashed curves show classical trajectories.

Figure 3 shows two examples of dissociation where R = 6 a.u. is passed at an intensity higher than 4×10^{13} W/cm^2, while the (1, 2) appearance intensity is just not achieved at any R. The pulse widths for these trajectories are 130 and 220 fs. With longer pulses the (0, 2) channel cannot be observed.

REFERENCES

[1] Augst S, Strickland D, Meyerhofer D D, Chin S L and Eberly J H 1989 *Phys. Rev. Lett.* **63** 2212

[2] Cornaggia C, Lavancier J, Normand D, Morellec J, Agostini P, Chambaret J P and Antonetti A 1991 *Phys. Rev.* A **44** 4499

[3] Schmidt M, Normand D and Cornaggia C 1994 *Phys. Rev* A **50** 5037

[4] Posthumus J H, Frasinski L J, Giles A J and Codling K 1995 *J. Phys B: At. Mol. Opt. Phys.* **28** L349-L353

[5] Posthumus J H, Giles A J, Thompson M R, Frasinski L J, Codling K, Langley A J and Shaikh W 1996 *The dissociation dynamics of diatomic molecules in intese laser fields* to be published

[6] Hatherly P A, Stankiewicz M, Codling K, Frasinski L J, Cross G M 1994 *J. Phys B: At. Mol. Opt. Phys.* **27** 2993-3003

GENERATION OF COHERENT VUV RADIATION USING RESONANCE-ENHANCED FOUR-WAVE DIFFERENCE-MIXING OF NANOSECOND AND FEMTOSECOND LASER PULSES IN KRYPTON

H. H. Fielding[1], Q. Hong[1], S. Solans[1], A.J. Langley[2], S. Schlorholz[2], W. Shaikh[2] and P.F. Taday[2]

[1]Department of Chemistry, King's College London, Strand, London WC2R 2LS

[2]Central Laser Facility, Rutherford Appleton Laboratory, Chilton, Oxon OX11 0QX

INTRODUCTION

Four-wave (third-order) frequency mixing of laser radiation is a well-established method for extending tunable, coherent laser sources into the vacuum ultraviolet (VUV) region ($\lambda < 200$ nm). Although non-resonant four-wave mixing (FWM) schemes using nanosecond lasers have relatively low conversion efficiencies ($10^{-7} - 10^{-6}$), the presence of a resonance at the two-photon level can increase the conversion efficiency considerably ($\geq 10^{-4}$). Such resonance-enhanced FWM schemes using the noble gases (Ar, Kr, Xe) have been widely exploited for the generation of intense, broadly tunable, narrow bandwidth (<1cm^{-1}), coherent, VUV radiation, for example [1-3]. In these experiments, the output of one visible or UV narrow bandwidth laser ω_1 is set to be in two-photon resonance with a transition in the nonlinear gas and the output of a second, tunable, narrow bandwidth laser ω_2 is scanned over a range of wavelengths to generate tunable VUV radiation at the sum or difference frequency $\omega_{vuv} = 2\omega_1 \pm \omega_2$. The power of the VUV radiation is determined by the relationship [4]

$$P_{vuv} \propto P_1^2 P_2 N^2 \chi^2 F \qquad (1)$$

where P_i is the power of the radiation with frequency ω_i, N is the number density of the nonlinear atoms and χ is the third-order nonlinear susceptibility tensor. F is a dimensionless phase-matching parameter which is a function of the wavevector mismatch, $\Delta k = k_{vuv} - (2k_1 \pm k_2)$, and the confocal parameters of the fundamental beams b_i. For a Gaussian beam in the tight-focusing limit ($b / L < 0.1$, where L is the path length of the beam through nonlinear gas), the phase-matching parameter $F \propto e^{-|\Delta k|L}$ [4] and, therefore, the power of the VUV radiation has the form

$$P_{vuv} \propto N^2 e^{-|C|N} \qquad (2)$$

where $C = \Delta k / N$ is the phase-mismatch per nonlinear atom. The VUV power can be maximised for specific fundamental laser powers and confocal parameters by changing the pressure of the nonlinear gas. This has been demonstrated by Marangos et al. [2] who used the $5p - 4p$ transition in Kr at $2\omega_1 = 94\,093.7$ cm^{-1} in a resonance-enhanced difference-mixing scheme to generate radiation over the wavelength range $\lambda_{vuv} = 200 - 120$ nm.

Since the development of high intensity femtosecond laser sources in the UV region, progress has recently been made in the generation of high power femtosecond VUV laser pulses by amplification of femtosecond seed pulses, generated by FWM processes, in excimer gain modules. For example, Tunnermann et al. [5,6] have demonstrated that it is possible to generate high power (up to 2.8mJ), short pulses of VUV radiation down to 133nm using near resonance-enhanced difference-mixing of fixed wavelength femtosecond radiation with tunable nanosecond radiation in Xe. More recently, Glownia et al [7] exploited the same near resonance-enhanced difference-mixing scheme in Xe using two femtosecond lasers to generate VUV pulses with up to 60μJ of amplified light at 155nm.

In this report, we present the results of an experiment in which we employ a resonance-enhanced FWM scheme, to generate femtosecond-scale pulses of coherent VUV radiation by difference-mixing narrow bandwidth radiation, in two-photon resonance with the $5p[1/2,0] \leftarrow 4p$ transition in Kr (fig1), with tunable femtosecond radiation. This approach has the advantage of providing true resonance-enhancement and, also, it is relatively easy to generate narrow bandwidth radiation in the UV by frequency doubling or tripling commercial, high power, nanosecond dye lasers.

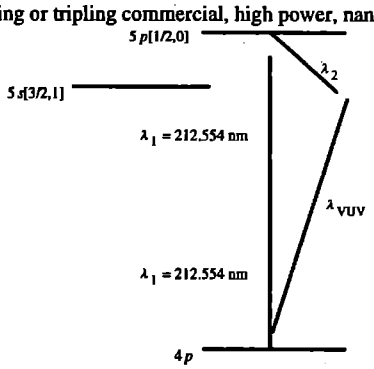

Fig 1 Resonantly-enhanced four-wave mixing scheme in Kr used for the generation of VUV femtosecond-scale pulses. λ_2 is centered around 740 nm and λ_{vuv} is centered around 124 nm

EXPERIMENTAL

The experimental arrangement is illustrated schematically in figure 2. A Quanta-Ray PDL-2 dye laser, pumped by the frequency-doubled output of a nanosecond Nd:YAG laser (Spectron SL805G-10), produced light at 637.662nm (60mJ in a 6ns pulse with 0.1 cm^{-1} bandwidth at 10 Hz). The output of the dye laser was frequency tripled using KD*P and BBO crystals to generate approximately 110 μJ of UV light at 212.554 nm which is in two-photon resonance with the $5p[1/2,0] \blacklozenge 4p$ transition in Kr. A Pellin-Broca prism was used to separate the 212.554 nm light from the fundamental and frequency-doubled radiation. The output of an argon-ion pumped Ti:Sapphire laser (Spectra-Physics Tsunami) was amplified at 10 Hz in a three-stage dye-amplifier [8] to generate nearly transform-limited 86 fs pulses centered around 740 nm (fwhm 6.3 nm, 150 μJ).

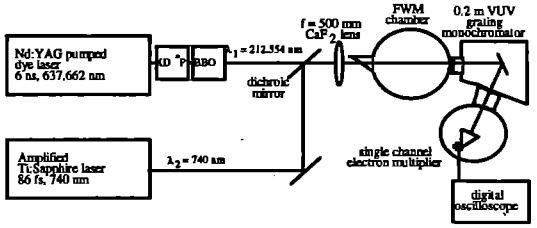

Figure 2 Schematic diagram of the four-wave mixing experiment for generating VUV radiation using nanosecond and femtosecond laser pulses

The UV and IR beams were then combined at a dichroic mirror and focused collinearly into a FWM cell using a 50cm focal length CaF_2 lens. Adjustment of a collimating lens in the path of the IR beam after the amplifier enabled both beams to be focused to a coincident point; the spatial overlap of the two beams at the focus was optimised by focusing them through a 50 μm pinhole onto a CCD camera with microscope objective. The FWM cell had a thin (mm) quartz entrance window arranged at Brewster's angle to the vertically polarised UV and IR radiation and a thin (3mm) MgF_2 exit window.

The UV and IR beams were focused a few centimetres in front of the MgF_2 exit window to minimise reabsorption of the generated VUV radiation whilst ensuring that the beam foci remained in the cell.

The sum-difference VUV radiation at 124nm was separated from the fundamental UV and IR radiation using a 0.2m grating monochromator (Acton Research Corporation VM-502) and detected using a single channel electron multiplier (Philips X919BL) having an efficiency of 0.03counts/photon at 124nm. The optical pathway after the FWM cell was evacuated to 10^{-4} - 10^{-5} mbar to reduce reabsorption of the generated VUV radiation.

RESULTS AND DISCUSSION

The VUV intensity was measured as a function of Kr pressure in the FWM cell and the results are presented in figure 3.

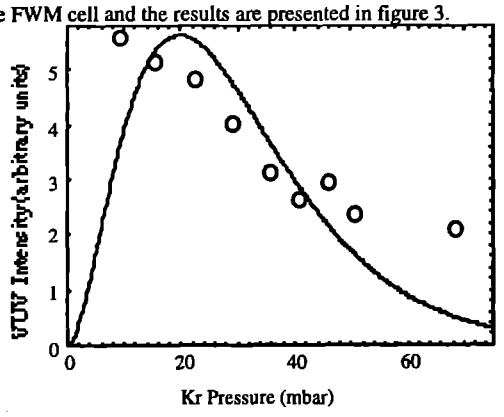

Figure 3 Intensity of the VUV radiation as a function of Kr pressure at λ_{vv} = 124 nm

The solid curve is fitted using equation (2). The number of VUV photons produced by the resonance-enhanced FWM process can be estimated by using the known spectral response of the single channel electron multiplier and measuring the relative loss of the 212.554nm radiation through the FWM chamber and monochromator and making the assumption that the relative loss of VUV radiation was of a similar magnitude. Although these assumptions are not unreasonable for the purposes of obtaining an order of magnitude estimate, they prevent an absolute pulse energy being quoted. At optimal Kr pressures of $\leq$ 20 mbar, approximately 10^7 photons/pulse were produced which corresponds to a pulse energy of approximately 0.02 nJ. For input energies of E_1 = 110 μJ and E_2 = 150 μJ, this implies an energy conversion efficiency of approximately 10^{-7} from the resonant radiation. It should be noted that the temporal overlap between the femtosecond and nanosecond pulses is only 10^{-1} and that including this in the estimation of the conversion efficiency gives a peak efficiency of around 10^{-6}.

Enhancement of the third order susceptibility tensor χ, and hence the VUV intensity (equation 1), is extremely sensitive to the precise wavelength of the narrow bandwidth UV radiation. In these experiments we were able to maximise the resonance enhancement by scanning the wavelength of the visible dye laser to within approximately 0.003nm (corresponding to approximately 0.4 cm^{-1} at the two-photon level) of the $5p - 4p$ two-photon resonance. No VUV signal could be observed by our detection system when the visible dye laser was tuned more than 0.025 nm away from the resonance.

The confocal parameter of the narrow bandwidth, nanosecond beam focused by a 50 cm lens was b_1 = 2.6 cm. The fitted curve in figure 3 corresponds to b_1 = 0.04 cm; Δk, the phase mismatch, was calculated using the Sellmeier formula for Kr [9]. The difference between the calculated and fitted values can be explained in terms of departures from the tight-focusing condition. Comparison with the experimentally measured VUV intensity shows the calculated curve to be less steeply sloped on the low pressure side of the peak and rather more steeply sloped on the high pressure side. These discrepancies can be attributed to a modification of the dispersion of the gas by competition between VUV generation and two-photon absorption followed by photoionisation. It is also likely that irregular beam profiles and the large bandwidth of the femtosecond radiation are contributing factors in the departure from theory.

For negatively dispersive four-wave mixing schemes it is possible to add a positively dispersive buffer gas to increase the conversion efficiency of the FWM process by phase-matching the system and making $\Delta k = 0$. This negative dispersion is achieved by choosing the wavelength of the tunable laser to be such that the wavelength of the VUV radiation is shorter than, but relatively close to, a transistion of high oscillator strength [10]. However, in the work presented here, the wave-vector mismatch is positive for the VUV wavelength of 124 nm which is just longer than the $5s[3/2,1]$ Kr resonance line at 123.583nm. Nonetheless, even unphase-matched, this resonance-enhanced difference-mixing scheme generates around 10^7 photons in a femtosecond-scale pulse which is sufficiently intense for single-photon spectroscopy. Currently, we are unable to measure the temporal profile of the VUV pulses; however, since the four-wave interaction only occurs for around 10^{-11} s (approximately 10^{-5} times the duration of the narrow bandwidth nanosecond pulses) it is not unreasonable to assume that the pulses of VUV radiation generated by four-wave difference-mixing are of the order of hundreds of femtoseconds. Inevitably, group-velocity dispersion will contribute to pulse broadening of the resulting VUV radiation. In future work we aim to measure the temporal profile of the VUV light using similar techniques to those recently proposed by Le Blanc et al [11] and, indeed, it will be interesting to investigate the VUV pulse width as a function of gas pressure and also to investigate the effect of scanning the VUV radiation through the Kr resonance line at 123.583nm.

CONCLUSIONS

In conclusion, we have demonstrated that resonance-enhanced four-wave difference-mixing of two narrow bandwidth nanosecond laser pulses and one femtosecond laser pulse offers a convenient method of producing tunable, intense ($\approx 10^7$ photons/pulse), coherent VUV radiation with femtosecond-scale pulses. Similar sum-mixing schemes could also be employed for the generation of short-pulse radiation further in the VUV. The development of laboratory sources of bright, tunable, coherent VUV femtosecond radiation has immediate applications in time-resolved electronic and molecular spectroscopy.

ACKNOWLDGEMENTS

This research was performed in the Central Laser Facility at the Rutherford Appleton Laboratory with financial support from the Engineering and Physical Sciences Research Council, King's College London, The Leverhulme Trust (QH) and the European Union (SS). The authors are grateful to Dr J.P. Marangos and the Blackett Laboratory Laser Consortium at Imperial College for the loan of the VUV grating monochromator.

REFERENCES

1.G Hilber et al, J Opt Soc Am B4 1753 1987
2. JP Marangos et al, J Opt Soc AmB 7 1254 (1990)
3. HH Fielding et al, Chem Phys 155 257 1991
4. GC Bjorkland, IEEE J Quant Electr 11 287 (1975)
5. A Tunnermann et al, Phys Rev A 46 2707 1992
6. A Tunnermann et al, IEEE J Quant Electr 29 1233 1993
7. J H Glownia et al, J Opt Soc Am B 11 2427 1994
8. AJ Langley et al, Appl Opt 33 3875 1994
9. A Bideau-Mehu et al, Spectrosc Radiat Transfer 25 395 1981
10. AH Kung et al, Appl Phys Lett 22 801 1973
11. SP Le Blanc, Z Qi and R Sauerbrey, Optics Letts 20 312 1995

THE POTENTIAL OF FEMTOSECOND LASER MASS SPECTROMETRY

K.W.D. Ledingham, R.P. Singhal, H.S. Kilic, T. McCanny, D. Smith and S. Wang
Department of Physics and Astronomy, University of Glasgow, Glasgow G12 8QQ, Scotland
C. Kosmidis
Department of Physics, University of Ioannina, GR-45110 Ioannina, Greece
A.J. Langley and W. Shaikh
Central Laser Facility, Rutherford Appleton Laboratory, Chilton, Didcot, Oxon OX11 0QX, UK

INTRODUCTION

The report describes the results of a series of experiments relating to multiphoton ionisation time of flight studies of molecules which were performed in the femtosecond laboratory at L.S.F. over the past 12 months.

EXPERIMENTAL AND THEORETICAL BACKGROUND

In a series of experiments over the last few years [1-10], the Glasgow group has demonstrated that resonance enhanced multiphoton ionisation (REMPI) coupled to time of flight (TOF) mass spectrometry can be used to detect, at ultra-trace levels (ppb), a great number of environmentally sensitive molecules e.g. urban pollutants, explosive molecules as well as medically and biologically important substances such as drugs of abuse and large biomolecules.

These experiments were carried out using Nd:YAG and Excimer pumped dye laser systems at nanosecond pulse lengths. It was shown for explosive molecules that a unique wavelength dependent fragmentation fingerprint for the whole family of nitro-hydrocarbon explosives could be obtained using specific wavelengths in the UV. This entailed dissociating the NO_2 radicals from the explosives with one photon, dissociating these further to NO neutrals which were resonantly ionised by the further absorption of two photons. All nitro compounds gave this unique fingerprint down to ppt sensitivity levels. The different members of the group could be further distinguished by studying the hydrocarbon fragments.

However one of the disadvantages of the REMPI approach in the nanosecond regime especially for the detection of thermally labile molecules e.g. explosives is that there is almost never any parent molecule ion formation. The reason for this is that the intermediate excited states from which the parent ionisation levels may be reached by the absorption of further photons are invariably dissociative with lifetimes typically hundreds of femtoseconds. The most sensitive as well as selective laser mass spectrometric approach for the detection of molecules is one which combines the detection of the parent mass in conjunction with a unique fragmentation pattern.

THE RESULTS OBTAINED FROM THE FS RUNS IN AUGUST 1995 AND MARCH/APRIL 1996

The idea of these experiments was to determine whether the fast up pumping to the molecular ion state could defeat the dissociation lifetimes and produce a large parent mass ion and make FLMS more useful than REMPI for thermally labile molecules. With ≤15μJ of laser power at 275 nm and 90fs, we demonstrated that FLMS at this wavelength, in the middle of the Ti sapphire double range, has enormous power as a general wavelength for ultra-trace chemical analysis.

In the August 1995 run, we completed the femtosecond dissociation studies of NO_2, nitromethane, nitrobenzene, the three isomers of nitrotoluene, dinitrotoluene, trinitrotoluene and carbon disulphide. The results showed that for most of these molecules a large parent mass peak was obtained but that in the two where o parent ion peak was obvious, the number of fragment ions produced was more than an order of magnitude greater than with nanosecond laser pulses increasing the detection sensitivity by his amount.

For the March/April 1996 run only some initial results are available. During this run, we have measured the fragmentation pattern for a number of different molecules using 750 nm laser pulses. At 750 nm the parent ion peak is dominant and the use of 750 nm light might provide for a simpler laser set up with cleaner and more easily interpretable mass spectra with the resultant increase in selectivity. We are currently evaluating the relative merits of the use of the red and blue lights for analytical detection of molecules.

Pump-probe measurements on NO_2 and some other molecules were carried out for both 375/375 nm and 375/750 nm combinations. They delay time was varied from about -500 fs to +2 ps. Such measurements will shed further light on the dissociation dynamics of the parent molecule and its fragments. Polarisation sensitivity was also studied for the 375/750 nm pump probe data.

In the following we discuss the results obtained for femtosecond multiphoton ionisation (MPI) and dissociation (MPD) of NO_2 and some nitro-molecules.

MPI/MPD OF NO_2 AT 375 NM AND 90 FS LASER PULSES

Figure 1 shows a NO_2 energy level diagram and the relevant MPI/MPD pathways. In measurements made in Glasgow, with 10 nanosecond laser pulse duration, only an ion peak due to NO is observed. This is due to the fast dissociation of the NO_2 molecule after absorbing a 375 nm photon. However, at 90 fsec the dissociation is substantially defeated by the fast up-pumping rate and a sizeable NO_2 ion peak is also observed.

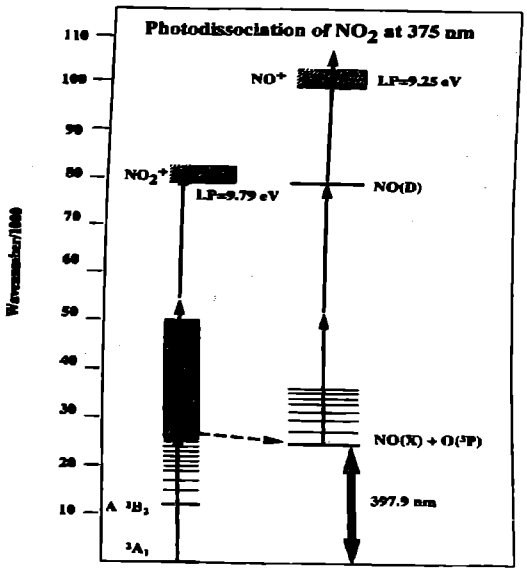

Fig 1 A NO_2 energy level diagram showing the dissociative state in the molecule. The multiphoton pathways in NO_2 and NO using 375 nm photons are indicated.

In order to account for the dependence of NO and No_2 ion yields on the laser parameters, a knowledge of the various excitation and ionisation cross-sections of NO and NO_2 is required. The dissociation rate of the NO_2 excited state is also needed. Apart from the two-photon ionisation cross-section of NO_2, these values are available in the published literature. A rate equations model was used to model theoretically the MPI/MPD of NO_2 for both the

nanosecond and femtosecond laser pulses. The results are shown in Figures 2 and 3. The excellent description of the experimental data over the very wide pulse durations supports the assumptions made about the competition between the ionisation an dissociation of NO_2 and demonstrates that fsec lasers can provide the parent mass ion yields by defeating the dissociation pathway in NO_2. The results have been accepted for publications [11] in Chemical Physics Letters.

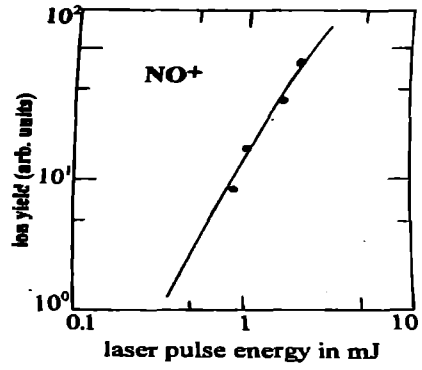

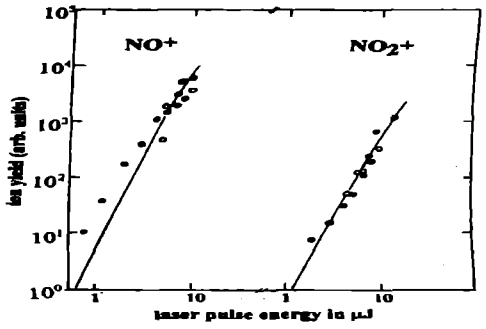

Figure 2: The yield of NO ions when NO_2 was irradiated by 375nm 10nsec pulses, and Figure 3: The yield of NO and NO_2 ions when NO_2 irradiated by 375nm 50 fsec laser pulses.

MPI/MPD OF SOME NITRO-MOLECULES AT 375 NM AND 90 FS LASER PULSES

Femotosecond mass spectrometry (FLMS) is expected to produce bigger parent ion peaks or/and substantial yields of large mass fragment ions than has been possible with nanosecond laser pulses. This would improve the selectivity and sensitivity of detection of the nitro-molecules which include the explosive molecules.

In Figure 4, we show spectra obtained with ns and fs lasers for nitrobenzene. The larger abundance of heavier mass fragment ions and the parent ion peak is obvious at 90 fsec. A second observation concerns with the very much higher efficiency, about a factor of 500 larger, with which fs pulses produce ions in comparison with the ns pulses. In Figure 5, a similar comparison for the molecule nitromethane is shown. Again the basic features pointed out in Figure 4 are reproduced here as well.

These results have been published [12] in Rapid Communications in Mass Spectrometry 9, 1522-27 (1995).

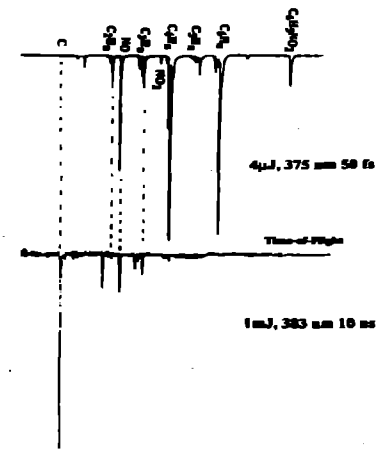

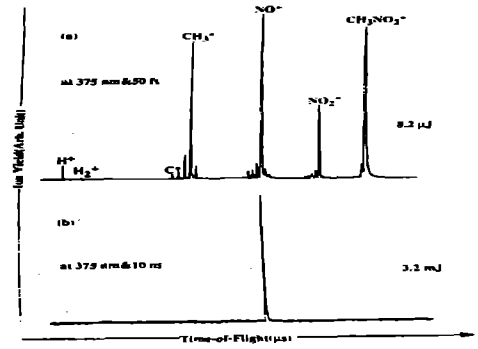

Figure 4: A comparison of the fsec and nsec excitation for nitrobenzene and figure 5: A comparison of fsec and nsec TOF spectrum for nitromethane.

REFERENCES

1. A. Marshall, A. Clark, R. Jennings, K.W.D. Ledingham and R.P. Singhal, Meas .Sci. Technol. 2. 1078-1082, 1991.
2. A. Marshall, A Clark, R. Jennings, K.W.D. Ledingham and R.P. Singhal, Int. J. of Mass Spec. and Ion Processes, 112, 273-283, 1992.
3. A. Clark, K.W.D. Ledingham, A. Marshall and R.P. Singhal, Spectrochimica Acta B 47, 799-808, 1992.
4. A. Marshall, A. Clark, R. Jennings, K.W.D. Ledingham, J. Sander and R.P. Singhal, Int. J. Mass Spectr. and Ion Process, 116, 143-156, 1992.
5. A. Clark, K.W.D. Ledingham, A. Marshall, J. Sander and R.P. Singhal, Analyst, 118, 601-607, 1993.
6. A. Clark, C. Kosmidis, R.M. Deas, K.W.D. Ledingham, A. Marshall, J. Sander and R.P. Singhal, J. Phys. D. Appl. Phys. 26, 1-10, 1993.
7. C. Kosmidis, K.W.D. Ledingham, A. Clark, A. Marshall, R. Jennings, J. Sander and R.P. Singhal, Int. J. Mass Spectrom. Ion Proc. 135, 229-242, 1994.
8. A. Marshall, A. Clark, R.M. Deas, C. Kosmidis, K.W.D. Ledingham, W. Peng and R.P. Singhal, Analyst **119**, 1719-1724, 1994.
9. A. Marshall, A. Clark, K.W.D. Ledingham, J. Sander, R.P. Singhal, C. Kosmidis and R.M. Deas, Rapid Communications in Mass Spectrometry **8**, 521-526, 1994.
10. C. Kosmidis, A. Marshall, A. Clark, R.M. Deas, K.W.D. Ledingham and R.P. Singhal, Rapid Communications in Mass Spectrometry **8**, 607-614, 1994.
11. R.P. Singhal, H.S. Kilic, K.W.D. Ledingham, C. Kosmidis, T. McCanny, A.J. Langley and W. Shaikh, Chemical Physics Letters, Accepted for Publication 1996.
12. K.W.D. Ledingham, H.S. Kilic, C. Kosmidis, R.M. Deas, A. Marshall, T. McCanny, R.P. Singhal, A.J. Langley and W. Shaikh, Rapid Communications in Mass Spectrometry 9, 1522-1527, 1995.

MULTIPHOTON PROCESSES IN ORGANIC MOLECULES USING VUV LASER PHOTONS

K.W.D. Ledingham[1], R.P. Singhal[1], H.S. Kilic[1], Shi-liang Wang[1], T. McCanny[1], D.J. Smith[1], I.C.E. Turcu[2] and R. Allott[2]

[1]Department of Physics, University of Glasgow, Glasgow G12 8QQ, Scotland
[2]Central Laser Facility, Rutherford Appleton Laboratory, Chilton
Didcot, Oxfordshire OX11 0QX, UK

INTRODUCTION

Vacuum ultraviolet (VUV) absorption processes have been utilised to study molecular structures, thresholds of ionization of atoms and molecules, quantum yields of photoionization and photodissociation processes and autoionization structures. It has been known for some time[1] that multiphoton processes using nanosecond laser pulses on thermally labile molecules can cause extensive fragmentation making analysis of these molecules difficult or impossible. There are two methods to defeat these fragmentation processes: firstly to use ultrashort laser pulses which can often defeat the intermediate dissociative states[2,3] or secondly to use single VUV photons to bypass completely any intermediate dissociative states[4]. Both of these methods should give large parent mass peaks which are necessary for unambiguous analytical analysis.

There are two common methods for the production of VUV photons <150 nm in wavelength: a) third harmonic generation in xenon (118 nm) using the 355 nm output of a Nd.YAG and b) four wave mixing. Both of these methods are quite difficult to produce and the laser intensities are rather small.

It was felt that the plasma source in the VUV laboratory might be a new and unique source of tuneable VUV photons suitable for these single photon experiments. Before however tackling the single photon ionization of gas phase molecules with photons from this source, it was felt necessary to carry out multiphoton experiments on these molecules with photons getting progressively shorter using the excimer lasers in this laboratory at 248 nm and 157 nm.

RESULTS AND DISCUSSION

A series of gas phase experiments were carried out using the 248 nm, 7ps, KrF excimer laser in conjunction with a linear one meter time of flight mass spectrometer. The ionization and dissociation multiphoton spectra for the molecules NO, NO_2, nitromethane, nitrobenzene, three isomers of nitrotoluene, H_2O and CS_2 were obtained. These were carried out for a series of different laser fluxes to investigate the power dependence of the fragmentation spectra.

After considerable effort the F_2 laser was set up and the 157 nm beam was directed into the TOF mass spectrometer. Unfortunately the only available VUV optics to focus the laser was a very long focal length lens. This resulted in the focal point of the laser in the ion region of the TOF mass spectrometer having considerable spatial dimensions which made the mass resolution far from optimal. None the less the ionization/dissociation mass spectra for all of the above molecules were recorded at 157 nm. It is hoped that some of these runs will be repeated in the future with much improved resolution.

CONCLUSIONS

It has been shown conclusively that as the wavelength is reduced into the UV regime from 248 to 157 nm the size of the parent peak becomes larger for the thermally labile molecules and indeed the overall efficiency of ionization also increases. This is corroboration of earlier work done in Glasgow on nitrobenzene[4] but at longer wavelengths.

At RAL there exists the world's brightest, repetitive, laboratory sized plasma x-ray source. This results from the very high temperature (10^6K) attainable by delivering 10^{15}Wcm^{-2} laser light on target. The source is based on a picosecond pulse train which is amplified in two stages by KrF Excimer lasers operating at 248 nm. The combination of ps laser pulses with a very tight focal spot leads to this extremely high power density. The soft X-rays so generated have a wide spectral range from 200 - 30 nm and hence with an appropriate monochrometer, a very effective single photon facility for mass spectrometry can be set up. It is expected that after the present upgrade of the facility is finished, the X-ray flux will be sufficient to carry out these important single photon experiments.

REFERENCES

1) A. Marshall, A. Clark, K.W.D. Ledingham, J. Sander R.P. Singhal, C. Kosmidis and R.M. Deas, Rapid Commun.Mass Spectrom., 8, 521, 1994.

2) K.W.D. Ledingham, H.S. Kilic, C. Kosmidis, R.M. Deas, A. Marshall T. McCanny, R.P. Singhal, A.J. Langley and W. Shaikh, Rapid Commun. Mass Spectrom. 9, 1522, 1995.

3) K.W.D. Ledingham, C. Kosmidis, S. Georgiou, S. Couris and R.P. Singhal Chem. Phys.Lett. 247, 555, 1995.

4) J.H. Arps, C.H. Chen, M.P. McCann and I. Datskou, Applied Spectroscopy, 7,1211, 1989

5) C. Kosmidis, K.W.D. Ledingham, A. Clark, A Marshall, R. Jennings, J. Sander and R.P. Singhal, Int.J.Mass Spectrom. and Ion Processes 135, 229, 1994.

'LINE FREE' XUV CONTINUUM EMISSION FROM A PICOSECOND TABLE-TOP LASER-PLASMA LIGHT SOURCE

J.T.Costello[1], A. Gray[1], J-P. Mosnier[1], W. Whitty[1], O. Meighan[1], C. L. S. Lewis[2], A. MacPhee[2], R. Allott[3], A Lamb[3], and I. C. E. Turcu[3]
[1]School of Physical Sciences, Dublin City University, Dublin 9, Ireland
[2]Queens University of Belfast, Belfast BT7 1NN, Northern Ireland
[3]Rutherford Appleton Laboratory, Chilton, Didcot OX11 OQX, United Kingdom

INTRODUCTION

The advent of table-top lasers capable of generating picosecond/ subpicosecond pulses with energies in the range of mJ's to hundred's of mJ's has permitted the study of laser-target interactions at ultra-high irradiances (>10^{18} W/cm^2). High harmonics of the laser frequency[1], stimulated Raman backscatter[2], hard X-rays with energies up to 1MeV[3] subpicosecond FIR emission[4] and laser wake-field accelerated electrons[5] have all been observed from such plasmas. However most experiments have been concerned with incoherent X-ray (photon energy > keV) emission[6,7,8,9,10,11,12,13]. Where X-ray pulse durations were measured they were predominantly on a picosecond time scale.

On the other hand plasmas formed by table-top long pulse length lasers (20 - 100 ns. typ.) with moderate pulse energies (10's mJ-100's mJ) have become well established light sources in many laboratories. For typical on target irradiances of 10^{12} W/cm^2 such plasmas are brightest at sub-keV photon energies with emission durations which are comparable to the laser pulse width[14] and increase to typically 100's of nsec. with decreasing photon energy into the VUV[15].

The observation of clean line-free continuum emission from such plasmas formed on rare earth and 5d metal targets[15] opened up the possibility of a high brightness, table top continuum light source for photoabsorption applications which had been exclusively limited to synchrotron light sources. To date long pulse laser plasma continua have been used as secondary VUV light source standards[16], for photoelectron spectroscopy[17] soft X-ray lithography[18], VUV reflectivity measurements[19], near-edge x-ray absorption spectroscopy (NEXAFS)[20], pulsed laser deposition dynamics[21] and XUV/VUV photoabsorption of laser produced plasmas[22,23].

A recent important postscript in laser plasma continua development is an experiment at Vulcan[24] which demonstrated that XUV continua with sub nanosecond pulse durations were possible. Measurements of a thulium plasma spectrum driven by a 80psec, ASE free incident laser pulse showed continuum emission on a time scale of ~ 100psec.

We report here the results of a preliminary experiment, motivated by the above developments, in which a picosecond laser driver is used at moderate on target irradiance to generate sub-nanosecond 'line-free' XUV continuum emission from high-atomic number plasmas . Time integrated dispersive spectroscopy was used to record the evolution of XUV continuum emission as a function of target atomic number. The 'spectral purity', single shot sensitivity and upper time limit on the duration of broad band XUV emission were established.

EXPERIMENTAL

Plasmas were generated by focusing 7ps/248nm pulses of energy (20 mJ typ.) from a KrF laser system[25] via a 1m f/10 plano convex lens onto continuous tape and cylindrical targets *in vacuo.* to an irradiance of ~10^{13} W/cm^2. A schematic diagram of the experimental setup used to record time integrated spectra is shown in Figure 1.

Spectra were recorded using a Flat Field Spectrometer (FFS) similar to that discussed by Kita et al[26] operated in two modes: for high resolution ($\Delta\lambda$ ~ 1Å) with an entrance slit (width = 75μm) ~230mm from the grating centre and for high

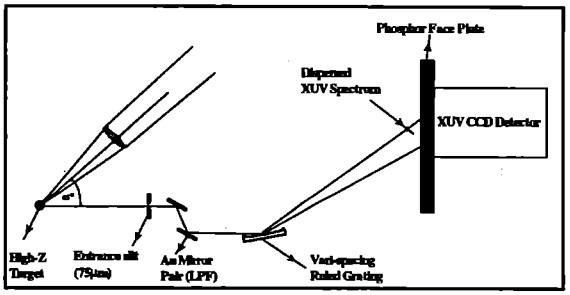

Figure 1. Experimental setup

throughput in slitless mode with a source-grating distance of ~900mm. The dispersed XUV spectrum fell on a phosphor coated faceplate and the resulting visible image was read out by a synchronised CCD camera system. The 1024 pixel length of the CCD covered a range of ca. 110 eV at ca. 85 eV corresponding to a sampling interval of approximately 0.1 eV per pixel. High order spectral contributions from plasma light of photon energy > 200 eV were significantly reduced using a pair of gold mirrors oriented at a grazing angle of 8°. The reflectivity of the mirror pair was less than 0.04 for energies above 200eV. This resulted in the spectral region 100 - 300 eV being virtually free from order sorting problems. Light emerging from this optical low pass filter was coincident with the optic axis of the spectrometer as the mirrors were aligned parallel to each other.

In order to study the duration of plasma emission time resolved results were obtained with a Kentech streak camera. It was decided not to streak dispersed spectra due to the lack of toroidal coupling optics between source and spectrometer which resulted in insufficient flux per CCD pixel. Instead a simple thin film of CHO was used for XUV filtering. The XUV window defined by the gold mirror pair and a 0.4μm thick CHO filter has a peak transmission of 18% at approximately 145 eV and provides a FWHM bandpass of 85 eV. However, while the CHO provides excellent VUV blocking it has a small transmission in the UV and visible region of the spectrum which may result in a long 'tail' superimposed on the XUV emission pulse.

RESULTS

Time integrated, predominantly first-order, spectra of Mylar ($C_{10}H_8O_4$), Copper and Samarium obtained with the FFS operating in high resolution mode are shown in the 100-200 eV energy range in Figure 2. The spectra obtained are uncorrected for the combined reflectivity of the gold mirror pair/grating and the phoshpor spectral response. They represent an average of 500 laser pulses on target with a mean energy of 15 mJ per pulse. The y-axis in Figure 2. represents CCD count values obtained for copper and samarium with an offset added to the Mylar spectrum. The transition from predominantly line emission to 'line free' continuum emission is observed as the target atomic number is increased. At high resolution samarium produces a smooth continuum, whereas XUV emission from copper is more intense but with increased discrete structure.

The single-shot sensitivity of the source was demonstrated by removing the entrance slit to allow increased XUV flux to fall on the detector plane. A single shot emission spectrum from a lead plasma with an average of 200 CCD counts/pixel is shown (with an offset) in Figure 3. From the detector calibration[27] this corresponds to 2200 VUV photons/pixel or 3 X 10^4 photons/mm^2

at 110 eV in the detector plane. The system gain could be increased by a factor

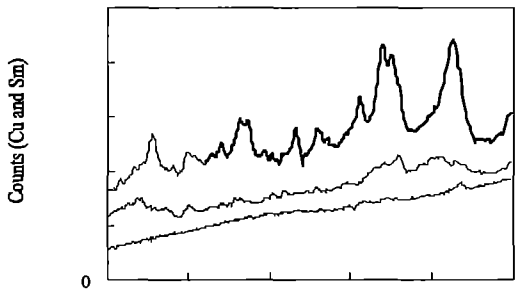

Figure 2. XUV spectra of CHO, Cu and Sm demonstrating the transition from 'line dominated' to 'line free' continuum emission with increasing target Z. Flat field spectrometer operated with a 75 μm wide entrance slit.

of greater using toroidal coupling optics resulting in sufficent flux yields for applications requiring single-shot sensitivity such as reaction kinetics and dynamics of laser ablation/ depostion.

The relative intensities of XUV continua produced by the high atomic number metals lead, gold and samarium are shown (uncorrected for optical reflectivities and detector response) in Figure 3. The spectra represent an average of 50 laser pulses on target with a mean energy of 15 mJ per pulse. Lead produces the brightest continuum and it's low cost and ease of target machining make it highly favourable as an XUV, short pulse duration, continuum source.

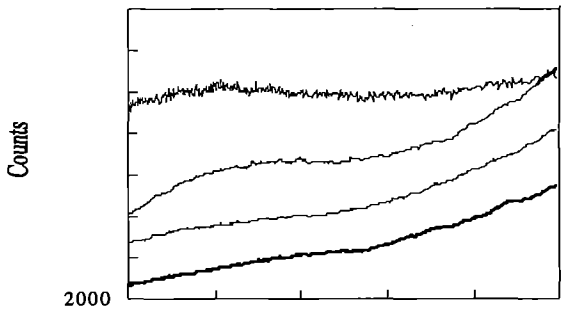

Figure 3. Spectra of Sm, Au and Pb taken under identical conditions. Traces are average shot signals from the accumulation of 50 laser shots on target with the spectrometer operated in slitless mode.

The spectral reproducibility of the source was investigated by calculating the ratio Io/Io for a series of successive lead spectra. The results obtained lie within ±5% of unity and serve to demonstrate the high degree of spectral integrity obtainable with this source.

Figure 4. shows the duration of emission from a lead plasma. Photon energies detected lay in the spectral window defined by the gold mirror pair and a 0.4μm thick CHO transmission filter (see inset Fig 4.) The emission pulse risetime was of ~150ps was limited by the focus voltage of the streak camera but not the slow decay time resulted in a real FWHM of ~750ps. This duration is long in comparison with the result obtained by Davidson[24] who measured pulse durations of ~100ps at 30Å (413eV) for a thulium target with an 80ps incident laser pulse. Two main factors are believed to contribute to this result. (1) The CHO filter provides excellent blocking in the VUV but it has a non-negible transmission in the UV and visible regions of the spectrum which may provide a long 'tail' superimposed on the XUV emission pulse. (2) A 20ns, 25mJ Amplified Spontaneous Emission (ASE) pulse was transmitted to the the target resulting in a dilute pre-plasma. Hence the main 7 psec pulse interacts not simply with a solid target but with a dilute expanding plasma. In the presence ASE generated preplasmas Kieffer et al. [28] observed X-ray emission pulses longer by a factor of five or so over plasmas produced with with a high-intensity-contrast laser pulse. However, further experiments with controlled ASE and sub 10 picosecond time resolution will be required to settle this question.

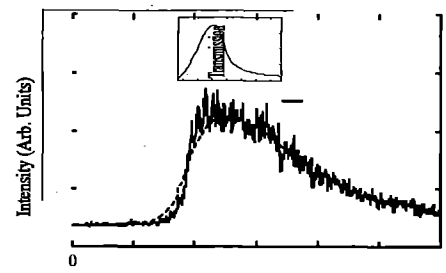

Figure 4: Streak image of Pb continuum pulse - XUV filter window (inset)

REFERENCES

1. JJ Macklin, JD Kmetec, & CL Gordon III, Phys Rev Lett **70**, 766 1993.
2. CB Darrow, C Coverdale, MD Perry, WB Mori, C Clayton, K Marsh, and C Joshi, Phys Rev Lett **69**, 442 1992.
3. JD Kmetec, CL Gordon, III, JJ Macklin, BE Lemoff, GS Brown, and SE Harris, Phys Rev Lett **68**, 1527 1992.
4. H Hamster, A Sullivann, S Gordan, W White, and RW Falcone, Phys Rev Lett **71**, 2725 1993.
5. A Modena, Z Najmudin, AE Dangor, CE Clayton, KA Marsh, C Joshi, V Malka, CB Darrow, C Danson, D Neely, and F Walsh, Nature, **377**, 606 1995.
6. M Murnane, HC. Kapteyn, and RW Falcone, Phys Rev Lett **62**, 155 1989.
7. B Soom, H Chen, Y Fisher, and DD Meyerhofer, J Appl Phys, **74**, 5372 1993
8. D Umstadter, X Liu, and J Workman, Proc Soc Photo-Opt Instrum Eng **1860**, 80 1993
9. JF Pelletier, M Chaker, Y Beaudoin, CY Côté, and JC Kieffer, Proc Soc Photo-Opt Instrum Eng **2041**, 222 1994
10. P Audebert et al, J Phys B**27**, 3303 1994.
11. R Shepherd et al , Rev Sci Instrum **66**, 719 1995
12. JC Kieffer and M Chaker, J of X-ray Sci & Tech **4**, 312 1994
13. GT Schappert et al, AIP Conf Proc **318**, 97 1994
14. J-P Mosnier, S Bac, R Barchewitz, ET Kennedy, M Collins and JT Costello, J Elec Spec Relat Phenom 1996 *in press*
15. PK Carroll et al, Appl Opt, **19**, 1454, 1980
16. G O'Sullivan et al, Opt Lett, **7**, 31 1982.
17. Ch Heckenkamp, U Heinzmann, G Schönhense, DD Burgess, AP Thorne and JEG Wheaton, J Phys D**14**, L203 1981.
18. P Gohil, H Kapoor, D Ma, MC Pekerar, TJ McIlrath, and ML Ginter, Appl Opt, **24**, 2024 1985.
19. ML Bortz and RH French, Appl Phys Lett **55**, 1955 1989
20. GD Kubiak et al, J Vac Sci Tech B**8**, 1643 1990
21. K Murakami et al, AIP Conf Proc **288**, 375 1994.
22. JT Costello, JP Mosnier, ET Kennedy, P. K. Carroll, and G O'Sullivan, Physica Scripta, **T34**, 77 (1991).
23. ET Kennedy et al, Opt Eng **33**, 3984 1994.
24. S Davidson, PhD Thesis, QUB 1993
25. ICE Turcu et al, Proc Soc Photo-Opt Instrum Eng **2015**, 243 1994.
26. Toshiaki Kita et al, **22**, 512 1983.
27. AG MacPhee et al, RAL Report RAL-94-042, 161 1994
28. JC Kieffer and M Chaker, J X-Ray Sci Tech **4**, 312 1994

X-RAY FOCUSING WITH MICROCHANNEL PLATES

A. N. Brunton,[1] A. S. Tremsin,[1] J. E. Lees[1], G. W. Fraser,[1] J. Page, [1] I. C. E. Turcu,[1] R. M. Allott[2], N. Lisi,[2] N. S. Kim[2] and W. B. Feller[3]

[1]X-ray Astronomy Group, Dept. of Physics and Astronomy, Leicester University, University Rd., Leicester, LE1 7RH, U.K.
[2]Rutherford Appleton Laboratory
[3]Nova Scientific Inc., 54 Main St., 7 Cedar Court, Sturbridge, MA 01566, U.S.A.

INTRODUCTION

Microchannel plate (MCP) X-ray optics have been an ongoing area of research in the Leicester X-ray Astronomy Group for some years now[1,2,3,4] While our primary interest in these devices is as imaging optics for astronomy, they may find terrestrial applications in the fields of semiconductor device lithography[5] or materials analysis.Following our successful 1994 optic testing run[3,4] on the RAL point-like repetititive laser-plasma X-ray source, when prototype 85 micron channel plates were tested, we applied for further time to test new 8 micron square channel MCP optics as they became available from Nova Scientific Inc.

EXPERIMENTS

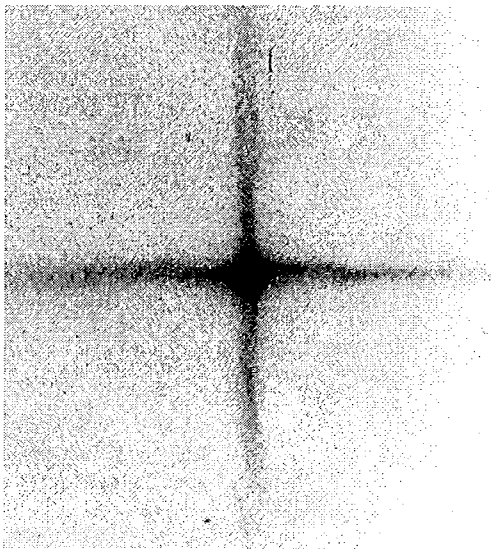

Fig 1 Point-to-point focused image 60:1 plate from Boule A central focus is 0.6mm fwhm

Batches of microchannel plates are manufactured in long blocks or 'boules' [6] from which individual MCP blanks are sliced prior to etching and polishing. Optics from two separate boules were investigated by illumination with 1.59keV X-rays emitted from an aluminium target tape. Experiments were performed in ambient helium at atmospheric pressure.The two families of plates will be designated "Boule A"(work with earlier plates from this boule is described in ref 4) and "Boule B" which is a later, supposedly improved,boule from the same manufacturers. In each case the channels were 8 microns square. The channel length to diameter ratios of the two Boule A plates and five Boule B plates varied between 30:1 and 100:1. Images were recorded on Kodak DEF X-ray film, these were then scanned with a Joyce-Loebl Mk3c microdensitometer using the calibration curve of Rockett *et al.*[7] in order to obtain detailed information on the foci.

The Boule A optics gave excellent results - much better than those reported in ref 4. Figure 1 shows an image of the focal plane X-ray distribution from a 60:1 plate in a geometry where the source-optic and optic-image distances were both 30cm - chosen to optimise the throughput. The microdensitometer revealed a focal spot of width 7arcmin fwhm and an intensity gain of 65. The improvement in performance over the earlier Boule A plates[4] is attributed to a new, less aggressive, etching process which had yielded channels which were almost perfectly square in cross-section. The plates of ref. 4 had channels with rather rounded-off corners due to a strong etch designed to increase the open area.

Five plates from Boule B were available for testing, all with L:D ratios of 100:1. The foci produced by these plates were of very poor quality (fig. 2). Comparison of lab images with the results of a ray-trace simulation suggest that a twisting of the channels or groups of channels (multifibres) along the length of the boule at the time of manufacture is to blame for the shortcomings of the image.

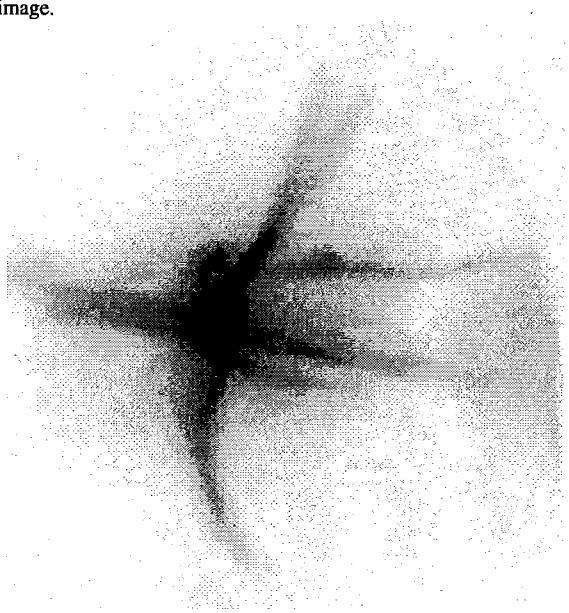

Fig 2 Point-to-point focused image Boule B scale as fig 1

CONCLUSIONS

We have demonstrated formation of a sharp X-ray image (7 arcmin or 0.6mm fwhm) with high intensity gain (65) by MCP optics with small (8 micron) channels. This indicates that the technology has matured to the point where our goals for astronomical optics have almost been achieved. Furthermore, this work has highlighted the critical nature of certain manufacturing processes. Figure 2 shows the catastrophic effects of channel torsion while comparison of figure 1 with the results presented in ref 4 highlights the importance of perfecting the etch.

REFERENCES

1. G. W Fraser, A. N. Brunton, J. E. Lees,J. F. Pearson,W. B.Feller, Nucl. Instr. Meth. A324 404 (1993)
2. G. W. Fraser, A. N. Brunton, J. E. Lees, I. C. E. Turcu CLF Annual Report 1994.
3. I. C. E. Turcu, A. N. Brunton, G. W. Fraser, J. E. Lees, Proc. SPIE 2523 11 (1995)
4. A. N. Brunton, G. W. Fraser, J. E. Lees, W. B. Feller, P. L. White, Proc. SPIE 2514 40 (1995)
5. A. N. Brunton, A. S. Tremsin, J. E. Lees, G. W. Fraser, I. C.E.Turcu, R. M. Allott, N. Lisi, N .S. Kim, W. B. Feller, CLF Annual Report 1996.
6. J. L. Wiza Nucl. Instr. Meth. 162 587 (1979)
7. P. D. Rockett, C. R. Bird, C. J. Hailey, D. Sullivan, D. B.Brown, P. G. Burkhalter. Appl. Opt. 24 2536 (1985)

MICROCHANNEL PLATE (MCP) BASED COLLIMATORS FOR X-RAY LITHOGRAPHY OF SEMICONDUCTOR DEVICES

A. N. Brunton,[1] A. S. Tremsin,[1] J. E. Lees,[1] G. W. Fraser,[1] J. Page, [1] I. C. E. Turcu,[2] R. M. Allott[2], N. Lisi,[2] N. S. Kim[2] and W. B. Feller[3]

[1] X-ray Astronomy Group, Dept. of Physics and Astronomy, Leicester University, University Rd., Leicester, LE1 7RH, U.K.

[2]Rutherford Appleton Laboratory

[3]Nova Scientific Inc., 54 Main St., 7 Cedar Court, Sturbridge, MA 01566, U.S.A.

INTRODUCTION

In order to continue the relentless miniaturisation of semiconductor devices that we have seen since theirr inception, some workers are using soft (~1keV) X-rays to expose the resist in the photolithographic process by which they are made. Diffraction considerations set limits, which are very hard to overcome, on the smallest features that may be etched by the current ultra-violet technology. X-rays of ~1nm wavelength are not as susceptible to diffraction problems. The preferred X-ray source is the synchrotron, which can provide a very intense almost parallel soft X-ray beam. Howevèr the cost of these machines is huge. Many semiconductor manufacturers seek alternatives .

One such alternative is the laser-plasma X-ray source.[1,2] Indeed considerable lithography work has been done with the RAL source. [3] The inherently diverging beam from the X-ray emitting plasma complicates the design of the lithography mask and the stepper which would move the silicon wafers into position for exposure in an industrial system. If a collimator optic (fig 1) were used to convert the diverging beam into a parallel one then the specifications of these components could be significantly relaxed.

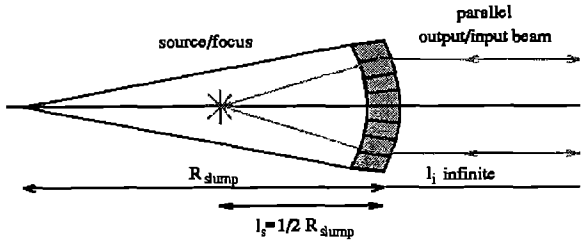

Fig 1 Collimator with source positioned at half radius of curvature gives uniform parallel output beam

COLLIMATORS

Collimators have been designed at Leicester, based on spherically curved circular pore microchannel plates[4)] ground to a special cross-section. The technical problems associated with making such a device are far from trivial.

Prototype collimators have been tested using the laser plasma source. Experiments have been performed with collimators of different channel diameters (10-25 micron) and which have undergone slightly different manufacturing processes. Fabrication problems identified by our work at RAL are slowly being overcome by the manufacturers, Nova Scientific Inc.

EXPERIMENTAL RESULTS

Fig 2 shows a Kodak DEF X-ray film image, exposed by 1.2keV X-rays emitted from a copper target tape. This image summarises the state of affairs at the end of our RAL run in February 1996. The collimator used to obtain this image had 25 micron channels and a nominal 1m radius of curvature. This curvature, rather larger than that which will be used in the final high-throughput version, implies that a source-collimator distance of 0.5m must be used to produce a parallel output beam. The source distance used to form fig 2 was 1m, the film was postioned 34cm behind the collimator.

The expected result from such an illumination is a uniform circular illuminated field, the X-rays having passed straight through the optic with no reflection and hence no collimation. That is, the beam should still be divergent (fig 1).

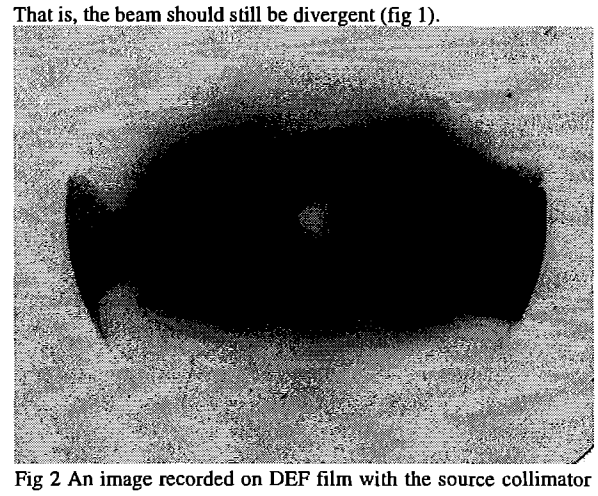

Fig 2 An image recorded on DEF film with the source collimator an collimator-film distances set to be 1m and 34cm respectively

What we see is rather different: The image is not a complete circle and has a circular unexposed region in its centre. This indicates problems when the MCP "core glass" is etched away to leave open channels. In some regions, particularly the centre where the channels are longest, the channels are not being etched out properly. An electron microscope examination confirmed this finding. Further work at Nova since these results were obtained is now believed to have solved this problem.

The image has two components which are easily distinguishable on the original X-ray film, one transmitted, as expected, with no reflection and the second reflected. The presence of a reflected component indicates an error in the "slump radius". The slumping is a proprietary process which is under further development at Nova.

CONCLUSIONS AND FURTHER WORK

We have experimented with a combination of laser-plasma source and collimator which could be used for X-ray lithography. The collimator technology is, however, not yet mature. Progress has been made, driven by the results obtained using the RAL source which is invaluable for testing these collimators. Collimators supplied to Leicester since this work was done suggest that the problems are starting to be ironed out. Further work is governed by a feedback loop of testing which must be iterated until the optic quality is sufficient to fulfil the lithography requirements.

REFERENCES

1. I. C. E. Turcu, I. N. Ross, G. J. Tallents, App. Phys. Lett. 63 3046 (1993)
2. I. C. E. Turcu and 18 co-authors Proc. SPIE 2015 243 (1994)
3. I. C. E. Turcu and 7 co-authors Microelectronic Eng 23 207 (1994)
4. G. W. Fraser, A. N. Brunton, J. E. Lees, J. F. Pearson, D. L. Emberson, Nucl. Instr. Meth. A334 579 (1993)

THE EFFECTS OF LASER WAVELENGTH AND LASER PULSE LENGTH ON METALLIC FILMS PREPARED BY PULSED LASER DEPOSITION.

A. M. Widdowson[1], T. J. Jackson[1,*], R. Allott[2], I. C. E. Turcu[2], S. B. Palmer[1] and C. McCoard[2].

[1]Department of Physics, University of Warwick, Coventry, CV4 7AL, UK.

[2]Rutherford Appleton Laboratory

*Present address Department of Material Science and Metallurgy, University of Cambridge, CB2 3QZ, UK.

INTRODUCTION

Pulsed laser deposition (PLD) has become a widely used technique for the production of thin films. A limiting factor for the PLD technique is the production of liquid droplets ejected from the target which collect on the films. Work on the deposition of superconducting oxides revealed that short UV laser wavelengths were efficient in producing smooth droplet free films and that reduction in the laser wavelength, λ, led to fewer droplets being present [1,2]. The situation in metal deposition, however, is less clear [3]. The thermal diffusion depth, $L_{th}=(2\kappa\tau_p/c_{pm}\rho_m)^{1/2}$, where κ is the thermal conductivity, c_{pm} is the molar specific heat capacity, ρ_m the molar density and τ_p is the laser pulse length, and the optical absorption length, $\alpha^{-1}=\lambda/4\pi k$, where k is the extinction coefficient, are important parameters in governing droplet formation, [4], determining the depth to which the laser energy is absorbed into the target [5]. In YBCO, α^{-1} is the longer of these two length parameters, L_{th}~10nm for τ_p=10ns compared with α^{-1}~50nm, [4], and therefore governs the ablation process. Hence an obvious consequence of reducing λ is to make the ablation process more surface specific, leading to smoother evaporation from the target and fewer droplets. For metals L_{th} is the dominant parameter, with L_{th}~1μm and α^{-1}~20nm, [4]. For this reason one might expect that wavelength dependence is less marked and that a shorter pulse length would be of greater importance in obtaining surface specific ablation.

We report studies of the influence of λ for nanosecond (ns) pulses and of the influence of τ_p at fixed wavelength in order to elucidate the laser-target interaction in Ni and Ag. In particular the deposition rates of the films and the density of droplets deposited on them are measured.

EXPERIMENTAL DETAILS

A picosecond (ps) laser producing a pulse train operating at λ =248nm and a UV ns laser operating at λ=193nm, 248nm and 351nm were used in this work. The ps pulse train consisted of a 20ns pulse envelope operating at a repetition rate of 20Hz and contained sixteen, 5ps pulses, [6]. A Questec 2440 laser provided the pulsed ns source, operating at fixed maximum energy. The beam was attenuated using a series of glass and quartz plates to obtain the energy required for ablation. The beam was focussed to produce fluences ranging up to 20J/cm^2. All the depositions were carried out in vacuum at ~10^{-6}mbar. The target was placed at 45° to the incoming laser beam and material ejected from the target was collected onto glass substrates. Preferential etching of the target surface caused as a result of the laser hitting the target at45° was minimized by rotating the target and by moving the focusing lens up and down, [7]. This ensured that a constant plume direction was maintained during deposition. Before films were grown the rate of deposition as a function of laser pulse energy was determined using a 5MHz crystal quartz oscillator. From these deposition rates a series of Ni and Ag films 25-50nm thick were grown over a range of fluences using the laser conditions described above. To estimate the droplet density and area, digital SEM images of the films were taken and analysed using an image processing package.

RESULTS AND DISCUSSION

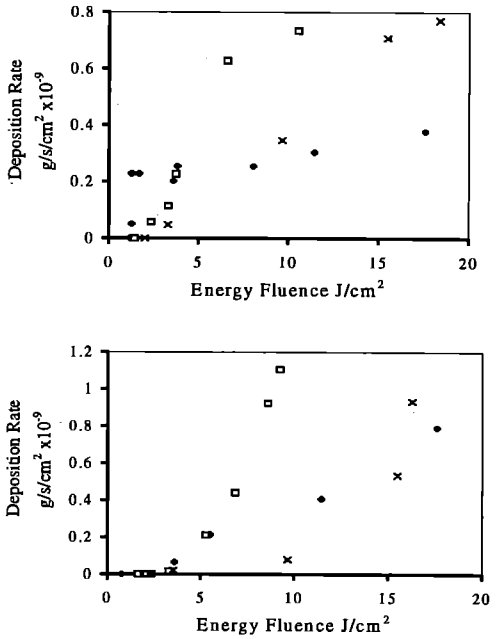

Figure 1 Mass deposition Rate vs Energy Fluence at λ=193nm(♦), 248nm(□) and 351nm(×), τ_p=20ns for (a) Ag and (b) Ni.

Figures 1(a) and (b) show the deposition rates for Ag and Ni at 193nm, 248nm and 351nm. From these figures we see that the threshold fluences for ablation decrease with decreasing wavelength. In addition for Ag we see that at shorter wavelengths a lower fluence is required to reach saturation of the deposition rate. Saturation is governed by the shielding arising from the plasma, which is characterised by the plasma frequency $\omega_p=\sqrt{(n_0e^2/m_e\varepsilon_0)}$, where n_0 is the electron density in the plasma, e the electronic charge and m_e the mass of the electron. The plasma is able to shield the target from the laser beam by absorption. The conditions for shielding as a result of absorption by the plasma depends on whether the photon frequency, ω, is greater than or less than ω_p. At high fluence ionization increases thus increasing the electron density, which in turn increases the plasma frequency. If the plasma frequency rises above the photon frequency, i.e., $\omega<\omega_p$, absorption in the plasma increases through inverse brehmsstrahlung, shielding the target from the laser beam. At shorter wavelengths the higher energy photons provide increased ionization in the plume giving rise to saturation of the deposition rate at lower fluences, as seen in Ag. This trend in the deposition rate is not observed for Ni. This is surprising since the first ionization potential for Ni is similar to that of Ag and one might therefore expect similar ion densities in the plasma. Clearly other processes are involved in reaching saturation conditions and further work is needed to investigate this.

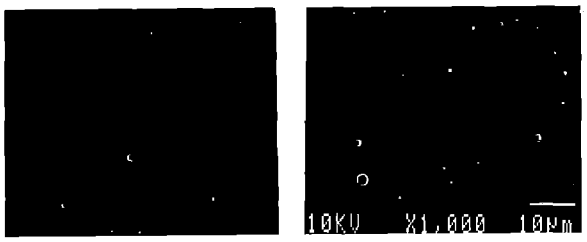

Figure 2 Ni films (a) fluence=9.8J/cm^2, thickness=26nm, λ =193nm, τ_p=20ns, droplet density (3.2±0.5)x10^{-3}μm^{-2}; (b) fluence=10.0J/cm^2, thickness=33nm, λ=351nm, τ_p=20ns.

Droplet density has been studied as a function of λ. In figures 2(a) and (b), two Ni films grown at 193nm and 351nm respectively are compared. The films being compared are grown at the same fluence to the same thickness, allowing a direct visual comparison. It is clear that there are more droplets on the film grown at 351nm. This is confirmed by the quantitative analysis, showing that fewer droplets are present on the films grown at shorter wavelength. A similar trend is seen for Ag films,[8].

The formation of droplets is expected if the amount of material removed from the target is greater than the evaporation rate at the target surface. Assuming that material is removed as vapour from the target by thermal evaporation, i.e., no droplet expulsion, then the depth/pulse ablated from the target can be estimated, see [9].

$$\text{depth/pulse} \approx \frac{p_{vs} T_s^{1/2} \tau_p}{M^{1/2} \Delta H_{lv}} \text{x1.53x10}^6 \text{ nm/pulse} \qquad (1)$$

where ΔH_{lv} is the latent heat of fusion, p_{vs} the vapour pressure, T_s is the surface temperature and M the molecular weight. We find that the measured removal rate at the target is far higher than estimated from the evaporation model implying that material is being expelled in the liquid state as droplets. For example in the ns regime the calculated rate of material removal in Ni is 14.8nm/pulse and the measured value is 1000nm/pulse.

For ps pulses the fluences required for deposition, ~0.01J/cm^2, are much lower than for ns pulses. By reducing τ_p, L_{th} is reduced from ~500nm to ~10nm in Ni and Ag. This confines the absorbed energy nearer to the target surface promoting efficient vaporization and thus reducing the fluences required for ablation. As for ns pulses, saturation of the Ag deposition rate is seen [8].

Figures 3(a) and (b) show Ag films grown with ns and ps pulses. These film have the same thickness since a comparison of fluences between ns and ps pulses is not available. Clearly more debris is present on the Ag film grown with ps pulse. A similar trend is seen in Ni, [8]. Part of the reasoning behind using the ps pulse was to reduce L_{th} making the ablation process more surface specific thus reducing the number of droplets, this has not been the case. As for ns pulses the

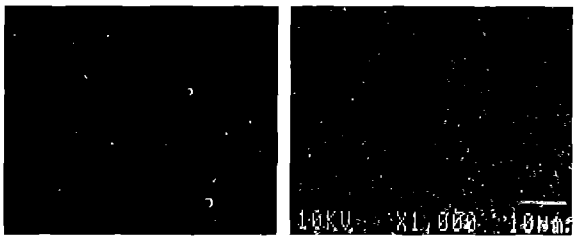

Figure 3 Ag films (a) fluence=7.2J/cm^2, thickness=28nm, λ =248nm, τ_p=20ns, droplet density (3.2±0.5)x10^{-3}μm^{-2}; (b) fluence=0.11J/cm^2, thickness=28nm, λ=248nm, τ_p=5ps.

rate of removal of material from the target, ~1nm/pulse, greatly exceeds the removal rate calculated from (1), ~10^{-3}nm/pulse, suggesting that droplets will be present on films deposited using ps pulses. In addition we suggest that the production of droplets is effected by the number of leading pulse edges. In the ps regime the target 'sees' sixteen times more pulses in an equivalent ablation period than in the ns regime. A comparison between films grown using ns and ps pulses at a repetition rate of 20Hz is required and further work to investigate the effect of the ps pulse repetition rate is planned at RAL.

CONCLUSION

Laser wavelength weakly influences the droplet emission from the metals Ni and Ag in which a small decrease in the droplet density at 193nm compared to 351nm is observed. We see that ps pulse lengths are not sufficient for the reduction of droplets and that the number of leading pulse edges also influences the presence of droplets. We find that the saturation fluence of the deposition rate of Ag decreases with decreasing wavelength. This is attributed to the increased photon energy giving rise to higher ion densities in the plume. However these saturation characteristics are not observed in Ni deposition rates.

ACKNOWLEDGEMENTS

The authors acknowledge the LSF at RAL for provision of facilities and the UK EPSRC for funding the programme.

REFERENCES

1 D S Misra and S B Palmer 1991 *Physica C* **176** 43
2 A Koren, A Gupta, R J Baseman, M I Lutwyche and R B Laibowitz 1989 *Appl. Phys. Lett.* **55** 2450
3 H Dupendant, J P Gavigan, D Givord, A Lienard, J P Rebouillat and Y Souche 1989 *Appl. Surf. Sci.* **43** 369
4 J P Gavigan 1990 *Proceedings of NATO ASI on the Science and Technology of Nanostructured Magnetic Materials.*
5 S Preuss, E Matthias and M Stuke 1994 *Appl. Phys. A* **59** 79
6 I C E Turcu et al 1994 *Applications in Laser Plasma Radiation* **2015** 243
7 T J Jackson, N J Appleyard, M J Cooper, D H Richards and S B Palmer 1995 *Meas. Sci. Technol.* **6** 128
8 A M Widdowson, T J Jackson, S B Palmer, R Allott, I C E Turcu and C McCoard submitted to *J. Phys. D Appl. Phys.*
9 R Kelly and J E Rothenberg 1985 *Nuclear Instruments and Methods in Physics Research* **B7/8** 755

DEEP, THREE DIMENSIONAL LITHOGRAPHY WITH A LASER-PLASMA X-RAY SOURCE AT 1NM WAVELENGTH

ICE Turcu, CM Mann*, SW Moon*, R Allott, N Lisi, BJ Maddison*, SE Huq** and NS Kim
Rutherfor Appleton Laboratory,
Central Laser Facility
*Space Science Facility
**Central Microstructures Facility

LIGA[1] is the new technology that replaces the milling and drilling machine for generating microstructures of dimensions of hundreds of micrometers and smaller, and resolution of well sub-micrometer and even tens of nanometers. For this end it uses a number of processes:

(a) lithographic transfer of the image from a mask into photoresist, with resolution of tens of nanometers when x-rays are used for imaging, and aspect ratios 10:1 or larger;

(b) electroplating (Galvanoformung, in German) the structure formed on the photoresit; and

(c) using the resulting metal structure as a die for moulding (Abformung, in German) mass produced devices.

It is therefore a new precision-tool making technology, which justifies the use of rather expensive synchrotron radiation. Nevertheless the x-ray exposures on the synchrotron beamline takes many hours (even 24 hours for one millimetre deep structures) because the PMMA photoresist used has very low sensitivity and the x-ray wavelength is very short, typically 0.2nm. This short wavelength used, also requires very thick gold absorber features on the x-ray mask, typically 15μm or more, which are expensive and time-consuming to.manufacture.

The present work describes, for the first time[2], a new method of performing deep lithography, with:

(a) softer x-rays of 1nm wavelength, generated by a compact laser-plasma x-ray source;

(b) more sensitive, chemically amplified photoresist;

(c) thinner, 3μm thick gold absorber features on the x-ray mask;

(d) a sequence of x-ray exposures, each penetrating 12μm deep in resist, followed by exposed resist removal (by developing) and re-exposure until the desired depth is reached;

(e) this results in reduced total x-ray exposure times of 10minutes for a 48μm deep structure.

The technique is applied successfully to fabricate 2.5 THz waveguides for microwave detector research in the Space Science Department (SSD) of Rutherford Appleton Laboratory (RAL).

The RAL laser-plasma source of soft x-rays[3, 4] is used to expose the lithographic cell containing the wafer, such that the distance between the point-like (10μm diameter) source and the wafer is 23mm, and the exposed area on the wafer is $1cm^2$. The plasma source was operated with a copper tape target in atmospheric pressure helium, and the lithographic cell contains a 10μm thick beryllium window/filter, which allows only the ~ 1nm wavelength x-rays (copper L-shell emission) emitted by the plasma to expose the resist. Otherwise, the exposure cell is also at atmospheric pressure helium as the rest of x-ray chamber. The absence of vacuum exposure has beneficial effects on the chemically amplified photoresist and allows fast injection of the exposure cell into the x-ray chamber, through a helium purge pipe.

The silicon wafer is spin-coated with 48μm thick photo-resist: AZ PF514 chemically amplified x-ray resist (Hoechst) with a ~30 times higher sensitivity then PMMA, and very good etching and mechanical properties. The very high resolution of AZ PF514 allowed the printing of 180nm wide transistor gates, reported in an earlier publication[5]. The 3μm thick gold absorber was directly deposited on the resist, using an inexpensive, standard mask-making machine in the Central Microstructures Facility (CMF) at RAL. This **integral mask** arrangement was chosen in order to simplify the realignment of the mask after each exposure/development step, which in the present experiment, was repeated four times.

The x-ray exposures are measured absolutely by means of a calibrated p-i-n x-ray diode filtered with the same thickness of beryllium foil as the lithographic exposure cell. A fluence of I_i= $200mJ/cm^2$ of 1nm wavelength x-rays allowed the development and removal of 12μm thick resist each exposure step. The exposure time was 2minutes/step for a laser-plasma repetition rate of 20Hz. This exposure dose/step is 10 times the surface fluence (I_e=$20mJ/cm^2$) required for exposing AZ PF514 photo-resist, for example for manufacturing transistor gates[5], which is consistent with an x-ray penetration of ln(10)=2.3 times the 1/e absorption depth at 1nm wavelength, which is t_e~5μm, and is the inverse of the resist absorption coefficient μ.

Next, it will be shown that by using four repeated exposures, the total x-ray fluence required to penetrate 48μm of resist is ~250 times smaller (and total exposure time shorter) compared to a single continuos exposure. Using Beer's law for calculating the irradiation fluence $I(t_i)$ needed for a selected exposure (and etching) depth t_i :

$I(t_i) = I_e \exp(t_i / t_e)$, with the above notations.

The irradiation $I(t_n)$ required for a depth of $t_n = n\, t_i$ is:

$D(t_n) = D_e \exp(n t_i / t_e)$, in a continuos exposure, but also

$D(t_n)^* = n\, D(t_i) = n D_e \exp(t_i / t_e)$, with the $D(t_i)$ exposure repeated

n times, and the resist removed (developed) after each exposure. With the values used in the present experiment:

$$D(t_n) / D(t_n)^* = (1/n) \exp[(n-1)\, t_i / t_e] = (1/4) \exp[(4-1)\ 12\mu m / 5\mu m\ ] = 248.1$$

If the ratio of the resist sensitivities, AZPF514 chemically amplified versus PMMA, is taken into account, the improvement in exposure time at this x-ray wavelength is ~6,700 times. This great reduction in exposure time allows the use of the plasma source, less powerful then the synchrotron, to demonstrate deep x-ray lithography in the present work.

Fig. 1 shows a 48μm structure patterned by 1nm wavelength x-rays generated by the RAL plasma source. The quality of the etching is very good, the striations on the vertical walls being due to imperfection in the edges of the gold absorber, which can be readily remedied if required. The imprints of the four exposure/development stages can be seen on the central element of the structure. An special technique in mask configuration, the **embedded mask,** is used to obtain the **true three-dimensional** structure: (a) the gold absorber defining the large rectangles was deposited on a first layer of resist, 24μm thick, (b) after which another layer of resist, 24μm thick, was spin coated on top of it, (c) and finally the top gold absorber is deposited to generate the central feature of the structure. The central structure is 100μm long, 25μm wide and 48μm high. A much higher aspect ratio cylindrical structure was generated (near side of Fig. 1) by a mask imperfection.

The next step in the LIGA technology is the metal plating of the resist structure. Fig. 2 shows the mirror image in gold, of the structure printed in photoresist. It constitutes a new method of fabricating high precision 2.5 THz waveguide structures.

In conclusion, deep structures can be generated with < 10 minute total exposure time, in chemically amplified resist, using compact laser-plasma x-ray source generating 1nm wavelength radiation. By using the RAL plasma x-ray source at its full 1Watt power the total exposure times can be reduced further by an order of magnitude. This would allow the exposure cell to be moved further away from the point-like plasma source (say to 5cm or 10cm) to allow a larger wafer area to be exposed to x-rays with reasonable radiation divergence angle.

The use of repeated exposure/etching of the photoresist together with the higher sensitivity of the chemical amplified resist results in a ~6,700 fold reduction of exposure time compared with a continuos (single) exposure of PMMA resist at the same wavelength.

The use of 1nm wavelength x-rays, and the repeated exposure/etching technique, reduces dramatically the thickness (to a few micrometers) of the gold absorber required to mask the x-rays, compared to the standard LIGA exposures carried out at ~0.2nm wavelength, which require gold absorber thickness of tens of micrometers, and make the masks expensive and time consuming to manufacture. The thinner gold absorber allows the use of integral masks which do not require realignment during several exposure/etching processes and also can generate true three- dimensional structures, as demonstrated. The integral gold masks survive intact the repeated etching of the resist. Obviously, thinner absorber features on the mask will have smaller aspect ration and therefore will allow higher resolution lithography.

It was shown that true three-dimensional structures with very good quality walls, can be generated with the above techniques in high sensitivity chemically amplified photoresist. The resist structures can be replicated in solid gold to fabricate high precision 2.5 THz waveguide structures.

The process could be automated to take full advantage of the short x-ray exposure times. A robot could be loaded with 20 exposure cells, such that while one cell is irradiated, the one before it undergoes post exposure backing of the resist, the one before undergoes developing, and so on, with the 19th preceding cell ready for the next x-ray exposure. The process-automation is made easier by the fact that x-ray exposures are performed at ambient atmospheric pressure in helium gas, such that no pressure change occurs between the cell irradiation stage and processing stages. This technique could open up new applications for the LIGA technique, in high volume, cost efficient, mass production of micro-components, compared to the present use of LIGA restricted to low volume, high added value tool-making, which tools, in their turn will be used for mass production. There are many aspects in which the two techniques are complementary, and two examples are chosen: flexibility and the height of the microstructure. The standard LIGA generates very high structures, > 1millimeter, but requires long design preparation and exposure time, and the availability of a synchrotron beam. The new LIGA technique, presented in this work, could be limited to a few hundred micrometer high structures, but will have fast turn-around of new microstructure designs, and the manufacturer could afford to own the compact plasma x-ray source.

The LIGA technique described in the present work could be used, to generate on the same substrate, both deep, three dimensional structures, typically of micrometer size, as well as ultrahigh resolution, ~100nm structures[5] with very exciting implications in integrating micro-mechanical, -optical, and -electrical devices. All this is made possible by using 1nm x-ray wavelength which is required in printing the ~100nm structures: at shorter wavelength the aspect ratio of the absorber features on the mask become prohibitive.

REFERENCES

1. W Ehrfeld, D Munchmeyer, "Three-dimensional microfabrication using synchrotron radiation", Nucl Instrum Meth Phys Res **A303**, 523-31 (1991).

2. ICE Turcu, CM Mann, BJ Maddison, "Deep pattern lithography", International Patent Application, PCT/GB96/00421 (1996).

3. ICE Turcu, IN Ross, C McCoard, "1Watt plasma x-ray source at hν ~ 1keV", RAL Report **TR-95-025**, 183 (1995)

4. ICE Turcu, IN Ross, C McCoard, "Picosecond KrF laser-plasma source generating 1nm x-rays at 1Watt average power"; Proc Conf on Lasers and Electro-optics **CLEO95**, CPD33 (1995).

5. CM Reeves, ICE Turcu, PD Prewett, AM Gundlach, JT Stevenson, AJ Walton, AWS Ross, RA Lawes, P Anastasi, R Burge, P Mitchell, "Fabrication of 200nm field effect transistor by x-ray lithography with a laser-plasma x-ray source", Electronics Lett. **31**, 2218-9 (1995).

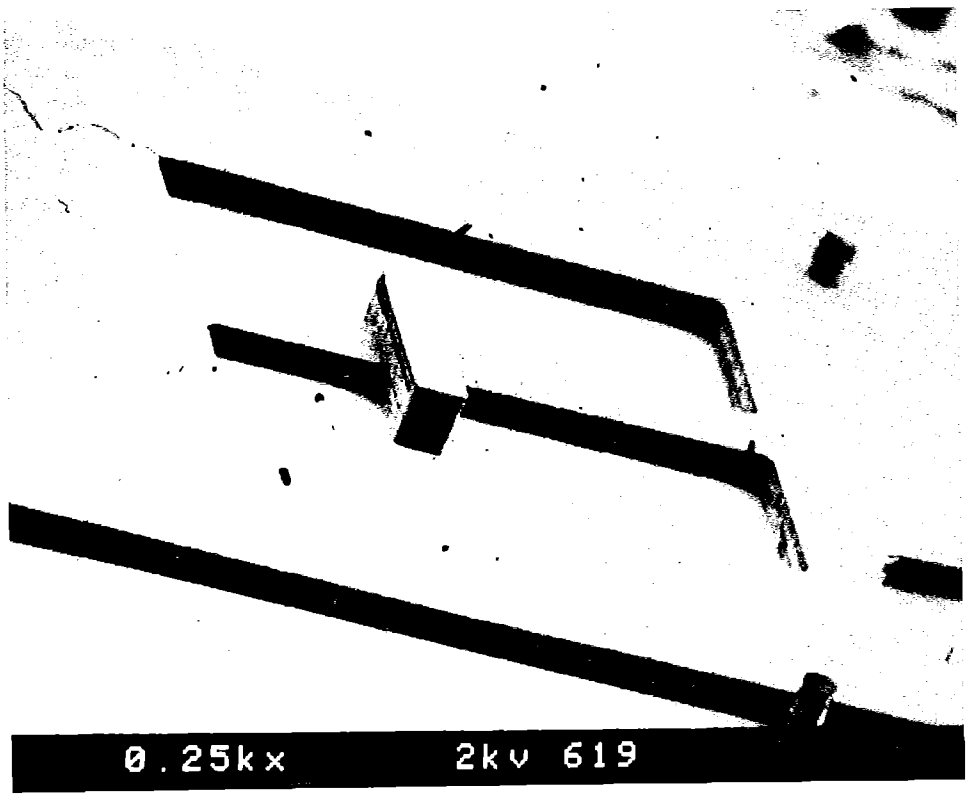

Fig. 1. Scanning electron micrograph of a three-dimensional, 48μm deep structure patterned by 1nm wavelength x-ray lithography into AZ PF 514 chemically amplified resist, using: a <10 minute total exposure time from a compact, laser-plasma x-ray source; 3μm thick gold absorber integral mask as well as embedded mask; four repeated resist exposure and etching stages, each removing a 12μm resist thickness. The structure is a 2.5 THz waveguide former. (Courtesy Dr CM Mann, SSD at RAL).

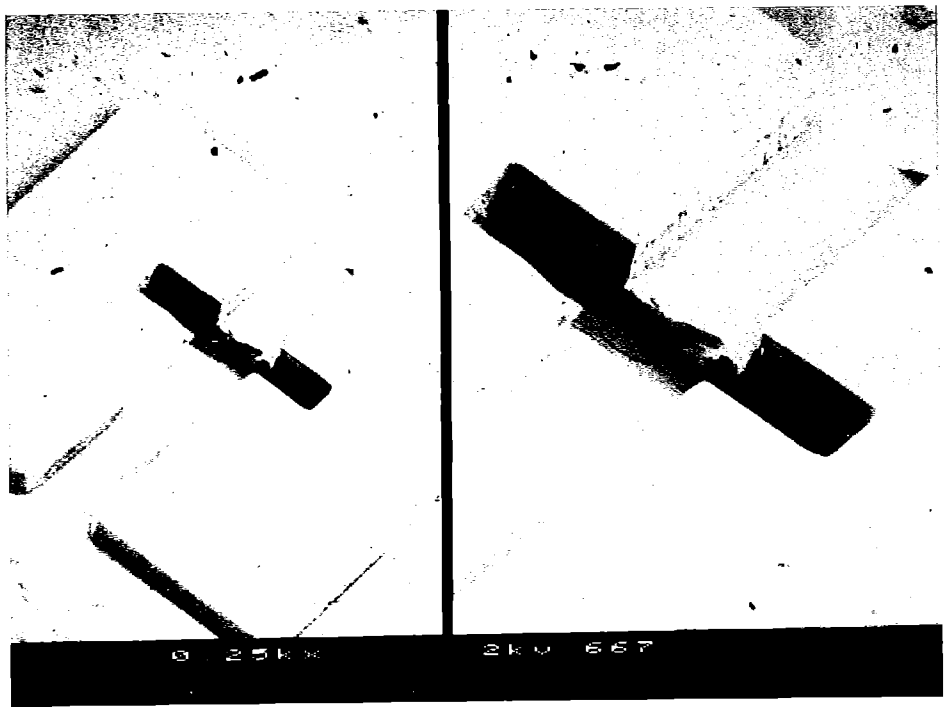

Fig. 2. 2.5 THz waveguide structure fabricated in gold, by plating the photoresist structure of Fig. 1.

A RESEARCH STUDY INTO THE FEASIBILITY OF USING LASER-PLASMA X-RAY LITHOGRAPHY FOR FUTURE DEEP SUBMICRON IC MANUFACTURING

C M Reeves[1], I C E Turcu[2] and P Prewett[3]

[1]Central Microstructure Facility, Rutherford Appleton Laboratory
[2]Central Laser Facility, Rutherford Appleton Laboratory
[3]Department of Electrical Engineering, University of Edinburgh

INTRODUCTION

Recent work at the LSF at RAL, in collaboration with the University of Edinburgh, the CMF at RAL, Leica Lithography Systems and King's College London, has provided a first demonstration of the use of the LSF laser-plasma X-ray source for deep submicron X-ray lithography.[1] These demonstrations involved integration of the X-ray exposures with a prototype 0.2 micron silicon field effect transistor (FET) process developed at Edinburgh. The results are worldclass and match the achievements of AT&T, who lead this type of research in the USA.[2]

DEVICE RESULTS

We reported our first functional X-ray defined FETs in early 1995. These devices had 0.2 micron gate lengths and were designed for n-channel operation. The process as reported in last year's LSF review involved the use of AZPF514 chemical amplified resist (with sensitivity of 20mJ/cm^2) and a 1x magnification gold-over-nitride mask technology. The University of Edinburgh provided access to their exploratory 0.18 micron device process and carried out all device integration work. The LSF provided all the X-ray exposures and the CMF at RAL provided facilities for resist processing and evaluation. Leica Lithography Systems patterned the X-ray masks which were prepared at King's College London.

Since the first n-channel device demonstrations, the partners have collaborated further and achieved two key new results. Firstly, the work has been expanded to encompass p-channel as well as n-channel devices - this is vital in order to open the way for complementary circuits as required for most very large scale integration (VLSI) designs. We reported functional 0.2 micron devices in both n-channel and p-channel configurations at Micro- and Nano- Engineering in Aix-en-Provence in September 1995.[3] Typical electrical results are indicated in figures 1 and 2 for 0.2 micron n-channel and p-channel devices respectively. Secondly, and perhaps more importantly, the partners have refined the mask fabrication and resist processing techniques to achieve linewidth resolutions down to the 0.13 microns as compared with our earlier results which were limited to 0.18 micron resolution.[3] Figure 3 shows an example of 0.13 micron lines defined in AZPF514 X-ray resist. This is very significant as the whole issue as to which new lithographic approaches will prove suitable for the 0.13 micron device generation (4Gbit circuits) remains hotly debated with X-ray, DUV optical, electron beam and ion beam as possible candidates. Already, the X-ray approach based on the LSF laser-plasma source looks promising and certainly deserves further investigation.

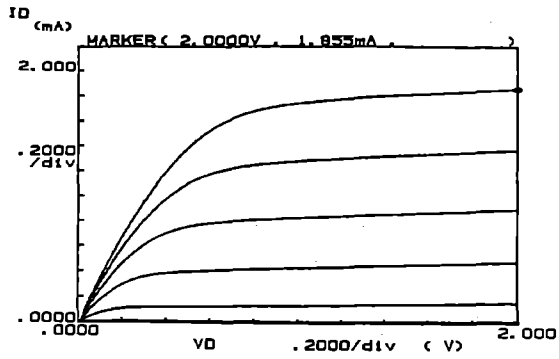

Figure 1: I-V Characteristic of a 0.2 micron n-channel FET defined by laser-plasma X-ray lithography.

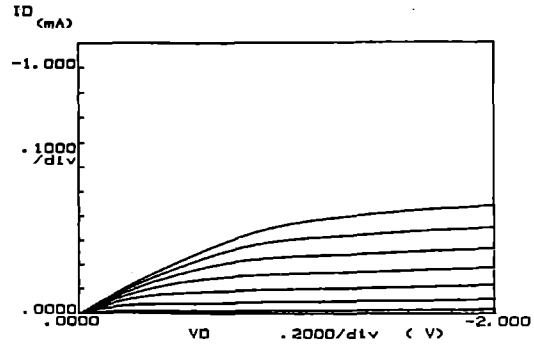

Figure 2: I-V Characteristic of a 0.2 micron p-channel FET.

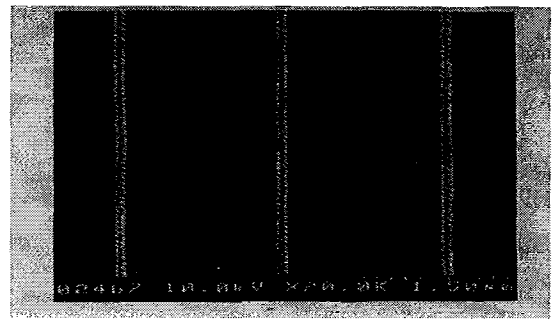

Figure 3: Electron micrograph showing 0.13 micron lines patterned in X-ray resist material.

This LSF collaboration in X-ray lithography provides an interesting link between the UK academic R&D community and the UK's semiconductor manufacturing base - the latter comprising mainly of inward investors in Scotland, north east England and Wales. With 0.35 micron manufacturing now being introduced into the UK for 64Mbit DRAM circuits, questions concerning the best lithographic strategies for the follow-on 0.25 micron, 0.18 micron and then 0.13 micron technologies must

soon be answered. To date, best lithographic strategies for 0.18 micron and 0.13 micron remain far from clear. In both cases, the laser-plasma X-ray approach provides an interesting option.

UPGRADE OF LSF SOURCE

Concerning the worldclass work on laser-plasma X-ray lithography at the LSF, it is clear that the continued exploration of the source for deep submicron lithography requires that the source be upgraded to increase the output power by a factor of x25. This is necessary to bring exposure times down from 4 minutes/chip to less than 10 seconds/chip. This requirement for shorter exposure times is a key element of the recent LSF upgrade proposal to EPSRC.

SUMMARY

This review has summarised the recent achievements of experiments using the LSF laser-plasma X-ray source for advanced lithography trials. The work has produced functional n-channel and p-channel transistors with 0.2 micron gate lengths and further demonstrated pattern resolution down to 0.13 microns as required for future 4Gbit circuits.

1 I.C.E. Turcu *et al.*,' 180nm X-ray Lithography with a High Repetition Rate Laser-Plasma Source', Microelectronic Engineering 27 (1995) p 295.

2 G.E.Rittenhouse *et al.*, 'Sub-0.1μm NMOS Transistors Fabricated Using Laser-Plasma Point-Source X-ray Lithography', IEEE Electron Device Letters, 16, No 7, July 1995, p 322.

3 C.M.Reeves *et al.*, 'Fabrication of 200nm field effect transistors by X-ray lithography using a laser-plasma X-ray source', Microelectronic Engineering 30 (1996) p 187.

LASERS *for* SCIENCE FACILITY (LSF): OPERATIONS AND DEVELOPMENT

R. Allott[2], I. Cormack[1], K. Henbest[3], A. J. Langley[1], P. Matousek[4], A. W. Parker[3,5], A. D. Scully[5], M. Scully[4], W. Shaikh[1], P. F. Taday[1,4], S. M. Tavender[3], M. Towrie[4,6], E. Turcu[2], W. Twigger[3]

Rutherford Appleton Laboratory

OPERATIONS FACTS AND FIGURES

This year a total of 41 RAL-based experiments were carried out over 160 weeks of laser time. LSF Loan Pool lasers were loaned for over 6 years worth of time to 17 university research groups.

[1]FEMTOSECOND SCIENCE LABORATORY

This has been a most productive year in the femtosecond laboratory with 11 experiments being carried out. We resumed operations in the Spring of 1995 following the successful reorganisation of the laboratory. This year a total of 9 refereed papers have been published and at least 10 conference presentations made reporting work from the fs laboratory.

Technical developments at the beginning of the year improved the lasers performance by a factor of ten. This was achieved with the successful amplification of 50 fs pulses derived from a new Spectra-Physics short-pulse oscillator - Tsunami. The amplified system specifications now are: 50 fs and 100 μJ at 750 nm. This improvement, combined with a new *f*/2 focusing parabolic mirror made by Optical Surfaces Ltd., results in focused intensities at sample of $>10^{15}$ Wcm^{-2}. Up to 13 μJ can be obtained at 375 nm by frequency doubling the laser output using a 0.2 mm thick, type I BBO crystal.

Several new research programmes were initiated, all of which are described elsewhere in this Annual Report. One of these, by Prof. K Codling's group from Reading, sought to explore the symmetry of fragmentation of molecules exposed to fundamental (750 nm) and second-harmonic (375 nm) fs pulses. The pump/probe techniques developed for these experiments were instrumental in the success of Dr K. Ledingham's (Glasgow) feasibility studies to develop the ultrasensitive technique of femtosecond laser mass-spectrometry. The time-resolution in both these experiments, measured by cross-correlating the fundamental and UV pulses, was better than 90 fs.

Two other new groups explored the possibilities of generating VUV, with the aim of developing a facility for spectroscopy. In the first of these, Dr H Fielding's group (Imperial College) generated fs VUV pules at 124 nm by four-wave difference mixing in Xe with an estimated 10^7 photons/pulse. This work is described in a paper in Optics Communications **123**(1,2,3), 129 (1996). The second research programme in this area, initiated by Prof. R. Donovan (Edinburgh), obtained VUV by harmonic generation in gasses. By focusing the fundamental 750nm, 100μJ pulses of 50fs pules to an intensity of $5x10^{14}Wcm^{-2}$ third (250nm) and fifth (150nm) harmonics were made in xenon and argon. Higher focused intensities resulted in plasma formation. Xenon gave the most efficient harmonic conversion producing 10^8 and $5x10^4$ VUV photons at the third and fifth harmonic respectively. Measurements established that fifth harmonic intensity was linearly dependent on the 750nm pulse intensity, indicating that the harmonic plateau had been reached. Similar results were obtained when the experiment was extended to use both these gases in a jet. The observation of higher harmonics was limited in this initial study by the detectors used.

[2]LASER-PLASMA X-RAY LABORATORY

The team running the laboratory has increased with the arrival of Dr Ric Allott from Swansea. Dr Nicola Lisi (Italy) has joined for one and a half years as an Italian EU fellow, and Dr Nam-Seong Kim (Korea, KAIST) for half a year as visiting scientist.

During the year, the Laser-Plasma X-Ray Laboratory scheduled 49 experimental weeks and 2 weeks were used for maintenance. New emission wavelengths from the hot plasma source were investigated in view of increasing the range of applications. These include; the XUV emission continuum (Dublin, EU experiment) for absorption spectroscopy, and the VUV emission continuum (LSF, Glasgow and Oxford) for biology and chemistry applications.

New applications of the x-ray source were: deep (50μm) 3-dimensional lithography for LIGA micromachining technology (RAL, in-house collaboration between Central Laser Facility, Space Science Department and Central Microstructure Facility); radiobiology of yeast cells by selective irradiation of the cell membrane and nucleus (Milan, EU experiment). The short wavelength excimer laser line of 157nm was used for the first time to generate single photon ionisation of macromolecules for mass spectroscopy (Glasgow). The R&D contract with JMAR Industries Inc. was completed successfully and resulted in a new, commercial laser-plasma x-ray source for x-ray lithography, in California.

A number of scientific investigations continued: the x-ray DNA damage and repair (Birmingham), as well as the direct comparison of biological effects of α-particle and x-ray radiation with (MRC-Radiobiology Unit and CRC Gray Lab); x-ray optics/beamline based on Micro-Channel-Plate technology (Leicester); the DNA study with UV laser radiation: 249 nm and 351nm (Birmingham) and 193 nm (MRC and Leicester); picosecond/nanosecond UV laser ablation and thin magnetic film deposition (Warwick).

The x-ray work resulted in seven publications, two patent applications, seven conference presentations, five lectures at national and international research organisations, and five publications in specialist magazines.

[3]NANOSECOND SCIENCE LABORATORY

The major development has been the replacement of the two XeCl excimer lasers. After much consideration and consultation with users over what would best suit the breath of science performed within this laboratory it was decided to replace one laser with the new solid state OPO laser technology and the other, following strong support to keep an intense 308nm photolysis source, to upgrade with the modern generation XeCl laser. The OPO system chosen is a Sunlite OPO pumped by a Continuum Nd:YAG laser tunable from 450 to 1680nm with high output energies (up to 50mJ @500nm) compared with the excimer/dye lasers. The bandwidth of the laser is 0.1 cm-1 and a frequency doubling option extends the wavelength range down to 225nm. Wavelength changes are facilitated with the removal of messy and time-consuming dye changes, for example; during a TR^3 study the triplet spectrum of benzophenone was recorded using the OPO at 500nm, minutes later this laser was tuned (by computer) to 460nm and without any optical realignment the TR^3 spectra of redox photo-products reacting with the triple benzophenone were being recorded. A full report giving the specifications of the OPO system can be found elsewhere in this report. The new excimer laser is a Lumonics Pulsemaster 848. This laser delivers a higher pulse energy, 400mJ, than the previous excimer lasers and this has increased the output from the FL3002 dye laser by up to 50%. The laser flash photolysis equipment was upgraded with a new Bentham monochromater, purchased for the facility by Dr A Beeby (Durham) from EPSRC grant funds, making data collection much simpler by enabling computer selection of the monitoring wavelength.

Throughout the year the nanosecond laboratories were scheduled for a total of 48 weeks. Although a serious laser failure on one of the excimer laser led to nearly 4 weeks of downtime a total of 10 journal publications (including 2 JACS papers) have resulted from work carried out during the period. One highlight is the study of pea seedling amine oxidase (Dr R. Bisby, Salford). TR^3 spectra indicate that the radical intermediate incorporates a substrate nitrogen atom and that the radical is strongly bound to a proton. This work has gone on to look at the intermediates in copper amine oxidase which catalyses the oxidation of amines to aldehydes. Staffing levels were increased with a new SO, Dr

Kevin Henbest, who joined the LSF in October, and is based in the ns laboratory. Dr Thierry Fournier, EU fellow, has continued to collaborate with visiting research groups.

[4]ULTRAFAST SPECTROSCOPY LABORATORY

The new laboratory is equipped with a widely tunable femtosecond source. The apparatus, based on optical parametric amplifiers (OPAs), provides two synchronised, independently tunable (480-730nm) 200fs laser pulses at a repetition rate of 40 kHz for pump/probe investigations such as time-resolved absorption and time resolved resonance Raman spectroscopies. The lasers arrived in May 1995 and the unique OPA systems were developed and assembled in-house within only three months. Complete details about the apparatus can be found in this section of the Annual Report.

Trial transient absorption and ps-TR^3 experiments took place between October and December 1995. Transient absorption capabilities were demonstrated using photochromic systems (Prof F Wilkinson) which required 395 nm sample excitation, and a white light continuum probe. Spectra were recorded at around 585 nm using the CCD camera/spectrograph detection system. For higher sensitivity photodiode system capable of operating at mutikilohertz repetition rate is now being developed. Picosecond TR^3 performance has been tested by investigating the electronically excited states of *p*-quaterphenyl and *trans*-stilbene. For the former compound the unique ability to independently tune the pump photon wavelength (quantum energy) while varying the probe wavelength has enabled the Raman excitation profile of the electronically excited, S_1' state of *p*-quarterphenyl to be obtained. This initial investigation forms the basis of the first two scheduled experiments in May 1996 to investigate the subtleties of early relaxation dynamics, IVR, structural changes, etc., of newly excited molecules in solution and will continue the success of the earlier work (York/RAL). A full description of the new OPA has been published, Optics Comm. **127** (1996) 307, and the work has been the attention of two short news articles in Laser Focus and Opto & Laser Europe.

[5]LASER MICROSCOPY LABORATORY

A wide-field fluorescence microscope capable of generating gated images with durations as short as 120 ps has been established in the first phase to develop a fluorescence microscope within the LSF. The apparatus has been used to map the intracellular fluorescence lifetime of a phthalocyanine sensitizer, currently undergoing clinical trials in Photodynamic Therapy (PDT), enabling determination of the intracellular distribution of the sensitizer. This work is to be extended as part of scheduled experiments in July 1996.

Work also commenced on fluorescence lifetime imaging experiments to determine the intracellular distribution of physiologically important ions, such as H^+ and Ca^{2+}. Suitable lifetime probes have been characterised *in vitro*, and will be incorporated into cells for *in vivo* measurements aiming to establish what pH changes occur during PDT.

Construction of the confocal hardware and electronics, representing the second phase of development of the microscope, has been completed, and the first steady-state fluorescence images were generated in November, and incorporation of the gated intensifier to enable time-resolved fluorescence imaging is expected to be accomplished by summer 1996. The feasibility of fluorescence microscopy utilising two-photon excitation of fluorophores absorbing in the UV was also demonstrated using the scanning optics developed for the confocal microscope. The use of two-photon excitation circumvents the need to use very expensive quartz objective lenses, and avoids cellular damage that would be inflicted by the use of direct UV excitation. The technique will also be of interest to chemists and material scientists wishing to perform UV excitation below the surface of UV absorbing materials. The versatile laser microscope will begin full scheduled operation from September 1996.

[6]LOAN POOL

This year there were a total of 79 months allocated for 7 laser systems, the lasers currently available in the Pool are listed below. The majority of the allocated time was used for research in gas phase spectroscopy and reaction dynamics using the nanosecond lasers. This included the work by Prof Simons (Oxford) who made structural assignments of the conformers of organic molecules in jet formed clusters using laser spectroscopy, Dr McKendrick (Edinburgh) made good progress in the study of reactions of oxygen atoms with hydrocarbons and in the inelastic electronic energy transfer of simple molecules and Dr Jones (Edinburgh) investigated the high resolution electronic spectroscopy biologically important molecules.

The titanium sapphire was used in the investigation of materials with potential in the Optoelectronics industries (Dr Maczmarek, ORC) and also in a feasibility study to generate nuclear spin polarised xenon (Prof Adams, MRC). The use of polarised Xenon and Helium *in vivo* promises to bring improvements in NMR imaging, in particular the lungs. The argon ion lasers were used by Dr Lees (UoCL) for C-H activation photochemistry, by Prof Walsh for the study of the reaction kinetics of germanium and tine containing transients and Prof Steen (Liverpool) to develop an imaging sensor for laser welding.

There has been considerable interest in the Community for a reliable source of narrow linewidth infrared radiation with nanosecond time resolution. Its main use would be in the state resolved vibrational excitation of molecules in gases and clusters. To access the infrared a Continuum dye laser system with difference frequency option was purchased, from the grant for the Loan Pool upgrade, and has been successfully installed in Birmingham University where Dr Sims and Prof Smith are using it to study reaction dynamics at ultra-low temperatures. This system was purchased in place of the Scanmate OPPO which unfortunately failed to meet specification and returned to Lambda-Physik. To further enhance the infrared capability of the Loan Pool the NSL3 system will be upgraded to have difference frequency generation as an option.

The Questek laser was no longer economically viable to run in the Loan Pool and was retired in October. The LSFP awarded this laser to Dr McKendrick (Edinburgh) where it will be used as a photolysis source for his studies in reaction and collision dynamics. A Lambda-Physik 205 fluoride optimised laser replaced the Questek and this is currently in use by Prof Ashfold (Bristol) for the study of diamond deposition and cutting.

Also, as part of the facility upgrade boxcar integrator equipment, pulse generators, power meters and monitor etalons have been purchased.

Table: Loan Pool Laser Systems

Laser System	Operating Parameters
NSL1 Quanta Ray GCR -11	1064nm/320mJ, 532nm/155mJ, 355nm/70mJ, 266nm/30mJ/10Hz
plus with PDL-3 dye laser	400-900nm/45mJ max/<0.08cm^{-1} bandwidth
NSL2 - Spectron SL805G	1064nm/1000mJ, 532nm/450mJ, 355nm/250mJ, 266nm/80mJ/10Hz
plus PDL-2 dye laser/WEX	260-900nm/50mJ/0.1cm^{-1} bandwidth
NSL3 - Spectron SL805G	1064nm/1000mJ, 532nm/450mJ, 355nm/250mJ, 266nm/80mJ/10Hz
plus PDL-2 dye laser/WEX	260-900nm/100mJ max/0.1cm^{-1} bandwidth
NSL4 - Continuum 8010 seeded Nd:YAG and ND6000 dye laser with IR option	220nm-4.5μm/100mJ max/<0.1 cm^{-1} bandwidth/10Hz
NSL5 - Lambda-Physik 205 Excimer laser	157nm/5mJ, 193nm/300mJ, 249nm/400mJ, 351nm/200mJ/50Hz
CWL1 - Spectra Physics 2025 Argon Ion	5W visible/0.4W UV single line
CWL2 - Spectra Physics titanium sapphire	680-1040nm/500mW max

DEVELOPMENT OF A LASER CONFOCAL FLUORESCENCE MICROSCOPE HAVING SUB-NANOSECOND TIME RESOLUTION

A.D. Scully[1,3], A.J. MacRobert[2], A.W. Parker[1] and D. Phillips[3]

[1]LSF, Rutherford Appleton Laboratory
[2]National Laser Medical Centre, UCL Medical School
[3]Department of Chemistry, Imperial College of Science, Technology and Medicine

INTRODUCTION

The confocal laser-scanning microscope (CLSM) has become a widely used tool in a number of research disciplines. The best known is probably biomedicine, but in addition, it is has found widespread use in the production environment, such as semiconductor and microelectronic device manufacturing. The main feature of the CLSM is that it provides relatively high resolution (≥0.1 μm) nondestructively, allowing specimens to be examined in their natural environment.

The most common configuration for the confocal fluorescence technique uses a point source of light focused to a diffraction-limited spot on the sample. The fluorescence from the sample is then detected through a spatial filter that isolates the detected area to that exactly coincident with the illuminating spot, as illustrated in Fig. 1.

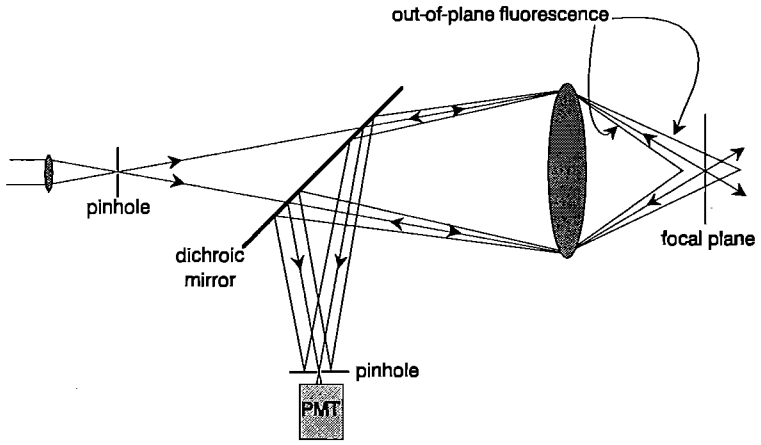

Fig. 1. Schematic diagram of point-scanned confocal microscope.

Fluorescence originating from focal planes other than that of the objective lens is rejected, resulting in a greatly reduced depth of field compared with conventional wide-field fluorescence microscopy. Either the sample or the excitation beam is scanned and a photodetector measures the intensity of the fluorescence originating from each point in the illuminated field enabling a high contrast image to be produced from only the in-focus fluorescence. A 3-D rendering of the fluorescing material may be constructed by combining the information obtained at mutiple focal planes.

The point-scanned confocal technique, however, has a number of deficiencies in practice. It is an inherently slow procedure to collect the information required to generate a fluorescence image. Image acquisition times for many commercially available confocal microscopes is of the order of seconds. This precludes examination of rapid intracellular phenomena taking place on the sub-second timescale. Perhaps more serious drawbacks are the deleterious effects of photobleaching and photosaturation of the sample. Photobleaching results from gradual destruction of the fluorophore upon exposure to the highly focused laser beam and ultimately results in a loss of fluorescence signal. Photosaturation arises when the rate at which fluorophores are excited exceeds the rate of decay back to their ground electronic state resulting in a depletion of fluorophores available for excitation. Photosaturation is a function of illumination intensity and, in some cases, can be overcome by attenuation of the excitation light.

One solution to these problems is to scan a focused line of excitation over the sample and to spatially filter the fluorescence signal using a slit. This modification enables 2-D steady-state fluorescence images from each focal plane to be acquired in real time and alleviates the problems of photobleaching and photosaturation associated with point-scan systems. The compromise for these improvements in performance is axial resolution, which, although significantly better than that obtainable using a conventional fluorescence microscope, is inferior to that of a point/pinhole-based CLSM.

FLUORESCENCE MICROSCOPE DESIGN

The design of the "direct-field" line-scanning CLSM developed in this work is based loosely on that described by Brakenhoff and co-workers [1] and its construction represents the final stage of the CLSM development in the Laser Microscopy Laboratory. The excitation source consists of a cavity dumped dye laser (Spectra Physics, model 3500) that is pumped synchronously by a mode-locked Nd^{3+}/YAG laser (Spectron, model SL901). The duration of the dye laser pulses is approximately 10 ps. The excitation wavelength range available is, typically, 580nm - 620 nm. A shematic diagram showing the layout of the confocal optics is presented in Fig. 2. The laser excitation beam is focused through a slit located at the line-generation plane (LGP) using a cylindrical lens (CL). A demagnified image of the slit is then relayed to the primary image plane (PIP) of the microscope (Olympus, IMT-2) which is projected into the object plane by the microscope objective (MO). The double-sided scanning mirror (SM), located in the pupil plane of the first beam-steering lens (BSL1), scans the line of excitation across the sample. The emitted line of fluorescence is collected by MO, descanned by SM and returns to the dichroic mirror (DM) following the same path as the excitation line. The fluorescence is reflected by DM towards the adjustable slit (AS) which is placed in a conjugate plane to LGP. The fluorescence eminating from the slit is then scanned using the other side of SM, in the pupil plane of the beam-steering lens (BSL2), projecting an image of the slit onto the 2-D detector.

The detector is comprised of an 18 mm diameter gated optical image intensifier (GOI) (Kentech Instruments, Didcot, U.K.) capable of gate durations ranging from ~120 ps to ~1 ns, and a

luminous gain of ~10^3 in a single-stage microchannel plate. The sync out signal from the dye laser cavity dumper module is amplified and used to trigger a low-jitter, digital pulse/delay generator (Kentech Instruments, Didcot, U.K.) which supplies an appropriate trigger signal to the GOI high voltage pulser unit. The phosphor output is coupled using either a f/0.85 camera lens (Fujinon, CF25L), or a tapered fibre-optic bundle, to the chip of an 8-bit scientific grade CCD camera (Cohu, 4910) capable of on-chip integration times of tens of seconds at room temperature. Camera control is performed using a commercial framegrabber package (Oxford Framestore Applications).

For steady-state fluorescence imaging, the GOI is operated in DC mode and the double-sided scanning mirror oscillates at 25 Hz, resulting in two scans of the field per video frame and yielding real-time fluorescence images on the video monitor. This facilitates the location of the sample region of interest for the fluorescence lifetime imaging (FLIM) measurements. Gated fluorescence images are obtained in an analogous manner, except that the GOI is operated in pulsed mode.

TWO-PHOTON FLUORESCENCE MICROSCOPY

The excitation path in the confocal optics described above can also be used for two-photon excitation of UV-absorbing fluorophores. Two-photon excitation arises when the photon density at the focal plane is sufficiently high that there exists a finite probability that two coincident visible photons can be absorbed by a UV-absorbing fluorophore. The inherent high spatial resolution of two-photon fluorescence microscopy derives from the quadratic dependence of two-photon absorption rate and fluorescence intensity on the incident laser intensity. When the laser beam is focused, this quadratic dependence results in fluorescence emission being highly localised to the immediate vicinity of the focal point, where the laser beam is most intense. Fluorescence intensity falls off rapidly in the lateral direction due to the focused laser beam profile, and also in the axial direction due to the high beam divergence on both sides of the focal plane. Two-photon fluorescence microscopy provides a unique means of probing fluorescence from intrinsic biological UV-absorbing fluorophores, such as the tryptophan residues associated with some proteins, without the need to use potentially harmful UV radiation. It also opens the way for monitoring polymer miscibility using currently available UV-absorbing fluorescent probes.

REFERENCES

1. G.J. Brakenhoff, K. Visscher, J. Microscopy, 171, 17 (1993).

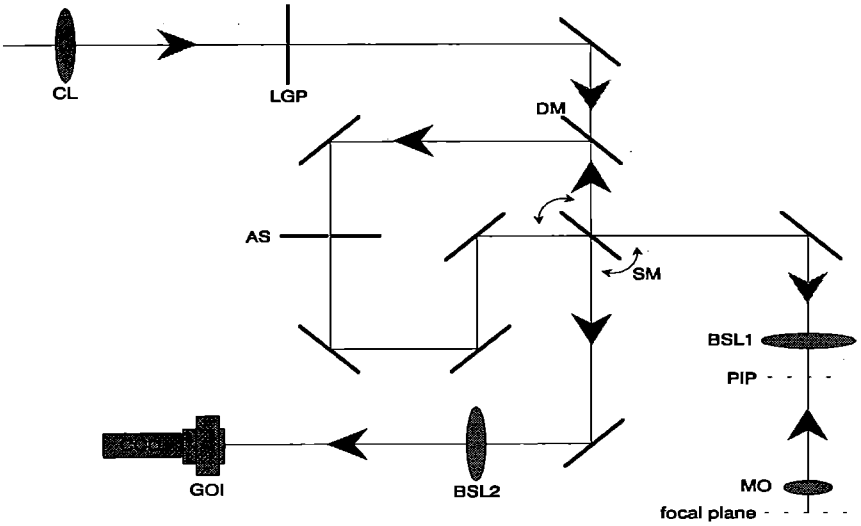

Figure 2. Schematic diagram of optical path for CLSM.

SOLID STATE OPO LASER TECHNOLOGY IN THE NANOSECOND LABORATORY

K Henbest, S M Tavender, M Towrie, A W Parker and W Twigger.

Rutherford Appleton Laboratory

INTRODUCTION

In early February the Nanosecond Science Laboratory was upgraded with new solid state laser technology. A Sunlite Extra™ OPO laser pumped by a Continuum YAG was installed. The laser has many attractive features. It produces nanosecond pulses that can be continuously tuned from 450-1680 nm. The need to use messy dyes which are time consuming to change is removed. The output energies are higher in comparison to existing excimer/dye systems. Fast changes between required wavelengths are possible and two ns TR^3 experiments using different probe wavelengths have recently been run in only twenty minutes. Defined wavelength regions can be scanned automatically at adjustable speeds and complex sequences of repeat scans programmed. The UV-LITE frequency doubling system extends the wavelength range to 225 nm using a series of BBO and KDP crystals. The energy output of the laser as a function of wavelength is shown in figure 1.

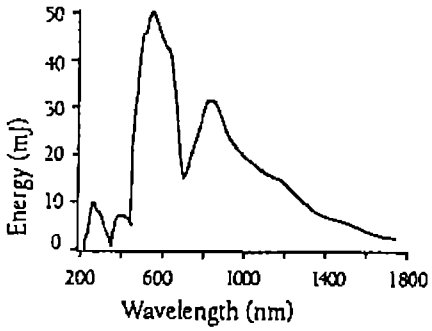

figure 1: Energy output of OPO laser

LASER SYSTEM

A schematic diagram of the sunlite optical layout is shown in figure 2. A seeded, frequency tripled Nd:YAG produces a single mode 355 nm pulse of radiation to pump the OPO. The OPO consists of three BBO crystals, the oscillator and two amplifiers which are rotated to maximise output. The first BBO crystal is incorporated in a sealed oscillator cavity and pumped with 80mJ of 355 nm light. The non-linear properties of the BBO produce two wavelengths of light, the 'signal' and the 'idler'[1]. By rotating a movable mirror set on a sine drive a range of wavelengths for both signal and idler can be generated. The output of the oscillator is then passed through two more BBO crystals in a single pass amplification system, pumped with 200mJ of 355 nm, to give the final output. Dichroic mirrors are used to separate the laser output which is made up of both the idler and signal wavelengths. The output energy is adjusted by rotating each individual BBO crystal using a computer controlled alignment system.

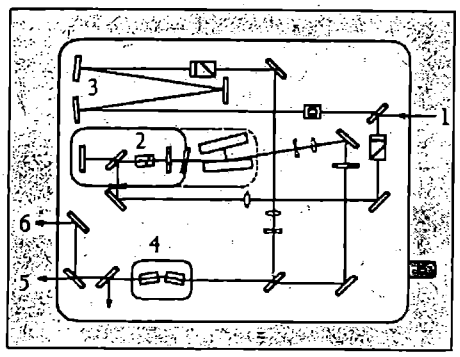

figure 2: Diagram of optical layout:

1. Pump input
2. ExtRA™ oscillator
3. Optical delay
4. Amplifier
5. Idler output
6. Signal output

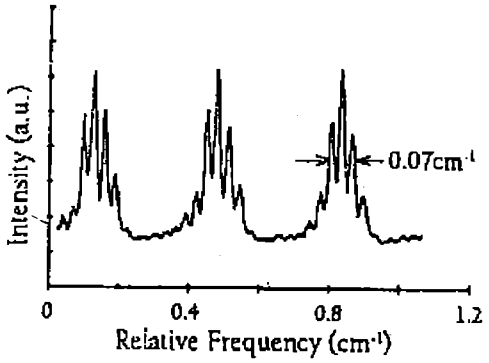

figure 3: sub 0.1cm^{-1} bandwidth-100 shot average of etalon fringes (FSR-0.33cm^{-1}).

To achieve the sub 0.1 cm^{-1} bandwidth the oscillator disperses the resonated signal wave in the extraordinary plane of the BBO crystal. The narrow acceptance angle in this plane reduces the bandwidth of the output by a factor of two over an ordinary resonance oscillator. The bandwidth is shown in figure 3.

The laser has produced high quality spectra for time resolved resonance Raman spectroscopy. Future scheduled experiments will include transient absorption and REMPI.

The specifications of the laser are given below

SUNLITE SPECIFICATIONS

FUNDAMENTAL	
Energy (at peak,mJ)	50
Repetition rate (Hz)	10
Tuning range (nm)	450-1680
Linewidth (cm^{-1})	0.1
Pulsewidth (nsec)	3-5
Jitter (nsec)	±1

UV-LITE	
Signal range (nm)	230-352
Frequency doubled	
Signal energy (at peak, mJ)	10
Idler range (nm)	358-460
Frequency doubled	
Idler energy (at peak, mJ)	5

REFERENCE

1 *Solid State Laser Engineering*, 3rd Edition, Walter Koechner, ed., Spring Verlag, Berlin, 1992.

DOUBLY TUNABLE FEMTOSECOND SOURCE

P.Matousek[1], A.W.Parker[1], M.Scully[1], P.F.Taday[1], W.T.Toner[2], M.Towrie[1]

[1]Rutherford Appleton Laboratory
[2]Clarendon Laboratory, University of Oxford

INTRODUCTION

Many time-resolved spectroscopy techniques require two broadly and independently tunable synchronised light pulses to excite and probe short-lived intermediates. In this report we report on the design of a multikilohertz repetition rate system capable of providing the above specification and tunable from the ultraviolet to the visible part of the spectrum for time-resolved absorption and resonance Raman spectroscopies. More details can be found in our recent publication on the apparatus[1].

Whilst conventional dye laser technology is able to meet the above criteria it tends to be restricted by a relatively narrow tuning range and the synchronisation of independent laser oscillators on femtosecond time-scales presents difficulties. However, optical parametric oscillators (OPOs) and optical parametric amplifiers (OPAs) pumped by high repetition rate titanium sapphire based ultra-fast lasers hold considerable promise and Laenen and Laubereau[2] have recently demonstrated the generation of two independent short pulses tunable in the infra-red using two synchronously pumped OPOs. Travelling wave optical parametric amplifiers[3-6] offer impressive pulse energy and wide tunability while avoiding the problems associated with maintaining resonance cavity length in optical parametric oscillators. We have developed a 40 kHz system using a single white light continuum (WLC) source to seed two OPAs pumped at 400 nm. The design of the seeded OPAs is based on that of Reed et al.[6] who pumped a single seeded OPA, but a somewhat higher energy regenerative amplifier operating at a lower repetition rate enables two independently tunable OPAs to be pumped.

DESCRIPTION OF THE SYSTEM

A block diagram of the system is shown in Fig. 1. An output pulse (130 fs, 800 nm) from a femtosecond Ti:Sapphire laser (Tsunami, Spectra Physics) is amplified up to 17 μJ in a Ti:Sapphire regenerative amplifier (Spitfire, Spectra Physics/Positive Light) pumped by a Q-switched intracavity frequency doubled Nd:YLF laser (Merlin, Spectra Physics/Positive Light) at 40 kHz repetition

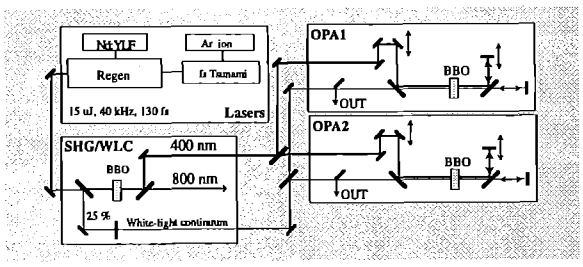

Figure 1 A block diagram of the parametric amplifier system.

rate. The oscillator and regenerative amplifier are tunable over the range 770 to 850 nm with over 10 μJ/pulse output. Single-filament white-light continuum is generated by *c.* 1.5 μJ, 800 nm pulses focused into a 3 mm thick sapphire crystal. To seed the OPAs the WLC beam is split in two using a 50 % broadband beamsplitter. The remaining light at the fundamental frequency is frequency doubled in a 1 mm thick type I BBO crystal cut at 29°. Each pump beam, is suitably delayed and focused into the 2-pass OPAs consisting of type I BBO crystals cut at 29°.

SINGLE OPA OPERATION

A typical tuning curve for a single OPA pumped with 2 μJ at 400 nm is shown in figure 2. The energy is *c.* 200 nJ per pulse over the range 510 to 720 nm representing pump to signal conversion efficiency of 10 %. The bandwidth over the range up to 600 nm averaged 165 cm^{-1}. When 10 nm bandwidth filters were introduced, operation was possible up to 780 nm with a bandwidth of c. 200 cm^{-1}, at the cost of reducing the output energy in the 630 to 780 nm wavelength range to *c.* 100 nJ per pulse. Energies in excess of 20 nJ were obtained out to 1700 nm. When the OPA was pumped at 3 μJ pulse energy a signal pulse energy of 280 nJ at 533 nm was obtained.

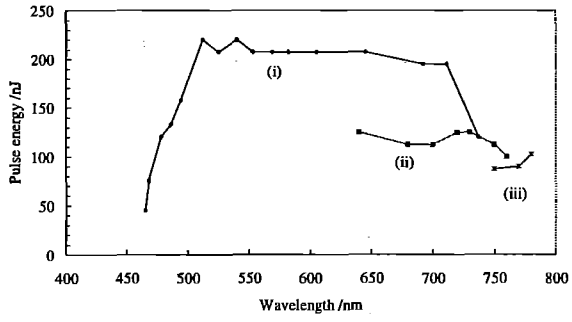

Figure 2 Tuning curves of the single OPA pumped at 400 nm with 2 μJ. The curves marked (i) were obtained without using interference filters to control the OPA bandwidth. The (ii) curves were obtained with 10 nm bandpass interference filters inserted after the WLC source. The curves (iii) were also obtained with interference filters but in a modified configuration where signal was picked off earlier on the return path before hitting the dichroic mirror.

The uncompressed OPA output was chirped with a typical autocorrelation width of 400 - 500 fs (FWHM). A double-pass prism pulse compressor enabled the autocorrelation width to be reduced to as little as 90 ± 15 fs at 590 nm corresponding to 64 ± 10 fs pulse width assuming a Gaussian profile. The bandwidth was 240 cm^{-1}, i.e. close to the transform limit (see Fig. 3).

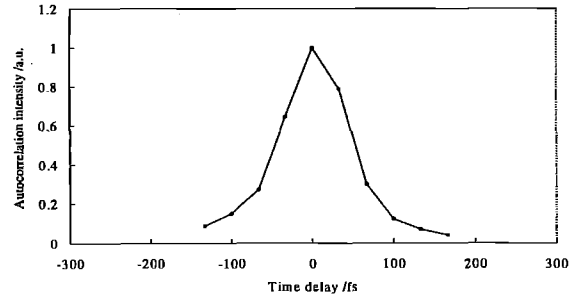

Figure 3 Normalised autocorrelation function of the compressed output pulses from the OPA1 at 590 nm. Fitting to Gaussian yielded an autocorrelation width of 90 fs (FWHM).

To extend the tuning range into the UV the OPA signal output was mixed with the 800 nm beam remaining after frequency doubling. Pulse energies of 25 nJ were obtained at 329 and 349

nm with an energy conversion efficiency of 30 % relative to the signal pulse energy at the input to the frequency mixing crystal. Typical energy conversion for frequency doubling of the uncompressed OPA output was around 10 %.

DOUBLE OPA OPERATION

When two OPAs were each pumped with 1 μJ at 400 nm, independently tunable signal pulses were available at pulse energies of 40 - 75 nJ over a 480 - 730 nm spectral range (see Fig 4) with a bandwidth of 205 ± 85 cm^{-1}. Above 600 nm, the bandwidth was kept below 250 cm^{-1} using 10 nm bandwidth interference filters inserted after the WLC collimating lens.

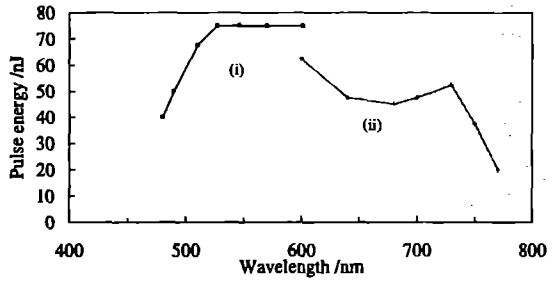

Figure 4 Tuning curves of the two OPA layout pumped at 400 nm with 1 μJ. The (i) curves were obtained without using interference filters to control the OPA bandwidth. The (ii) curves were obtained with 10 nm bandpass filters inserted after the WLC source.

The cross correlation widths between the uncompressed OPA outputs were measured to be between 540 - 610 fs (FWHM). Prism pulse compression of the OPA outputs reduced the cross correlation to 150 ± 10 fs (FWHM) for the combination of 595 and 600 nm (see Fig. 5) of partially compressed pulses. The autocorrelation FWHM for these outputs were 160 ± 20 fs and 130 ± 40 fs respectively.

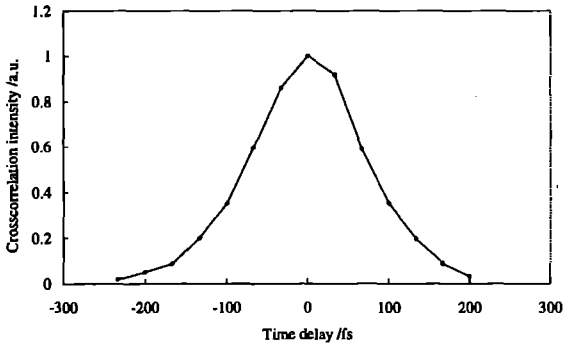

Figure 5 Normalised crosscorrelation function of the two OPAs with a width of 150 fs (FWHM) for compressed pulses.

PICOSECOND TR³ SPECTROSCOPY

The system has been used in the picosecond time-resolved resonance Raman study of p-quaterphenyl. Independent tunability allowed the measurement of Raman excitation profiles of the electronically excited molecule, as demonstrated in Figure 6. The spectra of p-quaterphenyl were obtained at fixed pump wavelength (277 nm, THG) and different probe wavelengths (OPA) at the time delay of 50 ps. More details and the analysis of the results can be found in the Chemistry section.

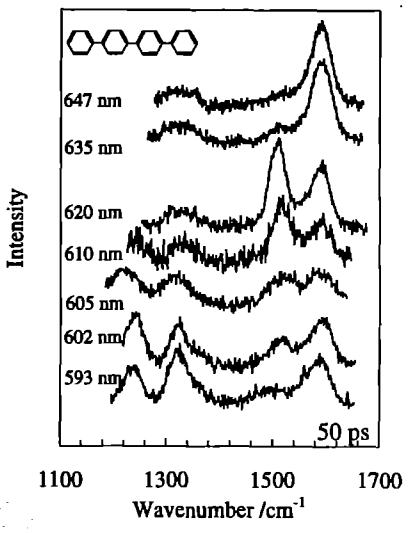

Figure 6 ps-TR³ spectra of S_1 p-quaterphenyl at the time-delay 50 ps obtained at different probe wavelengths. The pump wavelength was fixed 277 nm.

FEMTOSECOND TRANSIENT ABSORPTION SPECTROSCOPY

To test the suitability of the system for time-resolved transient absorption spectroscopy we have used the laser dye DDTTCI. Figure 7 shows the time resolved transient spectra following excitation into the S_1 state of the molecule. The pump wavelength was 800 nm and was probed with the white light continuum.

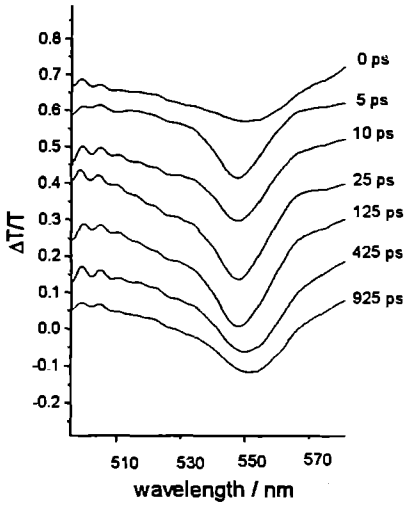

Figure 7 Transient absorption spectra of DDTTCI. The spectra are offset for clarity.

Following previous studies[7] of the naphthoxazine-spiro-indolines we have used the OPA to probe the formation of the B-form of this class of molecule. Figure 8 shows the rise of the B-form in 1-butanol, following excitation at 395 nm. The probe wavelength was 585 nm.

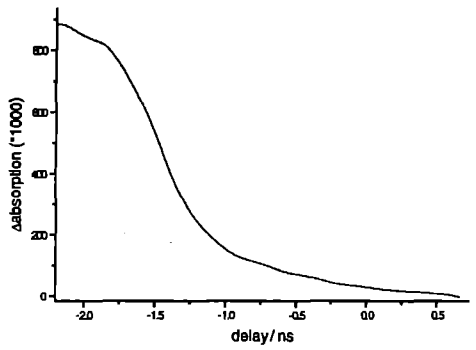

Figure 8 Rise of the B form of a photochromatic material, following excitation at 395 nm. Data was obtained by probing at 585 nm.

CONCLUSIONS

A system, based on optical parametric amplifiers, generating doubly tunable femtosecond synchronised pulses has been built and its basic characteristics measured. The OPAs each generate 40 - 75 nJ over a 480 - 730 nm spectral range with bandwidth 205 ± 85 cm^{-1}. Pulse compression showed that the outputs of the two OPAs are well synchronised to within 150 fs at 595 and 600 nm. When only one OPA is pumped, the conversion efficiency of pump to signal saturates at *c.* 10 %, giving up to 280 nJ at 533 nm for 3 μJ pump energy.

The system has been used in picosecond time-resolved resonance Raman and femtosecond absorption experiments.

ACKNOWLEDGEMENT

This development has been supported by an EPSRC grant (GR/J76392) with partial BBSRC funds.

REFERENCES

1. P.Matousek, A.W.Parker, P.F.Taday, W.T.Toner, M.Towrie, Two Independently Tunable Femtosecond Pulses Generated in the Visible at the Repetition rate 40 kHz using Optical Parametric Amplifiers, Optics Comm., in press.
2. R.Laenen, A.Laubereau, SPIE 2379 (1995) 202.
3. G.P.Banfi, C.Solcia, P.Di Trapani, R.Danielius, A.Piskarskas, R.Righini, R.Torre, Optics Comm. 118 (1995) 353.
4. R.Danielius, A.Piskarskas, A.Stabinis, G.P.Banfi, P.Di Trapani, R.Righini, J.Opt.Soc.Am. B 10 (1993) 2222.
5. U.Emmerichs, H.J.Bakker, H.Kurz, Optics Comm. 111 (1994) 497.
6. M.K.Reed, M.K.Steiner-Shepard, D.K.Negus, IEEE J. Quantum Electron. 31 (1995) 1614.
7. F. Wilkinson, D.R.Worrall, J.Hobley, L.Jansen, S.L.Williams, A.J.Langley, P.Matousek, J.Chem.Soc., Faraday Trans. 92 (1996) 1331.